UNIVERSITY OF NOTTINGHAM

SCHOOL OF CIVIL ENGINEERING

Quasi-Static Characterisation of Asphalt Mixtures

by

Stuart Thomas Dunhill

Thesis submitted to the University of Nottingham
for the degree of Doctor of Philosophy

September 2002

to my parents

Table of Contents

page

page

page

Abstract

A modern road pavement is a highly complex structure. Paving materials can exhibit non-linear and time dependent material properties whilst subjected to complicated three-dimensional loading conditions that are functions of the specific construction of each pavement. Nevertheless, empirical or linear elastic techniques, which cannot fully describe such factors, are often used in road engineering to assess pavement deterioration. An alternative approach is the use of finite element techniques, incorporating more complex constitutive models, to describe the response of asphalts and other paving materials.

This thesis is concerned with the experimental determination of the model parameters necessary for the characterisation of two UK asphalt mixtures, for use in a dynamic plasticity based constitutive model to simulate paving material response. The constitutive model is under development at Delft University of Technology in the Netherlands, where it will be implemented in a three-dimensional finite element code. The thesis describes the constitutive framework for the material response model. It also details the experimental work and numerical verification undertaken in the study to enable the determination of the basic model parameters required to describe a 10 mm dense bitumen macadam and 30/10 hot rolled asphalt mixture, for use in the constitutive model.

The characterisation of the mixtures has been undertaken through a series of quasi-static uniaxial compression and tension tests, which due to the significant influence of strain rate and temperature on the response of the asphaltic materials, were undertaken over a range of displacement rates and temperatures.

Through specification of key model parameters as functions of material strength, temperature and strain rate, and the development of relationships describing the hardening and softening characteristic of the mixtures, the constitutive model has been successfully utilised to simulate the temperature and rate dependent stress-strain response of the asphalt mixtures to compressive loads.

Acknowledgements

I would like to thank all those who have contributed to this research in some way either through providing assistance, advice, encouragement or funding.

I would like to particularly thank the following persons and organisations:

- Dr Gordon Airey, my supervisor, for his guidance, advice, support and friendship throughout my studies. Thanks also go to Dr Andrew Collop and Professor Stephen Brown for giving their time and assistance to this project.

- The Nottingham Asphalt Research Consortium, the Institution of Highways and Transportation and the Worshipful Company of Paviors for their financial support.

- The members of the Section of Structural Mechanics at Delft University of Technology, especially Tom Scarpas for extending his time, enthusiasm and support, to Cor Kasbergen, Xueyan Liu and Sandra Erkens for their assistance and for making my time at Delft both informative and enjoyable.

- My colleagues in the Pavement and Geotechnics Research Division at the University of Nottingham, especially Barry Brodrick for his advice regarding the experimental work and to Mick, Aaron and Lawrence for their work in the bitumen laboratory. Thanks must also go to all the members of the P&G tea club, particularly Annette, Bezhard, Jackie, Mike, Nick and Tony with whom I have had many enjoyable, although largely irrelevant discussions, over a distracting game of bridge.

- Finally I would like to thank my parents, for their continued support, understanding and constant encouragement.

Declaration

The work described in this thesis was conducted at the University of Nottingham, School of Civil Engineering between October 1998 and September 2001. I declare that the work is my own and has not been submitted for a degree of another university.

Chapter 1 - Introduction

1.1 Background

For pavement design purposes, extensive use has been made of linear elastic theory applied to layered systems [Shell International Petroleum, 1978; Brown *et al.*, 1986]. However, such approaches, many of which are routinely used in road engineering to assess pavement deterioration, ultimately do not fully describe the complex behaviour of asphaltic materials, and generally involve simplifications of the pavement structure. Whilst satisfactory results may be obtained for pavements of relatively thick asphalt construction, provided the stiffness of the asphalt layer is accurately specified, linear elastic analysis is inappropriate for pavements of thinner asphalt construction, where the non-linear characteristics of the pavement are more prominent [Brown, 1997]. Typically, thin or low volume pavements account for much of the lightly trafficked road network, a sector that represents approximately 95% of pavements in the UK [British Road Federation, 1999]. The application of inappropriate analysis tools for this category of a road has resulted in the use of uneconomic standards, in a sector where funds are particularly restricted [Dunhill *et al.*, 2000]. Therefore, if improved design standards are to be developed, then alternative analysis and evaluation methods, that can fully describe the behaviour of asphaltic and other paving materials are required.

The use of constitutive modelling is well established in many fields of engineering such as soil or rock mechanics, concrete technology, and structures. Asphaltic materials represent a difficult medium for the engineer to model due to their complex physical structure and correspondingly complex behaviour. It is well documented that asphaltic materials are both loading rate and temperature dependent and exhibit elastic, viscous and plastic behaviour. Traditionally the numerically intensive computer simulations required to model such complex material behaviour have been prohibitive in terms of computation processing time and storage space required to generate a solution to the problem. However the continuing increases in computing power and advances in numerical procedures now facilitate the implementation of complex constitutive models into incremental numerical techniques such as finite

element (FE) methods. To apply this approach to pavement structures, a constitutive model capable of describing the elastic and inelastic strain rate, temperature and stress dependent nature of asphaltic materials is required. The development of such constitutive models for asphalts and other paving materials, once implemented in FE codes, will provide versatile tools to facilitate the analysis and study of pavement response, performance and damage modes, such as rutting and cracking.

1.2 Research Philosophy and Objectives

In the recent past a three-dimensional, strain rate sensitive, history and temperature dependent constitutive model for asphaltic and other paving materials was developed at Delft University of Technology [Scarpas *et al.*, 1997 and 1998a]. The model, in a prototype formulation, has been implemented in a three-dimensional FE code and used to simulate damage response in Dutch pavement structures. A prerequisite to enable this model to be used for the investigation of the mechanisms that lead to damage modes within UK pavements, is the availability of model parameters describing realistic UK asphalt mixtures. This therefore defines the objective of this thesis, which is the experimental determination and numerical verification of the model material parameters necessary for the characterisation of UK asphalt design mixtures for use in the constitutive model described above.

An important stage in the development of any theoretical constitutive model is the availability of experimental data for the determination, calibration and verification of the model and the material parameters. Thus, a key element in the development of the constitutive model has been the development of appropriate material characterisation tests to determine the necessary model input parameters [Erkens *et al.*, 1998 and 2000a]. A three-dimensional response model should be based on the generalisations of numerous stress states. However, the response of asphalt mixtures is state of stress dependent, therefore to evaluate a one-to-one relationship between a state of stress and the corresponding response, the state of stress in any representative laboratory test must be uniform. This excludes many standard pavement engineering tests, such as the indirect tensile fatigue test, where a non-uniform stress state exists. Thus, in this study, characterisation is undertaken using data from quasi-static uniaxial laboratory

experiments, carried out at a range of displacement rates and temperatures. Two asphalt mixtures were chosen for full characterisation. These were a continuously graded 10 mm dense bitumen macadam [British Standards Institution, 1993] and a gap graded type F 30/10 hot rolled asphalt [British Standards Institution, 1985], selected to represent the two generic types of asphalt mixtures traditionally utilised in the construction of UK lightly trafficked pavements.

1.3 Scope of Research

The scope of this thesis consists of a literature review followed by four chapters, each detailing one aspect of the work undertaken, and a final chapter in which the main conclusions and recommendations for future research are presented. The literature review serves as an introduction to both pavement engineering and constitutive modelling, providing the reader with the necessary background knowledge appropriate to this study. Chapter 3 presents the framework for the dynamic plasticity based constitutive model that is used in this study. The model material parameters are discussed and their physical relationships described. The experimental work and data analysis necessary for the determination of the model material parameters based on loading rate and temperature controlled uniaxial laboratory tests are identified. This chapter also contains a review of previous research relating to the investigation of asphaltic material properties using monotonic (quasi-static) laboratory tests. In Chapter 4 details of the experimental work undertaken in this study are given. The development of the experimental apparatus and test methodology for the uniaxial compression test, based on the work undertaken by Erkens *et al.* [1998], is presented. The development of the experimental apparatus and test methodology for the uniaxial tension test is presented and details regarding mixture selection, specimen development, manufacture and densities are discussed. In Chapter 5 the experimental programme and test results are presented and discussed. The test data is used to evaluate the elasticity model parameters, Young's modulus and Poisson's ratio, and the parameters for a general, temperature and strain rate dependant relationship, used to describe the compressive and tensile strengths of the mixtures are determined. Chapter 6 presents the determination of the model material parameters based on the results of the uniaxial compression and tension tests. In this chapter the expressions

used to describe the hardening and softening responses of the mixtures are presented and the material parameters for these relationships are derived as a function of both plastic work and equivalent plastic strain. The functions are then used to assess the characteristics of the model flow surfaces. Finally, numerical simulations of the compression tests are performed in order to verify the capabilities of the model using the experimentally determined model material parameters.

Chapter 2 - Literature Review

2.1 Introduction

The main aim of this chapter is to provide the reader with the relevant background knowledge applicable to this particular study. This has resulted in the literature review being divided into three main sections. The first section 'Pavement Engineering' covers areas such as fundamental asphaltic material properties, pavement loading, failure mechanisms and design methodologies. The second section 'Constitutive Relationships' serves as an introduction to the basic principles of constitutive modelling, focussing on plasticity theory. The final section 'Plasticity Based Models for Asphalt Mixtures' details three examples of plasticity based constitutive models and their application to modelling asphalt mixture response. Each of the above sections is introduced in this chapter as a necessary precursor to Chapter 3, in which the asphalt concrete response model used in this research is presented.

2.2 Pavement Engineering

2.2.1 Background

The purpose of a road pavement is to support the loads induced by traffic and to distribute these loads safely to the underlying soil (subgrade). Ultimately, the aim is to ensure that the transmitted stresses are sufficiently reduced so that they do not exceed the supporting capacity of the subgrade. Typically, a modern pavement consists of a number a discrete layers, selected for their engineering, structural and material properties, which when processed and compacted form a pavement structure. There are a number of different pavement structural types, but the two main types are the flexible (bituminous) and rigid (concrete) pavements. Recent statistics show that flexible pavement design accounts for 85% of road construction in the UK compared with only 10 % for rigid pavement design [Amadeus, 2000]. As the main structural component and the substantive constituent of flexible pavement design is generally the bituminous layers, this project is primarily concerned with modelling bituminous material response and issues regarding rigid pavements are not discussed further.

2.2.2 A Brief History of Flexible Pavement Construction

The Romans were the first pioneers in the art of road construction. By the fall of their Empire in the 5th Century AD, a road network, comprising some 90,000 km of trunk and 300,000 km of secondary roads, extended from Rome across Europe and into most of the known world [Sprague de Camp, 1963]. Although a Roman road would appear simplistic if compared to a modern highway, they were essentially well constructed and long lasting.

The fall of the Roman Empire put a halt to road construction in Europe for much of the first millennium AD. Local people had little use for the roads and without maintenance they slipped into disrepair. It was not until the 18th Century that roads of good construction, which were based on solid methodologies, would again become common place. Two such constructions were the roads developed by Thomas Telford (1757-1834) and John Loudon McAdam (1756-1836) [Read, 1996]. These two engineers independently recognised the need for good drainage, compacted layer construction and an impervious road surface. Telford's construction placed emphasis on providing a strong foundation, using large stones and thick layers with little regard given to construction costs. McAdam favoured a thinner construction of smaller angular materials watered to assist granular interlock, relying on the native soil for strength [Croney *et al.*, 1998]. These two designs dominated road construction for this period and indeed the macadam grading described in Section 2.2.4 is still based on McAdam's early work.

Bituminous materials (asphalts) were first used in road construction in the middle of the 19th Century where attempts were made to utilise rock asphalt from European deposits for road surfacings. In 1853 the first natural asphalts were used as a surfacing in Paris, when the Rue Begere was surfaced with asphalt from the Val de Travers region [Earle, 1974]. From this point there was a slow development of the use of natural products for surfacings, leading to the advent of coal tar, which was sprayed on the unbound macadam roads to overcome the problem of dust generated from early motorised traffic. This was followed later by the use of bituminous binders manufactured from crude oil [Airey, 1997].

During this period of development, asphalt surfacings were assumed to contribute

little to the overall strength of the pavement. The structural strength was provided primarily by the base, which was generally a concrete layer [Earle, 1974]. The Second World War, however, saw a shortage of cement for use in road construction as this material was needed for building works. This cement shortage led to the use of bituminous materials in full depth pavement construction; particularly paved airfields. It is from this period that the first concepts of modern flexible pavement design originate.

2.2.3 UK Flexible Pavement Construction

Figure 2.1 shows a generalised representation of a modern day UK flexible pavement.

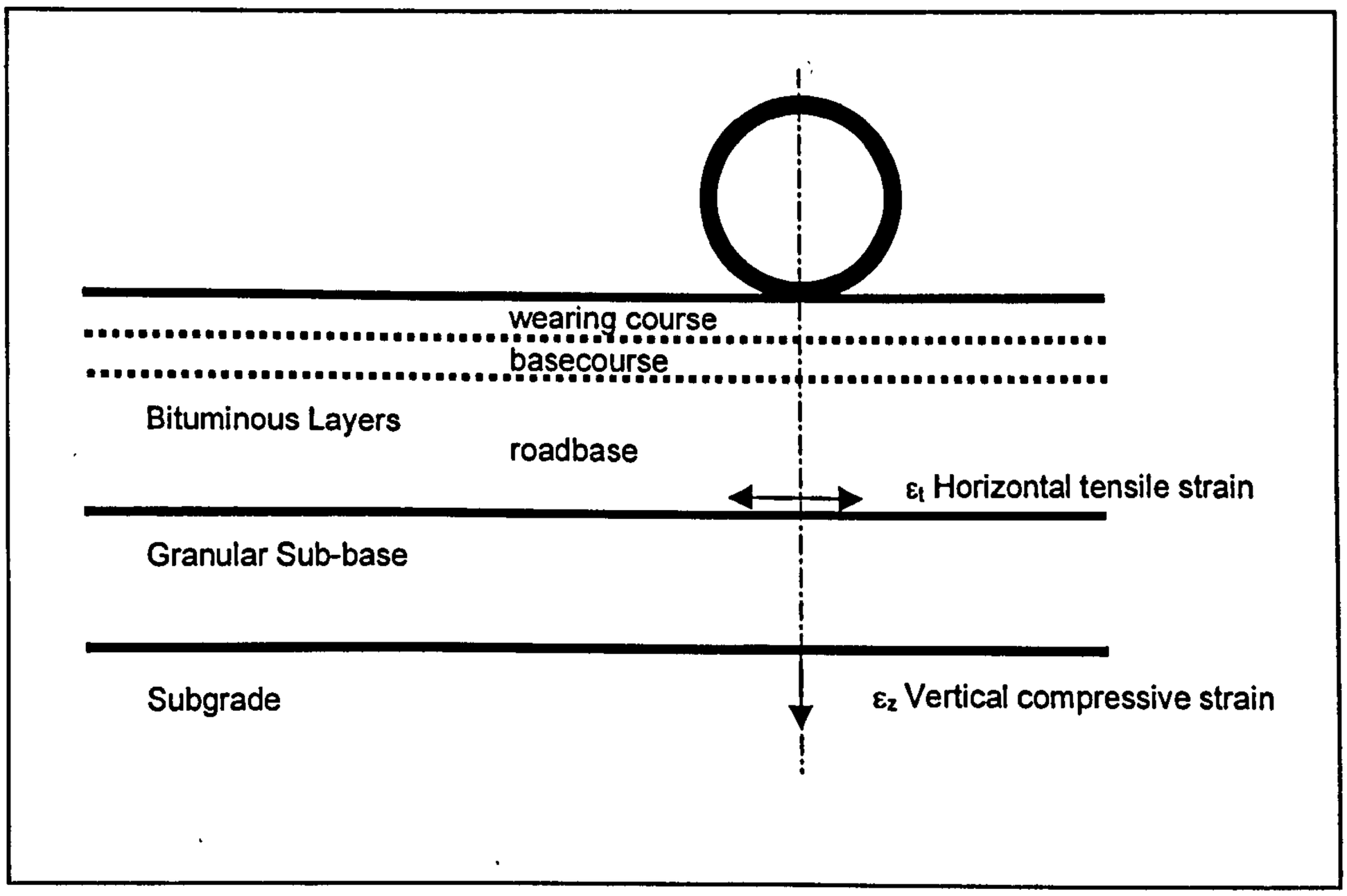

Figure 2.1: Typical UK flexible bituminous pavement

The pavement is composed of two main layer types; the bituminous layers, comprising the wearing course, basecourse and roadbase and the sub-base layer. Each layer of the pavement contributes to the overall performance of the road structure. The wearing course layer, which provides a running surface for the traffic, should be abrasion resistant and provide a safe level of skid resistance. The basecourse helps to distribute the traffic loads and provides a smooth surface on which to construct the

relatively thin wearing course. The roadbase is the main structural load-bearing layer within the pavement and is generally constructed of bituminous materials, although in some lightly trafficked situations a granular roadbase layer is possible [Dunhill, 1999]. The thickness of the roadbase layer is traditionally a function of the cumulative traffic loading to which the pavement is subjected, and the material properties of that layer. The function of the sub-base is to provide a uniform surface on which to construct the roadbase and surfacing layers, and to act as a haul road for site traffic during construction. The sub-base may also act as a drainage layer and is usually constructed of granular material [Department of Transport, 1994].

In view of the inconstancies in the UK, European and North American descriptions for bituminous materials, it should be noted that using the new European Committee for Standardisation (CEN) terminology, the aforementioned layers of a bituminous pavement should now be referred to as surface course, binder course and base course respectively [Read, 1998]. Figure 2.2 shows the new CEN terminology, which is used interchangeably, with traditional UK terminology throughout the reminder of this thesis.

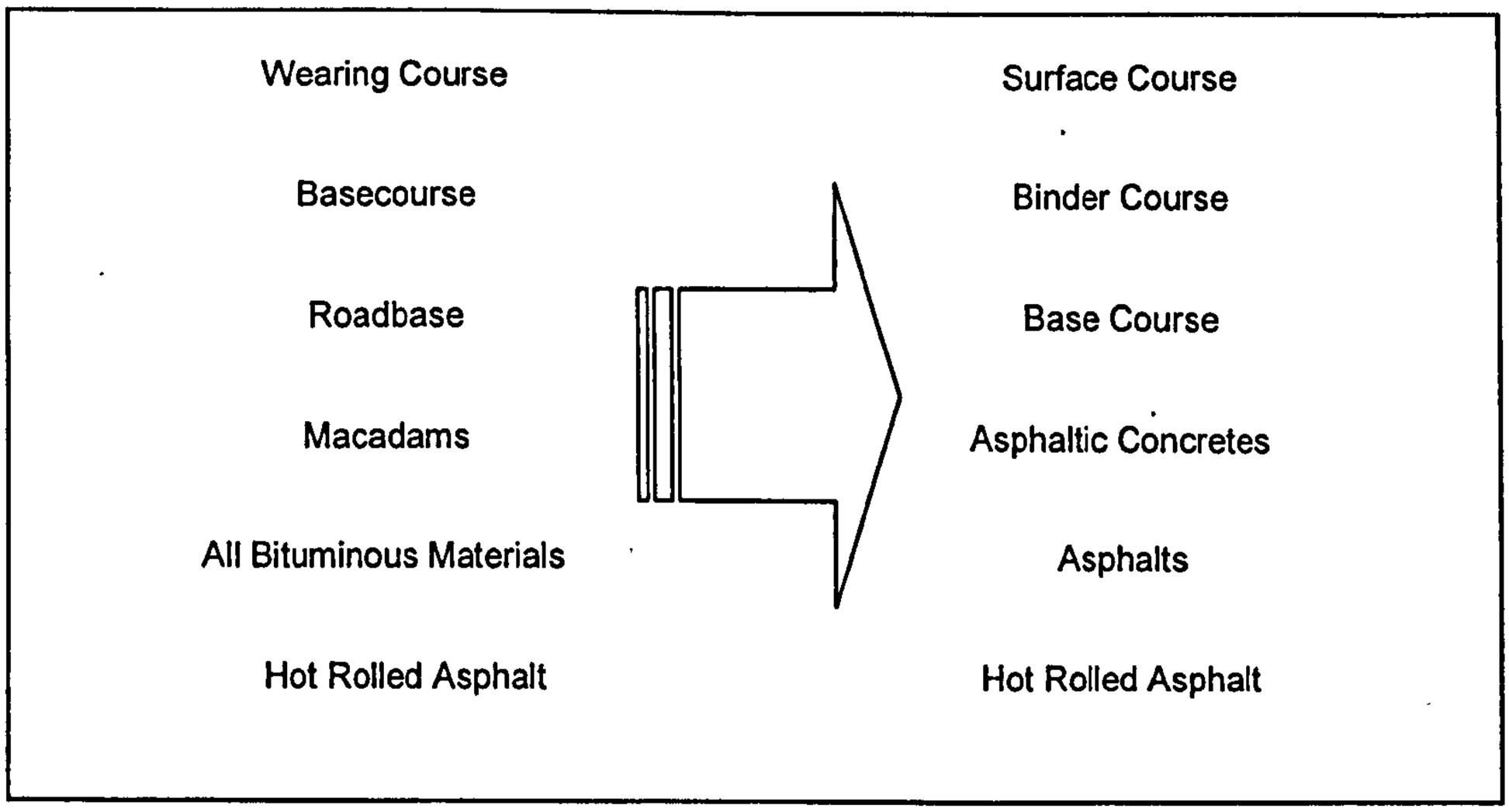

Figure 2.2: CEN terminology for paving materials

2.2.4 Asphalt Mixtures

Asphalt mixtures are a combination of mineral aggregates, filler, air and bitumen or bitumen based binder which are bound in a matrix. The range of possible compositions for an asphalt mixture is infinite, however the two types of mixtures traditionally used in the greater part of UK road construction are macadams (now referred to as asphaltic concretes, Figure 2.2) and rolled asphalts. The noticeable difference between the two classifications is the quantity and particle size distribution of the coarse aggregate. Macadams (asphaltic concretes) are generally made up of approximately equal amounts of each individual aggregate stone size, and are referred to as being continuously graded. Asphalts generally consist of a large proportion of fine aggregate and bitumen matrix, with differing amounts of single-sized coarse aggregate distributed throughout the mixture. This results in mixtures with very little intermediate sized material, commonly referred to as gap-graded. Figure 2.3 shows typical examples of the aggregate grading curves for both classifications.

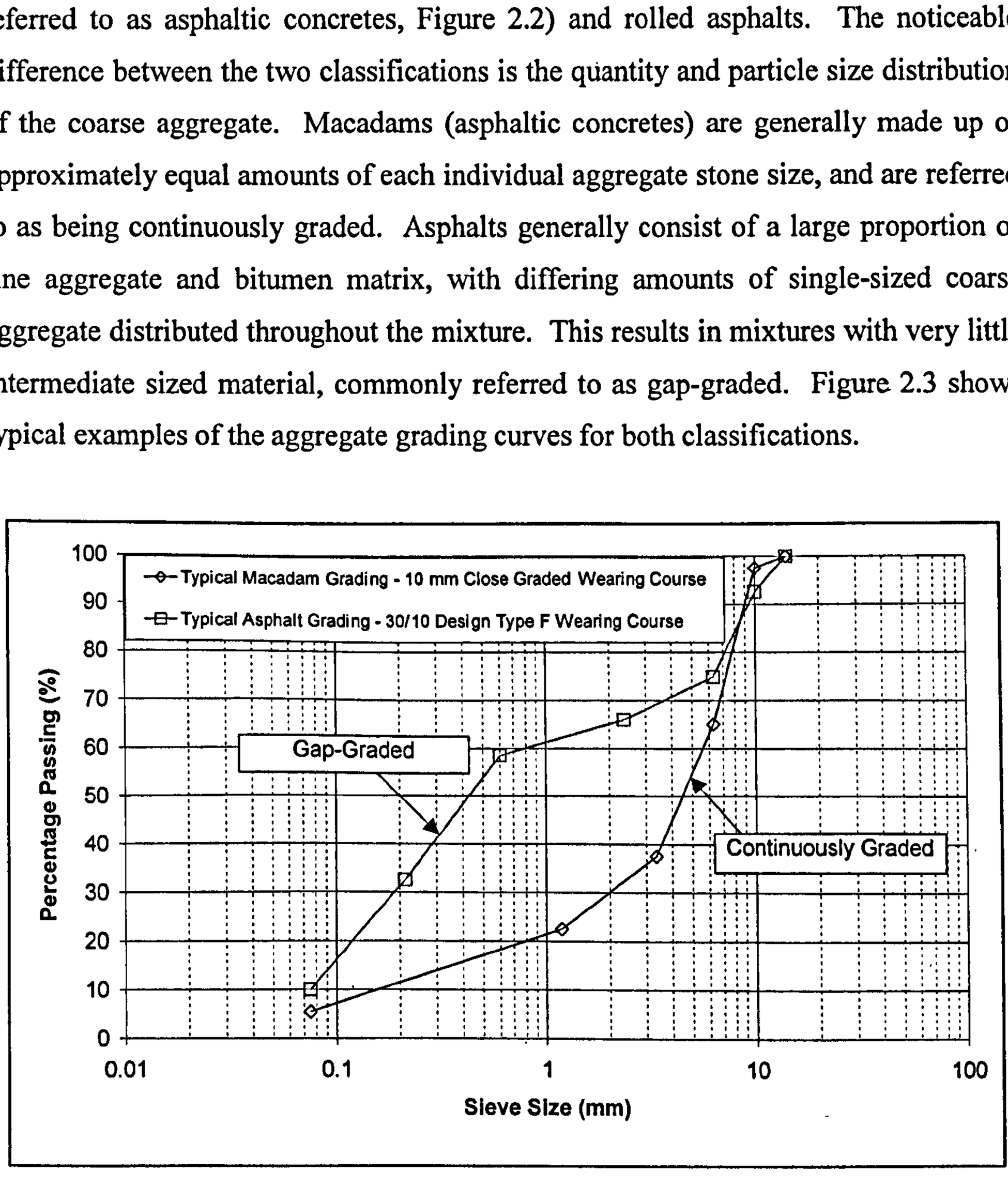

Figure 2.3: Aggregate grading curves for typical macadam and asphalt mixtures [British Standards Institution, 1992; 1993]

The composition of macadams is specified in BS 4987: Part 1 [British Standards Institution, 1993]. There are many types of macadam, but the type most commonly

used on UK lightly trafficked roads is dense bitumen macadam (DBM) [Dunhill, 1999]. The composition of asphalts is specified in BS 594: Part 1 [British Standards Institution, 1992]. Traditionally hot rolled asphalt (HRA) is the most commonly used asphalt on UK lightly trafficked roads [Dunhill, 1999]. Figures 2.4 and 2.5 show idealised cross sections through a continuously graded macadam and a gap-graded asphalt mixture respectively. It can be seen from Figure 2.4 that in the macadam mixture there is stone to stone contact between the coarse aggregate particles, forming a continuous framework throughout the mixture, referred to as the aggregate skeleton. It is this aggregate skeleton that provides the main mechanism for the material's resistance to permanent deformation and its load transmitting ability. Asphalts on the other hand, Figure 2.5, display little or no contact between coarse aggregate particles and therefore rely on the fine aggregate/sand/filler/bitumen mortar to resist deformation and transmit loads. The mortar must therefore have a high stiffness, which is usually achieved by using a relatively hard bitumen binder and a high filler content. As asphalts have a greater quantity of fine material than macadams, and therefore a larger total surface area, there is an increased demand for binder. As the bitumen binder is the most expensive constituent of asphalt mixtures, asphalts cost more to produce than macadams.

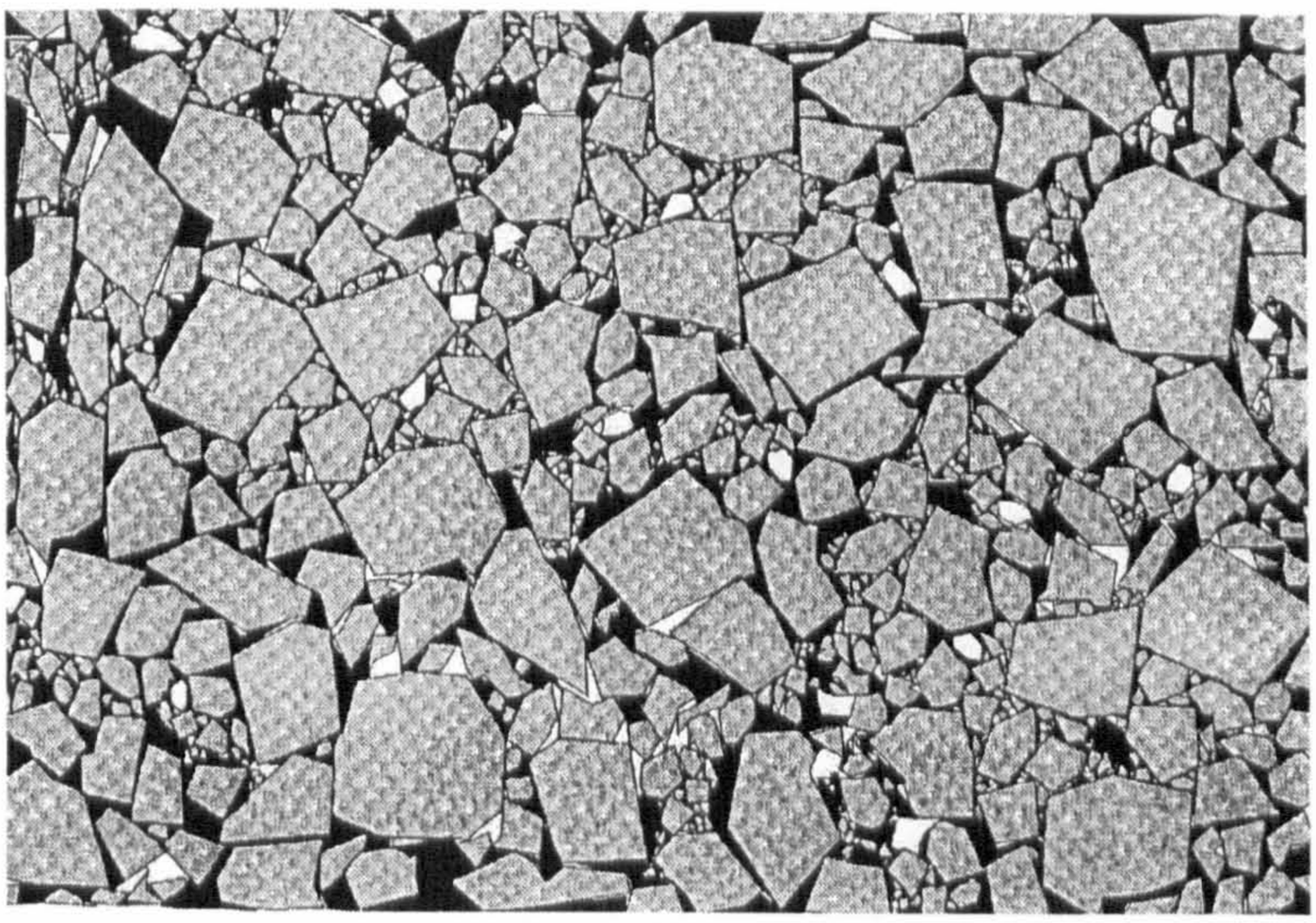

Figure 2.4: Section through an idealised continuously graded material

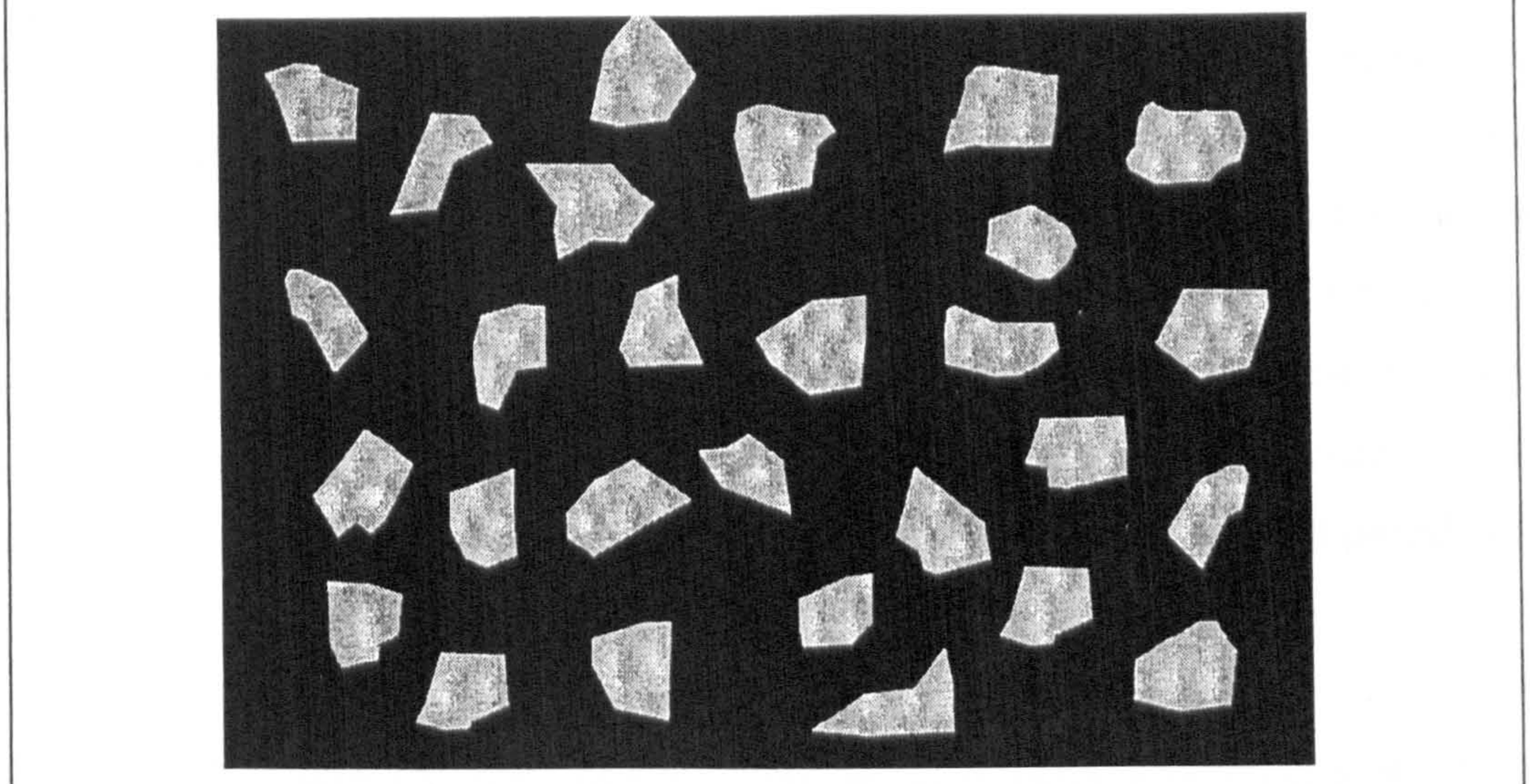

Figure 2.5: Section through an idealised gap-graded material

Bitumen is the only constituent of an asphalt mixture with the capacity to resist tensile strain. Therefore, asphalts, which generally have higher binder contents than macadams, generally have an increased resistance to fatigue cracking. Macadams on the other hand generally provide a better resistance to permanent deformation compared to asphalts, and can be stiffer, if compared with an asphalt composed of a similar maximum aggregate size and bitumen type.

2.2.5 Properties of Asphaltic Materials

As the substantive component in flexible pavement construction, understanding the behavioural characteristics of asphalt mixtures is critical to the development of effective pavement design methodologies. The mechanical properties of an asphalt mixture are strongly dependent on the properties of the binder and the volumetric proportions of the four mixture components.

Visco-Elastic Behaviour of Bitumen

Bitumen[1] is the most commonly used binder in asphalt mixtures. It is a thermoplastic

---

[1] In North America the term 'Bitumen' is referred to as 'Asphalt Cement' or simply 'Asphalt'

material that, in the two extremes, can behave either as an elastic, glass like solid or as a fluid depending on temperature and loading time. At low temperatures and/or short loading times bitumen response is predominantly elastic, whereas for high temperatures and/or long loading times the viscous properties are dominant. At intermediate temperatures, bitumen is visco-elastic in response. At these temperatures a bitumen exhibits both elastic and viscous behaviour and displays a time dependent relationship between applied stress or strain and resultant strain or stress. This intermediate range of temperatures and loading times are those that are prevalent in typical pavement structures.

Figure 2.6 illustrates the visco-elastic behaviour of bitumen subjected to an applied stress. The strain resulting from the applied stress shows an instantaneous elastic response, followed by a gradual increase in the strain with time, until the load is removed. On removal of the load, the elastic strain is recovered instantaneously and some additional recovery occurs with time, known as delayed elastic strain. The remaining viscous strain is irrecoverable, and is responsible for permanent deformation (rutting) experienced by a bitumen or asphalt mixture when loaded [Airey, 1997]. The elastic response of the bitumen dominates at short loading times and/or low temperatures, while the viscous response dominates at long loading times and/or high temperatures. The delayed elastic response is dominant at intermediate loading times and temperatures. The permanent strain of an asphalt mixture may also include an element of irrecoverable, instantaneous plastic strain in the aggregate fraction [Perl *et al.*, 1981; and Gibb, 1996]. The purely viscous component and the delayed elastic component constitute the time dependent deformation of the visco-elastic bitumen. Although none of the viscous deformation is recovered once the load is removed, the delayed elastic deformation is recovered but not immediately, as was the case for purely elastic deformation. The purely elastic component and the purely plastic component constitute the time independent deformation of the visco-elastic bitumen or visco-elastic-plastic asphalt mixture respectively [Perl *et al.*, 1981; Abdulshafi *et al.*, 1984; and Uzan *et al.*, 1985]. As the relative magnitude of the components change with loading time and temperature, both the magnitude and shape of material response shown in Figure 2.6 will change with loading time and temperature.

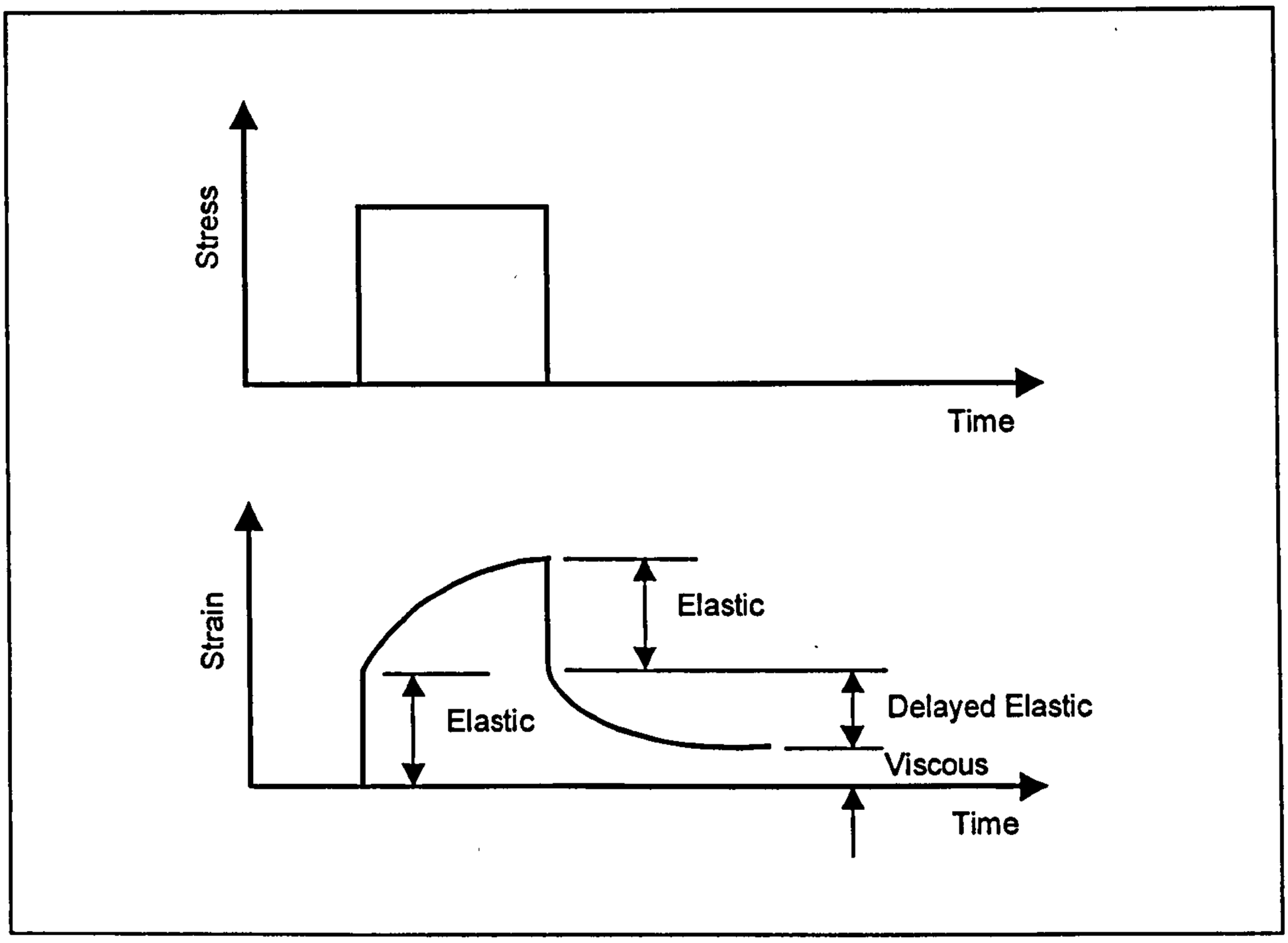

Figure 2.6: Visco-elastic response of bitumen to an applied load

Rheological models can be used to represent various types of material behaviour. To represent the visco-elastic properties of asphaltic materials, models are established by the combination of the Hookean model for an elastic spring (H) and the Newtonian or viscous damper (N) arranged either in series or in parallel. Two examples of this form of representation are shown in Figures 2.7 and 2.8. These are the Maxwell and Kelvin (or Kelvin-Voigt) models respectively, commonly used in pavement engineering to represent the behaviour of bituminous binders.

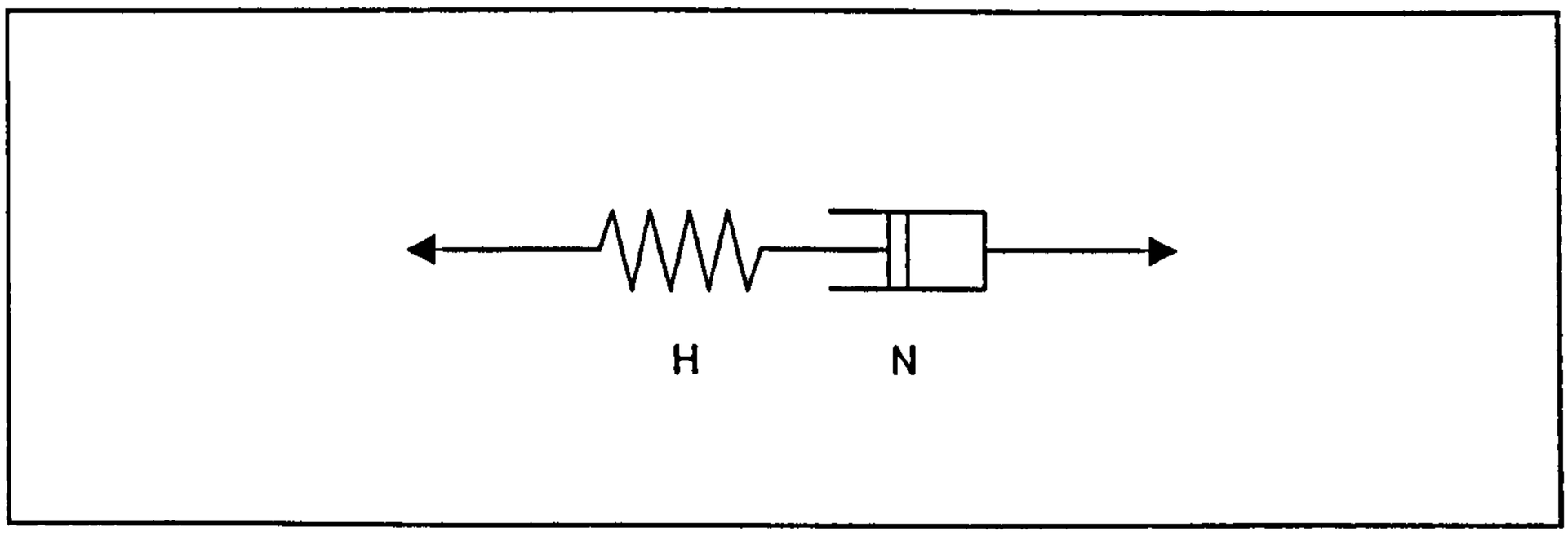

Figure 2.7: Visco-elastic Maxwell model

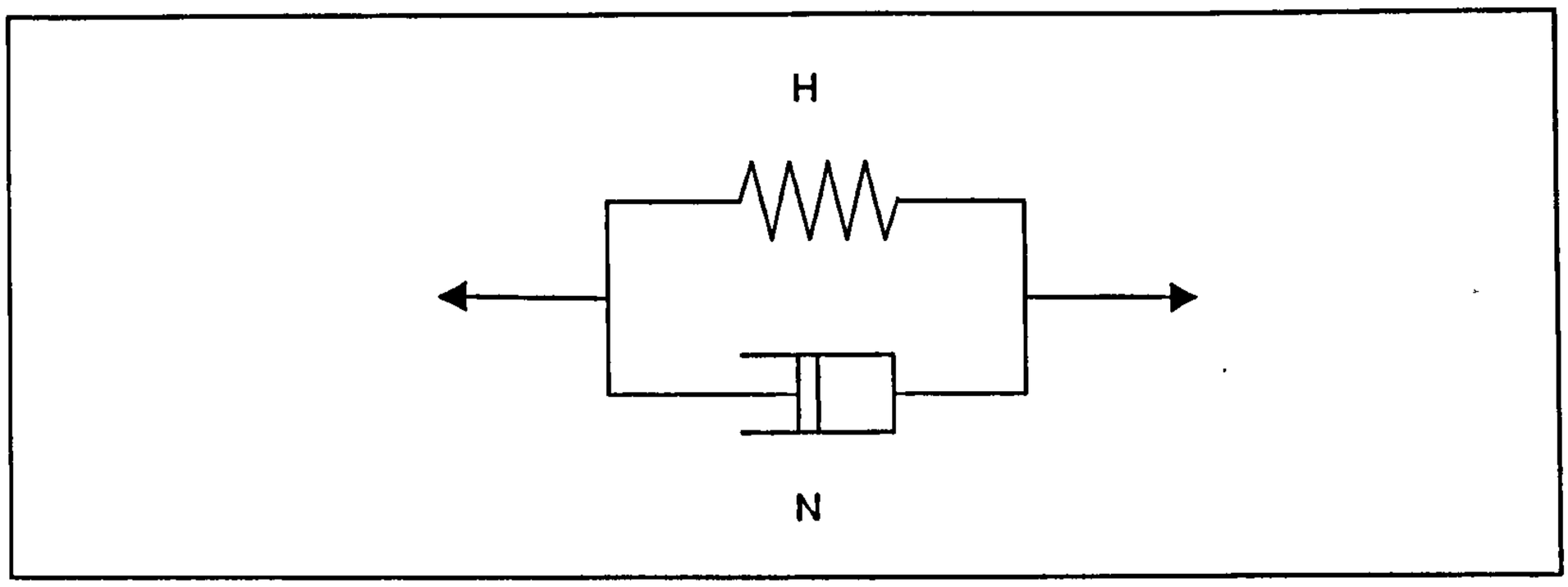

Figure 2.8: Visco-elastic Kelvin model

Binder Stiffness

The stress-strain relationship of a bituminous binder is characterised by both loading time and temperature, exhibiting both elastic and viscous behaviour. Therefore, the concept of Young's modulus, which applies to a purely elastic solid, and assumes the ratio of stress to strain is a single value, cannot be applied. Instead the term stiffness modulus, the ratio of stress to strain at a particular temperature and loading time, can be applied to visco-elastic materials [Van der Poel, 1954]. The ratio is defined as:

$$Stiffness_{(T,t)} = \frac{\sigma}{\varepsilon} \tag{2.1}$$

where, T, t = temperature and time

σ = stress

ε = strain

Van der Poel [1954] reported that a linear relationship between stress and strain is observed for bituminous binders at low temperatures and short loading times, where bitumen behaves as an elastic solid, becoming 'glassy'. In such conditions the stiffness modulus approaches a limiting value of approximately 3 GPa. Linearity is also maintained at high temperatures and long loading times where the material behaves almost entirely as a Newtonian fluid. However, at moderate temperatures and loading times, non-linear effects occur, and these become more marked with increases in deformation.

Following extensive dynamic and creep testing of over forty unmodified bitumens, Van der Poel [1954] developed a simple system, in the form of a nomograph, that could be used to predict or estimate the stiffness of a bitumen using routine binder test data. Van der Poel [1954] showed that two bitumens of the same Penetration Index (PI) at the same time of loading have equal stiffness at temperatures that differ from their respective softening points by the same amount. Van der Poel [1954] showed that using his nomograph, shown in Figure 2.9, given the penetration and softening point, it was possible to predict, to within a factor of two, the stiffness modulus of an unmodified bitumen for any conditions of temperature and time of loading.

Asphalt Mixture Stiffness

The stiffness of an asphalt mixture is an indicator of its ability to spread loads and protect the underlying layers by distributing the wheel loads and so influence the level of stresses and hence strains within the pavement structure. Determination of the stiffness modulus of an asphalt mixture is increased in complexity by the heterogeneity of the mixture components. Generally there are two categories of stiffness. These are, elastic stiffness under conditions of low temperatures and/or short loading times, used to calculate critical strains in traditional analytical pavement design, and viscous stiffness at high temperatures and/or long loading times, traditionally used to assess the resistance of a mixture to deformation [Whiteoak, 1990]. A range of methods can be used to measure the stiffness of asphalt mixtures. When testing at lower temperatures, techniques such as the bending or vibration test on a beam specimen may be used. When working at higher temperatures, direct methods such as uniaxial or triaxial tests on cylindrical specimens are popular.

An alternative way to determine mixture stiffness, where measurement is not possible, is by calculation, using methods such as those described by Bonnaure *et al.* [1977] or Brown *et al.* [1986]. These methods determine mixture stiffness as a function of bitumen stiffness and volumetric properties. However these methodologies can only be applied when the stiffness of the bitumen is greater than 5 MPa, where the assumptions of linear visco-elastic behaviour generally apply [Bonnaure *et al.*, 1977]. At bitumen stiffness modulus values less than 5 MPa, asphalt mixture stiffness not only becomes a function of binder and volumetric properties, but of a number of

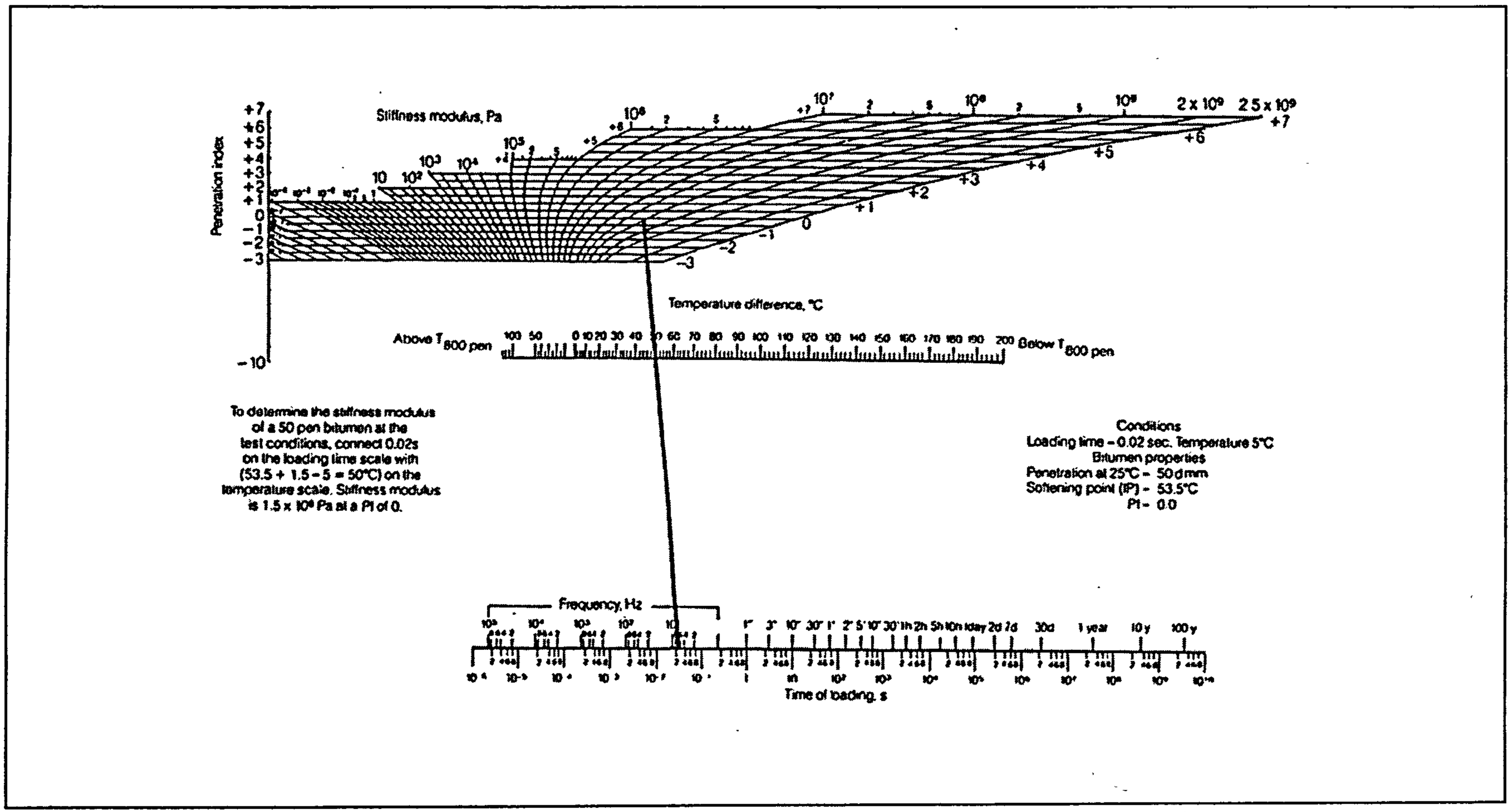

Figure 2.9: Nomograph for determining the stiffness modulus of bitumens [Reproduced from Whiteoak, 1990]

additional factors including the aggregate grading, its shape, texture, degree of interlock, and method of compaction. Under these conditions the viscous properties of the mixture are dominant.

2.2.6 Pavement Design

In order to design and evaluate road pavements it is necessary to have an understanding of their failure mechanisms. Pavements however, do not generally fail suddenly, but rather gradually over a period of time, until a terminal level is reached, which may be defined as failure. In traditional flexible pavement design the two main forms of structural failure are generally taken to be fatigue cracking and permanent deformation (rutting). In the UK empirical based performance criteria are used to define these mechanisms; a pavement is assumed to have reached critical conditions[1] when the wheel path rut depth is at 10 mm, failure is assumed to have occurred when this depth reaches 20 mm. Similar criteria are defined for fatigue cracking, where critical conditions correspond to the onset of fatigue cracking in the wheel path, and failure conditions are defined as evidence of extensive cracking in the wheel path.

From an analytical point of view the two aspects of material properties that are relevant to pavement design are the stress-strain characteristics that are required for the analysis of the structure and the performance characteristics which are used to determine the mode of failure. The material properties of asphalts change, depending on temperature variation, loading time and age. Loading of a pavement structure is itself time dependent, both in the duration of the applied load and the accumulated load history of the structure. It is also complex, with the magnitude and direction of the principal stresses depending on the distance and the relative position of the wheel load as it moves along. This is shown in Figure 2.10. Furthermore, in practice the stresses are applied three-dimensionally and a multitude of three-dimensional states of stress develop. The combination and interaction of the above factors result in a very complicated structural problem. Therefore it is not unexpected that most pavement design methodologies are largely empirically based or involve only simplified analytical design procedures [Hopman *et al.*, 1993].

---

[1] Critical conditions are defined as the latest time at which intervention could extend the life of a road.

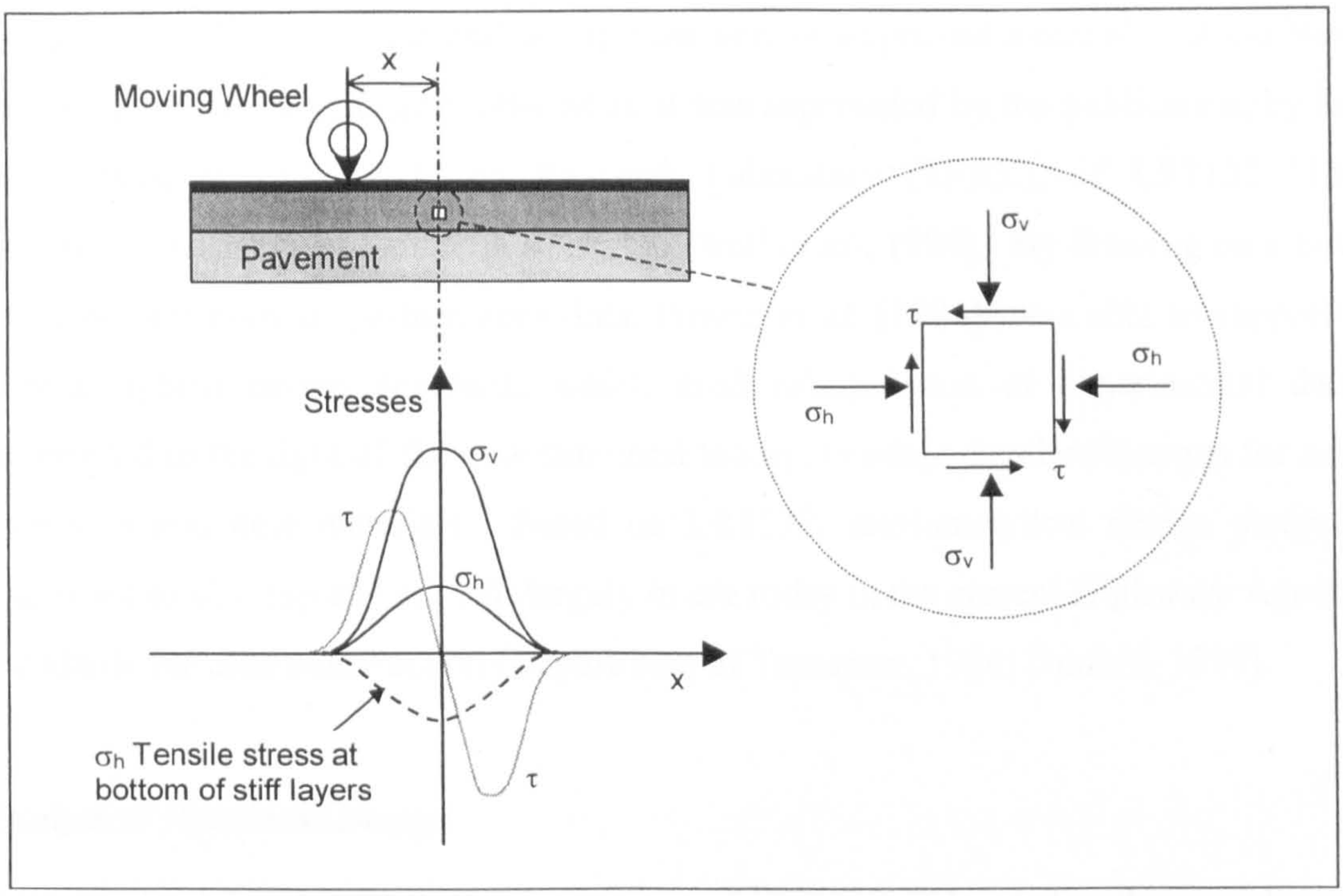

Figure 2.10: Stress induced in a pavement structure due to a moving wheel load [Reproduced from Paute *et al.*, 1993]

Empirical Pavement Design

Empirical design methods may be based solely on engineering experience, evolving over time, or the result of a systematic collection of performance data over a period of time and a statistical correlation of design variables with this performance information.

In the UK, empirical pavement design can be traced back to the late 1950's and early 1960's where much research effort, both in the UK and USA [Highway Research Board, 1962], was directed at extensive testing and monitoring of trial road sections to build up a database of pavement behaviour. This data formed the basis for the design method described in Road Note 29, published in 1960 [Department of the Environment and Road Research Laboratory, 1960], and revised for the second time in 1970, to include the concept of the equivalent standard axle loads [Department of Environment and Road Research Laboratory, 1970]. The chief limitations of this largely empirical approach were the inability to reliably accommodate traffic loading in excess of that already carried by the trial sections and the restricted possibilities of

the design method to assess and incorporate new or improved materials. Road Note 29 was in use in the UK until 1984 when it was superseded by the publication, by the then Transport and Road and Research Laboratory (TRRL), of LR1132 'The Structural Design of Bituminous Roads' [Powell *et al.*, 1984]. By drawing on a now much greater body of performance data, Powell *et al.* [1984] were able to support a semi-analytical design approach, which used extrapolation of experimental data, interpreted in the light of the new structural theory, to adapt standard designs for new situations and new materials. Based on LR1132, semi-analytical design methods continued to develop and are still largely in use today in the current Highways Agency Standards for road construction [Department of Transport, 1994; Dunhill, 1999].

Analytical Pavement Design

Recognition of road pavements as an engineering structure has led to the evolution of entirely analytical design methods. These methods use empirical data obtained from in-service roads to calibrate analytically determined pavement design criteria. Figure 2.11 shows a simplified flow chart of the analytical design process and serves to highlight the central part played by theoretical analysis [Brown, 1997].

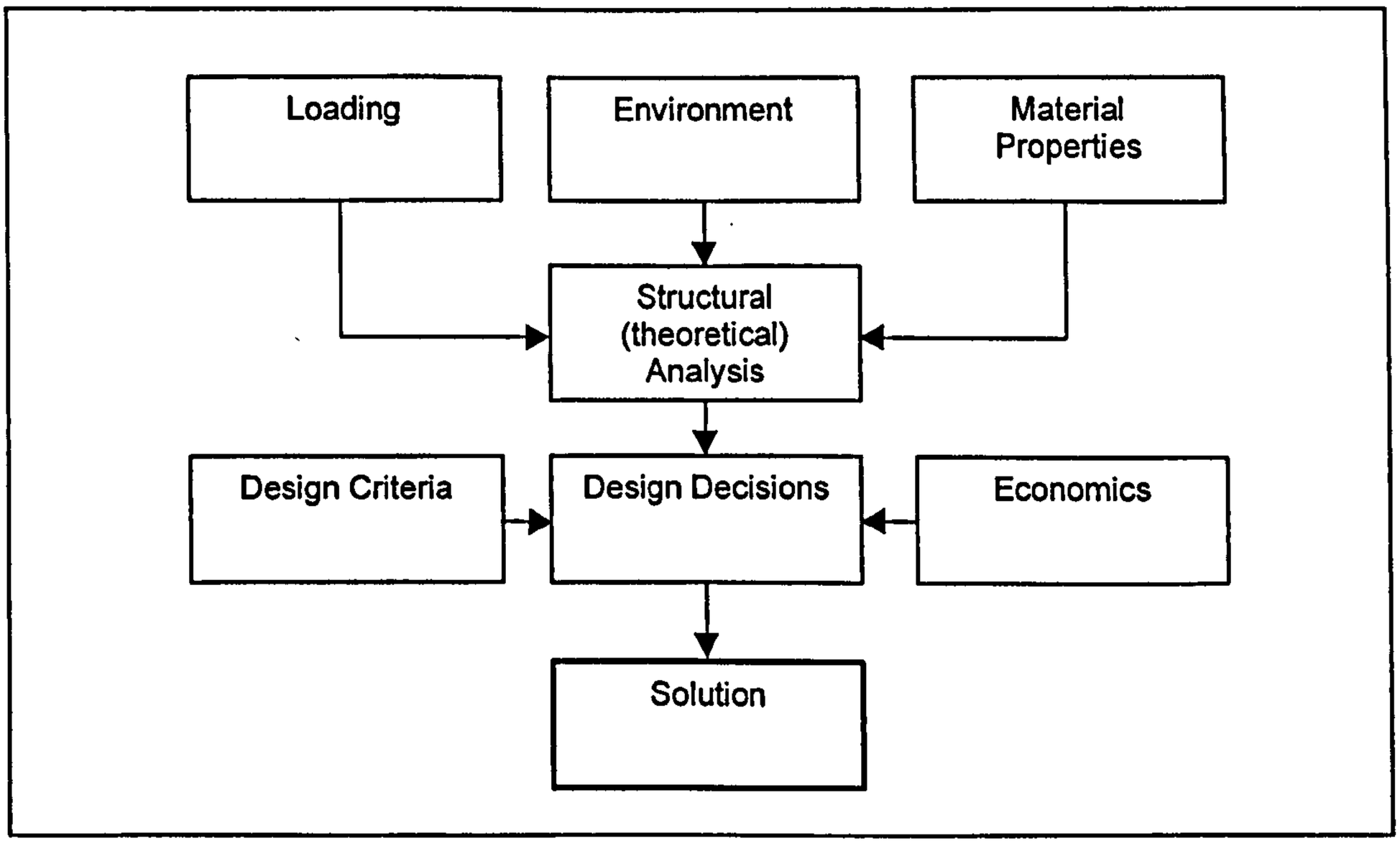

Figure 2.11: Simplified flow diagram for analytical pavement design [Adapted from Brown, 1997]

Typically, in the analytical design philosophy, a pavement is represented as a layered structure comprising of linear elastic materials, characterised by Young's modulus of elasticity and Poisson's ratio, which is subject to circular uniformly distributed loading. A range of different solution techniques has been incorporated into the analysis of traditional layered pavement systems, such as Odemark's method of equivalent thicknesses or layered analytical methods, for example those developed by the Shell International Petroleum Co Ltd. [1978] and Brown *et al.* [1986].

Method of Equivalent Thicknesses

In 1885 Boussinesq solved the equations for the response of a semi-infinite elastic solid [Bowles, 1979]. Based on the assumptions of static equilibrium, compatibility and Hooke's law, he established a fourth order differential equation that was solved for a point load perpendicular to the surface and for the centre line of a circular load. Boussinesq's closed form solutions allowed the calculation of stresses, strains both normal and shear, as well as displacements at any point of the halfspace under a point load or at the centre line of a circular load. However, no closed form solutions, such as Boussinesq's, exist for a layered system. Therefore, in 1949 Odemark presented a simplified method for dealing with such layered systems. This was done by a transformation of the layered system to semi-infinite halfspaces, on which Boussineq's closed form solutions were valid. The transformation is undertaken by calculating the 'equivalent thickness' of the pavement layer in such a way that the stiffness of each layer is maintained [Amadeus, 2000].

Layered Analytical Method

Layered analytical models are mathematically exact solutions, where the fourth order differential equation is solved for the given boundary conditions using numerical integration. These models give the response, in the form of stresses and/or strains induced by a wheel load at any point in a pavement structure. The pavement is represented as a multi-layered linear elastic structure, in which the layers are treated as being horizontally infinite and resting on a semi-infinite subgrade. Stresses and strains are then calculated at critical locations in the pavement structure. Typically, the two classical strain criteria, vertical compressive strain at the subgrade surface and horizontal tensile strain at the bottom of the asphalt layer (see Figure 2.1), are used as

the performance criteria to design against permanent deformation and fatigue cracking respectively. The calculated strains are then compared with permissible values to achieve the required design life and the pavement construction specified as necessary. Examples of this type of approach include procedures such as the Shell Pavement Design Method (SPDM) [Shell International Petroleum Co Ltd., 1978] and the Nottingham Analytical Design Method [Brown *et al.*, 1986]. Originally, layered analytical models of this type only considered linear isotropic layers, and uniform circular loading, although recent models can now also consider multiple wheel loads and some of the complex elements of asphaltic material behaviour such as cross anisotropy and visco-elasticity [Hopman *et al.*, 1997].

Analytical design methods, such as those described above based on layered elastic solutions, are of great importance to practising pavement engineers as they provide a strong design tool. Indeed, various layered elastic computer programs have been developed to analyse pavement systems, such as BISAR, and digitised versions of design procedures and methodologies, such as SPDM, are now readily available [Shell Global Solutions, 1998]. For relatively thick asphalt constructions, where the assumptions of linear elastic theory for a moving wheel load may be valid, satisfactory results can be obtained provided the stiffness of the asphalt layer is accurately specified [Brown, 1997]. However, such design methods are only valid within the confines of present experience and often involve the simplification of the pavement structure and loading conditions. Outside this experience such design methodologies become invalid, and the limitations of this approach need to be recognised, such as the inability of linear elastic approaches to detect inadmissible stress conditions within a pavement structure [Hopman *et al.*, 1993], or where thin asphalt construction is being used and the non-linear characteristics of the pavement structure are dominant, and therefore non-linear analysis is required.

Finite Element Method

As no analytical solution presently exists for non-linear stress-strain relationships, most of the pavement analysis accommodating non-linear behaviour has used the finite element (FE) approach. Non-linear FE analysis is essentially an approximate iterative method for calculating the behaviour of a real structure by performing an

algebraic solution of a set of equations describing an idealised model structure with a finite number of variables. In this model the real structure is represented by an assemblage of discrete subdivisions, of various sizes, called finite elements. The elements are considered interconnected at joints, termed nodes or nodal points. Each element is defined by its boundary geometry, its material properties and basic parameters such as thickness and/or volume. Blocks of finite elements, joined at the nodal positions form a mesh, which can be developed to model a particular design problem or structure. The behaviour of the complete idealised structure is determined as the aggregate behaviour of its elements. The basic equations of equilibrium, compatibility and state are set up and solved in terms of the discrete boundary variables and the behaviour within the elements is then derived from the values calculated at their boundaries. On the basis of nodal displacements, the stresses and strains can be computed at virtually any location within the structure. [NAFEMS, 1984].

The main advantages of FE methods over traditional layered elastic models, include:

- the ability to consider non-linear (inelastic) material characteristics,
- the versatility to study a wide range of pavement geometries and discontinuities,
- the ability to model complex loading conditions and tyre contact stresses, and
- the opportunity to incorporate complex material characteristics, such as cross and full anisotropy, visco-elasticity, material heterogeneity.

The Transport Research Laboratory (TRL) started using FE methods in pavement design in the 1970's, but were limited in the application of the method by the large amount of memory and computational time required to generate solutions. However, modern developments in computer technology have removed some of these limitations, enabling the increased use of FE methods for pavement response modelling [Almeida, 1993; Amadeus, 2000]. A distinction can be made between plane stress/strain two-dimensional FE methods, axial symmetric FE methods and three-dimensional FE methods. A second important distinction can be made between FE models on the basis of the constitutive model used to describe the material behaviour.

2.3 Constitutive Relationships

In the subsequent sections of this chapter a review of some of the general aspects of constitutive relationships are given. This review is not intended to be exhaustive in content, but to serve to introduce some of the basic principles, with particular regard to plasticity based constitutive models and their application in pavement engineering. Various sources on the subject of constitutive numerical modelling are available; the texts by Hill [1950], Desai *et al.* [1972 and 1977], Owen *et al.* [1980], Hinton [1992], Potts *et al.* [1999] and Becker [2001] were used to collate the information presented within the initial stages of this review.

2.3.1 Elasticity

A central part in the numerical treatment of physical problems is the description of the relationships between physical quantities such as stress, strain and time. These descriptions are called constitutive relationships. The basic constitutive relationship upon which many others are based is that of elasticity. A linear elastic material is one that obeys Hooke's Law of proportionality between stress and strain. In three-dimensional bodies this can be generalised as:

$$\{\sigma\} = [D]\{\varepsilon\} \tag{2.2}$$

where, $\{\sigma\}$ and $\{\varepsilon\}$ are the stress and strain vectors respectively and [D] is the constitutive matrix[2]. The simplest specialisation of the constitutive matrix is that of a homogenous linear elastic isotropic material. For such a material only two independent elastic constants are required to define the matrix, which becomes symmetrical. Typically, the constants used are Young's modulus of elasticity, E, and Poisson's ratio, ν, where the constitutive matrix is given by Equation (2.3).

---

[2] The reader should note that in this context the vectors $\{\sigma\}$ and $\{\varepsilon\}$ represent stress and strain tensor components in column matrix format.

$$[D]=\frac{E}{(1+v)(1-2v)}\begin{bmatrix} 1-v & v & v & 0 & 0 & 0 \\ & 1-v & v & 0 & 0 & 0 \\ & & 1-v & 0 & 0 & 0 \\ & & & 0.5-v & 0 & 0 \\ & Sym & & & 0.5-v & 0 \\ & & & & & 0.5-v \end{bmatrix} \quad (2.3)$$

The number of independent terms required to describe the constitutive matrix however, increases considerably, from five, when considering cross anisotropy, to 21 for fully anisotropic material behaviour. A logical first step to improving linear elastic relationships such as that outlined above is to make the elastic material parameters dependent on stress and/or strain level. As only two material parameters are required to define isotropic elastic behaviour this is relatively straightforward. However, this is much more difficult for anisotropic behaviour due to the increased number of parameters. As a consequence most non-linear elastic models assume isotropic material behaviour.

In FE analysis an incremental approach is often used for non-linear elastic analysis. Essentially this incremental technique approximates material behaviour as piecewise linear. The total applied load is divided into small increments and each increment is applied individually. Provided the increments are small, the material behaviour may be assumed to be linear during the load increment, and a new stiffness can be used in each load increment. If only a few increments are used, this method produces a solution that tends to drift away from the exact solution. For this reason it is common to combine incremental and iterative approaches to arrive at an exact solution (see Figure 2.12).

In linear FE analysis the displacements are linearly related to the applied loads, and hence the material behaviour is elastic and completely reversible. However it has been readily shown that asphalt mixtures can exhibit non-linear stress-strain relationships, displaying both viscous and plastic behaviour. As such, the elastic constitutive relationships applied in linear FE analysis are unsuited to modelling asphaltic material response. Therefore non-linear FE analysis must be used. Traditionally non-linear FE problems can be grouped into three classifications:

- material non-linearities,
- geometric non-linearities, and
- boundary non-linearities (such as the tyre-pavement interface).

Material non-linearities correspond to conditions where the stress-strain relationships are non-linear. As such, understanding this type of non-linearity is of paramount importance in the development of accurate constitutive models and is discussed below. Geometric non-linearity refers to conditions where changes in the geometry of a structure due to its displacement under load are taken into account in analysis of its behaviour. Boundary non-linearity occurs in contact problems, in which two surfaces come into or out of contact, and the displacements and stresses of the bodies are not linearly dependent on the applied loads. Further details on both these forms of non-linearity can be found in Desai *et al.* [1972], Hinton [1992] and Becker [2001] but will not be discussed further in this thesis.

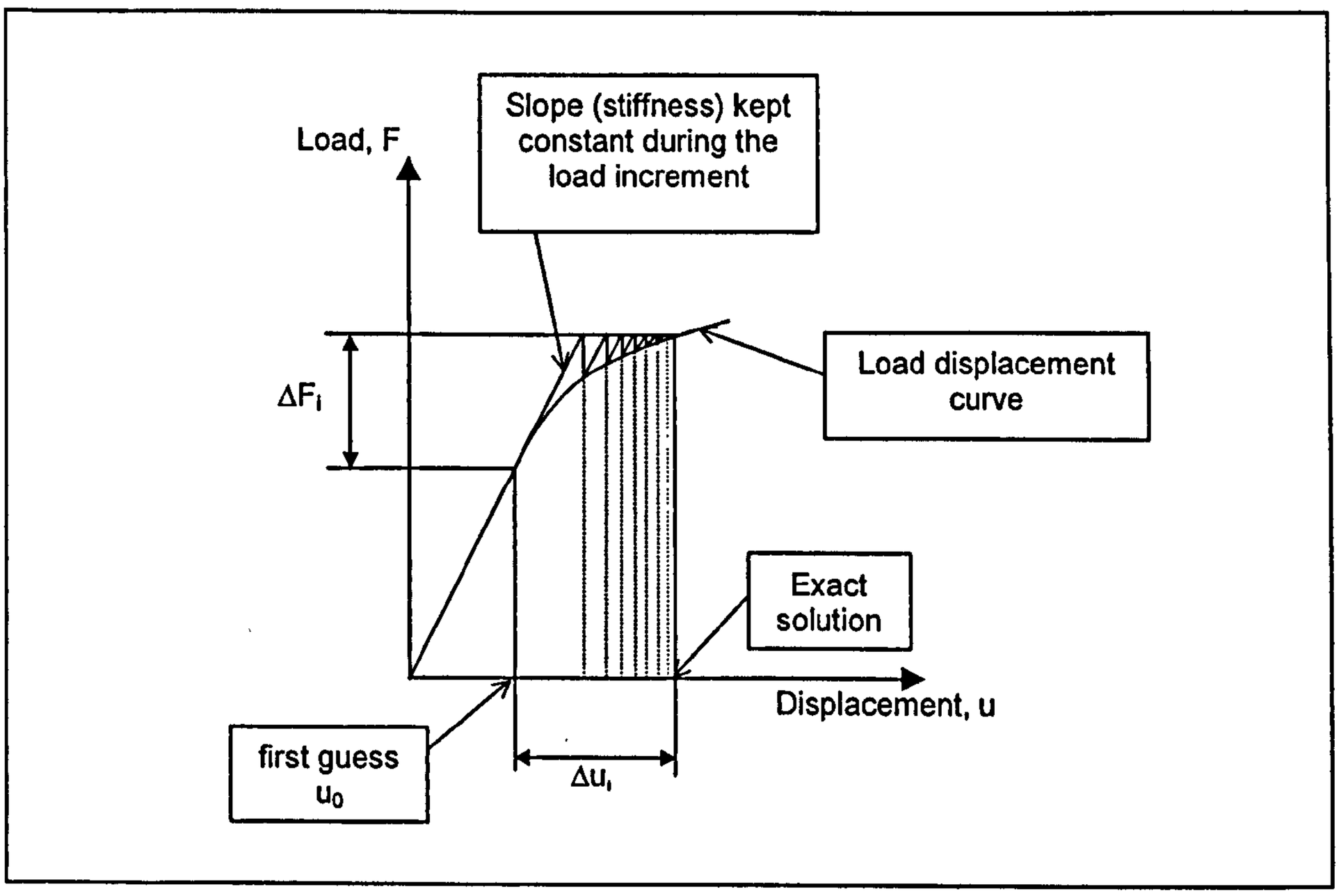

Figure 2.12: Schematic representation of an iterative procedure applied during a load increment

Departure from linear FE analysis implies that the linear elastic constitutive equations are no longer valid, hence the constitutive matrix [D] is no longer constant. The non-

constant matrix represents complex constitutive relationships, corresponding to the adopted non-linear material model. By definition, the material (constitutive) matrix relates components of stress to components of strain in a multi-axial state. Often for various reasons, such as insufficient experimental evidence, non-linear models of multi-axial material behaviour rely on generalisations of uniaxial concepts. This in turn requires the definition of some functional relationships between components of stress and strain. The challenge in the development of such relationships is that they should provide both adequate physical representation of the observed mechanical behaviour, and also sound numerical performance.

2.3.2 Plasticity

In soil mechanics, plasticity based models have been recognised as a class of models that can provide some degree of both physical realism and sound numerical performance, having themselves benefited from the establishment of the underlying theory from preceding developments in metal plasticity. Asphaltic materials, which are composed of aggregates, bitumen and air voids are to some extent analogous to soils which are composed of soil solids, water and air. Indeed, Nijboer [1948] was the first to apply soil mechanics principles to the characterisation of asphalt mixtures. He distinguished between the behaviour of various asphalt mixtures under constant rate triaxial loading, using the parameters ϕ, the angle of internal friction, and c, the cohesion (see Section 2.4.1).

Elasto-plasticity models have been successfully used to describe the response of materials such as soils and concrete that exhibit both elastic recoverable and plastic permanent strains. Such models use the concept of a yield point or yield surface (in multi-axial models) to separate the elastic material behaviour from the plastic response. In the formulation of elasto-plastic models it is common to use linear-elastic laws to describe material behaviour prior to the proportional limit. In the zone between the proportional limit and the yield point, piecewise linear formulations can be applied to model non-linear elastic material behaviour. To model the plastic or inelastic material behaviour beyond the yield point, it is necessary to have an understanding of the basic laws that govern plasticity.

Plasticity theory is the name given to the mathematical study of stress and strain in plastically deforming solids. The theory of classical plasticity is based on the existence of a yield condition, a flow rule and hardening and/or softening rules. The situation is complicated by the fact that different materials exhibit different plastic characteristics. Therefore different yield criteria must be employed. The identification of an appropriate yield criterion for asphaltic materials is a key stage in the development of a suitable constitutive model for implementation into a FE pavement model.

2.3.3 Uniaxial Elasto-plastic Behaviour

As already indicated, models for multi-axial material behaviour are generally based on generalisations of one-dimensional concepts. Therefore before presenting the formulation for a multi-axial constitutive model, first consideration is given to the uniaxial case. Figure 2.13 shows the idealised uniaxial stress-strain curve for a general element of material that is loaded monotonically by applying strain.

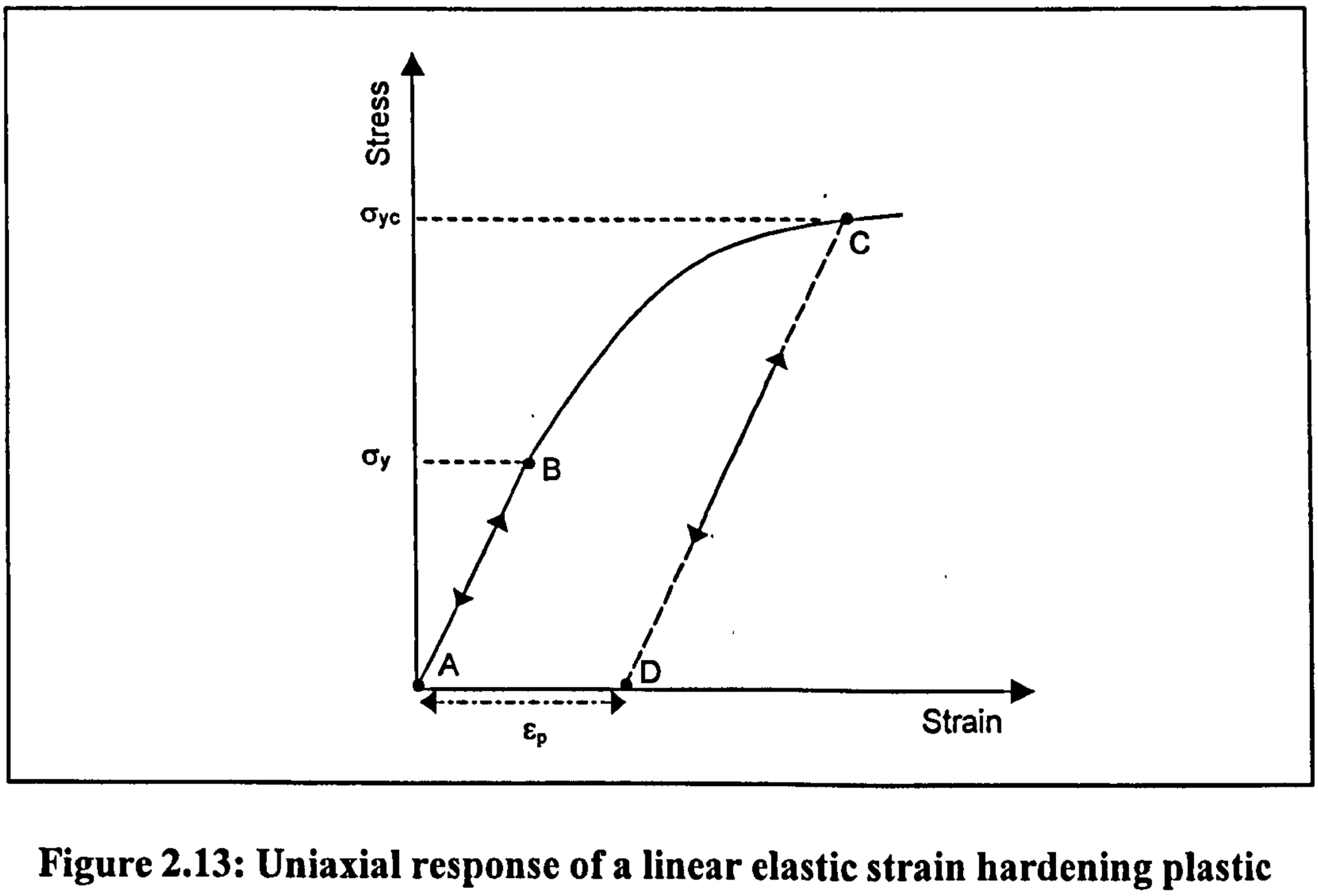

Figure 2.13: Uniaxial response of a linear elastic strain hardening plastic material element to monotonic compressive loading

Initially, when strained, the element behaves elastically, and loading/unloading results in movement up and down the path *AB*. If strained beyond point *B* to point *C* the

yield stress σ_y is exceeded and the element becomes plastic[3]. The characteristics of path *BC* are dependent on the type of material being loaded. For linear elastic-perfectly plastic materials, such as some metals, the path *BC* is a horizontal straight line. Such materials can be represented by the arrangement shown in Figure 2.14, know as the Prandtl model (where the friction slider *SV* is active for $\sigma \geq \sigma_y$). Material models such as this are bounded by a yield function separating the elastic behaviour from the plastic behaviour. The Tresca, Von Mises, Mohr-Coulomb and Drucker-Prager criteria, discussed later, represent some of the more common yield functions that are used to model elasto-plastic material behaviour.

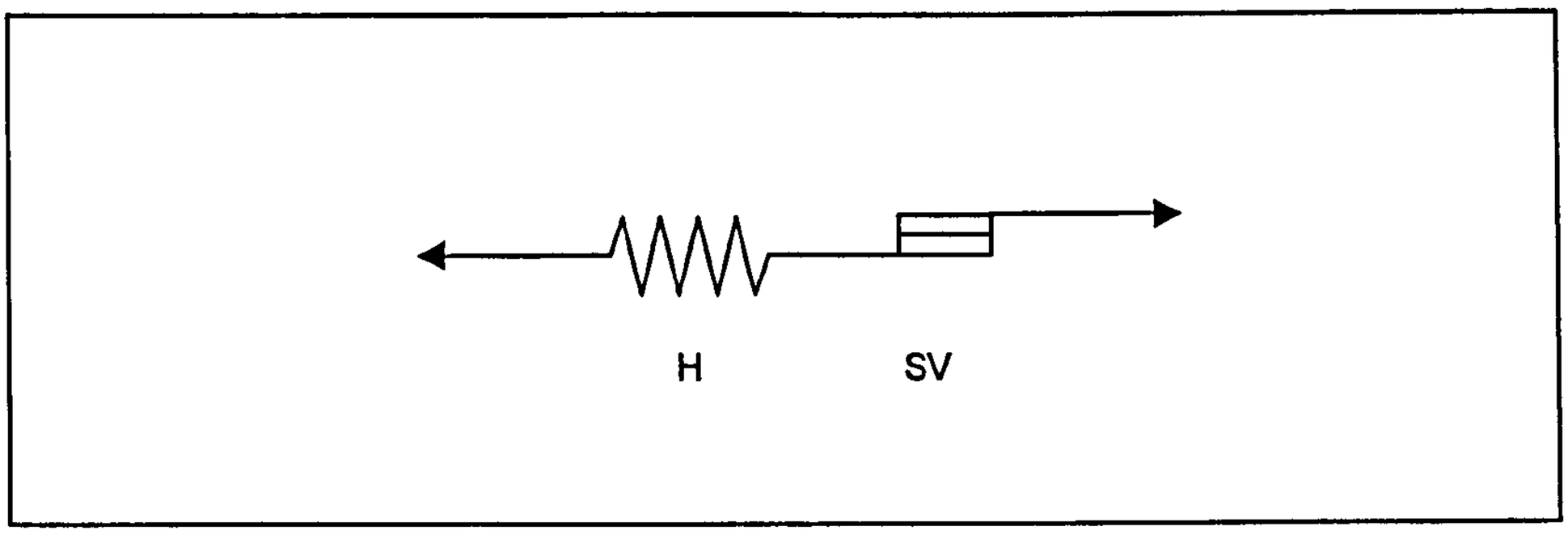

Figure 2.14: Elasto-plastic Prandtl model

For asphalts (see Figure 2.29, Section 2.4.2) and other paving materials, such as soils and granular materials the path *BC* is characterised by an increasing strain curve, as shown in Figure 2.13. At first the plastic strains are limited as they result in an increased resistance of the material to further deformations. In this condition the yielding response is gradual and the material is said to strain (or work) harden. Hardening can increase a materials resistance to a limited extent. However, once the applied stress attains the maximum strength of the material, the external work done exceeds the internal dissipation of energy in overcoming the resistance of the material to further strains, and failure occurs. After this point, for some materials, under

---

[3] The value of σ_y can be identified as a minimum level of stress in a material above which irreversible deformations occur after load removal. In other words σ_y represents the elastic limit of a material, or equivalently the onset of inelastic material response and is defined as the yield point.

certain loading conditions, a decrease in the resistance to strain can be observed and the material is said to strain (or work) soften. For path *BC*, in the plastic range, unloading from a point such as *C* will result in the elastic behaviour of the element, which will follow path *CD*, parallel to *AB*. When fully unloaded to point *D* the remaining plastic strain ε_p is equivalent to the plastic strain experienced straining along path *BC*. If the element were now to be reloaded the stress-strain curve would behave elastically following path *DC* until point *C* is reached[4], at which point the stress is equal to the new yield stress σ_{yc} and the element becomes plastic once again. For a strain hardening material the yield stress at point *C* is greater than the initial yield stress as it has increased as a result of plastic straining. For a strain softening material the yield stress at point *C* is less than the initial yield stress as it has decreased as a result of plastic straining. Strain or work hardening models are often used in geotechnical engineering as a more realistic way to model the behaviour of soils and granular materials.

2.3.4 Multi-axial States of Stress

If the above concepts of elasto-plastic material models are to be of general use in the three-dimensional analysis of pavement structures, then the uniaxial behaviour must be translated into general multi-axial stress and strain space. Figure 2.15(a) illustrates the stresses on a cubic element in a pavement structure[5]. The element strains could also be shown in a similar manner. On each plane of the cube, one component of normal stress and two components of shear stress represent the resultant stress. These stresses can be described in terms of the stress tensor given in Equation (2.4).

$$\sigma_{ij} = \begin{bmatrix} \sigma_{xx} & \sigma_{xy} & \sigma_{xz} \\ \sigma_{yx} & \sigma_{yy} & \sigma_{yz} \\ \sigma_{zx} & \sigma_{zy} & \sigma_{zz} \end{bmatrix} \tag{2.4}$$

---

[4] In reality the path from D up to C would not coincide with the descending line CD, but would be close to it and a slight rounding of the curve near the C would be observed. This represents a hysteresis loop caused by the loss of energy during the cycle of loading and reloading.

[5] For clarity and because they would simply be equal and opposite, the stresses on the three planes away from the reader are not shown.

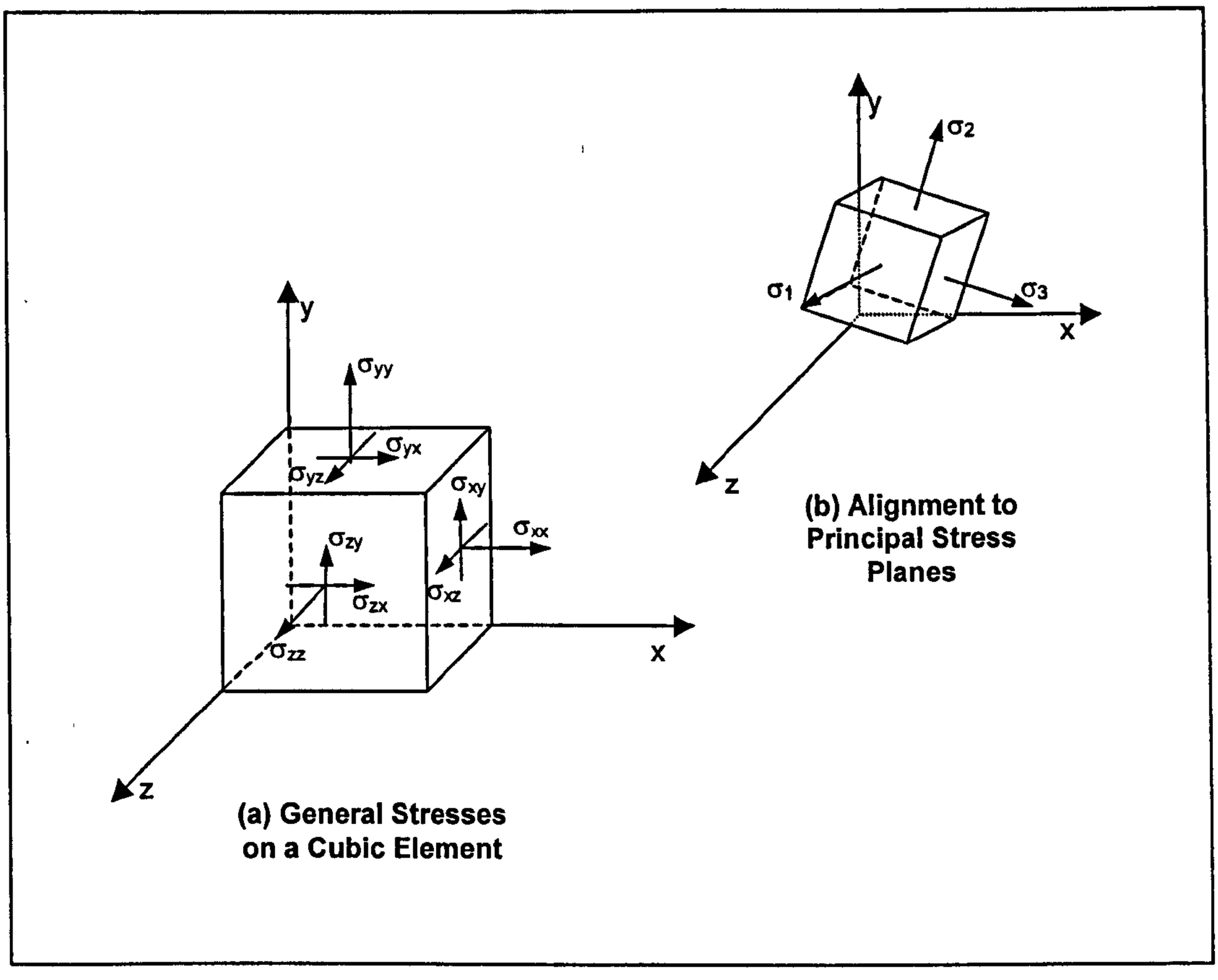

Figure 2.15: General stresses on a cubic element

There also exist three orthogonal planes in the element on which the resultant stress is the normal stress, with the components of shear being zero, Figure 2.15(b). These planes are called the principal stress planes and the associated normal stresses are called the principal stresses, σ_1, σ_2 and σ_3. These stresses always act on the same planes and have the same magnitude. They are therefore invariant to the choice of axes. Consequently, the state of stress can be fully defined by either specifying the six component values for a fixed direction of the coordinate axis, or by specifying the magnitudes of the principal stresses and the direction of the principal stress planes.

For isotropic materials, however, material properties are independent of orientation, and only the stress magnitudes, and not their directions are required. It is therefore possible to define the state of stress for an isotropic material using just the three principal stresses, or some set of three combinations of these. The principal stresses are the solutions to Equation (2.5).

$$\sigma^3 - I_1\sigma^2 + I_2\sigma - I_3 = 0 \tag{2.5}$$

in which
$$I_1 = \sigma_{xx} + \sigma_{yy} + \sigma_{zz} = \sigma_1 + \sigma_2 + \sigma_3 \tag{2.5a}$$

$$I_2 = \begin{vmatrix}\sigma_{xx} & \sigma_{xy}\\ \sigma_{yx} & \sigma_{yy}\end{vmatrix} + \begin{vmatrix}\sigma_{yy} & \sigma_{yz}\\ \sigma_{zy} & \sigma_{zz}\end{vmatrix} + \begin{vmatrix}\sigma_{zz} & \sigma_{zx}\\ \sigma_{xz} & \sigma_{xx}\end{vmatrix} = \sigma_1\sigma_2 + \sigma_2\sigma_3 + \sigma_3\sigma_1 \tag{2.5b}$$

$$I_3 = \begin{bmatrix}\sigma_{xx} & \sigma_{xy} & \sigma_{xz}\\ \sigma_{yx} & \sigma_{yy} & \sigma_{yz}\\ \sigma_{zx} & \sigma_{zy} & \sigma_{zz}\end{bmatrix} = \sigma_1\sigma_2\sigma_3 \tag{2.5c}$$

I_1, I_2 and I_3 are referred to as the first, second and third stress invariants. Since the principal stresses are physical quantities independent of the choice of coordinate axes, the invariants are also independent of the chosen coordinate system.

In constitutive modelling it is often convenient to describe the stress state in terms of volumetric (hydrostatic) and deviatoric components. The hydrostatic stress component, σ_m, can be written as:

$$\sigma_m = \frac{1}{3}\sigma_{ij} = \frac{I_1}{3} \tag{2.6}$$

The deviatoric stress component, s_{ij}, is then expressed in the form:

$$s_{ij} = \sigma_{ij} - \delta_{ij}\sigma_m \tag{2.7}$$

where, δ_{ij} = Kronecker delta

for which
$$\delta_{ij} = \begin{cases}0 \text{ if } i \neq j\\ 1 \text{ if } i = j\end{cases} \tag{2.7a}$$

In a similar manner to the resultant stress the deviator stress also has principal values and invariants. These are referred to as s_1, s_2 and s_3 where J_2 and J_3 are used to

represent the second and third deviatoric stress invariants respectively. In analogy to Equation (2.5) the principal deviatoric stresses are the solutions to Equation (2.8).

$$s^3 - J_2 s - J_3 = 0 \tag{2.8}$$

in which $$J_2 = \frac{1}{2}\left(s_{xx}^2 + s_{yy}^2 + s_{zz}^2\right) + \sigma_{xy}^2 + \sigma_{yz}^2 + \sigma_{zx}^2$$

or $$J_2 = \frac{1}{2}\left(s_1^2 + s_2^2 + s_3^2\right) \tag{2.8a}$$

$$J_3 = s_{xx}s_{yy}s_{zz} + 2\sigma_{xy}\sigma_{yz}\sigma_{zx} - s_{xx}\sigma_{yz}^2 - s_{yy}\sigma_{xz}^2 - s_{zz}\sigma_{xy}^2$$

or $$J_3 = \frac{1}{3}\left(s_1^3 + s_2^3 + s_3^3\right) \tag{2.8b}$$

As shall be seen later, it is often convenient to work with quantities expressed in invariant form.

2.3.5 Yield Functions

In the uniaxial model presented earlier, the yield stress σ_y, represented by a point on the stress strain curve, was used to define the stress level at which purely elastic stresses stopped occurring and plastic straining occurred, or vice versa. For multi-axial situations however there can be several non-zero components of stress, hence this representation is no longer viable. Therefore a yield function, F, is used; the exact form of which depends on the postulated yield criterion. It is defined as a scalar function of stress, expressed in terms of either stress components or stress invariants, and the state parameters k:

$$F[\sigma_{ij}, k(\varepsilon_{ij}^p)] = 0 \tag{2.9}$$

If Equation (2.9) were to be expressed in principal stress space, with $\sigma_2 = 0$, the yield function would plot as a curve, as shown in Figure 2.16(a).

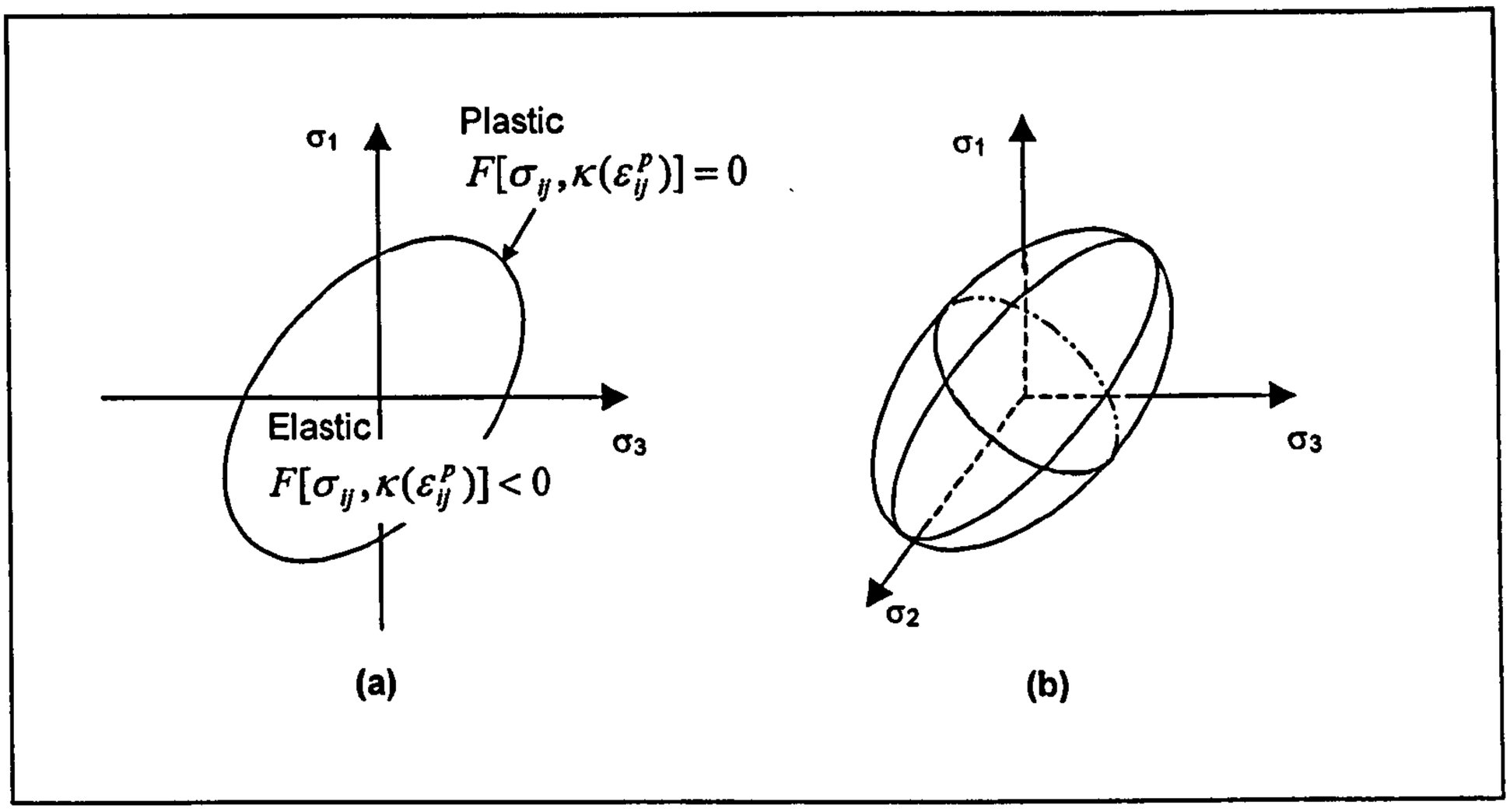

Figure 2.16: (a)Yield curve; (b)Yield surface

The value of the yield function, F, is used to identify the type of material behaviour. Elastic material behaviour occurs for $F[\sigma_{ij}, k(\varepsilon_{ij}^p)] < 0$, the space enclosed by the yield curve in Figure 2.16(a). Plastic (or elasto-plastic) material behaviour occurs for $F[\sigma_{ij}, k(\varepsilon_{ij}^p)] = 0$, which corresponds to states of stress on the yield curve.

If σ_2 is not set to zero, then Equation (2.9) represents a yield surface (or flow surface) when plotted in three-dimensional principal stress space, Figure 2.16(b). The size of this yield surface can change as a function of the state parameters k, which are related to hardening/softening rules by plastic straining, ε_{ij}^p (see Section 2.3.7). If the yield function were to be expressed in terms of stress components, as opposed to stress invariants, the yield function would form a surface in six-dimensional space. As it is not possible to draw such a surface, making visualisation difficult, the advantages of assuming isotropic material behaviour, and hence working with invariant quantities, are apparent.

A true yield surface for a material may be determined through laboratory experiments. This can be achieved by testing material samples under various combinations of stress situations, from which a locus of yield points on a common deviatoric plane can be found, which in turn will define the yield surface. For isotropic materials, principal

directions for σ_1, σ_2 and σ_3 can be interchanged and consequently the trace of the yield surface in the deviatoric plane must be symmetric with respect to the principal axes, thus reducing the number of test conditions required.

Classical Plasticity Models

Often, for an isotropic material, a failure criterion in combination with experimental data is used to represent the yield surface in principal stress space. As different classes of materials exhibit different characteristics, various yield criteria have been developed. Three classical failure theories are represented in Figure 2.17.

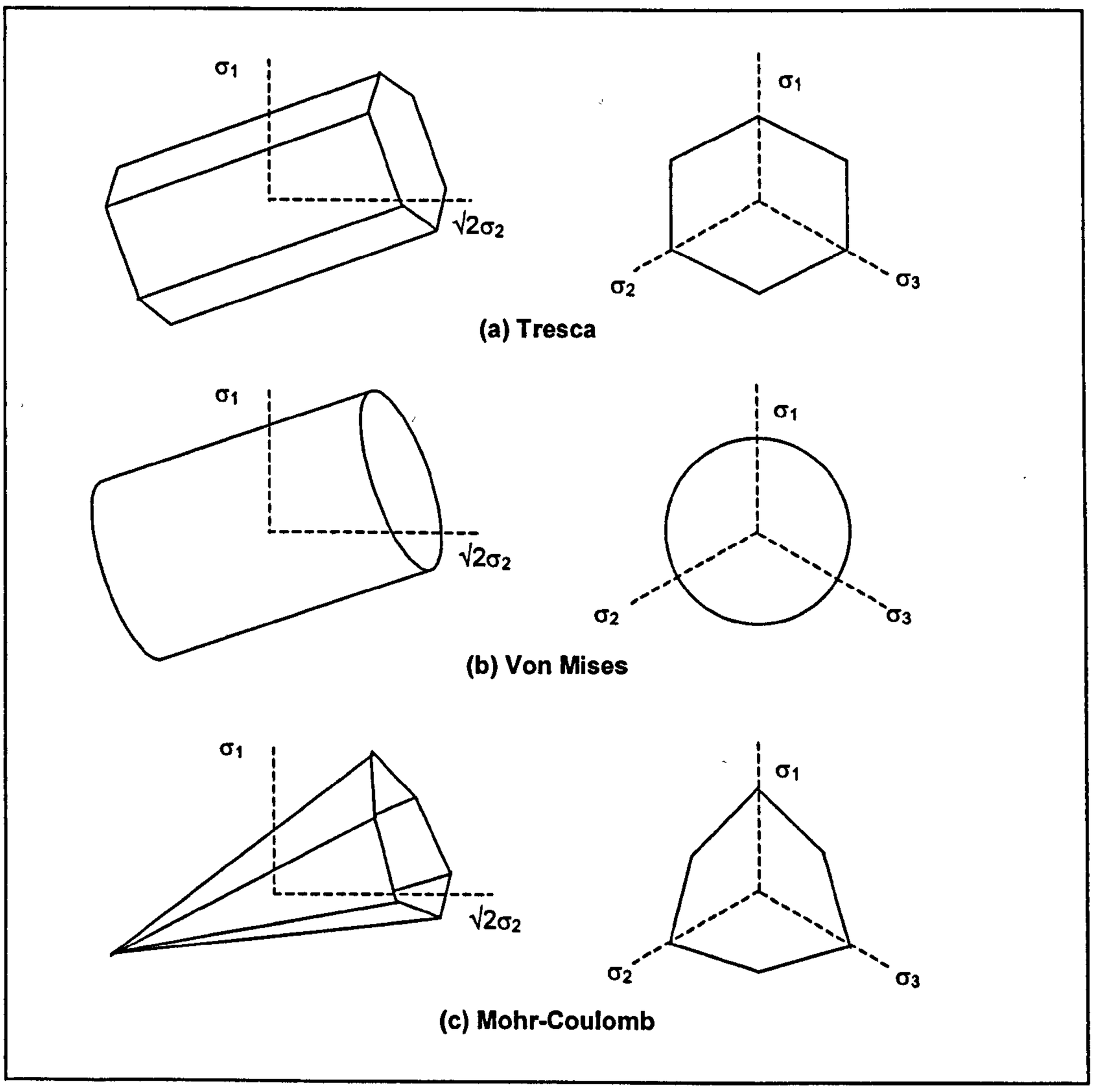

Figure 2.17: Multi-axial representation of classical failure criterion

The figure shows the Tresca maximum shear strength, Von Mises maximum distortion energy and Mohr-Coulomb friction slip theories. The Tresca (1864) and Von Mises (1913) yield criteria were developed within metal plasticity and when presented in principal stress space plot as a regular hexagonal prism and a cylinder respectively. The surfaces are this shape due to the presumption that yield is caused by a deviatoric state of stress and is independent of the hydrostatic state of stress. This may be appropriate in metallurgy, were material behaviour is assumed to be the same in compression and tension, however this is not the case for so called frictional materials such as sand, concrete and rocks, for which volumetric effects do play a significant role in yielding. Brown *et al.* [1980 & 1984] have shown this to also be true for asphalt mixtures, where extensive triaxial testing of asphalt mixtures showed the mixture response to be a function of the hydrostatic as well as the deviatoric stresses.

In classical plasticity, for frictional materials, the Mohr-Coulomb (1773) yield criterion (a generalised form of the Coulomb friction failure law) is used. When plotted in principal stress space the yield function forms an irregular hexagonal cone, Figure 2.17(c). In similarity to the Tresca yield criteria, the Mohr-Coulomb yield function has corners when plotted in principal stress space. These corners imply singularities in the yield function. To deal with singularities in FE analysis requires elaborate computer code, which inevitably consumes greater computing resources, consequently earlier modelling pioneers sought simplifications. Therefore, Drucker and Prager (1952) presented an approximation of the Mohr-Coulomb yield criterion as a modification of the Von Mises yield criterion. The influence of the hydrostatic stress component on yielding was introduced by the inclusion of an additional term in the Von Mises expression.

Von Mises: $$F = J_2^{\frac{1}{2}} - k = 0 \tag{2.10}$$

Extended Von Mises: $$F = \alpha I_1 + J_2^{\frac{1}{2}} - k = 0 \tag{2.11}$$

where k and α are experimentally determined material parameters. The extended Von

Mises or Drucker-Prager yield criterion, as it has become known, has the form of a circular cone in principal stress space, Figure 2.18(a), and can be shown to coincide with either the outer or inner apices of the Mohr-Coulomb hexagon, Figure 2.18(b). In Section 2.4.1 it is shown that the Drucker-Prager yield criterion can be used to model some of the behavioural aspects of asphalt mixtures [Abdulshhafi *et al.*, 1984 and Tan *et al.*, 1994].

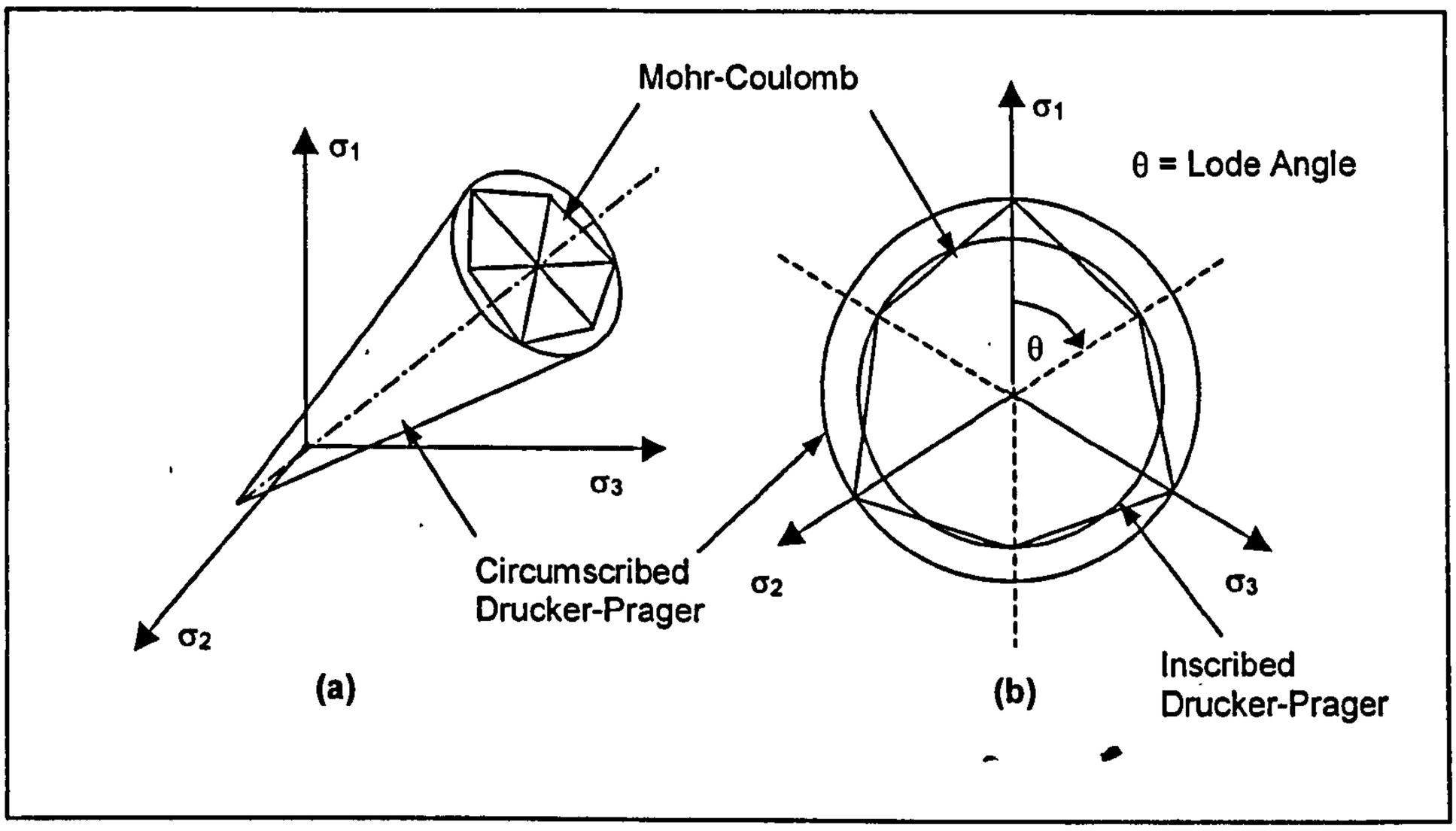

Figure 2.18: Representation of the Mohr-Coulomb and Drucker-Prager yield criterion in (a) Principal stress space; (b) The deviatoric plane

The classical yield criteria presented above have been criticised on the grounds that they do not adequately model the behaviour of materials such as soils. The non-frictional plastic models (Tresca and Von Mises) ignore the fact that soils and rock do have volumetric components to their shear strengths. However, their major deficiency is that the failure surface is adopted as the yield surface, whereas for most geologic materials yielding actually occurs well below the failure surface, often initiating very early. This has also been shown to be true of asphalt mixtures at typical service temperatures, (see Section 2.4.1) [Abdulshafi *et al.*, 1984]. Therefore, it is necessary to define a yield function for continuous yielding behaviour (see below and Section 2.3.7).

Cap and Single Surface Models

'Cap' type yield models represent one approach to modelling continuous yielding response. For such models it is common to define two surfaces, one to describe continuous yielding and one to describe finial state or failure. Figure 2.19 shows a family of yield criteria forming 'caps' to the open-ended Drucker-Prager envelope. As the stress changes from *A* to *B*, the yield criterion also moves as the result of strain hardening. If the stress is reversed, then the material behaves elastically and the yield criterion remains fixed through point B, this is analogous to the strain hardening uniaxial case discussed in Section 2.3.3. If the stress level is then increased to a point on the current yield locus, such as *C*, the material will again become plastic. Therefore the criterion is a reflection of past loading (plastic strain). The critical state concept, first proposed in 1958 by Roscoe, Scholfield and Worth, belongs to this class of models. The advantage of such models is that they provide a unified framework for continuously yielding materials such as soils in which the deviatoric and volumetric stress states are interrelated.

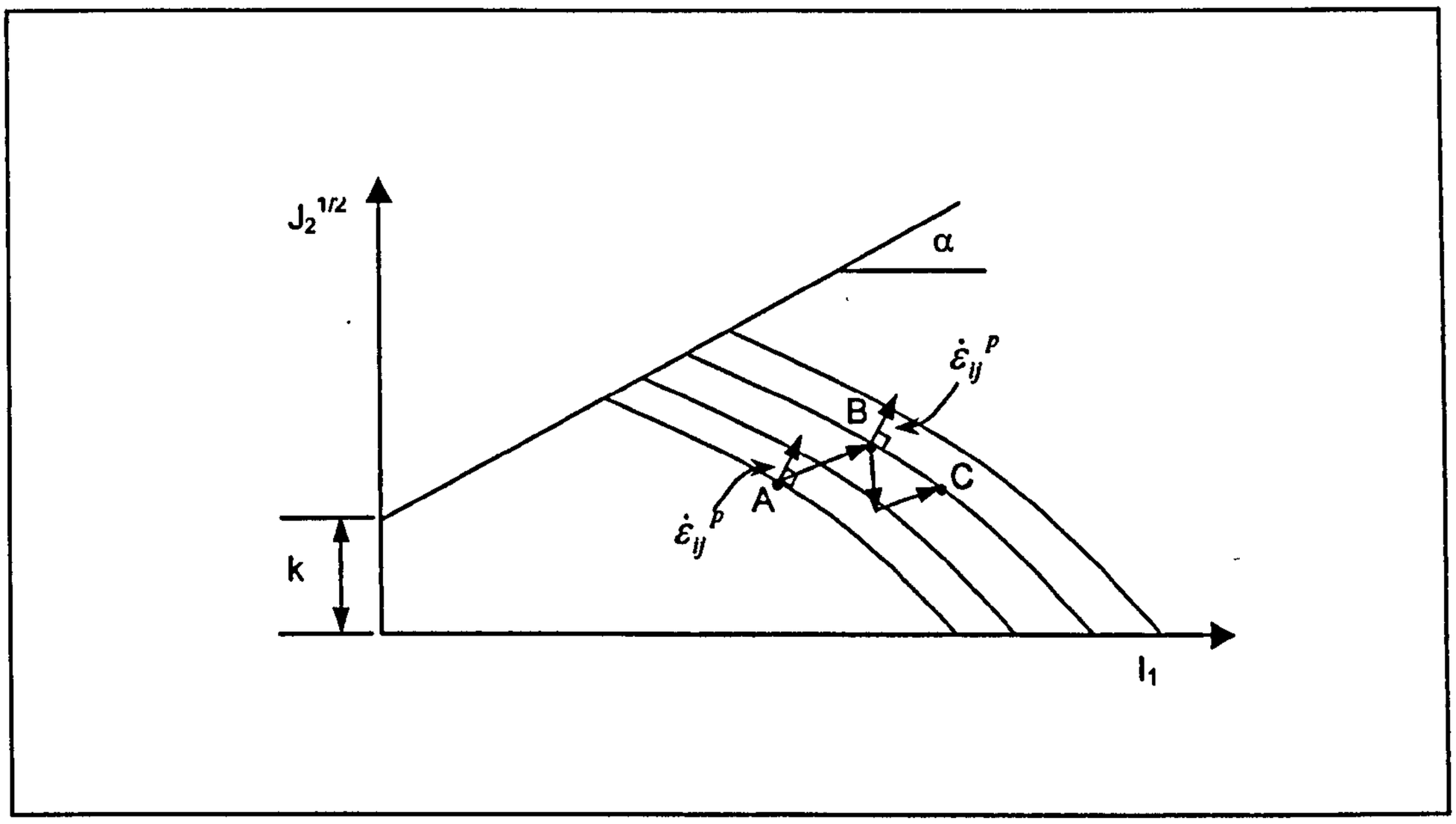

Figure 2.19: Example of strain hardening capped yield criterion

The intersection of two or more independent surfaces that comprise the yield surface of capped models such as the critical state models results in corner point singularities, which can give rise to potential numerical difficulties. To overcome these limitations, various mathematical expression have been postulated for the yield surface, and lead

to some researchers developing single surface yield and plastic potential functions (see Sections 3.3.2 and 2.3.6 respectively) to eliminate the need for multi-surface yield functions altogether [Desai *et al.*, 1986; Lade *et al.*, 1995].

2.3.6 Plastic Potential Functions and the Flow Rule

The yield criterion defines when plasticity will occur but does not reveal the nature of the plastic behaviour. After initial yield, the behaviour of a strain (or work hardening) material is partly elastic and partly plastic. During any increment of stress, the changes of the strain are assumed to be divisible into elastic and plastic components:

$$d\varepsilon_{ij} = d\varepsilon_{ij}^{e} + d\varepsilon_{ij}^{p} \tag{2.12}$$

where, $d\varepsilon_{ij}^{e}$ = elastic strain increment

$d\varepsilon_{ij}^{p}$ = plastic strain increment

The elastic strain increment is related to the stress increment by an incremental form of the relationship given in Equation (2.2). In order to derive the relationship between the plastic strain increment and the stress increment an assumption of material behaviour is made. In uniaxial models it is implicitly assumed that the plastic strain increment will take place in the same direction as the imposed stress. However for the multi-axial case, the situation is more complex, as there are potentially six components of both stress and strain. Therefore in the mathematical theory of plasticity, as well as the yield surface description and subsequent evolution, it is necessary to have some means of specifying the growth of the plastic strain. This is done by assuming that the plastic strain increment is proportional to the stress gradient of a quantity termed the plastic potential, Q, so that:

$$d\varepsilon_{ij}^{p} = d\lambda \frac{\partial Q}{\partial \sigma_{ij}} \tag{2.13}$$

where, $d\lambda$ is a factor of proportionality, termed the plastic multiplier, and the plastic

potential function is similar to the description of the yield surface, F, and is of the form:

$$Q[\sigma_{ij}, m(\varepsilon_{ij}^{p})] = 0 \tag{2.14}$$

where m is a vector of state parameters. Equation (2.13) is termed the flow rule, and is represented diagrammatically in Figure 2.20, which shows a segment of a plastic potential surface plotted in principal stress space.

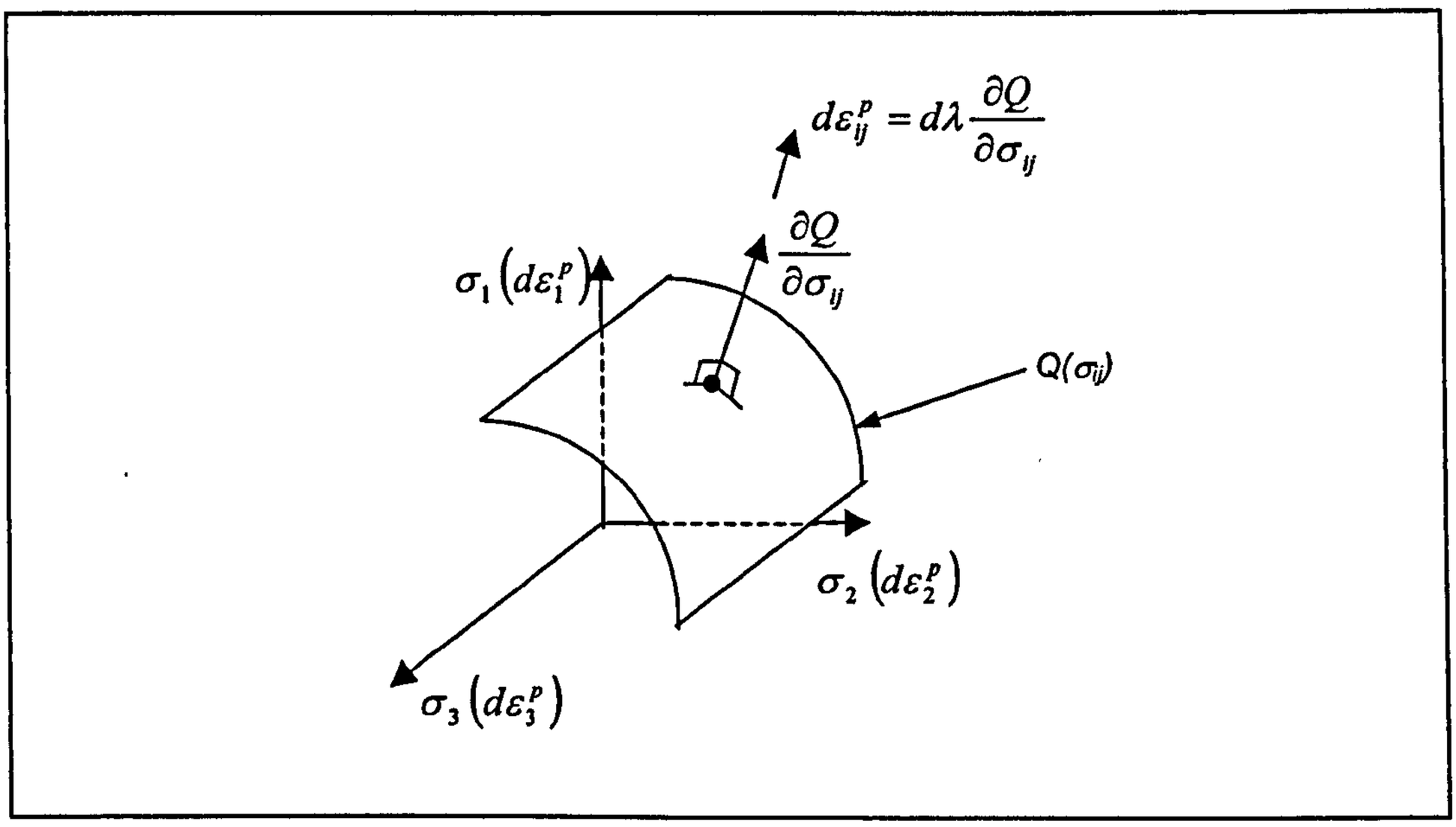

Figure 2.20: Plastic potential surface in principal stress space

The outward vector normal to the plastic potential surface at the current state of stress has components that provide the relative magnitudes of the plastic strain increment components. It should be noted that the normal vector only provides an indication of the relative sizes of the strain components. The value of the scalar parameter $d\lambda$ controls the magnitude, and is dependent on the specified hardening/softening rule. If the plastic potential surface coincides with the yield surface, then the flow rule is said to be associative and the incremental plastic strain vector is then normal to the yield surface and the normality condition is said to apply. In this case the flow rule becomes:

$$d\varepsilon_{ij}^{p} = d\lambda \frac{\partial F}{\partial \sigma_{ij}} \tag{2.15}$$

In a general case, where the yield and plastic potential functions are not coincident, the flow rule is said to be non-associated. Whether a flow rule is associative or non-associative has an effect on the cost implication in FE analysis. An associated flow rule results in symmetric constitutive and stiffness matrices. For a non-associated flow rule both matrices are non-symmetric, the inversion of which is much more costly, both in terms of storage and computation time. For metals, experimental results give good agreement with associative plasticity formulations, however it has been shown that for frictional materials the normality conditions may not necessary apply [McDowell, 2000].

2.3.7 Hardening and Softening Rules

The hardening/softening rules prescribe how the state parameters k vary with plastic straining. For a perfectly plastic material, no hardening or softening rules are required and consequently the state parameter k is constant. In multi-axial situations it is common to relate k to a measure of the total plastic deformation, termed the effective, generalised or equivalent plastic strain. Such hardening/softening rules are then called strain hardening/softening rules. Alternatively, k can be related to the change in plastic work. Such hardening/softening rules are then called work hardening/softening rules.

Typical examples of hardening and softening rules, which can be either 'isotropic' or 'kinematic' in nature, are shown in Figure 2.21. An isotropic hardening rule, Figure 2.21(a), implies that the yield surface expands (or shrinks for softening conditions) in a uniform manner i.e. the position vectors of points on the yield surface change their magnitude by a common factor. Kinematic hardening, Figure 2.21(b), describes the translation of the initial yield surface into a new position without a change of its shape and size, and is important in modelling cyclic behaviour, see Section 2.3.8. The combination of these two principal hardening rules leads to a mixed hardening rule, where the initial yield surface both expands and translates as a consequence of plastic flow.

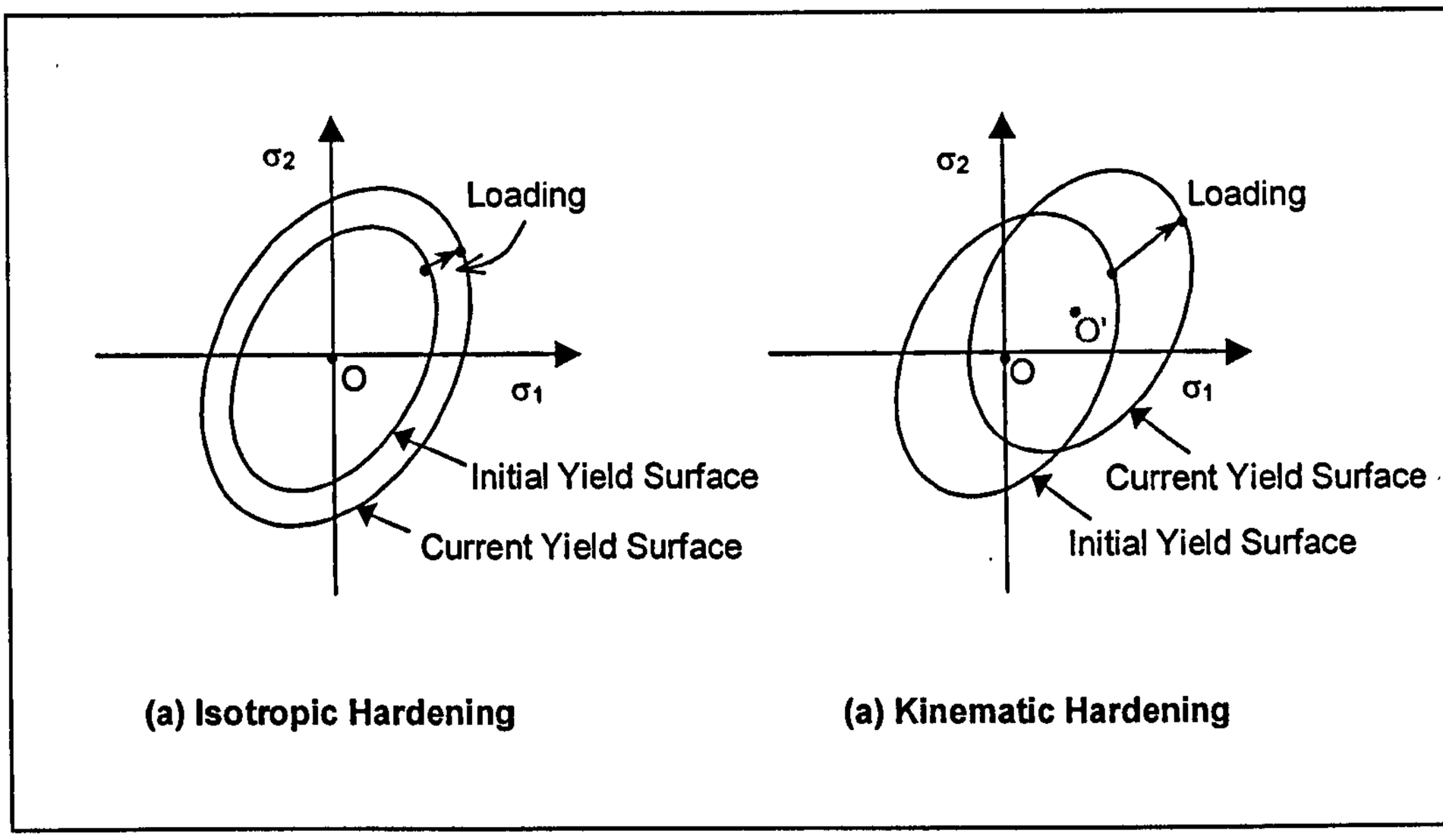

Figure 2.21: Isotropic and kinematic hardening

2.3.8 Constitutive Models for Cyclic Loading

Plasticity based models such as those described in this chapter were originally developed for monotonic loading conditions, such that on primary loading, large plastic strains occur, but on subsequent unloading/reloading cycles, within the yield surface, only purely elastic strains are produced. In such models the size of the elastic region becomes very large. This is not suitable for modelling the response of materials under cyclic loading conditions, such as those experienced in a pavement structure, where in reality, all unloading reloading cycles result in the gradual accumulation of permanent strain and hysteretic material behaviour. Therefore various models or modifications to existing models have been proposed that can account for this type of material behaviour [Desai *et al.*, 1986 & 1990; Bonaquist *et al.*, 1997].

Cyclic loading models generally account for hysteretic behaviour and additional permanent deformations by permitting the yield surface to translate and/or contract on unloading. Desai *et al.* [1986 and 1990] proposed that factors such as non-associativeness and induced anisotropy due to friction and cyclic loading should be introduced as corrections or perturbations to a basic model. The proposed model

considers induced anisotropy by treating it as a manifestation of deviation from normality by using the theory of non-associative plasticity. The model involves the motion of a single potential surface, Q, which visits and intersects the 'fixed' field of yield surfaces, F. The model allows for the continuous accumulation of induced anisotropy during loading unloading and reloading. Figure 2.22 shows a schematic of the general anisotropic hardening model, δ_2, (see Section 3.3.2) in $I_1 - \sqrt{J_2}$ stress space. The plastic potential Q moves in the field of yield surfaces F, defined by the basic model, δ_0, which range from an initial surface F_o, corresponding to the limit of an observed (or chosen) elastic range, to the ultimate failure envelope. For convenience Q is chosen as the initial surface F_o. Surface Q can intersect the fixed surfaces at the stress point during loading, unloading and reloading. Surfaces F serve to define virgin loading and initiation of unloading and reloading, to govern the magnitude of plastic strain increments, and to retain memory of maximum pre-stress. Surface Q acts as the plastic potential during virgin and non-virgin loading, and governs the directions of the plastic strain increments. During non-virgin loading (unloading and reloading), Q also serves as a loading surface allowing for elastic behaviour within its domain, and plastic behaviour beyond its boundaries.

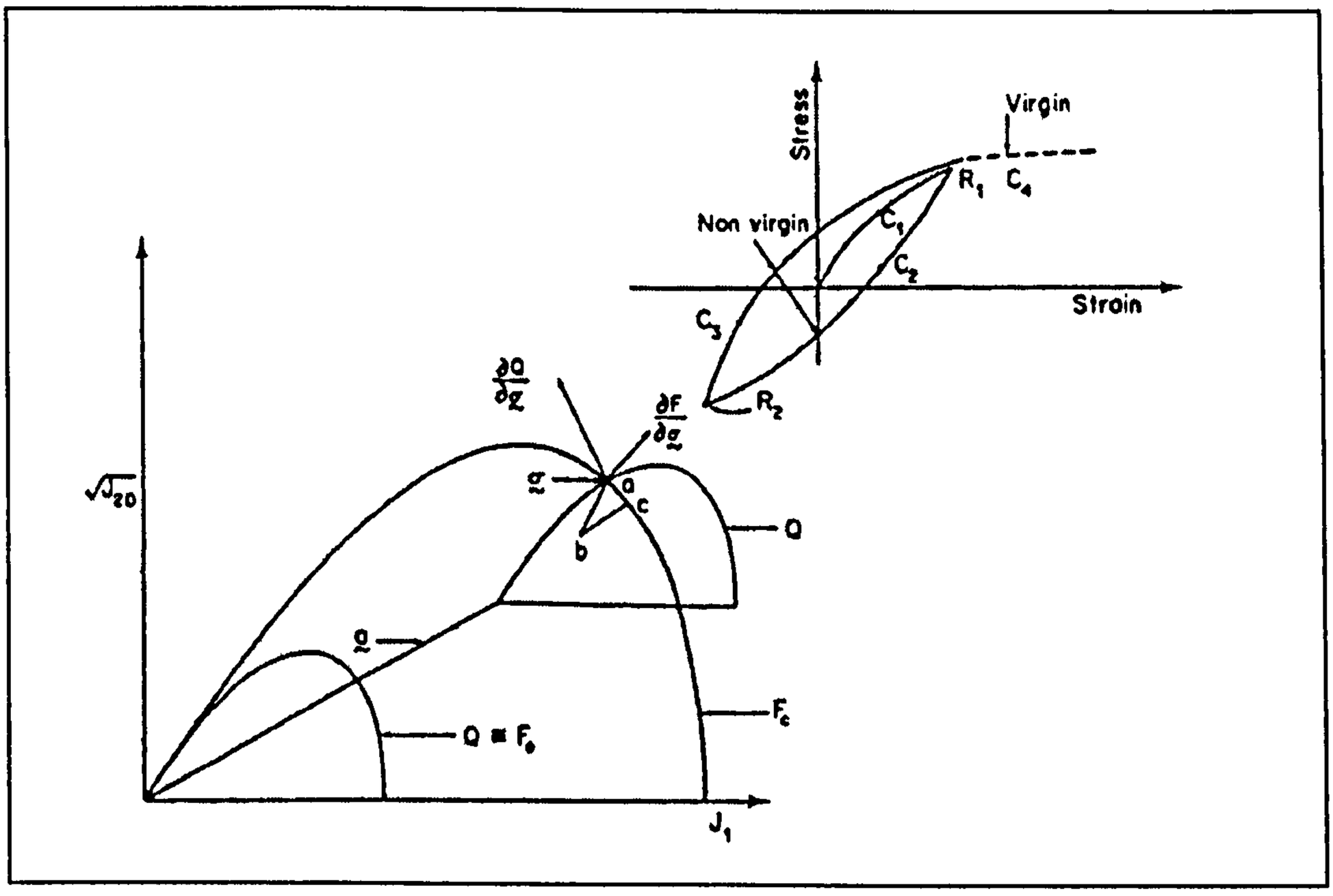

Figure 2.22: Anisotropic hardening model δ_2

[Reproduced from Desai *et al.*, 1986]

Bonaquist *et al.* [1997] proposed a bounding surface approach based on the work by Mroz (1978) to model repeated loading conditions of granular materials, as applied to the Desai hierarchical single surface (HISS) modelling approach (see Section 3.3.2). In contrast to the relatively complex anisotropic hardening model, described above, Bonaquist *et al.* [1997] favour a less complex isotropic model, which although incapable of accounting for the hysteresis loop formed during unloading and subsequent reloading, is capable of modelling the overall permanent deformation behaviour. In the bounding surface approach two yield surfaces are used to describe the repeated loading behaviour of the material, Figure 2.23.

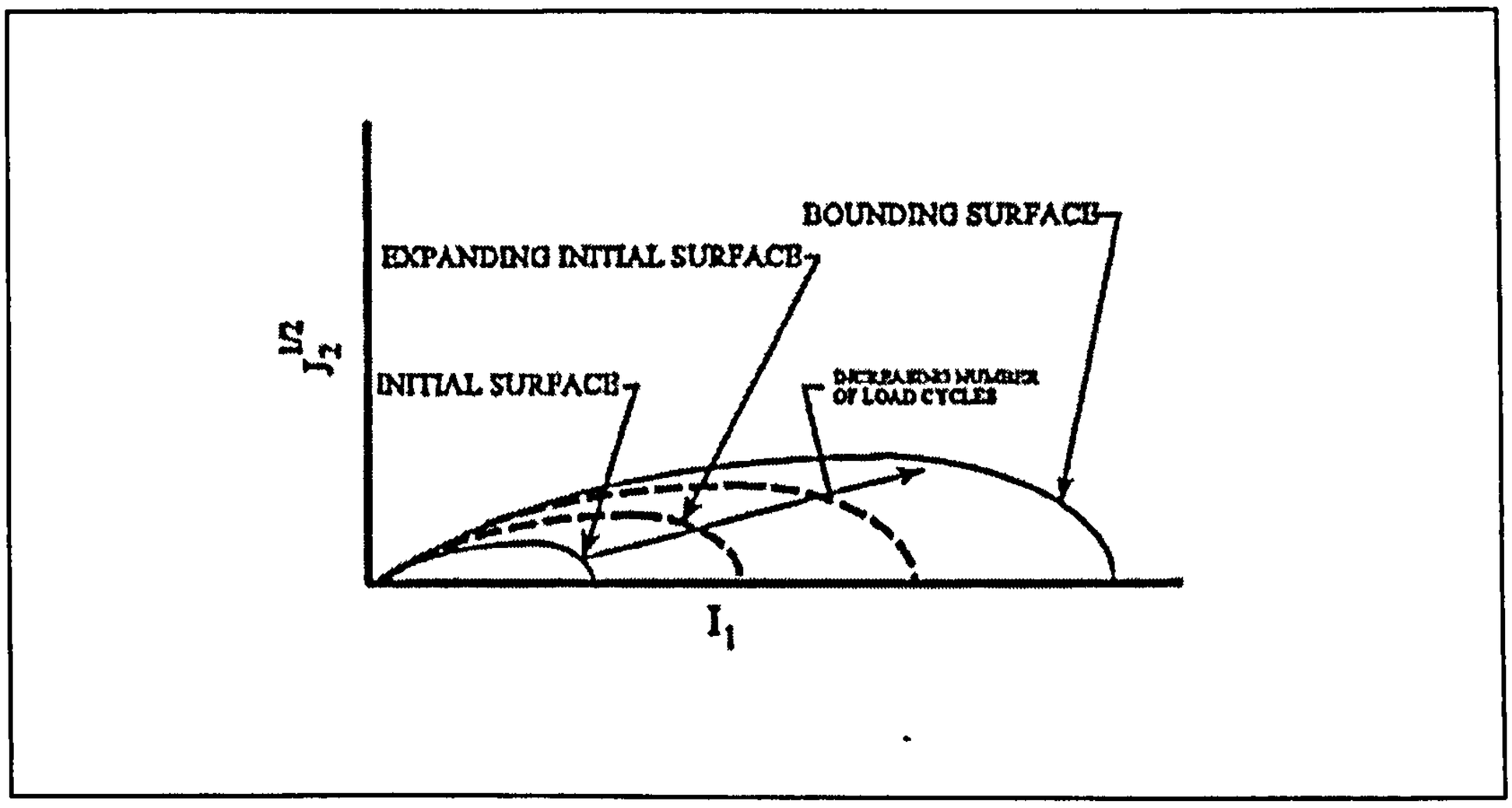

Figure 2.23: Schematic of the bounding surface concept

[Reproduced from Bonaquist *et al.*, 1997]

The first yield surface is the initial surface, which describes the past loading history of the materials. The second surface is the bounding surface, which describes the current state of stress. During repeated loading the initial surface expands while the bounding surface remains stationary. Elastic behaviour corresponds to states of stress within the initial surface, with elastic-plastic behaviour corresponding to states of stress between the initial surface and the bounding surface. When the two surfaces coincide, the response is purely elastic and no additional permanent deformation occurs. The location of the bounding surface is obtained from the basic hierarchical model for the applied stress state, and is characterised by the plastic strain trajectory for the

bounding surface, ξ_b, given by Equation (2.16):

$$\xi_b = \left[\frac{a_1 \left(\frac{I_1}{p_a} \right)^n}{\frac{\gamma I_1^2 - J_2}{p_a^2}} \right]^{1/\eta_1} \tag{2.16}$$

where a_1 and η_1 are material parameters relating to the hardening behaviour or rate at which the subsequent yield surface develops. The deformation behaviour for each load application is also obtained from the basic hierarchical model for the corresponding initial surface. The location of the initial surface changes with the number of load applications and is determined from repeated loading tests. It is characterised by, ξ_i, which represents the sum of the plastic strains that remain effective after unloading. Bonaquist *et al.* [1997] propose a function for the definition of ξ_i, such that the location of the initial surface expands quickly when the number of load repetitions is small, then asymptotically approaches the bounding surface after a large number of load repetitions:

$$\xi_i = \xi_o + \left(1 - \frac{1}{N^{a_2}}\right)(\xi_b - \xi_o) \tag{2.17}$$

where ξ_o = initial location of the initial surface

N = number of load cycles

a_2 = repeated load hardening coefficient

The rate of the expansion of the yield surface during repeated loading is controlled by the exponent a_2, which is determined through repeated load tests.

2.4 Plasticity Based Models for Asphalt Mixtures

2.4.1 Classical Plasticity – Drucker-Prager Yield Criterion

Tan *et al.* [1994] used an idealised elastic-perfectly plastic constitutive model, with a

Drucker-Prager yield criterion, to describe the behaviour of an asphalt mixture loaded in compression until failure, using axisymmetric FE analysis to predict both failure strain and failure stress. A granite based continuously graded asphalt mixture, with a 60/70 penetration grade bitumen binder, of 5.5% by mass, was used in the study. Material properties for the model were determined through monotonic, triaxial compression tests on cylindrical specimens.

To study the effects of temperature, strain rate and confining pressures on the material properties, two sets of triaxial tests were undertaken. In the first set, a series of asphaltic specimens were loaded to failure at a constant confining pressure and deformation rate (50.8 mm/min) for test temperatures ranging from 40°C to 60°C. The tests were then repeated for a range of confining pressures (from 0 to 400 kPa). The maximum deviator stress was then plotted as Mohr circles, from which a Coulomb failure envelope for each temperature could be determined, Figure 2.24. From this the material properties ϕ, the angle of internal friction and c, the cohesion of the asphaltic mixture were recorded. In the second set of experiments a series of specimens were loaded in triaxial compression, until failure, at a constant confining pressure and a constant temperature (40°C) for different test deformation rates, ranging from 4 mm/min to 60 mm/min. In a similar manner to the first set of tests, each condition was repeated at various confining pressures and a failure envelope for each strain rate was defined, Figure 2.25. Combining the results of both experimental sets, Tan *et al.* [1994] observed the friction angle to be independent of both test temperature and strain rate, whereas the cohesion was found to be strongly dependent on both temperature and strain rate.

From these and similar results reported by Nijboer [1948], Tan *et al.* [1994] concluded that the fiction angle, ϕ, is primarily a function of the aggregate contact friction and interlocking and that the cohesion, c, is predominantly governed by the binder and fines mixture properties, whose mechanical behaviour is controlled by binder viscosity.

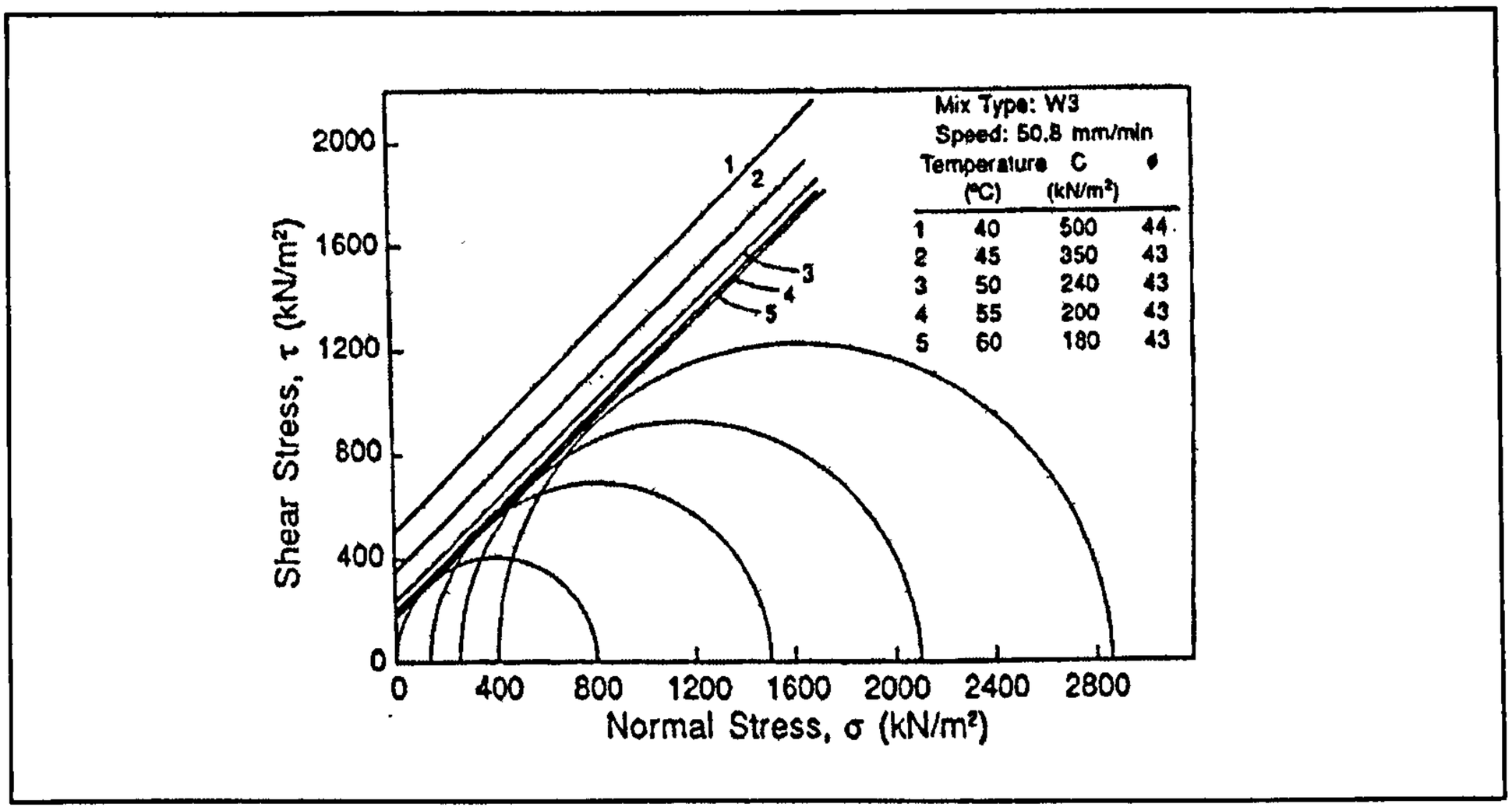

Figure 2.24: Mohr circles and failure envelopes at constant test temperatures

[Reproduced from Tan *et al.*, 1994]

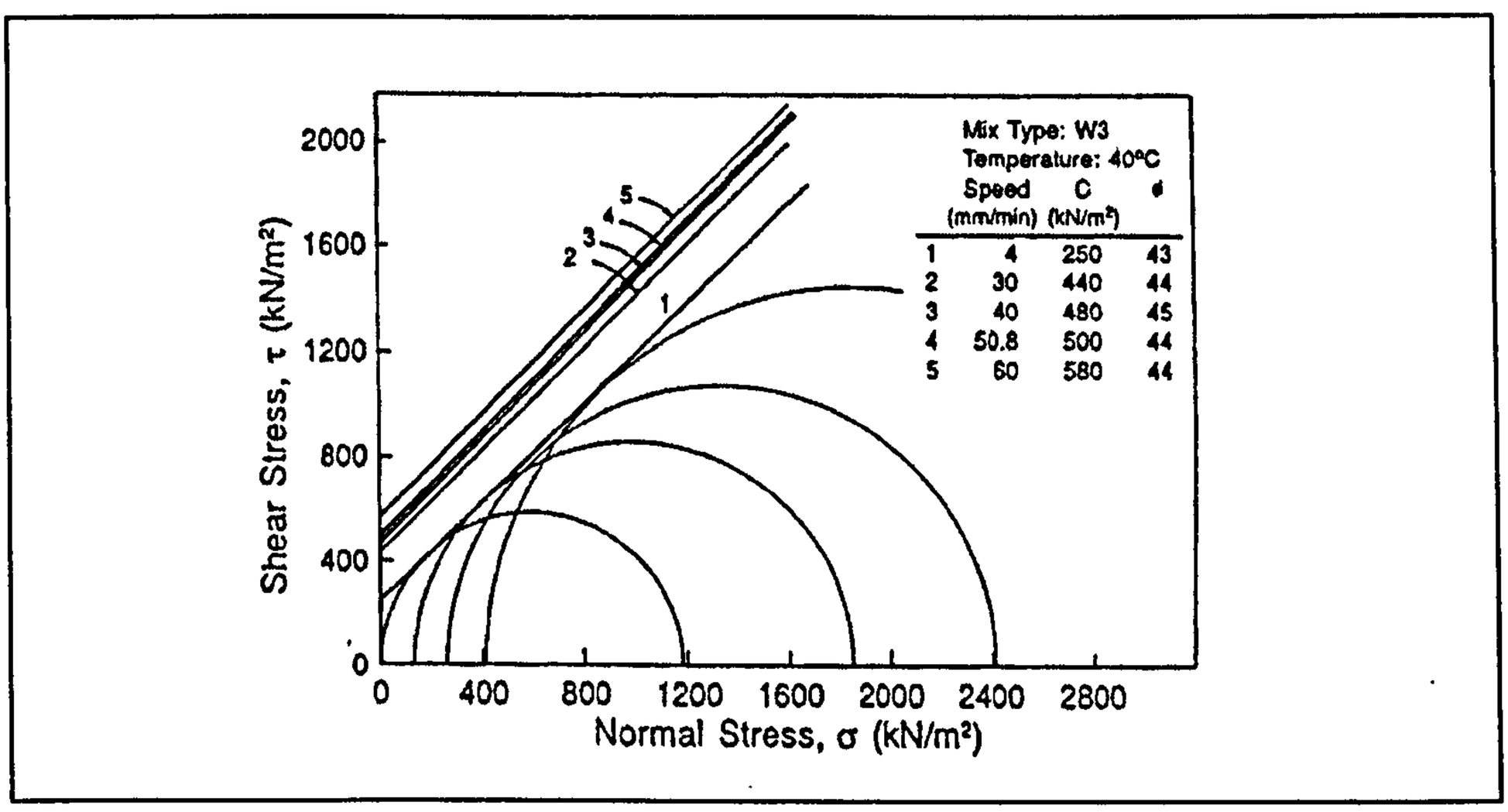

Figure 2.25: Mohr circles and failure envelopes at constant strain rates

[Reproduced from Tan *et al.*, 1994]

To model the stress-strain response of the asphalt mixture up to ultimate load Tan *et al.* [1994] used a plasticity model based on the Drucker-Prager yield criterion described by Equation (2.11). For a stress state on the yield surface Equation (2.11) represents a straight line on a I_1 - $J_2^{1/2}$ plot and the material parameters α and k can be

determined from the slope and intercept of the general failure envelope (Figure 2.19). Alternatively they can be calculated by matching the Drucker-Prager criterion at the external apices of the Mohr-Coulomb criterion, Figure 2.18(b), for which the following relationships can be determined for triaxial compression:

$$\alpha = \frac{2\sin\phi}{\sqrt{3}(3-\sin\phi)} \tag{2.18}$$

$$k = \frac{6c\sin\phi}{\sqrt{3}(3-\sin\phi)} \tag{2.19}$$

These relationships were used in the axisymmetric FE program NONSAP to calculate the material properties for the Drucker-Prager model. Due to symmetry, one quarter of the cylindrical triaxial compression specimen was modelled, using 60 eight-node axisymmetric rectangular elements. Nodal point loads along the side of the specimen represented the confining pressures, with the monotonic load represented by a series of load increments. The elastic modulus of the asphalt mixture was estimated from the initial slope of the triaxial test carried out at the same confining pressure, temperature and strain rate as was modelled. The FE model was used to simulate the stress-strain failure curves of four triaxial tests at confining pressures of 0, 130, 260 and 400 kPa, with the assumed material properties: E = 134 MPa, c = 180 kPa, ϕ = 43° and ν = 0.45. From the failure loads determined from these simulations Mohr's circles could be plotted and a Coulomb envelope determined, as shown in Figure 2.26. An excellent agreement between the numerically simulated and assumed values of c and ϕ was observed. From this Tan *et al.* [1994] concluded that the Drucker-Prager yield criterion could be used for simulating the failure conditions of asphalt mixtures.

Figure 2.27 shows two examples of a comparison between the FE model predicted stress-strain curves and their equivalent experiment measurements. The model can be used to describe the stress-strain behaviour in the elastic range up to peak stress reasonably well. The model was found to predict accurately the peak stress at failure, but to underestimate the axial strain at failure. After passing the peak yield stress,

strain softening behaviour can be observed in the experimental results. However, this post-failure condition could not be modelled using the idealised elastic-perfectly plastic model selected.

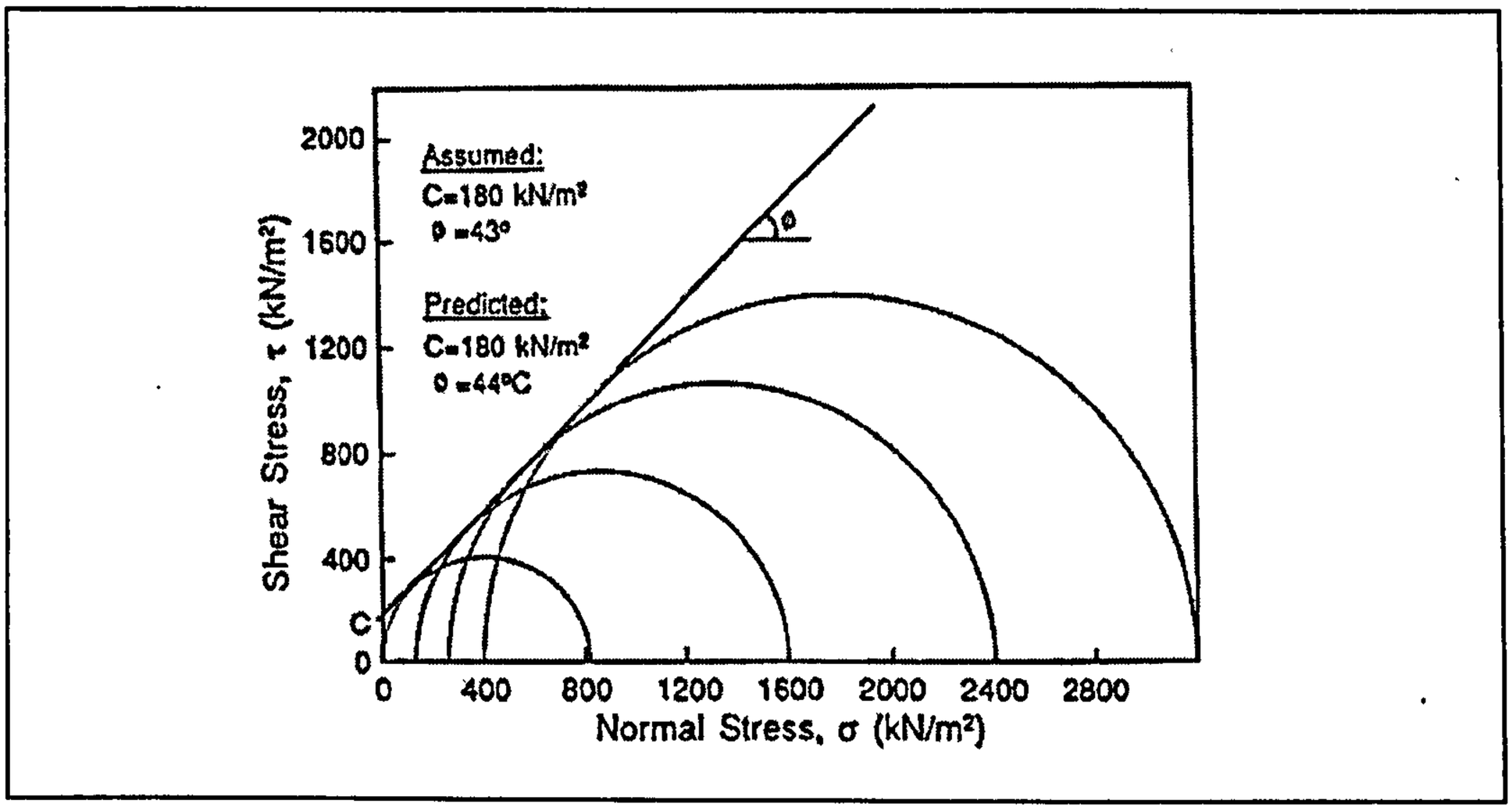

Figure 2.26: Mohr circles and failure envelopes for numerically simulated triaxial tests [Reproduced from Tan *et al.*, 1994]

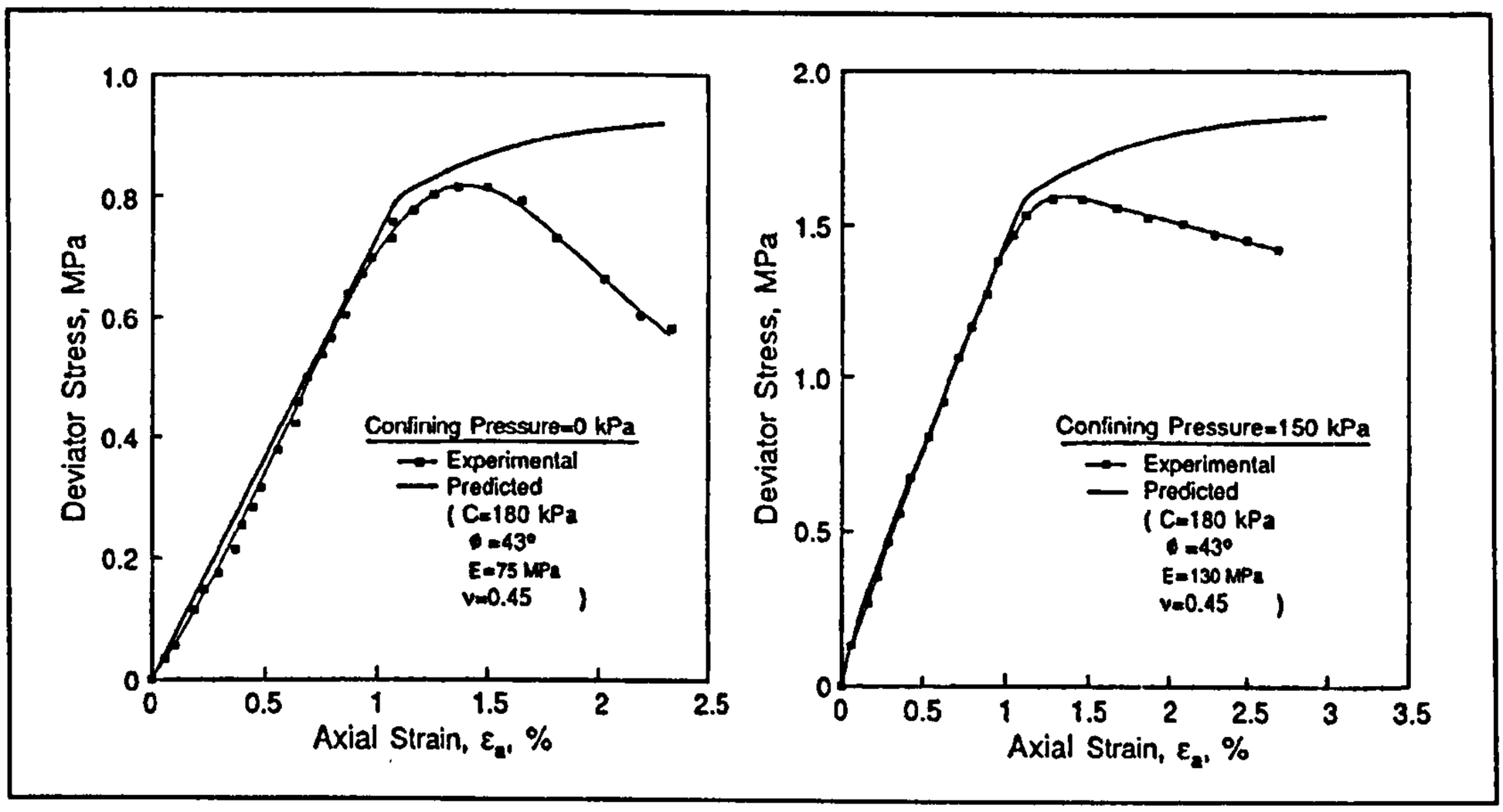

Figure 2.27: Comparison of finite element generated and experimental stress-strain curves [Reproduced from Tan *et al.*, 1994]

Combination Visco-Elastic-Plastic Model

Abdulshafi *et al.* [1984] derived a theoretical 'one-dimensional combo visco-elastic-plastic' constitutive model to characterise asphaltic mixtures and to predict rutting. The theoretical model was then supplemented by an experimentation phase to identify the required material parameters. Incremental creep tests combined with unconfined compression and indirect tensile strength tests were carried out on five laboratory prepared recycled asphaltic mixtures[6]. The model was composed of a Burger[7] type rheological arrangement connected in-series with a friction slider with a Drucker-Prager yield criterion. The total strain was decomposed into groupings of the time-independent response in an elastic-plastic component and the time-dependent response in a visco-elastic component. Therefore, two separate models were constructed, the first to describe the elastic-plastic component and the second the visco-elastic component. In the former model, the elastic strain is related to the total stress through Hooke's Law. The plastic strain is obtained by assuming a Drucker-Prager yield criterion, with associated flow rule and isotropic hardening, with the hardening parameter being a function of plastic work. In the second model, incremental creep phase loading conditions were imposed on the governing differential equations in order to obtain the appropriate form of the constitutive equation. The two models were then combined together, relating the strain increment to the stress increment by a single visco-elastic-plastic compliance, which is a function of the material parameters and time:

$$d\varepsilon_1(t) = C_{VEP}\,\sigma_1 \tag{2.20}$$

in which

$$C_{VEP} = \left(\underbrace{\left(\frac{t}{\eta_2}\right) + \left(\frac{1}{E_1}\right)\left[1 - \exp\left(-\frac{E_1}{\eta_1}t\right)\right]}_{\textit{visco-elatic model}} + \underbrace{\left(\frac{1}{E_2}\right) + \left\langle \frac{n_1^2}{H(W_p)} \right\rangle}_{\textit{elastic-plastic model}} \right) \tag{2.20a}$$

---

[6] Although triaxial testing of the asphalt mixtures was cited as a suitable experimental method for parameter determination, the authors' preference was to employ evaluation methods routinely in use in asphalt testing.

[7] A Burger rheological model consists of a Maxwell and Kelvin model (Figures 2.7 and 2.8) connected in series.

where, C_{VEP} = visco-elastic-plastic compliance

E_1 = uniaxial elastic spring coefficient in the visco-elastic model

E_2 = uniaxial elastic spring coefficient in the elastic-plastic model

η_1 = in parallel (with E_1) Newtonian damper viscosity coefficient

η_2 = in series Newtonian damper viscosity coefficient

t = time scale

n_1 = flow parameter

$H(W_p)$ = hardening parameter

In the experimental verification of the theoretical model, a true yield surface for the asphalt mixtures was determined based on the results of creep tests carried out at 70°F (≈ 21°C). Yielding was found to occur at around 75 psi (≈ 0.52 MPa) in compression and 3 psi (≈ 0.021 MPa) in tension. These values were found by plotting the relationship between the steady-state creep rate at different stress levels versus the stress, where the relationship between stress and the steady-state strain rate, $\dot{\varepsilon}_{ss}$, is of the form:

$$\dot{\varepsilon}_{ss} = A\sigma^n \tag{2.21}$$

in which A and n are material constants that are stress dependent. For low stress and strain levels if asphalt mixtures are to be considered linear visco-elastic, then $n = 1$ and $A\sigma$ = constant. However, at high stress and strain levels the material behaviour is expected to become non-linear. For the visco-elastic-plastic model proposed, the friction slider represents the element that possesses material non-linearity. Consequently a plot of steady-state creep rate versus stress level, Figure 2.28, could be used to determine the stress level at which non-linearity occurs, which was termed the yield point. Back extrapolation to $\dot{\varepsilon}_{ss} = 0$ was then used to determine the yield stress for compressive and tensile states.

From Figure 2.28 it can also be observed that, for the compressive creep test data, the material coefficients A and n do not change until a stress level in excess of 60 psi, thus substantiating the previous linear visco-elastic hypothesis for asphalt mixtures at

lower stress and strain levels. Based on this work Abdulshafi *et al.* [1984] proposed that plastic deformation should be accounted for in pavement characterisation as actual stress levels on pavement surfaces can exceed 75 psi (≈ 0.52 MPa).

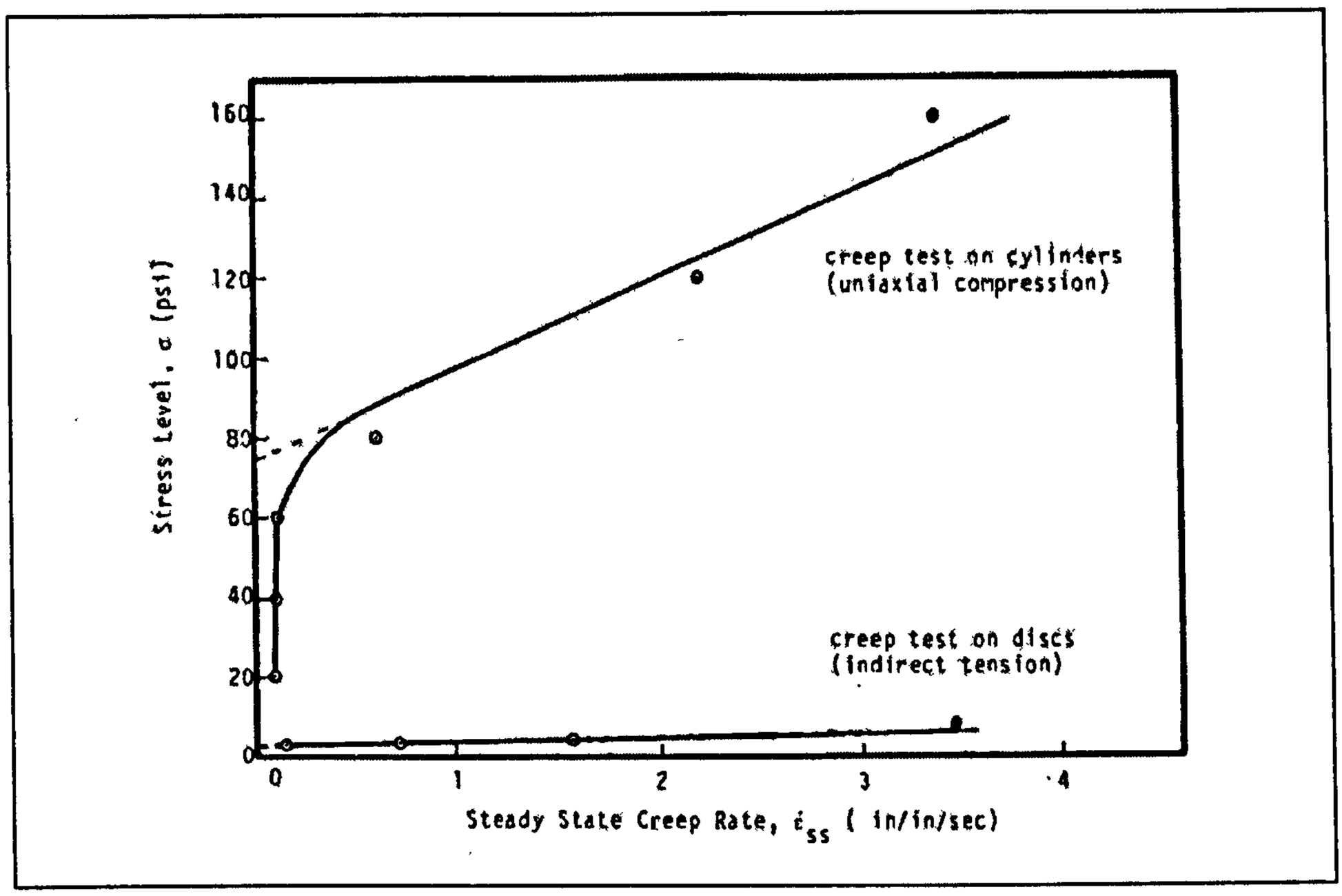

Figure 2.28: Steady-state deformation rate versus stress level curve

[Reproduced from Abdulshafi *et al.*, 1984]

2.4.2 Visco-Plasticity

It has been shown above, that plasticity models can be used to simulate some of the behavioural aspects of asphaltic materials. However, one of the fundamental assumptions of classical plasticity, that of time independence of the equations of state, makes the simultaneous description of the plastic and rheological properties of a material impossible. The resulting simulated material response is therefore time independent, meaning that all non-liner effects happen instantaneously (although in FE analysis a pseudo-time is frequently used in order to trace the evolution of non-linear behaviour). Therefore, Scarpas *et al.* [1997] proposed that visco-plasticity, a phenomenological approach to modelling materials that exhibit both plastic and creep behaviour could provide a suitable framework in which to develop a response model for asphaltic materials, which display time dependent viscous properties.

Scarpas *et al.* [1997] presents a framework for, and the preliminary stages of, an investigation undertaken at Delft University of Technology, whose goal is the development and finite element implementation of a three-dimensional, strain rate sensitive, temperature and history dependant constitutive model of asphaltic concrete. In a prototype formulation the constitutive model has been implemented in a three-dimensional FE code and used to simulate material damage response and to investigate the dynamic non-linear response of asphalt pavements to the Falling Weight Deflectometer (FWD), at discrete temperatures. In the preliminary phase of the investigation, the results of uniaxial tests carried out on a Dutch dense asphalt mixture were used to identify the basic components of the formalistic model and their interaction [Scarpas *et al.* 1997].

Figure 2.29 diagrammatically represents the idealised behaviour that is observed during an incremental creep test on an asphalt mixture.

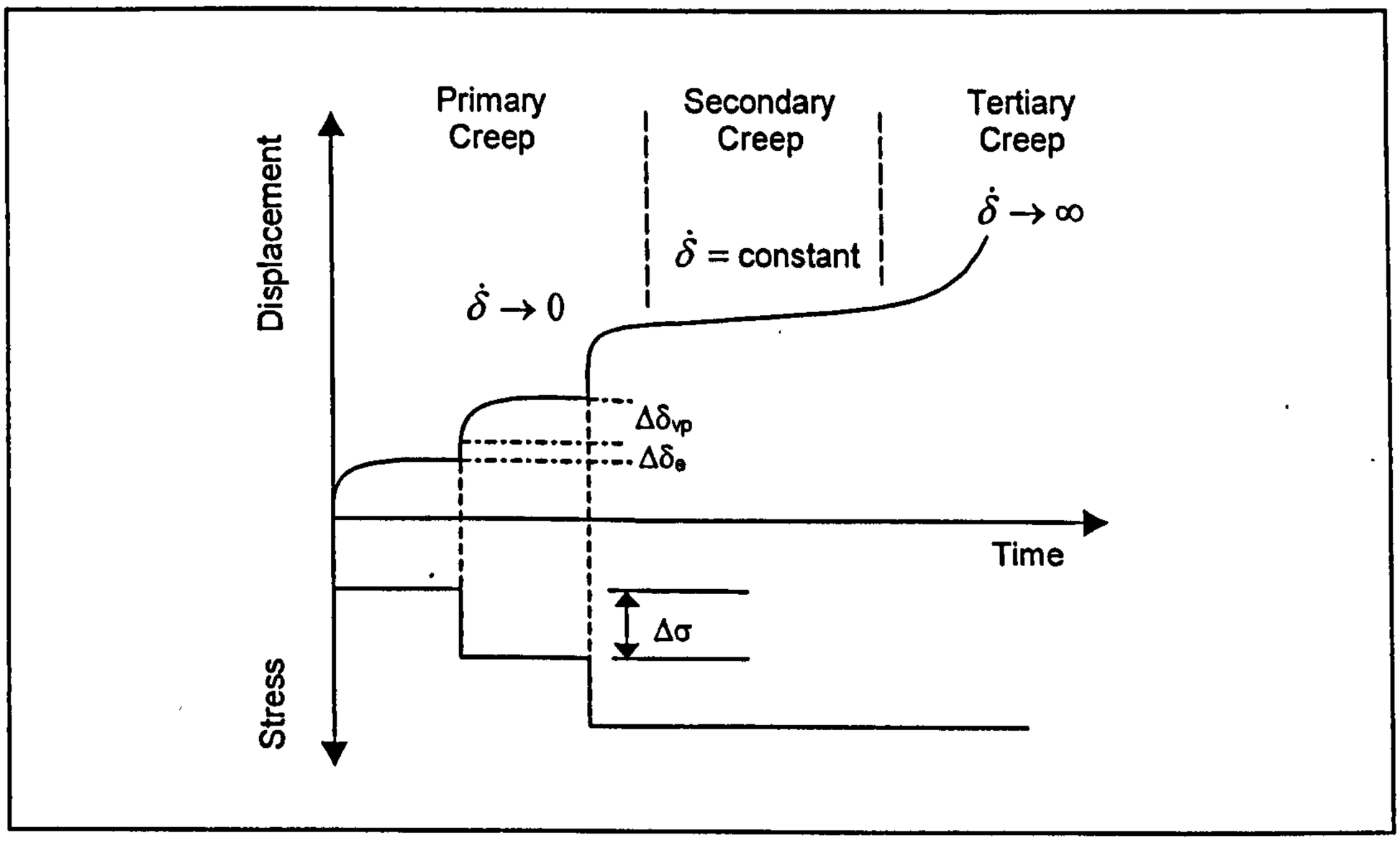

Figure 2.29: Idealised incremental creep test on an asphaltic mixture [Reproduced from Scarpas *et al.* 1997]

Three time dependent phases of material response can be observed in Figure 2.28; these are primary creep, secondary creep and tertiary creep. Retaining the

fundamental to classical plasticity notions of a yield surface, decomposition of strains and hardening, Scarpas *et al.* [1997] present Perzyna [1966] type visco-plasticity as a framework in which to model these three observed stages of time dependent asphaltic concrete response. A brief review of visco-plasticity is presented in Appendix A, from which, according to Perzyna [1966] and in analogy to classical incremental plasticity, the visco-plastic strain rate vector, $\dot{\varepsilon}_{ij}^{vp}$, can be determined by means of a flow rule, expressed as:

$$\dot{\varepsilon}_{ij}^{vp} = \Gamma\langle\Phi(F)\rangle\frac{\partial g}{\partial \sigma_{ij}} \tag{2.22}$$

in which Γ is an experimentally determined material fluidity parameter, $\langle\Phi(F)\rangle$ is the visco-plastic flow function and $(\partial g/\partial\sigma_{ij})$ is some measure of the direction of the visco-plastic straining[8]. In analogy with classical plasticity, Section 2.3.5, a geometric locus of states of stress corresponding to the same level of viscous flow, k_h, defines the flow (yield) surface:

$$F(\sigma_{ij}, k_h) = 0 \tag{2.23}$$

For elastic states of stress, inside the flow surface:

$$F(\sigma_{ij}, k_h) < 0 \tag{2.23a}$$

whereas, for a state of stress outside the flow surface[9]:

$$F(\sigma_{ij}, k_h) > 0 \tag{2.23b}$$

---

[8] For definitions of Γ and $\langle\Phi(F)\rangle$ see Appendix A, Equation A.6 and Equations A.11 - A.14 respectively.

[9] The presence of stresses outside the yield surface constitutes the main difference between the theories of classical plasticity and visco-plasticity, and is in fact the generating cause of visco-plastic effects.

Referring again to Figure 2.29, during the primary creep phase, arrest of the viscous flow can be observed when the rate of deformation, $\dot{\delta}$, tends to zero. This would imply that straining of the asphalt mixture results in an increased resistance to further deformations, i.e. the material is exhibiting strain or work hardening (see Sections 2.3.3 and 2.3.7). Scarpas *et al.* [1997] propose that this could be simulated by assuming that as a result of viscous straining, the size of the flow surface increases until it encompasses the imposed state of stress, implying a functional relationship of the type:

$$k_h = k_h\left(\varepsilon_{ij}^{vp}\right) \tag{2.24}$$

where, ε_{ij}^{vp} = visco-plastic strain

For stress levels below a critical limit, hardening of the asphaltic mixture is responsible for the arrest of viscous flow. However, for larger stress levels, flow does not arrest and initiation of the secondary creep phase is observed, Figure 2.29. The presence of a critical stress limit indicates that hardening does not continue indefinitely. Without this critical limit the arrest of viscous flow would occur for any stress level, implying that a material had infinite strength. In the prototype model formulation, the above critical limit stress is extended to a general 'secondary creep initiation surface' for multi-axial states of stress. Specification of a suitable functional form of k_h then ensures that the flow surface expands only up to the size of this secondary creep initiation surface [Scarpas *et al.*, 1997]. Thus, for a state of stress outside the secondary creep initiation surface, the visco-plastic flow function $\langle\Phi(F)\rangle$ is constant. Therefore, according to Equation (2.22) the resulting rate of change of visco-plastic strain is constant throughout the secondary creep phase of material response.

The final phase of the creep test, tertiary creep, Figure 2.29, is initiated after a certain period of constant viscous flow (secondary creep). It is characterised by a rapid increase in deformations and eventual loss of load carrying capacity of the specimen. Comparing the similarities between rate controlled monotonic displacement tests and

incremental creep tests Scarpas *et al.* [1997] conclude that material strength degradation can be considered the cause of initiation of the tertiary creep phase. With reference to Figure 2.30, Scarpas *et al.* [1997] highlight the fundamental equivalency of the aforementioned tests.

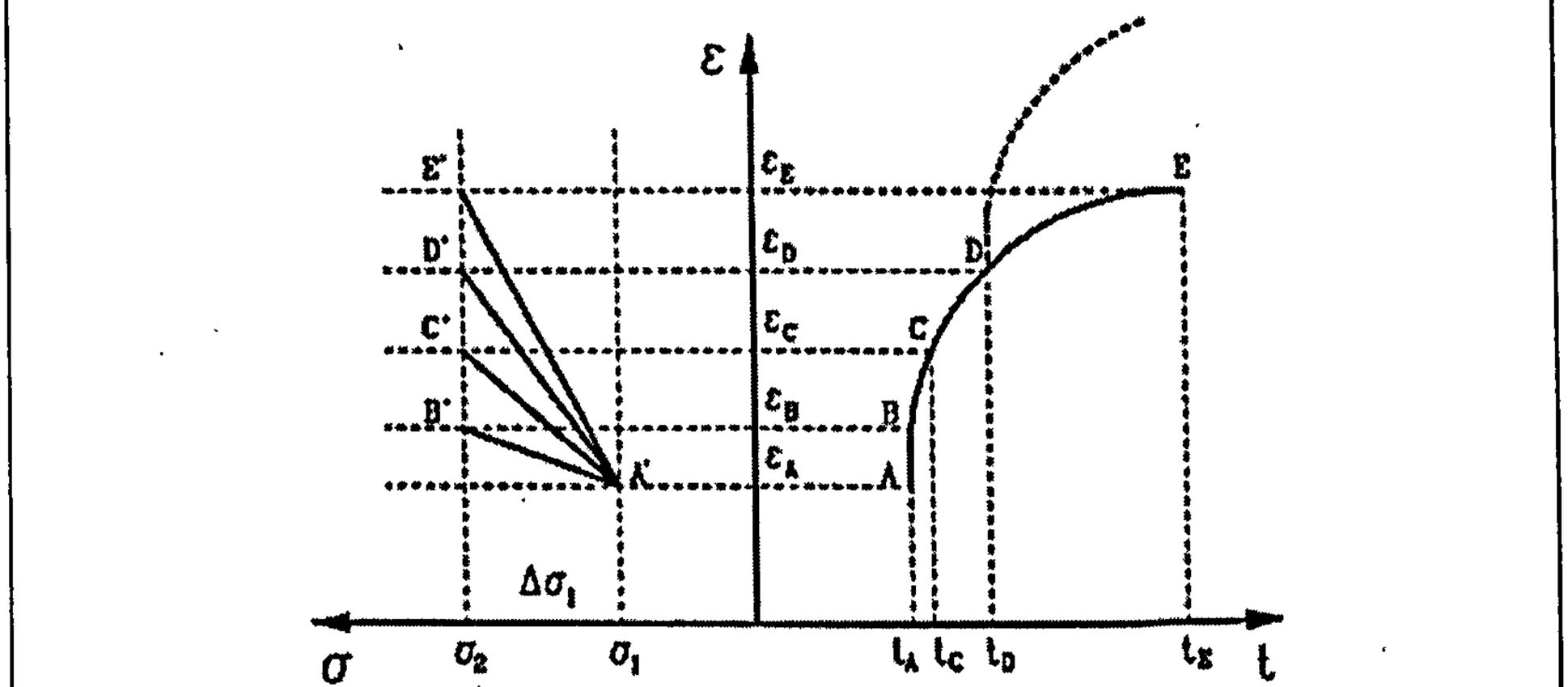

Figure 2.30: Influence of loading rate on creep response

[Reproduced from Scarpas *et al.* 1997]

The figure shows a typical step of the incremental creep test during the primary creep phase, where path *ABE* denotes the ε - t response of the asphalt mixture to the applied stress increment $\Delta\sigma_1$ at time t_A. This response plots as line $A'E'$ in σ - ε space. Arrest of the material flow can be observed to occur at time t_E. However, if instead of waiting for the arrest of viscous flow at t_E, the next stress increment is applied at time t_D then, the observed increment of strain corresponding to $\Delta\sigma_1$ is equal to $\Delta\varepsilon_D = \varepsilon_D - \varepsilon_A$, which plots as line $A'D'$ in σ - ε space. Therefore, if progressively shorter time intervals are considered corresponding smaller increments of strain will be recorded. This results in an apparent stiffing effect in the response of the material such that:

$$\frac{\Delta\sigma_1}{\Delta\varepsilon_E} < \frac{\Delta\sigma_1}{\Delta\varepsilon_D} < \frac{\Delta\sigma_1}{\Delta\varepsilon_C} \tag{2.25}$$

This stiffening effect is a consequence of the smaller time increments that prevent the full extent of viscous flow developing. Reducing the time intervals between successive stress increments is physically equivalent to performing the test at increasingly faster loading rates. Therefore, if in addition, the magnitude of the stress increment is also reduced, the incremental creep test becomes fundamentally equivalent to the rate controlled monotonic test. Scarpas *et al.* [1997] comment that the rate induced hardening effect typical of monotonic tests (such as those shown in Figure 2.25) can be interpreted as a manifestation of the retarded viscous flow of the material.

Scarpas *et al.* [1997] postulate that in actual engineering tests the development of viscous flow has a detrimental effect on the ultimate strength of a material. Where the ultimate strength represents a hypothetical monotonic test performed at an infinitely fast loading rate. Therefore, for realistic loading rates and uniaxial test conditions Scarpas *et al.* [1997] specifies the apparent strength of the material as a decaying function of the ultimate strength. In analogy to this uniaxial case an 'ultimate strength surface', F_u, is then postulated to represent the multi-axial strength of the material:

$$F_u\left(\sigma_{ij}, k_s\right) = 0 \tag{2.26}$$

in which, k_s, controls the size of the surface and is defined as a decaying function of viscous flow, such that the size of the flow surface, or 'apparent strength surface', diminishes until it encompasses the imposed state of stress.

$$k_s = k_s\left(\varepsilon_{ij}^{vp}\right) \tag{2.27}$$

Thereby Scarpas *et al.* [1997] specify the initiation of tertiary creep when the imposed state of stress in the material exceeds the progressively diminishing size of the apparent strength surface.

On the basis of the model components identified above a prototype constitutive formulation, utilising an adapted form of the basic Desai HISS model as the flow

surface (see Section 3.3), was implemented in the FE code CAPA-3D (Computer aided pavement analysis in three-dimensions) and used to simulate damage, due to a circular uniformly distributed load, in a visco-plastic material specimen [Al-khoury, 1993; Scarpas *et al.*, 1997]. Due to axial symmetry one quarter of a cylindrical specimen was modelled, shown in Figure 2.31(a). Considering the deflections of the material specimen, shown in Figure 2.31(b), Scarpas *et al.* [1997] describe an overall double bending flexural mode of deformation, with curvature reversal near the edge of the loaded area. Scarpas *et al.* [1997] report that the elements under the vicinity of the load are subject to large shearing deformations and that due to the double bending mode some elements are subject to compression in the horizontal direction and some to tension.

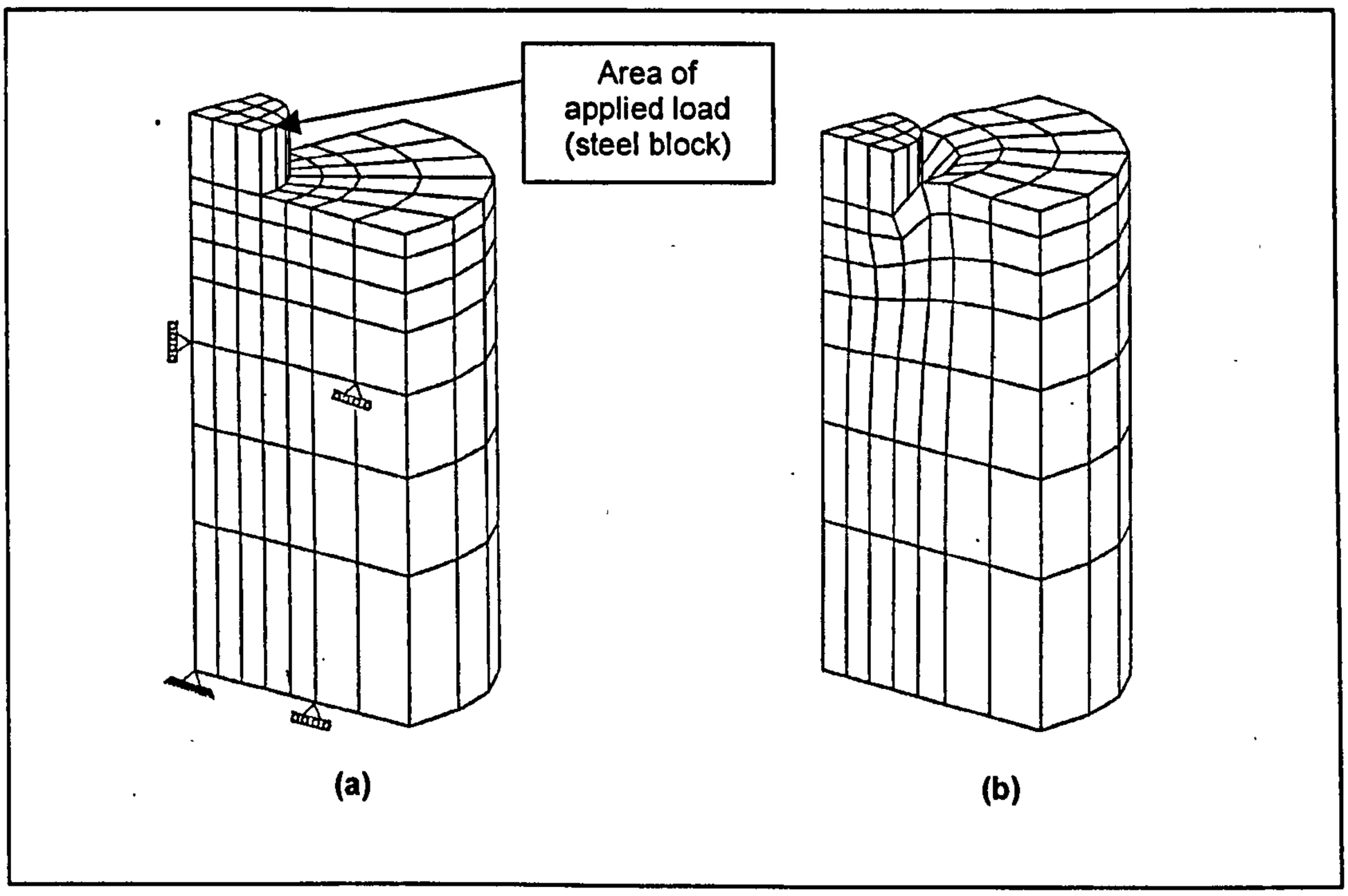

Figure 2.31: Simulated visco-plastic material specimen showing a) Initial one quarter FE mesh; and b) Loaded FE mesh [Reproduced from Al-khoury, 1993]

Figure 2.32 shows the damage distribution in the material specimen during various stages of loading, in which damage is defined as the magnitude of plastic strain in the material, given by Equation (2.28).

$$\xi = \sum d\xi \tag{2.28}$$

in which,

$$d\xi = \left(d\varepsilon_{ij}^{p} \cdot d\varepsilon_{ij}^{p}\right)^{\frac{1}{2}} \tag{2.28a}$$

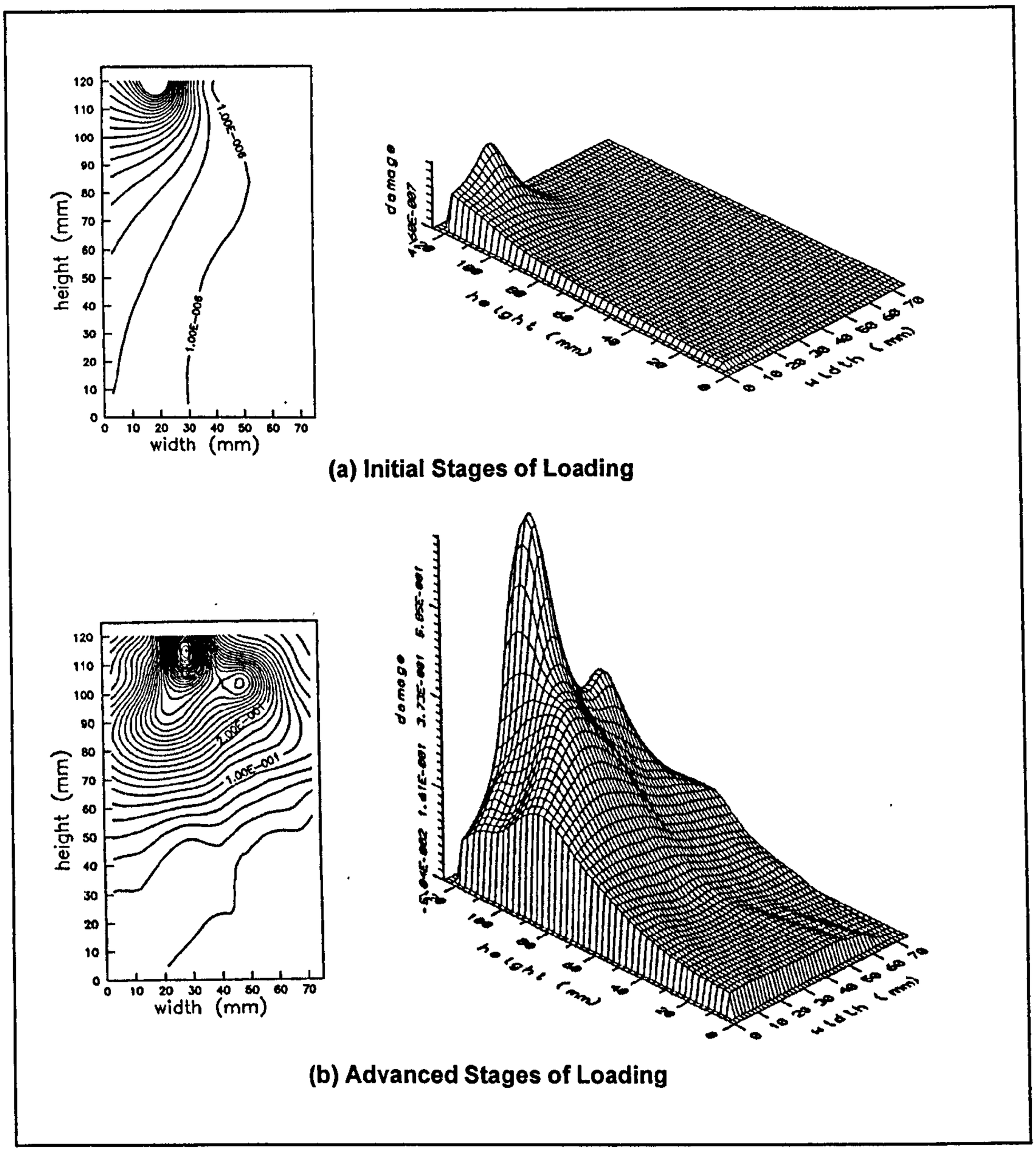

Figure 2.32: Simulated distribution of damage in a visco-plastic material specimen a) Initial stages of loading; b) Advanced stages of loading [Reproduced from Scarpas *et al.*, 1997]

Scarpas *et al.* [1997] use the damage plots shown in Figure 2.32 in support of the conjecture that damage induced in a pavement due to load, will vary in both the

vertical but also the horizontal directions. The plots show that as the degree of confinement decreases, i.e. the state of stress in the horizontal direction changes from compressive under the centre of the load, to tensile at the outer load edges, the level of damage induced in the material increases. Scarpas *et al.* [1997] state that neglecting this influence of the horizontal stress component, constitutes one of the main pitfalls of non-linear pavement simulation by multi-layer approaches, where the material properties are assumed constant across the thickness of a layer.

2.5 Summary

In this chapter it has been shown that asphaltic materials only satisfy the assumptions of linear elastic theory under limited conditions. These are at low temperatures and short loading times where the materials act as glassy solids, or at high temperatures and long loading times where asphaltic materials behave as Newtonian fluids. At intermediate temperatures and loading times, typical of in-service pavement conditions, asphaltic materials generally exhibit non-linear stress-strain relationships and display not only elastic but also viscous and plastic strains as a result of typical wheel loading. Traditional pavement design methods generally make use of linear elastic theory to describe asphaltic material response and approximate techniques for dealing with the non-linear behaviour of the pavement foundation. However, these techniques, which are routinely used in pavement engineering to assess pavement deterioration, ultimately do not fully describe the complex behaviour of asphalts and other road paving materials. They do not take into account the visco-elastic, plastic and non-linear behaviour of asphalts and involve the simplification of both the pavement structure and the loading conditions. However, as computational and numerical capabilities have developed, more realistic modelling of pavements has become possible. Finite element methods provide a basis for this and can be used to address some the complexities of asphaltic material response, whilst also providing the versatility to enable the study of a wide range of pavement geometries and loading conditions.

A key area in the use of FE methods is the identification and/or development of appropriate constitutive material models for asphalts and other paving materials. In

this chapter plasticity based models have been identified as a class of material models that offer both realism and sound numerical performance. It has been shown that classical plasticity models, that take account of both hydrostatic and deviatoric stress states, such as Drucker-Prager based yield models, can be used to predict some aspects of asphalt mixture response, such as compressive failure (peak) stress [Tan *et al.*, 1994]. However, such classical models do not take into account the pre-peak hardening and/or post peak softening response exhibited by asphaltic materials and therefore fail to simulate accurately material strain response. Nor do such models take into account the time dependant nature of asphaltic material response. It has been shown through a combination of plasticity and traditional visco-elastic rheological based models that some of the time dependent properties of asphalt mixtures can be simulated, and that at typical in-service temperatures of approximately 20°C, asphalt mixtures display continuous yielding [Abdulshafi *et al.*, 1984]. Based on the response of asphalt mixtures to creep testing, the basic components of a formalistic strain rate sensitive model for asphalt mixtures has been presented [Scarpas *et al.*, 1997].

The chapter has identified the need for a plasticity based, hydrostatic and deviatoric stress state sensitive, continuously yielding, strain hardening/softening constitutive model that can describe strain rate, temperature and time dependent material properties as being a necessary pre-requisite to enable greater accuracy in the description of asphaltic material behaviour.

Chapter 3 - Asphalt Concrete Response Model

3.1 Introduction

This chapter presents the framework for the constitutive model used in this study. The model, developed recently at Delft University of Technology, incorporates many of the necessary prerequisites identified in Chapter 2, such as rate, temperature, hardening and softening effects, that are required for the accurate modelling of asphaltic material response, whilst also providing the functionality of FE implementation. In the first sections of this chapter the constitutive framework for the model is presented and the model material parameters are discussed. This is followed by an outline of the required experimental work and the presentation of a methodology for the determination of the material parameters based on results from monotonic laboratory tests. In the final section a review of previous research, relating to the investigation and characterisation of asphaltic materials by means of monotonic laboratory experiments, is presented.

3.2 Background

Scarpas *et al.* [1997, 1998a & 1998b] and Erkens *et al.* [2000b] present a review of an extensive investigation into the response of asphalt concrete that was undertaken in the recent past at Delft University of Technology in the Netherlands. The goal of this Asphalt Concrete Response (ACRe) project was the development and finite element implementation of a three-dimensional, strain rate sensitive, loading history and temperature dependent constitutive model for asphaltic materials. In the preliminary phases of this investigation, the basic formalistic components of the model were identified from a series of simple laboratory tests (Section 2.4.2) [Scarpas *et al.*, 1997]. The results from these tests were then used for both model development and calibration (Section 3.3) [Scarpas *et al.*, 1998a], and also to define additional test requirements for the experimental procedures subsequently developed by Erkens *et al.* [1998 and 2000a] (Sections 3.4 and 3.5.4).

3.3 ACRe Constitutive Model Formulation

In the following section the constitutive framework for the ACRe model, described above, is presented. Details of some of the previous stages of the model development and prototype formulation can be found in Scarpas *et al.* [1997] and have been presented in Section 2.4.2. The current formulation of the model is based within the framework of dynamic plasticity. By retaining the fundamentals of the classical plasticity notions of flow surface, decomposition of strains, hardening and softening, Scarpas *et al.* [1998a] presents the theory as an attempt to provide a realistic, unified phenomenological modelling approach for materials, such as asphalt, that exhibit rate dependent inelastic deformations.

3.3.1 Constitutive Framework

In analogy to inviscid incremental plasticity, the total strain rate can be divided into elastic and plastic components:

$$\dot{\varepsilon} = \dot{\varepsilon}_e + \dot{\varepsilon}_p \tag{3.1}$$

where the elastic component, $\dot{\varepsilon}_e$, is related to the stress vector by the elasticity matrix $[D_e]$, see Section 2.3.1, expressed as:

$$\dot{\varepsilon}_e = [D_e]^{-1} \cdot \dot{\sigma} \tag{3.2}$$

and the plastic rate component, $\dot{\varepsilon}_p$, after yielding is defined as:

$$\dot{\varepsilon}_p = \dot{\lambda} \frac{\partial F}{\partial \sigma} \tag{3.3}$$

with the standard Kuhn-Tucker conditions imposed:

$$\dot{\lambda} \geq 0 \quad , \quad F \leq 0 \quad , \quad \dot{\lambda} \cdot F = 0 \tag{3.4}$$

where $\dot{\lambda}$ is a constant of proportionality[1], and F is a response surface associated with a locus of states of stress, σ, corresponding to a certain magnitude of inelastic response. The evolution of plastic flow is determined by the consistency condition:

$$\dot{F}(\sigma, \dot{\varepsilon}, T, k) = 0 \tag{3.5}$$

where, $\dot{\varepsilon}$ = strain rate

T = temperature

k = some measure of hardening/softening

The model formulation can be used to distinguish two main phases of inelastic material response. These are illustrated in Figure 3.1.

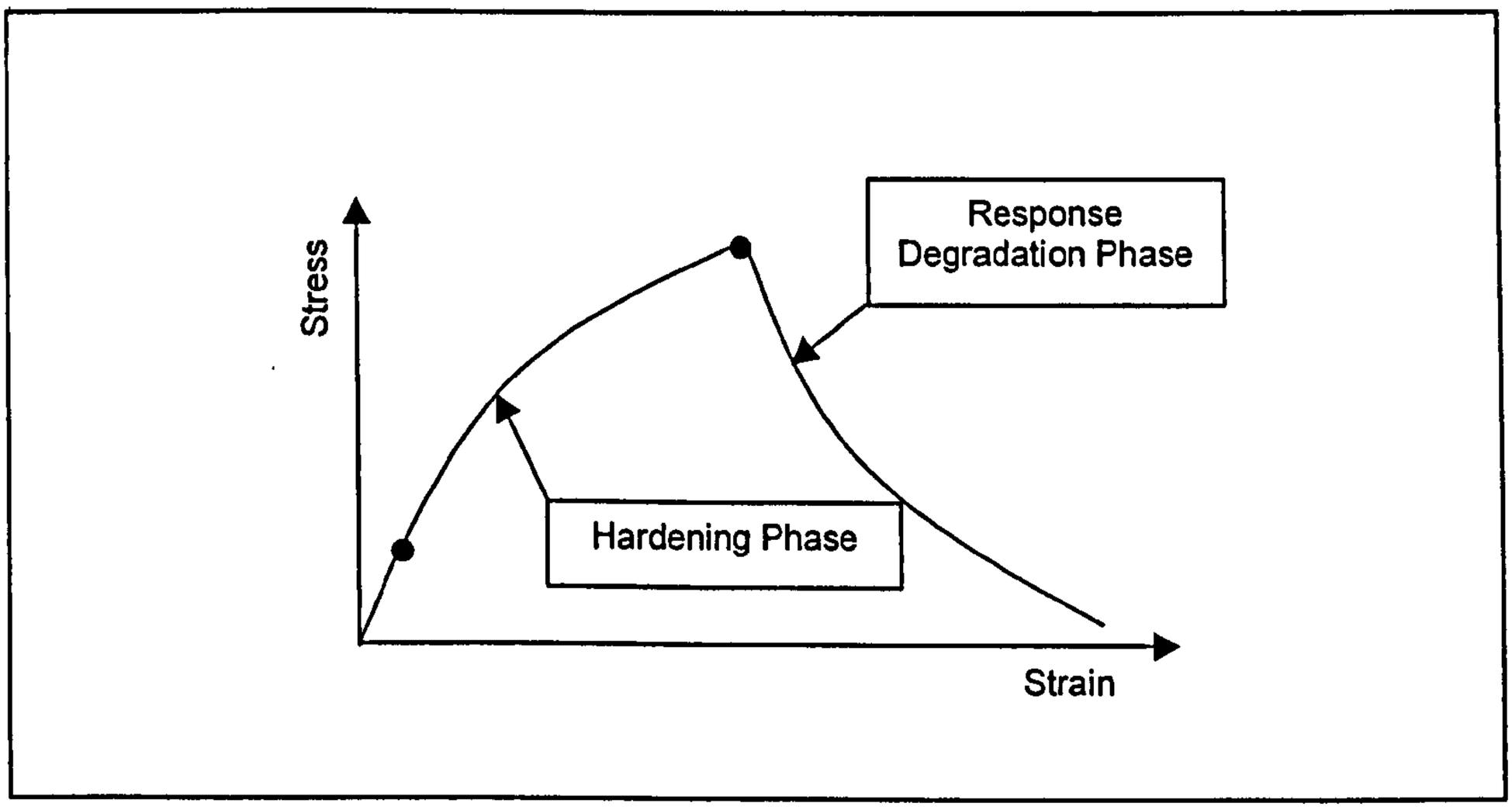

Figure 3.1: Illustration of the two main phases of model material response [Adapted from Erkens *et al.*, 2000b]

These phases comprise the hardening response phase, covering the range from zero

---

[1] Which for Perzyna type visco-plasticity, described in Appendix A, is analogous to $\dot{\lambda} \equiv \Gamma\langle\Phi(F)\rangle$.

stress to peak response, and the softening response (or response degradation) phase, covering the range from the peak response to response annihilation. The same constitutive framework was selected by Scarpas *et al.* [1998a] for the simulation of all phases of material response. However, different flow surfaces are utilised to represent the hardening and softening phases of material response.

3.3.2 Hardening Response

To simulate the inelastic phase of the material hardening response, utilisation of a single flow (yield) surface was deemed sufficient [Scarpas *et al.*, 1997]. The flow surface chosen is of the form proposed by Desai *et al.* [1986] (see below), which was selected, amongst other reasons, to provide the generality required to model the many types of geologic materials encountered in a typical pavement profile [Scarpas, 1999].

Desai Flow Surface Characteristics

Desai *et al.* [1980, 1986, and 1990] proposed a hierarchical concept for the development of constitutive models to account for the various factors that influence behaviour of geological materials. A key ingredient of this concept is the use of single surface yield and potential functions, thus eliminating the need for hydrostatic caps or multi-surface yield functions and the corresponding computational intensive intersection singularities. The hierarchical single surface (HISS) approach permits the evolution of models of progressively higher grades based on the simplest category. A schematic of this approach is shown in Figure 3.2. The basic hierarchical model, δ_0, is an isotropic hardening model with associated flow. The model consists of a series of yield surfaces, which expand with increasing plastic strains as shown in Figure 3.3. The yield function is defined in stress invariant space as:

$$F_D \equiv \frac{J_2}{p_a^2} - F_b \cdot F_s = 0 \tag{3.6}$$

in which F_b is the basic function, describing the shape in I_1 - $\sqrt{J_2}$ space, which in the ACRe model has been modified by Scarpas *et al.* [1997] to accommodate the tensile strength of asphaltic materials, expressed as:

$$F_b = \left[-\alpha \left(\frac{I_1 - R}{p_a} \right)^n + \gamma \left(\frac{I_1 - R}{p_a} \right)^2 \right] \tag{3.6a}$$

and F_s is the shape function, describing the shape in the deviatoric plane, defined as:

$$F_s = (1 - \beta \cos 3\theta)^m \tag{3.6b}$$

where,
$$\cos 3\theta = \frac{\sqrt{27}}{2} \cdot \frac{J_3}{J_2^{3/2}} \tag{3.6c}$$

in which, I_1, is the first stress invariant, J_2 and J_3 are the second and third deviatoric stress invariants, defined in Section 2.3.4; α, R, n, γ, β, m are experimentally determined material parameters, p_a, is the atmospheric pressure (with stress units) and θ is the Lode angle.

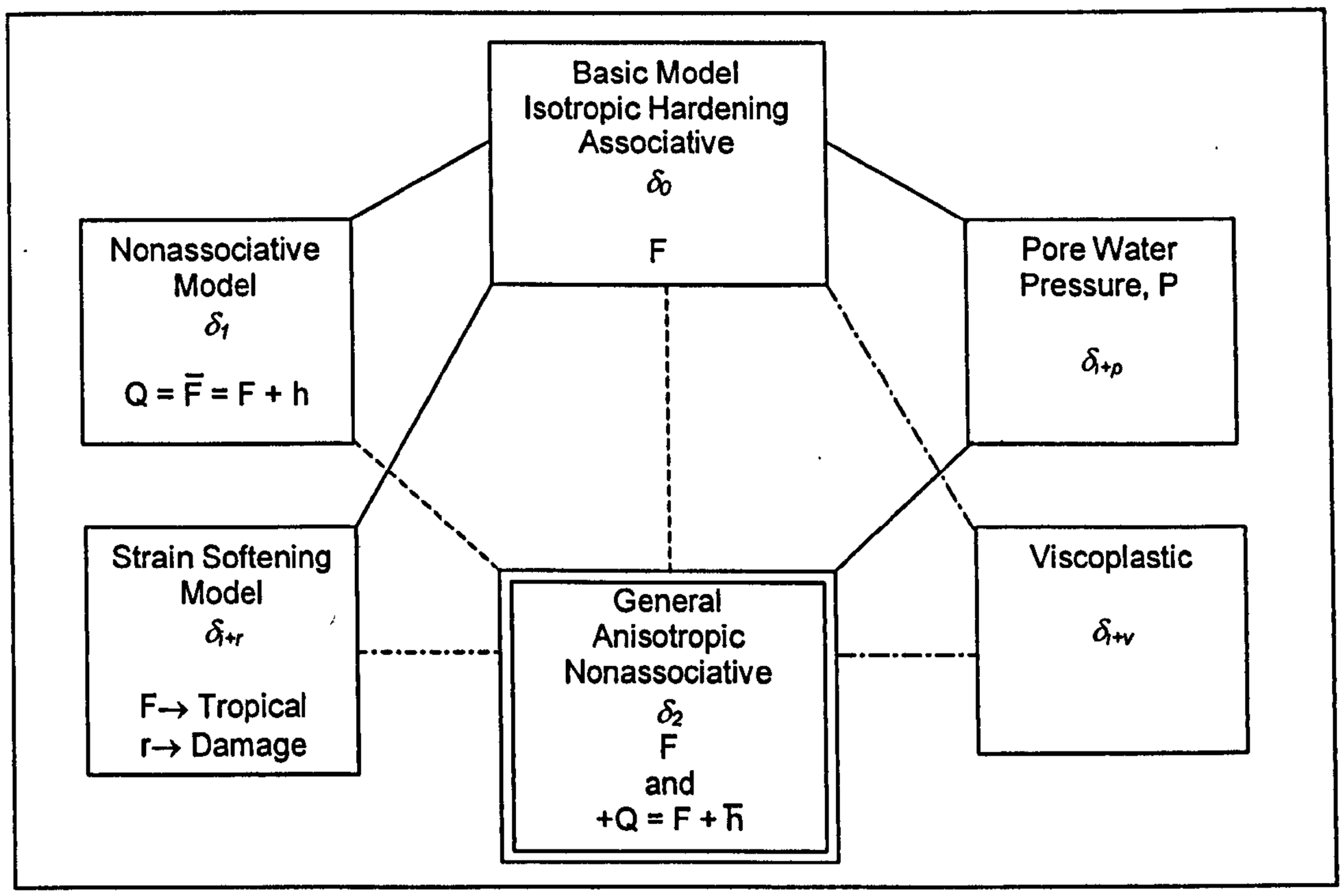

Figure 3.2: Schematic of the hierarchical single surface modelling approach [Adapted from Desai, 1990]

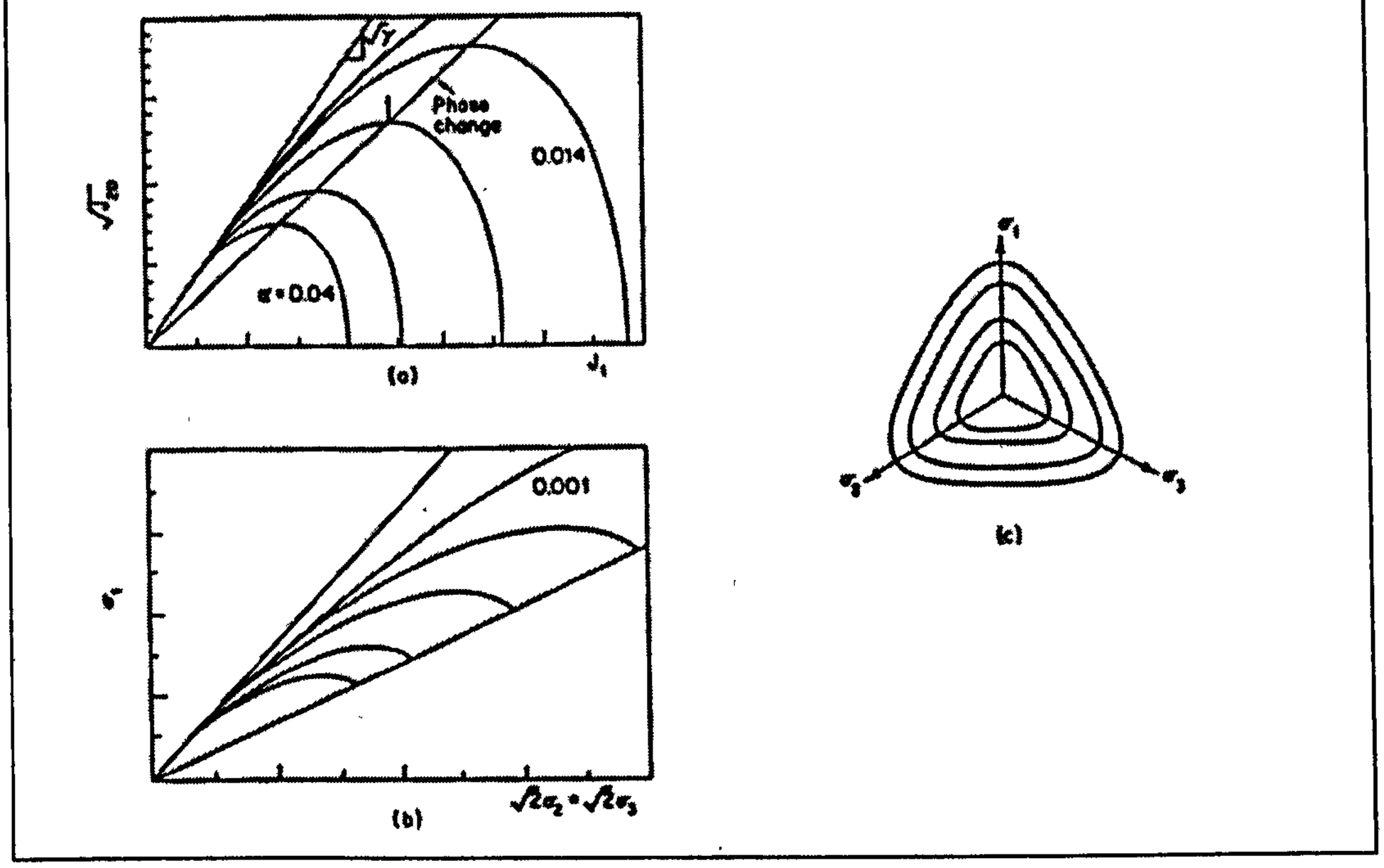

Figure 3.3: Plot of yield function in various stress spaces: (a) I_1-$\sqrt{J_2}$ space; (b) Triaxial space; (c) Deviatoric space [Reproduced from Desai *et al.*, 1986]

The exact characteristics (size, shape and position in three-dimensional space) of the flow surface depend of the material parameters, which will vary for different materials. Each of the parameters controls a specific aspect of material response. Parameter α is a hardening function controlling the growth of the size of the flow surface. For elastic states of stress α retains a constant value, but for inelastic, hardening states of stress, α decreases until $\alpha = 0$. This corresponds to peak stress, where hardening stops, see Figure 3.4. The influence of the size of α on the flow surface is shown in Figure 3.5. As α decreases the size of the flow surface increases until peak stress is reached. For peak stress ($\alpha = 0$), Equation (3.6) can be compared to the Drucker-Prager failure envelope described in Section 2.3.5, and the peak response surface (or ultimate envelope, see below) is attained. The parameters γ, β and m are material functions associated with the ultimate envelope, where, the ultimate envelope is defined as the locus of points corresponding to asymptotic stress to stress-strain curves for different tests (defined in this study by peak stress response). The classical states such as critical and failure are below or coincide with the ultimate state. The peak response surface is characterised by an open plane in I_1 - $\sqrt{J_2}$ space, the slope of which is defined by parameter γ, Figure 3.5.

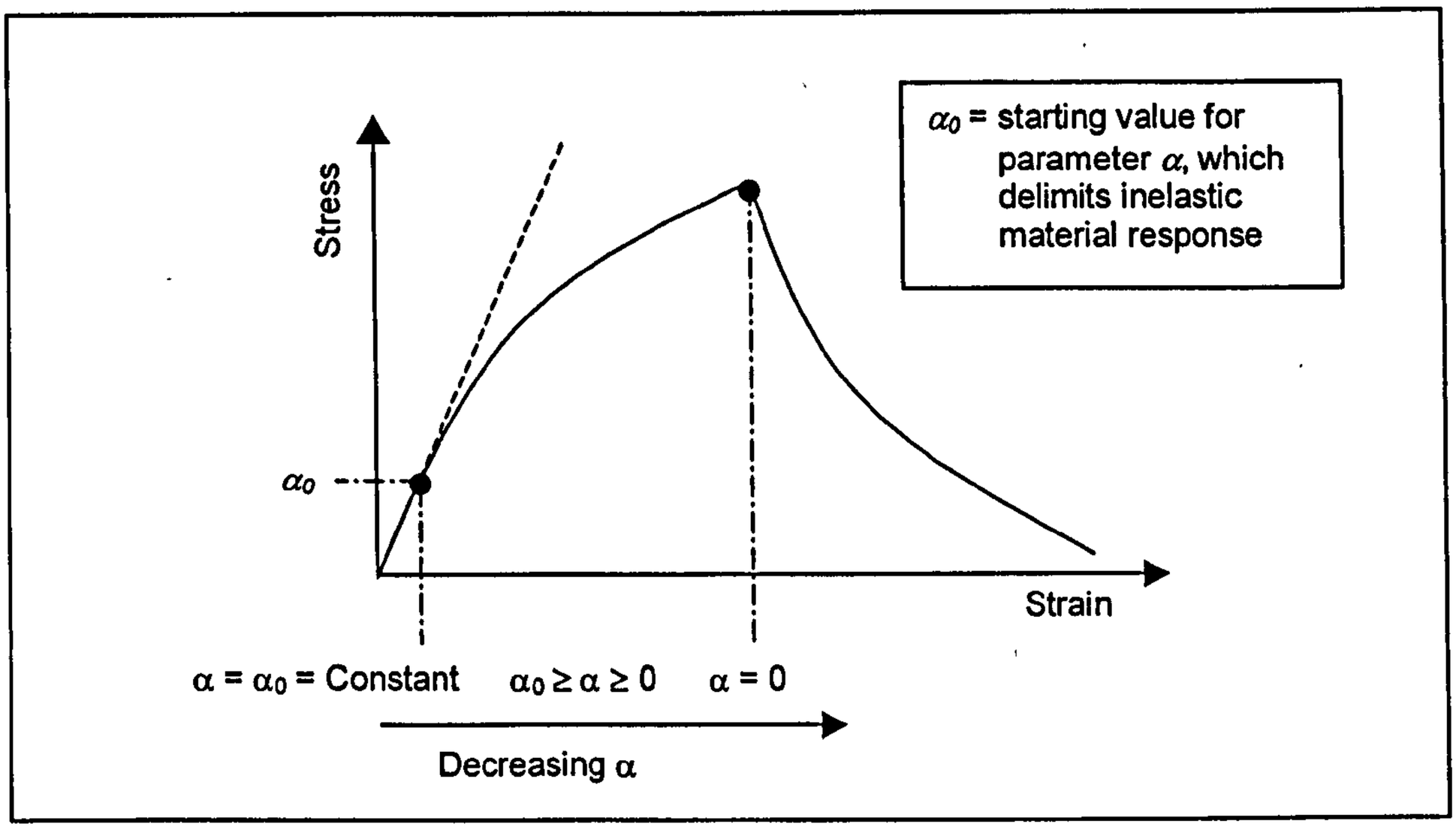

Figure 3.4: Hardening response

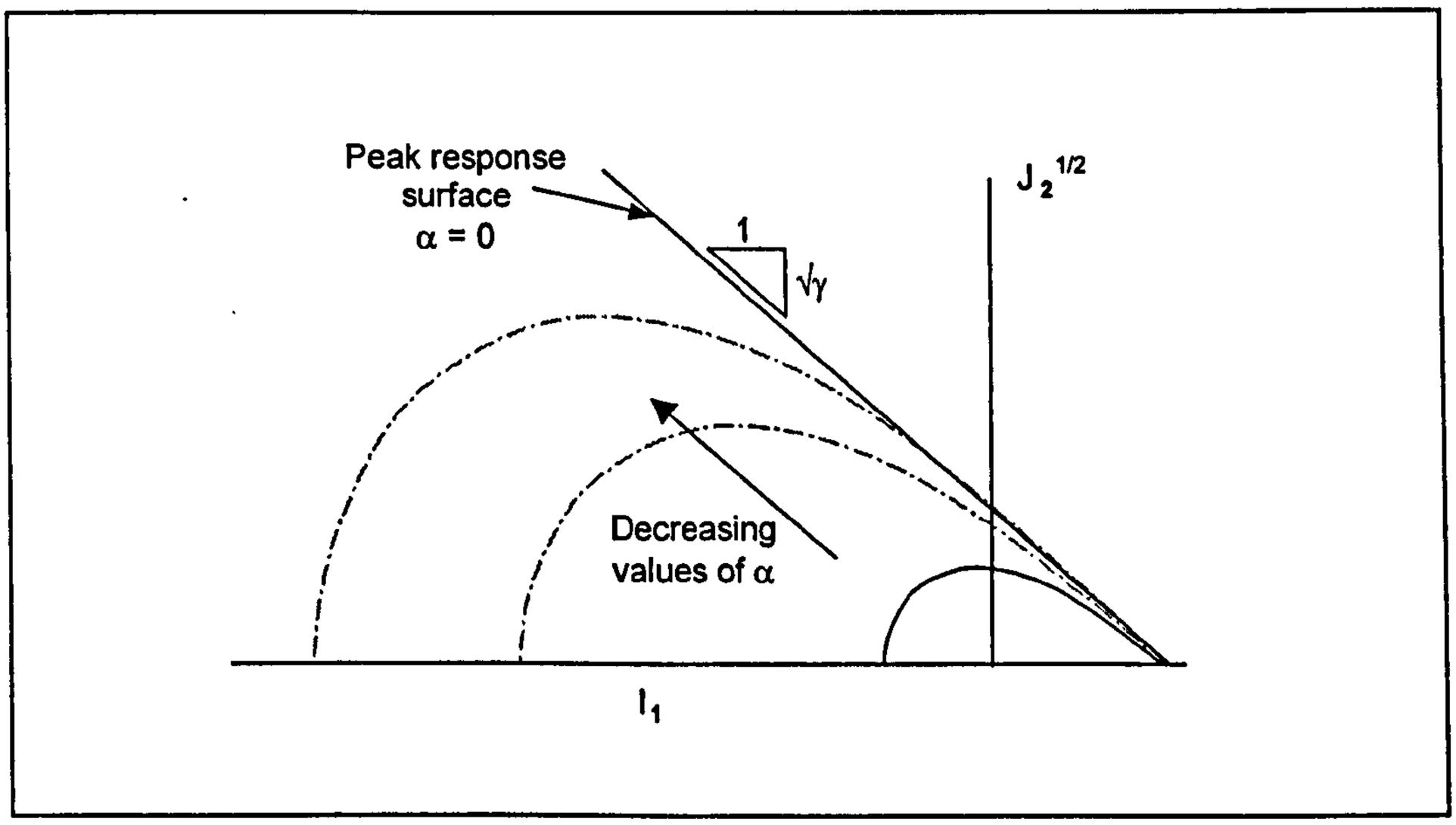

Figure 3.5: Influnce of parameter α on the size of the flow surface, plotted in I_1 - $\sqrt{J_2}$ space

The function F_D in Equation (3.6) for $F_s = 0$ represents a closed surface in I_1 - $\sqrt{J_2}$ space, with a circular cross section in the deviatoric plane, here parameter n acts as a shape parameter. It determines the position of the apex of the flow surface in the I_1 - $\sqrt{J_2}$ plane. For $n = 2$ the surface has an elliptical form in I_1 - $\sqrt{J_2}$ space. Known as the phase change or transition parameter, n, delimits the state of stress at which

dilation occurs. Changes in the value of n therefore influence both the shape and the size of the flow surface, Figure 3.6.

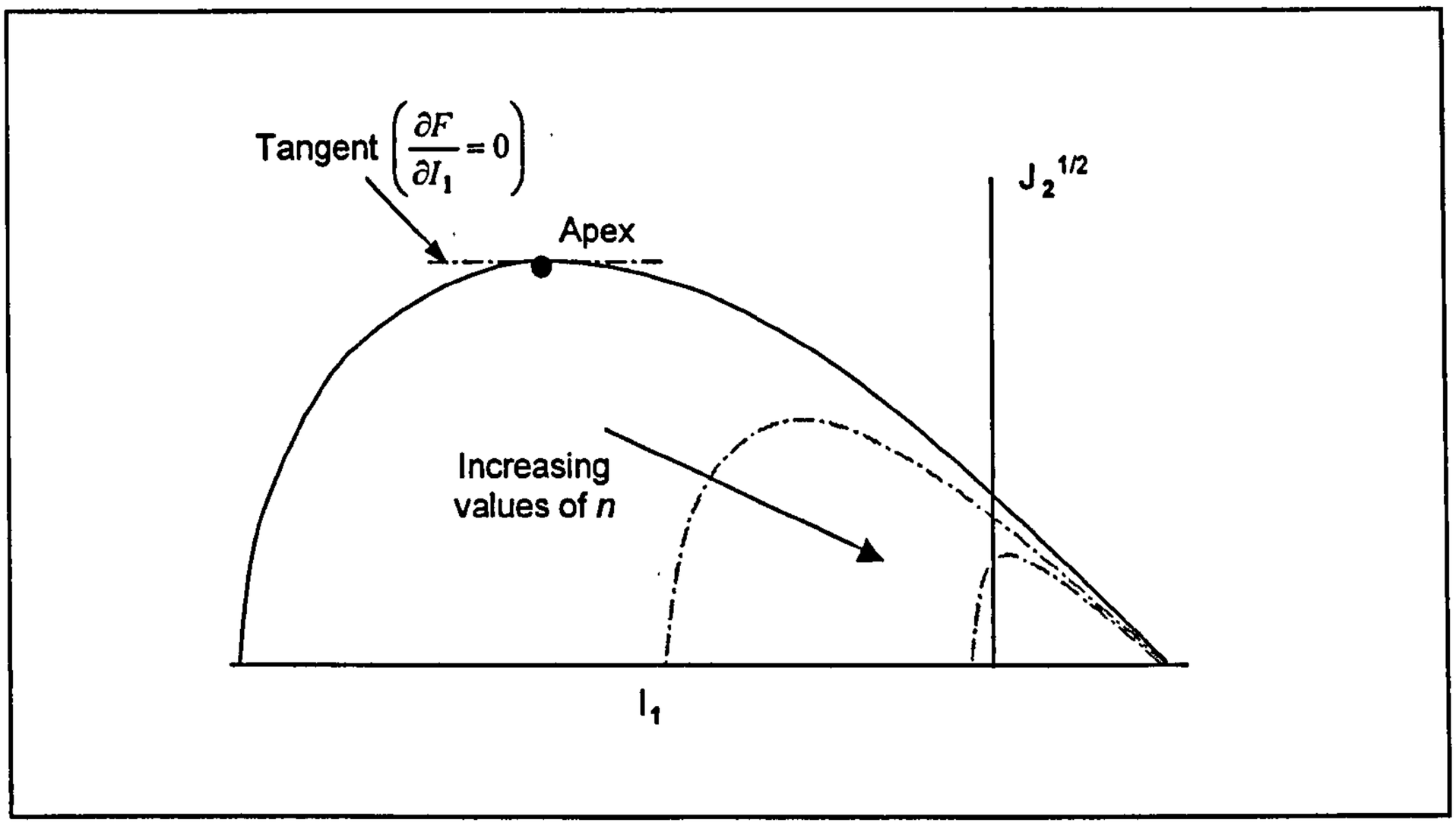

Figure 3.6: Influence of parameter n on the shape of the flow surface, plotted in I_1 - $\sqrt{J_2}$ space [Adapted from Erkens *et al.*, 1998]

The function F_s in Equation (3.6) modifies the shape of the flow surface in the deviatoric plane, Figure 3.3(c), to shapes appropriate for a given material. Here parameters β and m define the shape. For many geologic materials parameter m is found to be equal to -0.5 [Desai *et al.*, 1986 & 1990]. For some materials such as concrete and rock the yield surface may change shape with varying levels of confinement. For such materials experimental evidence indicates that for low confinement levels the shape of the surface in the deviatoric plane is triangular while for higher levels of confinement the trace tends to a circular form [Al-khoury, 1993]. Desai *et al.* [1986 and 1990] propose that this can be incorporated by treating parameter β as a function of I_1.

The parameter R defines the three-dimensional tensile strength of a material. For cohesionless materials $R = 0$. For cohesive and adhesive materials such as asphalts, parameter R takes a positive value. For increasing values of R the flow surface is shifted in the direction of the positive I_1 axis, Figure 3.7.

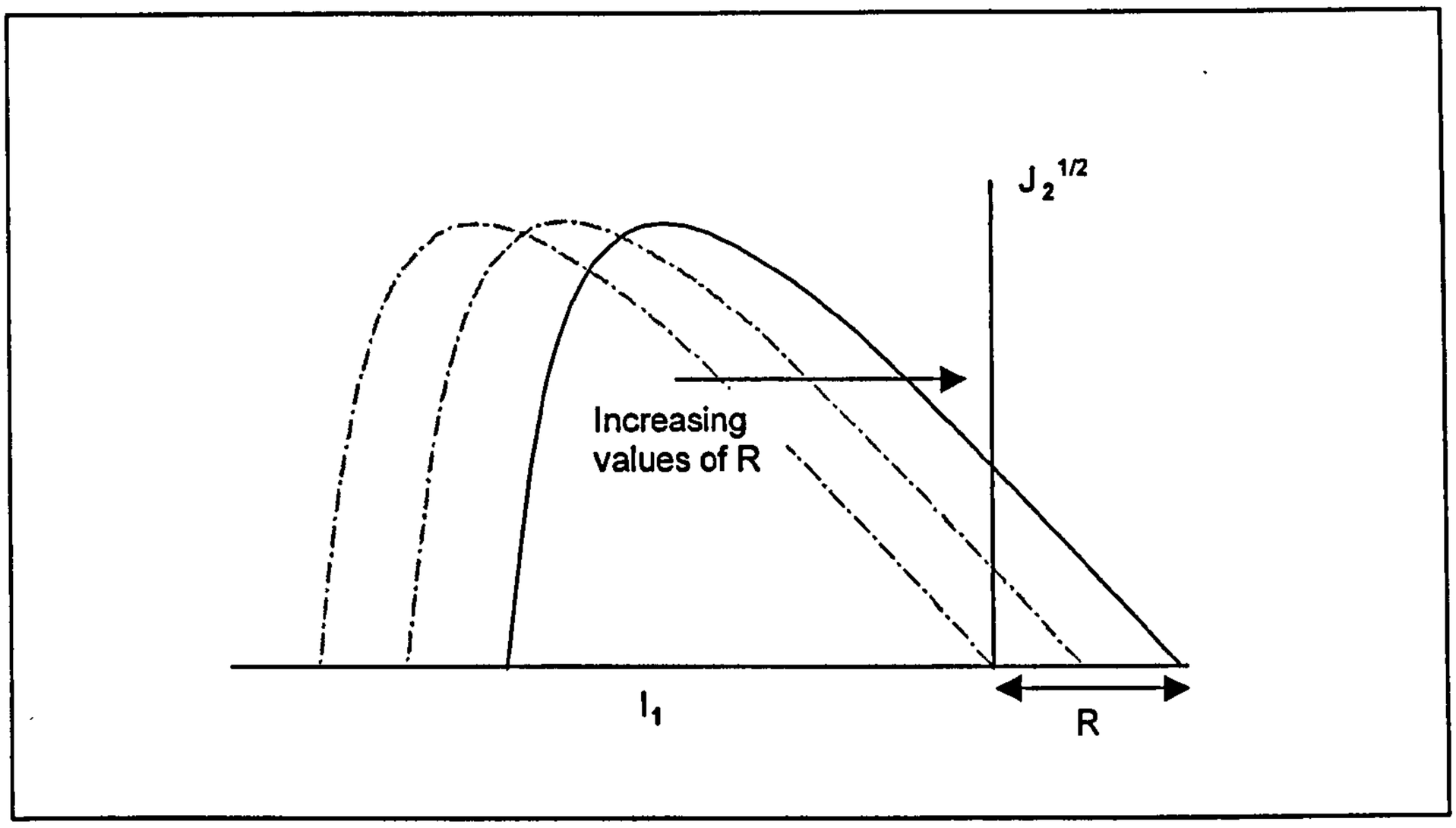

Figure 3.7: Influence of parameter *R* on the position of the flow surface, plotted in I_1 - $\sqrt{J_2}$ space

The Desai HISS modelling approach has been used to successfully simulate various types of geologic material response such as soil [Al-Klouary, 1993], sand [Desai *et al.*, 1986], granular material [Bonaquist *et al.*, 1997], concrete [Desai *et al.*, 1986] and rock [Desai *et al.*, 1986; Varadarajan *et al.*, 2001]. In the ACRe model Scarpas *et al.* [1997, 1998a and 1998b] utilise the adapted form of the basic HISS model given in Equation (3.6), to define both the hardening response simulation (see below) and the overall isotropic softening of material response that results from compressive loading (see Section 3.3.3).

Hardening Response Simulation

As discussed above material hardening is controlled by parameter α. As α decreases the size of the flow surface increases, until peak response where $\alpha = 0$ and the surface becomes an open plane in I_1 - $\sqrt{J_2}$ space. By defining α as a decreasing function of some physically increasing quantity, such as plastic work, Equation (3.7) [Scarpas *et al.*, 1997, 1998a; and Airey *et al.*, 2002] or equivalent plastic strain, Equation (3.8) [Desai *et al.*, 1986; Erkens *et al.*, 2000b], strain rate and temperature, the characteristics of the material hardening response, as shown in Figure 3.1, can be simulated.

$$\alpha = \alpha\left(\dot{\varepsilon}, T, W_p\right) \tag{3.7}$$

$$\alpha = \alpha\left(\dot{\varepsilon}, T, \xi_p\right) \tag{3.8}$$

where, W_p = plastic work

ξ_p = equivalent plastic strain

3.3.3 Softening Response

In the proposed model, for $\alpha = 0$, the peak response of a material is attained. For deformation levels beyond those corresponding to $\alpha = 0$ two independent mechanisms are specified to control the subsequent material response degradation. These are an isotropic softening criterion, to simulate the overall response surface degradation that is observed as a result of compressive loading, and an independent cracking softening criterion that is used to control the tensile softening response.

γ Degradation

To control the post peak softening response, an isotropic measure of response degradation is introduced to regulate reduction of the Desai surface, Figure 3.8. This is incorporated in the model by specifying γ as a decaying function of some increasing physical quantity, such as post fracture plastic work, Equation (3.9) [Scarpas *et al.*, 1998a; Airey *et al.*, 2002] or equivalent post fracture plastic strain, Equation (3.10), the strain rate and the temperature.

$$\gamma = \gamma\left(\dot{\varepsilon}, T, W_{pf}\right) \tag{3.9}$$

where, W_{pf} = post fracture plastic work

$$\gamma = \gamma\left(\dot{\varepsilon}, T, \xi_{pf}\right) \tag{3.10}$$

where, ξ_{pf} = post fracture equivalent plastic strain

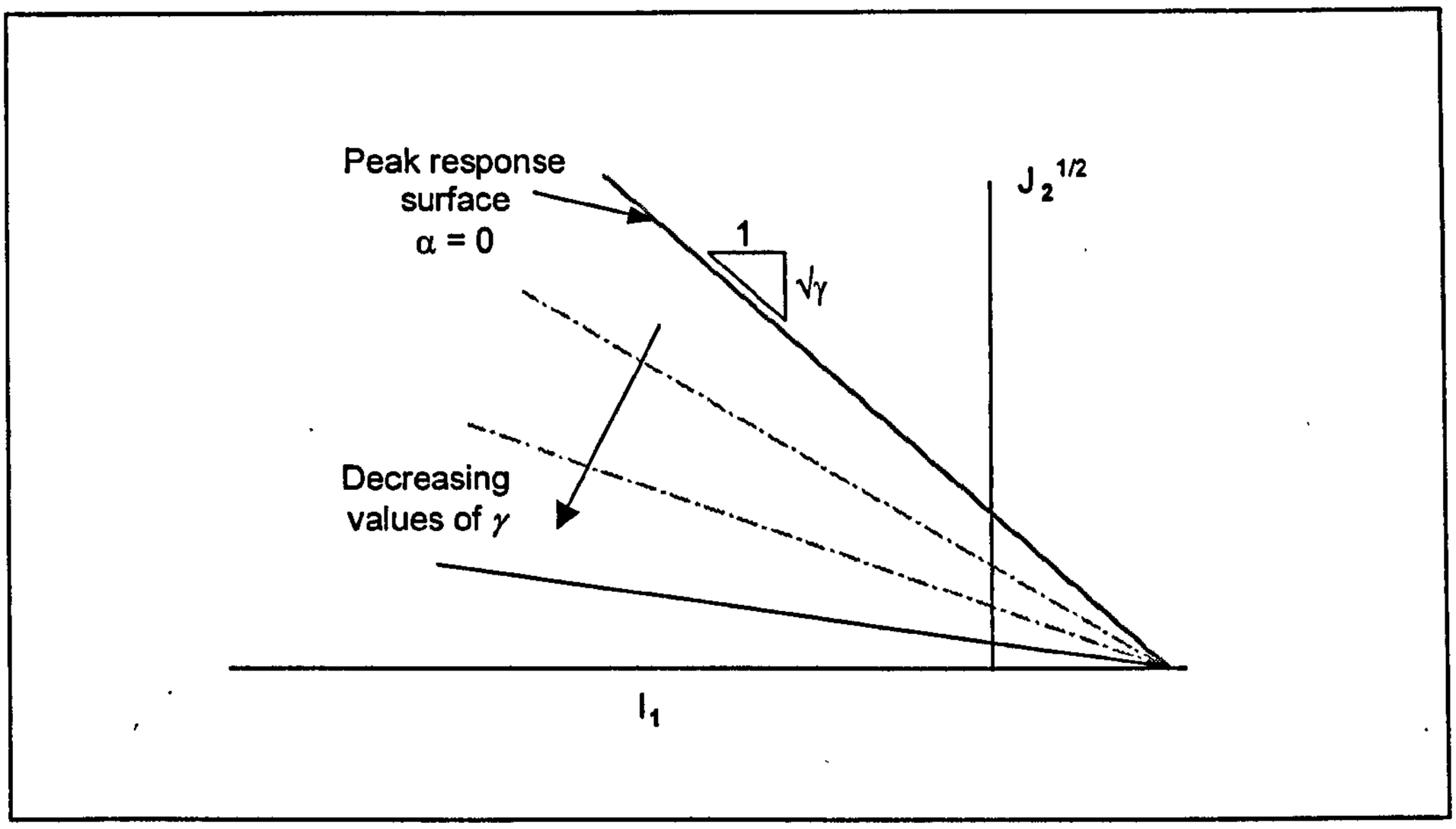

Figure 3.8: Softening response – Desai surface degradation

As stated above, the primary purpose of the isotropic softening formulation is to simulate the overall material response degradation that is observed experimentally as a result of compressive loading. Therefore, Erkens *et al.* [2000b] introduce γ degradation for compression paths only. Here, after response degradation initiation, in all subsequent steps, the principal values of the plastic strain vector are computed. An equivalent plastic strain measure is then constructed, Equation (3.11), consisting only of increments of compressive principal plastic strain components.

$$\bar{\varepsilon}_{p,c} = \int d\bar{\varepsilon}_{p,c} \tag{3.11}$$

in which $$d\bar{\varepsilon}_{p,c} = \left(d\varepsilon_I \cdot d\varepsilon_I\right)^{\frac{1}{2}} \quad : \quad d\varepsilon_I < 0 \tag{3.11a}$$

where, $\bar{\varepsilon}_{p,c}$ = compressive principal plastic strain vector

$d\varepsilon_I$ = compressive principal plastic strain

Isotropic softening, due to the development of compressive principal strains, can then be ensured by specifying:

$$\gamma = \gamma\left(\dot{\varepsilon}, T, \bar{\varepsilon}_{p,c}\right) \tag{3.12}$$

Cracking

Tensile loading is largely directional and thus does not significantly influence cross-directional material strength. Therefore, for cyclic states of stress, such as those typically encountered in pavement engineering, it is desirable that tensile cracking of the material in one direction of the loading cycle does not adversely weaken the compressive strength of the material during stress reversal [Scarpas *et al.*, 1998a]. To account for this aspect of material response Scarpas *et al.* [1998a and 1998b] have incorporated a softening criterion, the main purpose of which is to control the tensile softening response and which is independent of the overall γ softening (described above).

This criterion is introduced along fixed orthogonal material axes by specifying that, for states of stress exceeding the magnitude of the fracture surface, a plane of cracking is introduced perpendicular to the principal tensile stress direction if Equation (3.13) is satisfied [Erkens *et al.*, 2000b].

$$\varepsilon_n \geq \frac{f_{tu}}{E} \tag{3.13}$$

where, ε_n = strain normal to the plane of potential cracking

f_{tu} = tensile strength at crack initiation

On a crack plane, a Hoffman type criterion is then utilised to control the subsequent softening response [Scarpas *et al.*, 1998a]. In the current formulation isotropic softening of the form given in Equation (3.14) is postulated.

$$\sigma^2 + q \cdot \left(\tau_s^2 + \tau_t^2\right) = f_t^2\left(\dot{\delta}, T, k\right) \tag{3.14}$$

in which, σ = the normal stress on the crack plane

τ_s, τ_t = shear stress components

f_t = uniaxial tensile strength

k = some measure of softening

In previous publications, Scarpas *et al.* [1998b], the plastic strain normal to the crack plane after crack initiation, ε_{cr}^{p}, has been used as the softening measure. In this case an exponential decay of tensile strength with ε_{cr}^{p} was postulated. However, the determination of the exact form of this tensile cracking softening function is outside the scope of this study, which focuses on the determination of material parameters relating to the hardening and overall softening functions of the model described in Sections 3.3.2 and 3.3.3. The reader is therefore referred to Scarpas *et al.* [1992, 1998a and 1998b] and to Erkens *et al.* [2000b] for further details relating to the tensile cracking model capabilities.

3.3.4 Algorithmic Aspects

Scarpas *et al.* [1998] present details of the numerical techniques utilised for the implementation of the constitutive model described in this section in a three-dimensional FE code. During the hardening phase only the Desai surface is active. However, during the response degradation phase both the Desai and Hoffman surfaces are assumed active. Therefore, two main algorithms are utilised in the model. The first algorithm is used to specify the Desai surface hardening response, and if no cracking has occurred, the same Desai surface algorithm is specified to control softening response. Otherwise if cracking is apparent the stresses are first resolved along the three orthogonal directions defined by the cracking plane, then depending on the situation, the Desai surface algorithm is applied in combination with a Hoffman surface reduction algorithm. Full details of the numerical algorithms are given in Scarpas *et al.* [1998a] and Erkens *et al.* [2000b].

3.3.5 Damage Simulation of Asphalt Pavements

The constitutive model described in this section has been implemented in the three-dimensional FE code INSAP (Incremental non-linear structural analysis package) and has been used by Erkens *et al.* [2000b] for the simulation of damage response within

the asphalt layers of two Dutch flexible pavement structures. Both pavement structures were modelled using the same subgrade and sub-base constructions, but with different asphalt layer properties and construction. The sub-base was specified as a 250 mm granular layer on a 15 m sand sub-grade. For the asphalt layers two thicknesses, of 120 mm and 150 mm, with respective stiffness moduli of 1000 MPa and 3000 MPa were selected. Due to axisymmetry a quarter of the pavement structure was simulated using a 1040 element mesh. On the basis of uniaxial compression tests and preliminary uniaxial tension tests the basic model parameters required for the characterisation of a sand asphalt mixture (see Section 3.5.4) for use in the ACRe model were identified[2], and used for simulation of the inelastic response of the asphalt layers [Erkens *et al.*, 1998, 2000a & 2000b]. The pavement structures were subjected to a series of successive half-sinusoidal load pulses of 25 ms duration and 0.707 MPa, which is typical of FWD[3] pulses used in the Netherlands. Figures 3.9 and 3.10 show cross-sectional plots through the asphaltic layers of the two pavement structures. The plots display the development of damage, presented in the form of contours, with respect to increases in the number of load pulses. Three types of contour plots are used to represent the damage accumulation within the pavement structures. These are a deviatoric damage plot, a volumetric damage plot and a total damage plot. The total damage, given by Equation (2.28), can be subdivided into volumetric and deviatoric components as given in Equations (3.15) and (3.16) respectively. Compressive volumetric damage is typically associated with deformations leading to inelastic compaction of a material. Tensile volumetric damage is typically associated with deformations leading to cracking (Mode I). Deviatoric damage is the result of tensile-compressive states of stress and can lead to Mode II associated cracking.

$$\xi_V = \sum d\xi_V = \sum \frac{\left| d\varepsilon_{ij}^p \right|}{\sqrt{3}} \tag{3.15}$$

---

[2]As only limited tension data was available the model parameters were considered preliminary.

[3] The falling weight deflectometer (FWD) is an apparatus used for non-destructive structural evaluation of pavement structures. The device loads the pavement in a manner such that the load pulse resembles that from moving traffic. Deflection sensors are used to record the vertical displacements at the surface of the pavement. These deflection data are then commonly used to back-calculate layer moduli to infer critical strains for maintenance and rehabilitation purposes.

$$\xi_D = \sum d\xi_D = \sum \left(d\xi^2 - d\xi_V^2 \right)^{\frac{1}{2}} \tag{3.16}$$

where, ξ_V = volumetric damage

ξ_D = deviatoric damage

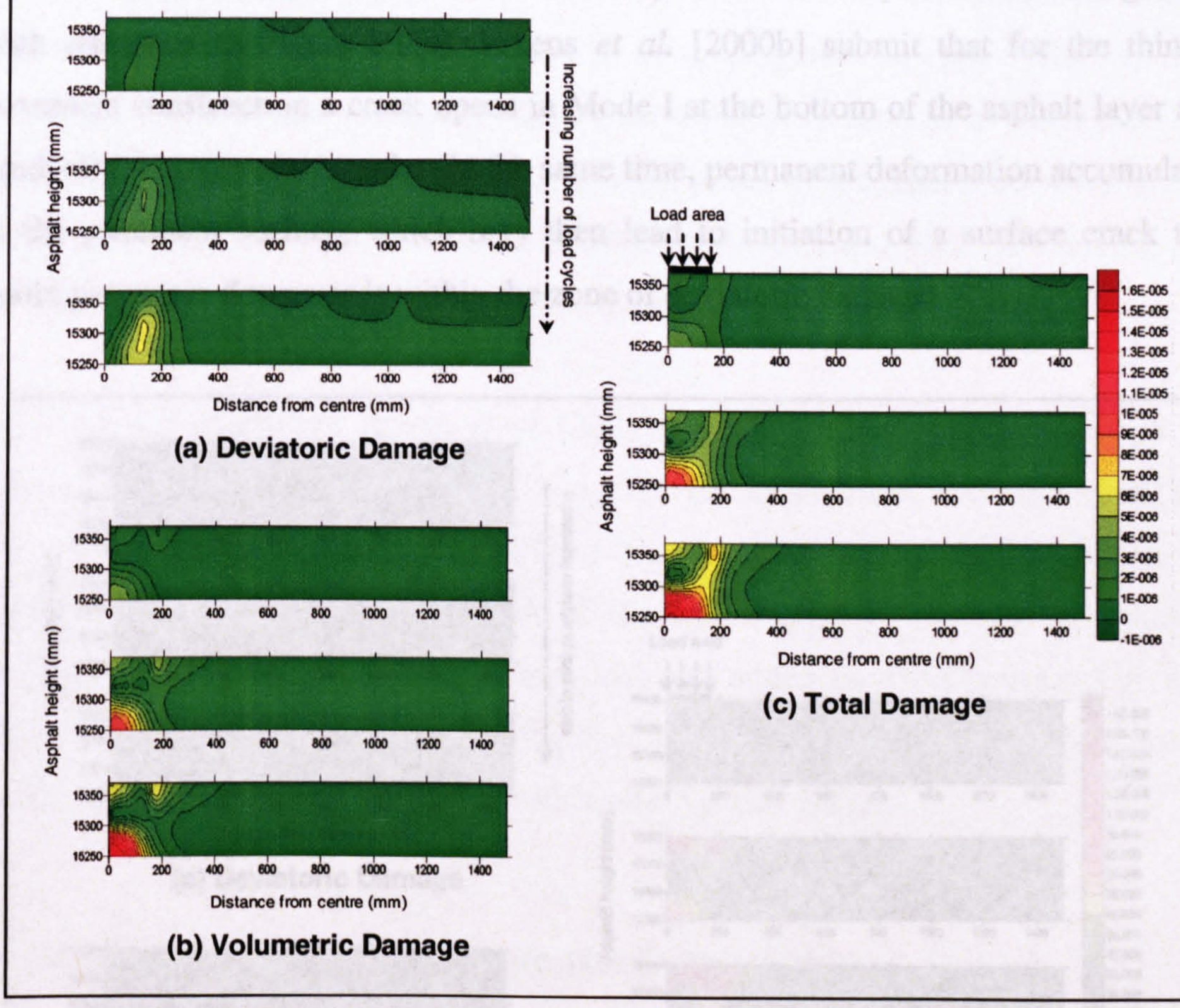

Figure 3.9: Cross-sections through 120 mm asphalt layer pavement showing (a) Deviatoric, (b) Volumetric and (c) Total damage contours [Adapted from Erkens *et al.*, 2000b]

Based on analysis of the in-time response of each pavement, Erkens *et al.* [2000b] make the following observations regarding the development and propagation of damage within the asphaltic layers.

For the thinner pavement construction, shown in Figure 3.9, deviatoric damage can be observed to initiate at the load edge and to gradually increase throughout the depth of

the pavement, Figure 3.9(a). Tensile volumetric damage is initiated and gradually develops at the bottom of the asphaltic layer, indicating the gradual propagation of a crack, Figure 3.9(b). With increases in the number of load pulses, compressive volumetric damage can be seen to develop directly under the load, indicating compaction (rutting) of the pavement surface. Also the gradual development of tensile volumetric damage at the periphery of the load can be observed. Taking into account the observations drawn from the analysis of the components of damage, and with reference to Figure 3.9(c), Erkens *et al.* [2000b] submit that for the thinner pavement construction a crack opens in Mode I at the bottom of the asphalt layer and gradually propagates upwards. At the same time, permanent deformation accumulates at the pavement surface, which may then lead to initiation of a surface crack that could propagate downwards within the zone of deviatoric damage.

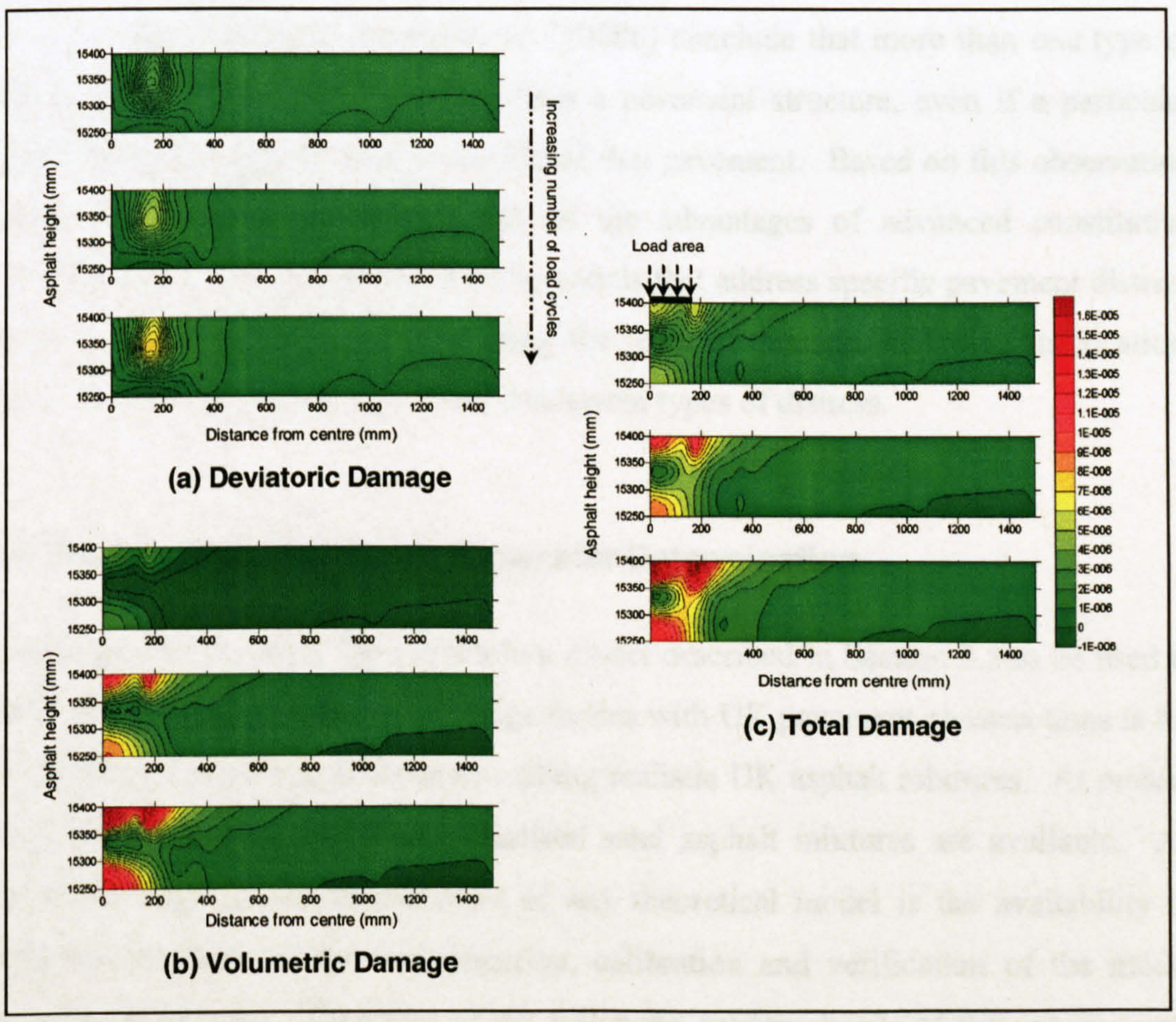

Figure 3.10: Cross-sections through 150 mm asphalt layer pavement showing (a) Deviatoric, (b) Volumetric and (c) Total damage contours [Adapted from Erkens *et al.*, 2000b]

For the thicker pavement constructions, shown in Figure 3.10, deviatoric damage is observed to initiate in the region near the periphery of the load area and to spread gradually throughout the asphalt layer, Figure 3.10(a). Two concentrated areas of volumetric damage can be identified on the surface of the pavement structure, Figure 3.10(b). These are a compressive zone directly under the load and a tensile zone at the load edge. Incorporating the observations drawn from analysis of the individual components of damage Erkens *et al.* [2000b] submit that for the thicker pavement, Figure 3.10(c), a surface crack appears to be developing near the edge of the load area where curvature reversal occurs. The tensile volumetric damage at the top of this crack indicates that it starts in Mode I, but most probably propagates downwards into the depth of the asphalt layer in a combination of Mode I and Mode II cracking. At the same time, rutting type damage occurs under the loaded area.

From the above analysis Erkens *et al.* [2000b] conclude that more than one type of damage can develop concurrently within a pavement structure, even if a particular type becomes dominant later in the life of that pavement. Based on this observation Erkens *et al.* [2000b] highlight one of the advantages of advanced constitutive modelling, which is the transition from models that address specific pavement distress types, to models capable of identifying the form of damage, including its location, extent and the interaction with other concurrent types of distress.

3.4 Methodology for Model Parameter Determination

A prerequisite to enable the constitutive model described in Section 3.3 to be used to investigate the development of damage modes with UK pavement constructions is the availability of model parameters describing realistic UK asphalt mixtures. At present only data describing Dutch and idealised sand asphalt mixtures are available. An important stage in the development of any theoretical model is the availability of experimental data for the determination, calibration and verification of the model material parameters. Therefore in the following section details of the experimental work required for material characterisation are presented.

3.4.1 Identification of Experimental Work

The material response of asphaltic materials is state of stress dependent, therefore to assess a one-to-one relationship between a state of stress and the corresponding response, the state of stress in any representative laboratory test must be uniform. This excludes many standard pavement engineering material tests, such as the indirect tensile fatigue test, which exhibit non-uniform stress states.

Table 3.1 is a summary of the laboratory tests, as proposed by Desai *et al.* [1986 and 1990], that are required to determine the material parameters for the HISS constitutive model. Desai *et al.* [1990] state that it is desirable to use at least three conventional triaxial compression (CTC) tests, with different confining stresses, with at least one tension extension (TE) stress path, combined with a simple shear (SS) stress path to reliably determine the parameters for boundary value problems. As a minimum, however, it is possible to obtain an approximate set of parameters from only one CTC test and as a recommended minimum, Desai *et al.* [1986 and 1990] suggest that one CTC test combined with one TE or conventional triaxial extension (CTE) test is advisable.

Table 3.1: Tests required for parameter determination [Desai, 1990]

Criterion	*Test(s)*
Absolute minimum	1 CTC
Recommended minimum	1 CTC, 1 TE or CTE
Desirable	3 CTC, 1 TE, 1 SS

Ideally, if the full simulative capabilities of the asphalt concrete response model presented in Section 3.3 are to be engaged, then multi-axial tests at different stress paths, strain rates and temperatures are required for the characterisation of asphalt mixtures. However, triaxial equipment that can apply high confinement is expensive and unavailable at this time, and by using only lower confinement, the area of response that can be evaluated is extremely limited. Therefore, a methodology based on the work undertaken at Delft University of Technology, will be used to determine the required material parameters based on laboratory results obtained from uniaxial tests [Scarpas *et al.*, 1997; Erkens *et al.*, 1998, 2000a and 2000b]. By taking

advantage of the cohesive nature of asphalt it is possible to determine the basic[4] material parameters required for material characterisation in the constitutive model, through two test types, namely:

- monotonic uniaxial compression tests, and
- monotonic uniaxial tension tests.

Effectively these are the uniaxial equivalents of the recommended minimum tests described in Table 3.1. Due to the significant influence of loading rate and temperature on the response of asphaltic materials the above uniaxial tests will be required to be undertaken over a range of temperatures and displacement rates.

3.4.2 Model Parameter Determination

Based on the results of monotonic uniaxial compression and uniaxial tension tests the basic material parameters for the hardening and isotropic compressive softening section of the constitutive model can be determined.

Evaluation of Desai Flow Surface for a Uniaxial State of Stress

For uniaxial states of stress:

$$\sigma_1 = \sigma \tag{3.17}$$

$$\sigma_2 = \sigma_3 = 0 \tag{3.17a}$$

therefore, Equation (3.6) for the Desai surface can be simplified substantially, as:

$$I_1 = \sigma_1 + \sigma_2 + \sigma_3 \quad = \sigma \tag{3.18}$$

---

[4] To determine parameter β requires data from multi-axial experiments (see Section 6.3)

$$J_2 = \frac{1}{2}\left(s_1^2 + s_2^2 + s_3^2\right) \tag{3.19}$$

$$= \frac{1}{2}\left[\left(\sigma_{xx} - \sigma_m\right)^2 + \left(\sigma_{yy} - \sigma_m\right)^2 + \left(\sigma_{zz} - \sigma_m\right)^2\right] \tag{3.19a}$$

$$= \frac{1}{2}\left[\left(\frac{2\sigma}{3}\right)^2 + \left(-\frac{\sigma}{3}\right)^2 + \left(-\frac{\sigma}{3}\right)^2\right] \quad = \frac{1}{3}\sigma^2 \tag{3.19b}$$

$$J_3 = \frac{1}{3}\left(s_1^3 + s_2^3 + s_3^3\right) \tag{3.20}$$

$$= \frac{1}{3}\left[\left(\sigma_{xx} - \sigma_m\right)^3 + \left(\sigma_{yy} - \sigma_m\right)^3 + \left(\sigma_{zz} - \sigma_m\right)^3\right] \tag{3.20a}$$

$$= \frac{1}{3}\left[\left(\frac{2\sigma}{3}\right)^3 + \left(-\frac{\sigma}{3}\right)^3 + \left(-\frac{\sigma}{3}\right)^3\right] \quad = \frac{2}{27}\sigma^3 \tag{3.20b}$$

$$\cos 3\theta = \frac{\sqrt{27}}{2} \cdot \frac{J_3}{J_2^{3/2}} \tag{3.21}$$

$$= \frac{\sqrt{27}}{2} \cdot \frac{\frac{2}{27}\sigma^3}{\left(\frac{1}{3}\sigma^2\right)^{3/2}} \quad = \frac{\sqrt{27}}{2} \cdot \frac{\frac{2}{27}\sigma^3}{\sigma^3\sqrt{\frac{1}{27}}} \quad = 1 \tag{3.21a}$$

giving,
$$F_D = \frac{\frac{1}{3}\sigma^2}{p_a^{\,2}} - \left[\left[-\alpha\left(\frac{\sigma - R}{p_a}\right)^n + \gamma\left(\frac{\sigma - R}{p_a}\right)^2\right] \cdot (1 - \beta)^{-1/2}\right] \tag{3.22}$$

where, σ = uniaxial stress (MPa)

m = -0.5

Based on the data obtained from the two uniaxial test types, relationships can be

developed to describe the compressive and tensile strengths of the mixtures as a function of temperature and strain rate (see Chapter 5):

$$f_c = f_c(T, \dot{\varepsilon}) \tag{3.23}$$

$$f_t = f_t(T, \dot{\varepsilon}) \tag{3.24}$$

At peak stress, the hardening parameter α is zero and the uniaxial stress, σ, is equal to the compressive or tensile strengths of the material, given by the expressions above. Also at this stage in the derivation of the material parameters, as only uniaxial test results will be available, the influence of the Lode angle on the material response will not be examined and parameter β is assumed to be zero (see Section 6.3). This is equivalent to assuming a circular shape for the yield surface in the deviatoric plane. Therefore Equation (3.22) reduces further:

$$F_D = \frac{\frac{1}{3}\sigma^2}{\cancel{p_a^2}} - \left[\left[-\alpha\cancel{\left(\frac{\sigma - R}{p_a}\right)^{n}}^{\to 0} + \gamma\left(\frac{\sigma - R}{\cancel{p_a}}\right)^2\right] \cdot \cancel{(1-\beta)^{-1/2}}^{1}\right]$$

$$F_D = \frac{1}{3} f_{c,t}{}^2 - \left[\gamma\left(f_{c,t} - R\right)^2\right] \tag{3.25}$$

where, $f_{c,t}$ = uniaxial compressive or tensile material strength

Therefore, at peak stress response the only unknown parameters in Equation (3.25) are R and γ. Both of these can be computed from a plot of the failure surface, defined in two-dimensional space as the line intersecting the uniaxial compressive and uniaxial tensile strength points, see Figure 3.11. Parameter R is defined as the intercept with the I_1 axis of the failure surface, Equation (3.26). Once a relationship for R has been identified, Equation (3.25) can be solved for γ.

$$R = I_1 - \frac{\Delta y}{\Delta x} \cdot \sqrt{J_2} \tag{3.26}$$

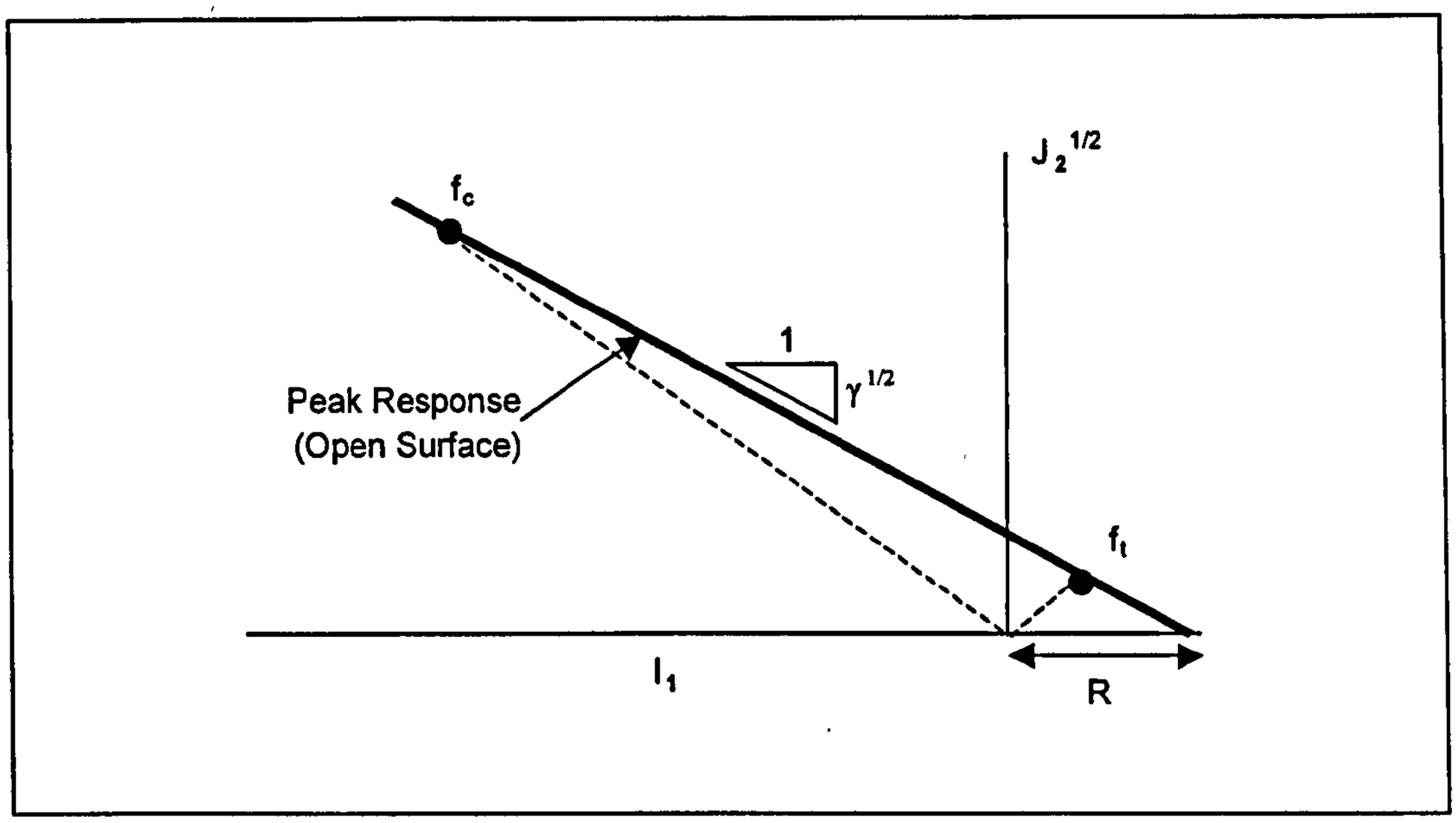

Figure 3.11: Plot showing failure surface in two-dimensional stress invariant space

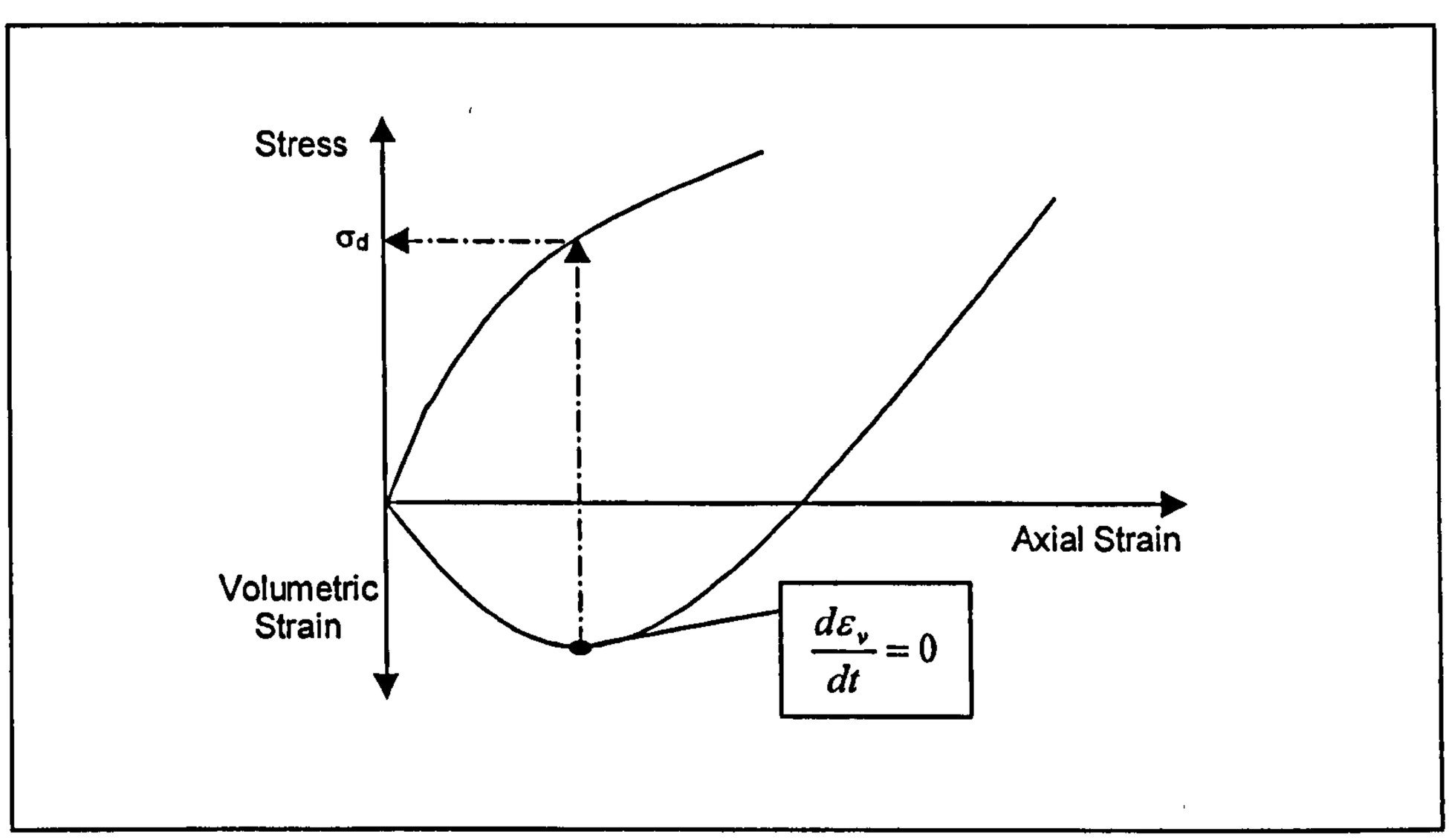

Figure 3.12: Determination of the state of stress delimiting the onset of dilation

The model parameter *n* is determined from the compressive test data. It is related to the onset of dilation, which can be caused by the opening of internal cracks within a

test specimen. At the beginning of a uniaxial compressive test the axial strain exceeds the radial strain, and therefore the volume of the specimen decreases. As dilation occurs the volume of the specimen will increase. Parameter n is evaluated for the state of stress delimiting this dilation, σ_d. It can be determined from the inversion point of the change in the volumetric strain, see Figure 3.12.

Once the other material parameters have been calculated, as α is the only unknown in Equation (3.6) it becomes possible to compute parameter α for all stress levels during the hardening response:

$$\alpha = \frac{-\frac{J_2}{p_a^2}\cdot\sqrt{(1-\beta\cos 3\theta)}+\gamma\left(\frac{I_1-R}{p_a}\right)^2}{\left(\frac{I_1-R}{p_a}\right)^n} \tag{3.27}$$

which, for a uniaxial case and where, $\beta = 0$, reduces to Equation (3.28).

$$\alpha = \frac{-\frac{\sigma^2}{3p_a^2}+\gamma\left(\frac{\sigma-R}{p_a}\right)^2}{\left(\frac{\sigma-R}{p_a}\right)^n} \tag{3.28}$$

where, σ = stress corresponding to the current level of plastic work or equivalent plastic strain (see Section 6.6)

3.5 Monotonic Characterisation of Asphaltic Materials

Various studies have been undertaken by previous researchers focusing on the investigation and characterisation of the response of bitumen and asphalt mixtures to monotonic loading conditions. As the experimental programme will consist of a series of monotonic uniaxial compression and tension tests in this section of the chapter, a brief summary of similar works relevant to this study is presented.

3.5.1 Pure Bitumens in Tension

Heukelom [1966] presents an investigation into the relationship between elongation at break and the stiffness modulus of bitumens. A series of constant rate ductility tests were carried out on a range of pure bitumens. From these, Heukelom observed that the elongation at break for road bitumens (PI –1.0 to +0.5) is a function of the stiffness modulus for a stiffness range of 0.1 to 100 kg/cm^2 (≈ 9.8 kPa to 9.8 MPa). Extending this work for other stiffness ranges, Heukelom developed a master curve for road bitumens showing the relationship between elongation at break and stiffness modulus, Figure 3.13.

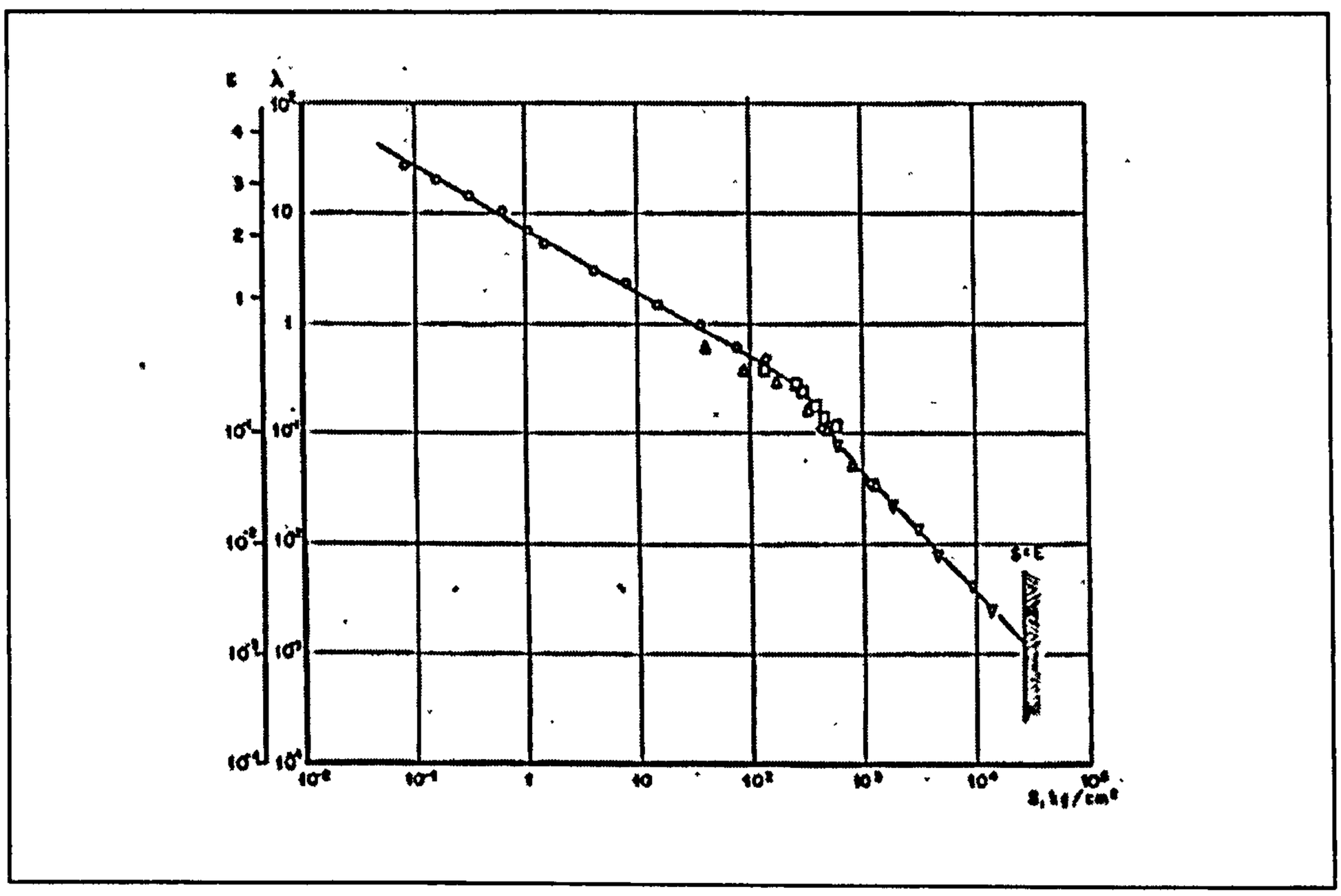

Figure 3.13: Elongation at break (λ) of road bitumens, observed with four test methods using constant rates of elongation, as a function of stiffness modulus [Reproduced from Heukelom, 1966]

Relating the elongation at break to the tensile strain at break (see second axis on Figure 3.13) Heukelom showed that the tensile strength at break is also a function of the stiffness modulus at break, and therefore could be computed directly. Figure 3.14 shows a representation of the tensile strength of plain bitumens as a function of the stiffness modulus as determined by Heukelom [1966]. It can be seen that the tensile

strength increases with increasing stiffness modulus until at peak strength of approximately 55 kg/cm^2 (≈ 5.4 MPa) at a stiffness modulus of 400 to 500 kg/cm^2 (≈ 39 MPa to 49 MPa) after which a decrease in the tensile strength can be observed.

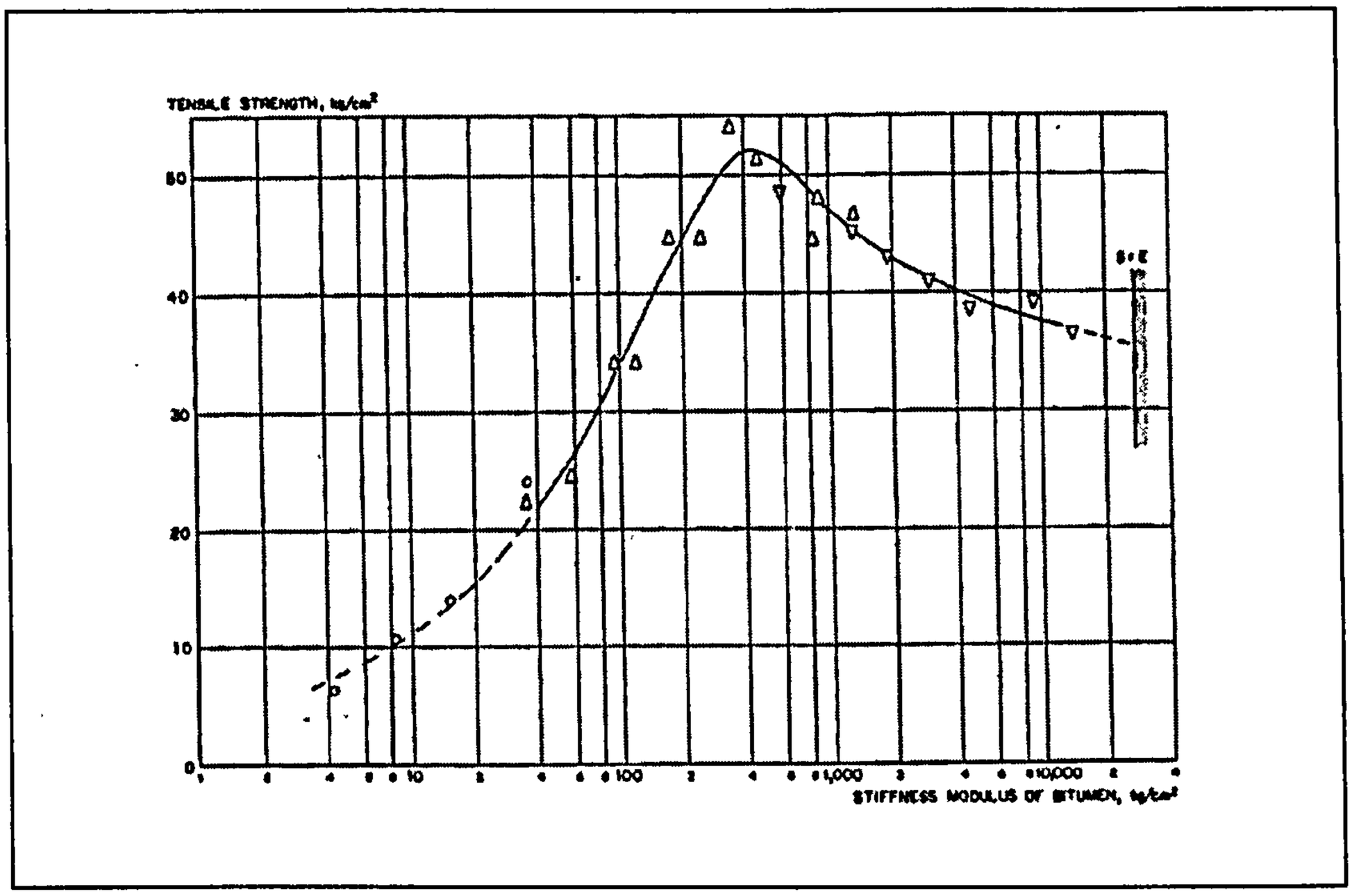

Figure 3.14: Tensile strength of plain bitumens as a function of stiffness modulus [Reproduced from Heukelom, 1966]

Similar results have also been reported more recently by Cheung [1995] who carried out constant strain rate uniaxial tensile tests on a 50 pen grade bitumen, for a range of temperatures (-50°C to 30°C). At the high temperatures and low strain rates the bitumen specimens were found to neck before fracture, whereas at the low temperatures and high strain rates fracture before necking was more common. Plotting the fracture data in terms of fracture stress, Cheung [1995] observed that all the specimen failures occurred between the stress range of 1 MPa to 3 MPa, and that there was no significant dependence of the fracture stress on the temperature or strain rate. Cheung [1995] suggests that for constant strain rate tests at temperatures higher than the glass transition, fracture is controlled by the tensile stress applied to the specimen. For an applied strain rate, the stress increases with strain, but at a decreasing rate, until a maximum value is attained. If this maximum value is smaller than the fracture stress, the specimen necks rather than breaks. Conversely, whenever

the applied strain rate is large enough to sustain a stress that is comparable to the fracture stress, the specimen breaks before it necks. Therefore, Cheung [1995] submits that the value of the fracture strain is an indication of the time taken to attain fracture stress, during which there is accumulation of the creep strain, the value of which depends on the applied strain rate.

3.5.2 Pure Bitumens in Compression

Heukelom [1966] reports on the results from constant elongation rate compression tests carried on plain bitumens at various temperatures. Heukelom [1966] observed that during the compression tests, cracking of the specimens occurred in the direction of the applied stress, and was visible from approximately the moment when maximum stress was recorded. It was not until the latter stages of the test that breakdown in the region of the largest shear stress was observed. This type of cracking, running parallel to the applied compressive stress, along planes perpendicular to the maximum principal tensile strain, is termed 'axial splitting' and can be observed in brittle materials such as concrete and rock [Neville, 1981; Vardoulakis *et al.*, 1998] and has also been reported in asphalt mixtures [Starodubsky *et al.*, 1994; Erkens *et al.*, 1998].

Based on these observations Heukelom [1966] proposed that excessive tangential strain is the governing factor that determines the maximum stress obtained in a compression test. Where the tangential strain, ε_t, is defined as the tensile strain produced in the absence of extraneous tangential stress and results from compressive axial strain, ε_a, given as:

$$\varepsilon_t = -\nu \cdot \varepsilon_a \tag{3.29}$$

For the plain bitumens tested (for which $\nu \approx 0.5$), Heukelom found that the tangential strain at break was approximately equal to the tensile strain at break, for equivalent stiffness modulus' < 500 kg/cm^2 (≈ 49 MPa).

3.5.3 Asphalt Mixtures in Tension

Heukelom [1966] states that the stress and strain in a bitumen is proportional to the

stress and strain applied to the mixture containing the bitumen, independent of the bitumen stiffness. Heukelom [1966] proposed that a 'mix factor', *M*, which depends on the bitumen content, type and grading of aggregate, mix density or void content, could be used to estimate the tensile strength of a mixture using the stiffness of its constituent bitumen through Equation (3.30). Heukelom [1966] states that it is likely that this factor would be constant, for a given mixture, for all deformation rates and/or temperatures.

$$\sigma_{Tmix} = M_T \cdot \sigma_{bit} \tag{3.30}$$

where,
σ_{Tmix} = tensile strength of the mixture
σ_{Tbit} = tensile strength of the bitumen
M_T = M_T (bitumen content, type and grading of aggregate, mix density or void content)

To demonstrate this hypothesis Heukelom [1966] carried out a series of tensile tests on a number of types of asphalt mixtures, at various strain rates and temperatures. Combining the results of these tests with those for plain bitumens (see Section 3.5.1), Heukelom [1966] produced a plot showing the relative tensile strength as a function of the stiffness modulus of the constituent bitumen, for the asphalt mixtures and plain bitumens. From this plot, shown in Figure 3.15, the uniformity of the relationship between relative tensile strength and the stiffness modulus of the bitumen is evident. It can also be observed that the asphalt mixtures obtain a maximum strength value at a similar stiffness to the plain bitumens, i.e. 500 to 600 kg/cm^2 ($\approx$ 49 – 59 MPa).

Reporting on the distress characteristics of asphalt concrete mixtures, with respect to fracture under a single load application, Monismith *et al.* [1973], presents an investigation into uniaxial and biaxial tension and compression states of stress. Monismith *et al.* [1973] report similar results to those observed by Heukelom [1966] for a range of asphalt concrete mixtures, comprising differing aggregate gradations, aggregate type, bitumen content and bitumen type, subject to tensile states of stress. In addition, Monismith *et al.* [1973] reported the following influences of 'mix factor' properties on the ultimate tensile characteristics of a mixture:

- void content – general increase in strength with decrease in void content,
- aggregate gradation – within the limits of dense graded aggregate, tensile strength increases with increase in the fineness of the grading, and
- bitumen content – there is an optimum bitumen content for maximum tensile strength.

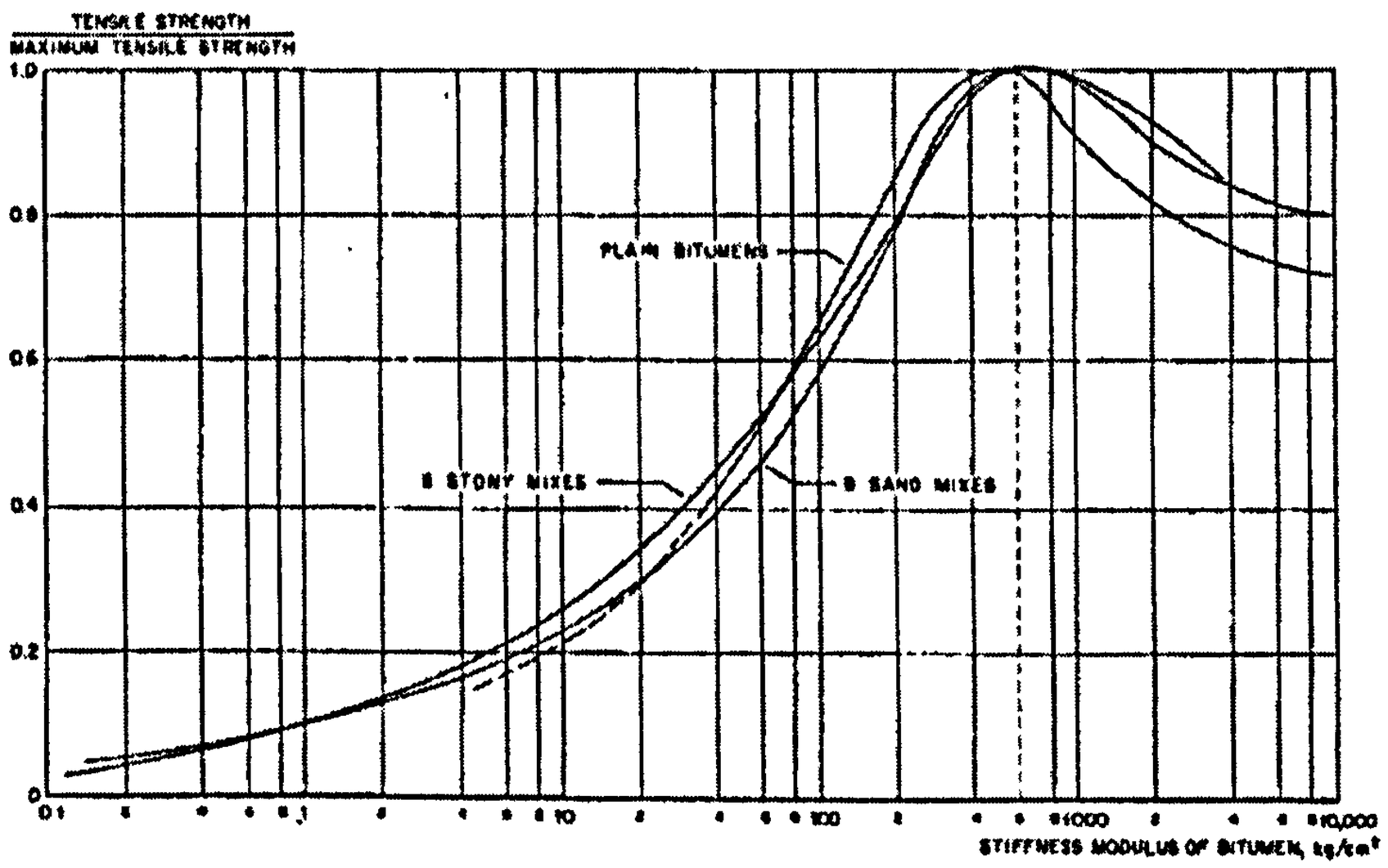

Figure 3.15: Average relative tensile strength as a function of bitumen stiffness, for 8 asphalt mixtures, 9 sand asphalt mixtures and plain bitumen [Reproduced from Heukelom, 1966]

3.5.4 Asphalt Mixtures in Compression

Investigating the response of the asphalt concrete mixtures to uniaxial compressive states of stress, Monismith *et al.* [1973] report a similar trend to that observed for the tensile states of stress, shown in Figure 3.16. It was observed that the compressive strength increased with increased binder stiffness, reaching a maximum value, ranging from 5000 – 9000 PSI (≈ 34 – 62 MPa), at stiffness moduli of approximately 6000 kg/cm^2 (≈ 588 MPa). For binder stiffness moduli greater than this, a decrease in the compressive strength of the mixtures was observed.

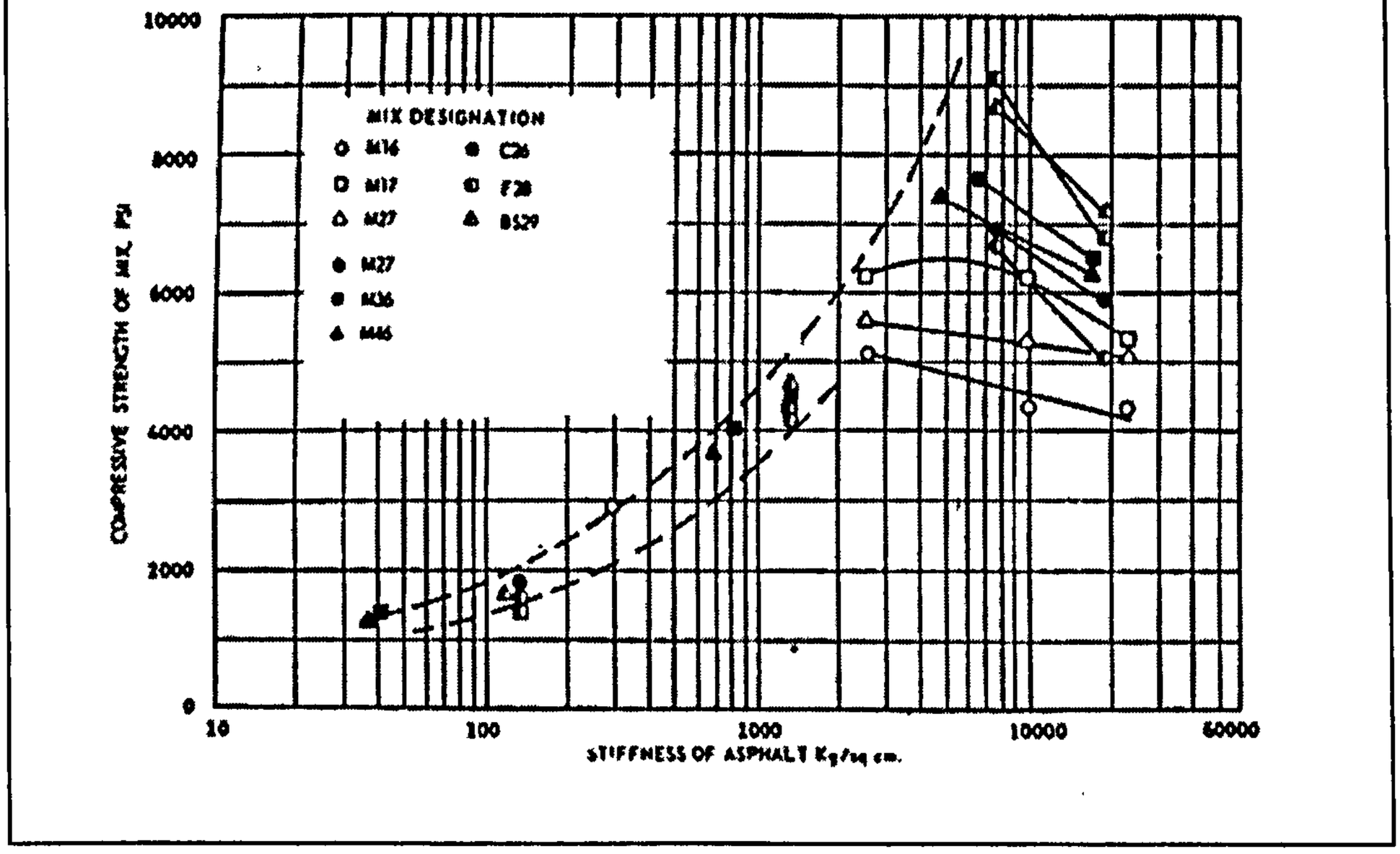

Figure 3.16: Compressive strength of asphalt concrete mixtures as a function of bitumen stiffness [Reproduced from Monismith *et al.*, 1973]

As part of the ACRe project discussed in Section 3.2, Erkens *et al.* [1998] carried out uniaxial constant rate compression tests on a 45/60 penetration grade sand asphalt mixture. The mixture design details for the sand asphalt are given in Table 3.2.

Table 3.2: Sand asphalt mixture design

Constituent	*Percentage by Mass (%)*	*Percentage by Volume (%)*
Sand	77.1	66.3
Filler	14.3	11.8
Bitumen Binder (45/60 Pen)	8.6	19.3
Air Voids	-	2.6

Uniaxial compression tests were carried out at deformation rates of 0.1, 1 and 10 mm/s and temperatures of 0, 15 and 30°C, so that the influence of these factors on the material response could be incorporated into the material model. On the basis of the results obtained, general expressions describing the apparent compressive strength

(see Section 5.3.6), Young's modulus and Poisson's ratio as functions of loading rate and temperature were determined [Erkens *et al.*, 1998 & 2000a]. The results were also used to determine preliminary model material parameters for the Desai flow surface, as described in Section 3.3.2.

In the development of the ACRe uniaxial compression test, Erkens *et al.* [1998 and 2000a] investigated the confining effects of the loading platens and the influence of specimen height to diameter ratio (h/D) on the apparent compressive strength of the test specimens. Erkens *et al.* [1998] review a number of different anti-friction methods that are commonly used in other similar engineering fields, such as concrete and soil mechanics. From this review it is apparent that confinement of a specimen's ends, at the loading platens, results in an overestimation of the compressive strength of the material being tested. A range of solutions to minimise this confining friction were considered, including:

- glycerine and talc mixture with graphite powder,
- Teflon foil sandwich (a layer of bearing grease between two layers of Teflon foil),
- rubber inter-layers, and
- plastic brush plates.

The plastic brush plates were rejected due to the difficulties associated with integrating them into the test configuration, and the expected uniform cracking pattern, at the brush/specimen interface, that their use would produce. Glycerine and talc mixtures combined with graphite powder are commonly employed in creep tests on asphalt mixtures, however for the case of uniaxial compression tests Erkens *et al.* [1998] reported no observed friction reduction. Similar results were obtained using the Teflon foil and bearing grease, which resulted in too large a confinement of the specimen ends. A series of trial tests were undertaken using rubber inter-layers positioned between the specimen and loading platens. However, this method was also rejected due to the tensile stresses generated in the contact planes resulting from the larger deformations of the rubber as compared with the asphalt mixture, and the tendency of the rubber to rupture, leading to an uneven stress distribution.

Based on the evaluation of the above methods, Erkens *et al.* [1998] submit that an appropriate interlayer, for use as friction reduction between an asphalt specimen and the loading platens in an uniaxial compression test, should have low yield strength, high ultimate strain and high resistance to rupture. Erkens *et al.* [1998] identify a thin foil of 'Luflexen'[5] sandwiched between two thin layers of soap as meeting the above criteria. Using this method of friction reduction, Erkens *et al.* [1998] observed uniform specimen deformation, with the failure mode taking the form of axial splitting, comparable to that observed by Heukelom [1966] for pure bitumen (see Section 3.5.2). Similar results were also reported by Starodubsky *et al.* [1994], who carried out uniaxial and low confinement triaxial constant displacement rate compression tests, at 8.5 milli-strain min^{-1} ($\approx 1.4x10^{-3}$ mm/s), on a number of asphalt specimens, with varying bitumen contents, compaction effort, aggregate type, height to diameter ratios, and end plate lubrication. Lubricated tests were conducted with a) no lubrication, b) with aluminium foil + paraffin paper + 4 mm thick bitumen pad, and c) aluminium foil + paraffin paper + 1.2 mm thick rubber pad. Starodubsky *et al.* [1994] report that the specimens tested without lubrication developed failure by inclined macrocracking, which were considered shear failures, whereas those tested with the friction reducing pads demonstrated less shortening and a less pronounced barrel form, with the failure mode reverting to axial splitting.

Erkens *et al.* [2000a] demonstrate the effect of height to diameter (h/D) ratio on the apparent strength of asphalt mixture specimens when tested in compression, Figure 3.17. The figure shows the apparent compressive strength for the sand asphalt mixture given in Table 3.2, for a range of specimen h/D ratios, tested at 0.05 s^{-1} at 30°C. The open squares indicate tests undertaken without friction reduction, and the closed circles represent the same test with friction reduction. From the results it was apparent that there was an increase in strength with a decrease in h/D ratio for tests conducted without friction reduction, and that h/D ratios ≥ 2 are required to determine a 'true' apparent compressive strength. Whereas, for tests with the friction reduction system, reliable 'true' apparent strengths were obtainable for ratios as low as 0.5.

---

[5] Luflexen is a Metallocen-based Linear Low Density Polyethylene (mLLDPE).

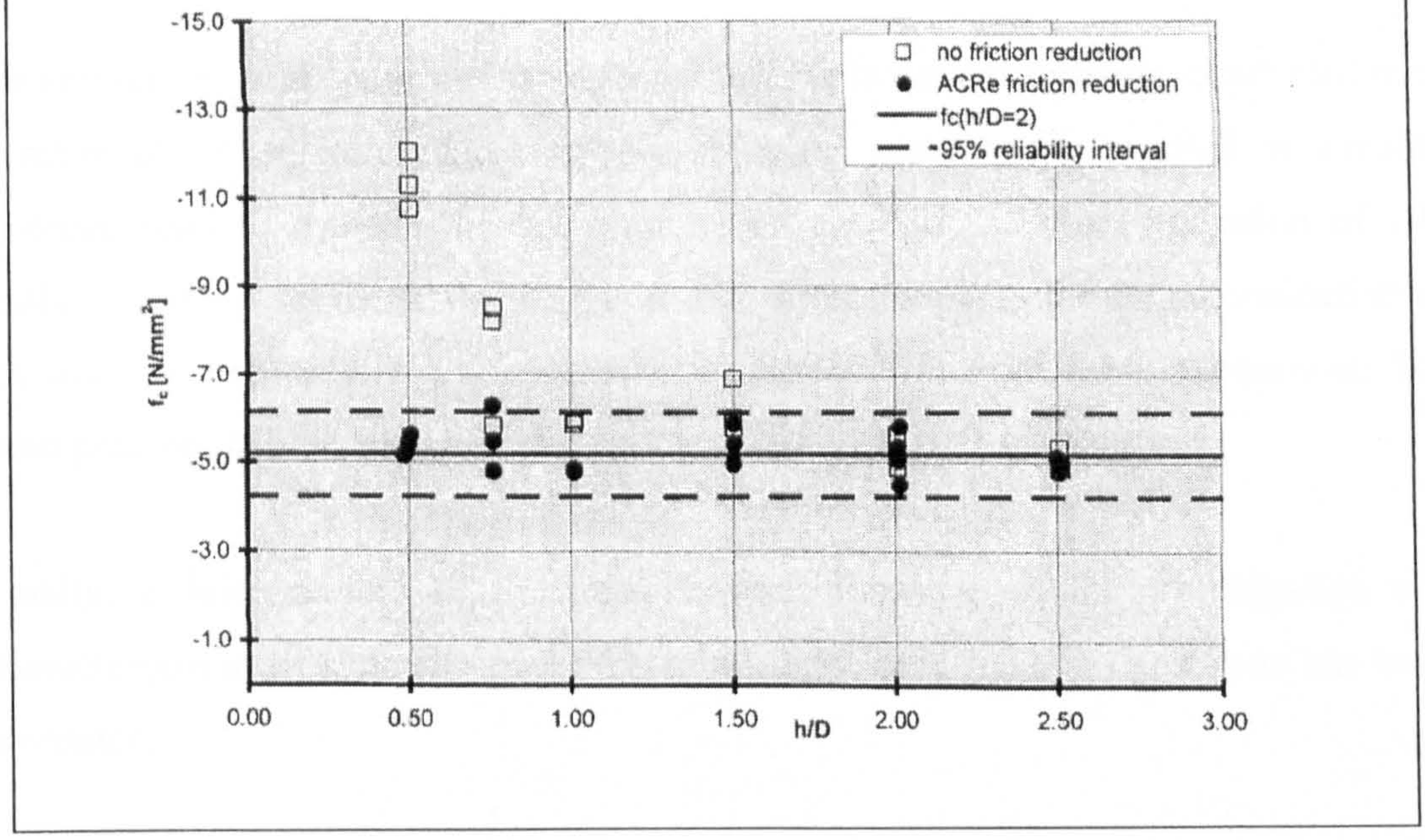

Figure 3.17: Effect of the height to diameter ratio on the apparent compressive strength of asphalt specimens with and without friction reduction (T = 30°C and strain rate = 0.05 s^{-1}) [Reproduced from Erkens *et al.*, 2000a]

3.6 Summary

In this Chapter the framework for a dynamic plasticity based constitutive model, which meets many of the pre-requisites that were identified in Chapter 2 as necessary for the accurate description of asphaltic material behaviour, has been presented. This Asphalt Concrete Response (ACRe) model has been developed at Delft University of Technology to incorporate rate and temperature effects, and can be utilised to simulate both material hardening and material degradation. The main components of the ACRe model formulation have been presented and the material parameters that are integral to the definition of the model's flow surfaces have been discussed. The model employs a Desai type single surface yield function to simulate material hardening and the overall material softening that is observed as a result of extended loading, and an independent Hoffman type criterion to simulate material cracking. In this study, research focus has been placed on the determination of the model parameters concerned with the Desai type flow surface. The potential advantages to be gained from the application of advanced constitutive models, such as the ACRe model, to the

investigation of damage modes within pavements structures has been highlighted.

Monotonic uniaxial compression and monotonic uniaxial tension tests, conducted over a range of temperatures and displacement rates, have been identified as suitable material tests to provide the basic necessary data for the characterisation of UK asphalt mixtures for use in the ACRe model. A methodology for the determination of the main model material parameters based on the data from these experiments has been presented.

Finally, a brief review of previous research focusing on the investigation and characterisation of asphaltic materials using monotonic loading conditions has been presented.

Chapter 4 - Experimental Work

4.1 Introduction

In Chapter 3 monotonic uniaxial compression and uniaxial tension tests have been identified as suitable laboratory experiments from which the basic material parameters for the ACRe model can be determined. This chapter presents the experimental work that was undertaken in this study for characterisation of two UK asphalt mixtures into the ACRe model. In the first sections of the chapter, material selection, specimen development, manufacture and densities are discussed. In the later sections of the chapter, experimental development, apparatus, instrumentation and the experimental procedures for the two uniaxial tests are presented.

4.2 Required Tests for Material Characterisation

The cohesive nature of asphalt means that it is possible to determine the basic material parameters required by the ACRe model through two test types, namely:

- monotonic uniaxial compression tests, and
- monotonic uniaxial tension tests.

Due to the significant influence of loading rate and temperature on the response of asphaltic materials, the above uniaxial tests were required to be undertaken over a range of temperatures and displacement rates.

4.3 Material Selection

Two asphaltic mixtures were chosen for characterisation. These were a 10 mm close graded wearing course macadam (formerly known as 10 mm dense wearing course macadam) [British Standards Institution, 1993] and a Type F 30/10[1] design hot rolled

[1] The mixture designation numbers 30/10 refer to the nominal coarse aggregate percentage content of the mixture and the nominal maximum aggregate size in mm in the mixture respectively.

asphalt wearing course [British Standards Institution, 1985]. These materials were selected to represent the two generic types of asphalt mixtures used in UK road construction, namely DBM's and HRA's (see Section 2.2.4), and also to allow the comparison of a continuously graded versus gap graded composition. To allow unbiased analysis of the effect of the different aggregate structures on the material response, it was decided to use the same penetration grade bitumen binder in both mixtures. A third, binder rich, 0/3 design hot rolled asphalt mortar wearing course [British Standards Institution, 1985] was also selected for additional compressive testing.

Preliminarily calculations indicated that for specimens incorporating aggregate sizes greater than 10 mm, the compressive failure load at fast loading rates and low temperatures would exceed the maximum capacity of the available hydraulic equipment (see Appendix B). Therefore, the choice of maximum aggregate stone size, and hence mixture type, was limited to 10 mm.

4.3.1 Mixture Design

The mixture designs for the DBM and HRA materials are shown in Tables 4.1 and 4.2 respectively, and represented schematically in Figure 4.1. Limestone aggregate and 100 penetration grade bitumen were used to produce the mixtures, with the binder content by mass for the DBM and HRA mixtures being 5.5% and 7% respectively. The target void content for both mixtures was set at 4%. The aggregate grading for the DBM and HRA mixtures are shown in Figures 4.2 and 4.3 respectively.

Table 4.1: DBM mixture design

Constituent	*Percentage by Mass (%)*	*Percentage by Volume (%)*
Coarse Aggregate	53.9	47.2
Fine Aggregate	37.8	33.1
Filler	2.8	2.5
Bitumen Binder (100 Pen)	5.5	13.2
Air Voids	-	4.0

Table 4.2: HRA mixture design

Constituent	*Percentage by Mass (%)*	*Percentage by Volume (%)*
Coarse Aggregate	29.8	25.6
Fine Aggregate	13.0	11.2
Sand	40.9	35.2
Filler	9.3	8.0
Bitumen Binder (100 Pen)	7.0	15.9
Air Voids	-	4.0

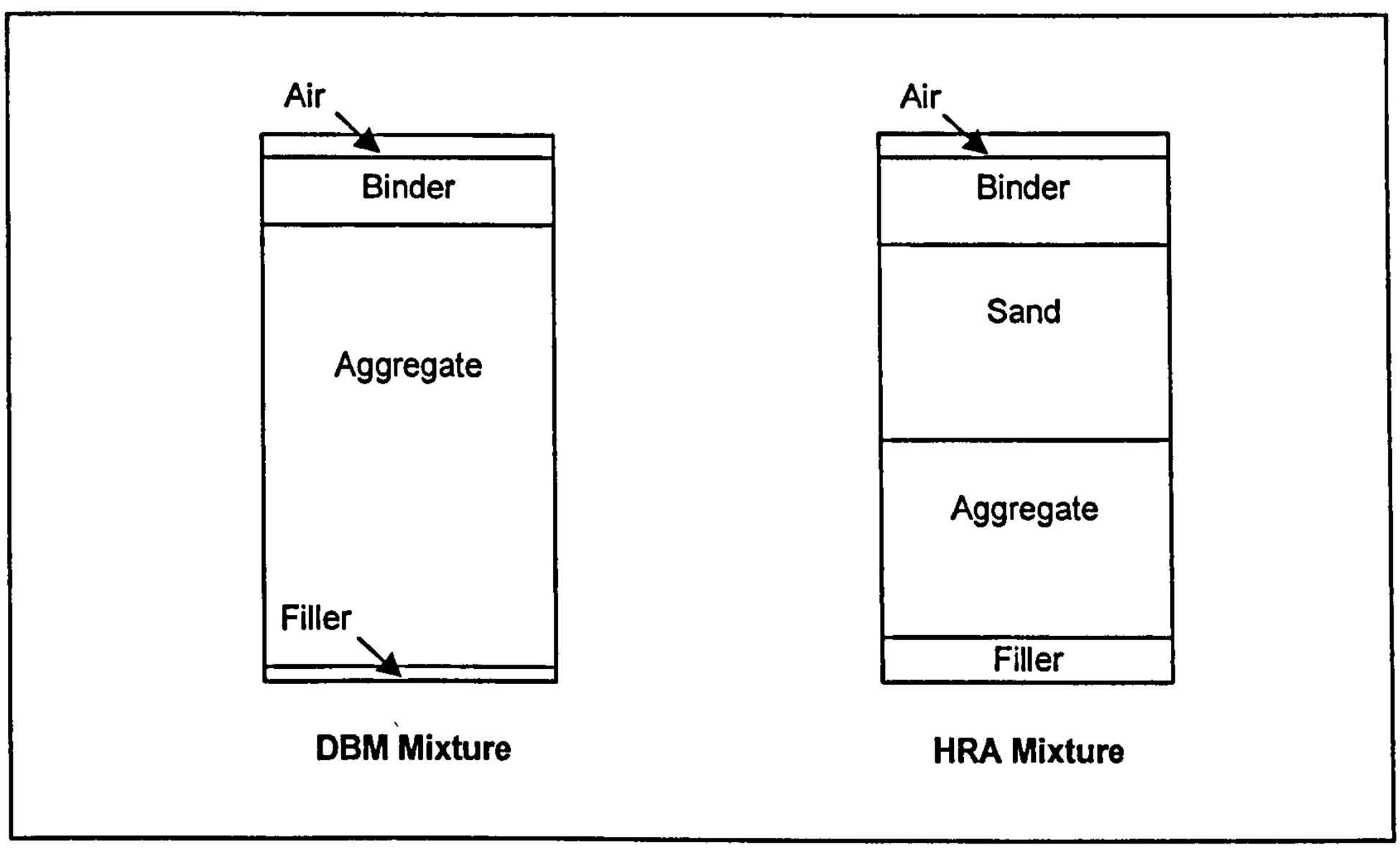

Figure 4.1: Schematic representation of DBM and HRA materials

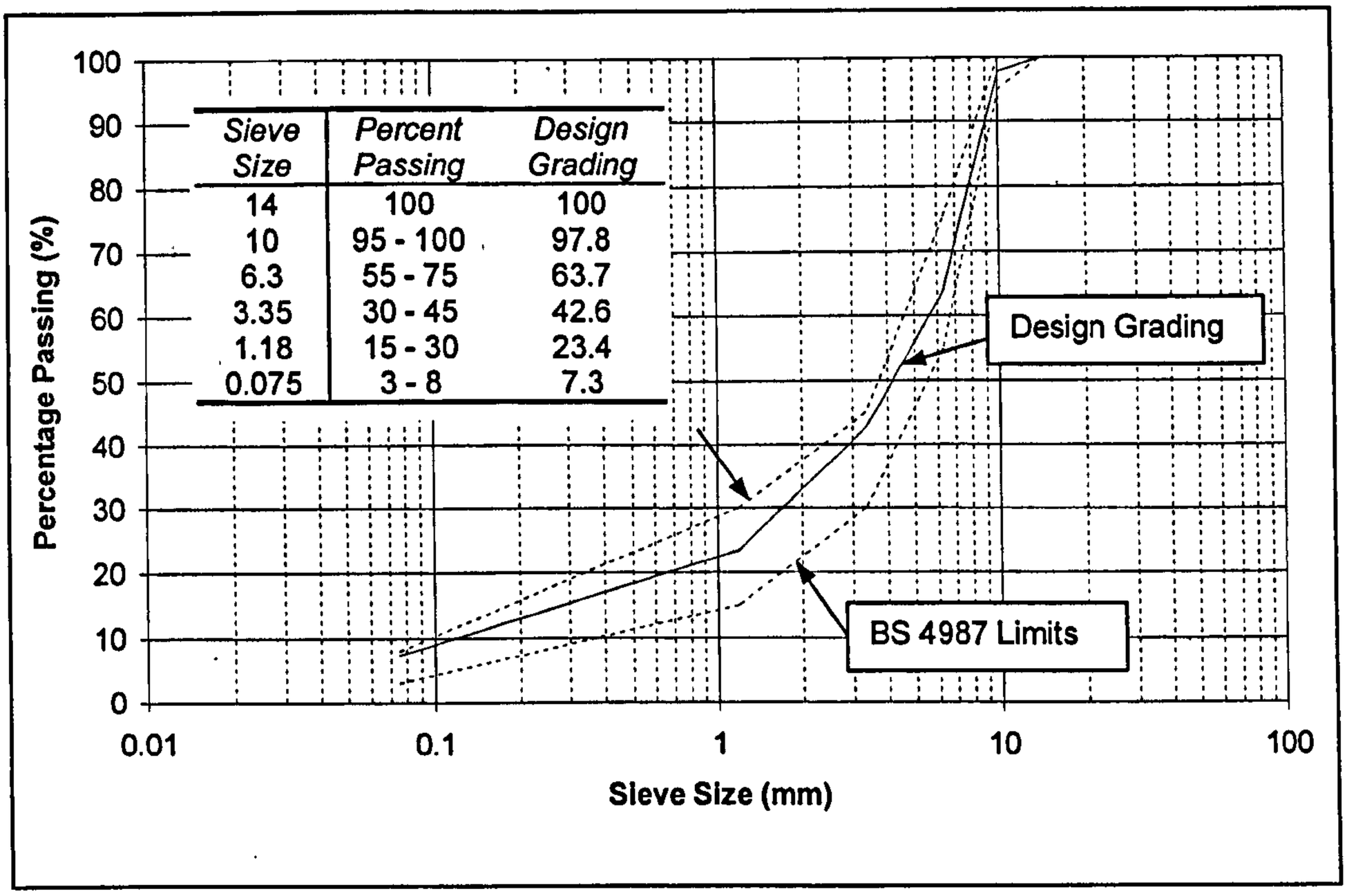

Sieve Size	Percent Passing	Design Grading
14	100	100
10	95 - 100	97.8
6.3	55 - 75	63.7
3.35	30 - 45	42.6
1.18	15 - 30	23.4
0.075	3 - 8	7.3

Figure 4.2: DBM aggregate gradation

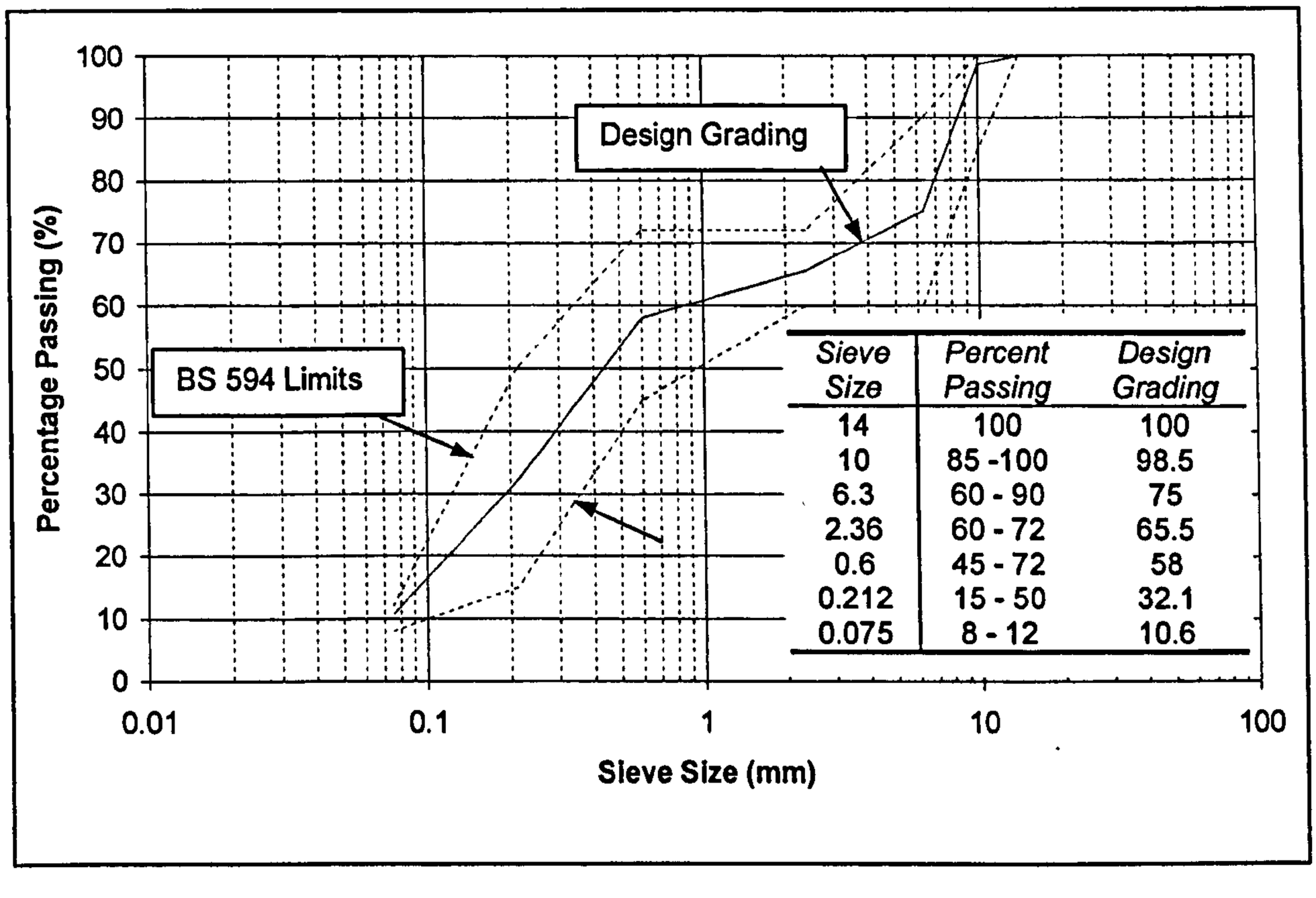

Sieve Size	Percent Passing	Design Grading
14	100	100
10	85 -100	98.5
6.3	60 - 90	75
2.36	60 - 72	65.5
0.6	45 - 72	58
0.212	15 - 50	32.1
0.075	8 - 12	10.6

Figure 4.3: HRA aggregate gradation

Additional monotonic uniaxial compression tests were also undertaken on a HRA mortar mixture. A 0/3 Type F design HRA mortar mixture was selected for testing

due to its high binder content. The mixture design for the HRA mortar is shown in Table 4.3, and schematically in Figure 4.4. Limestone aggregate and 100 penetration grade bitumen were used to remain consistent with the DBM and HRA mixtures. The aggregate gradation is shown in Figure 4.5.

Table 4.3: HRA mortar mixture design

Constituent	*Percentage by Mass (%)*	*Percentage by Volume (%)*
Fine Aggregate	12.6	10.4
Sand	64.5	53.4
Filler	12.6	10.4
Bitumen Binder (100 Pen)	10.3	21.9
Air Voids	-	4.0

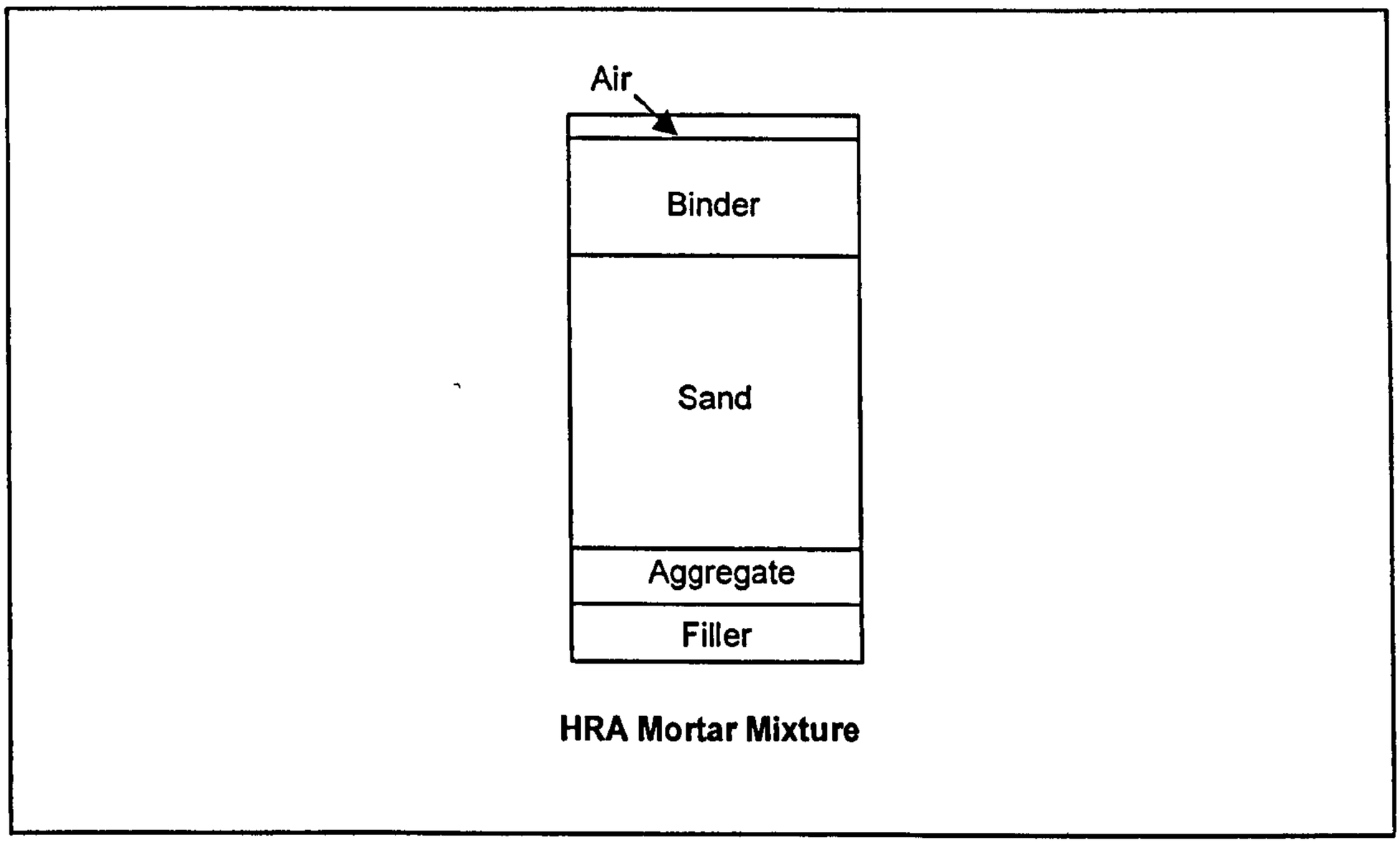

Figure 4.4: Schematic representation of the HRA mortar

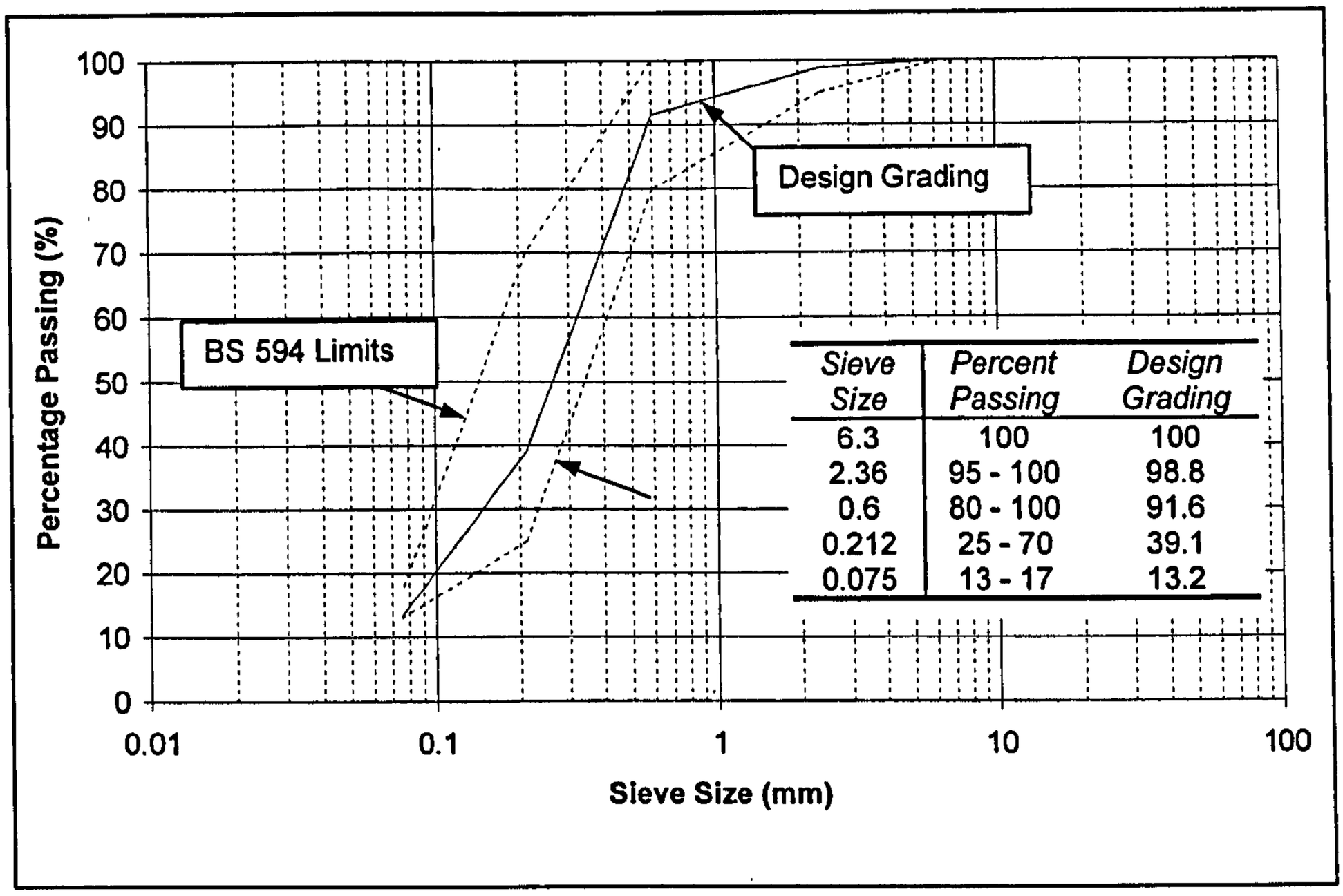

Figure 4.5: HRA mortar aggregate gradation

4.3.2 Mixing

Mixing was carried out following similar procedures to that outlined by the Asphalt Institute [Asphalt Institute, 1988]. This defines the mixing temperature as being equivalent to a bitumen viscosity of 170 ± 20 centistokes. Before mixing, the required aggregate batches were sorted in accordance with the predetermined gradations (Figures 4.2, 4.3 and 4.5) and heated in a thermostatically controlled oven to within ± 5°C of the required mixing temperature. At the same time the bitumen was also heated to within ± 5°C of the required mixing temperature. The aggregate and binder were then maintained at the mixing temperature for approximately four hours. The aggregate was then placed in a preheated sun-and-plant mixer. A small hollow was made in the aggregate into which the appropriate mass of bitumen was poured and the aggregate and the bitumen were then mixed for approximately two minutes.

4.4 Specimen Development

The material response of asphalt mixtures is state of stress dependent. Therefore to assess a one-to-one relation between a state of stress and the corresponding response,

horizontal ram drives the mould back and forth to simulate a rolling action. Prevention of compaction below a height of 120 mm was achieved by fitting a notched steel jig over the top of the mould. After compaction, the slabs were left to cool and then stripped from the moulds, cored and trimmed to produce the compression test specimens as detailed below in 'Preliminary Trials 3'. All specimens were then stored at 5°C until required for testing.

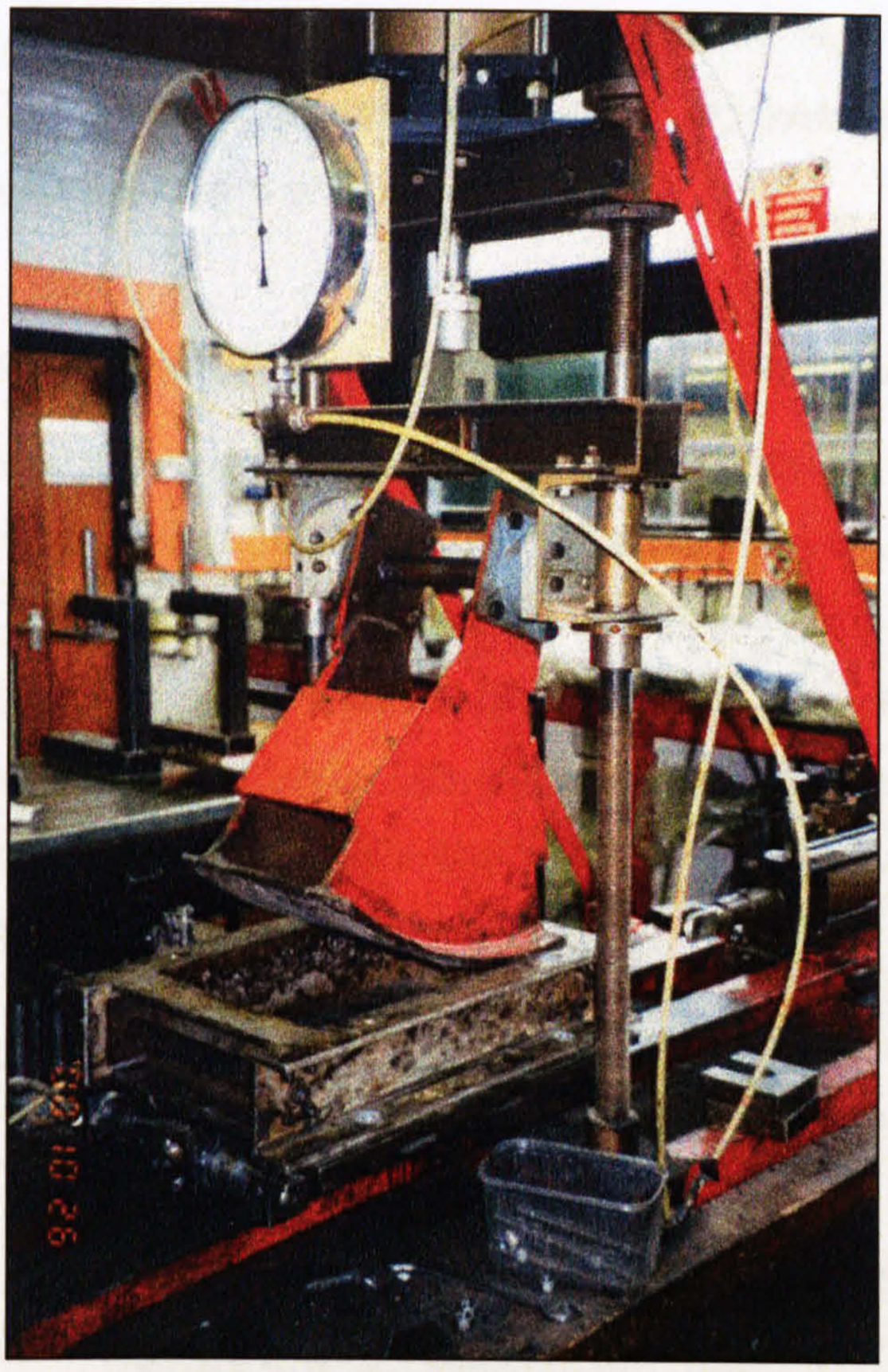

Figure 4.6: Nottingham laboratory roller compactor

Preliminary Trials 1 – Vertically Cored Specimens from Roller Compacted Slabs

Initially it was intended to core the slabs vertically to allow the production of 15 samples per slab. The slabs were therefore compacted to a height of 120 mm. Fifteen samples were then cored vertically through the slab, such that no sample was taken within 50 mm of the slab edges. A wet cutting core drill with a 49 mm internal cutting diameter was used for the coring. The cores cut from the slab measured 120

mm in length and 49 mm in diameter. They were trimmed to approximately 100 mm in length using a masonry saw taking care to ensure both ends of the specimen were parallel. Visual inspection however, revealed inconstancies in the homogeneity of the DBM specimens cored in this manner. On investigation it was discovered that a density/air void content gradient was present in the DBM slabs manufactured using the roller compactor. An approximately 6% variation was evident between the measured mixture density of the top and bottom halves of a specimen cored from a DBM slab, compared to less than 1% for a specimen cored from a HRA slab. This variability for the DBM specimens was considered to be unacceptable and therefore, this method of specimen coring was rejected.

Preliminary Trails 2 – Cored Specimens from Vibration Compacted Samples

A method similar to that described in Section 4.4.2 'Uniaxial Tension Specimen Manufacture' was investigated as a possible alternative method of compression test specimen manufacture. The method, which was principally the same as that used to manufacture the tensile specimens[3], was used to produce cubic samples 150 mm by 150 mm in plan and 120 mm in depth. Four cores measuring 120 mm in length by 49 mm diameter were cut from the sample and trimmed to 100 mm in length using a masonry saw (see Figure 4.7).

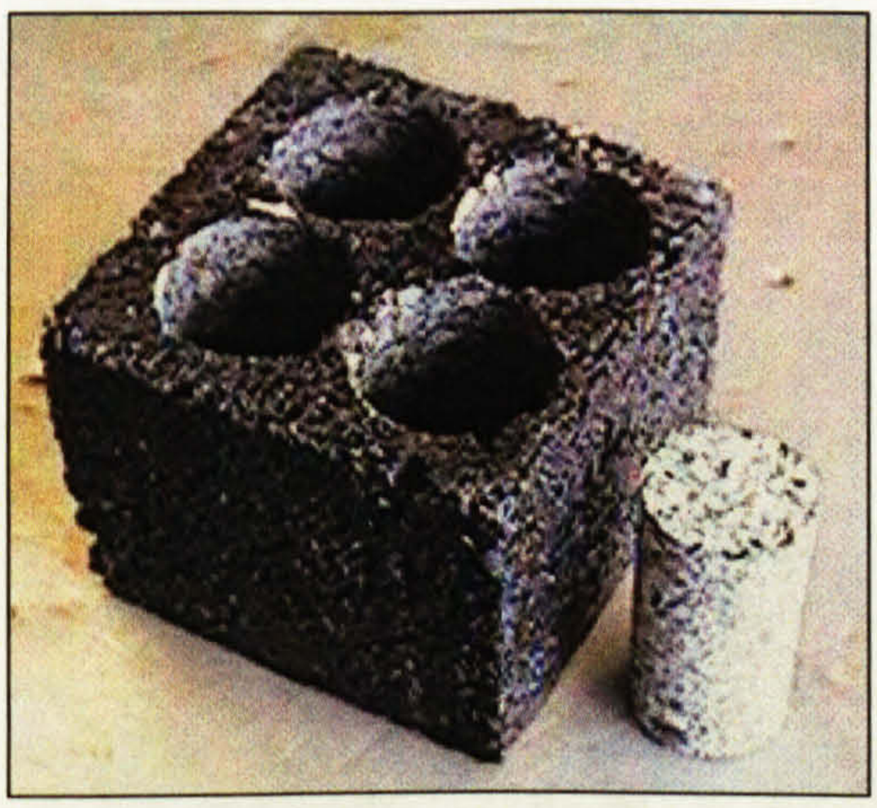

Figure 4.7: Cored 150 mm^3 sample

[3] The notable difference was the use of the concrete mould without the semi-circular inserts and the use of a 149 mm^2 Kango foot to compact the mixture.

However, it was found difficult to achieve homogenous specimen compaction of the DBM mixture, to a depth of 120 mm, using this method of production. Moreover taking the cores from close proximity to the mould walls may have resulted in boundary effects being inherent in the specimens. Therefore this method of manufacture was also rejected.

Preliminary Trials 3 – Horizontally Cored Specimens from Roller Compacted Slabs

By coring the roller compacted slabs horizontally, three cores measuring 404 mm in length by 49 mm in diameter could be cut from the slabs, such that none were taken from within 50 mm of the slab edges. Figure 4.8 shows a typical cored slab. The central sections of the cores were then cut and trimmed using a masonry saw, discarding approximately 50 mm from each of the core extremities, and taking care to ensure that the alignment of the specimen ends was parallel. This allowed the production of three specimens per core. Once trimmed, the density and air void content of the specimens were determined as outlined in Section 4.5. The mixture densities of specimens cut from horizontal cores for both DBM and HRA slabs were found on average to vary by less than 1%. It was therefore concluded that homogeneous samples could be achieved by coring the roller compacted slabs horizontally. Figure 4.9 shows typical HRA, DBM and HRA mortar compression test specimens ready for instrumentation. Using this method for the manufacture of the uniaxial compression test specimens allowed the production of nine specimens per slab.

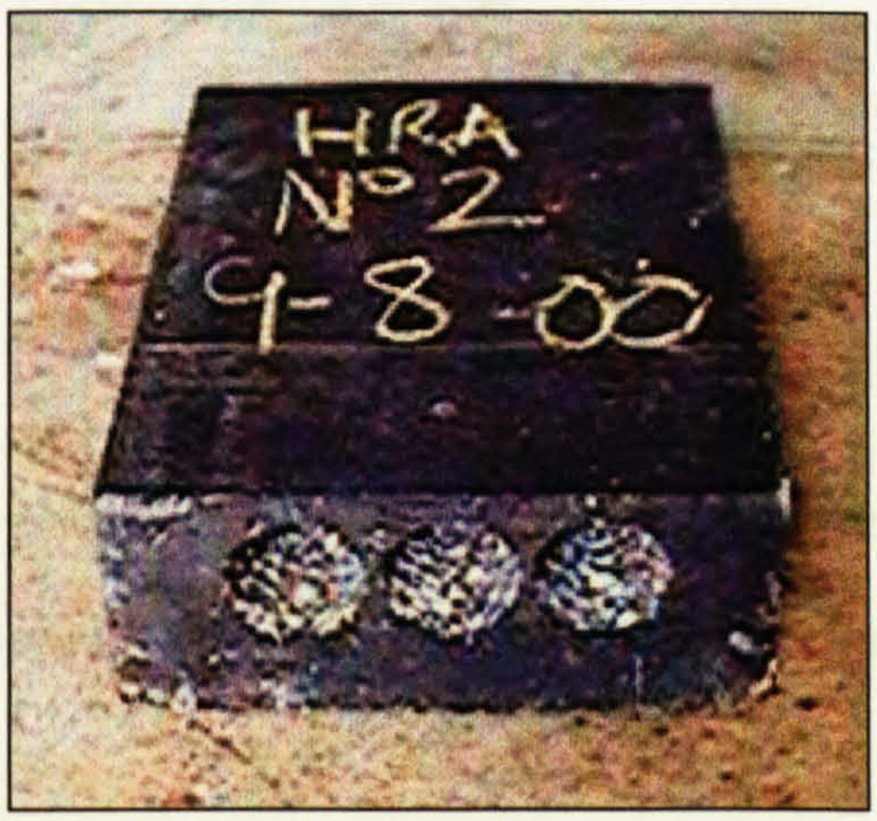

Figure 4.8: Typical cored slab (HRA mixture)

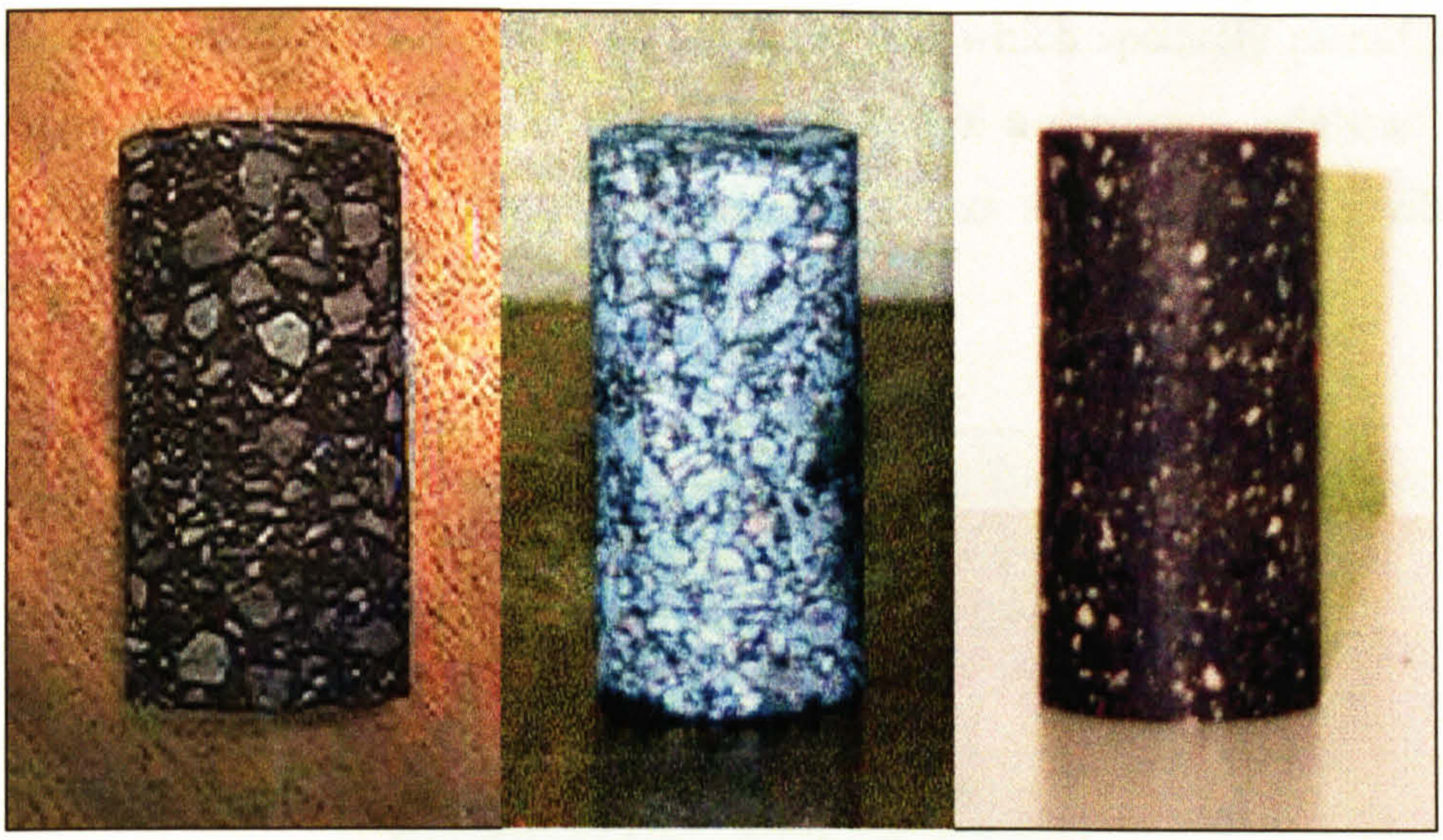

Figure 4.9: Typical HRA, DBM and HRA mortar compression specimens

4.4.2 Uniaxial Tension Specimen Manufacture

A prismatic 'dog-bone' shaped specimen was developed for the uniaxial tension test. Figure 4.10 shows a schematic of the specimen with dimensions.

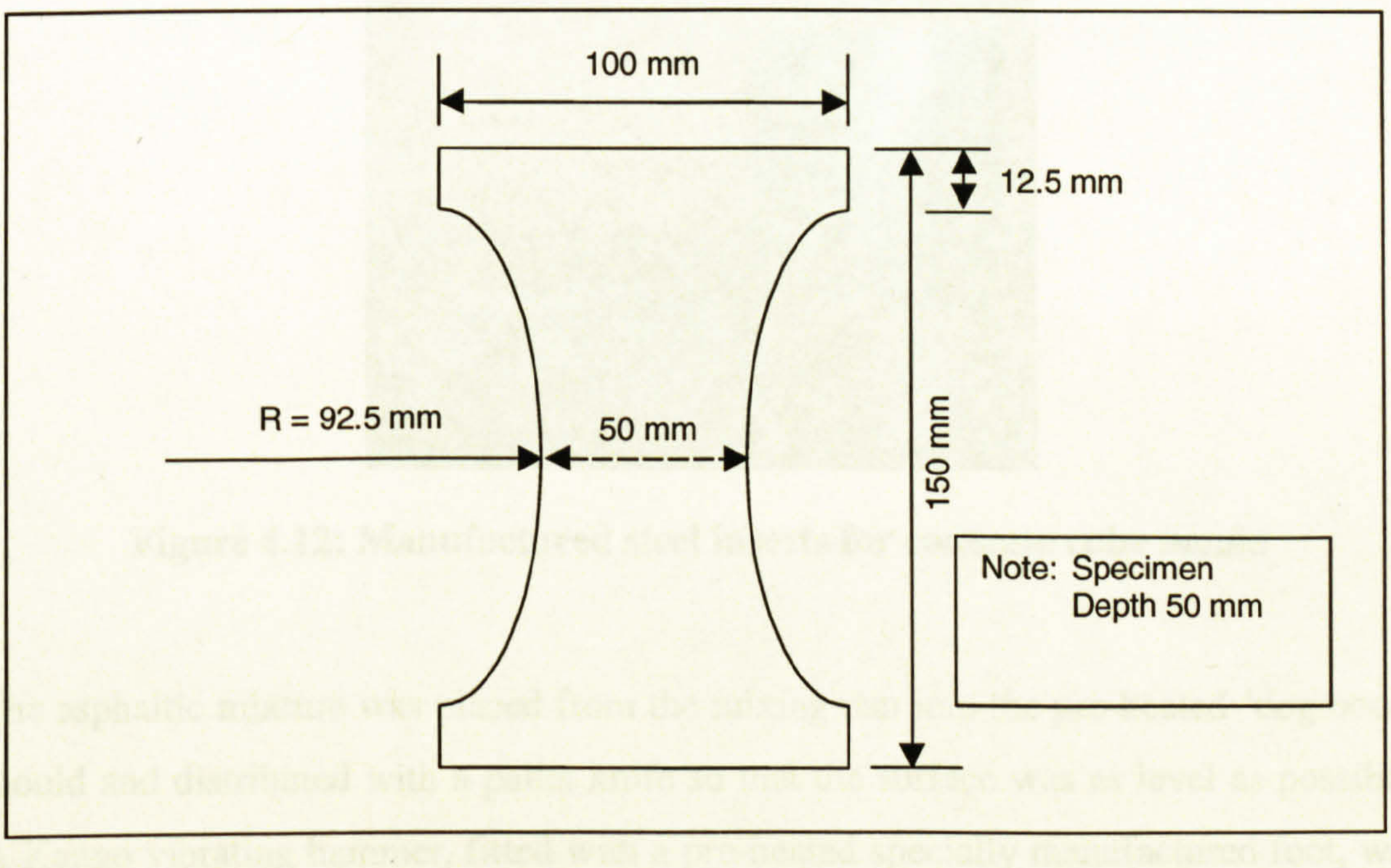

Figure 4.10: Schematic of tension specimen showing dimensions

The minimum specimen dimension of 50 mm was selected to be 5 times the maximum aggregate size. The specimens were manufactured using a converted 150

mm concrete cube mould shown in Figure 4.11, into which specially manufactured steel inserts were placed, Figure 4.12. This resulted in a specimen height to width ratio of 1.5. Compaction of the tensile specimens was achieved using a vibrating hammer compactor.

Figure 4.11: Standard 150 mm concrete cube mould

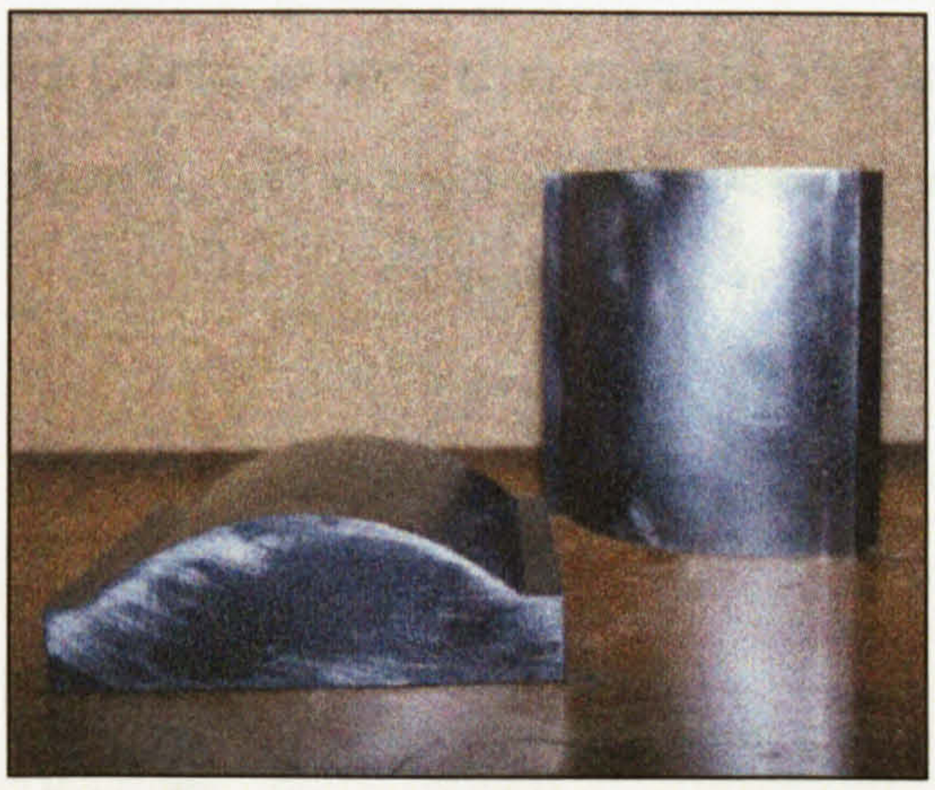

Figure 4.12: Manufactured steel inserts for concrete cube mould

The asphaltic mixture was placed from the mixing pan into the pre-heated 'dog bone' mould and distributed with a pallet knife so that the surface was as level as possible. A Kango vibrating hammer, fitted with a pre-heated specially manufactured foot, was then used to compact the material. Previous to this both the mould and Kango foot had been sprayed with a silicone lubricant to reduce adhesion of the sample to the apparatus. The Kango hammer and completed 'dog bone' mould are shown in Figure 4.13. The method of compaction was based on the Percentage Refusal Density

method (PRD) in BS 598 Part 104 [British Standards Institution, 1989]. The material was compacted from the top for a period of 1 or 1.5 minutes for the HRA and DBM mixtures respectively (predetermined from compaction trials, see below). After which the foot-screws were loosened and the whole assembly rotated through 180° and refastened, so that what was the top of the mould became the bottom. Each sample was then driven into contact with the new base plate using the vibrating hammer, and compacted for a further period of 1.5 or 2 minutes for the HRA and DBM mixtures respectively. Towards the end of the second compaction phase a steel rule was used to check the depth from the top of the mould to the compacted material in four places. The DBM material was compacted to a thickness of 70 mm (80 mm depth from the mould top) and the HRA mixture to a thickness of 120 mm (30 mm from mould top). Each sample was allowed to cool overnight before the mould was carefully stripped, after which the sample was trimmed using a masonry saw to produce specimens 50 mm in depth. The DBM samples had 10 mm of material trimmed from each side whereas the larger HRA samples were first cut in two and then 10 mm trimmed from each half. Measurements for density and air void content were then undertaken as outlined in Section 4.5. All samples were then stored at 5°C until required for testing. Figure 4.14 shows typical DBM and HRA tensile specimens ready for instrumentation.

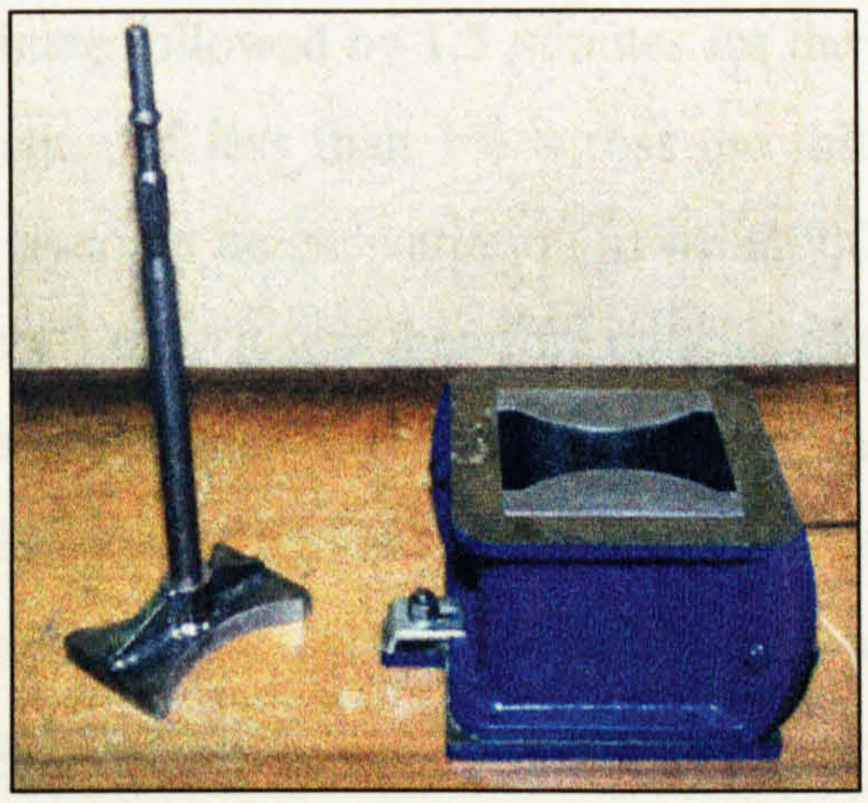

Figure 4.13: Kango hammer foot and completed mould

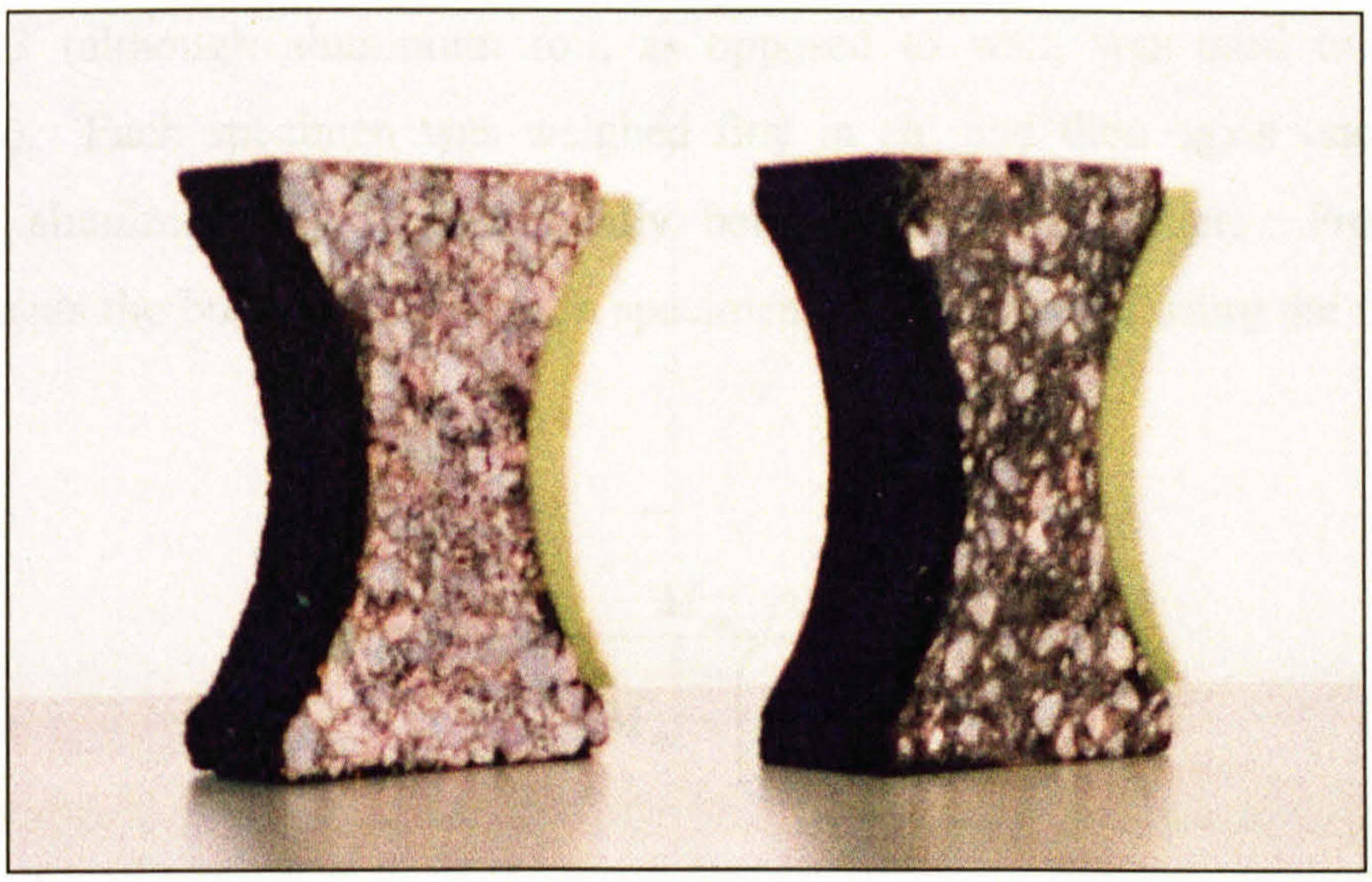

Figure 4.14: Typical DBM and HRA tension test specimens

Preliminary Trials – Compaction

Preliminary compaction trials were undertaken to investigate specimen homogeneity. These were followed by a series of trials to determine the ideal compaction time required to achieve the target specimen density for each mixture type. Varying target depths and compaction times were investigated. Vertical and horizontal sections were cut from compacted specimens and their densities determined to assess the homogeneity of the compaction procedure. It was found that a compaction time of 1.5 minutes followed by 2 minutes on the opposite side for the DBM samples and a compaction time of 1 minute followed by 1.5 minutes for the HRA samples, achieved an average density variation of less than 1% across the thickness of the specimens (vertical sections). The average height variation in density (horizontal sections) was found to be approximately 1.6%. It was therefore concluded that this procedure could be used to produce satisfactorily homogenous specimens. As the compaction of the asphaltic materials was influenced by the skill of Kango hammer operator, density/air void checks were undertaken on each sample and only those within ± 1% of the target void content were selected for testing.

4.5 Specimen Densities

The determination of specimen bulk density was carried out in accordance with BS

598 Part 3 (although aluminium foil, as opposed to wax, was used to seal the specimens). Each specimen was weighed first in air, and then again once it was sealed in aluminium foil before finally being weighed in water. From these measurements the bulk density of each specimen was determined using the following equation:

$$\rho = \frac{M_{au} \cdot \rho_w}{M_{ac} - M_{wc} - \left(\frac{M_{ac} - M_{au}}{S_{gf}}\right)} \tag{4.1}$$

where ρ = bulk density of the specimen

ρ_w = density of water (1000 kg/m^3)

M_{au} = mass of the specimen in air uncoated (kg)

M_{ac} = mass of the specimen in air coated with aluminium foil (kg)

M_{wc} = mass of the specimen in water coated with aluminium foil (kg)

S_{gf} = relative density, aluminium foil tape (1650 kg/m^3)

A theoretical maximum density of 2443 kg/m^3, 2589 kg/m^3 and 2284 kg/m^3 was estimated for the HRA, DBM and HRA mortar materials using the following equation:

$$\rho_{\max} = \frac{M_A + M_B}{\left(\frac{M_B}{G_b}\right) + \left(\frac{M_A}{G_a}\right)} \cdot \rho_w \tag{4.2}$$

where

$$M_A + M_B = 100 \tag{4.2a}$$

in which ρ_{max} = maximum theoretical density

M_A = aggregate content percent by mass of total mixture

M_B = binder content percent by mass of total mixture

G_b = specific gravity of the bitumen

G_a = specific gravity of the aggregate

ρ_w = density of water (1000 kg/m^3)

The air void content (V_v) of each specimen was then calculated as a percentage using the following equation:

$$V_v = \left(1 - \frac{\rho}{\rho_{max}}\right) \cdot 100 \qquad (4.3)$$

Tables 4.5 and 4.6 show the variation in the air void content, characterised by a mean value, minimum, maximum and standard deviation (S.d.) for the test specimens used in the uniaxial compression and uniaxial tension tests respectively.

Table 4.4: Air voids content analysis for compression test specimens

Mixture	*No. of Specimens*	*Air Void Content (%)*			
		Mean	*Minimum*	*Maximum*	*S.d.*
DBM	27	3.19	2.45	4.07	0.55
HRA	27	3.30	2.36	4.63	0.68

Table 4.5: Air voids content analysis for tension test specimens

Mixture	*No. of Specimens*	*Air Void Content (%)*			
		Mean	*Minimum*	*Maximum*	*S.d.*
DBM	27	4.15	3.20	4.98	0.48
HRA	27	4.14	3.16	4.97	0.52

The results of the air void content analysis for the HRA mortar are shown in Table 4.6. It can be seen that although a target air void content of 4 % was specified the achievable average air void content of the specimens was approximately 6 %.

Table 4.6: Air voids content analysis for HRA mortar compression test specimens

Mixture	*No. of Specimens*	*Air Void Content (%)*			
		Mean	*Minimum*	*Maximum*	*S.d.*
HRA mortar	9	6.05	5.14	6.96	0.52

4.6 Uniaxial Compression Test Development and Procedures

The monotonic uniaxial compression test was used to determine the elasticity material parameters E and ν and the ACRe model parameters α, n and γ, described in Chapter 3. Further details on these parameters and the methods for their determination are given in Chapters 5 and 6.

4.6.1 Specimen Preparation

Prior to testing, the ends of each compressive test specimen were sanded to minimise any surface roughness, and the height and diameter carefully measured using a pair of vernier callipers. The mid-height position was marked on each sample, onto which four grooved plastic guide strips were glued at approximately 90° intervals, as shown in Figure 4.15.

Figure 4.15: Compression specimen with plastic guide strips

This was done to enable a wire to be passed around the circumference of the specimen in order to measure the radial displacement (see Section 4.6.3). The plastic guides were cut from a 50 mm diameter pipe, therefore ensuring conformity with the specimen curvature.

4.6.2 Test Equipment

Figure 4.16 shows a schematic of the apparatus used for the uniaxial compression tests undertaken in this study. The test apparatus consists of a temperature controlled cabinet mounted on a MAND loading frame, a 100 kN servo-hydraulic actuator, an axially mounted load cell and specimen instrumentation. A 'Rubicon' digital servo-control system is used to operate the frame. A separate digital computer is used for data acquisition. An external pump supplied the hydraulic power. As no temperature control was originally available on either of the MAND or INSTRON loading frames (see Section 4.7.2) both were fitted with temperature control cabinets, with a –5°C to 50°C operating range, supplied and installed by Cooper Research Technology Ltd.

During a test a monotonic displacement is applied to the specimen through the hydraulic actuator, which passes through holes in the top and bottom sections of the temperature control cabinet. A precision linear variable differential transformer (LVDT), connected to the actuator piston, continuously monitors the crosshead stroke during a test, and provides a feedback signal for the control system. The control system compares this feedback signal with the input command signal, and the difference is amplified and fed to the servo-valve, which adjusts the oil flow to the actuator to reduce the difference between the input and output signals, so that the actuator responds precisely to the command signal. A load cell mounted axially on the actuator piston is used to record the applied load at pre-set time intervals during a test.

4.6.3 Compression Test Specimen Instrumentation

The compression test is undertaken using displacement control during which the specimen is instrumented to measure both axial and radial deformations. The axial displacement is measured using two axially mounted ± 25 mm stroke 0.1 % linearity

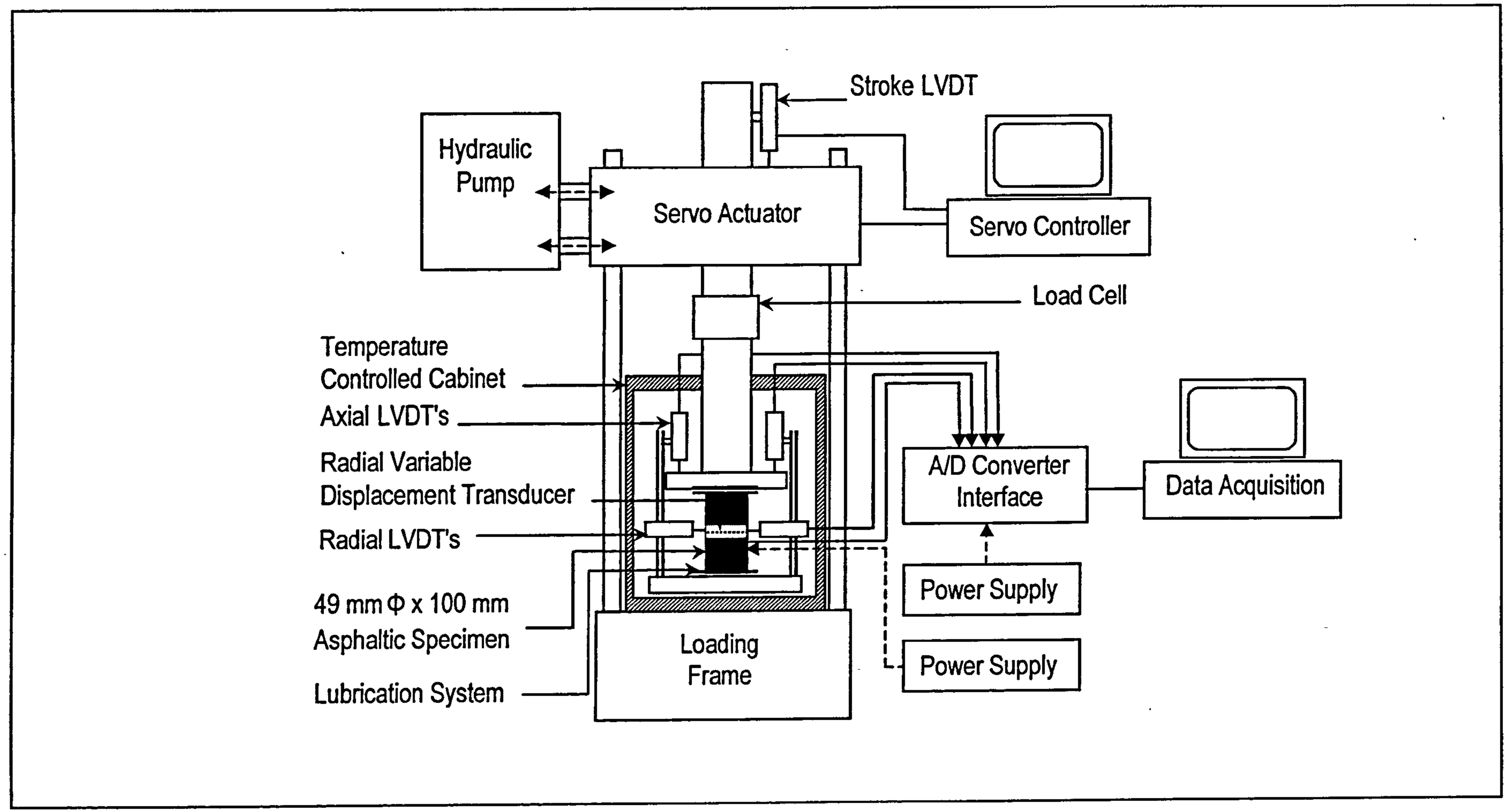

Figure 4.16: Schematic of the uniaxial compression test apparatus

LVDTs. To avoid the occurrence of damage from possible explosive compressive failure during a test, the axial LVDTs were mounted vertically, on brackets positioned at diametrically opposite locations above the specimen. The axial strain is then calculated from the average of these two measurements.

The radial displacement was measured using a combination of two different systems. The first consisted of LVDTs of the same type used for the axial measurements. These were mounted horizontally on brackets and positioned at diametrically opposite locations to measure the radial displacement of the specimen at mid-height. The second system employed a UniMeasure LX-PA-10 linear position measuring transformer that shall be referred to as a radial variable differential transformer (RVDT). The RVDT unit was also mounted in a fixed position in alignment with the central section of the specimen. A multi-stranded stainless steel wire, which wrapped around an internal capstan in the device, was extended around the specimen circumference using the plastic guides for positioning and attached to the specimen using a small metal clamp that was fixed to the sample. This arrangement is shown in Figure 4.17.

Figure 4.17: Photograph of the RVDT measurement system

Tension is maintained in the wire by an internal spring. As movement occurs, the extensible wire rotates the internal capstan, which in turn rotates a precision potentiometer. Therefore it is possible, through simple geometry, to relate the wire extension produced which is equal to the increase in circumference of the specimen,

to the average radial dilation of the specimen (see Appendix C). Using the RVDT measurement system it is possible to measure the dilation of the specimen at the same point throughout the duration of a test as the plastic guide strips ensure that the wire remains at the specimen mid-height throughout the duration of a test.

4.6.4 Uniaxial Compression Test Development

Friction Reduction at Loading Platens

The influence of friction between specimen and loading platens on compression test results is a well documented problem. It is known that, by inducing large lateral forces, the platens confine the ends of the specimen, which can lead to an overestimation of the compressive strength of the material being tested, and cause the well know barrel-shape specimen. Various researches, Starodubsky *et al.* [1994]; Vardoulakis *et al.* [1998] and Erkens *et al.* [1998 & 2000a], have shown that different types of rubber, plastic or bitumen sheets, combined with different types of lubricant can reduce or eliminate the friction at the loading plates (see Section 3.5.4). Therefore to minimise the confining effects of the loading plates, a friction reduction system similar to that proposed by Erkens *et al.* [1998] was employed in this study. This comprised a lubricated interlayer of plastic film, placed at each of the specimen loading platen interfaces. The plastic film used was a 50 μm thick metallocen-based linear low density polyethylene called 'Luflexen', supplied by Elenac UK limited. The 'Luflexen' was selected for its low yield strength and high ultimate strain characteristics. A range of preliminary tests were undertaken at 1 mm/s displacement rate at approximately 22°C (room temperature) to identify a suitable lubricant to be used in the experimental procedure. The results from these tests are shown in Figure 4.18. Both the liquid soap and the silicon grease lubricants performed equally well. Based on handing sensitively the liquid soap 'Zalpon' was selected for the test procedure. Through utilisation of the friction reduction system it was possible to minimise the effects of end confinement within the specimen. This was evident from the test results that exhibited up to an approximately 25 % reduction in the recorded peak strength of the specimens when the system was employed compared to tests undertaken with dry loading platens.

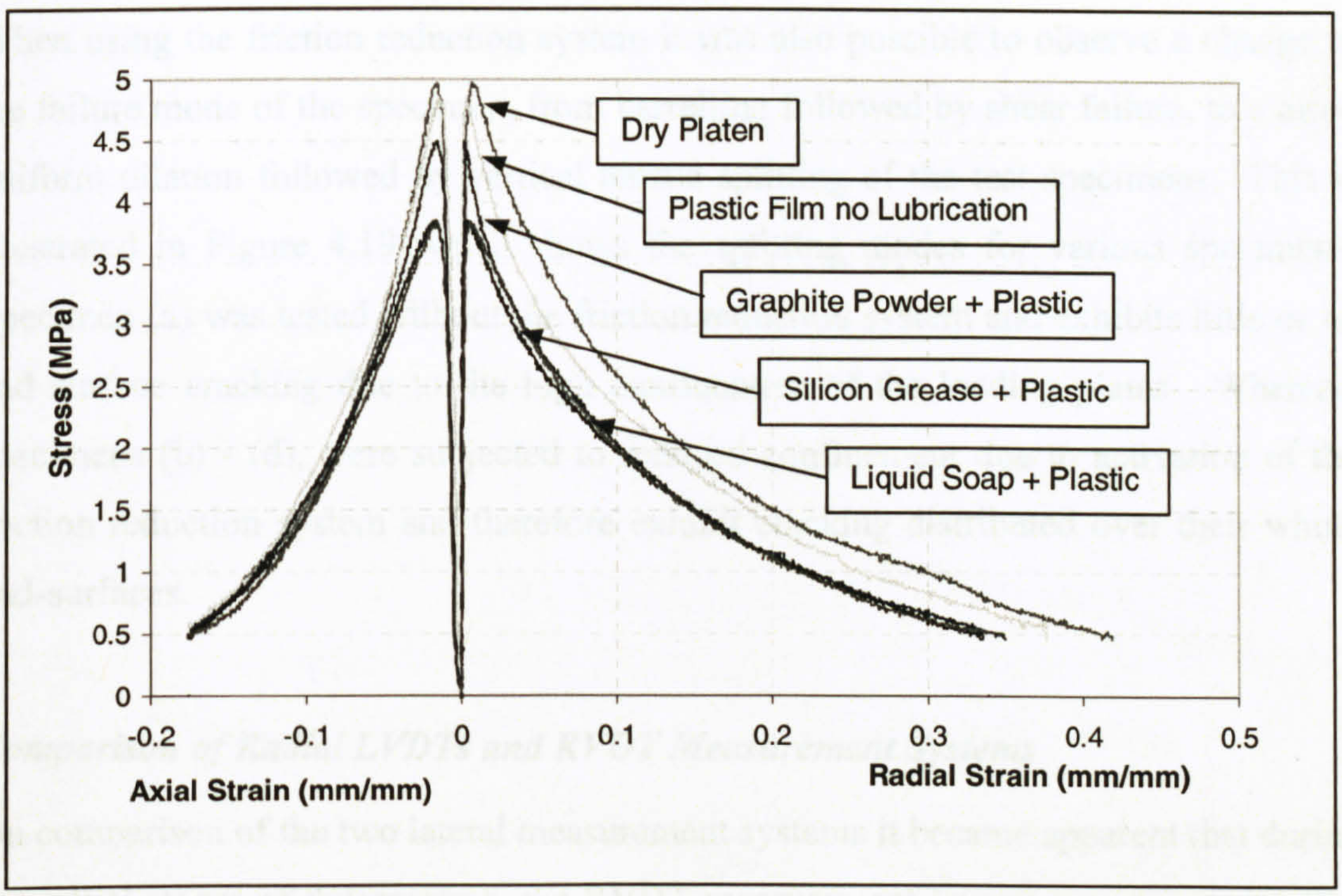

Figure 4.18: Preliminary compression tests for lubricate selection at 1 mm/s displacement rate at ≈ 22°C

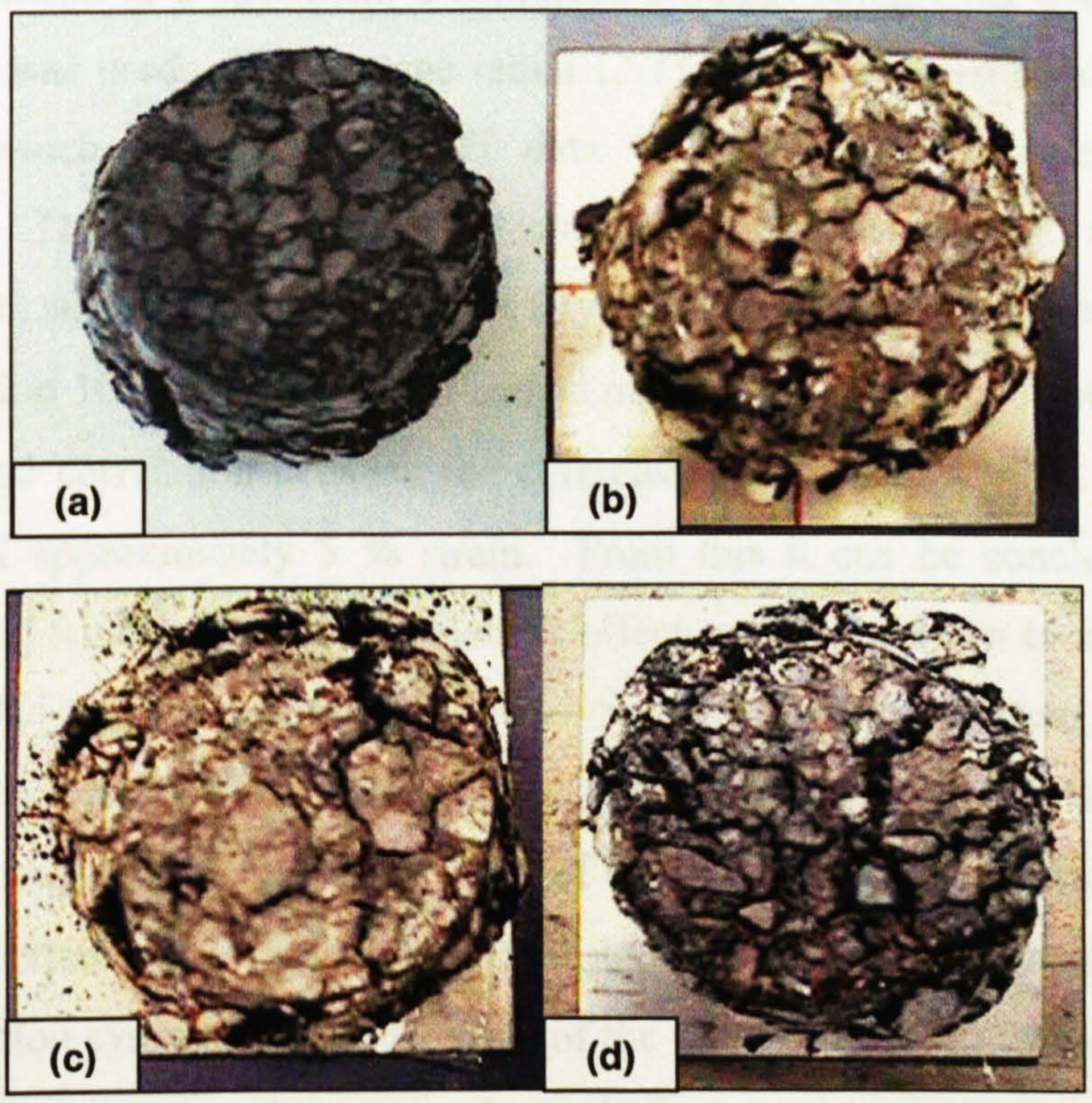

Figure 4.19: Specimen end surfaces (a) without the friction reduction system, and (b), (c) and (d) with the friction reduction system

When using the friction reduction system it was also possible to observe a change in the failure mode of the specimen, from barrelling followed by shear failure, to a more uniform dilation followed by vertical tensile splitting of the test specimens. This is illustrated in Figure 4.19 which shows the splitting modes for various specimens. Specimen (a) was tested without the friction reduction system and exhibits little or no end surface cracking due to the high confinement of the loading plates. Whereas, specimens (b) - (d), were subjected to reduced confinement due to activation of the friction reduction system and therefore exhibit cracking distributed over their whole end-surfaces.

Comparison of Radial LVDTs and RVDT Measurement Systems

On comparison of the two lateral measurement systems it became apparent that during the initial stages of deformation, the RVDT measurement system was not registering the full dilation of the specimen. This was considered to be due to friction between the extensible wire and the plastic guides, which had to be overcome before movement of the wire could take place. Therefore to achieve an overall picture of the lateral deformation of a specimen, a combined reading, comprising data taken from both systems was used. The average radial LVDT data was used up until the peak stress after which a corrected RVDT data was used for the remainder of the deformation. The RVDT reading was corrected using the average radial LVDT reading at peak stress. Figure 4.20 shows a typical example of this process for a HRA mixture tested at 10 mm/s at 20°C. It can be observed that from peak stress onwards there is a good correlation between the corrected RVDT and average radial LVDT readings until approximately 5 % strain. From this it can be concluded that the aforementioned friction reduction system is effective for strains up to approximately 5 %. After this point it is possible to observe a divergence of the two measurement systems, which, because each system is now measuring the strain at a different height on the specimen, indicates the occurrence of specimen barrelling. Similar results to this were reported by Erkens *et al.* [1998 and 2000a] who hypothesised that the friction reduction systems use the strength of the material to be activated. Therefore, the system becomes inactive somewhere during the post-peak response of the specimen, when the remaining strength is no longer sufficient to drive the system, see Figure 4.21. Therefore when the system is no longer active (post 5 % radial strain) the

end surfaces are again restrained and the specimen starts to barrel.

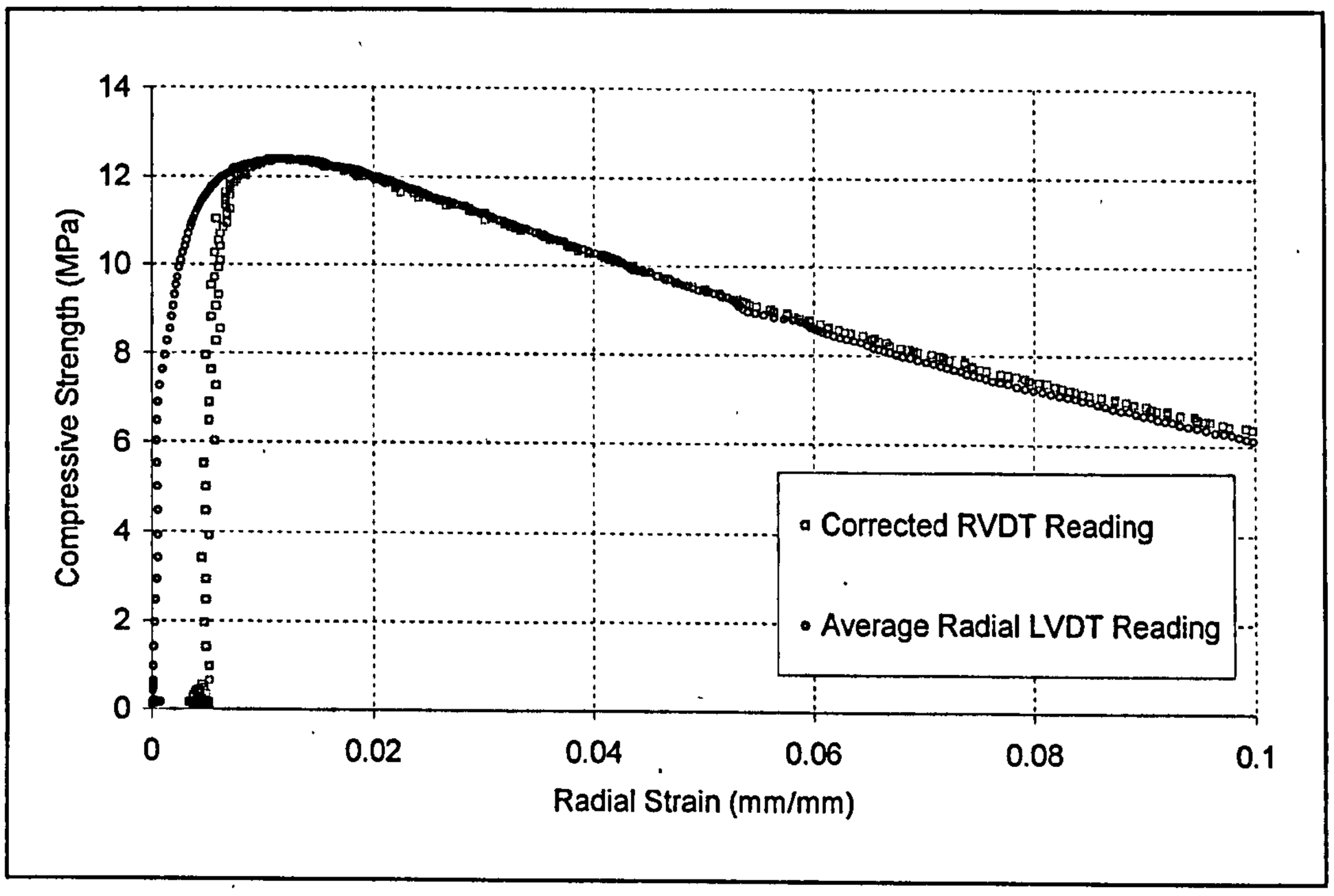

Figure 4.20: Plot showing a comparison of the radial LVDT and RVDT displacement measurement systems

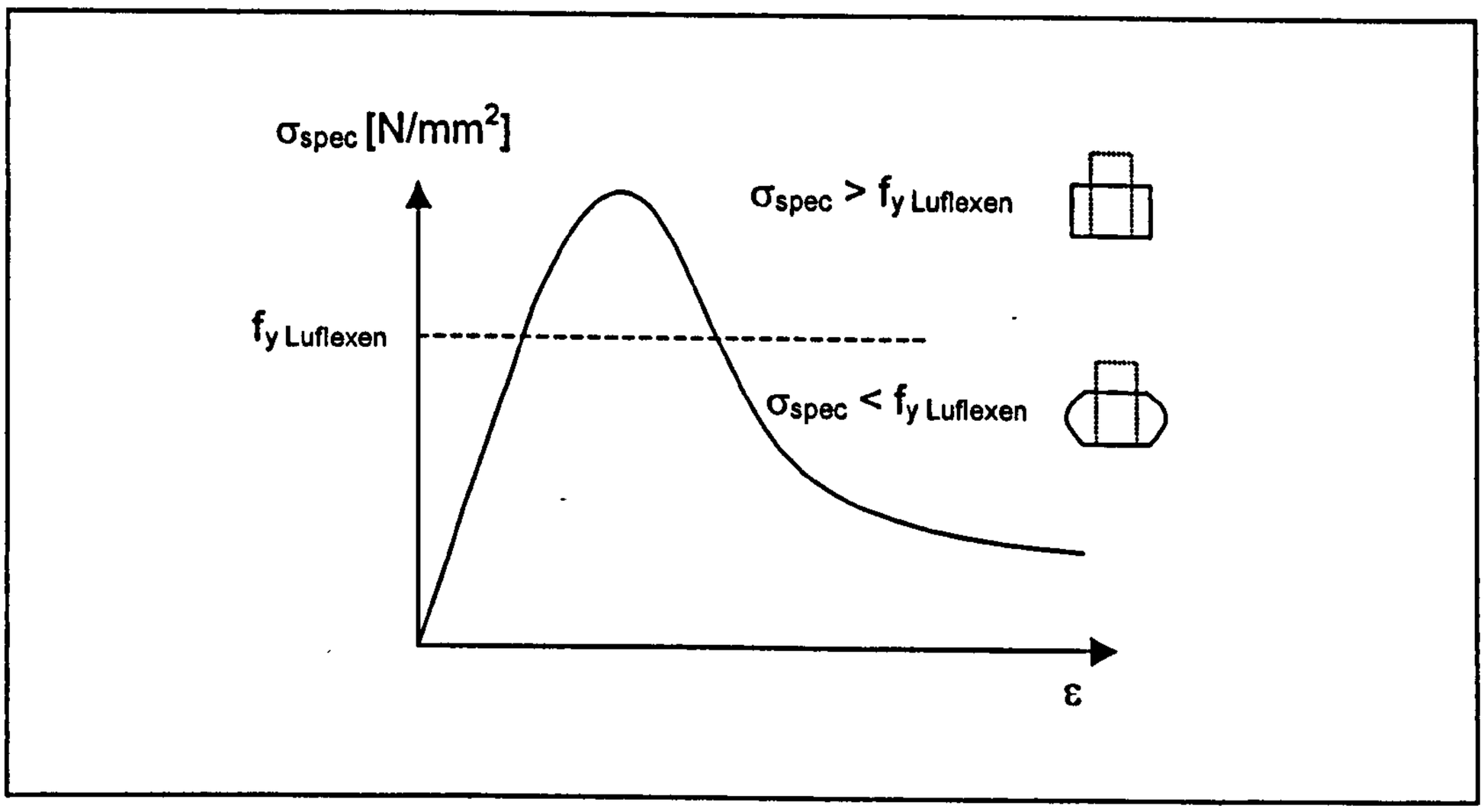

Figure 4.21: Plot showing activation zone of the friction reduction system [Reproduced from Erkens *et al.*, 1998]

4.6.5 Uniaxial Compression Test Procedure

The experimental apparatus is shown in Figure 4.16. Prior to the start of a test, the prepared compression samples were placed in a temperature controlled environment, set at the required testing temperature, for a period not less than 12 hours. When ready to start a test, a sample was taken from the conditioning environment and the specimen end surfaces were lubricated with the liquid soap as described in Section 4.6.4. The sample was then placed in the temperature controlled cabinet, also set at the required testing temperature, between the loading crossheads. The specimen was located centrally between two 100 mm square polished steel plates, whose surfaces had also been lubricated with the liquid soap. A thin layer of plastic film as detailed in Section 4.6.4 was then placed between the specimen and polished plates. The specimen was then instrumented as detailed in Section 4.6.3 and the actuator brought into position using the Rubicon control system, so that the higher loading crosshead was nearly touching the specimen end. The temperature controlled cabinet door was closed and the apparatus was then left for a period of 20 – 40 minutes, depending on the difference between the room and test temperature, to ensure a constant temperature regime within the cabinet. Before the start of the test, to avoid the risk of additional pulse loads due the actuator hitting the specimen during load application, a compressive pre-load of 0.25 kN was applied to the specimen. This pre-load also ensured that the specimen would not slide at the beginning of the test. Each test was undertaken in displacement control, throughout the duration of which two axial LVDT displacement measurements, the RVDT displacement measurement, two radial LVDT displacement measurements and the axial load were logged by a digital computer at pre-set time periods. Each test was carried out until an axial displacement of 17.5 mm was reached. During each test an ASCII file was created on the hard disc of the computer, which could then be copied and transferred for data analysis.

4.7 Uniaxial Tension Test Development and Procedures

Through the combination of the results from the monotonic uniaxial tension tests with their compressive equivalents, it is possible to determine the ACRe model parameters, R and γ, that are described in Chapter 3. Further details on these material parameters and their determination are given in Chapter 6.

4.7.1 Specimen Preparation

Prior to a test, each tensile specimen was carefully measured using a pair of vernier callipers and the positions of the LVDTs marked. The specimens were then fitted with a set of loading platens. The loading platens were bonded to the specimen ends using an 'Araldite' epoxy resin. To ensure the parallel alignment of the platens with each other and the specimen, a right angle jig, as shown in Figure 4.22 was constructed. Each sample was left for a minimum period of 24 hours to allow the resin to harden before testing. 'Pips' were then glued onto the specimen to enable measurement of the axial strain over an effective gauge length of 60 mm. This resulted in the displacement measurement being taken across a minimum of five aggregate particles, but still remote from the restrained specimen ends where spurious strain reading may occur.

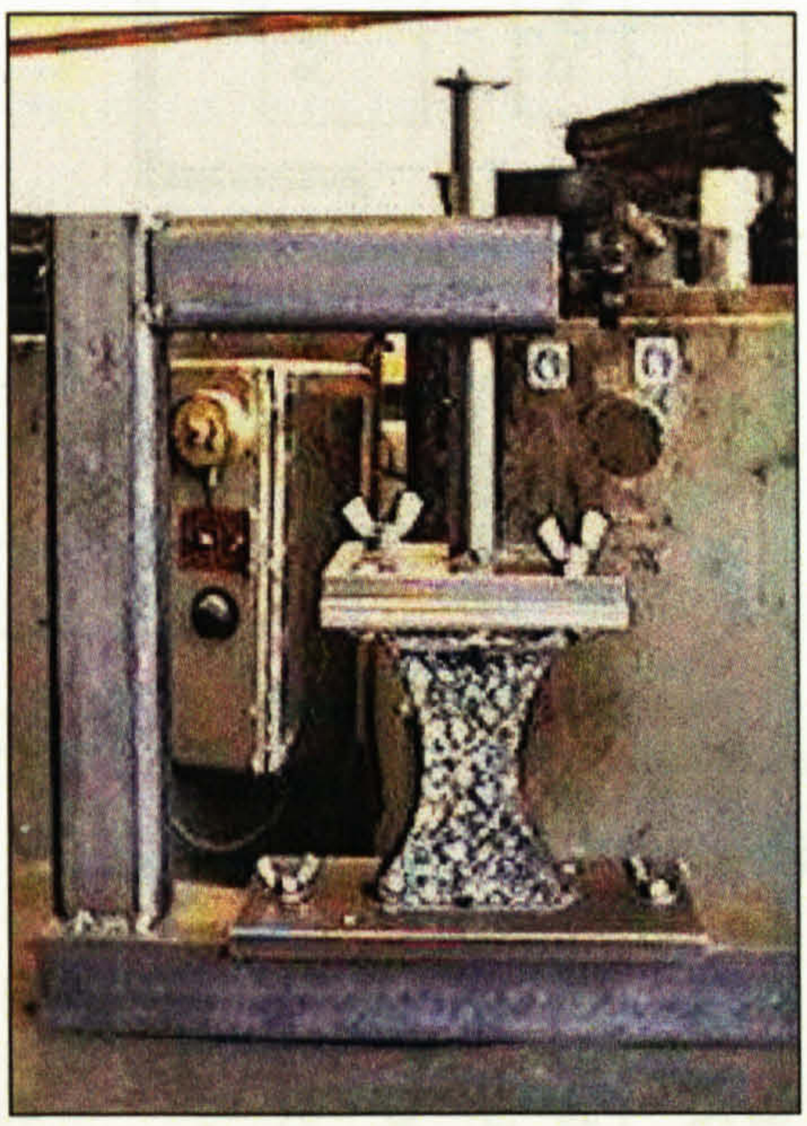

Figure 4.22: Jig for gluing loading platens to the tensile specimens

4.7.2 Test Equipment

Figure 4.23 shows a schematic of the apparatus used for uniaxial tension tests undertaken in this study. The apparatus consists of the specimen housed within a -5°C to 50°C temperature controlled cabinet, mounted on an Instron - 1332 100 kN loading frame, a servo-hydraulic actuator, an axially mounted load cell and on-specimen instrumentation. The load frame is controlled by a 'Rubicon' digital control system

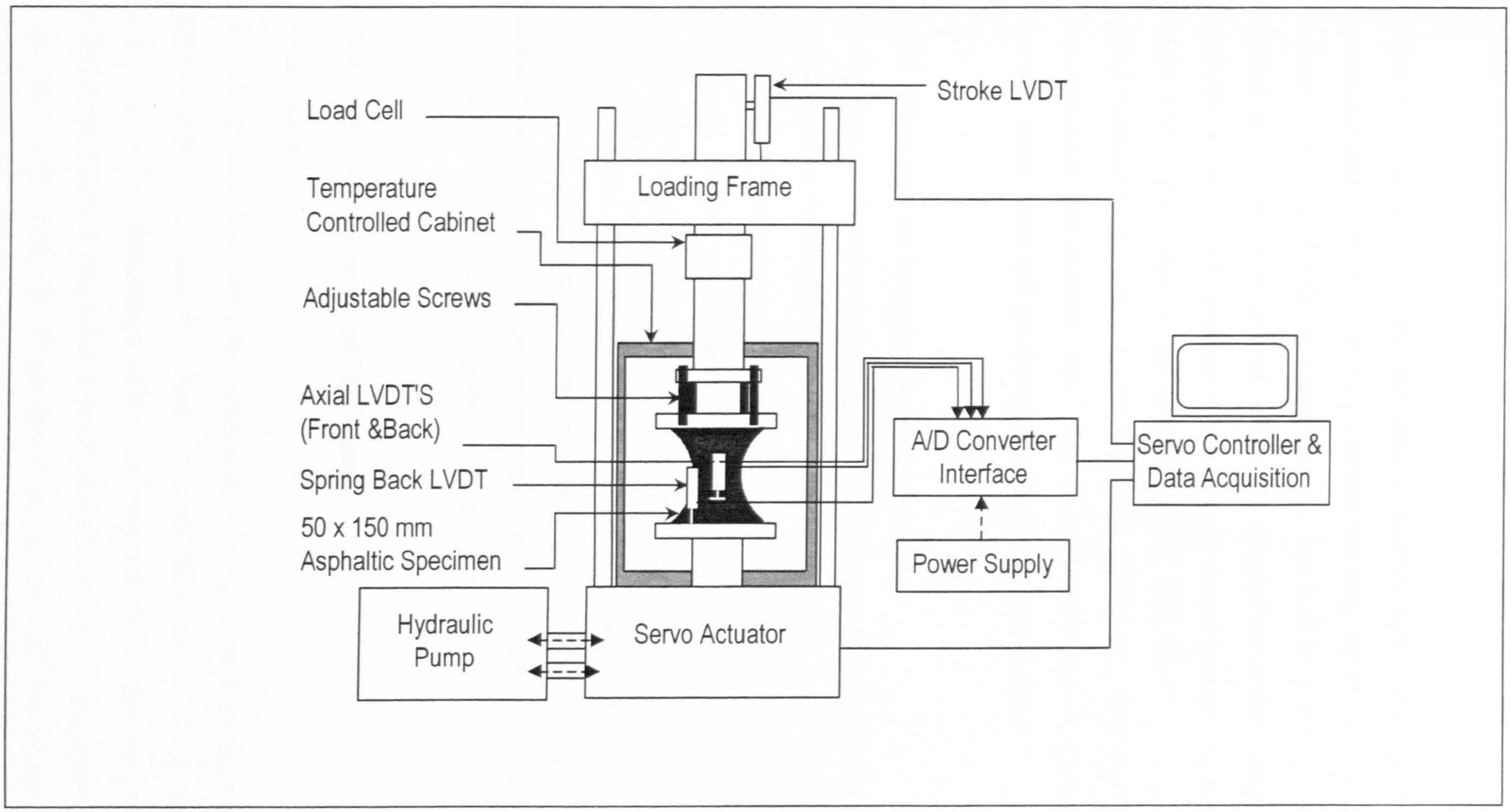

Figure 4.23: Schematic of the uniaxial tension test apparatus

that was also used for data acquisition. An external pump supplied the hydraulic power.

Using the loading platens the specimen is fastened to the upper and lower actuator crossheads and a system of bolts positioned between the top loading platen and the hydraulic ram are adjusted to compensate for any load eccentricity. Displacement is applied to the specimen, housed within the temperature control cabinet, through the hydraulic actuator. The position of the actuator is continuously monitored by a long stroke LVDT positioned on the actuator piston. This LVDT provides the feedback signal required by the servo-control system to calculate the load required to maintain the monotonic displacement rate. The applied load is then logged at pre-set time intervals using a load cell positioned axially on the actuator piston.

4.7.3 Tension Test Specimen Instrumentation

The tension test is undertaken using displacement control during which the specimen is instrumented with three LVDT's. The axial displacement is recorded by two ± 5 mm stroke LVDT's positioned centrally on each flat side of the prismatic specimen. The axial strain was then calculated as the average of these two deformation measurements. A third ± 5 mm stroke LVDT was used to measure spring back, as detailed by Scarpas *et al.* [1997], and was positioned to measure the recovered elastic strain over the lower section of the specimen. The cables from these transformers pass through a small access hole in the back of the temperature controlled cabinet. Figure 4.24 shows an instrumented tension specimen prior to the start of a test.

4.7.4 Uniaxial Tension Test Development

Pre-Loading

A series of preliminary tests was undertaken at room temperature (approximately 22°C) and at displacement rates of 0.1 mm/s, 1 mm/s and 10 mm/s. These results were then used to plot the displacement versus load response during the tests, see Figure 4.25. From these results it was evident, particularly at the slower displacement rates, that at the start of the test, the displacement controlled feedback system had difficulty adjusting to the initial 'play' in the experimental configuration. This resulted in spikes

in the initial loading curves. To overcome this problem a small pre-load of 0.05 kN was applied to the experimental arrangement just prior to the start of a test, thereby pre-tensioning the specimen and removing any 'play' in the system.

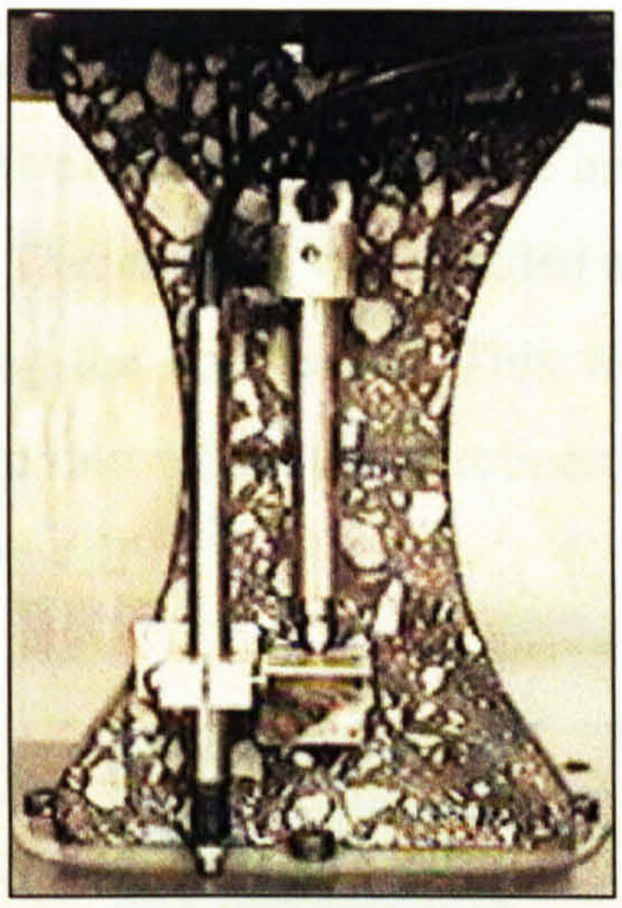

Figure 4.24: Instrumented tension test specimen

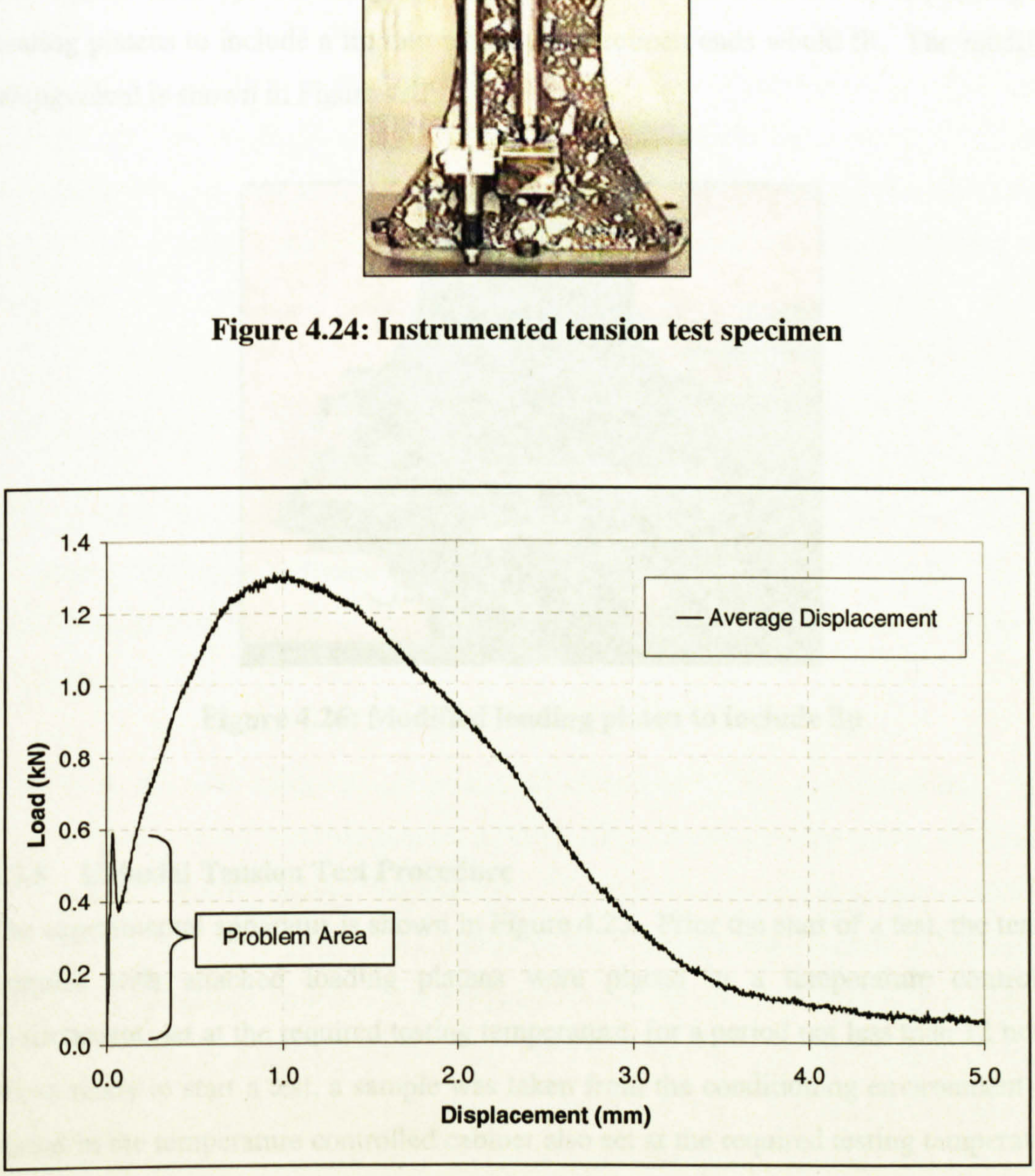

Figure 4.25: Preliminary test at 0.1 mm/s displacement rate at ≈22°C

Failure of Resin at Low Temperatures and/or Fast Displacement Rates

When testing at 5°C at displacement rates of 10 mm/s, the failure strength of the specimen was found to exceed the bond strength of the Araldite epoxy resin used to glue the sample to the loading platens. This manifested in failure taking place at the specimen resin bond interface. Therefore use of an alternative high strength 2-ton epoxy resin was instigated, however this proved to be brittle, resulting in failure taking place through the resin itself. Therefore, it was decided to increase the bond strength of the original resin by increasing the bond area. This was achieved by modifying the loading platens to include a lip into which the specimen ends would fit. The modified arrangement is shown in Figure 4.26.

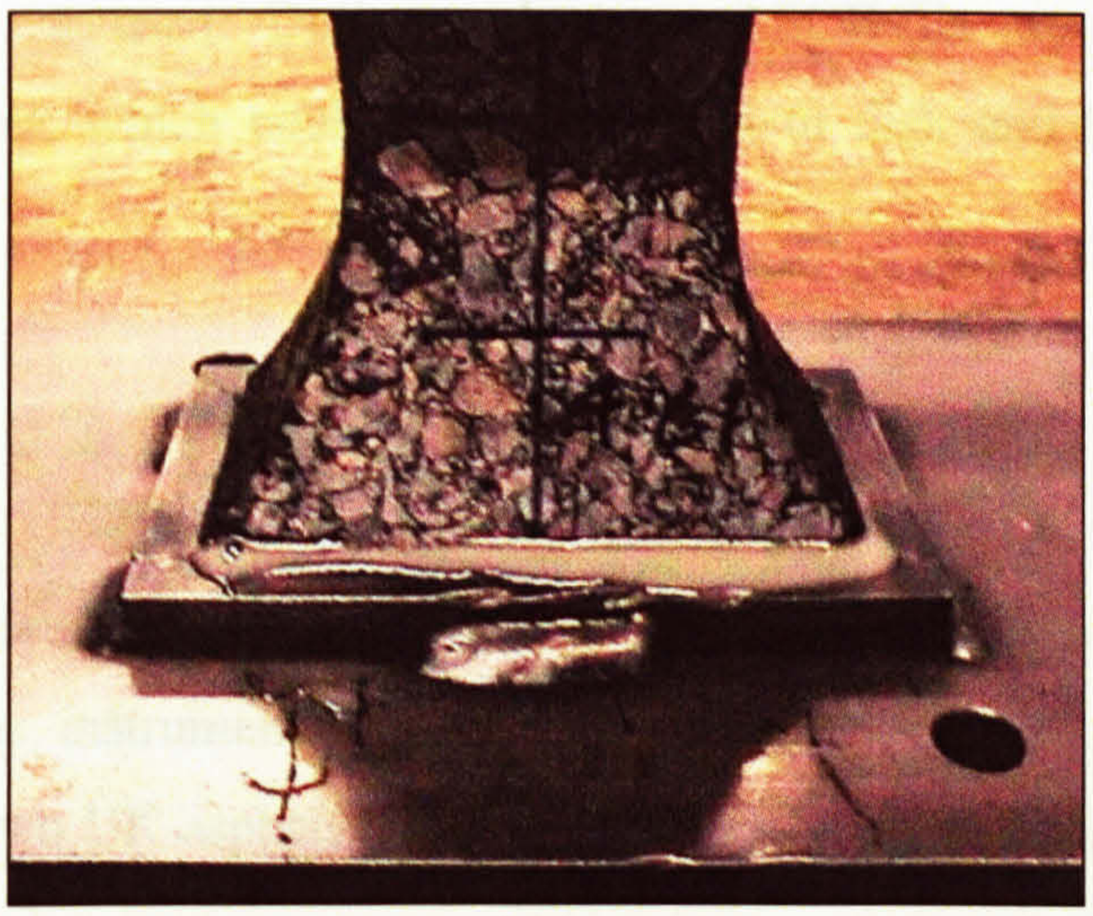

Figure 4.26: Modified loading platen to include lip

4.7.5 Uniaxial Tension Test Procedure

The experimental apparatus is shown in Figure 4.23. Prior the start of a test, the tensile samples with attached loading platens were placed in a temperature controlled environment, set at the required testing temperature, for a period not less than 12 hours. When ready to start a test, a sample was taken from the conditioning environment and placed in the temperature controlled cabinet also set at the required testing temperature. The specimen was instrumented as detailed in Section 4.7.3 and fastened to the actuator at the lower crosshead using the bottom loading platen. The specimen was then brought into position using the actuator, controlled via the Rubicon control system, so that the top loading platen could be fastened to the higher stationary crosshead. This

was done using a system of four bolts, which were adjusted two at a time until the registered load was zero ± 0.01 kN. The door to the temperature controlled cabinet was closed and the apparatus was then left for a period of 20 - 40 minutes to ensure a constant temperature regime within the cabinet. Before the start of the test a pre-load of +0.05 kN was applied to the specimen, followed immediately by commencement of the test. Each test was undertaken in displacement control, throughout the duration of which the two axial displacement measurements, the spring back displacement measurement and the axial load were logged by the Rubicon data acquisition unit at pre-set time periods. The test was carried out until there was complete fracture of the specimen or until the axial displacement reached 30 mm. It was possible to calibrate the load cell for 10, 20 50 and 100 kN ranges, therefore, during each test the lowest possible calibration was used. During each test an ASCII file was created on the hard disc of the computer, which could then be copied to disk and transferred for data analysis.

4.8 Summary

This chapter has detailed the manufacture and development of the experimental specimens, apparatus, instrumentation and test procedures required in this study for the characterisation of two UK asphalt mixtures for use in the constitutive model presented in Chapter 3.

Two main, and one additional asphalt mixture were selected for characterisation. These were a 10 mm DBM wearing course, a 30/10 HRA wearing course and a 0/3 Type F HRA mortar wearing course, respectively. The mix designs and aggregate gradations of each mixture are presented and details of the specimen manufacture processes are given. The uniaxial compression test utilised cylindrical specimens, 49 mm in diameter and 100 mm in height, which were manufactured by taking horizontal cores, longitudinally through slabs (measuring 404 mm x 280 mm x 120 mm) produced in the Nottingham Roller Compactor. A prismatic 'dog-bone' shaped specimen was developed for the uniaxial tension test, which by means of a reduced central cross-section allowed the development of fracture to take place in a repeatable and hence instrumented area. The tension specimens were manufactured using a 150 mm concrete

cube mould, into which specially manufactured semi-circular steel inserts were placed. The samples were compacted using a kango hammer, in a manner similar to that outlined in BS 598: Part 104, the Percentage Refusal Density Method.

Details of preliminary compression and tension tests are presented and the development of the experimental apparatus and test configurations are described. Both tests are undertaken in displacement control, in a temperature-controlled environment. The compression test specimen was instrumented to measure both axial and radial strains. The axial strains were recorded as the average of two axially mounted LVDT's and the radial strains were recorded using a dual measuring system comprising of a RVDT and the average of two horizontally mounted LVDT's. The tension specimen was instrumented to record the average axial displacement across the central part of the sample. In both test configurations the applied load was recorded by a load cell positioned axially on the hydraulic ram. To reduce the friction between the compression specimen and the loading platens a lubricating system, comprising a soap, plastic film, soap sandwich was employed at each of the specimen/loading platen interfaces in the compression test. Utilisation of this system resulted in an observed decrease in the measured compressive strength of the mixtures and an observed change in the failure mode, from barrelling followed by shear to a more uniform dilation followed by vertical tensile splitting of the test specimen.

Chapter 5 - Experimental Results

5.1 Introduction

This chapter presents the results of uniaxial monotonic compression and tension tests carried out over a range of temperatures and displacement rates. The chapter is broadly divided into four sections. The first section briefly presents details of the experimental programme. The second and third sections detail the results from the uniaxial compression and tension tests respectively. Within these sections the experimental results are presented and analysed, with discussion highlighting any observed trends in material behaviour. The results from the compression tests are then used to obtain the elasticity model parameters, i.e. Young's modulus and Poisson's ratio. A general temperature and strain rate dependent relationship that is used to describe both compressive and tensile strength is presented and the material strength parameters for each mixture are determined. In the final section the results from the two experimental configurations are combined to investigate the interaction between the compressive and tensile mixture characteristics.

5.2 Experimental Programme

Changes in temperature and displacement rate have a significant influence on the response of asphaltic mixtures. One of the final aims of the model when implemented in FE code, will be the simulation of the effect of these influences on material response. Therefore, it is necessary to characterise the material response over a range of temperatures, T, and displacement rates, v. The test conditions (temperature and displacement rate) for the experimental programme are shown in Table 5.1. Three repeats per test condition were undertaken, resulting in an experimental programme of 117 tests.

Table 5.1. Test conditions for the experimental programme

Test Type	*Mixture Type*	*Temperature (°C)*	*Displacement Rate (mm/s)*
Monotonic Uniaxial Compression	DBM, HRA	5	0.1, 1, 10
	DBM, HRA, HRA mortar	20	0.1, 1, 10
	DBM, HRA	35	0.1, 1, 10
Monotonic Uniaxial Tension	DBM, HRA	5	0.1, 1, 10
	DBM, HRA	20	0.1, 1, 10
	DBM, HRA	35	0.1, 1, 10

5.3 Uniaxial Compression Test Results

The uniaxial compression testing programme was carried out as detailed in Section 4.6 for each of the test conditions listed above in Table 5.1. The overall axial and radial deformations and loading forces were transformed into strains and stresses[1], from which the apparent compressive strength, f_c, defined as the peak compressive stress, the axial strain at peak stress, ε_a^{peak}, and the radial strain at peak stress, ε_r^{peak}, could be determined for each test condition. The elasticity parameters, Young's modulus and Poisson's ratio, were calculated from the axial and radial strains recorded at the beginning of each test using linear regression analysis (see Sections 5.3.7 and 5.3.8 respectively).

5.3.1 Summary of Compression Test Results

The compressive data, presented in summary form, is given in Tables 5.2, 5.3 and 5.4 for the DBM, HRA and HRA mortar mixtures respectively. Typical examples of the DBM and HRA material response are presented graphically in Figures 5.1 to 5.6, which show plots of the compressive stress (plotted as positive) versus the axial and radial strain curves for the range of applied displacement rates for each test temperature. Figure 5.7 shows a similar plot for the HRA mortar mixture that was tested at 20°C. Plots of the individual test results are shown in Appendix E.

---

[1] Due to signal interference the LVDT compressive data was filtered prior to analysis, see Appendix D.

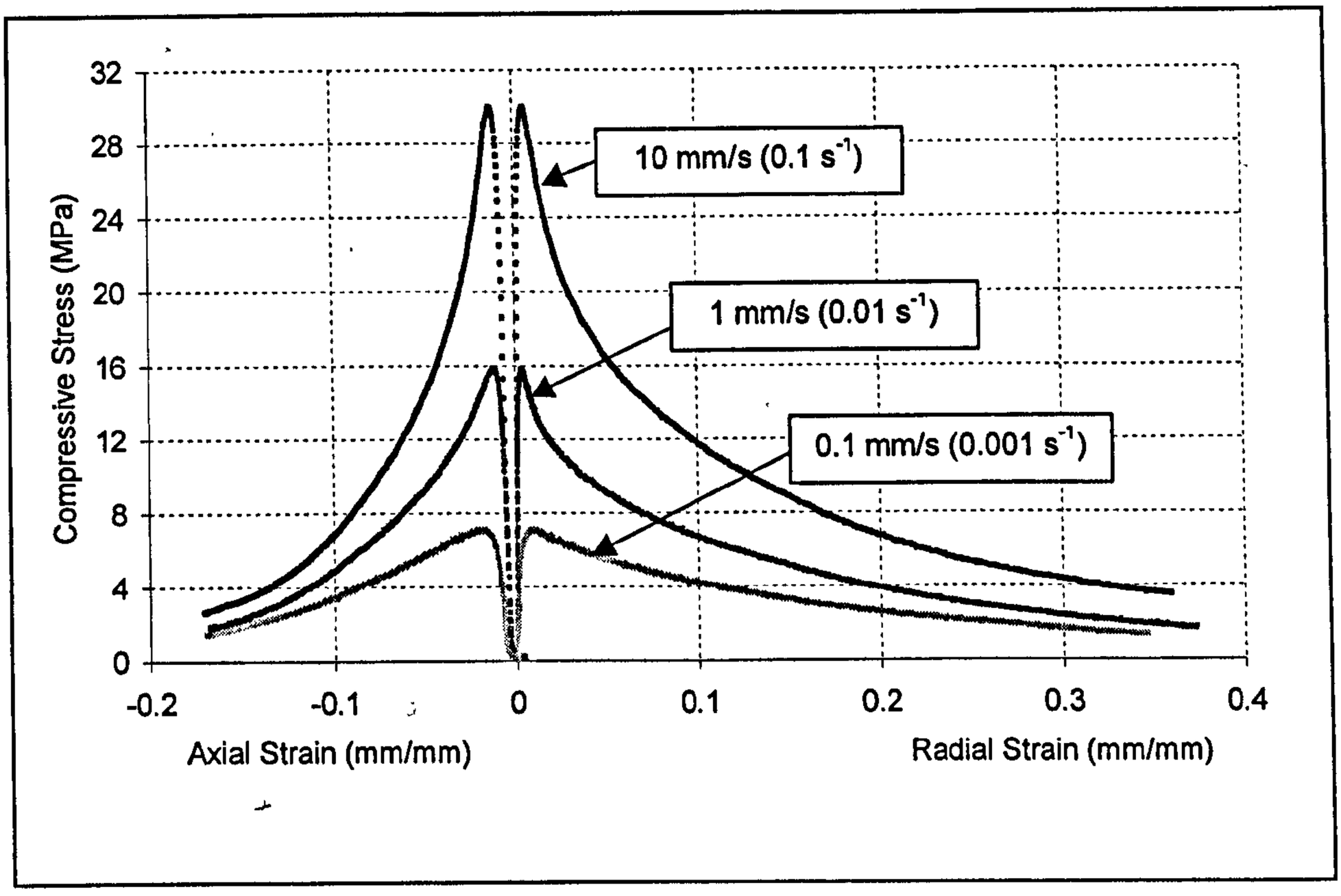

Figure 5.1: Typical uniaxial compression data - DBM mixture at 5°C

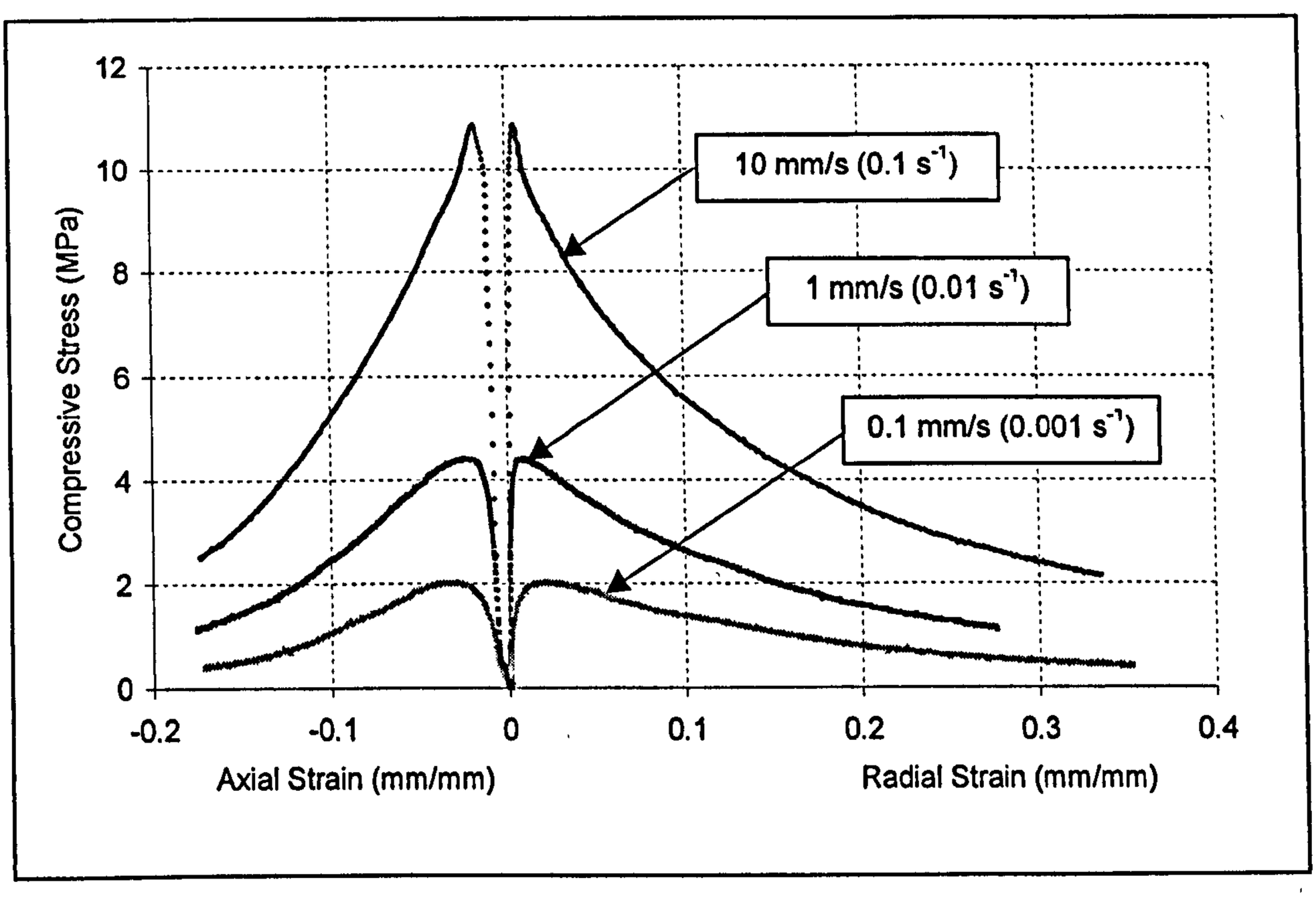

Figure 5.2: Typical uniaxial compression data - DBM mixture at 20°C

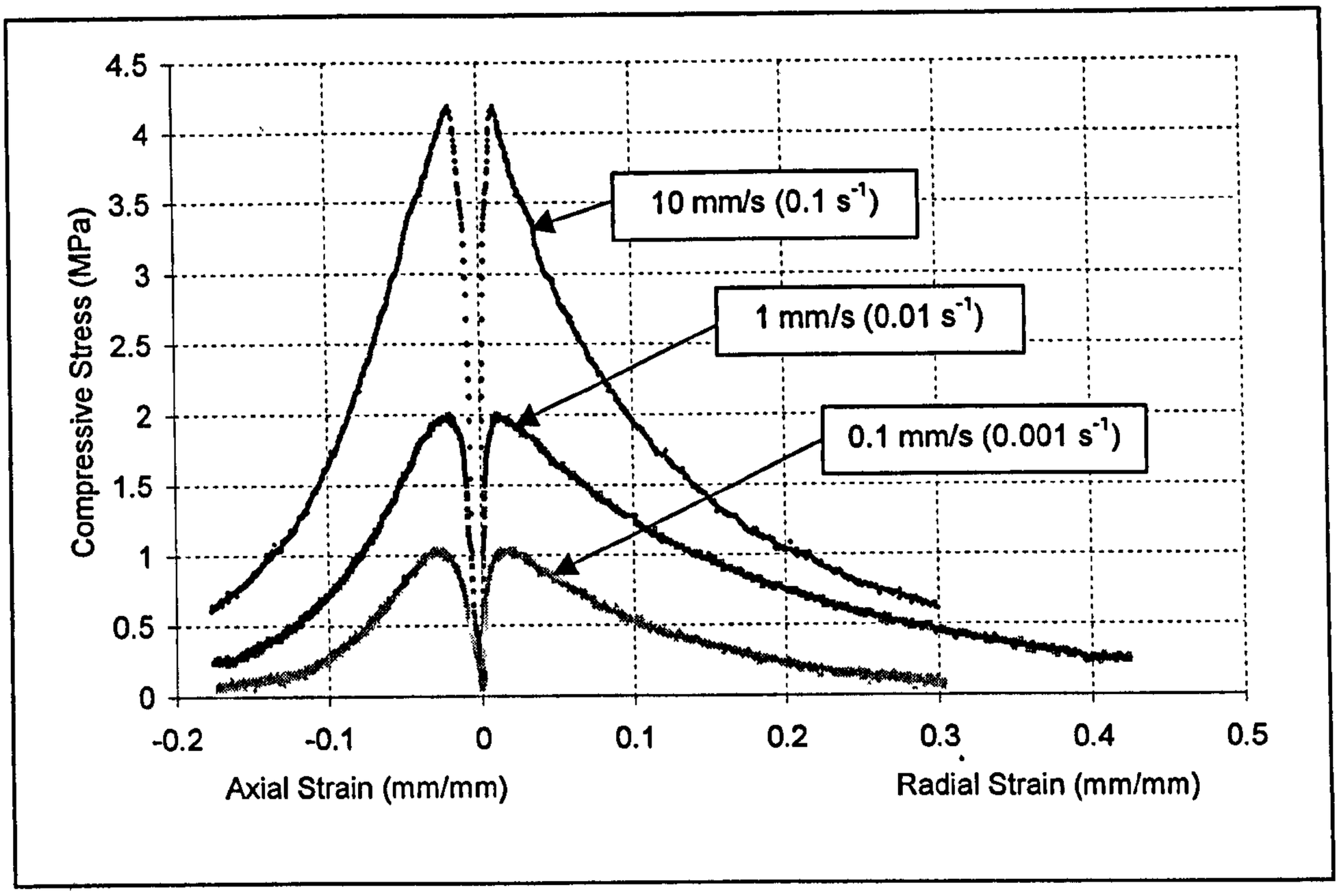

Figure 5.3: Typical uniaxial compression data - DBM mixture at 35°C

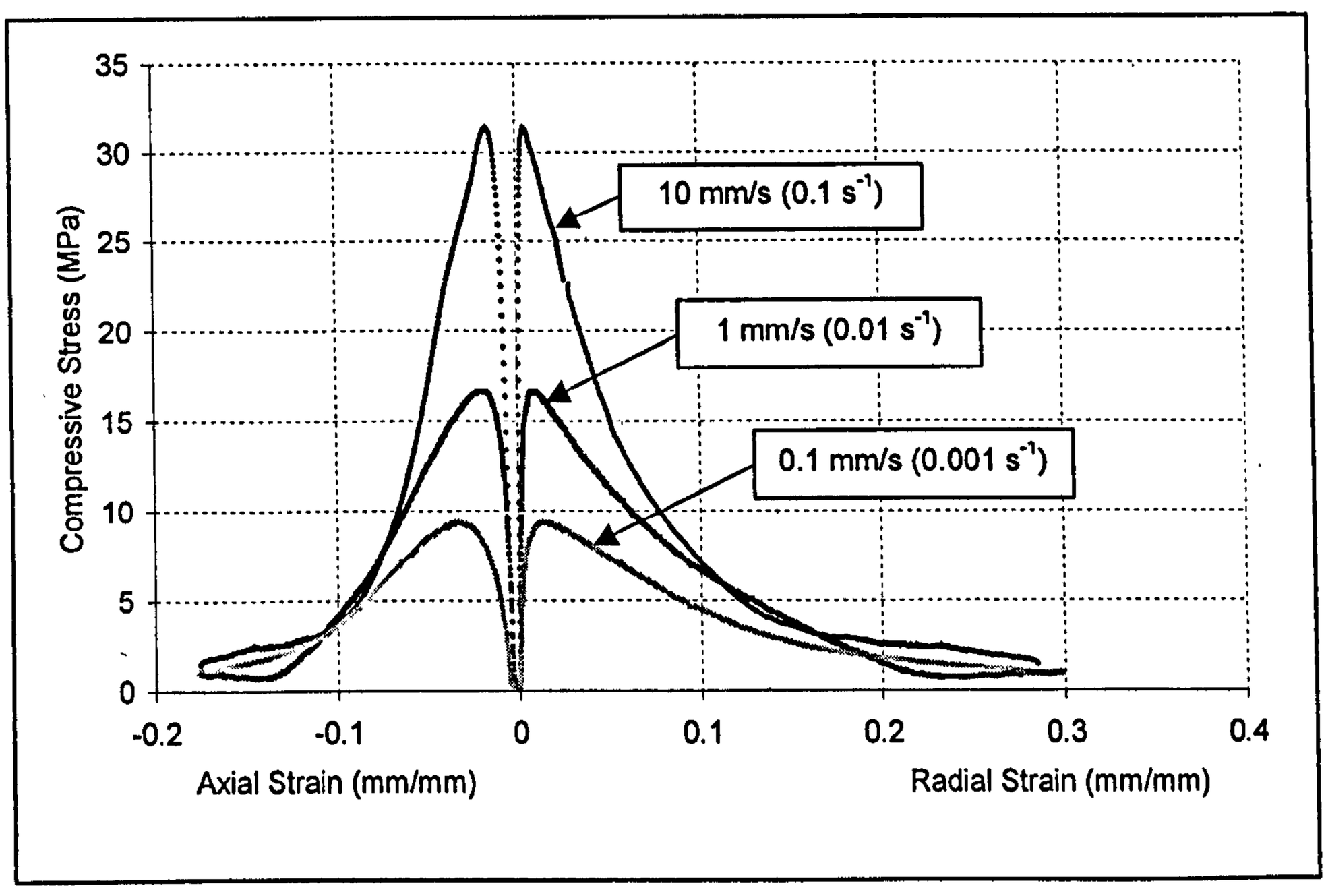

Figure 5.4: Typical uniaxial compression data – HRA mixture at 5°C

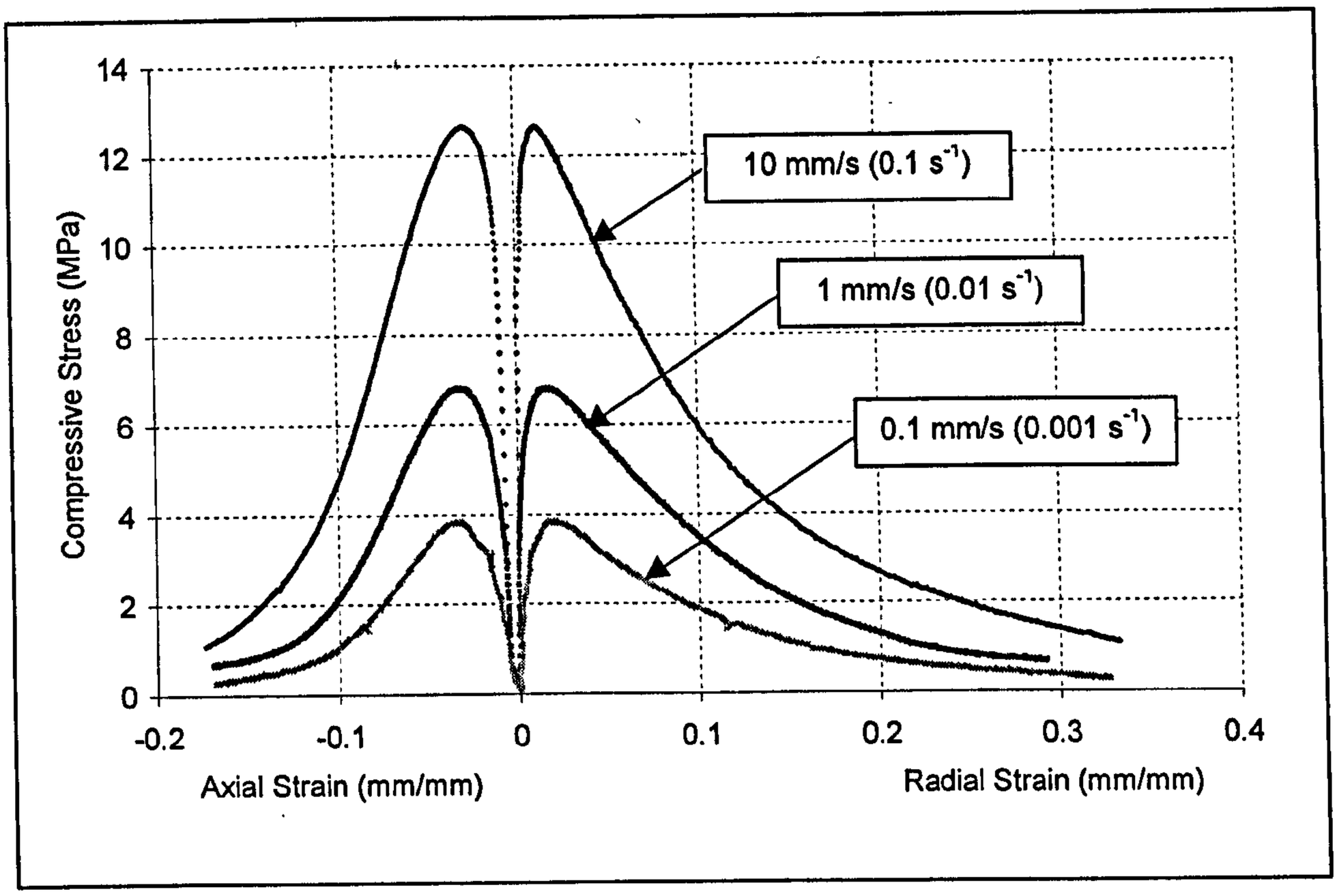

Figure 5.5: Typical uniaxial compression data – HRA mixture at 20°C

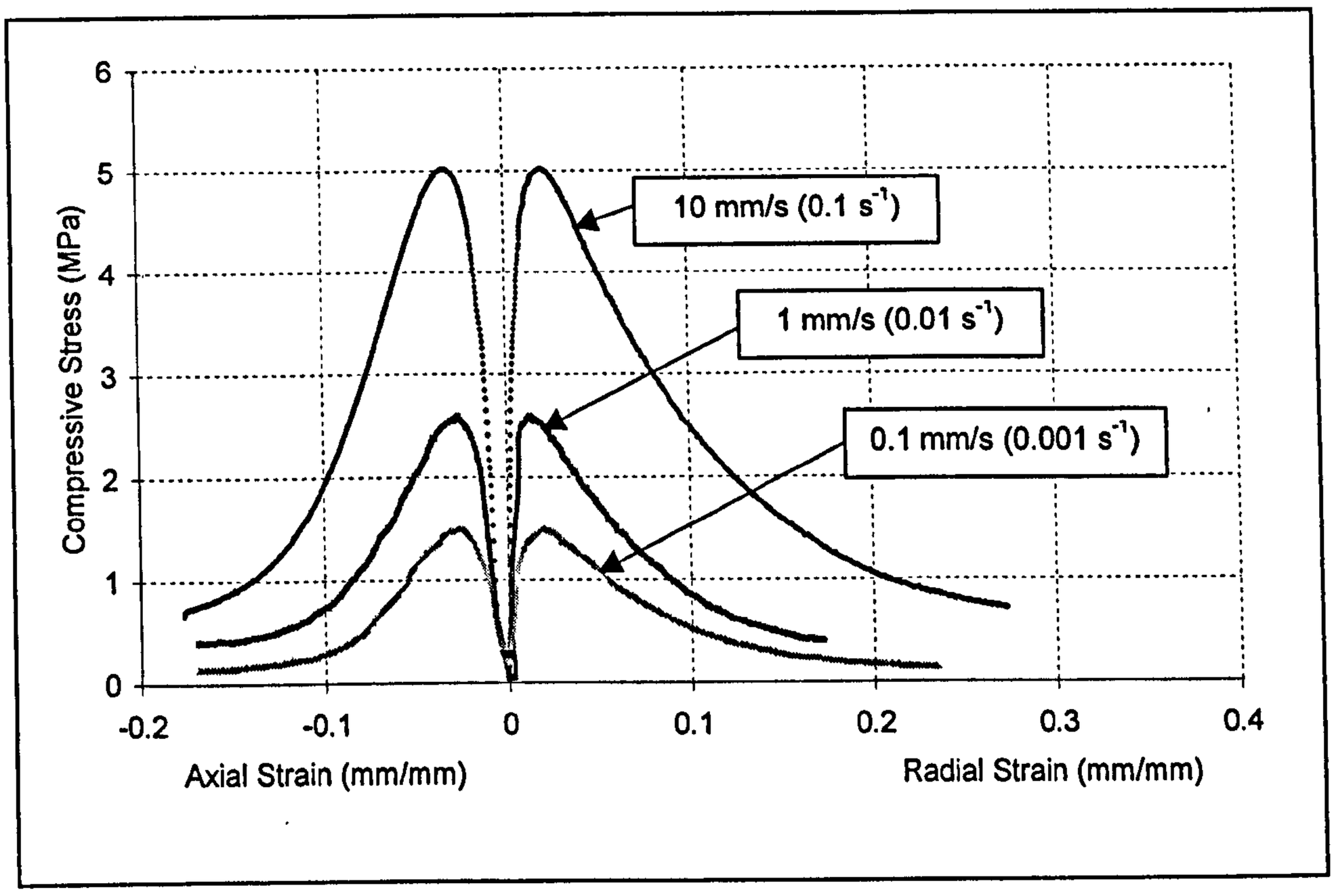

Figure 5.6: Typical uniaxial compression data – HRA mixture at 35°C

Table 5.2: Summary of uniaxial compression test data for the DBM mixture

Sample	T (°C)	Dispt. Rate (mm/s)	Strain Rate (1/s)	fc (MPa)	ε_a peak x10^{-3} (mm/mm)	ε_r peak x10^{-3} (mm/mm)	E (MPa)	ν
DBM5 0.1A	5	0.1	0.001	-7.15	-17.48	5.73	1455	0.36
DBM5 0.1B	5	0.1	0.001	-6.39	-14.93	7.19	1524	0.29
DBM5 0.1C	5	0.1	0.001	-7.14	-13.84	9.43	1224	0.23
Average	5	0.1	0.001	-6.89	-15.42	7.45	1401	0.29
DBM5 1A	5	1	0.01	-17.03	-9.12	4.07	3722	0.36
DBM5 1B	5	1	0.01	-14.31	-8.38	3.70	3604	0.24
DBM5 1C	5	1	0.01	-15.89	-9.34	3.99	3627	0.30
Average	5	1	0.01	-15.74	-8.95	3.92	3651	0.30
DBM5 10A	5	10	0.1	-28.98	-10.18	4.03	6558	0.27
DBM5 10B	5	10	0.1	-29.97	-9.29	6.16	6284	0.35
DBM5 10C	5	10	0.1	-28.64	-9.17	3.97	6362	0.31
Avearge	5	10	0.1	-29.20	-9.55	4.72	6401	0.31
DBM20 0.1A	20	0.1	0.001	-2.18	-31.33	22.33	332	0.39
DBM20 0.1B	20	0.1	0.001	-2.09	-33.06	19.30	378	0.28
DBM20 0.1C	20	0.1	0.001	-2.04	-25.10	19.34	335	0.38
Average	20	0.1	0.001	-2.10	-29.83	20.33	348	0.35
DBM20 1A	20	1	0.01	-4.42	-19.77	9.34	895	0.27
DBM20 1B	20	1	0.01	-4.36	-17.95	11.11	1140	0.20
DBM20 1C	20	1	0.01	-4.49	-15.70	8.62	936	0.38
Average	20	1	0.01	-4.42	-17.81	9.69	990	0.28
DBM20 10A	20	10	0.1	-10.85	-11.44	5.29	2189	0.32
DBM20 10B	20	10	0.1	-11.01	-10.60	5.88	2610	0.33
DBM20 10C	20	10	0.1	-11.01	-10.79	5.35	2198	0.38
Average	20	10	0.1	-10.96	-10.94	5.51	2332	0.34
DBM35 0.1A	35	0.1	0.001	-1.06	-27.13	19.07	91	0.36
DBM35 0.1B	35	0.1	0.001	-1.08	-31.57	20.08	86	0.30
DBM35 0.1C	35	0.1	0.001	-1.08	-30.06	32.92*	90	0.34
Average	35	0.1	0.001	-1.07	-29.59	19.58	89	0.33
DBM35 1A	35	1	0.01	-1.89	-19.72	11.62	409	0.44
DBM35 1B	35	1	0.01	-2.01	-16.65	10.85	302	0.37
DBM35 1C	35	1	0.01	-1.95	-22.42	23.44*	558	0.46
Average	35	1	0.01	-1.95	-19.60	11.24	423	0.42
DBM35 10A	35	10	0.1	-4.19	-13.70	10.49	813	0.45
DBM35 10B	35	10	0.1	-3.95	-14.31	9.66	816	0.41
DBM35 10C	35	10	0.1	-4.30	-12.39	7.15	895	0.35
Average	35	10	0.1	-4.15	-13.47	9.10	841	0.40

* Denotes a result excluded from the average

Table 5.3: Summary of uniaxial compression test data for the HRA mixture

Sample	T (°C)	Dispt. Rate (mm/s)	Strain Rate (1/s)	fc (MPa)	ε_a peak x10^{-3} (mm/mm)	ε_r peak x10^{-3} (mm/mm)	E (MPa)	ν
HRA5 0.1A	5	0.1	0.001	-9.42	-24.99	12.94	1130	0.23
HRA5 0.1B	5	0.1	0.001	-9.37	-23.58	15.45	1280	0.29
HRA5 0.1C	5	0.1	0.001	Corrupt Data				
Average	5	0.1	0.001	-9.40	-24.28	14.19	1205	0.26
HRA5 1A	5	1	0.01	-16.66	-16.09	8.59	2500	0.36
HRA5 1B	5	1	0.01	-16.95	-15.58	5.27	2560	0.23
HRA5 1C	5	1	0.01	-16.19	-16.14	9.96	2550	0.34
Average	5	1	0.01	-16.60	-15.94	7.94	2537	0.31
HRA5 10A	5	10	0.1	-29.63	-14.70	6.20	4792	0.31
HRA5 10B	5	10	0.1	-32.22	-11.57	5.31	5333	0.34
HRA5 10C	5	10	0.1	-31.42	-11.87	5.21	5412	0.22
Average	5	10	0.1	-31.09	-12.71	5.57	5179	0.29
HRA20 0.1A	20	0.1	0.001	-4.26	-30.83	18.36	352	0.30
HRA20 0.1B	20	0.1	0.001	-3.91	-32.09	20.52	363	0.23
HRA20 0.1C	20	0.1	0.001	-3.86	-28.24	21.15	334	0.29
Average	20	0.1	0.001	-4.01	-30.39	20.01	350	0.27
HRA20 1A	20	1	0.01	-6.76	-28.36	13.61	950	0.41
HRA20 1B	20	1	0.01	-6.68	-26.50	13.44	928	0.30
HRA20 1C	20	1	0.01	-6.84	-26.81	13.29	901	0.31
Average	20	1	0.01	-6.76	-27.22	13.45	926	0.34
HRA20 10A	20	10	0.1	-12.40	-20.78	12.16	1962	0.40
HRA20 10B	20	10	0.1	-12.85	-23.47	12.27	1768	0.32
HRA20 10C	20	10	0.1	-12.66	-23.27	12.03	1721	0.33
Average	20	10	0.1	-12.64	-22.51	12.15	1817	0.35
HRA35 0.1A	35	0.1	0.001	-1.42	-30.37	19.86	84	0.36
HRA35 0.1B	35	0.1	0.001	-1.34	-27.27	23.42	99	0.45
HRA35 0.1C	35	0.1	0.001	-1.50	-30.57	20.26	98	0.40
Average	35	0.1	0.001	-1.42	-29.40	21.18	94	0.40
HRA35 1A	35	1	0.01	-2.76	-29.96	13.56	228	0.45
HRA35 1B	35	1	0.01	-2.58	-30.06	13.50	216	0.37
HRA35 1C	35	1	0.01	-2.61	-26.29	12.61	198	0.41
Average	35	1	0.01	-2.65	-28.77	13.22	214	0.41
HRA35 10A	35	10	0.1	-5.15	-27.74	16.74	510	0.37
HRA35 10B	35	10	0.1	-4.60	-27.35	8.81	489	0.27
HRA35 10C	35	10	0.1	-5.03	-26.06	14.22	499	0.46
Average	35	10	0.1	-4.93	-27.05	13.26	499	0.37

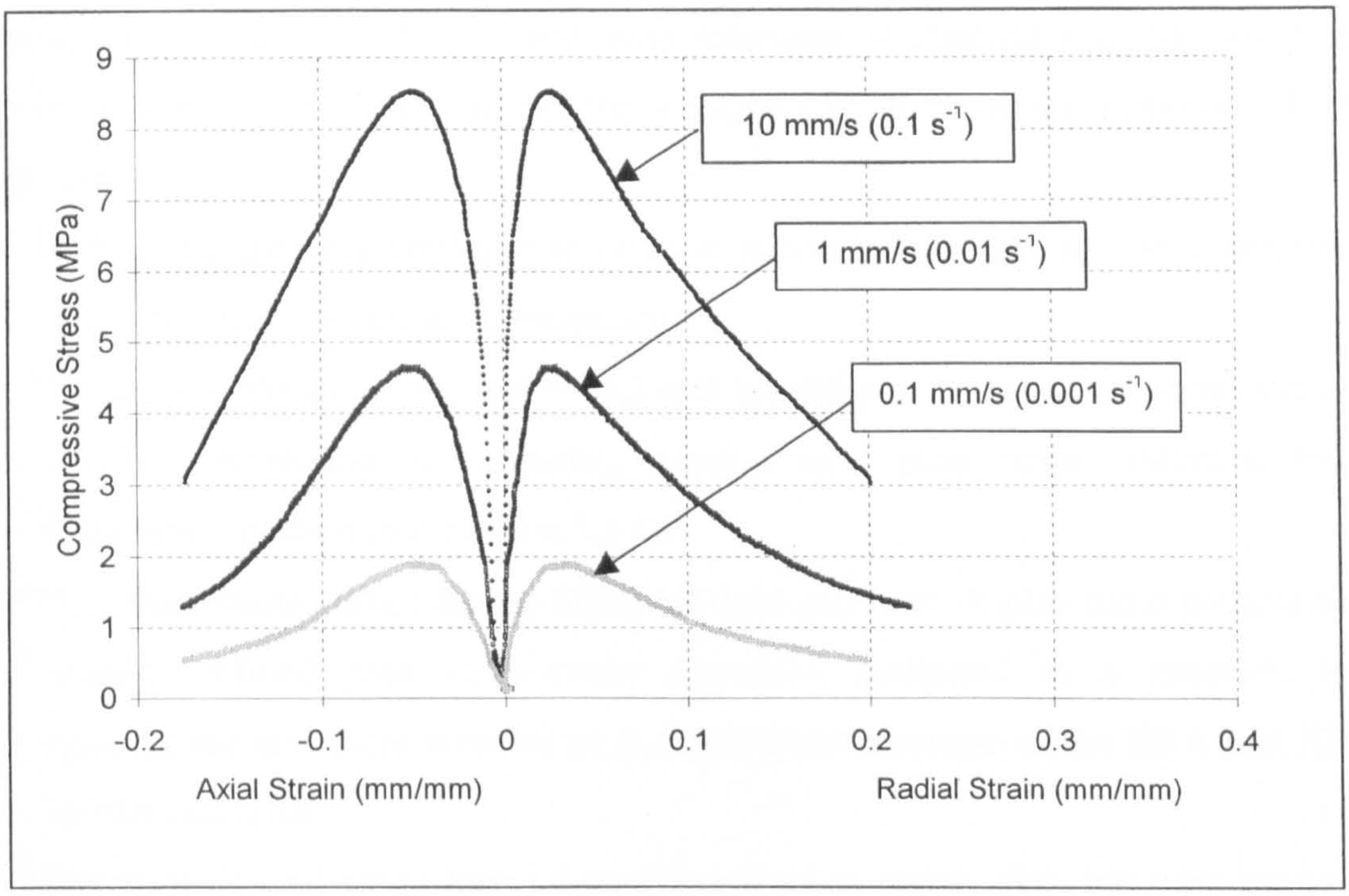

Figure 5.7: Typical uniaxial compression data – HRA mortar mixture at 20°C

Table 5.4: Summary of uniaxial compression test data for the HRA mortar mixture at 20°C

Sample	T (°C)	Dispt. Rate (mm/s)	Strain Rate (1/s)	fc (MPa)	ε_a^{peak} x10^{-3} (mm/mm)	ε_r^{peak} x10^{-3} (mm/mm)	E (MPa)	ν
HRAm20 0.1A	20	0.1	0.001	-1.78	-44.98	29.19	60	0.46
HRAm20 0.1B	20	0.1	0.001	Corrupt Data				
HRAm20 0.1C	20	0.1	0.001	-1.98	-48.89	34.03	72	0.23
Average	20	0.1	0.001	-1.88	-46.93	31.61	66	0.34
HRAm20 1A	20	1	0.01	-4.33	-44.27	26.74	356	0.34
HRAm20 1B	20	1	0.01	-4.93	-48.65	31.66	344	0.41
HRAm20 1C	20	1	0.01	-4.66	-51.01	28.28	329	0.40
Average	20	1	0.01	-4.64	-47.98	28.89	343	0.38
HRAm20 10A	20	10	0.1	-8.44	-46.35	29.10	872	0.41
HRAm20 10B	20	10	0.1	-8.54	-44.99	27.62	868	0.27
HRAm20 10C	20	10	0.1	-8.40	-45.82	26.71	894	0.41
Average	20	10	0.1	-8.46	-45.72	27.81	878	0.36

5.3.2 Observations on Compression Test Results

Comparing Figures 5.1 to 5.7, and with reference to Appendix E, the following observations can be made about the compressive stress-strain response of the mixtures.

- Each of the mixtures displayed an increase in compressive strength with increasing strain rate and/or decreasing temperature.
- For each of the mixtures, and for all test conditions, the stress-strain response is similar, comprising an ascending portion until peak stress, followed by a descending portion (see Section 5.3.4).
- The stress-strain curves for the DBM mixture generally display more pronounced, sharply defined peak stress-strain responses, compared to a generally less pronounced and more rounded peak stress-strain response of the HRA and HRA mortar mixtures.
- The tests showed some form of load introduction phase, even after the pre-load, (see Section 5.3.3).
- As a percentage of peak strength, the HRA mortar mixture exhibits the greatest residual strength at the end of the tests.
- For comparable test conditions, the DBM mixture generally exhibits greater residual strengths, as a percentage of peak strength, than the HRA mixture.
- At 5°C, after peak stress has been reached, the HRA mixture exhibits very rapid response degradation, particularly at the 10 mm/s displacement rate.

5.3.3 Load Introduction Phase

It was apparent from the test results that for most test conditions the axial stress-strain response exhibited a load introduction phase. This is represented in detail in Figure 5.8, which shows a plot of the axial strain versus compressive stress data for sample DBM20 10C. Despite the fact that the specimens were subject to a pre-load prior to the start of the test, the figure clearly shows an initial load introduction phase. This initial response is thought to be related to compression of the lubrication system and/or due to internal restructuring within the specimen[2] and is therefore not a true

---

[2] This type of effect is explained by Read [1996] as the thickening of the bitumen films in the direction normal to the applied load and the thinning of the films in the direction of the applied load.

measure of the material response. To correct for this phenomenon, linear regression analysis was performed on the steepest part of the slope, assuming that this corresponded to the linear elastic phase of the mixture response, Figure 5.8. Then, by extrapolating this slope to the beginning of the test, the response of the mixture as it would have been without these effects was determined.

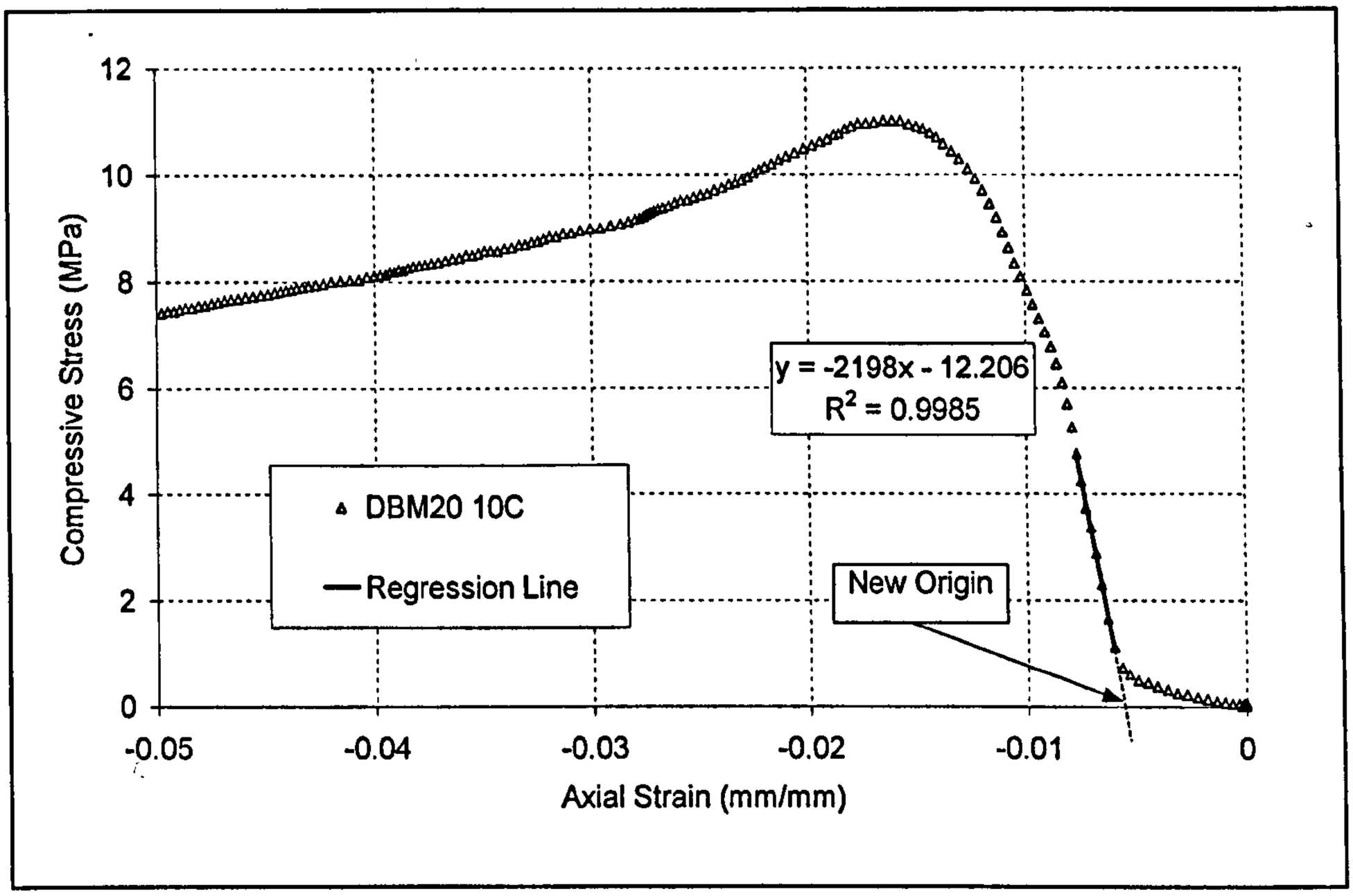

Figure 5.8: Detail showing load introduction phase

5.3.4 Compressive Stress-Strain Response Generalisation

In all the compression experiments the stress-strain relationships were similar, consisting of an ascending portion, until peak strength, followed by a descending portion. These observations have been reported by other researchers [Starodubsky *et al.*, 1994 and Erkens *et al.*, 1998]. It is therefore possible to make an idealised generalisation of the uniaxial monotonic compressive stress-strain response of asphalt mixtures irrespective of strain rate, temperature or mixture specifications.

It is possible to divide the stress-strain curve into four distinct areas as shown in Figure 5.9. These are, (1) an initial linear zone, (2) a inelastic strain hardening zone,

(3) the peak (apparent) strength response and (4) the descending strain softening zone. Effectively when modelling the material response, zone one is modelled as linear-elastic, (see Sections 5.3.7 and 5.3.8) with zones two and four modelled using plasticity hardening and softening functions (see Sections 6.6 and 6.7). This leaves zone three, the apparent strength response.

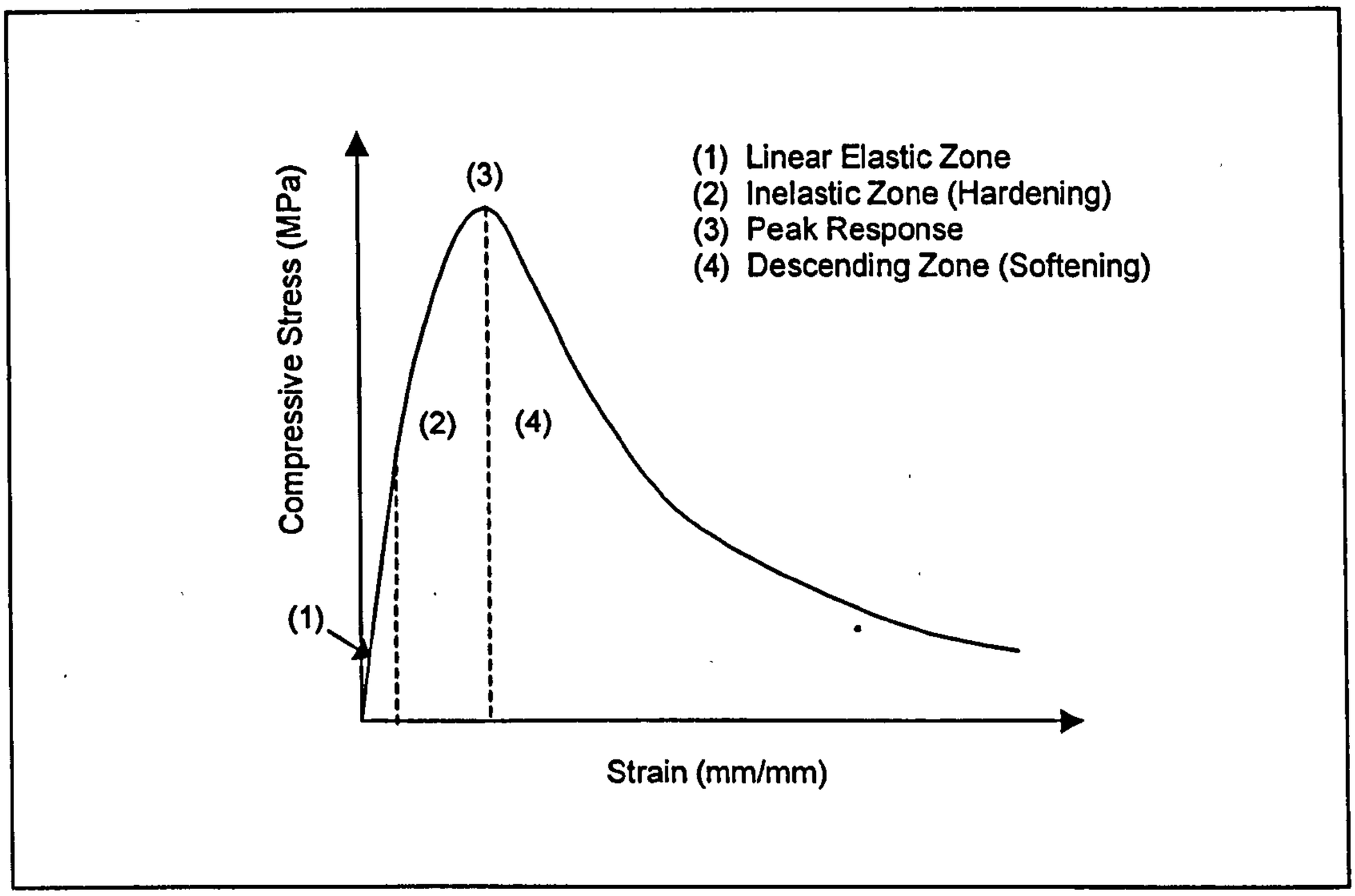

Figure 5.9: Generalised uniaxial compressive stress-strain response

5.3.5 Apparent Compressive Strength

The variation in the measured compressive strength of each mixture, for each test condition, was found to be small. The maximum relative error in the measured peak stress between three tests carried out under the same conditions was 7.1% (DBM at 5°C at 1 mm/s), with the average overall relative error in the compressive strength for the DBM and HRA mixtures for all test conditions found to be 2.9% and 2.8% respectively. Figure 5.10 shows the average compressive strength (compression negative) plotted as a function of strain rate and temperature for the DBM and HRA mixtures. The data shows the influence of strain rate and temperature on the material strength. A trend of increasing peak compressive strength with increasing strain rates and, more markedly, with decreasing temperature is exhibited by both mixtures.

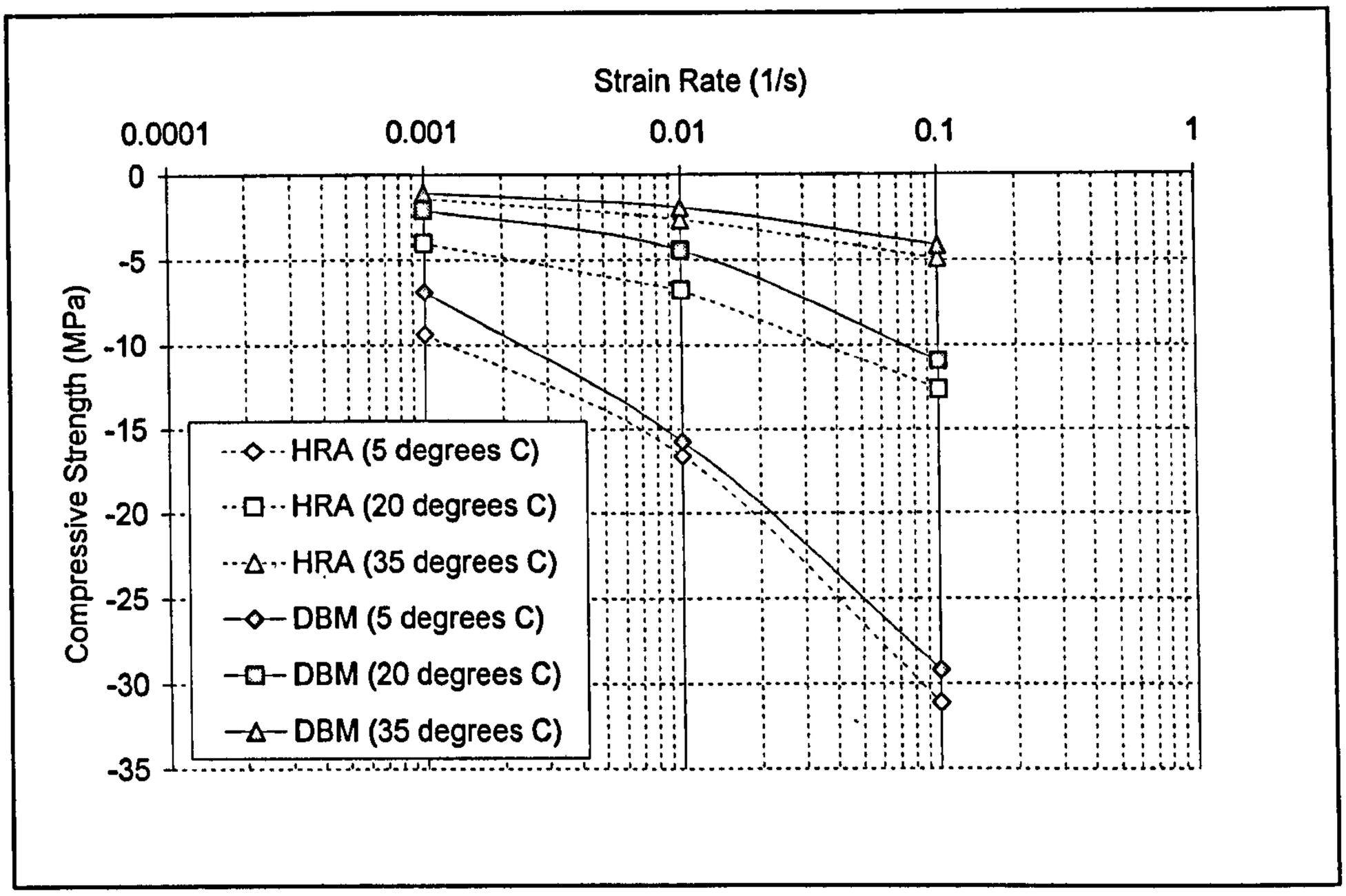

Figure 5.10: Average peak compressive strength of DBM and HRA mixtures as a function of strain rate and temperature

It can be observed that the two mixtures have a similar response, although the gap graded HRA mixture has a slightly higher average compressive strength than the continuously graded DBM mixture for any given strain rate and/or temperature. These observations indicate that binder content (13.2 % by volume for the DBM mixture compared to 15.9 % for the HRA mixture) is a more dominant factor, as opposed to the type of aggregate gradation, in determining the uniaxial compressive strength of a mixture. This is highlighted further by Figure 5.11, which shows the average peak compressive strength data for the DBM, HRA and HRA mortar mixtures (21.9 % binder content by volume) tested at 20°C. It can be seen that, although on average, the DBM mixture has stiffness moduli exceeding twice that of the HRA mortar mixture (see Section 5.3.7), both mixtures have similar average peak compressive strengths at the lower range of strain rates investigated.

Figure 5.12 presents a comparison of the average peak compressive strengths of the HRA mortar mixture, tested at 20°C, with the average peak compressive strength of the sand asphalt mixture characterised by Erkens *et al.* [1998, 2000a & 2000b].

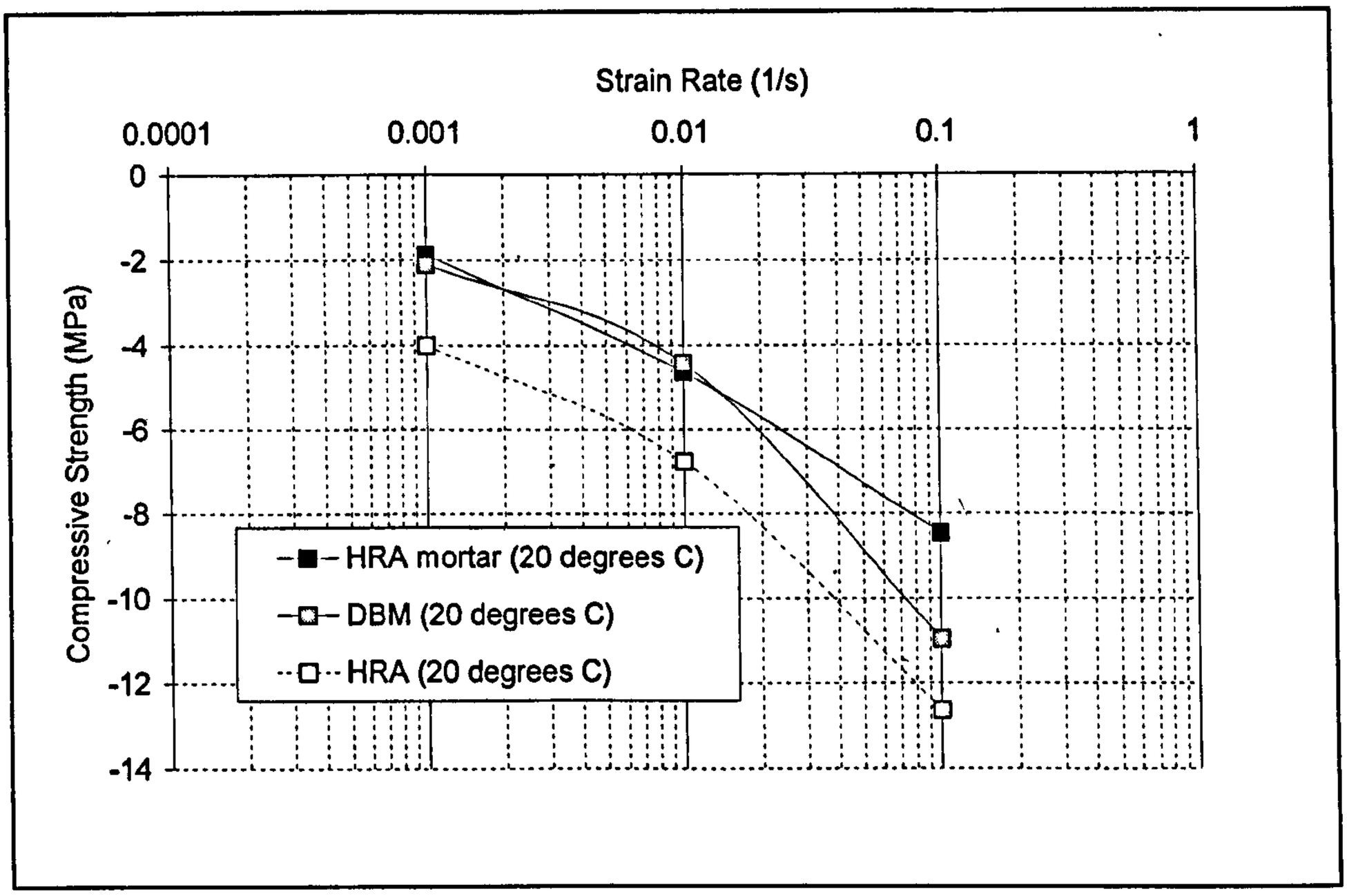

Figure 5.11: Average peak compressive strength of DBM, HRA and HRA mortar mixtures as a function of strain rate at 20°C

Details of the sand asphalt mixture are given in Table 3.2, the mixture has a binder content of 19.3 % by volume and was manufactured using a 45/60 penetration grade binder. Characterisation of the sand asphalt mixture was undertaken at temperatures of 0, 15 and 30°C [Erkens *et al.*, 1998]. Therefore, to allow a comparison with the data obtained in this study, the compressive strength of the mixture has been adjusted, for test temperatures of 5, 20 and 35°C, using Equation (5.7), and the regression parameters given in Table 5.5 (see Section 5.3.6). Effectively the two types of mixture can broadly be considered similar, with the exception of their binder penetration grades. Figure 5.12 shows that at 20°C the general trend in the response of the two mixtures is the same, increasing compressive strength with increasing strain rate. However, it can be observed that the sand asphalt mixture has the greater compressive strength, nearly twice that of the HRA mortar mixture at a strain rate of 0.1 s^{-1}. This observation reinforces the previous supposition of binder dominance, and would indicate that uniaxial compressive strength is sensitive to binder penetration grade, with harder binders resulting in greater compressive strengths.

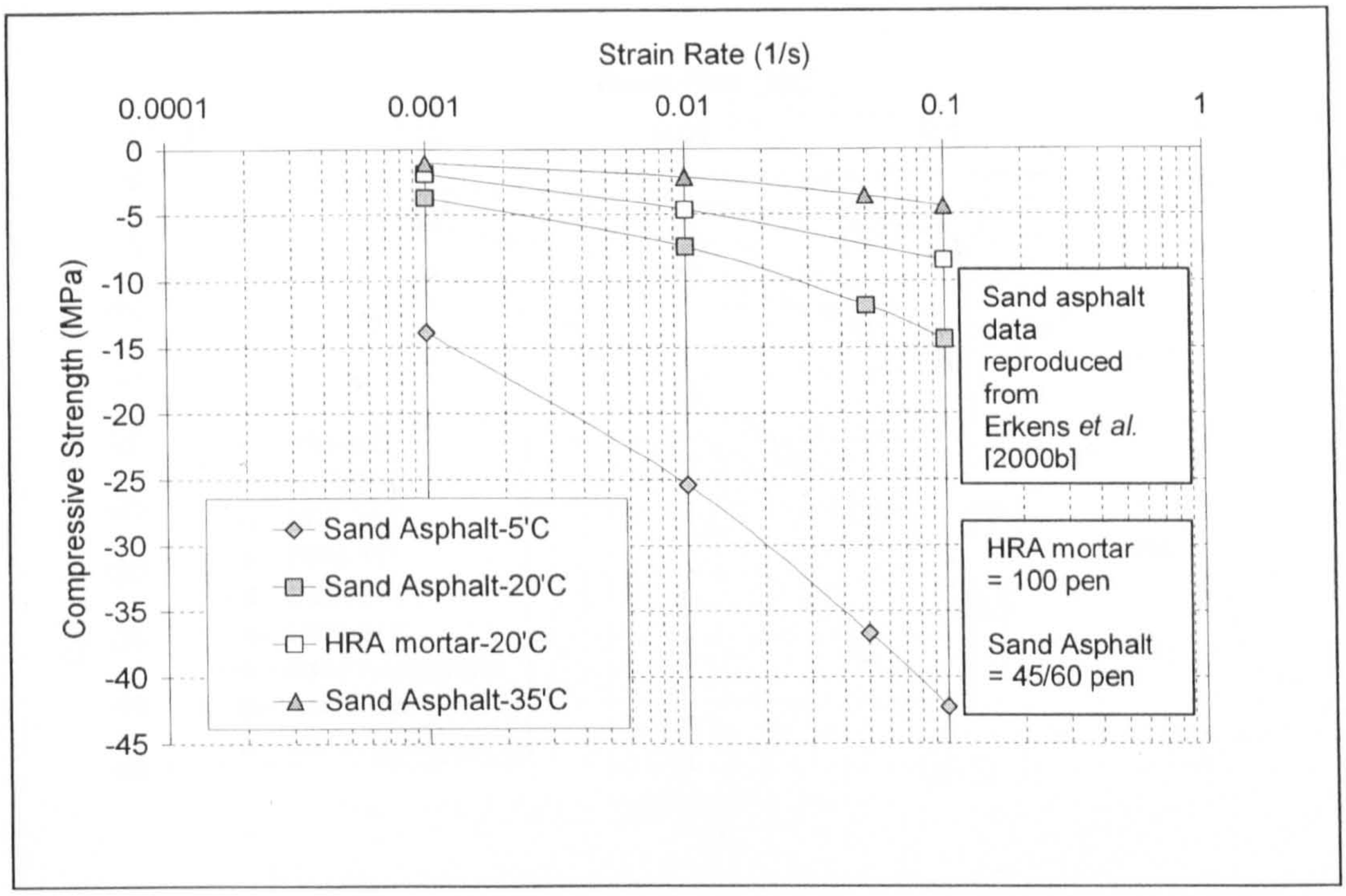

Figure 5.12: Comparison of average peak compressive strength of HRA mortar mixture (100 pen binder) at 20°C, versus the peak compressive strength of an idealised sand asphalt mixture (45/60 pen binder) characterised by Erkens *et al.* [1998, 2000a & 2000b] as a function of temperature and strain rate

Figure 5.13 presents a comparison of the peak compressive strength of the DBM and HRA mixtures, to the peak compressive strength of the sand asphalt mixture characterised by Erkens *et al.* [1998, 2000a & 2000b] adjusted, as above, for the temperatures used in this study. The figure shows that at 35°C the average compressive strengths of all three mixtures are similar. Whereas, at 20°C, at 0.001 s^{-1} the compressive strengths of the HRA and sand asphalt mixtures are similar, with the strength of the sand asphalt mixture surpassing that of the HRA mixture as the rate of strain is increased. At 5°C the average compressive strength of the sand asphalt mixture can be observed to exceed that of the DBM and HRA mixtures by approximately 1.7 and 1.45 times respectively. These observations would indicate that the effect of binder content and binder properties on the compressive strength of the mixtures become progressively more pronounced with decreases in temperature and/or increases in strain rate (i.e. increases in bitumen stiffness).

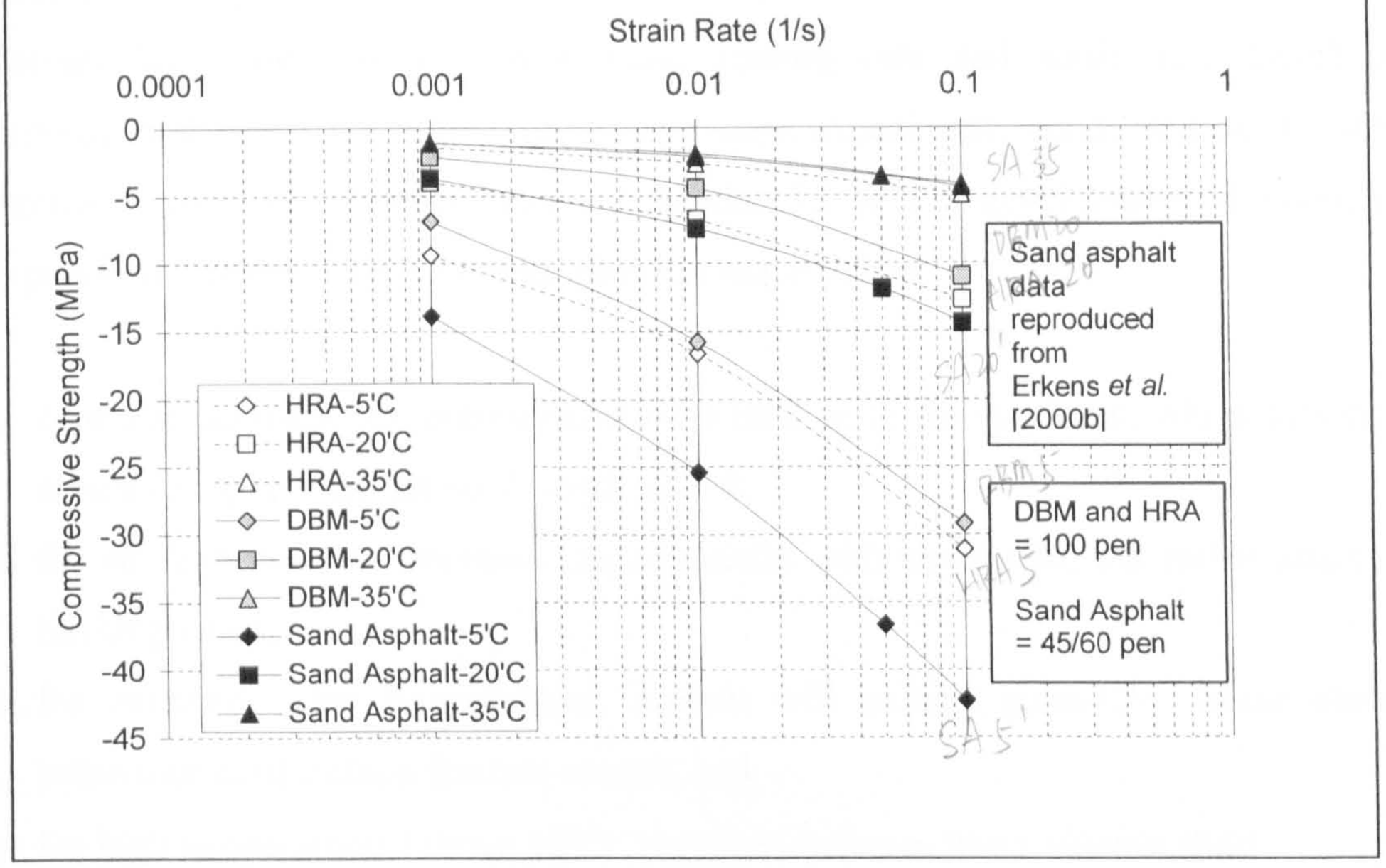

Figure 5.13: Comparison of average peak compressive strength of DBM and HRA mixtures (100 pen binder), versus the peak compressive strength of an idealised sand asphalt mixture (45/60 pen binder) characterised by Erkens *et al.* [1998, 2000a & 2000b] as a function of temperature and strain rate

5.3.6 Expression for Peak Compressive Strength Response

It is envisaged that the ACRe model will eventually be used in laboratory and road construction analysis [Scarpas *at al.*, 1999]. For these types of applications it is desirable to have general expressions for material strength and the model parameters. Development of the model in this way may enable the future required inputs to be limited, for example, to the type of mixture or mixture composition, the temperature profile and the strain rate. From these inputs FE analysis could be used to determine the temperature and strain rate at each integration point in the structure being analysed and from this the parameters for the model could be determined. This leads to the requirement that all the material parameters and the material strength must be expressed as functions of the strain rate, temperature, and eventually mixture composition. Therefore a key stage in the development of the model has been the determination of suitable functions to express the material strength and model parameters [Erkens *et al.*, 1998].

Erkens *et al.* [1998 and 2000a] developed expressions for the peak compressive strength as a function of temperature, loading rate and strain rate based on experimental data from monotonic compression experiments conducted on the sand asphalt mixture described in Table 3.2, Section 3.5.4. The development of a suitable expression was based on four main physical assumptions:

i. zero displacement rate corresponds to no loading of the specimen, which therefore means the specimen has no strength $f_c = 0$,
ii. the strength does not increase proportionally with strain rate, but rather attains a limiting value,
iii. for extremely low temperatures, asphalt will exhibit glass-like, linear elastic behaviour until sudden fracture occurs, and
iv. for high temperatures (above 160°C) bitumen behaves like a viscous fluid.

Based on these considerations an S-shaped transition relation was selected. Further to this, to determine the appropriate relationships to describe the influence of loading rate and temperature on the material strength, Erkens *et al.* [2000a] considered the asphalt mixture to be represented by a combination of Hookean springs and Newtonian dampers (see Section 2.2.5), in which the behaviour of the springs were independent of the loading rate and temperature, and hence any changes in response were due to the viscous dampers only. For which, the viscosity is given by Equation (5.1):

$$\eta = \frac{\tau}{\left(\frac{\partial \gamma}{\partial t}\right)} \tag{5.1}$$

where, η = coefficient of viscosity
τ = shear stress
γ = shear strain

For ideal linear viscous behaviour, the resistance to shear is expressed in terms of the shear modulus, G, defined as:

$$G = \frac{\eta}{t} \tag{5.2}$$

where the elastic and shear moduli are related by Equation (5.3).

$$E = 2(1+\nu)G \quad = \quad \frac{2(1+\nu)\eta}{t} \tag{5.3}$$

Therefore, considering the temperature and rate effects to be represented solely by the viscous components, the stress in a Newtonian damper can be expressed as:

$$\sigma = \frac{2(1+\nu)\eta}{t}\varepsilon \tag{5.4}$$

in which,
$$\frac{\varepsilon}{t} = \dot{\varepsilon} = \frac{v}{h} \tag{5.5}$$

where, h = specimen height

which substituting Equation (5.5) into Equation (5.4) gives:

$$\sigma = \frac{2(1+\nu)}{h}\eta \cdot v \quad = 2(1+\nu)\eta \cdot \dot{\varepsilon} \tag{5.6}$$

From Equation (5.6) Erkens *et al.* [1998] submit that the stress in a viscous material is proportional to the strain rate[3], and the viscosity, in which the viscosity represents the temperature effects, the logarithmic relation for which, on the bitumen test data chart (BTDC), is linear for S-class bitumens [Whiteoak, 1990]. Therefore based on these

---

[3] Equation (5.6) shows that the strength of an asphaltic material is related to strain rate rather than displacement rate. Therefore, the description of the material response should be independent of the specimen geometry and therefore should be expressed as a function of the strain rate.

factors, Erkens *et al.* [2000a] developed the expression given in Equation (5.7) to represent the compressive strength of the mixture as a function of both strain rate and temperature.

$$f_c = a\left(1 - \frac{1}{1 + \left[\dot{\varepsilon} \cdot \exp^{\left(b + \frac{c}{T}\right)}\right]^d}\right) \tag{5.7}$$

where,

f_c	=	compressive strength in MPa
$\dot{\varepsilon}$	=	strain rate in s^{-1}
T	=	temperature in degrees Kelvin
a,b,c,d	=	compressive strength non-linear regression parameters

Erkens *et al.* [2000a] suggest that the regression parameters a,b,c,d may represent the following physical influences of mixture response, and that these characteristics could vary with mixture composition and bitumen characteristics.

- parameter, a, is the maximum limiting strength of the mixture,
- parameters, b, and, c, control the beginning and end points of mixture transition (flow and glass points), and
- parameter, d, controls the rate of this transition, between zero and limiting strength, i.e. temperature sensitivity.

Table 5.5 gives the values of the regression parameters a through d for the sand asphalt mixture, as characterised by Erkens *et al.* [2000a]. On the basis of the regression analysis, parameter, a, the limiting compressive strength was found to be rather large, at –108 MPa. However, compressive strengths as high as 56.5 MPa were reported at test temperatures of 0°C and displacement rates of 10 mm/s, therefore providing possible basis for the value.

Table 5.5: Non-linear regression parameters [Erkens *et al.*, 2000a]

Regression Parameter	*Sand Asphalt Mixture*
a	-108
b	-86.3
c	24260
d	0.32
r^2	0.99

Determination of Non-linear Regression Parameters for DBM and HRA mixtures

Through non-linear regression analysis, using the statistical package SPSS, Equation (5.7) was used to describe the peak strength data given in Tables 5.2 and 5.3 for the DBM and HRA mixtures respectively. When performing the non-linear regression analysis, the parameters, *a*, *b*, *c* and *d*, were initially set at –1, 0, 1 and 1 respectively. An example of the output from the non-linear regression evaluation is shown in Appendix F. The iterative progress was stopped after 45 and 190 model evaluations for the DBM and HRA mixture respectively. The resultant fitted uniaxial compression non-linear regression constants for each mixture are shown in Table 5.6.

Table 5.6: Initial uniaxial compressive strength non-linear regression parameters – DBM and HRA mixtures

Regression Parameter	*DBM Mixture*	*HRA Mixture*
a	-76	-1625
b	-63.66	-80.92
c	18014	19045
d	0.39	0.27
r^2	0.99	0.99

With reference to the observed positive strength effects of binder content and penetration grade presented in Section 5.3.5, it can seen from Table 5.6 that the values obtained for the DBM mixture compare sensibly with the parameters given in Table 5.5 for the sand asphalt mixture. However, this is not true of the regression values determined for the HRA mixture, particularly parameter, *a*, (a possible indication of

the mixture's maximum strength). On the basis of the regression analysis, the HRA mixture would have a theoretical maximum compressive strength of 1625 MPa. This is obviously incorrect and was found to be the result of divergence of the HRA iterative evaluation progress after iteration 18. Therefore, it was decided to refit the data for the HRA mixture, but with three regression constants only, substituting parameter, *a*, for a predefined limiting strength of -106 MPa. This value was determined based on Equation (5.9), see Section 5.3.7, which gives the ratio of HRA mixture compressive strength to DBM mixture compressive strength, as a function of apparent stiffness, as 1.4. Therefore, the value for parameter, *a*, used in the HRA analysis was selected to be 1.4 times that determined for the DBM mixture. The refitted values for the HRA mixture are given in Table 5.7. Figure 5.14 shows a plot of the predicted peak compressive strengths, using the regression parameters given in Table 5.7, compared to the experimental data for both the DBM and HRA mixtures, as a function of strain rate and temperature. It can be observed that a good fit is obtained for both mixture types, with a standard deviation between the average experimental results and the predicted values of 0.31 and 0.42 for the DBM and HRA mixtures respectively. The actual numerical predicted values, at each of the test conditions, are presented in Tables 5.8 and 5.9 for the DBM and HRA mixtures respectively.

Table 5.7: Final uniaxial compressive strength non-linear regression parameters – DBM and HRA mixture

Regression Parameter	*DBM Mixture*	*HRA Mixture*
a	-76	-106
b	-63.66	-67.28
c	18014	18572
d	0.39	0.32
r^2	0.99	0.99

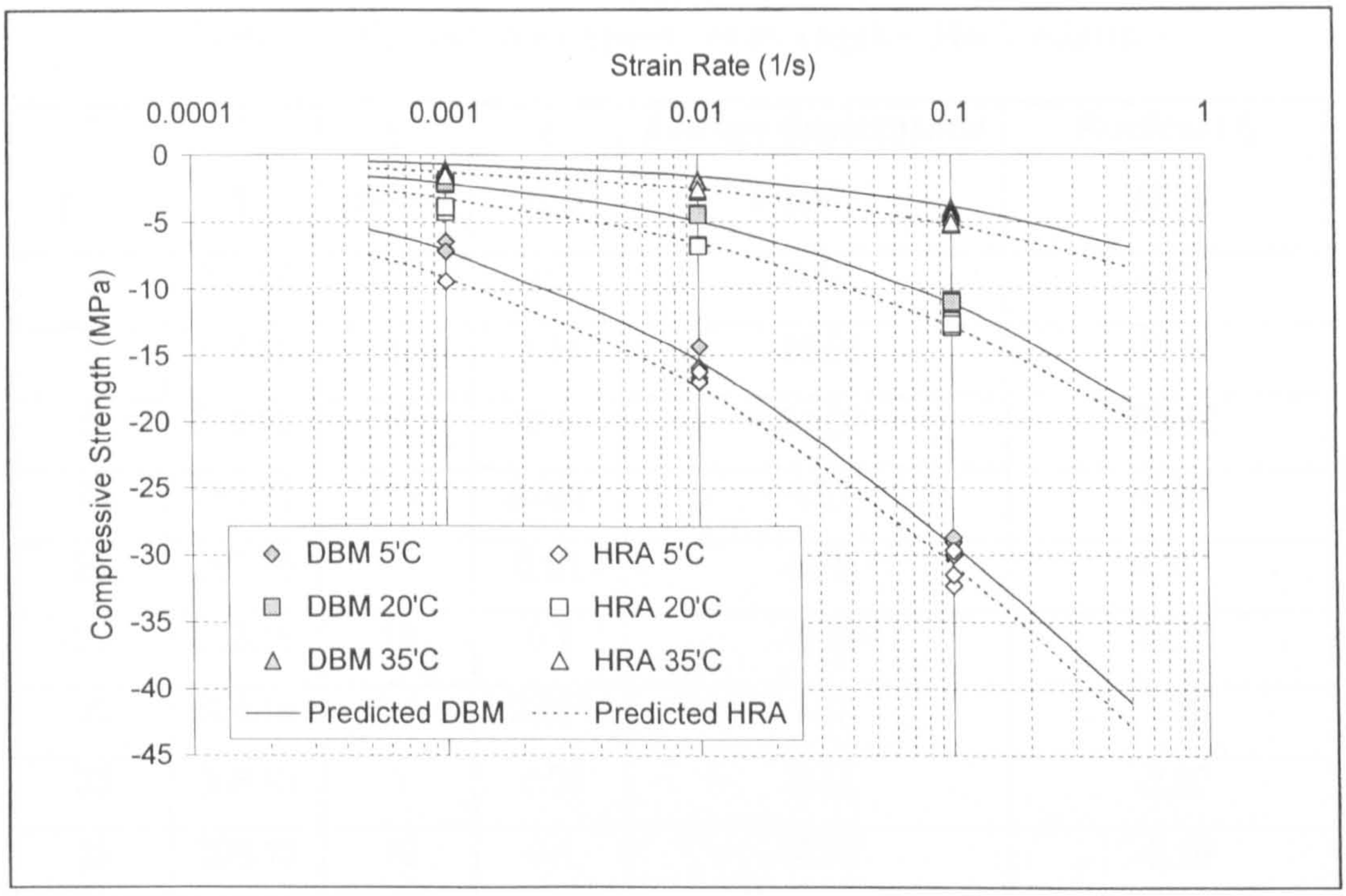

Figure 5.14: Predicted compressive strength (Equation (5.7), regression parameters Table 5.7) compared to experimental compressive strength data, as a function of strain rate and temperature

Table 5.8: Predicted compressive strength – DBM mixture

T (°C)	*T* (°K)	*v* (mm/s)	$\dot{\varepsilon}$ (s^{-1})	*Average Experimental* f_c *(MPa)*	*Predicted* f_c *(MPa)*
5	278.15	0.1	0.001	-6.89	-7.11
5	278.15	1	0.01	-15.74	-15.40
5	278.15	10	0.1	-29.20	-29.25
20	293.15	0.1	0.001	-2.10	-2.09
20	293.15	1	0.01	-4.42	-4.94
20	293.15	10	0.1	-10.96	-11.11
35	308.15	0.1	0.001	-1.07	-0.66
35	308.15	1	0.01	-1.95	-1.60
35	308.15	10	0.1	-4.15	-3.83
Standard Deviation					0.31

Table 5.9: Predicted compressive strength – HRA mixture

T (°C)	*T* (°K)	*v* (mm/s)	$\dot{\varepsilon}$ (s^{-1})	*Average Experimental* f_c *(MPa)*	*Predicted* f_c *(MPa)*
5	278.15	0.1	0.001	-9.40	-9.12
5	278.15	1	0.01	-16.60	-17.37
5	278.15	10	0.1	-31.09	-30.72
20	293.15	0.1	0.001	-4.01	-3.26
20	293.15	1	0.01	-6.79	-6.57
20	293.15	10	0.1	-12.64	-12.81
35	308.15	0.1	0.001	-1.42	-1.25
35	308.15	1	0.01	-2.65	-2.56
35	308.15	10	0.1	-4.93	-5.19
Standard Deviation					0.42

Figure 5.15 shows a plot of the trend in the predicted compressive strength for the DBM and HRA mixtures, using the regression parameters given in Table 5.7, as a function of strain rate and temperature. The figure shows the S-type transition relationship between compressive strength, temperature and strain rate. For intermediate temperatures and strain rates the response of the two mixtures can be observed to be similar, which is reasonable considering that they are composed of the same penetration grade and maximum aggregate stone size. However, at lower temperatures and increased strain rates the dominant binder properties of the HRA mixture can be seen. Also indicated in Figure 5.15 is the actual area of response covered by the compressive testing programme. From this it can be seen that the regression parameters are fitted on the basis of data from a limited area, hence making it difficult to establish whether the values found are realistic. Monismith *et al.* [1973] reports on an investigation into the compressive strength of 13 asphalt mixtures, with varying aggregate gradation, aggregate type, asphalt grade and asphalt content, see Section 3.5.4. Monismith *et al.* [1973] report that the maximum compressive strength of all the mixtures studied fell within the range of 34 to 62 MPa, see Figures 3.16, and 5.18, after which any further increases in the stiffness of the mixtures resulted in a decrease in the compressive strength. On the basis of these results it would appear that the maximum strength of the mixtures, as determined by the regression analysis,

are too large. Therefore, at this stage the regression parameters should be taken as just that, regression parameters, and should be considered valid only within (or close to) the constraints of the testing conditions given in Table 5.1. If further compressive test data was available, which would identify the maximum strength of the mixtures, then it would be possible to refit Equation (5.7) but using the experimentally determined maximum strength for parameter *a*.

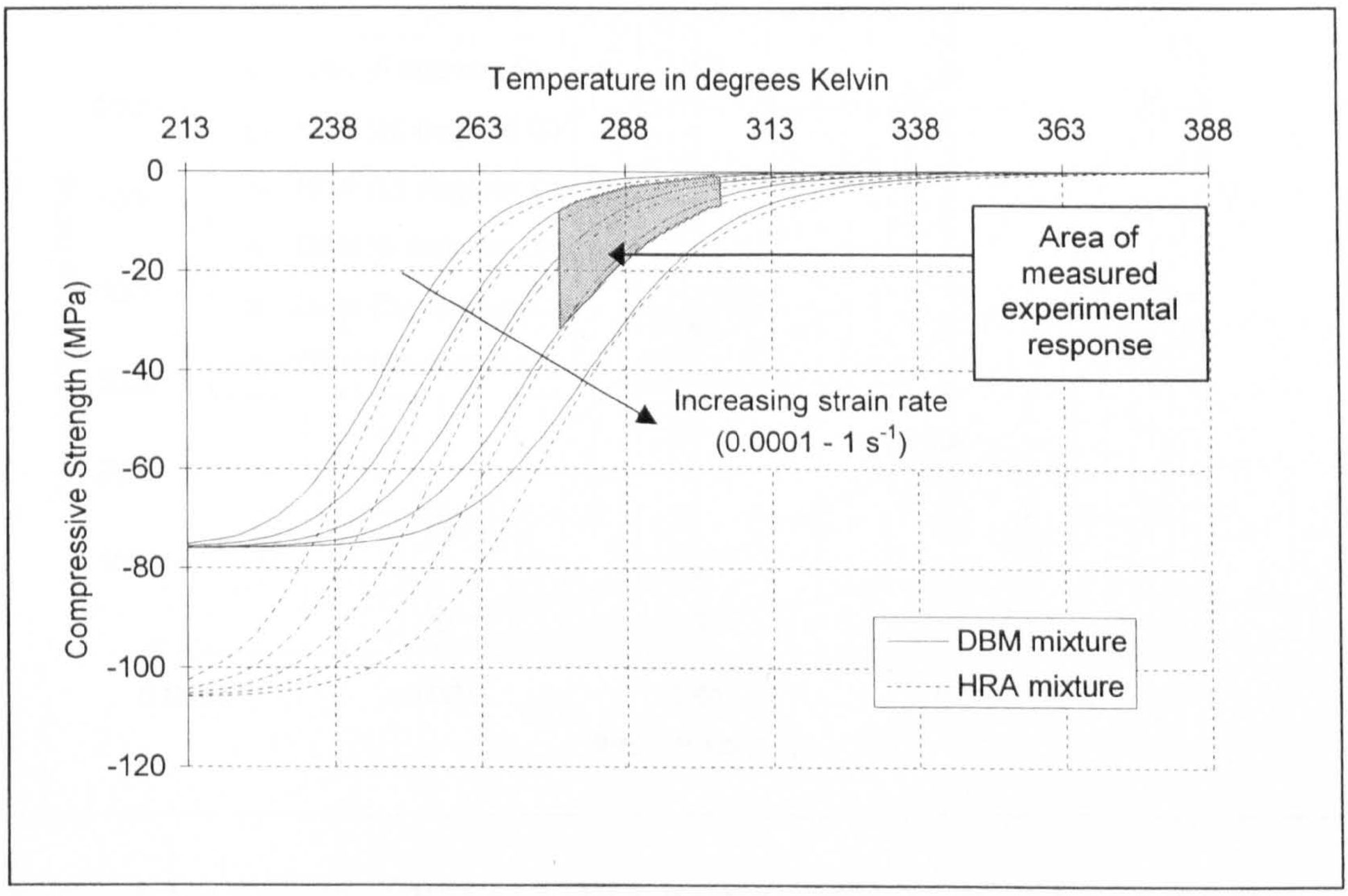

Figure 5.15: Plot showing trend in predicted compressive strength (Equation 5.7) as a function of temperature and strain rate – DBM and HRA mixtures

5.3.7 Young's Modulus

For the purpose of this study the Young's modulus or 'apparent stiffness' for each test condition was determined using linear regression analysis. The regression analysis was performed on the axial data taken at the beginning of each test, see Figure 5.8, (discounting the load introduction phase). An average value was then determined for each test condition. The calculated values are shown in Tables 5.2, 5.3 and 5.4 for the DBM, HRA and HRA mortar mixtures respectively. Figure 5.16 shows the average apparent stiffness values for the DBM and HRA mixtures at each test temperature plotted against the strain rate. In a similar manner to the apparent compressive

strength, Figure 5.16 shows that mixture stiffness is a function of temperature and strain rate. An increase in stiffness can be observed with a reduction in temperature and/or an increase in the strain rate, for both mixtures. As expected for comparable test conditions the stiffness of the continuous graded DBM mixture is generally greater than that of the gap graded HRA mixture, for equivalent test conditions.

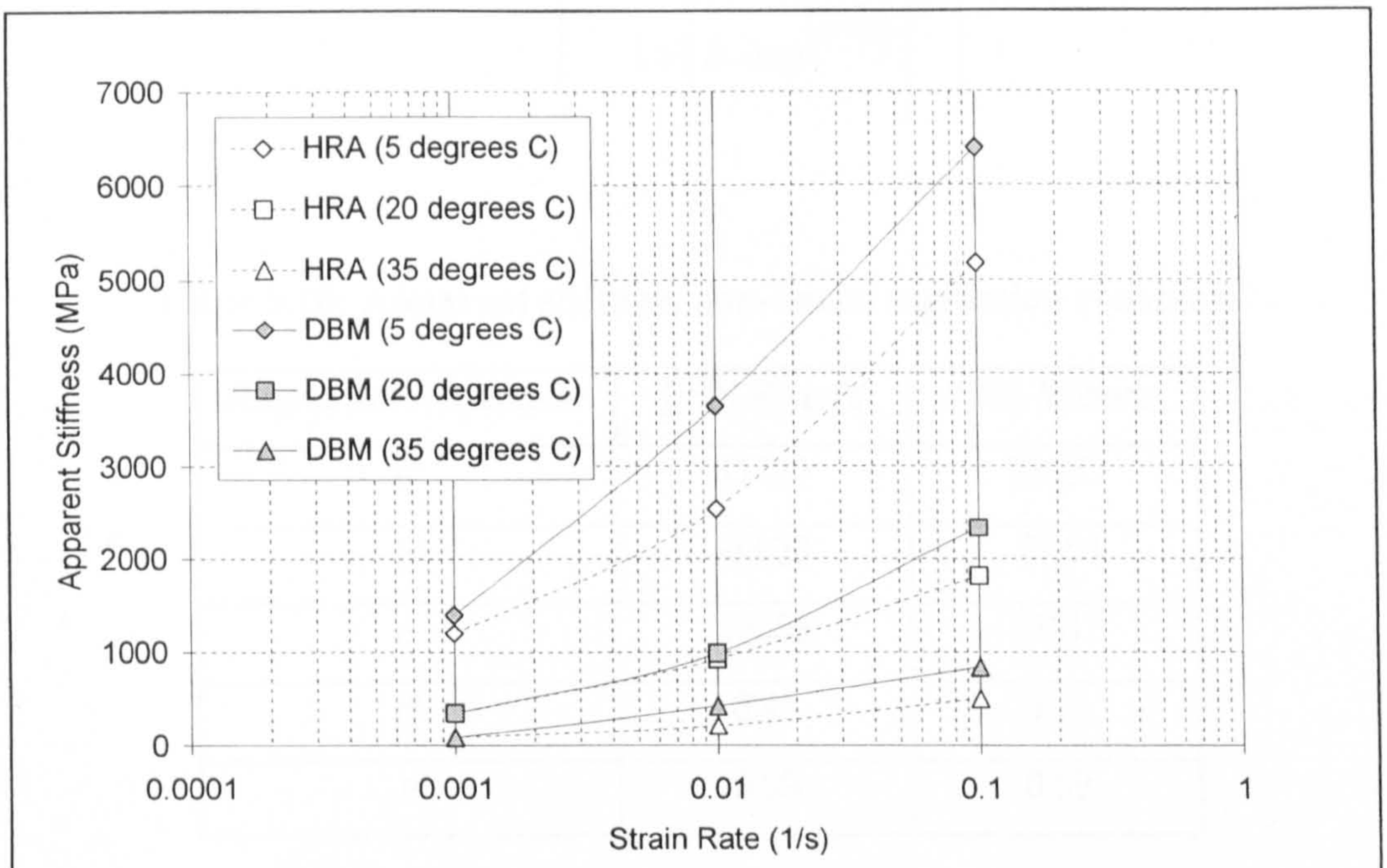

Figure 5.16: Average DBM and HRA mixture stiffness moduli as a function of strain rate and temperature

If the model is to be used for the non-linear simulation of asphaltic material response then eventually mixture stiffness will also be required as a function of temperature and strain rate. Due to the observed similarities between the trend in compressive strength and the trend in mixture stiffness it is possible to describe the apparent stiffness of the DBM and HRA mixtures using a relationship of form given in Equation (5.7). The compressive strength regression constants a, b, c and d are replaced by constants referring to the apparent stiffness of the mixture, Equation (5.8). The values of these constants, a', b', c' and d', determined through non-linear regression analysis are given in Table 5.10 for the DBM and HRA mixtures. Figure 5.17 shows the comparison between the experimental data and the predicted apparent stiffness determined using Equation (5.8). It can be observed that a good fit is achieved. Although again it

should be stated that these values can only be taken as valid within (or close to) the constraints of the experimental test conditions.

$$E = a'\left(1 - \frac{1}{1 + \left[\dot{\varepsilon} \cdot \exp^{\left(b' + \frac{c'}{T}\right)}\right]^{d'}}\right) \tag{5.8}$$

Table 5.10: Apparent stiffness non-linear regression constants

Regression Parameter	*DBM Mixture*	*HRA Mixture*
a′	11720	20320
b′	-63.28	-67.54
c′	18359	18617
d′	0.45	0.37
r^2	0.99	0.99

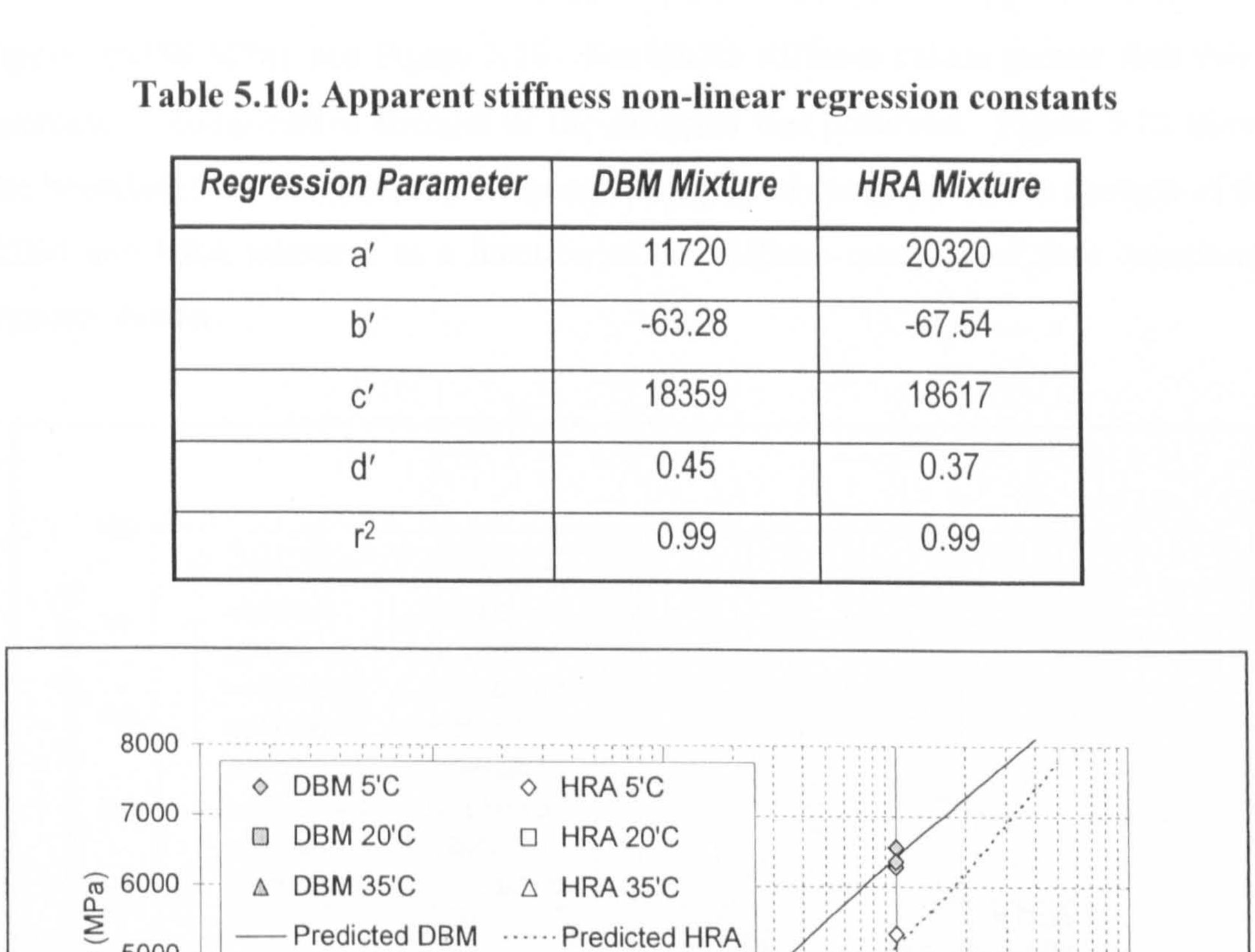

Figure 5.17: Predicted apparent stiffness using Equation (5.8) compared to experimental data

In Section 5.3.5 it was shown that the compressive strength of asphaltic materials is a function of temperature and strain rate, and therefore stiffness. Furthermore, it was observed that binder content and binder properties significantly influence the compressive strength of a mixture, particularly at lower temperatures and faster strain rates (higher stiffnesses) where their effects were found to be more pronounced. Similar results have been reported by Monismith *et al.* [1973], see Section 3.5.4, who found that the compressive strength of various asphalt mixtures increased with increasing stiffness. The mixtures were observed to reach a maximum value, ranging from 5000 – 9000 PSI (≈ 34 - 62 MPa), at binder stiffnesses of approximately 6,000 kg/cm^2 (≈588 MPa), see Figure 3.16. For binder stiffness values greater than this a decrease in compressive strength of the mixtures was observed. Figure 5.18 shows the boundaries for this data superimposed on a plot of the compressive strength of the DBM and HRA mixtures as a function of the stiffness modulus of their constituent bitumen binder.

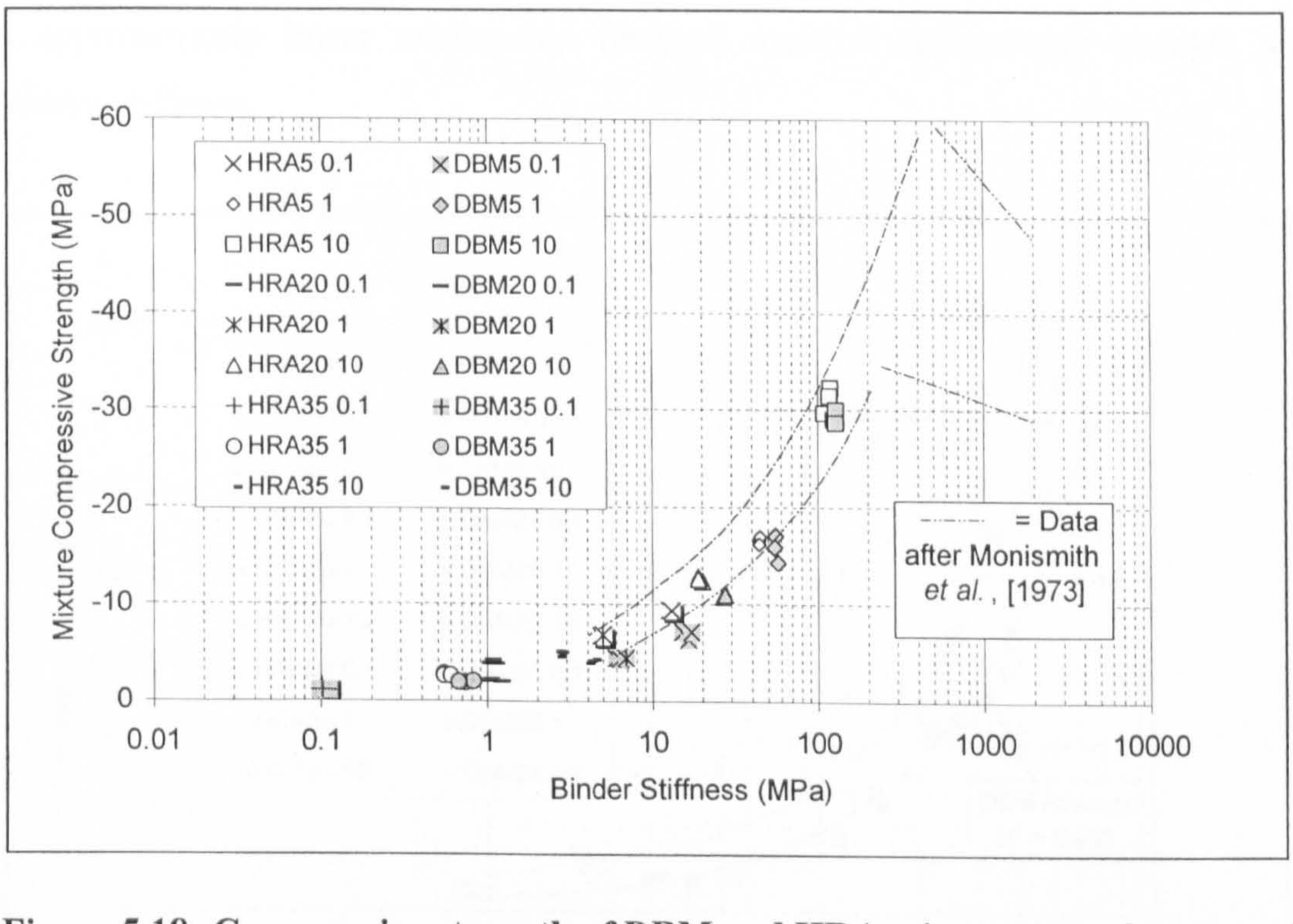

Figure 5.18: Compressive strength of DBM and HRA mixtures as a function of the stiffness modulus of their constituent bituminous binder

The stiffness modulus of the bitumen was estimated using the Van der Poel nomograph given in Figure 2.9 [Van der Poel 1954], based on the following binder

properties:

- softening point = 49.5°C
- penetration at 25°C = 106 dmm
- penetration index ≈ 0.75

The loading time was defined as the time taken to reach peak load and was calculated for each test condition from the axial strain at failure divide by the displacement rate.

For the test conditions, and hence stiffness range investigated in this study, the compressive strength does not attain a maximum value. Which, with reference to Figure 5.18, can be seen to be consistent with the results reported by Monismith *et al.* [1973]. Figure 5.19 shows a similar plot of compressive strength for the DBM and HRA mixtures but as a function of the apparent mixture stiffness. It can be observed that, for the range of temperatures and strain rates investigated in this study, there is an approximately linear relationship between material compressive strength and material stiffness.

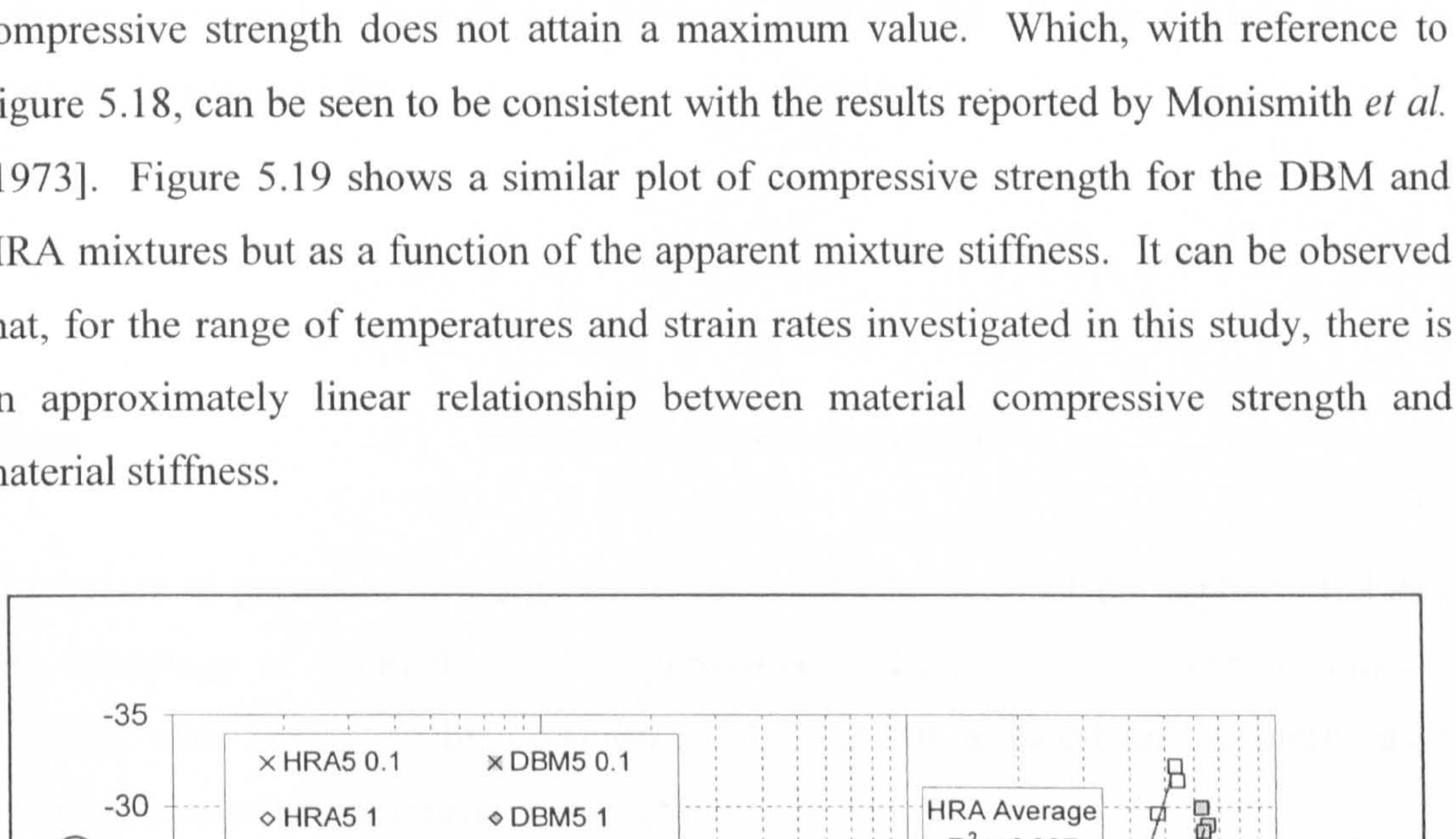

Figure 5.19: Compressive strength as a function of apparent mixture stiffness – DBM and HRA mixtures

This linear relationship can be seen more clearly in Figure 5.20, which shows a plot of apparent stiffness versus compressive strength for the DBM, HRA and HRA mortar mixtures. In this plot, the regression lines have been taken through zero, as a material with no stiffness will have no strength. It can be observed that a better fit is obtained for the DBM mixture, R^2 of 0.99 compared with 0.98 and 0.92 for the HRA and HRA mortar mixture respectively. This supports the earlier observation that the DBM mixture fails in a more brittle manner (as characterised by pronounced sharply defined peaks), when compared to the other two mixtures. Erkens *et al.* [1998] found a similar linear relationship between stiffness and compressive strength for the sand asphalt mixture, which for reference is also plotted in Figure 5.20. The relationship between compressive strength and apparent stiffness for all four mixture types is given by Equation (5.9):

$$E = -S \cdot f_c \tag{5.9}$$

where, S = material stiffness parameter

The values of parameter S are given in Table 5.11 for each of the asphalt mixtures. The advantage of using the above approximate relationship to determine mixture stiffness, over that given by Equation (5.8), is that it is based on the more easily measurable mixture compressive strength.

Table 5.11: Values of material stiffness parameter *S* for the DBM, sand asphalt, HRA and HRA mortar mixtures

Mixture	*Required Mixture Stiffness*
DBM	220
Sand Asphalt	189
HRA	157
HRA mortar	95

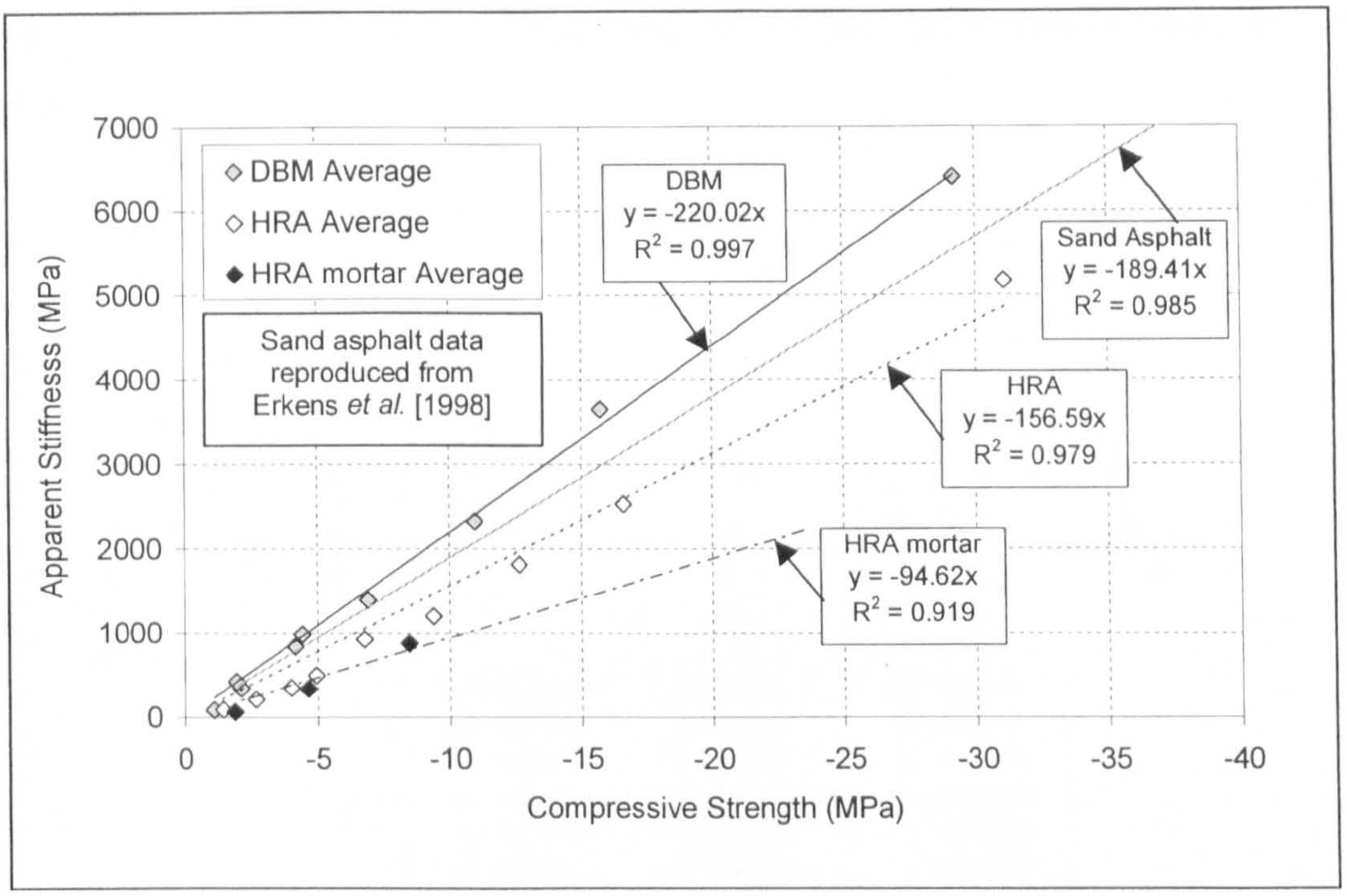

Figure 5.20: Average apparent stiffness versus average compressive strength – DBM, HRA, HRA mortar and sand asphalt mixtures

5.3.8 Poisson's Ratio

Poisson's ratio is defined as the negative ratio of the radial strain to the axial strain, as given in Equation (5.10). The variation of Poisson's ratio for different materials is within a narrow range generally between 0.1 and 0.5. A value of 0.5 is the largest possible theoretical value for an elastic material, and implies constancy of volume during deformation.

$$\nu = -\frac{\varepsilon_r}{\varepsilon_a} \tag{5.10}$$

The axial and radial strains corresponding to the same range of stress data, that was used in the calculation of the apparent stiffness in Section 5.3.7, were used to determine an average Poisson's ratio for each test. The results are shown in Tables 5.2, 5.3 and 5.4 for the DBM, HRA and HRA mortar mixtures respectively. Figure 5.21 shows a plot of Poisson's ratio versus apparent stiffness for the DBM and HRA mixtures. It can be seen that the value for Poisson's ratio shows a general decreasing

trend with increasing mixture stiffness and that similar values were obtained for each of the mixtures.

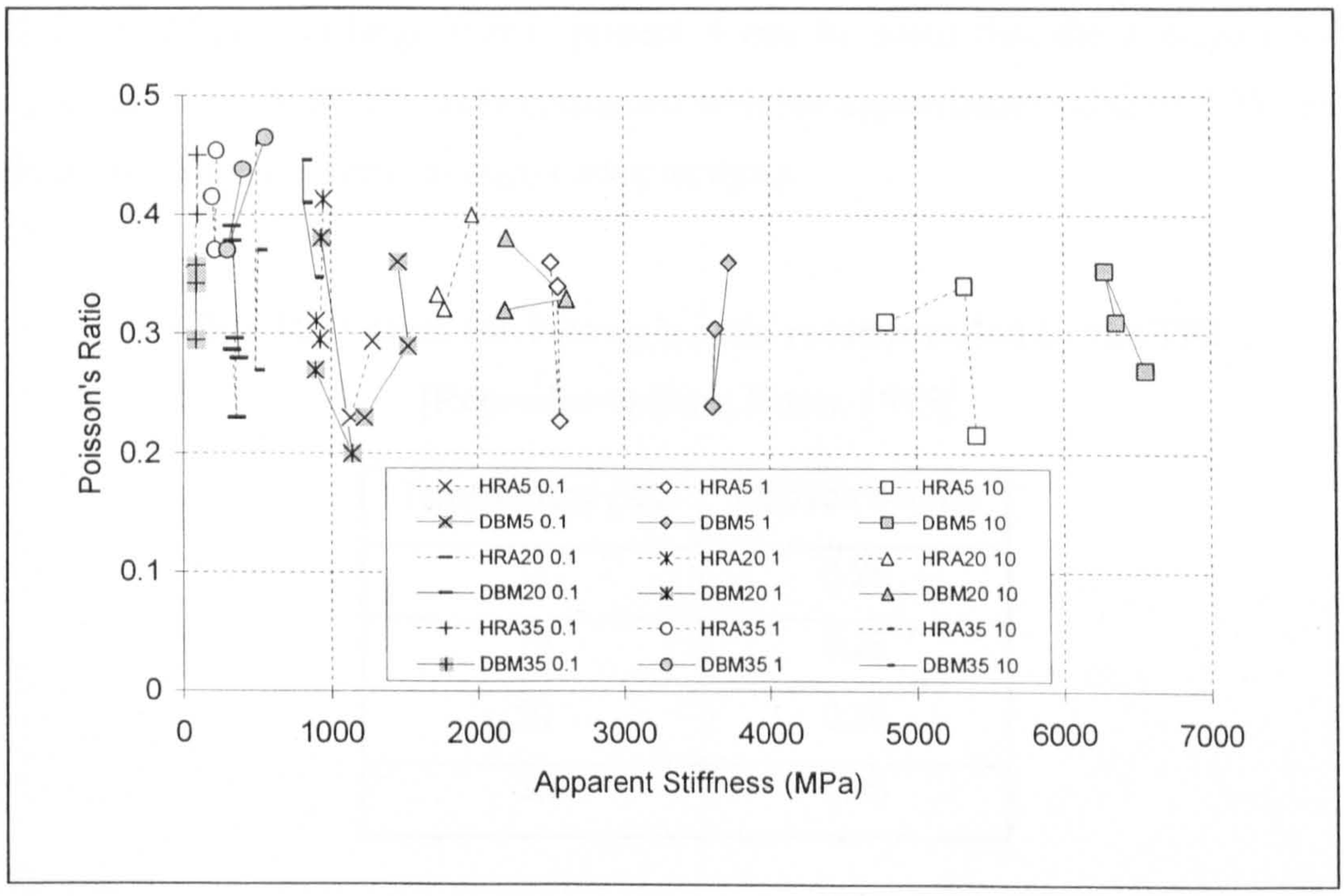

Figure 5.21: Poisson's ratio versus mixture stiffness – DBM and HRA mixtures

It can be seen from Figure 5.21 that the calculated Poisson's ratios display a large degree of scatter, ranging from 0.2 to 0.46 for the DBM mixture and from 0.22 to 0.46 for the HRA mixture. Previous research has found the value of Poisson's ratio for asphalt mixtures to lie somewhere in the range 0.1 to 0.45 [Alavi *et al.*, 1994; Read, 1996]. The TRL has published recommended temperature dependent values of Poisson's Ratio ranging from 0.25 to 0.45 [Nunn, 1995]. These values are given in Table 5.12. Linear interpolation is used between the values given in the table. Outside the temperature range, values of 0.25 and 0.45 are recommended as a minimum and maximum respectively.

Poisson's ratios as determined for the DBM and HRA mixtures are given as a function of strain rate, and as a function of temperature in Figures 5.22 and 5.23 respectively. For the ranges of rates of strains investigated, 0.001 to 0.1 s^{-1}, Figure 5.22 indicates that Poisson's ratio may broadly be considered independent of strain rate for both asphalt mixtures. Figure 5.23 shows the same data but plotted against temperature.

From this figure it is possible to observe a slight increase in Poisson's ratio with increasing temperature. The line in the figure is included for reference, and refers to the Poisson's ratio recommended by the TRL as given in Table 5.12. Although both figures highlight the large scatter present it can be noted that the average results, shown in Figure 5.24, are fairly consistent with the approximate value of 0.35 that is commonly used in pavement engineering analysis.

Table 5.12: Values for Poisson's ratio recommended by the TRL

[Reproduced from Nunn, 1995]

Temperature (°C)	*Poisson's Ratio*
0	0.25
10	0.25
20	0.35
30	0.45

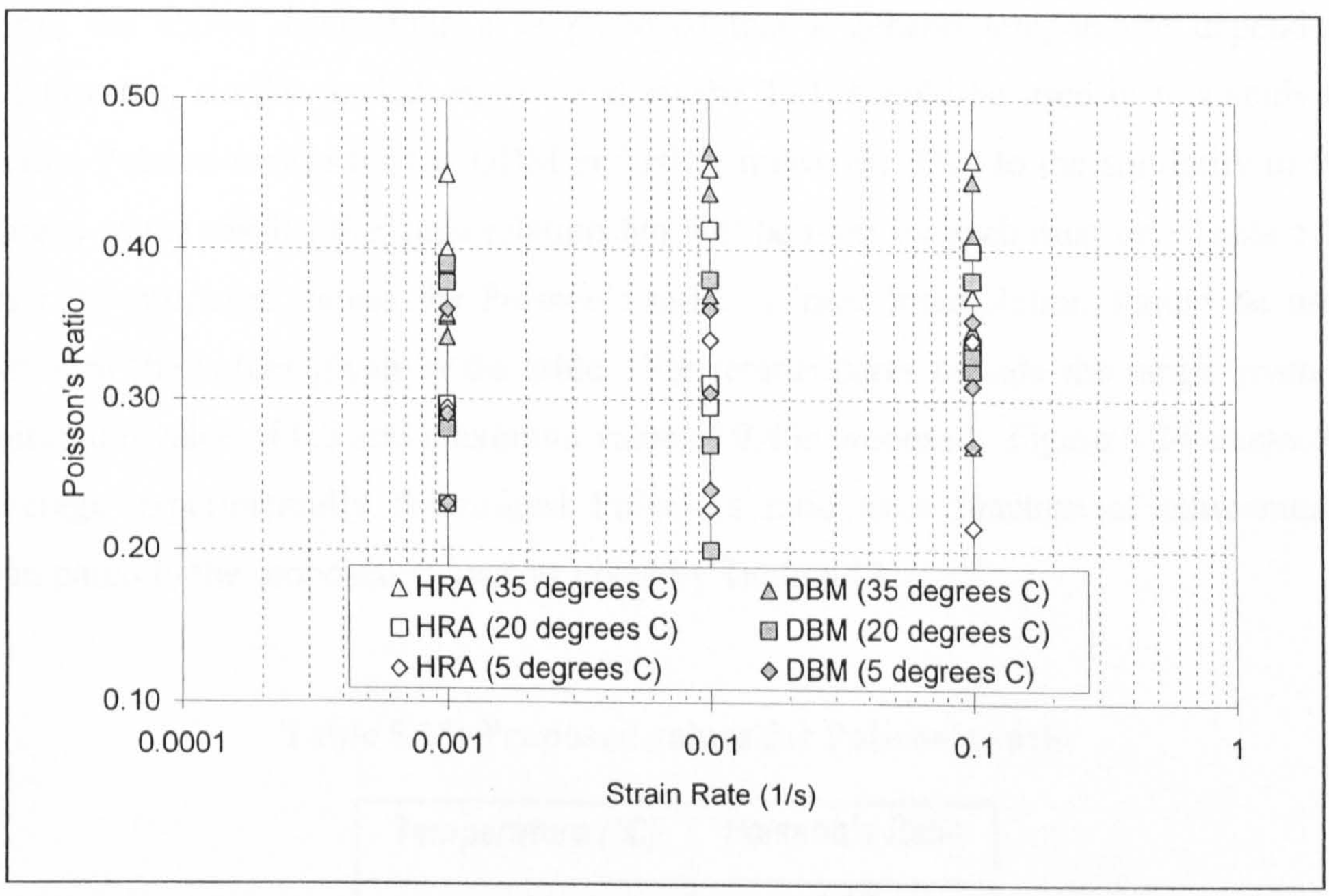

Figure 5.22: Poisson's ratio as a function of strain rate – DBM and HRA mixtures

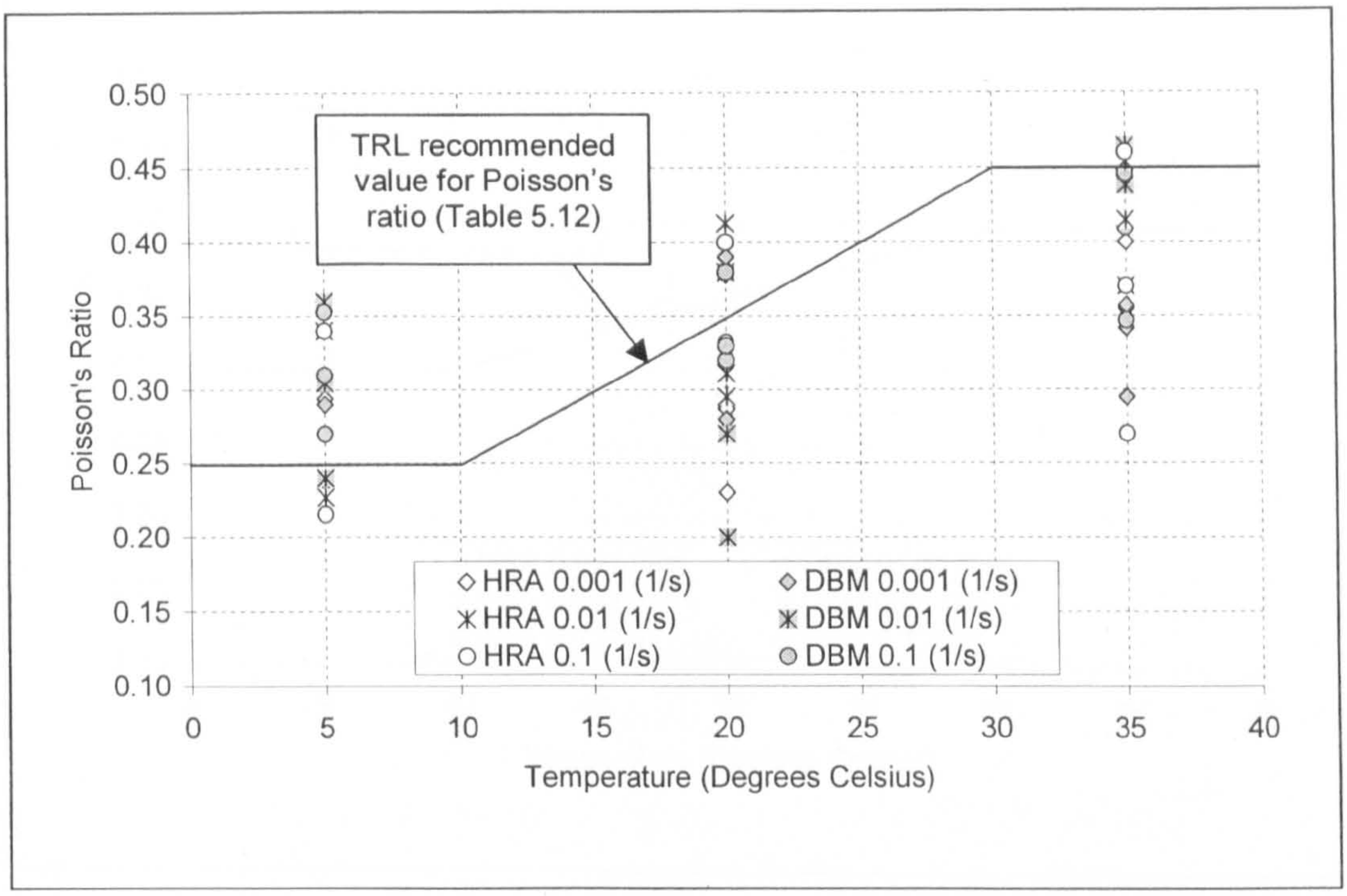

Figure 5.23: Poisson's ratio as a function of temperature – DBM and HRA mixtures

From the above discussions it is proposed that a general temperature dependent relationship, similar to that recommend by the TRL should be used in this study to define Poisson's ratio for the DBM and HRA mixtures. Due to the similarity in the spread of the results, the same relationship will be used for each mixture. Table 5.13 lists the proposed values for Poisson's ratio. Linear interpolation should be used between the values given in the table. For temperatures outside the range given, a minimum value of 0.3 and maximum value of 0.4 is proposed. Figure 5.24 shows the average experimentally determined Poisson's ratio as a function of temperature, compared to the proposed values, as given by Table 5.13.

Table 5.13: Proposed values for Poisson's ratio

Temperature (°C)	*Poisson's Ratio*
0	0.30
10	0.30
20	0.35
30	0.40

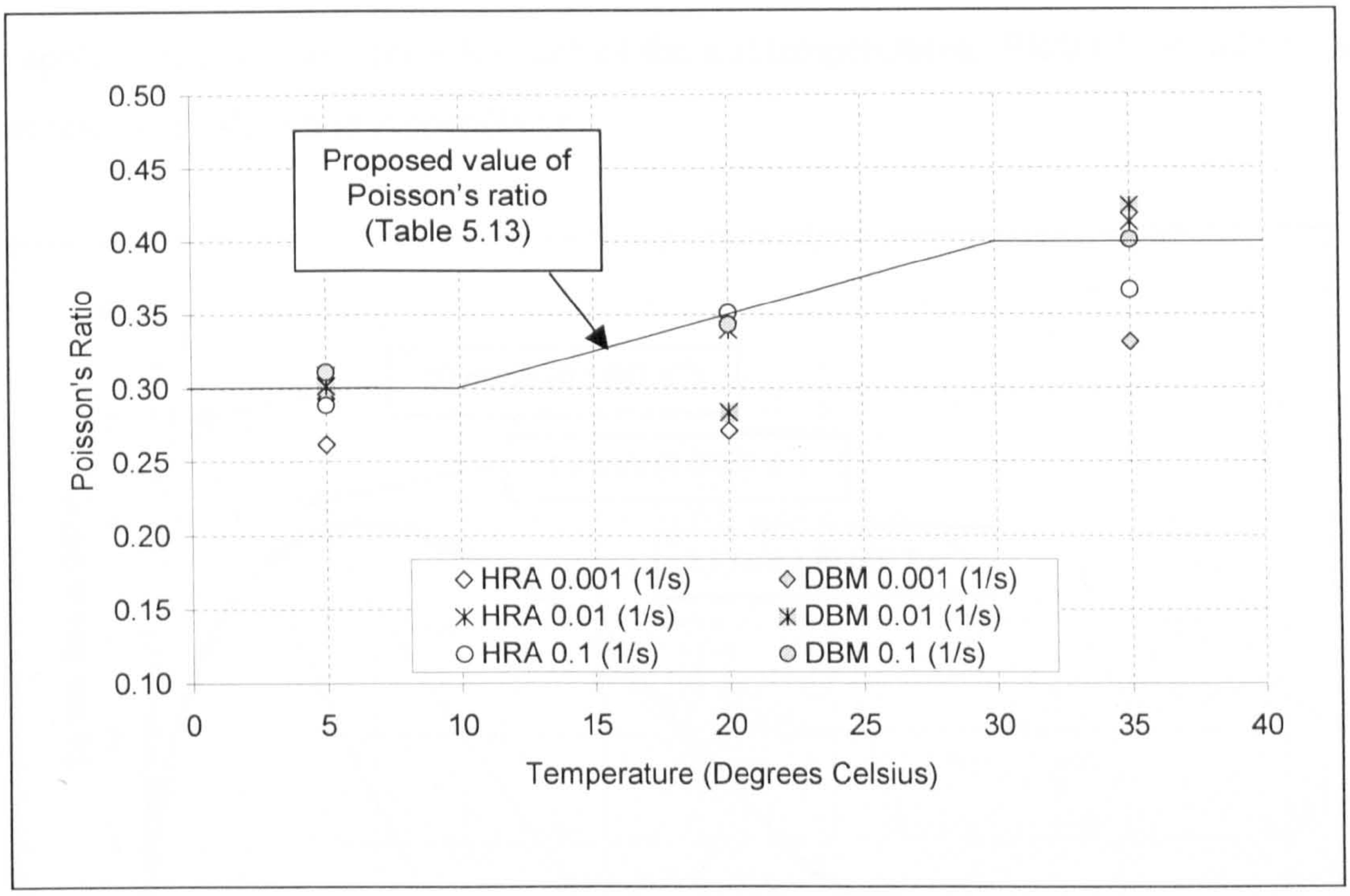

Figure 5.24: Average Poisson's ratio as a function of temperature compared to predicted values given in Table 5.13

5.4 Uniaxial Tension Test Results

The uniaxial tension testing programme was carried out as detailed in Section 4.7 for each of the test conditions listed in Table 5.1. The overall loading forces and axial deformations were transformed into stresses and strains, from which the apparent tensile strength, f_t, defined as the peak tensile stress, and the axial strain at peak stress, ε_a^{peak}, could be determined for each test condition. It should be noted that for the purposes of these transformations, the variation in the axial strains and stresses across the central instrumented section of the specimen, due to the slight change in the specimen width, were assumed to be negligible.

5.4.1 Summary of Tension Test Results

The data for the tensile testing programme is presented in summary form in Tables 5.14 and 5.15, for the DBM and HRA mixtures respectively. Typical examples of the DBM and HRA mixture material response are presented graphically in Figures 5.25 to 5.30, which show plots of the tensile stress versus the axial strain curves for the range

of applied displacement rates for each of the test temperatures. Plots of the individual test results are shown in Appendix G.

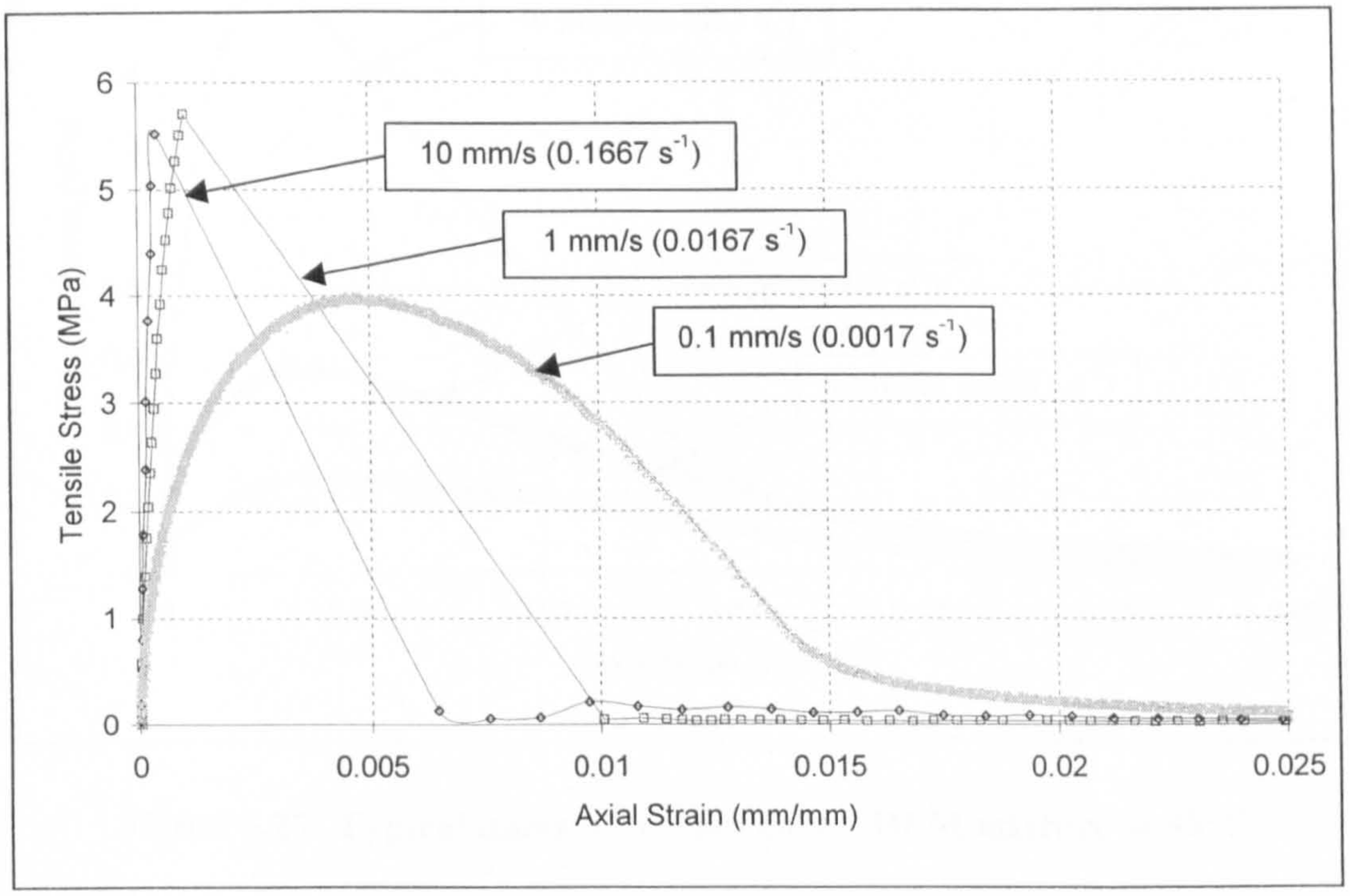

Figure 5.25: Typical uniaxial tension data – DBM mixture at 5°C

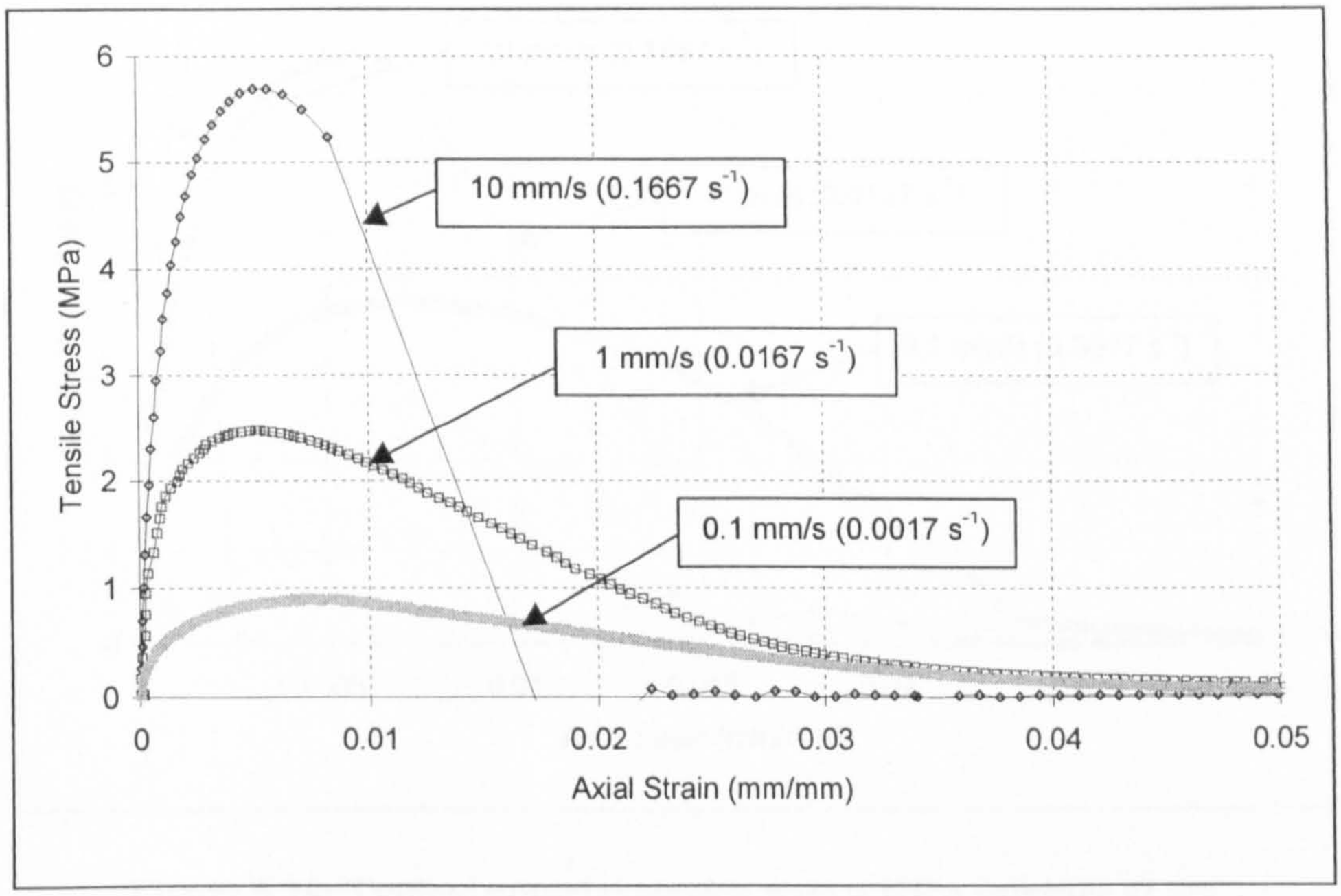

Figure 5.26: Typical uniaxial tension data – DBM mixture at 20°C

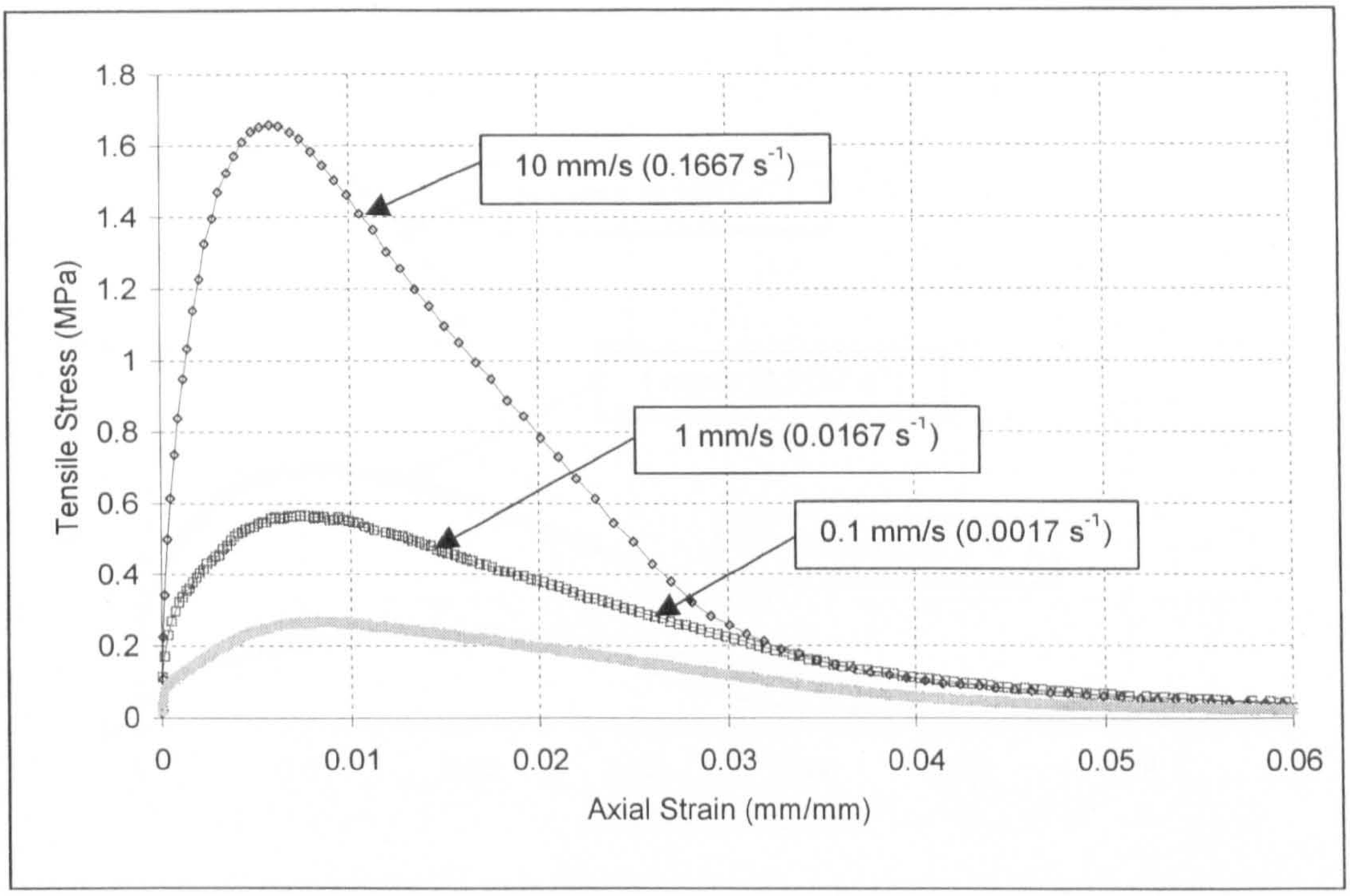

Figure 5.27: Typical uniaxial tension data – DBM mixture at 35°C

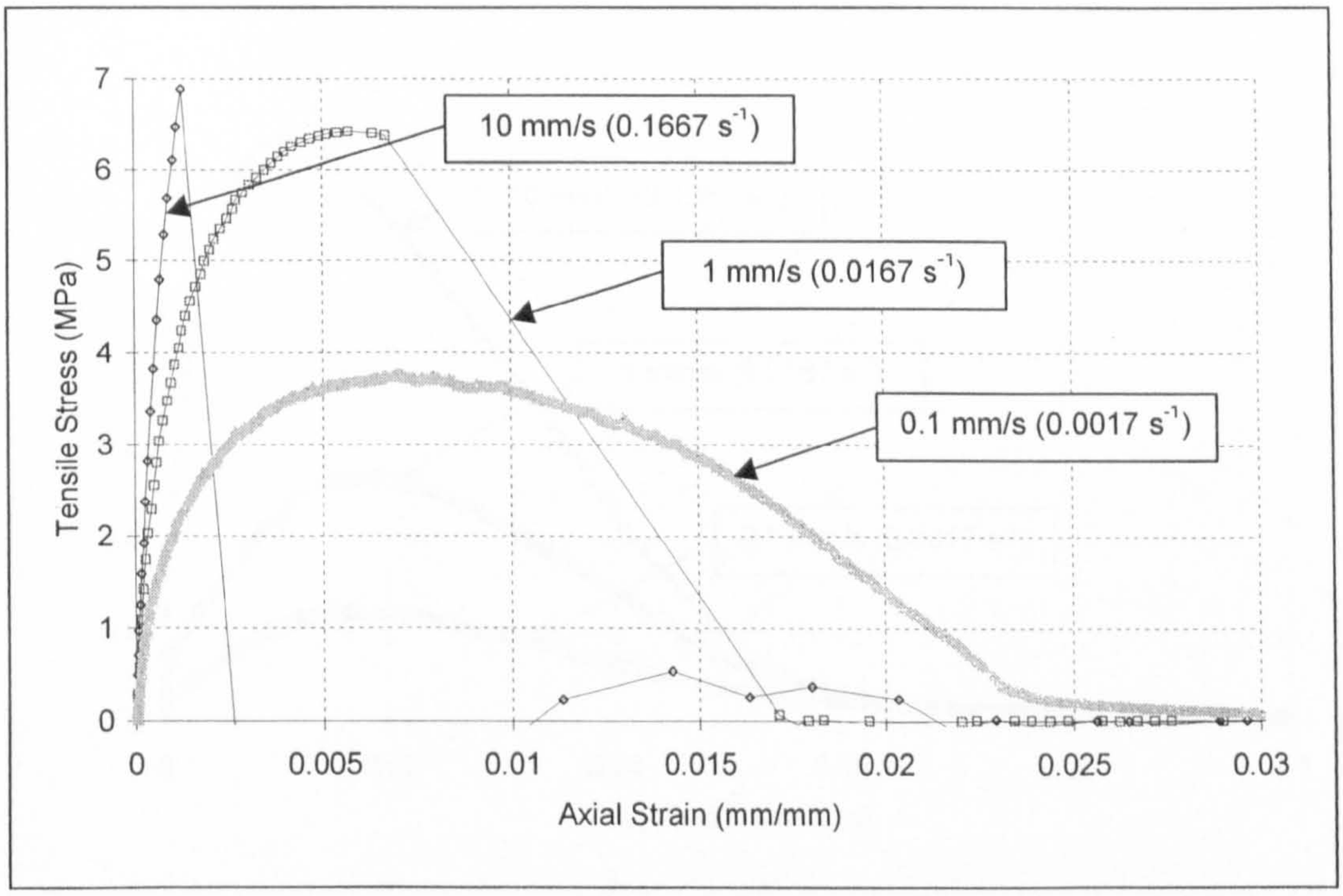

Figure 5.28: Typical uniaxial tension data – HRA mixture at 5°C

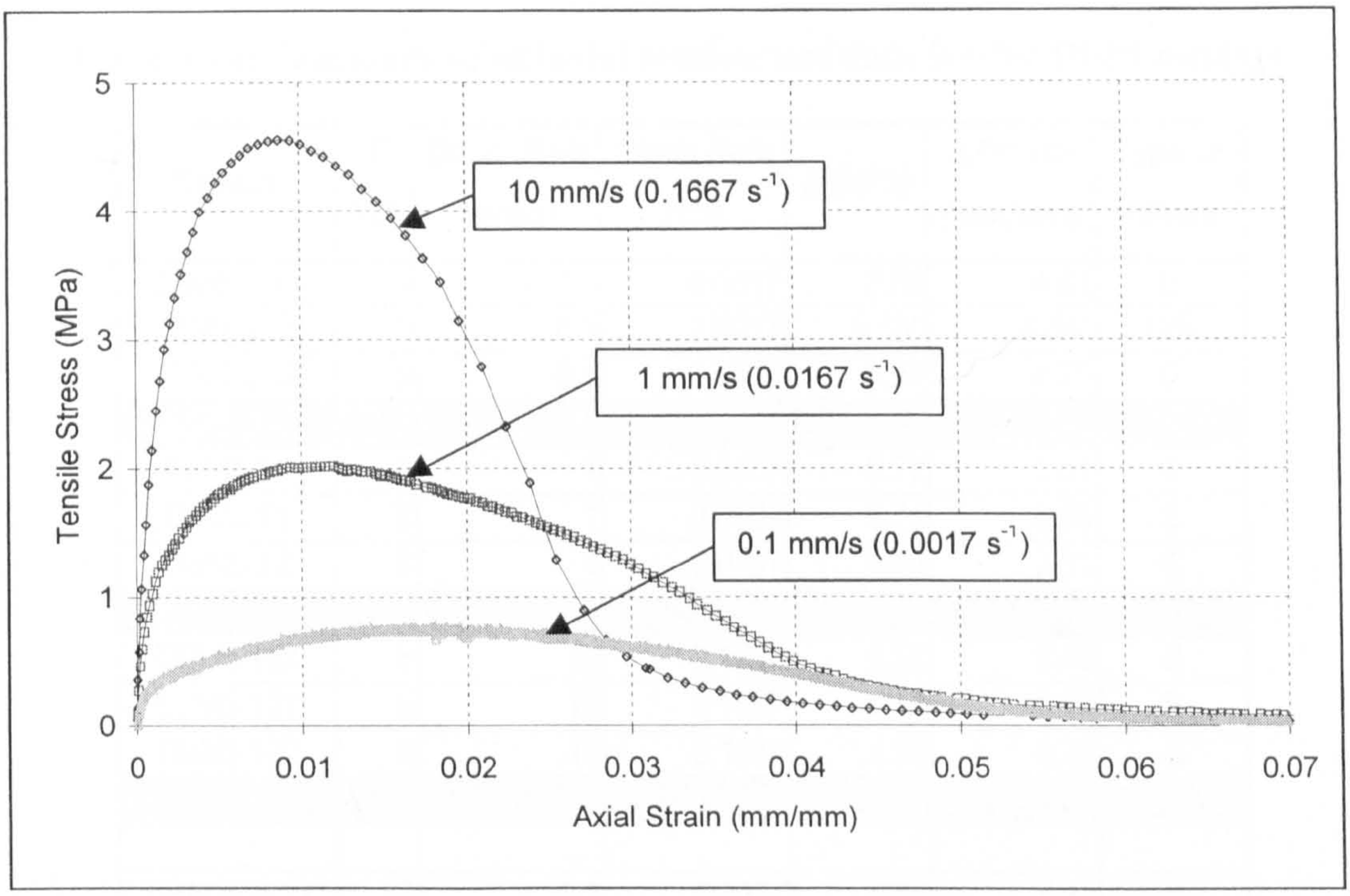

Figure 5.29: Typical uniaxial tension data – HRA mixture at 20°C

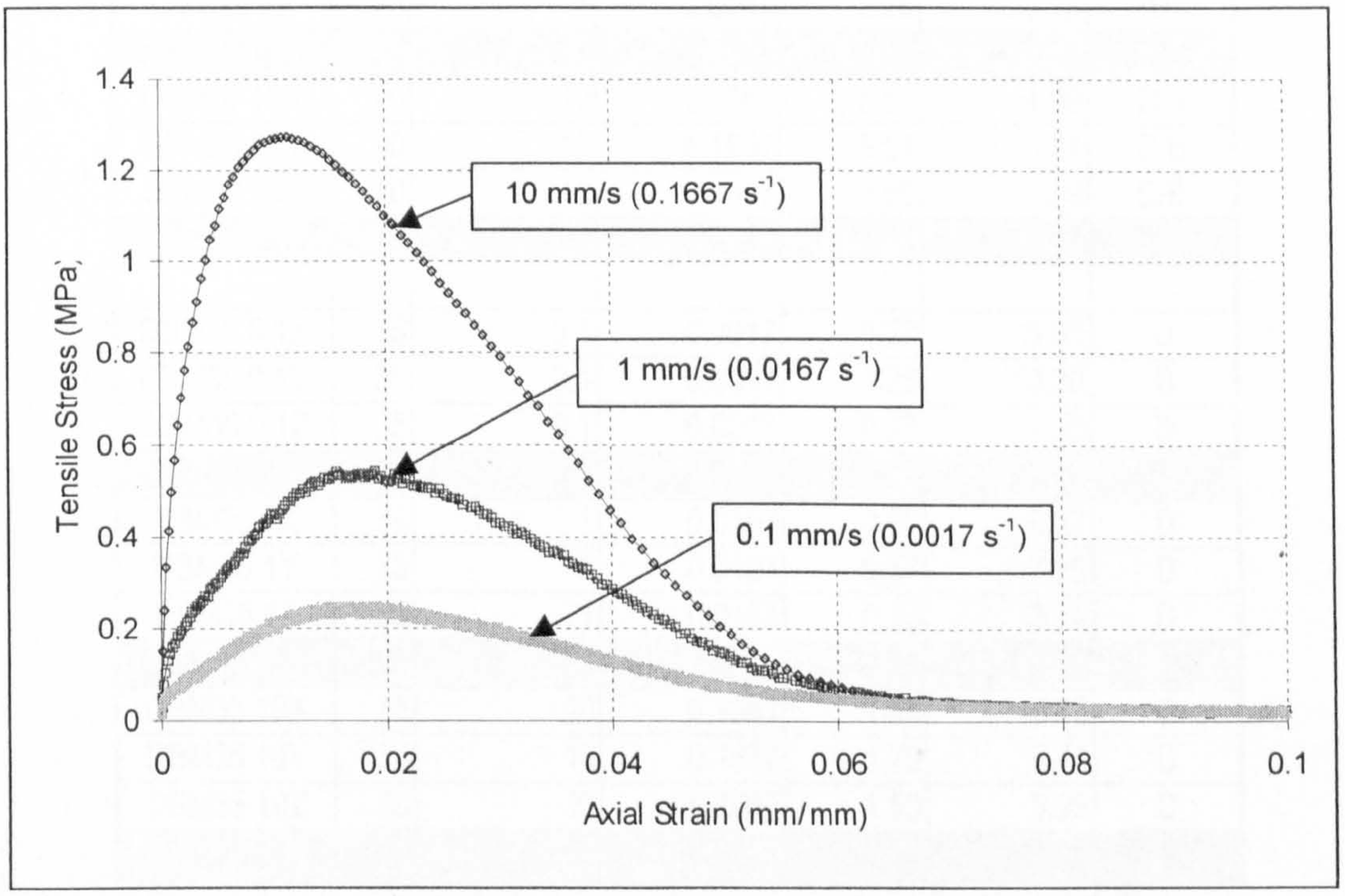

Figure 5.30: Typical uniaxial tension data – HRA mixture at 35°C

Table 5.14: Summary of uniaxial tension test data for the DBM mixture

Sample	T (°C)	Dispt. Rate (mm/s)	Strain Rate (1/s)	ft (MPa)	ε_a^{peak} x10^{-3} (mm/mm)	Type of Failure
DBM5 0.1X	5	0.1	0.0017	3.78	4.63	D
DBM5 0.1Y	5	0.1	0.0017	5.16*	4.84*	D/B
DBM5 0.1Z	5	0.1	0.0017	3.98	4.70	D
Average	5	0.1	0.0017	3.88	4.66	
DBM5 1X	5	1	0.0167	5.72	1.01	B
DBM5 1Y	5	1	0.0167	5.74	0.98	B
DBM5 1Z	5	1	0.0167	6.83	2.61	B
Average	5	1	0.0167	6.10	1.53	
DBM5 10X	5	10	0.1667	5.52	0.40	B
DBM5 10Y	5	10	0.1667	6.16	0.50	B
DBM5 10Z	5	10	0.1667	4.98	0.30	B
Average	5	10	0.1667	5.55	0.40	
DBM20 0.1X	20	0.1	0.0017	0.99	6.35	D
DBM20 0.1Y	20	0.1	0.0017	0.83	7.89	D
DBM20 0.1Z	20	0.1	0.0017	0.91	8.25	D
Average	20	0.1	0.0017	0.91	7.50	
DBM20 1X	20	1	0.0167	2.48	5.05	D
DBM20 1Y	20	1	0.0167	2.60	4.90	D
DBM20 1Z	20	1	0.0167	2.20	5.13	D
Average	20	1	0.0167	2.43	5.03	
DBM20 10X	20	10	0.1667	5.85	4.99	D/B
DBM20 10Y	20	10	0.1667	5.54	5.24	D/B
DBM20 10Z	20	10	0.1667	5.69	5.09	D/B
Average	20	10	0.1667	5.69	5.10	
DBM35 0.1X	35	0.1	0.0017	0.27	9.00	D
DBM35 0.1Y	35	0.1	0.0017	0.26	10.30	D
DBM35 0.1Z	35	0.1	0.0017	0.28	7.36	D
Average	35	0.1	0.0017	0.27	8.88	
DBM35 1X	35	1	0.0167	0.58	6.27	D
DBM35 1Y	35	1	0.0167	0.57	7.35	D
DBM35 1Z	35	1	0.0167	0.76	3.74	D
Average	35	1	0.0167	0.64	5.79	
DBM35 10X	35	10	0.1667	1.66	5.82	D
DBM35 10Y	35	10	0.1667	1.75	5.44	D
DBM35 10Z	35	10	0.1667	1.53	5.29	D
Average	35	10	0.1667	1.65	5.52	

* Denotes a result excluded from the average (see Section 5.4.3)

Table 5.15: Summary of the uniaxial tension test data for the HRA mixture

Sample	T (°C)	Dispt. Rate (mm/s)	Strain Rate (1/s)	ft (MPa)	ε_a^{peak} x10^{-3} (mm/mm)	Type of Failure
HRA5 0.1X	5	0.1	0.0017	5.39*	4.80*	D/B
HRA5 0.1Y	5	0.1	0.0017	3.18	6.94	D
HRA5 0.1Z	5	0.1	0.0017	3.78	7.06	D
Average	5	0.1	0.0017	3.48	7.00	
HRA5 1X	5	1	0.0167	7.42	5.64	B
HRA5 1Y	5	1	0.0167	6.42	5.69	B
HRA5 1Z	5	1	0.0167	6.22	7.43	B
Average	5	1	0.0167	6.69	6.25	
HRA5 10X	5	10	0.1667	6.47	1.11	B
HRA5 10Y	5	10	0.1667	6.92	1.26	B
HRA5 10Z	5	10	0.1667	5.83	0.81	B
Average	5	10	0.1667	6.41	1.06	
HRA20 0.1X	20	0.1	0.0017	0.78	18.02	D
HRA20 0.1Y	20	0.1	0.0017	0.81	14.90	D
HRA20 0.1Z	20	0.1	0.0017	0.91	13.72	D
Average	20	0.1	0.0017	0.83	15.54	
HRA20 1X	20	1	0.0167	2.17	9.56	D
HRA20 1Y	20	1	0.0167	2.02	11.93	D
HRA20 1Z	20	1	0.0167	1.71	12.87	D
Average	20	1	0.0167	1.97	11.45	
HRA20 10X	20	10	0.1667	4.99	7.74	D/B
HRA20 10Y	20	10	0.1667	4.56	8.73	D
HRA20 10Z	20	10	0.1667	4.00	8.44	D
Average	20	10	0.1667	4.52	8.30	
HRA35 0.1X	35	0.1	0.0017	0.20	28.37	D
HRA35 0.1Y	35	0.1	0.0017	0.21	22.32	D
HRA35 0.1Z	35	0.1	0.0017	0.25	17.79	D
Average	35	0.1	0.0017	0.22	22.83	
HRA35 1X	35	1	0.0167	0.47	20.00	D
HRA35 1Y	35	1	0.0167	0.45	18.65	D
HRA35 1Z	35	1	0.0167	0.54	18.94	D
Average	35	1	0.0167	0.49	19.20	
HRA35 10X	35	10	0.1667	1.27	13.73	D
HRA35 10Y	35	10	0.1667	1.25	12.78	D
HRA35 10Z	35	10	0.1667	1.26	11.11	D
Average	35	10	0.1667	1.26	12.54	

* Denotes a result excluded from the average (see Section 5.4.3)

5.4.2 Observations on Tension Test Results

Comparing Figures 5.25 to 5.30, and with reference to Appendix G, the following observations can be made with regard to the tensile stress-strain response of the mixtures.

- For most test conditions both mixtures displayed an increase in tensile strength with increasing strain rate and/or decreasing temperature.
- It is possible to distinguish two main types of tensile failure mode. Ductile failure, at higher temperatures and/or slower strain rates, or brittle failure, at lower temperatures and/or faster strain rates, (see Section 5.4.4).
- At the test conditions of 5°C a slight decrease in tensile strength of the mixtures can be observed between 1 mm/s and 10 mm/s displacement rates.
- In general the HRA mixture exhibits larger axial strains than the DBM mixture for equivalent test conditions.

5.4.3 Apparent Tensile Strength

The variations in the measured tensile strengths of the mixtures, for each of the test conditions were found to display some scatter, particularly the 5°C test conditions. On further investigation it became apparent that, for both mixtures, at the 5°C, 0.1 mm/s test conditions, two out of the three tests failed in a ductile mode, with the remaining failure taking a more brittle form. This resulted in relative errors of 15.7 % and 26.8 % for the DBM and HRA mixture, respectively, for the 5°C, 0.1 mm/s test conditions. On preliminary determination of the model material parameters it was found that the above scatter, at 5°C, 0.1 mm/s resulted in inconsistencies in the formation of the flow surfaces. Therefore, as the errors were considered to be large, it was decided to omit the results corresponding to the more brittle failure from the averages for the 5°C, 0.1 mm/s test conditions. This resulted in a maximum relative error in the measured peak stress between three tests carried out under the same conditions of 13.7 % (DBM at 35°C at 1 mm/s). The average overall relative error in the tensile strength for the DBM and HRA mixtures for all test conditions was found to be 6.5 % and 7.5 % respectively. Figure 5.31 shows a plot of the average peak tensile strength (tensile positive) plotted as a function of strain rate and temperature for the DBM and HRA mixtures. It can be seen from this figure that with increasing

strain rate and decreasing temperature, the peak tensile strength of the mixtures increases and then appears to reach a plateau level, followed by a slight decease in strength.

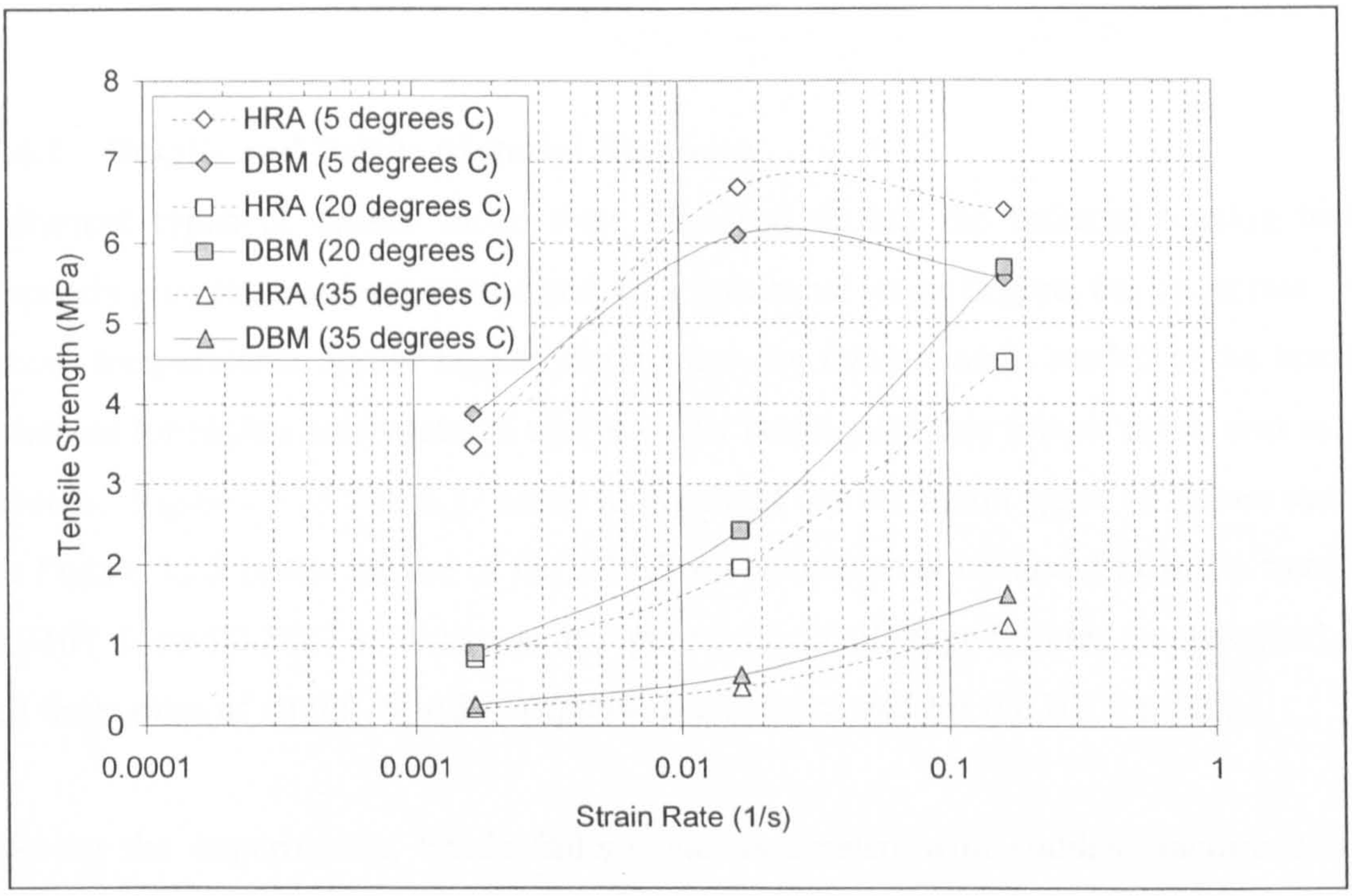

Figure 5.31: Average peak tensile strength of DBM and HRA mixtures as a function of strain rate and temperature

It can be observed that at the test temperatures of 20°C and 35°C the DBM mixture has a greater tensile strength than the HRA mixture for the strain rates investigated. However, it can be seen that at 5°C at the faster strain rates the HRA mixture has the greatest tensile strength. This is an interesting observation, as traditionally, the HRA mixture having the larger binder content would be assumed to have the higher fracture strength for all test conditions. This might therefore indicate the presence of additional influences in the failure of the specimens, or could be a result of the way in which the failure condition has been defined. The plateau represents the fracture strength of the mixtures. From Figure 5.31 it can be determined that the average fracture strength of the HRA mixture is approximately 6.8 MPa compared to approximately 6.1 MPa for the DBM mixture. It can be seen that at the test temperature of 5°C, at a displacement rate of 10 mm/s, a reduction in the average tensile strength of the mixtures can be observed. This type of behaviour is consistent

with the observations reported by Heukelom [1966], see Sections 3.5.1 and 3.5.3, for plain bitumens and asphalt mixtures. Heukelom found that after an optimum binder stiffness of approximately 49 – 59 MPa the tensile strength of asphaltic materials decreases with increasing binder stiffness.

5.4.4 Ductile and Brittle Material Response

Different types of failure mode were observed during the uniaxial tension tests, depending on the test temperature and, to a somewhat lesser degree, the strain rate. At lower temperatures and/or higher strain rates the failure mode tended to be brittle, whereas for higher temperatures and/or lower strain rates this failure mode was more ductile. Figures 5.25 and 5.27 serve to highlight the two main types of failure mode. In Figure 5.25 brittle failure of the DBM test specimen is observed at strain rates of 0.0167 s^{-1} and 0.1667 s^{-1}, whereas in Figure 5.27 ductile type failures are observed for all three rates of strain. Similar response is also observed for the HRA mixture.

During the experiments, brittle failure was associated with sudden fracture of the specimen, accompanied by an audible 'bang'. Such failures are characterised by relatively large tensile strengths and relatively small axial strains at failure. Conversely, for the ductile failure mode, it was possible to observe necking of the test specimens, and in some cases, mainly for the DBM mixture, multiple cracking planes. In such circumstances failures are characterised by relatively low tensile strengths and relatively large axial strains. The type of failure mode, ductile (D), brittle (B) or ductile/brittle (D/B) that characterised each test is given in Tables 5.14 and 5.15 for the DBM and HRA mixture respectively. Ductile/brittle failure modes were characterised by necking of the specimen before sudden fracture occurred, see Figure 5.26, at 10 mm/s displacement rate. The above information is also presented graphically in Figure 5.32, which indicates which type of failure mode each test was subject to, on a plot of tensile strength versus strain rate, as a function of temperature.

From Figure 5.32 it is possible to observe that the brittle failure modes generally took place at the lower temperatures, mostly 5°C, and at fast strain rates. This would indicate that the type of failure mode is a function of material stiffness, i.e. the stiffer the mixture the more brittle the failure mode. This is analogous to the work carried

out by Cheung [1995], see Section 3.5.1, on bituminous binders, who observed that for an applied strain rate, the stress increases with strain, but at a decreasing rate, until a maximum value is attained. If this maximum value is smaller than the fracture strength, the specimen necks rather than breaks. Conversely, whenever the applied strain rate is large enough to sustain a stress that is comparable to the fracture stress, the specimen breaks before it necks.

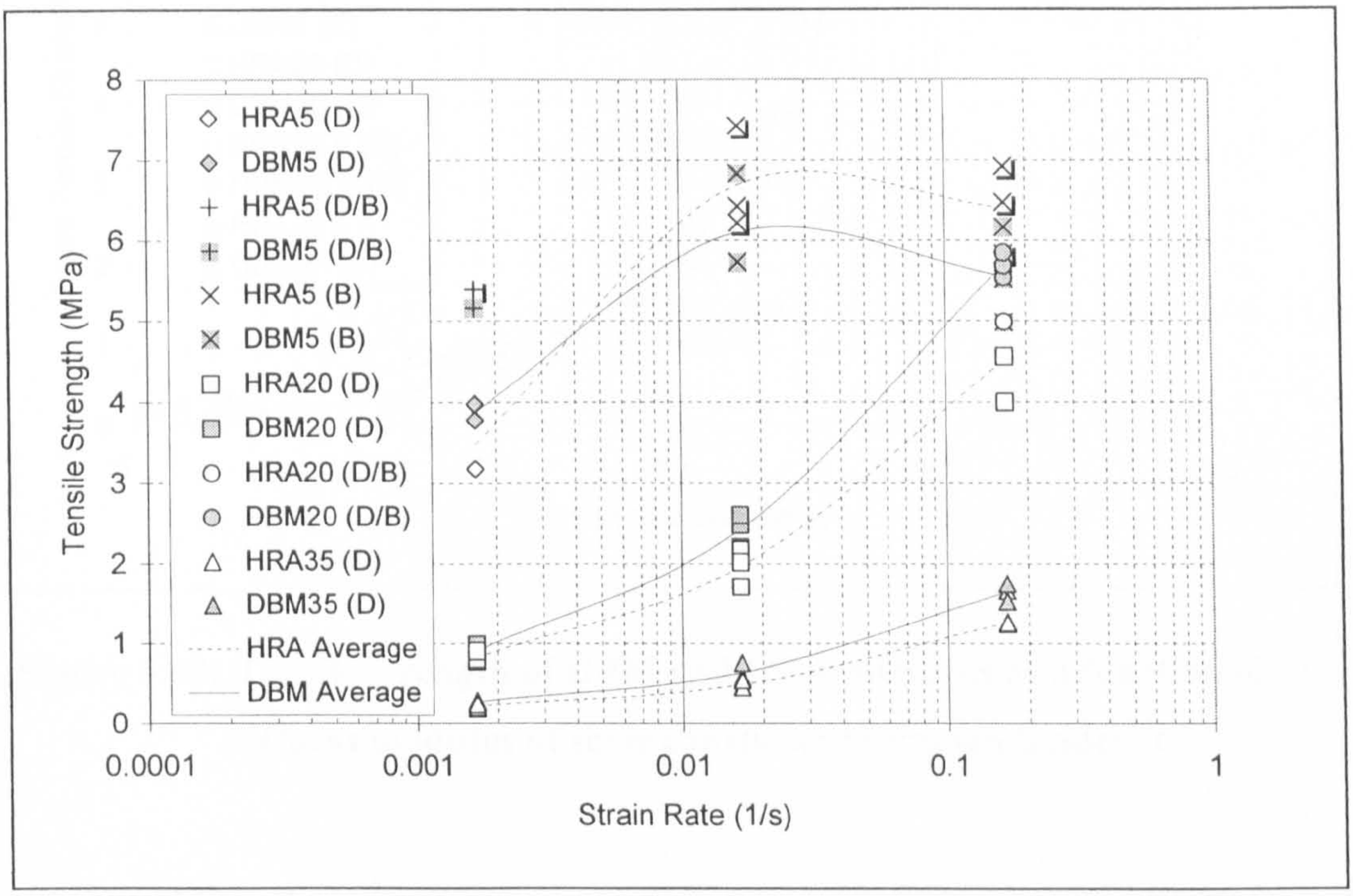

Figure 5.32: Individual tensile test failure mode type, shown on a tensile strength versus strain rate plot, at 5, 20 and 35°C

The information given in Figure 5.32 has been replotted in Figure 5.33, which shows a plot of the tensile strength of the DBM and HRA mixtures, but as a function of the stiffness modulus of their constituent bituminous binder. The stiffness modulus of the bitumen was estimated using the Van der Poel nomograph given in Figure 2.9, [Van der Poel, 1954] based on the following binder properties:

- softening point = 49.5°C,
- penetration at 25°C = 106 dmm
- penetration index ≈ 0.75

The loading time was defined as the time taken to reach peak load and was calculated for each test condition from the axial strain at failure divide by the displacement rate.

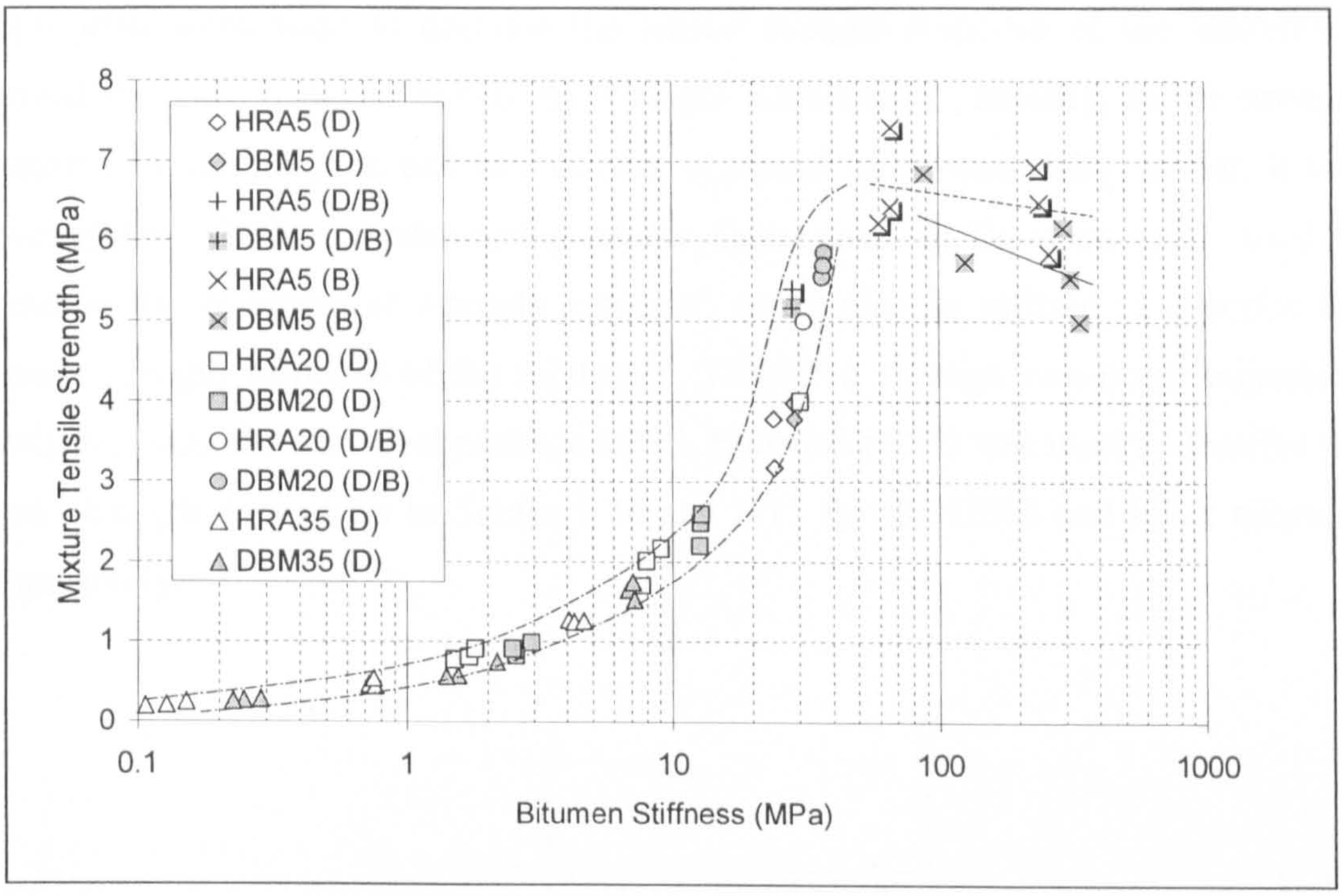

Figure 5.33: Tensile strength of DBM and HRA mixtures as a function of the stiffness modulus of their constituent bitumen binder

The result of this analysis, shown above in Figure 5.33, displays good agreement with the observations of Heukelom, reported earlier in Sections 3.5.1 and 3.5.3. It can be observed that the DBM and HRA mixtures display a similar range of response. At lower stiffness moduli the dashed line indicates this range, whereas at higher stiffness moduli where the response of each mixture is more distinct, the dotted line represents the HRA mixture response and the solid line represents the response of the DBM mixture. From Figure 5.33 it can be observed that brittle failures occur only after peak strength response at binder stiffness moduli of approximately 60 MPa or greater, i.e. only when the strain rate and temperature conditions are sufficient to allow the fracture strength of the mixtures to be attained. For binder stiffness moduli below approximately 30 MPa only ductile type failure can be observed. Between these two ranges, binder stiffness moduli of 30 – 60 MPa, both ductile and brittle failure conditions are observed.

5.4.5 Expression for Peak Tensile Strength Response

It has been shown above that different types of failure mode were exhibited by the specimens, depending on the mixture stiffness. Therefore, when selecting an appropriate expression to describe the tensile strength response of the mixtures it proved difficult to fit the data using a single relationship. Initially, as the strength response in compression and tension was observed to be essentially similar, it was investigated whether a relationship of the form given in Equation (5.7), used to describe the compressive strength response, could also be utilised to describe the tensile strength response of the mixtures. Therefore, through non-linear regression analysis, using the statistical package SPSS, Equation (5.11) was used to describe the peak strength data given in Tables 5.14 and 5.15 for the DBM and HRA mixtures respectively.

$$f_t = e\left(1 - \frac{1}{1 + \left[\dot{\varepsilon} \cdot \exp^{\left(f + \frac{g}{T}\right)}\right]^h}\right) \tag{5.11}$$

where, f_t = tensile strength (MPa)

e, f, g, h = tensile strength non-linear regression parameters

When performing the non-linear regression analysis, the parameters, e, f, g and h, were initially set at 1, 0, 1 and 1 respectively. The iterative process was stopped after 37 and 33 model evaluations for the DBM and HRA mixtures respectively. The resultant fitted uniaxial tension non-linear regression constants for each mixture are shown in Table 5.16. On first inspection the results of the regression analysis appear promising. Parameter, e, which is the tensile equivalent of parameter, a, indicates a theoretical limiting tensile strength of approximately 6 MPa and 7 MPa for the DBM and HRA mixtures respectively. These values are similar to the observed fracture strengths of 6.1 MPa (DBM) and 6.8 MPa (HRA) that were reported for the mixtures in Section 5.4.3. However, through using one set of regression parameters it was found that a favourable fit could only be obtained for the brittle type mixture failures.

At the higher temperatures (ductile failures) a less favourable fit was obtained, particularly for the lower strain rates. Therefore, the use of expressions with dual or multiple functions was investigated as a possible means to describe the tensile strength response, as a function of both strain rate and temperature.

Table 5.16: Uniaxial tensile strength non-linear regression parameters – DBM and HRA mixtures

Regression Parameter	*DBM Mixture*	*HRA Mixture*
e	6.08	7.07
f	-56.41	-66.93
g	17653	20441
h	0.97	0.68
r^2	0.98	0.98

Initially a temperature dependent relationship such as that proposed in Scarpas *et al.* [1997] was investigated. However as the type of failure mode has been found to depend on the material stiffness, i.e. the combined effects of temperature and strain rate, the selection of an appropriate temperature boundary for such an expression was found to be problematic. The tensile failure mode has been shown in Section 5.4.4 to vary depending on the material stiffness. At low stiffness moduli (binder stiffness ≤ 30 MPa) the failure mode is ductile. At intermediate stiffness moduli (binder stiffness 30 MPa – 60 MPa) both ductile and brittle failures occur and the results display scatter. At high stiffness moduli (binder stiffness ≥ 60 MPa) the fracture strength of the material is attained and the failure mode is brittle. Therefore a more applicable expression would be one segregated on the basis of stiffness. One possible form of such a function is given in Equation (5.12).

$$f_t = \begin{cases} f_t(\dot{\varepsilon}, T, x) & for \quad S_b > 30\,MPa \\ f_t(\dot{\varepsilon}, T, y) & for \quad S_b \leq 30\,MPa \end{cases} \tag{5.12}$$

where, x, y = material parameters

S_b = binder stiffness

Based on the above discussion the expression given in Equation (5.11) can be utilised with two sets of independent regression parameters to describe the ductile and brittle response ranges. The fitted tensile non-linear regression constants are presented in Table 5.17, for each of the mixtures, for the stiffness ranges given in Equation (5.12). Figure 5.34 shows a plot of the predicted peak tensile strengths, using the dual regression parameters, compared to the experimental data, for each of the mixtures.

Table 5.17: Dual function uniaxial tensile strength non-linear regression parameters – DBM and HRA mixtures

Regression Parameter	*DBM Mixture*		*HRA Mixture*	
	S_b >30 MPa	*$S_b \leq$ 30 MPa*	*S_b >30 MPa*	*$S_b \leq$ 30 MPa*
e	6.08	26.4	7.07	32.4
f	-56.41	-67.66	-66.93	-74.82
g	17653	19490	20441	21119
h	0.97	0.44	0.68	0.40
r^2	0.98	0.99	0.98	0.99

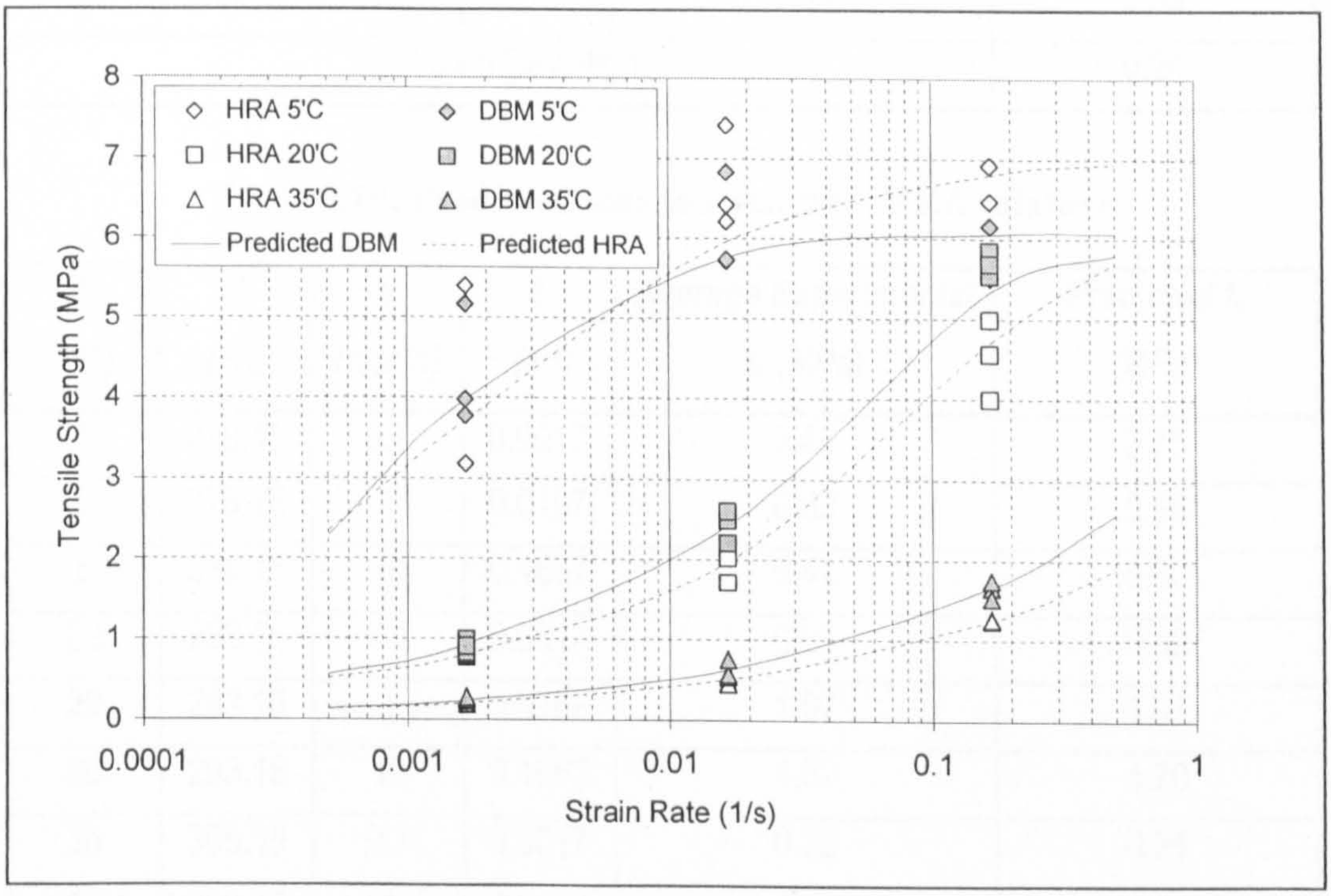

Figure 5.34: Predicted tensile strength (Equation (5.14), dual regression parameters Table 5.17), compared to tensile experimental data.

Through utilisation of the dual function, a much better data fit was possible, with an overall standard deviation of the predicted data to the average experimental data of 0.24 and 0.29 for the DBM and HRA mixtures respectively. A comparison of the numerical predicted values to the experimental data is presented in Tables 5.18 and 5.19 for the DBM and HRA mixtures respectively.

Table 5.18: Predicted tensile strength – DBM mixture

T (°C)	*T* (°K)	*v* (mm/s)	$\dot{\varepsilon}$ (s^{-1})	*Average Experimental* f_c (MPa)	*Predicted* f_c (MPa)
5	278.15	0.1	0.0017	3.88	3.99
5	278.15	1	0.0167	6.10	5.76
5	278.15	10	0.1667	5.55	6.05
20	293.15	0.1	0.0017	0.91	0.94
20	293.15	1	0.0167	2.43	2.42
20	293.15	10	0.1667	5.69	5.33
35	308.15	0.1	0.0017	0.27	0.24
35	308.15	1	0.0167	0.64	0.63
35	308.15	10	0.1667	1.65	1.66
Standard Deviation					0.24

Table 5.19: Predicted tensile strength – HRA mixture

T (°C)	*T* (°K)	*v* (mm/s)	$\dot{\varepsilon}$ (s^{-1})	*Average Experimental* f_c (MPa)	*Predicted* f_c (MPa)
5	278.15	0.1	0.0017	3.48	3.73
5	278.15	1	0.0167	6.69	5.96
5	278.15	10	0.1667	6.41	6.80
20	293.15	0.1	0.0017	0.83	0.82
20	293.15	1	0.0167	1.97	1.97
20	293.15	10	0.1667	4.52	4.70
35	308.15	0.1	0.0017	0.22	0.21
35	308.15	1	0.0167	0.49	0.51
35	308.15	10	0.1667	1.26	1.25
Standard Deviation					0.29

Figure 5.35 shows a plot of the overall trend in the predicted tensile strength of the DBM and HRA mixtures, using the dual regression constants given in Table 5.17, as a function of strain rate and temperature. The figure shows the S-shape transition relationship between tensile strength, temperature and strain rate. The sharp gradient of this transition indicates that the tensile characterises of the asphalt mixtures are highly temperature sensitive. A similar response is observed in both mixture types. Also marked on Figure 5.35 is the actual area of response covered by the tensile testing programme. Comparison of this, to the same area marked on Figure 5.15 for the compression test results, reveals that it has been possible to evaluate a much larger percentage of the whole area of tensile material response, using the same test conditions, than was possible in the compressive tests. This larger area of measured material response thereby increases the robustness of the determined material regression parameters, which is reflected in the more accurate predictions of the observed experimental data, characterised by the low values of standard deviation.

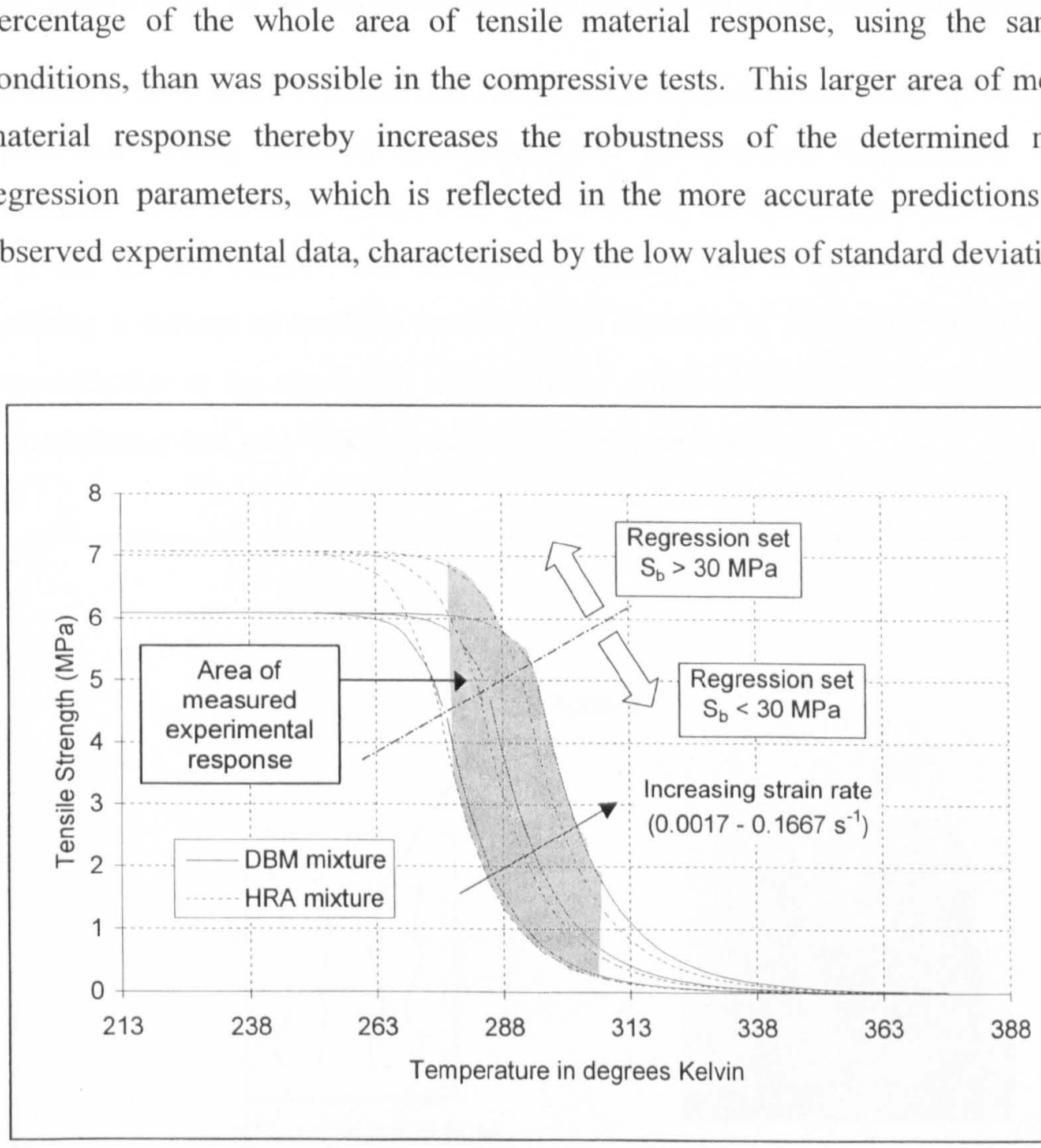

Figure 5.35: Plot showing trend in predicted tensile strength (Equation 5.14) as a dual function of strain rate and temperature – DBM and HRA mixtures

At present the ACRe model can only be used to analyse pavement structures at

discrete temperatures. Therefore, at this stage in the development, for the range of test conditions examined, it is practical to apply the dual form of Equation (5.14) but to segregate the type of material behaviour by temperature boundaries. This results in the 5°C test data being described by the regression parameters corresponding to $S_b >$ 30 MPa, and the 20°C and 35°C test data being described by the regression parameters corresponding to $S_b \leq 30$ MPa. However, it is recommended that future contributions segregate tensile failure mode on the basis of material (binder) stiffness.

5.5 Interaction of Compressive and Tensile Material Characteristics

In Section 3.5.2 it was reported that Heukelom [1966] observed 'axial splitting' of test specimens during constant elongation rate compression experiments on pure bitumens. The mode of failure that was observed for the compression experiments reported in this chapter was also predominantly that of 'axial splitting'. Axial splitting is defined as cracking parallel to the direction of the applied stress on planes perpendicular to the maximum tensile strain. Figure 5.36 shows a schematic of the axial splitting that was observed during the compression test.

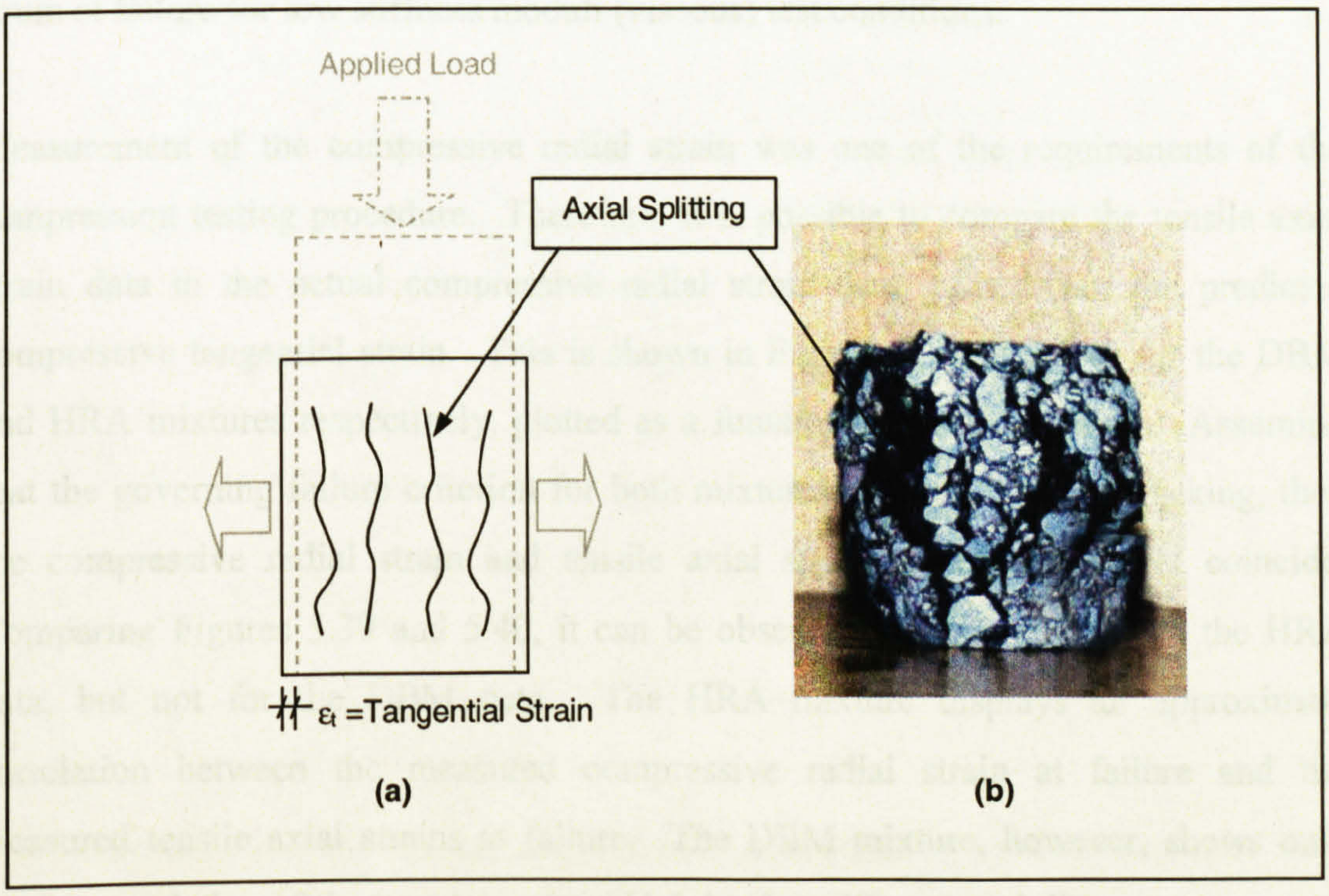

Figure 5.36: (a) Schematic representation of axial splitting during a compression test, and (b) Photograph of a DBM compression specimen showing axial splitting

Heukelom [1966] found that for pure bitumens the compressive tangential strain at break was approximately equal to the tensile strain at break, where the tangential strain at break is related to the axial strain at break by Poisson's ratio, as given in Equation (3.29). Heukelom also showed the elongation at break of pure bitumens in tension to be a decreasing function of binder stiffness, (Figure 3.13, Section 3.5.1). Similar plots to Figure 3.13 are shown in Figures 5.37 and 5.38 for the DBM and HRA mixtures respectively. The plots show a comparison of the tensile axial strain at failure, versus the compressive tangential strain at failure, determined using Equation (3.29), as a function of binder stiffness; in which the binder stiffness was calculated using the methods given in Sections 5.3.7 and 5.4.4. In each of the plots a logarithmic trendline describing the tensile axial strain data is given. It can be observed that for the DBM mixture there is reasonable correlation between the tensile axial strain at failure and the calculated compressive tangential strain at failure. However, for the HRA data, it is apparent that this correlation exists only at high binder stiffness values. At lower binder stiffness moduli the tensile material failure has been shown to be ductile. This is characterised by necking of the specimen, which results in larger tensile axial strains at failure. This is evident in the data for the HRA mixture, which shows the compressive tangential strain at failure to under predict the tensile axial strain at failure for low stiffness moduli (viscous) test conditions.

Measurement of the compressive radial strain was one of the requirements of the compression testing procedure. Therefore, it is possible to compare the tensile axial strain data to the actual compressive radial strain data, rather than the predicted compressive tangential strain. This is shown in Figures 5.39 and 5.40 for the DBM and HRA mixtures respectively, plotted as a function of binder stiffness. Assuming that the governing failure criterion for both mixtures is that of tensile cracking, then the compressive radial strain and tensile axial strains at failure should coincide. Comparing Figures 5.39 and 5.40, it can be observed that this is true for the HRA data, but not for the DBM data. The HRA mixture displays an approximate correlation between the measured compressive radial strain at failure and the measured tensile axial strains at failure. The DBM mixture, however, shows only partial correlation of the two data sets at high binder stiffness moduli.

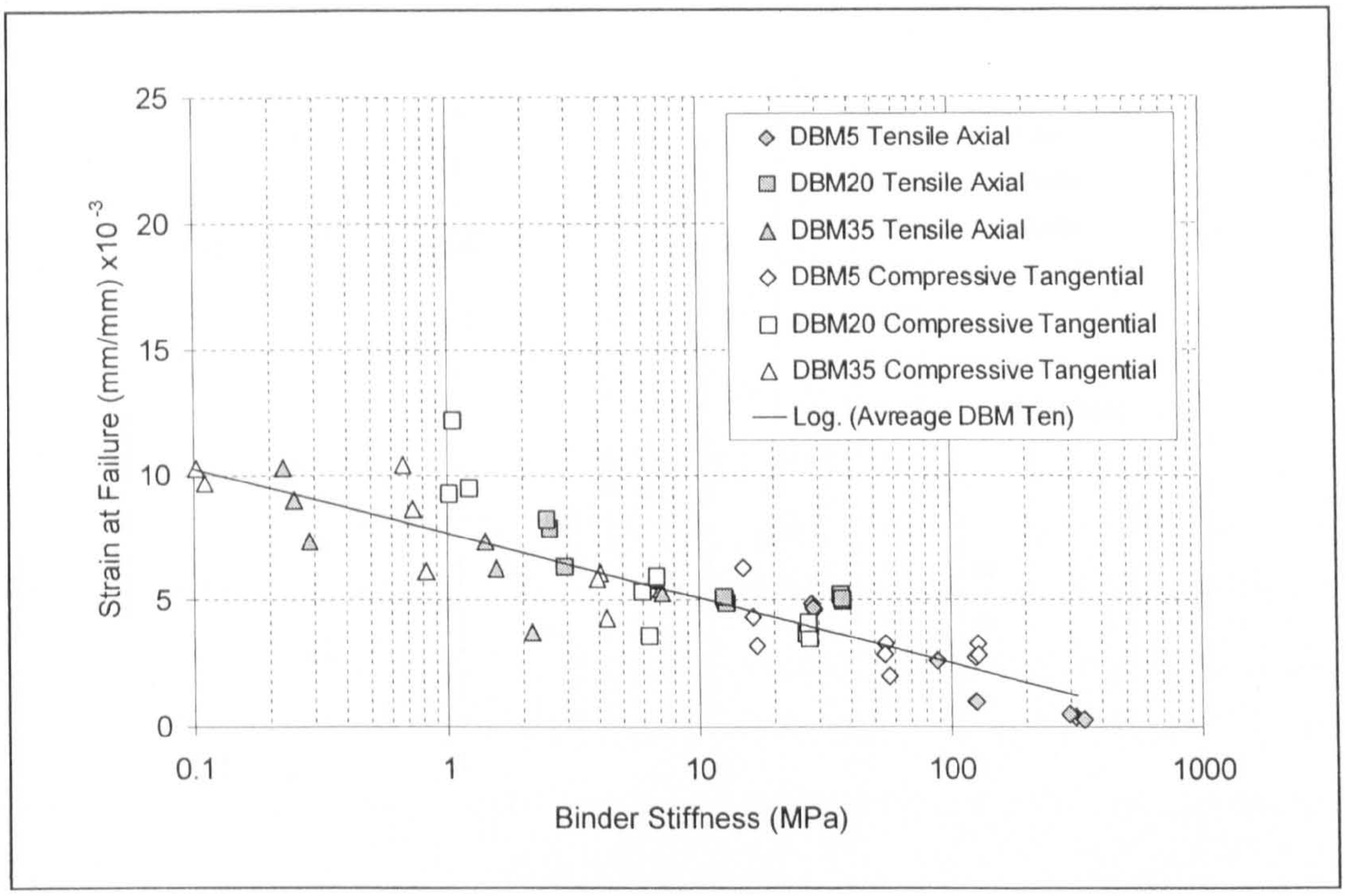

Figure 5.37: Comparison of the tensile axial strain at break versus the compressive tangential strain at failure, plotted as a function of binder stiffness – DBM mixture

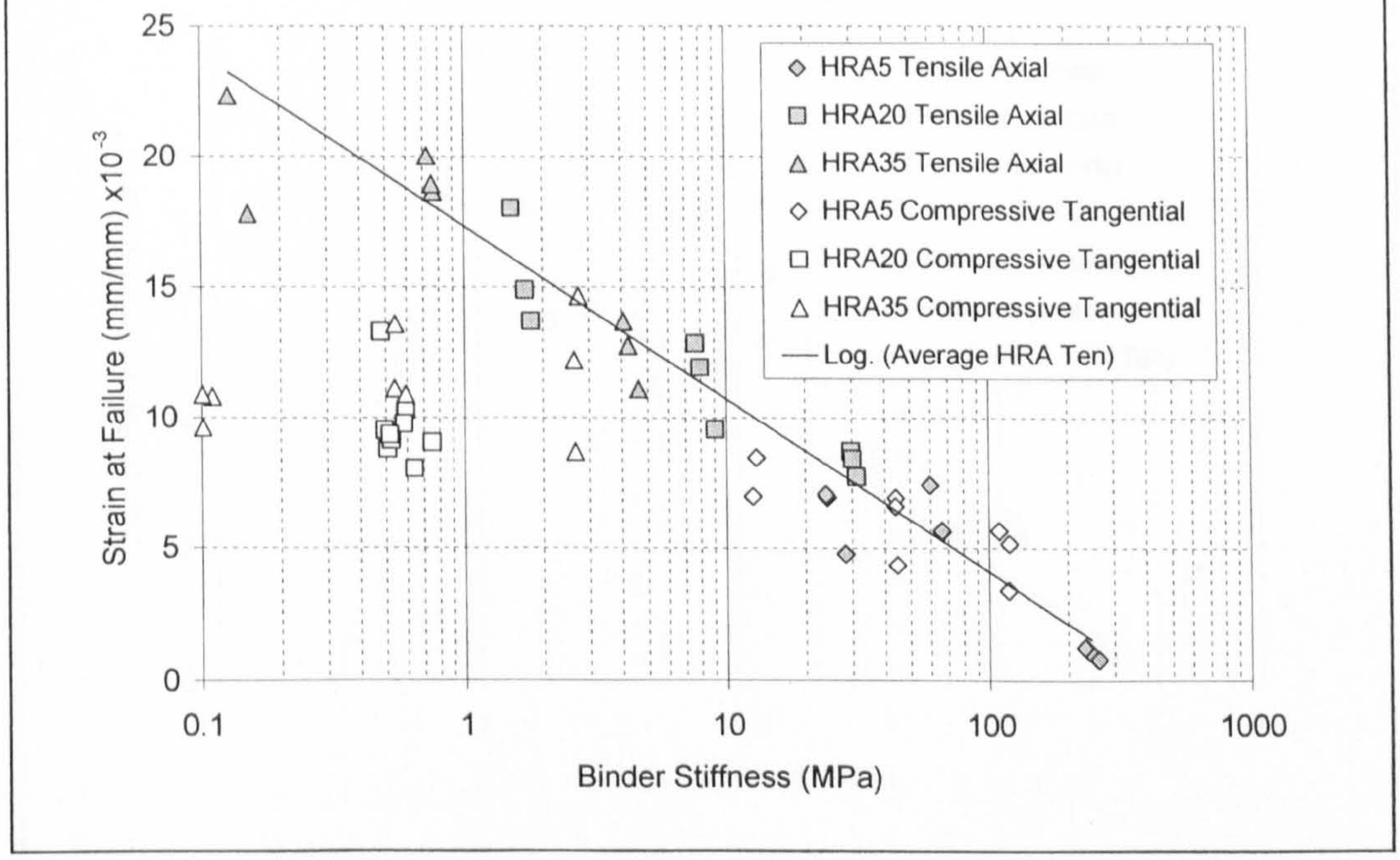

Figure 5.38: Comparison of the tensile axial strain at break versus the compressive tangential strain at failure, plotted as a function of binder stiffness – HRA mixture

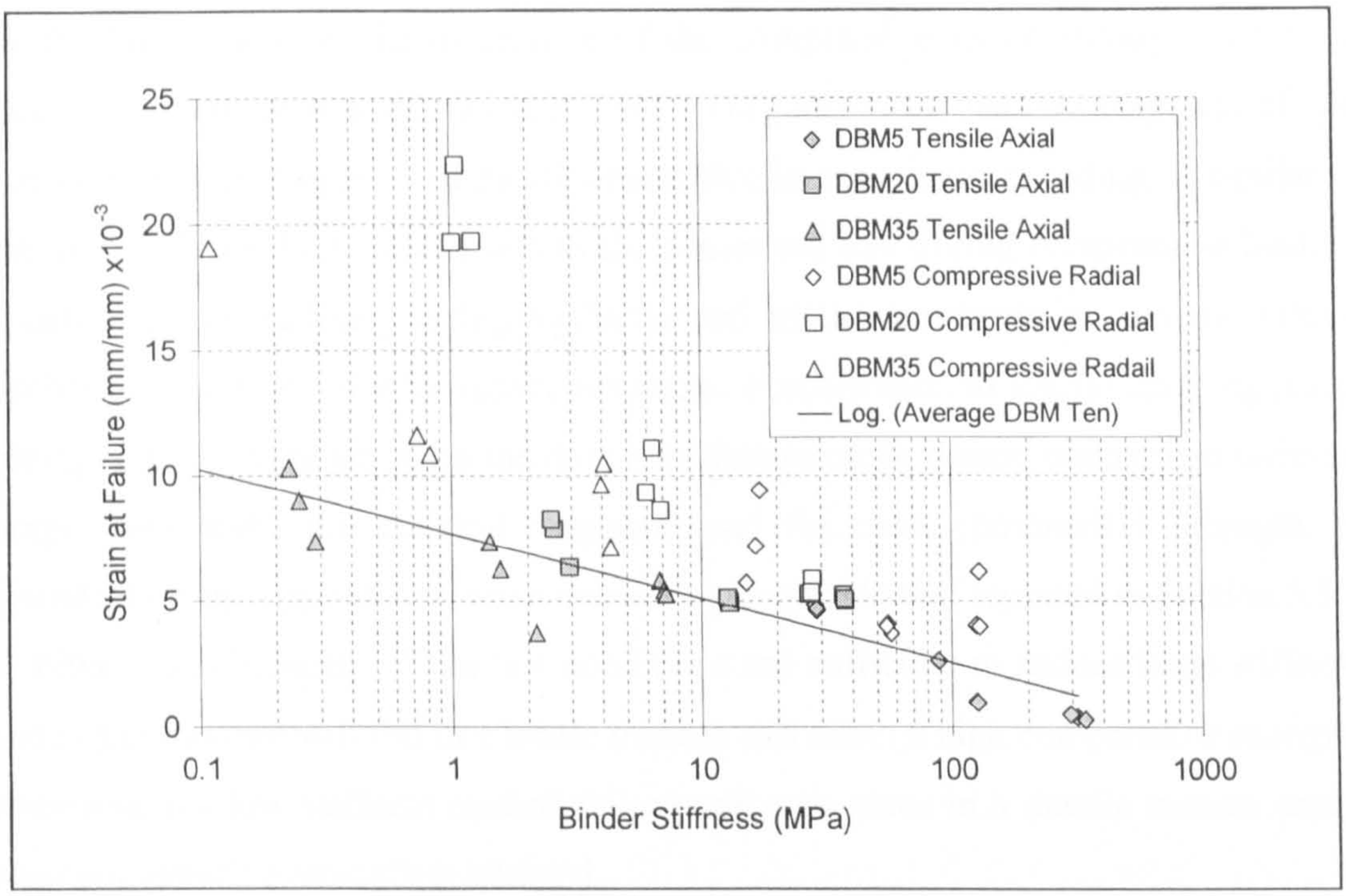

Figure 5.39: Comparison of the tensile axial strain at break versus the compressive radial strain at failure, plotted as a function of binder stiffness – DBM mixture

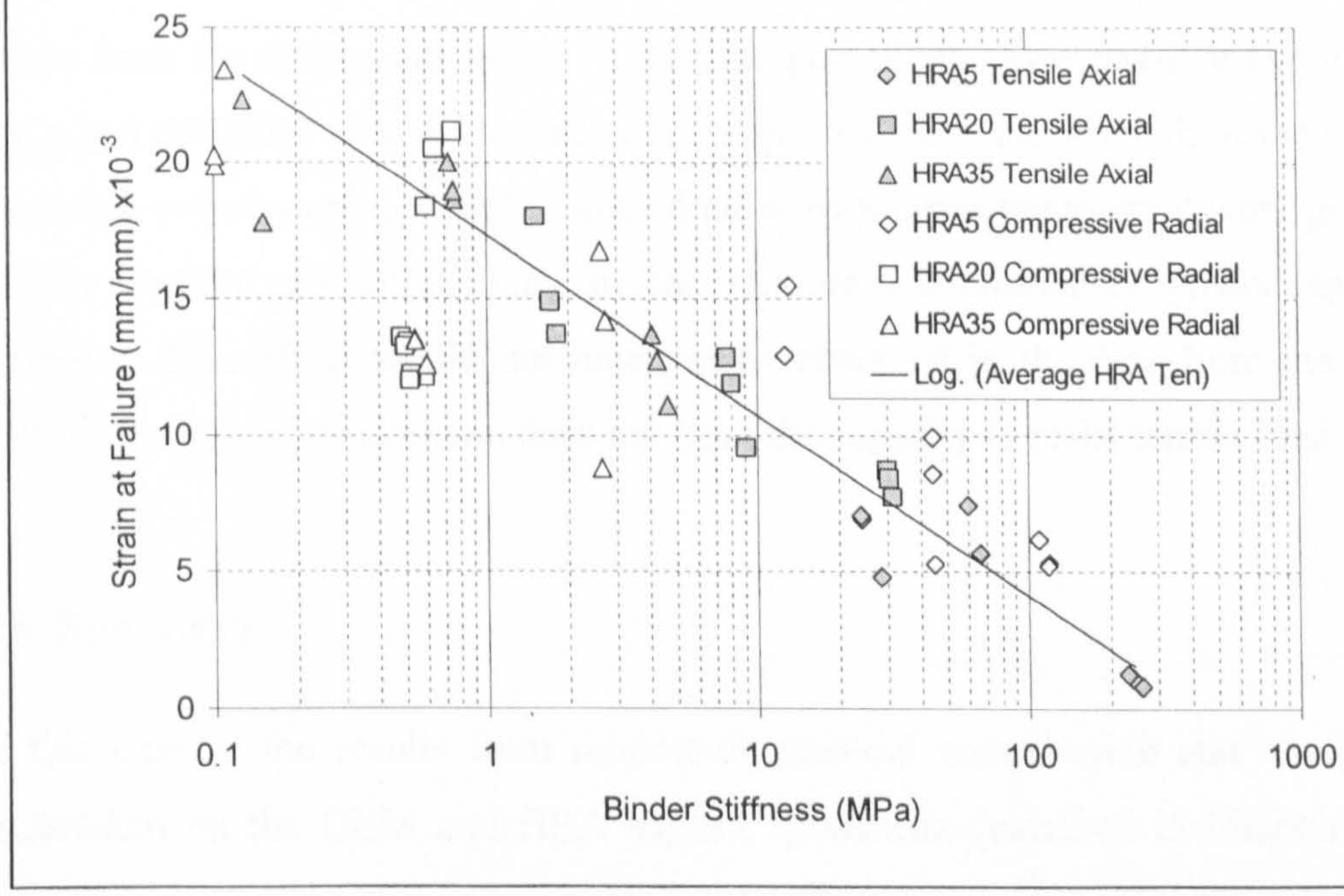

Figure 5.40: Comparison of the tensile axial strain at break versus the compressive radial strain at failure, plotted as a function of binder stiffness – HRA mixture

For the HRA mixture, the magnitude of the compressive radial strains and tensile axial strains are concurrent, Figure 5.40. This indicates that the response of the mixture to the development of radial strains, due to compressive loading, is similar to that for tensile loading. This leads to the conjecture that during compressive loading asphalt mixtures are likely to display ductile and brittle characteristics, similar to those described in Section 5.4.4 for tensile response. Furthermore, as tensile cracking (axial spitting) has been shown to be the dominant failure mode during unconfined uniaxial compression tests, the material response, and therefore compressive strength, is dependent on the applied stress in a manner analogous to that reported in Section 3.5.1 for bituminous binders. If the test conditions are sufficient to induce large stiffness moduli the mixture will fail in a brittle manner and attain a high compressive strength. Otherwise, for low stiffness moduli failure will take place in a ductile manner and a lower compressive strength is attained.

For the DBM mixture however, there is little agreement between the magnitude of the compressive radial and tensile axial strains, Figure 5.39. This would indicate the presence of some additional factor(s) influencing the failure mode of the DBM mixture. Based on the composition of the two mixtures it is likely that these factors derive from the differences in their aggregate gradations. One possible hypothesis is that when the DBM mixture is loaded in compression and the strength of the binder is exceeded, extra external work has to be done to over come the internal work generated due to friction and interlocking of the mixture's continuously graded aggregate skeleton. This effect would not however be observed in the data from the tension tests, as the aggregate skeleton does not have the capacity to resist tensile load.

5.6 Summary

In this chapter the results from monotonic uniaxial compression and tension tests undertaken on the DBM and HRA asphalt specimens described in Chapter 4 have been presented. The tests were carried out over a range of temperatures (5, 20 and 35°C) and displacement rates (0.1, 1 and 10 mm/s) to allow the influence of these factors to be incorporated into the ACRe model. To provide additional data, limited compression testing was also undertaken on the UK HRA mortar (also described in

Chapter 3).

Typical examples of both the compressive and tensile stress-strain material responses have been presented for each of the asphalt mixtures. The compressive stress-strain response curves for the three mixtures were found to be similar, and a trend of increasing compressive strength with increasing strain rate and/or decreasing temperature was observed. The data indicated that the apparent strength of an asphalt mixture is sensitive to both binder content and binder type (penetration grade), with increase in binder content/decreases in binder penetration grade producing increases in compressive strength of a mixture. The compression results were compared to similar data for a Dutch sand asphalt mixture [Erkens *et al.*, 1998] which indicted that the effects described above are more pronounced at lower temperatures and/or increased strain rates (higher stiffness). It was observed that at elevated temperatures and/or slower strain rates (lower stiffness) the apparent strengths of each of the asphalt mixtures were comparable. The tensile stress-strain response curves displayed a trend of increasing tensile strength with increasing strain rate and/or decreasing temperatures, up until a peak fracture strength of approximately 6.1 MPa and 6.8 MPa for the DBM and HRA mixtures respectively, after which a slight decease in strength was observed. Ductile and brittle type failure modes were observed to occur in the tensile tests. These were found to be linked to binder stiffness. If the test conditions were sufficient to induce high mixture stiffness moduli, capable of sustaining a stress comparable to the fracture strength of the mixture, the specimen would break before it necked. Otherwise, for lower stiffness conditions the stress increased with strain, but at a decreasing rate until a maximum value was attained, which if smaller than the fracture strength lead to necking of the specimen.

Details of a temperature and strain rate dependent relationship developed by Erkens *et al.* [1998, 2000a] to describe the strength response of asphaltic materials have been presented. The relationship has been used to express the peak strength response for the DBM and HRA mixtures for both uniaxial test configurations. The material parameters required to describe the compressive and tensile strengths were determined using non-linear regression techniques and have been compared to those determined for a Dutch sand asphalt mixture. A dual set of regression parameters, segregated on the bases of binder stiffness have been used to describe the tensile strength response.

The methodology utilised to determine the elasticity material parameters has been presented. The apparent stiffness (Young's modulus) and Poisson's ratio for the asphalt mixtures at each of the test conditions was determined though non-linear regression analysis performed on the initial linear zone of compressive test data. The apparent stiffness of both mixtures was found to increase with decreases in temperature and/or increases in displacement rate. An approximate linear relationship between compressive strength and apparent stiffness was observed for each of the asphalt mixtures. The values determined for Poisson's ratio were found to display scatter, although a general decreasing trend with increasing mixture stiffness could be observed. A temperature dependent relationship for Poisson's ratio has been proposed.

It has been shown that the dominant failure mechanism during a well lubricated uniaxial compression test is that of axial splitting and that furthermore, for the HRA mixture, the magnitude of the tensile strain is the governing factor determining the maximum stress obtained in such a test.

Chapter 6 - Determination of Model Material Parameters

6.1 Introduction

This chapter presents the determination of model parameters necessary for the characterisation of the 10 mm DBM and 30/10 HRA UK asphalt mixtures described in Chapter 4, for use in the ACRe material model. This is undertaken using the methodology outlined in Chapter 3. In the first sections of the chapter the model parameters relating to the elastic and shape function aspects of the constitutive model are discussed. The results from the uniaxial compression and tension tests presented in Chapter 5 are then used to define the failure envelopes for the DBM and HRA mixtures, from which the model parameters γ and R are determined. General, strain rate and temperature sensitive values for the phase change parameter, n, are identified. Functions describing the hardening and softening response of the mixtures in terms of both plastic work and equivalent plastic strain are presented and their associated material parameters are evaluated from the experimental data. In the final sections of the chapter the characteristics of the Desai model flow surface are discussed and numerical simulations are undertaken to assess the validity of the model using the experimentally determined model parameters.

6.2 Elasticity Parameters – Model Parameters E and ν

For isotropic materials two elasticity model parameters are required to perform a numerical simulation of the material response to load. These are, E, Young's modulus and, ν, Poisson's ratio. The methodology used for the determination of these material parameters for each of the asphalt mixtures has been described in Chapter 5. For the case of the numerical simulations presented in Section 6.8.3, Young's modulus was specified by Equation (5.8), utilising the apparent stiffness non-linear regression constants given in Table 5.10, and Poisson's ratio was specified using the values proposed in Table 5.13.

6.3 Shape Function – Model Parameters β and θ

The results from the uniaxial compression and tension tests presented in Chapter 5 were used to determine material parameters for the DBM and HRA mixtures for characterisation in the ACRe model. Therefore, as already discussed in Section 3.4.2, in the absence of additional stress paths, the influence of the Lode angle, θ, on the material response could not be examined. With regard to the ACRe model, Lode angle independence is equivalent to assuming parameter $\beta = 0$, i.e. a circular cross section in the deviatoric plane, Figure 6.1. Therefore Equation (3.6b) reduces to unity.

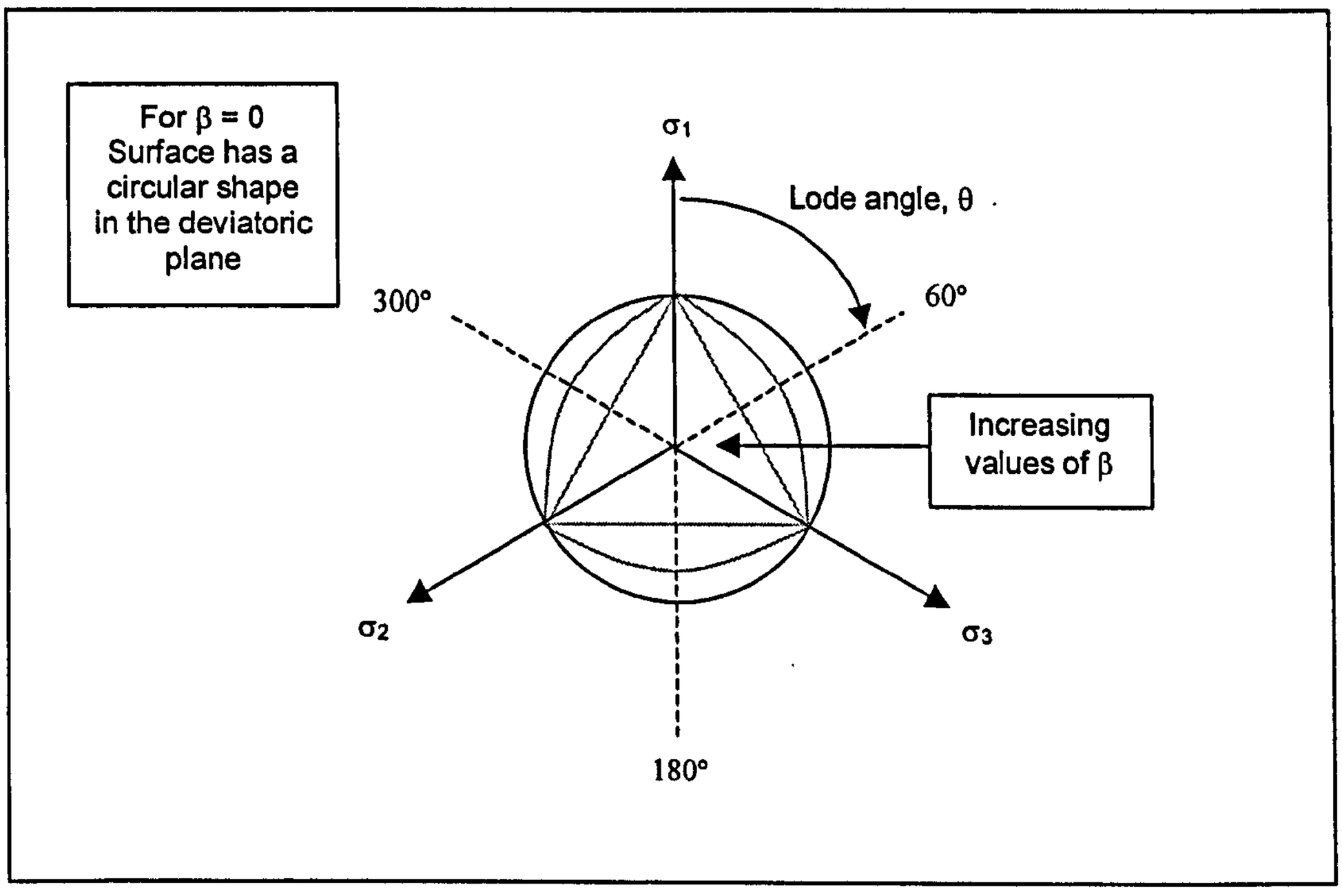

Figure 6.1: Influence of Lode angle and parameter β on Desai flow surface

Investigation of the effect of the Lode angle on the response of the asphalt mixtures would require triaxial or multi-axial tests undertaken over a range of strain rates and temperatures. If this data were available parameters γ and β could then be obtained using a least squares method [Desai *et al.*, 1990].

6.4 Peak Response Evaluation - Model Parameters *R* and γ

For peak stress response parameter α is zero, therefore Equation (3.6) for the Desai surface reduces, see Section 3.4.2, to become:

$$F_D = J_2 - \gamma(I_1 - R)^2 \tag{6.1}$$

The only unknowns in Equation (6.1) are the experimentally determinable material parameters γ and R. For each set of test conditions, temperature and strain rate, the peak compressive and tensile strengths of the DBM and HRA mixtures were plotted in I_1 - $\sqrt{J_2}$ space. These plots are shown in Figures 6.2 and 6.3 for the DBM and HRA mixtures respectively. As the uniaxial compression and tension experiments were undertaken at the same displacement rates, but not however, at the same strain rates, the tensile strength data was adjusted for the rates of strain used in the compression tests, i.e. 0.001, 0.01 and 0.1 s^{-1}. This could be achieved through interpolation of the experimental data, or as was the case in this study, through utilisation of Equation (5.14), using the regression parameters as described in Chapter 5. The adjusted tensile data is given in Table 6.1 for both the DBM and HRA mixtures.

Table 6.1: Tensile strength data adjusted for compressive strain rates

$\dot{\varepsilon}$ (s^{-1})	T (°C)	Average f_t (MPa) DBM Mixture	Average f_t (MPa) HRA Mixture
0.001	5	3.26	3.12
0.01	5	5.56	5.59
0.1	5	6.02	6.70
0.001	20	0.76	0.67
0.01	20	1.97	1.63
0.1	20	4.93	3.79
0.001	35	0.19	0.17
0.01	35	0.51	0.42
0.1	35	1.34	1.03

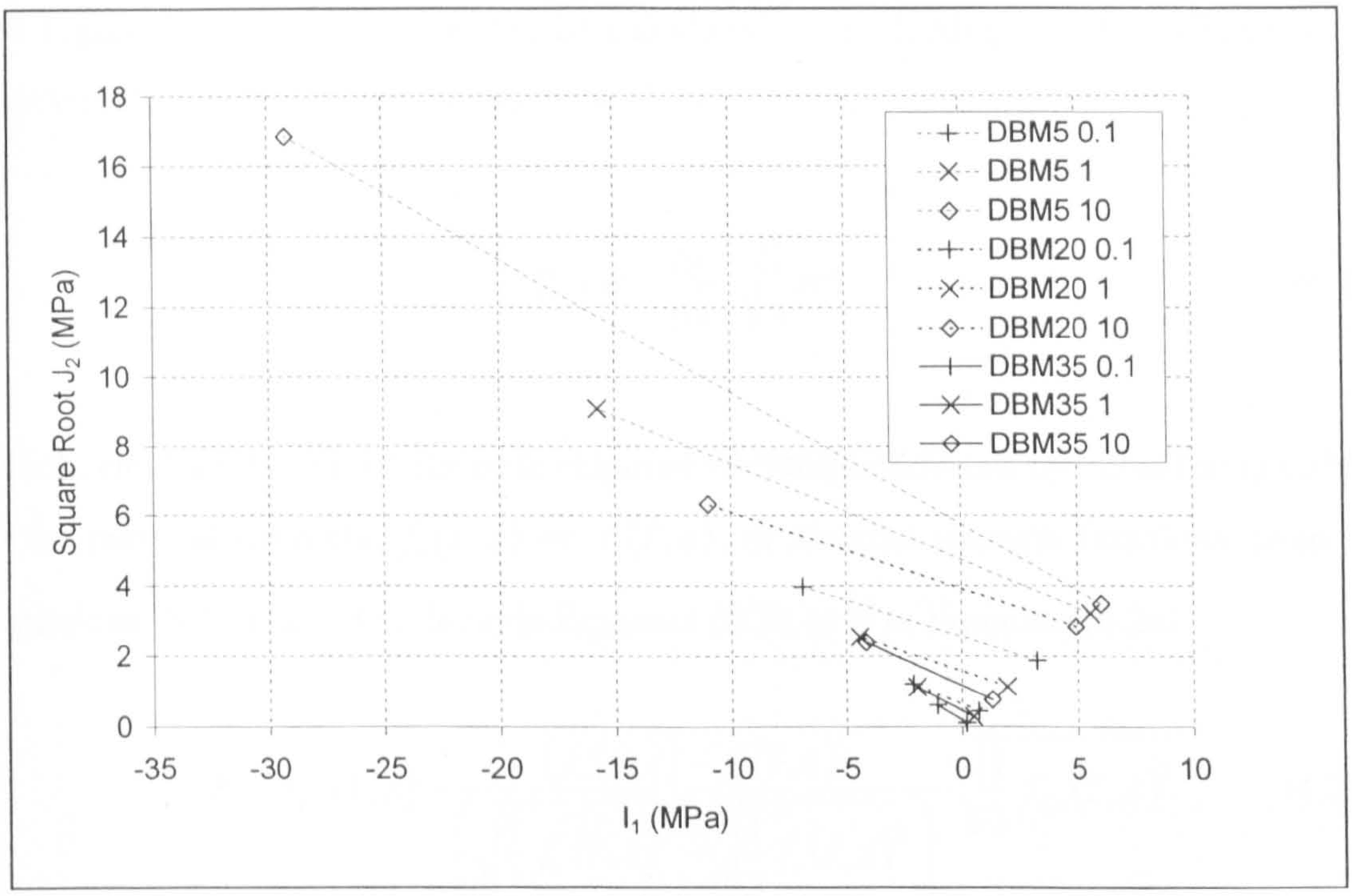

Figure 6.2: Average DBM peak (failure) response envelopes in I_1 - $\sqrt{J_2}$ space

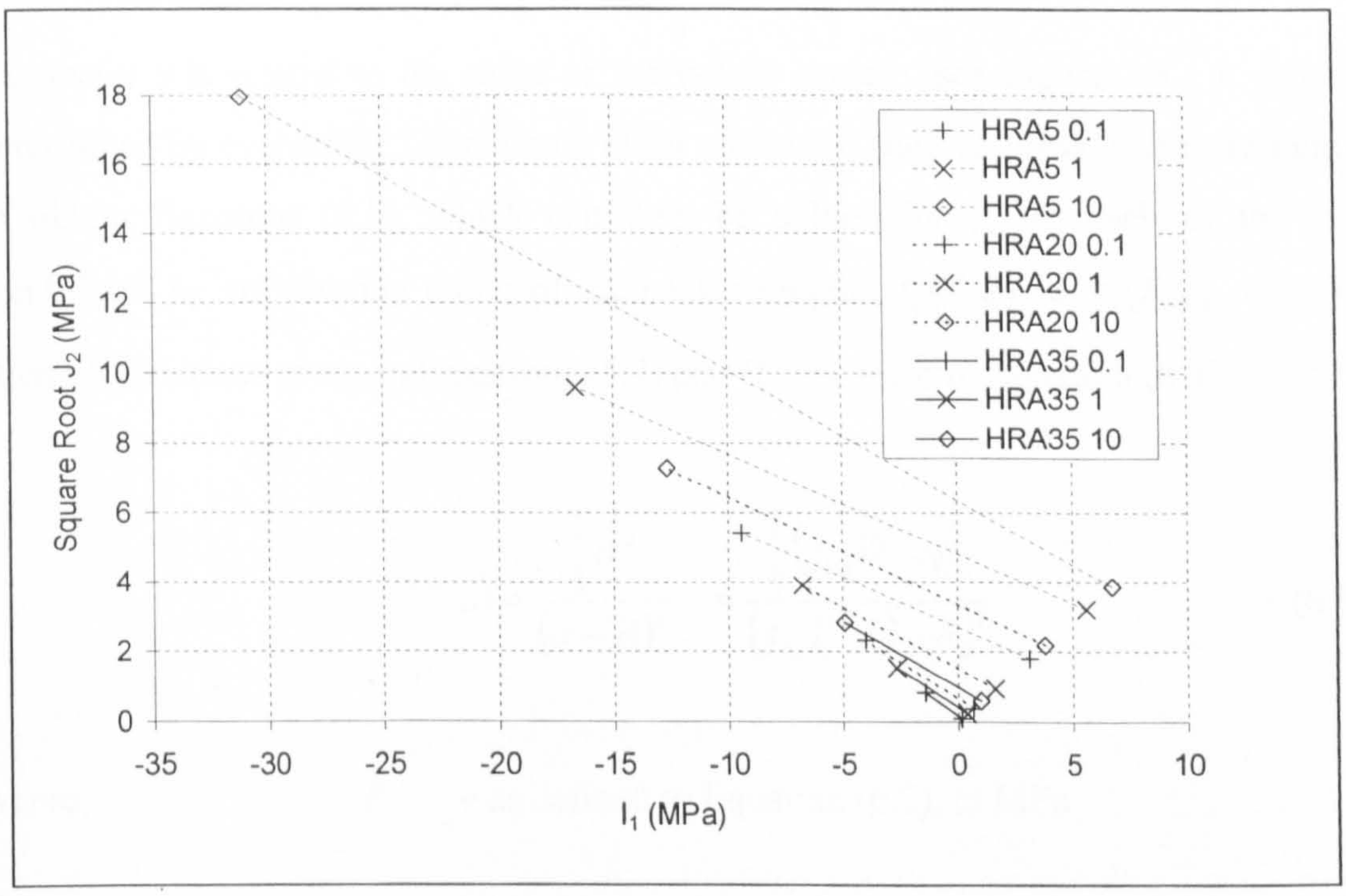

Figure 6.3: Average HRA peak (failure) response envelopes in I_1 - $\sqrt{J_2}$ space

Parameter R can be determined for each test condition. It is defined as the intersection of the peak response envelope joining the points $f_c(T, \dot{\varepsilon})$ and $f_t(T, \dot{\varepsilon})$ with the I_1 axis,

see Figure 3.11. Parameter R can be calculated by evaluating Equation (3.26) for a uniaxial state of stress, to give Equation (6.2):

$$R = \sigma - \frac{\Delta y}{\Delta x} \cdot \sqrt{\frac{1}{3}\sigma^2} \tag{6.2}$$

which, can then be solved for peak response (failure) conditions by substituting either of the material strengths, $f_c(T,\dot{\varepsilon})$ or $f_t(T,\dot{\varepsilon})$, or material strength functions given in Equations (5.7) and (5.11), for σ in Equation (6.2), to give Equation (6.2a).

$$R = f_{c,t}(T,\dot{\varepsilon}) - \frac{\left(f_c(T,\dot{\varepsilon}) - f_t(T,\dot{\varepsilon})\right)}{\left(\sqrt{\frac{1}{3}f_c(T,\dot{\varepsilon})^2} - \sqrt{\frac{1}{3}f_t(T,\dot{\varepsilon})^2}\right)} \cdot \sqrt{\frac{1}{3}f_{c,t}(T,\dot{\varepsilon})^2} \tag{6.2a}$$

where, $f_{c,t}(T,\dot{\varepsilon})$ = compressive or tensile strength in MPa

Parameter γ is related to the slope of the failure surface, see Figure 3.5. It can be determined by evaluating Equation (6.1) for a uniaxial state of stress, and rearranging to obtain Equation (6.3), which can then be solved for γ, for each of the test conditions, by substituting either of the peak strengths, $f_c(T,\dot{\varepsilon})$ or $f_t(T,\dot{\varepsilon})$, or peak strength functions given in Equations (5.7) and (5.11), for σ in Equation (6.3).

$$\gamma(T,\dot{\varepsilon}) = \frac{\frac{1}{3}\sigma^2}{(\sigma - R)^2} = \frac{\frac{1}{3}\left(f_{c,t}(T,\dot{\varepsilon})\right)^2}{\left(f_{c,t}(T,\dot{\varepsilon}) - R\right)^2} \tag{6.3}$$

where, R = as defined in Equation (6.2), in MPa

The values of R and γ, determined for each of the test conditions, are given in Tables 6.2 and 6.3 for the DBM and HRA mixtures respectively. During the hardening phase of material response parameter γ is constant. After peak response, during material degradation γ is used to control the overall reduction in the strength of the materials that is observed as a result of compressive loading (see Section 6.7).

Table 6.2: Values for model parameters R and γ for the DBM mixture

Sample	$\dot{\varepsilon}$ (s^{-1})	T (°C)	R	γ
DBM5 0.1A	0.001	5	11.98	0.047
DBM5 0.1B	0.001	5	13.31	0.035
DBM5 0.1C	0.001	5	12.00	0.046
Average	0.001	5	12.38	0.043
DBM5 1A	0.01	5	16.51	0.086
DBM5 1B	0.01	5	18.19	0.065
DBM5 1C	0.01	5	17.11	0.077
Average	0.01	5	17.19	0.076
DBM5 10A	0.1	5	15.20	0.143
DBM5 10B	0.1	5	15.07	0.148
DBM5 10C	0.1	5	15.24	0.142
Average	0.1	5	15.17	0.144
DBM20 0.1A	0.001	20	2.33	0.078
DBM20 0.1B	0.001	20	2.39	0.073
DBM20 0.1C	0.001	20	2.42	0.070
Average	0.001	20	2.38	0.073
DBM20 1A	0.01	20	7.11	0.049
DBM20 1B	0.01	20	7.19	0.048
DBM20 1C	0.01	20	7.02	0.051
Average	0.01	20	7.11	0.049
DBM20 10A	0.1	20	18.07	0.048
DBM20 10B	0.1	20	17.86	0.048
DBM20 10C	0.1	20	17.86	0.048
Average	0.1	20	17.92	0.048
DBM35 0.1A	0.001	35	0.46	0.161
DBM35 0.1B	0.001	35	0.46	0.164
DBM35 0.1C	0.001	35	0.46	0.164
Average	0.001	35	0.46	0.163
DBM35 1A	0.01	35	1.40	0.110
DBM35 1B	0.01	35	1.37	0.118
DBM35 1C	0.01	35	1.38	0.114
Average	0.01	35	1.38	0.114
DBM35 10A	0.1	35	3.94	0.089
DBM35 10B	0.1	35	4.06	0.081
DBM35 10C	0.1	35	3.89	0.092
Average	0.1	35	3.96	0.087

Table 6.3: Values for model parameters R and γ for the HRA mixtrue

Sample	$\dot{\varepsilon}$ (s^{-1})	*T* (°C)	*R*	γ
HRA5 0.1A	0.001	5	9.33	0.084
HRA5 0.1B	0.001	5	9.36	0.083
Average	0.001	5	9.34	0.084
HRA5 1A	0.01	5	16.83	0.083
HRA5 1B	0.01	5	16.68	0.085
HRA5 1C	0.01	5	17.08	0.079
Average	0.01	5	16.86	0.082
HRA5 10A	0.1	5	17.32	0.133
HRA5 10B	0.1	5	16.92	0.143
HRA5 10C	0.1	5	17.03	0.140
Average	0.1	5	17.08	0.139
HRA20 0.1A	0.001	20	1.59	0.177
HRA20 0.1B	0.001	20	1.62	0.167
HRA20 0.1C	0.001	20	1.62	0.165
Average	0.001	20	1.61	0.170
HRA20 1A	0.01	20	4.30	0.125
HRA20 1B	0.01	20	4.31	0.123
HRA20 1C	0.01	20	4.28	0.126
Average	0.01	20	4.30	0.125
HRA20 10A	0.1	20	10.92	0.094
HRA20 10B	0.1	20	10.75	0.099
HRA20 10C	0.1	20	10.82	0.097
Average	0.1	20	10.83	0.097
HRA35 0.1A	0.001	35	0.39	0.206
HRA35 0.1B	0.001	35	0.39	0.200
HRA35 0.1C	0.001	35	0.38	0.211
Average	0.001	35	0.39	0.206
HRA35 1A	0.01	35	0.99	0.180
HRA35 1B	0.01	35	1.00	0.173
HRA35 1C	0.01	35	1.00	0.174
Average	0.01	35	1.00	0.176
HRA35 10A	0.1	35	2.58	0.148
HRA35 10B	0.1	35	2.65	0.134
HRA35 10C	0.1	35	2.59	0.145
Average	0.1	35	2.61	0.142

Parameter γ is proportional to the ratio of the peak tensile strength to the peak compressive strength of the asphalt mixtures. Figure 6.4 shows the change in the computed average values for γ plotted as a function of the apparent stiffness moduli (see Section 5.3.7) for the DBM and HRA mixtures.

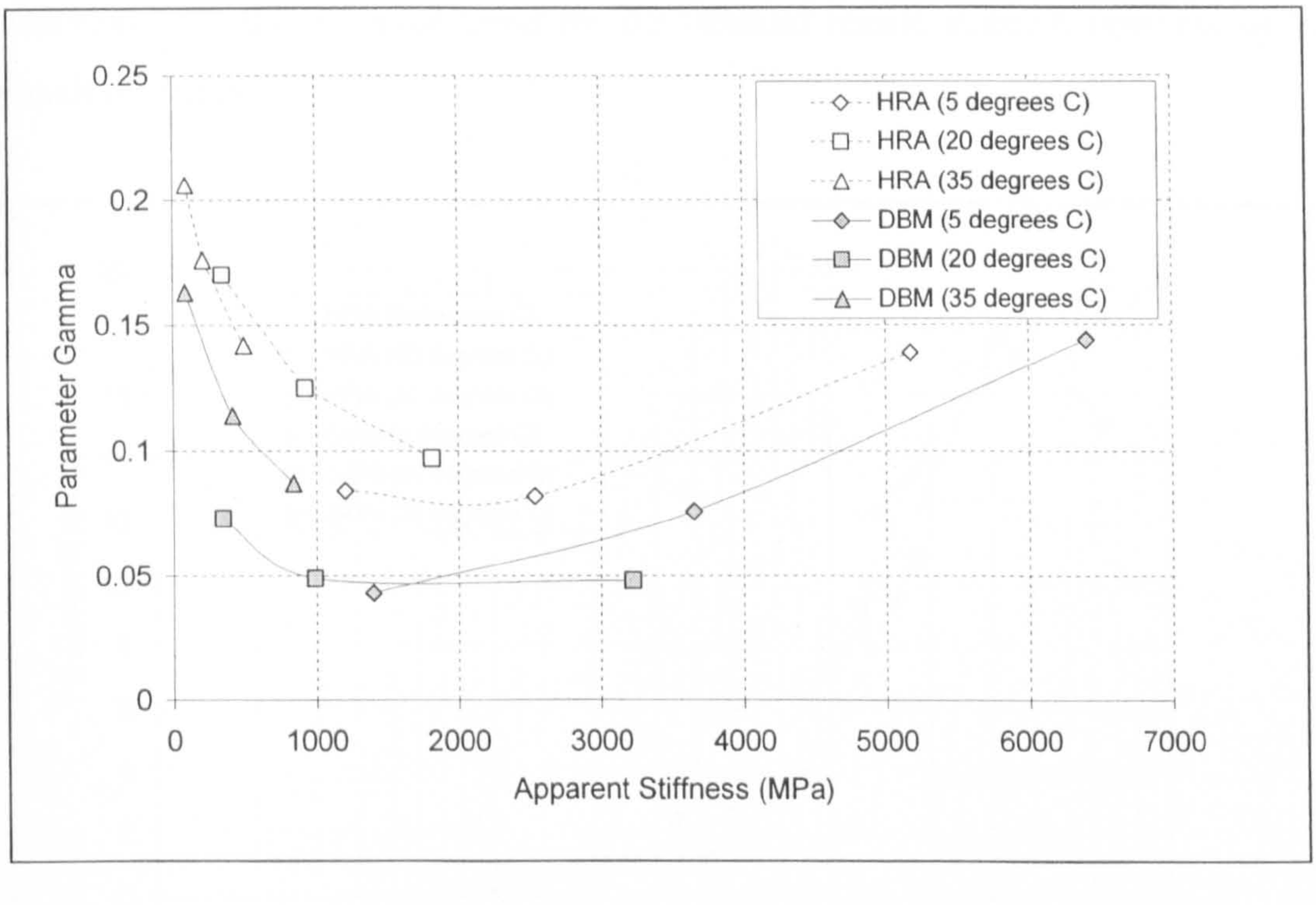

Figure 6.4: Plot showing computed average values for model parameter γ as a function of the apparent stiffness moduli for the DBM and HRA mixtures

From Figure 6.4 it can be observed that both of the mixtures display a similar trend in the change in parameter γ with changes in mixture stiffness. High values of γ are obtained at low stiffness moduli (high temperatures and slow strain rates) and decrease with increasing mixture stiffness to minimum values of approximately 0.049 and 0.083 for the DBM and HRA mixtures respectively, before increasing again with further increases in mixture stiffness. It can be observed that, for all test conditions, larger average values for parameter γ are obtained for the HRA mixture than for the DBM mixture. This is representative of the relative ratios defining the uniaxial compressive and uniaxial tensile strengths of the two mixtures, the value of which is larger for the HRA mixture.

Figure 6.5 shows the average values for parameter R plotted as a function of the

apparent stiffness for the DBM and HRA mixtures. The computed values for parameter R can be observed to increase with increases in apparent stiffness, until a peak value of approximately 17 MPa is reached for both of the mixtures. After this, further increases in mixture stiffness result in a decrease in the value of parameter R. Comparing Figure 6.5 to Figure 5.33 this trend for parameter R can be seen to be consistent with the observed trend for the uniaxial tensile strength response of the asphalt mixtures.

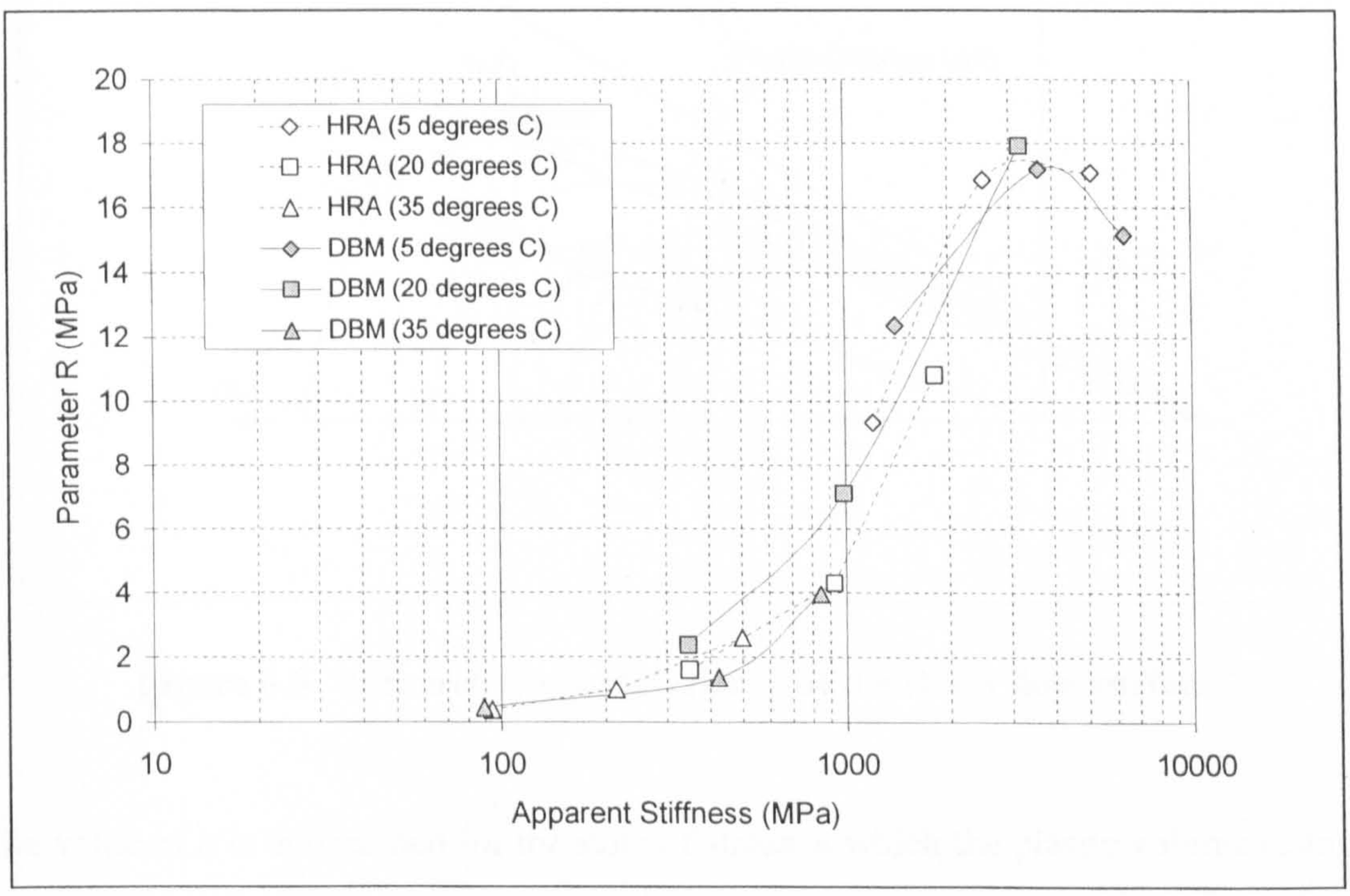

Figure 6.5: Plot showing computed average values for model parameter *R* as a function of the apparent stiffness moduli for the DBM and HRA mixtures

6.5 Phase Change - Model Parameter *n*

Parameter n determines the apex of the surface in the I_1 - $\sqrt{J_2}$ plane, and is related to the volume change in the material. As the model uses associated flow, the direction of the plastic strain increment is normal to the yield surface. Referring to Figure 6.6, it can be seen that if the normal to the yield surface has a component in the negative I_1 direction, then the material will tend to reduce in volume (compact) as plastic strains occur. This condition is typical of low $J_2^{1/2}$ to I_1 ratios, i.e. low shear stress and high confining stresses. Conversely, for high $J_2^{1/2}$ to I_1 ratios, the normal to the yield

surface has a positive plastic strain increment and the material tends to dilate. When the normal to the yield surface is perpendicular to the I_1 axis no plastic strain volume change will occur.

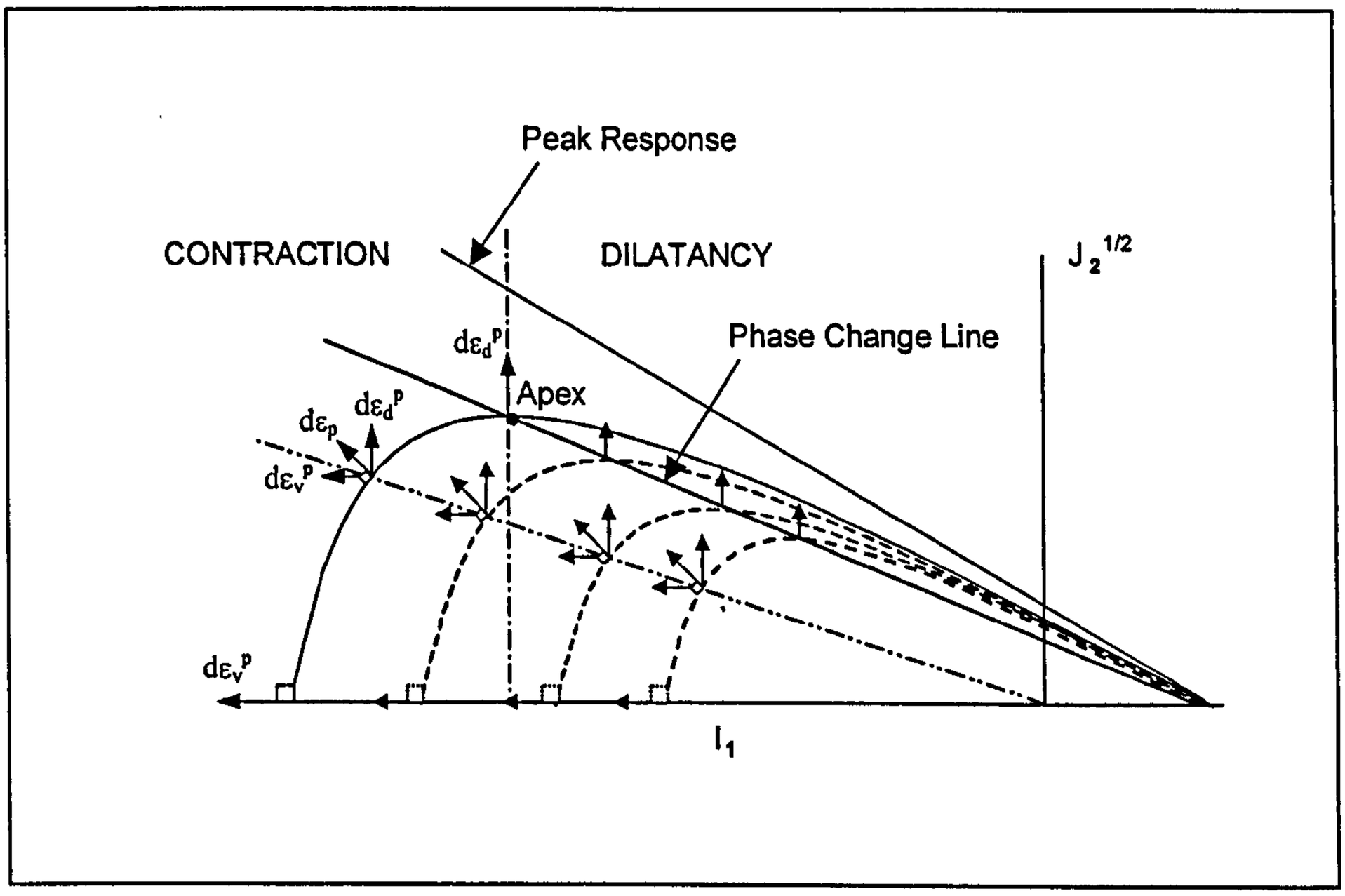

Figure 6.6: Volumetric characteristics of the Desai flow surface

The value of n is determined for the state of stress at which the plastic volume change ($d\varepsilon_v^p$) is zero, i.e. where the volumetric response changes from contraction to dilation. By taking the derivative of Equation (3.6) with respect to I_1, setting it equal to zero, substituting the result back into Equation (3.6) and simplifying, the condition for which no volume change occurs can be determined [Desai *et al.*, 1990; Bonaquist *et al.*, 1997]. This is Equation (6.4), which is the expression for the phase change line shown in Figure 6.6. For states of stress on the yield surface and above the phase change line dilation takes place and below the line compaction occurs. From Equation (6.4) it can be seen that for dilative materials parameter n must have a value greater than or equal to 2.

$$\sqrt{J_2} = \gamma^{1/2} \cdot \left(1 - \frac{2}{n}\right)^{1/2} \cdot (I_1 - R) \tag{6.4}$$

Evaluation of Equation (6.4) for a state of stress at which the volumetric strain, as a function of the axial strain, changes from a negative to positive gradient, Figure 3.12, allows the state of stress at which n is computed to be determined. Typical plots (compressive stress positive) showing the evaluation of n for the DBM and HRA mixtures at test conditions of 20°C and 10 mm/s are presented in Figures 6.7 and 6.8 respectively. A complete set of plots for the determination of parameter n for each compression test is given in Appendixes H and I for the DBM and HRA mixtures respectively.

It can be observed from Figures 6.7 and 6.8, and with reference to Appendixes H and I, that after some initial contraction the response of both mixture types, under all test conditions, is dilative. The numerical values determined for parameter n, for each of the test conditions, are summarised in Tables 6.4 and 6.5 for the DBM and HRA mixtures respectively, and represented graphically in Figure 6.9.

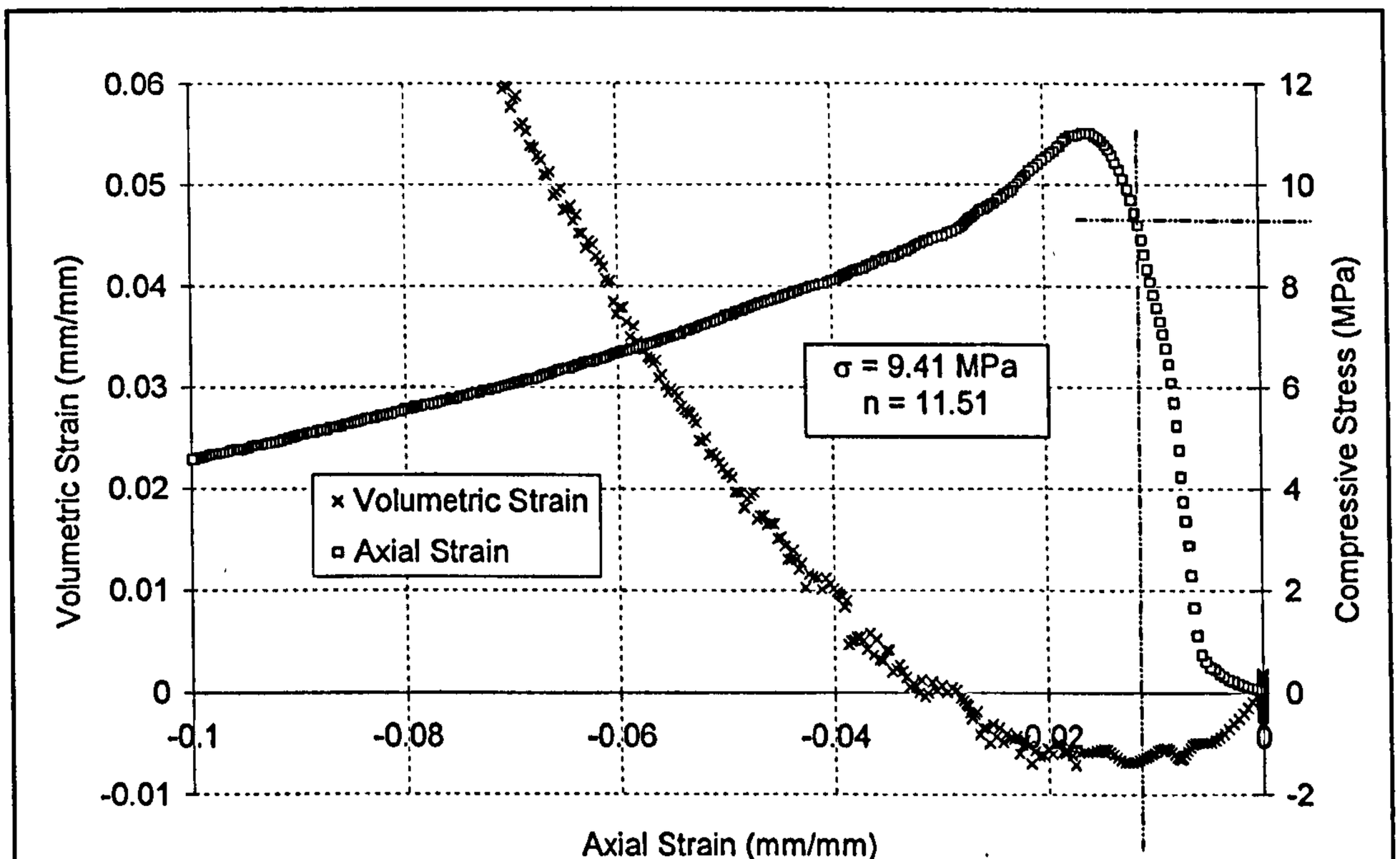

Figure 6.7: Example plot showing the evaluation of parameter n – DBM mixture at 20°C and 10 mm/s displacement rate

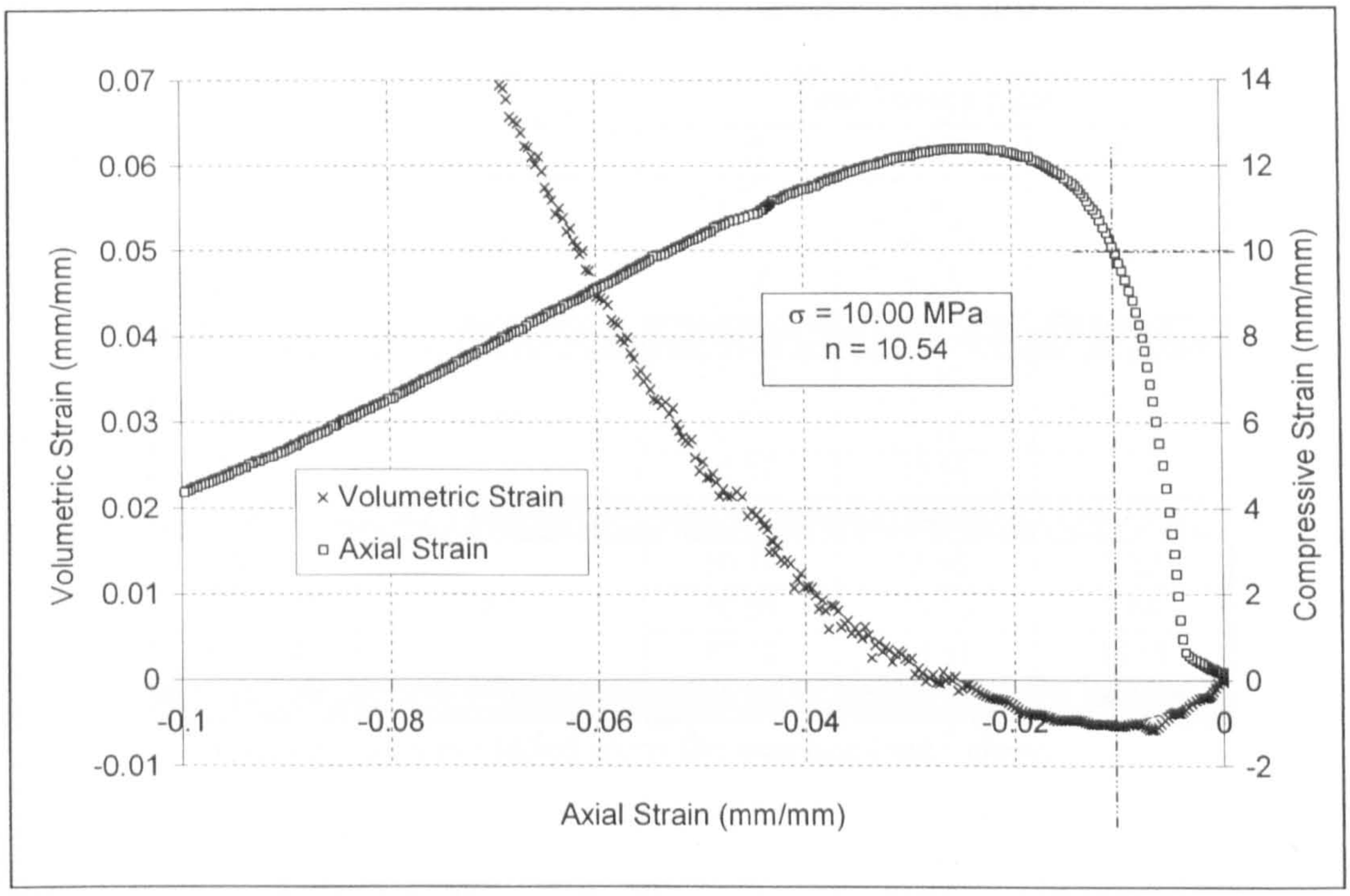

Figure 6.8: Example plot showing the evaluation of parameter *n* – HRA mixture at 20°C and 10 mm/s displacement rate

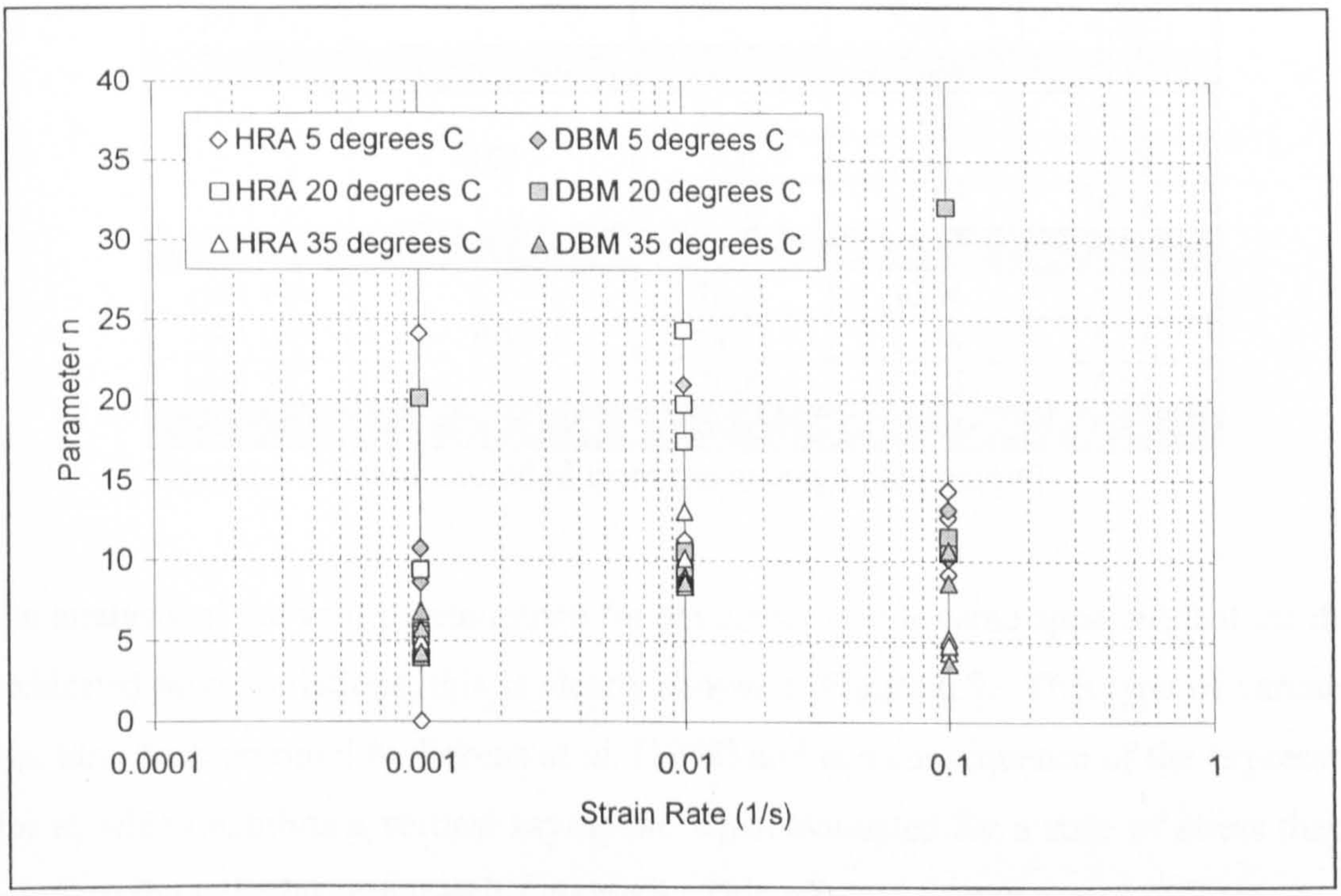

Figure 6.9: Graphical representation of parameter *n*, as a function of strain rate

and temperature – DBM and HRA mixtures

Table 6.4: Values for parameter *n* – DBM mixture

Sample	Strain Rate (s^{-1})	Test Temperature		
		5 ℃	20 ℃	35 ℃
DBM 0.1A	0.001	18.72*	5.41	6.86
DBM 0.1B		8.63	20.07*	5.73
DBM 0.1C		5.74	3.96	4.26
Average	0.001	7.19	4.69	5.61
DBM 1A	0.01	10.22	9.32	9.07
DBM 1B		20.96*	8.47	8.95
DBM 1C		10.07	10.59	8.61
Average	0.01	10.15	9.46	8.88
DBM 10A	0.1	10.19	32.06*	3.62
DBM 10B		10.96	10.92	8.64
DBM 10C		13.19	11.51	10.68
Average	0.1	11.45	11.21	7.65

*Denotes a result excluded from the average (see below)

Table 6.5: Values for parameter *n* – HRA mixture

Sample	Strain Rate (s^{-1})	Test Temperature		
		5 ℃	20 ℃	35 ℃
HRA 0.1A	0.001	24.14*	9.40*	4.52
HRA 0.1B		5.17	5.24	4.22
HRA 0.1C		-	5.61	4.98
Average	0.001	5.17	5.43	4.57
HRA 1A	0.01	11.29	17.41*	8.39
HRA 1B		NA	24.34*	13.08*
HRA 1C		8.99	19.74*	10.16
Average	0.01	10.14	-	9.28
HRA 10A	0.1	12.71	10.54	4.37
HRA 10B		14.37	11.44	5.22
HRA 10C		9.18	11.26	4.80
Average	0.1	12.09	11.08	4.80

*Denotes a result excluded from the average (see below)

On analysis of the values determined for parameter *n*, it became apparent that the data exhibited large variations, this is clearly shown in Figure 6.9. This type of variation has also been reported by Erkens *et al.* [1998] and is a consequence of the expression for *n*, which exhibits a vertical asymptote when evaluated for a state of stress that is equal to the uniaxial compressive strength. This effect is demonstrated in Figure 6.10, which shows parameter *n* as a function of the normalised stress. Where the

normalised stress, σ_{norm}, is given by Equation (6.5).

$$\sigma_{norm} = \frac{\sigma_d}{f_c} \tag{6.5}$$

where, σ_d = the state of stress delimiting the onset of dilation

It can be observed that for low values of σ_{norm}, which correspond to ductile type stress-strain curves, found at high temperatures and slow strain rates (for example Figures H.19 – H.21 and I.18 – I.20), or to very brittle type stress-strain curves, found at low temperatures and fast strain rates (for example Figures H.7 - H.9 and I.6 – I.8), the variation in parameter n is relatively small. However, for the remaining intermediate types of response, characterised by large ratios of σ_{norm}, the variation in n, for small changes in σ_d, is large.

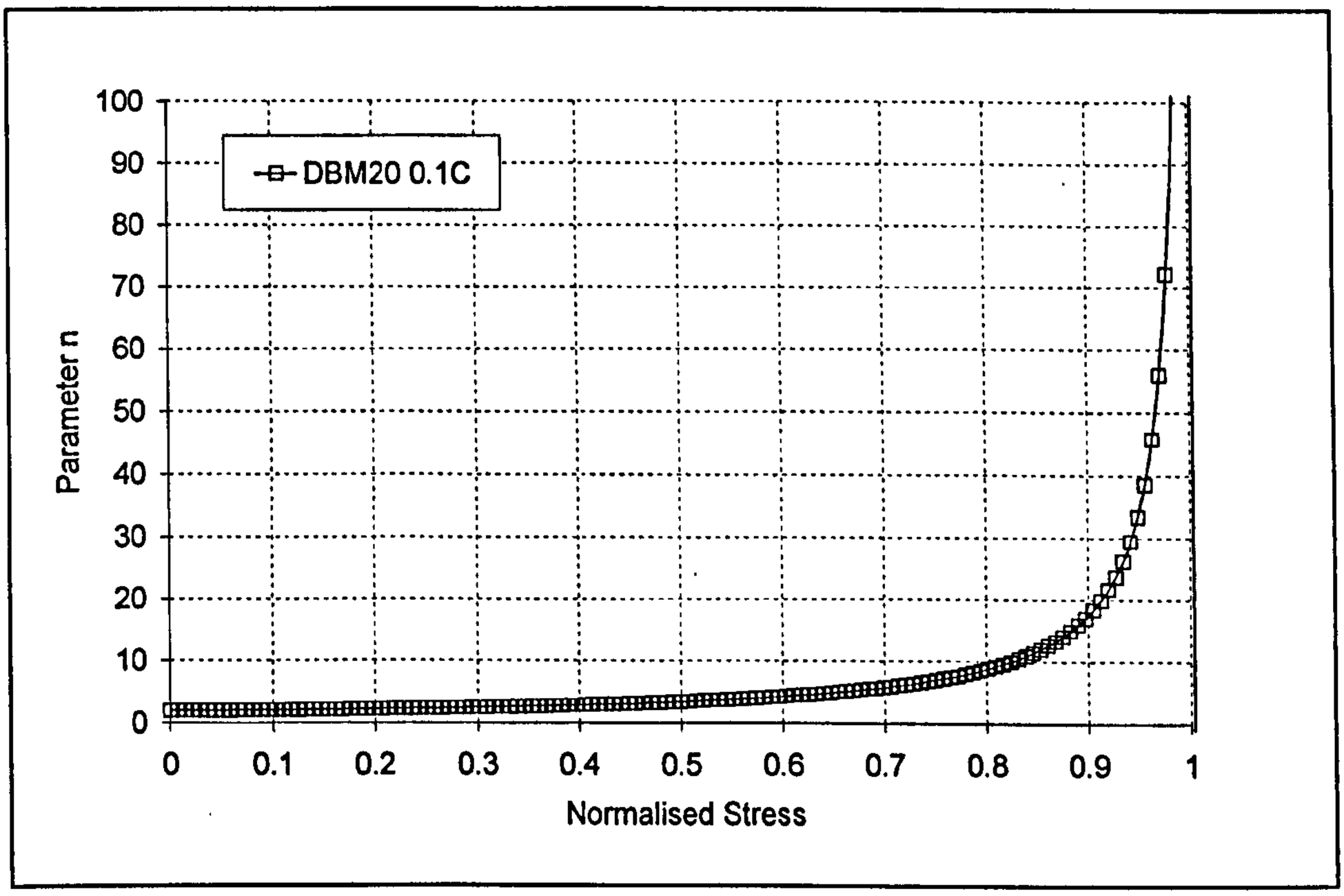

Figure 6.10: Parameter n as a function of normalised stress

Therefore, on the basis of the above discussion, any obvious extraneous values for parameter n, corresponding to variations caused by small changes in σ_d at high ratios of σ_{norm}, were discounted, and an average of the remaining (if any) results taken.

These averages are also shown in Tables 6.4 and 6.5 for the DBM and HRA mixtures respectively. Figure 6.11 shows a plot of the average *n* values as a function of strain rate and temperature, for both mixtures. With the exception of the 35°C, 0.1 s^{-1} data (see Section 6.6.1), Figure 6.11 shows a general trend of increasing *n* with increasing strain rate and possibly, although less marked, decreasing temperature. It can also be observed that similar values were obtained for both the DBM and HRA mixtures.

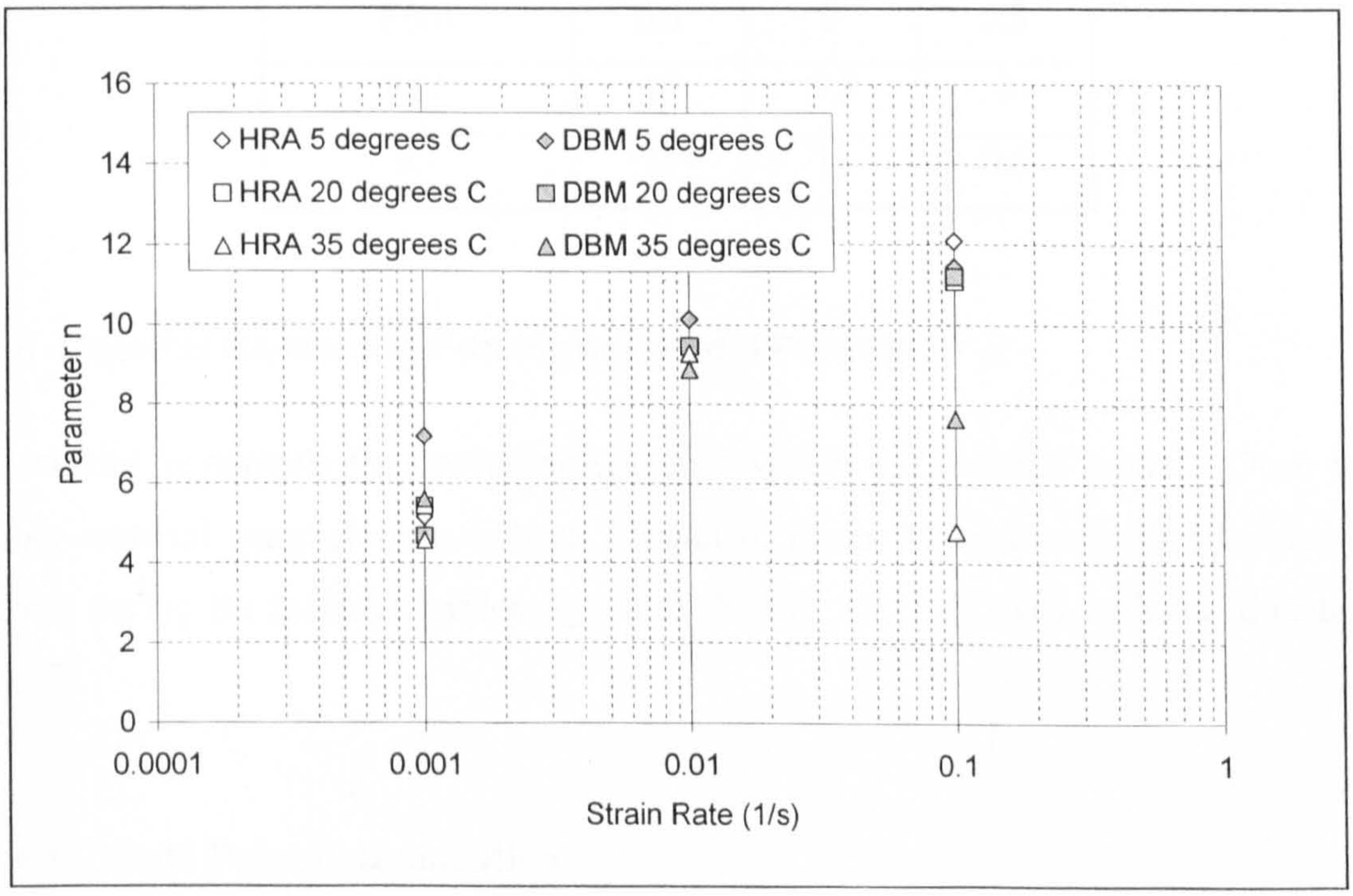

Figure 6.11: Average values for parameter *n* as a function of strain rate and temperature – DBM and HRA mixtures

For other dilative materials typical values for parameter *n* range from 2.5 to 4 for soils with larger values in the region of 5 to 7 used in the characterisation of concrete and rock [Desai *et al.*, 1986]. Other researchers have used values ranging from 2 – 3.3 for the characterisation of asphaltic materials[1] [Scarpas *et al.*, 1997 and 1998a; Erkens *et al.*, 2000b]. However, on the basis of the available experimental data, a strain rate and temperature dependent relationship was selected for *n*. Due to the similarity in the DBM and HRA data, combined with the discussed uncertainty in the determination of *n*, the same values were used to describe both the DBM and HRA mixtures. The

[1] A similar large variation in the values of parameter *n* was also reported by Erkens *et al.* [2000b].

selected values for parameter *n* based on the above considerations and the averages given in Tables 6.4 and 6.5 are listed in Table 6.6.

Table 6.6: Selected values for parameter *n*

Strain Rate (s^{-1})	Temperature		
	5 °C	20 °C	35 °C
0.001	6.5	6	5.5
0.01	10	9.5	9
0.1	12	11	9.5

6.6 Material Hardening Function – Model Parameter α

Parameter α controls the hardening response within the material model. Once the other material parameters have been computed, α can be evaluated for all states of stress during the inelastic hardening phase (Figure 5.9, Part two), utilising Equation (3.28).

6.6.1 Yield Point Determination

The state of stress at which inelastic material response starts can be determined from the compressive test data. Figure 6.12 shows an example plot of Poisson's ratio versus compressive stress (plotted as positive) for the DBM mixture tested at 35°C at a displacement rate of 10 mm/s. From this figure the state of stress delimiting inelastic material response can be approximated. Evaluation of Equation (3.28) for this state of stress allows, α_0, the starting value for parameter α to be computed.

At this stage, during analysis of the data, it became evident that at 35°C, at the slower strain rates, a portion of the data (i.e. the yield point) was being 'lost'. This was due to the initial load introduction phase, see Section 5.3.3, which, for test data at elevated temperatures and slower strain rates, represented a greater percentage of the overall response. This effect is shown diagrammatically in Figure 6.13 for two typical data sets.

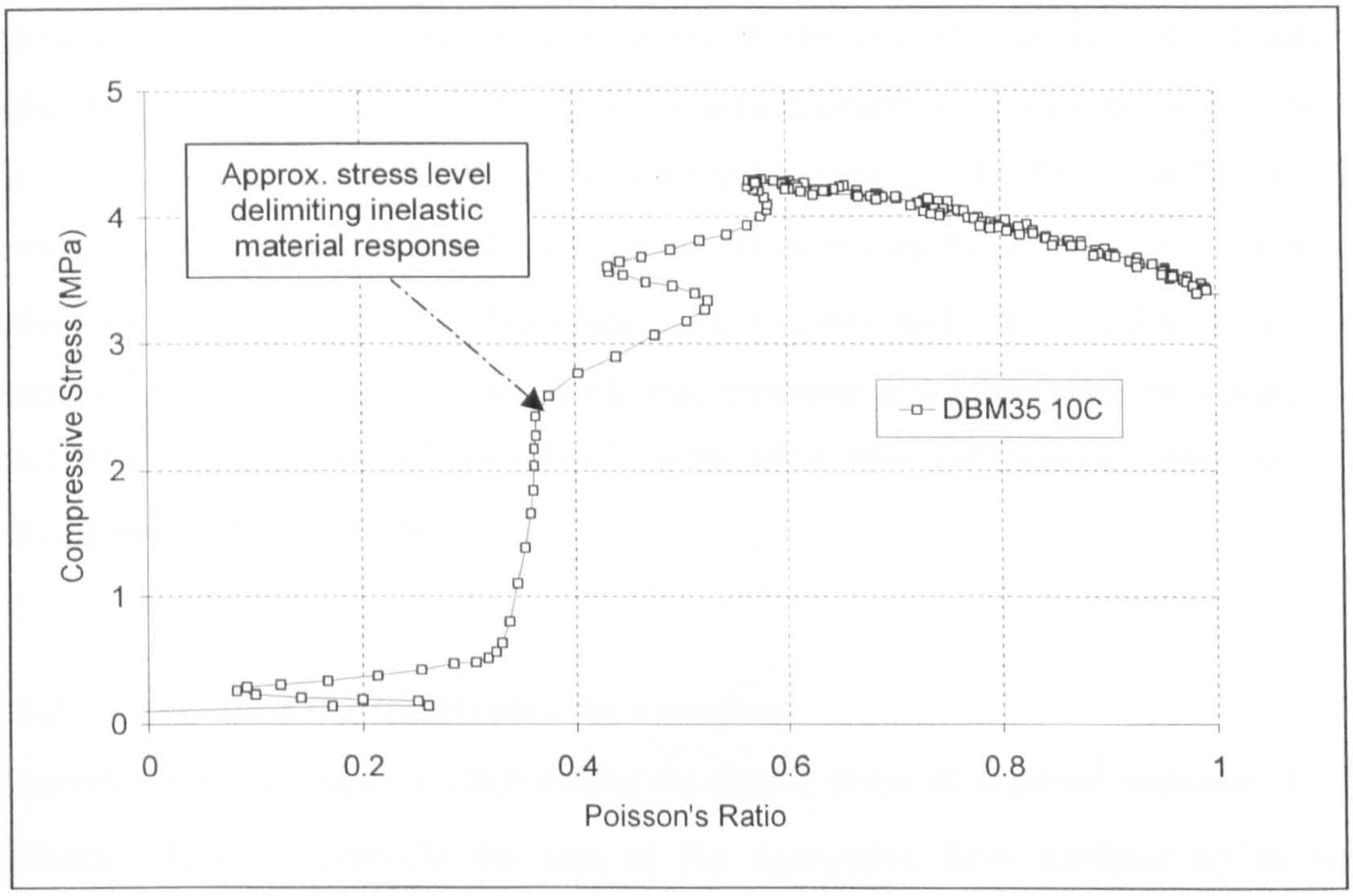

Figure 6.12: Plot showing stress level delimiting inelastic material response

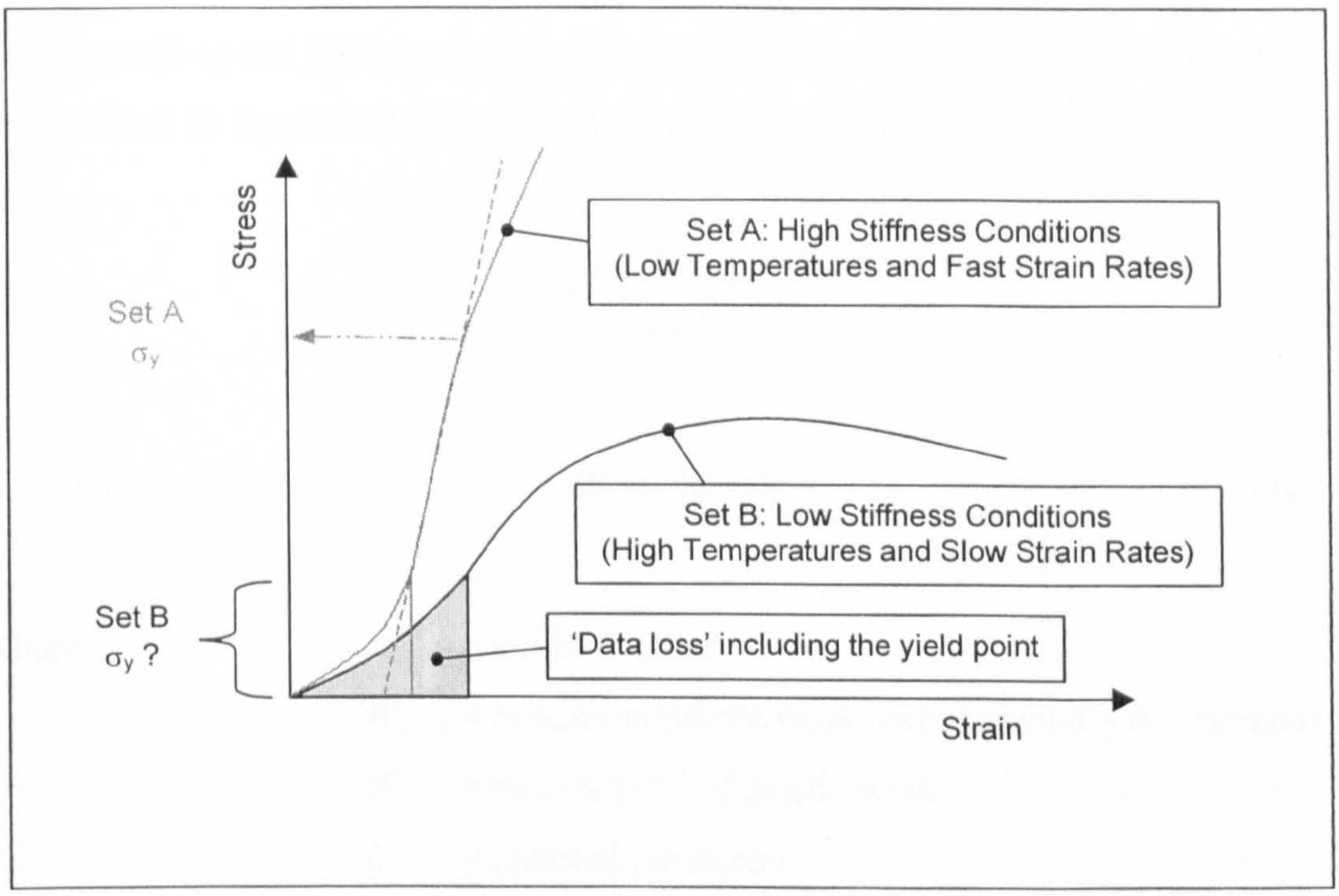

Figure 6.13: Diagram showing 'data loss' due to the initial load introduction phase for low stiffness test conditions

Set *A* in Figure 6.13 represents high stiffness test conditions and set *B* low stiffness conditions. For test conditions such as set *B*, the load introduction effect lead to difficulty in identifying the start of the inelastic material response phase, and hence the current level of plastic straining could not be determined. This was found to be more pronounced for the HRA data due to its increased binder content, and hence reduced mixture viscosity. This complication meant that for the 35°C it was not possible to reliably determine the hardening parameters at strain rates of $0.001s^{-1}$ for the DBM data, and $0.001s^{-1}$ and $0.01s^{-1}$ for the HRA data and therefore these data sets are not used in this section[2].

6.6.2 Expression for the Hardening Function

Parameter α has a constant value during the elastic phase of material response. In the inelastic phase, α controls the size of the successive flow surfaces up to peak response, see Section 3.3.2. This is achieved by specifying α as a decreasing function of a physically increasing quantity, temperature and strain rate. In this study α is specified both as a function of plastic work and as a function of equivalent plastic strain. In the current formulation of the ACRe model the expressions given by Equations (6.6) and (6.7) are to be used to specify the degradation of α as function of plastic work or equivalent plastic strain, respectively [Erkens *et al.*, 2000b].

$$\alpha = \frac{\alpha_1 \cdot \left(W_{p\lim} - W_p\right)}{1 + C \cdot W_p} \tag{6.6}$$

in which

$$W_p = \int \sigma \cdot d\varepsilon_p \tag{6.6a}$$

where,

α_1 = initial α value

$W_{p\,lim}$ = maximum plastic work (experimentally determined)

W_p = current level of plastic work

C = material parameter

---

[2] Note: this did not affect the softening response, for which, the determination of the parameters is independent of the yield point.

ε_p = plastic strain (experimentally determined)

$$\alpha = \frac{\alpha_1 \cdot \left(\xi_{p\lim} - \xi_p\right)}{1 + c \cdot \xi_p} \tag{6.7}$$

in which

$$\xi_p = \int \left(d\varepsilon_{ij}^p \cdot d\varepsilon_{ij}^p\right) \tag{6.7a}$$

where,

$\xi_{p\,lim}$ = maximum equivalent plastic strain (experimentally determined)

ξ_p = current level of equivalent plastic strain

c = material parameter

6.6.3 Parameter α as a Function of Plastic Work

The advantage of specifying α as a function of plastic work is that its computation can be based on axial strain data alone, without requiring information on the radial strains. Figure 6.14 shows a typical experimental plot of the relationship between parameter α and plastic work, during inelastic material hardening response, for the DBM mixture at displacement rates of 0.1, 1 and 10 mm/s at 20°C. A trend of decreasing alpha with increasing plastic work can observed. This trend was found to be similar for each of the displacement rates, however the magnitude of α was found to vary. Plots similar to this were also found for the other test temperatures and also for the HRA data.

As the value of parameter alpha was found to vary in magnitude for different test conditions, to facilitate a comparison of the overall range of data, α was normalised with respect to α_0 (the experimentally determined starting value for parameter α). Figures 6.15 and 6.16 show plots of normalised alpha versus plastic work for the DBM and HRA mixtures respectively; where normalised alpha, α_{norm}, is given by Equation (6.8).

$$\alpha_{norm} = \frac{\alpha}{\alpha_0} \tag{6.8}$$

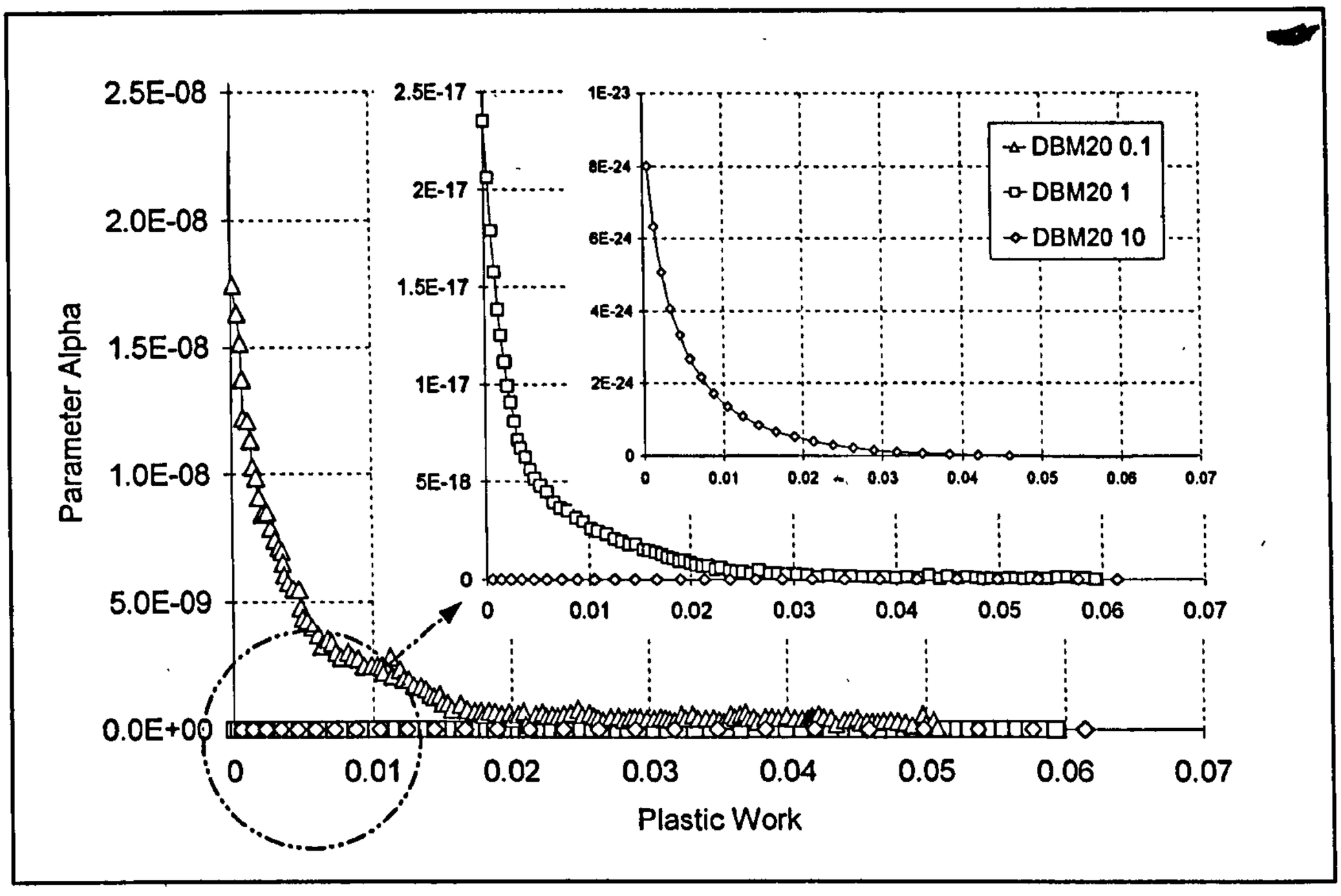

Figure 6.14: Parameter α as a function of plastic work – DBM mixture at displacement rates of 0.1, 1 and 10 mm/s at 20°C

With the notable exception of the 5°C, 10 mm/s test data, a general trend of increased levels of plastic work with increasing strain rate and decreasing temperature was evident for both mixture types[3]. This observation would seem logical as it implies that, as an asphalt mixture becomes stiffer a greater level of external work is required to overcome the internal dissipation of energy generated by the mixture's resistance to further straining. Contrasting the response of the two mixtures, it can be seen from the typical examples shown in Figures 6.15 and 6.16 that the HRA data exhibits a greater maximum level of plastic work compared to the DBM data. This is a reflection of the relative sizes of the inelastic hardening response zones of the mixtures, which is larger for the HRA mixture due to its increased straining capacity.

---

[3] Note: This observed dependency of the development of W_p on temperature and displacement rate is in contrast to the data reported by Scarpas *et al.* [1998a], who observed the level of plastic work for a Dutch asphalt concrete mixture to be insensitive to these factors.

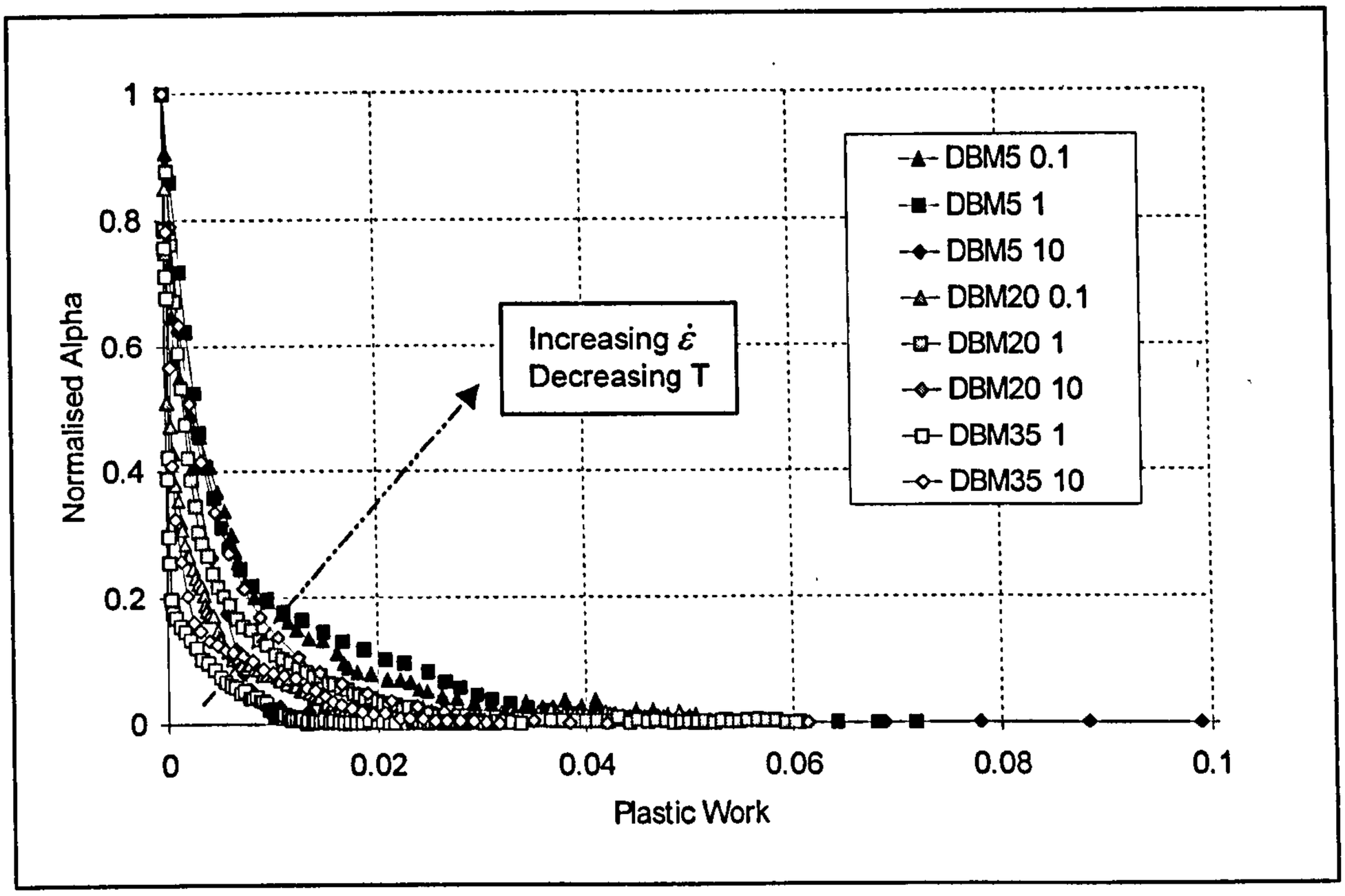

Figure 6.15: Typical plot of normalised α versus plastic work, as a function of strain rate and temperature – DBM mixture

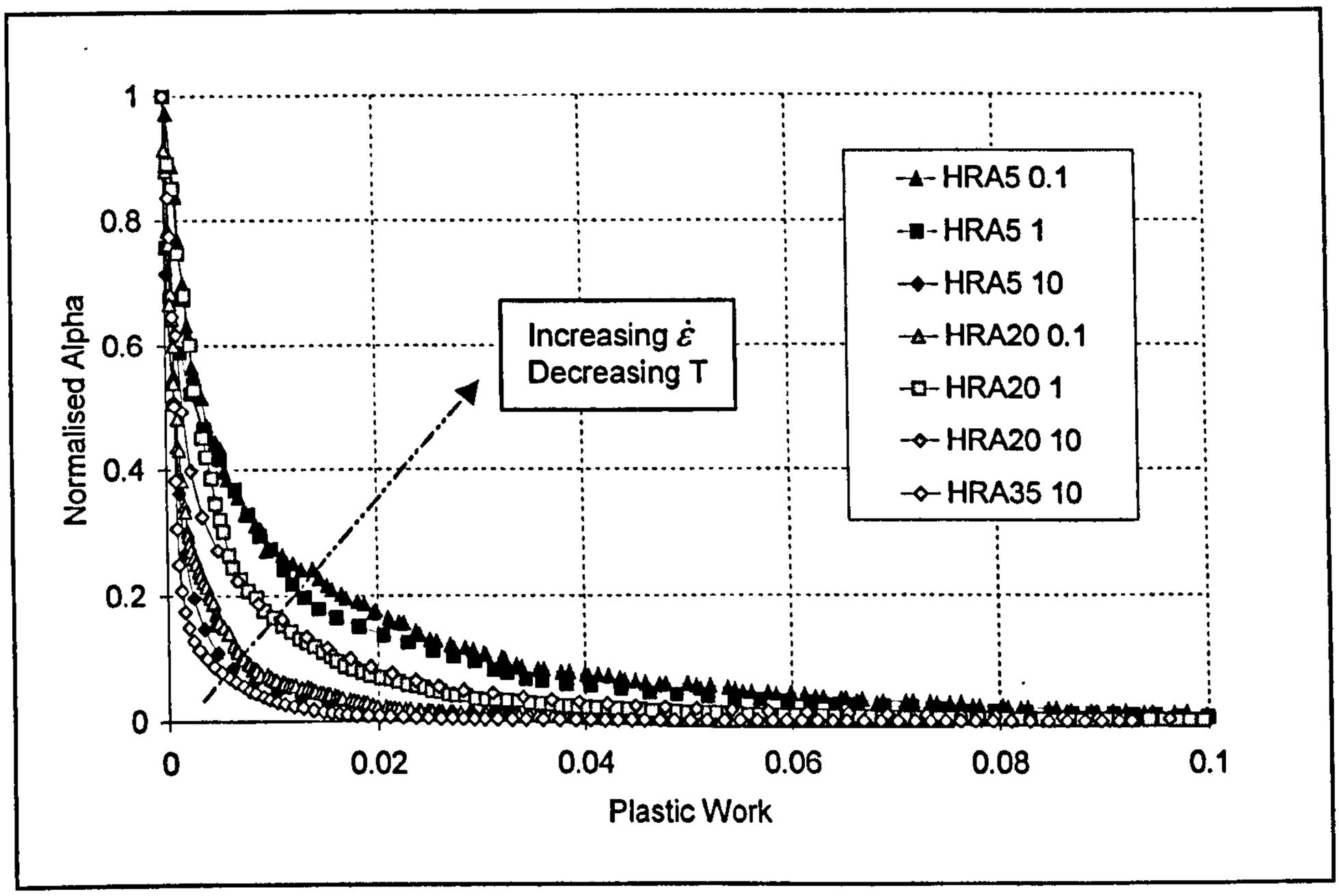

Figure 6.16: Typical plot of normalsied α versus plastic work, as a function of strain rate and temperature – HRA mixture

Through non-linear regression of Equation (6.6) over the range of experimental data, using a data analysis package entitled 'Table Curve 2D' [SPSS Inc, 1996], it was possible to determine average values for the hardening function parameters, for each set of experimental conditions. These average values are shown graphically in Figures 6.17 to 6.20, and given numerically in Tables 6.7 and 6.8 for the DBM and HRA mixtures respectively, along with the starting value for alpha, α_0. The value of α_0 delimits the onset of inelastic material response and hence specifies the size of the elastic region of the flow surfaces (see Section 6.8.1).

Table 6.7: Average values for the hardening function parameters given in Equation (6.6), derived as a function of plastic work – DBM mixture

T (°C)	$\dot{\varepsilon}$ (s^{-1})	α_1	$W_{p\,lim}$	C	α_0
5	0.001	3.562E-11	0.05568	394	1.921E-12
	0.01	2.112E-20	0.06902	447	1.631E-21
	0.1	1.060E-25	0.11527	918	1.217E-26
20	0.001	5.863E-07	0.04279	463	2.469E-08
	0.01	7.334E-16	0.05251	397	3.851E-17
	0.1	6.932E-24	0.05581	229	7.016E-24
35	0.01	4.266E-10	0.02582	3188	1.039E-11
	0.1	3.881E-14	0.03052	1098	1.197E-15

Table 6.8: Average values for the hardening function parameters given in Equation (6.6), dervied as a function of plastic work – HRA mixture

T (°C)	$\dot{\varepsilon}$ (s^{-1})	α_1	$W_{p\,lim}$	C	α_0
5	0.001	7.697E-11	0.14610	190	1.134E-11
	0.01	1.003E-20	0.14963	383	1.504E-21
	0.1	2.781E-26	0.18675	1404	5.297E-27
20	0.001	1.191E-6	0.06910	950	8.200E-08
	0.01	3.393E-15	0.12481	425	4.223E-16
	0.1	1.310E-21	0.17567	350	2.302E-22
35	0.1	2.084E-13	0.08014	1700	1.658E-14

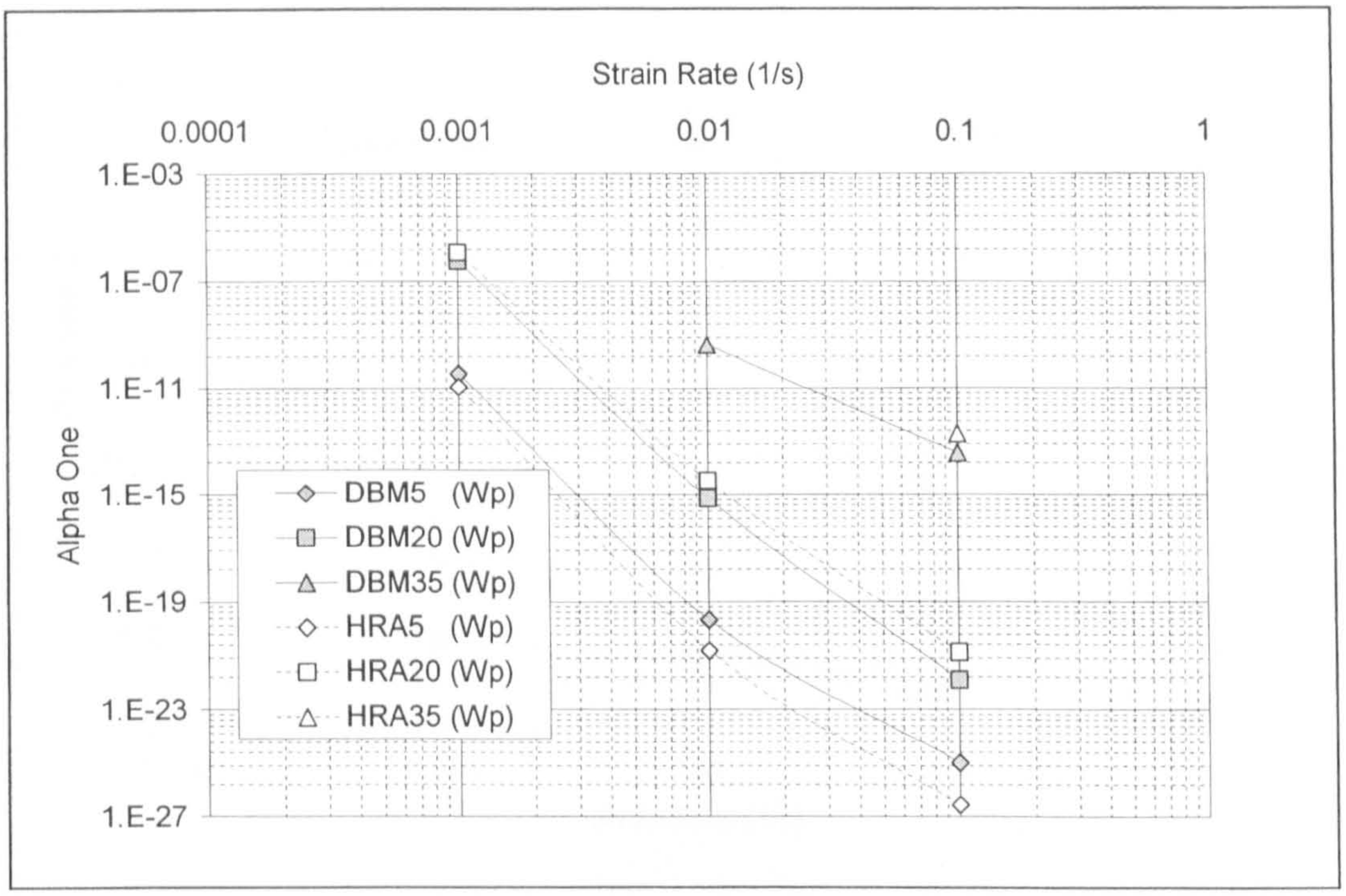

Figure 6.17: Plot showing the trend in the average values of the hardening function parameter α_1, as a function of plastic work, with respect to changes in strain rate and temperature - DBM and HRA mixtures

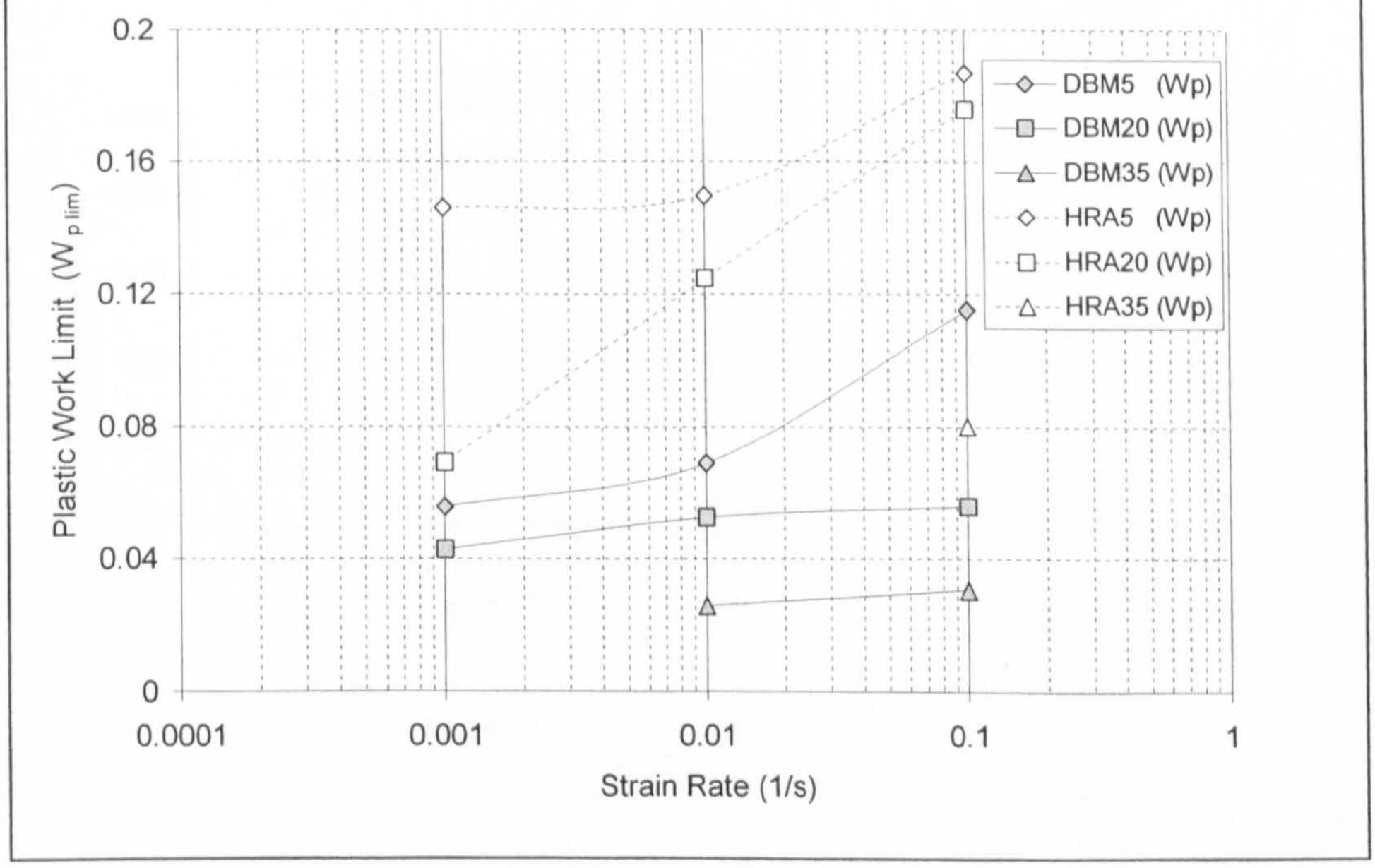

Figure 6.18: Plot showing the trend in the average values of parameter $W_{p\,lim}$ (the maximum level of plastic work) as a function of strain rate and temperature - DBM and HRA mixtures

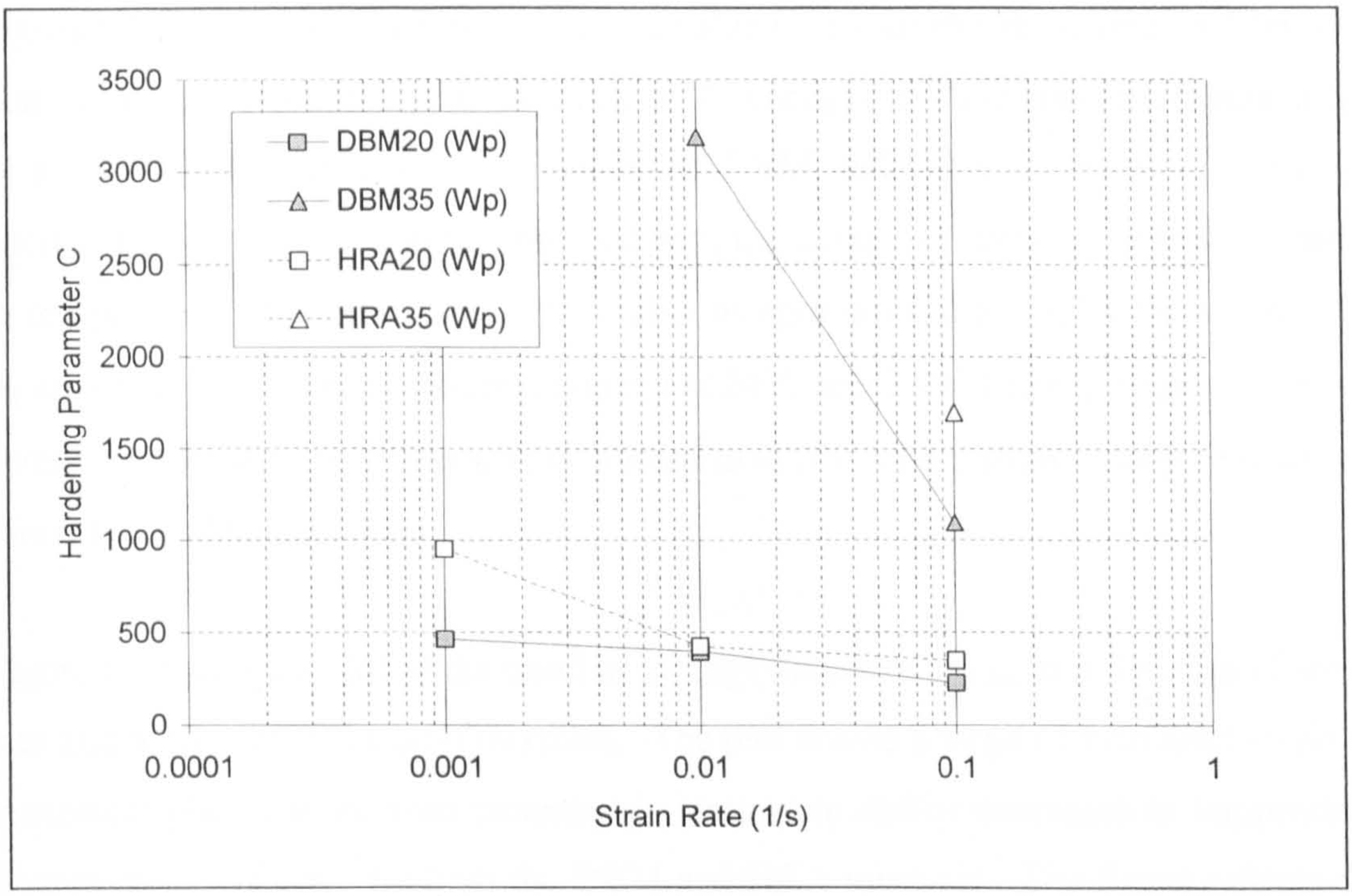

Figure 6.19: Plot showing the trend in the average values of the hardening function parameter *C*, as a function of plastic work, with respect to changes in strain rate at 20°C and 35°C – DBM and HRA mixtures

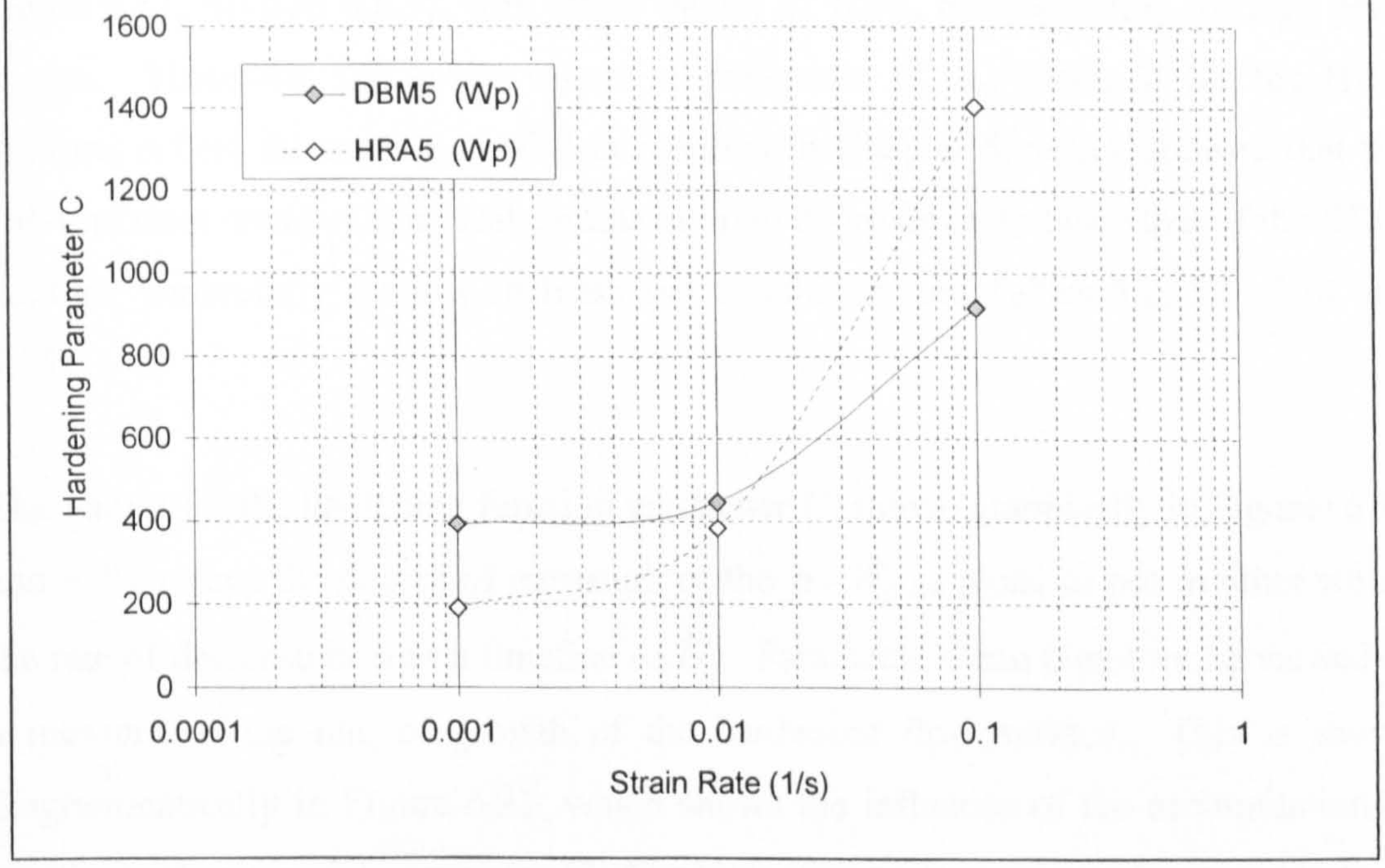

Figure 6.20: Plot showing the trend in the average values of the hardening function parameter *C*, as a function of plastic work, with respect to changes in strain rate at 5°C – DBM and HRA mixtures

Figure 6.17 shows the trend in the average value for parameter α_l, determined through non-linear regression analysis, with respect to changes in strain rate and temperature as a function of plastic work, for both the DBM and HRA mixtures. A trend of decreasing values of α_l can be observed with increases in strain rate and/or decreases in temperature. For equivalent test conditions approximately similar magnitudes for α_l are obtained for each mixture, although at 20°C and 35°C slightly larger values are determined for the DBM mixture, compared to at 5°C where slightly larger values are found for the HRA mixture.

Figure 6.18 shows a plot of the trend in average values of $W_{p\,lim}$ as a function of strain rate and temperature for both mixtures. The plot shows a trend of increased levels of maximum plastic work with increases in strain rate and/or decreases in temperature (increases in stiffness) for both the DBM and HRA mixtures. The figure reflects the earlier observation that, for equivalent test conditions, the HRA mixture exhibits greater levels of maximum plastic work than was observed for the DBM mixture. In the ACRe model parameter $W_{p\,lim}$ (or $\xi_{p\,lim}$ in the case of ξ_p specification) controls the amount of straining that takes place during the inelastic hardening response (see Figure 6.51, Section 6.8.3), with larger values of $W_{p\,lim}$ corresponding to large peak strains. Therefore, the larger values of parameter $W_{p\,lim}$, obtained for the HRA mixture, reflect the experimental data reported in Chapter 5, which showed that the HRA mixture could exhibit peak strains of up to approximately twice that of the DBM mixture, particularly for low stiffness test conditions (see Tables 5.2, 5.3, 5.14 and 5.15).

The values for the hardening function parameter C, shown graphically in Figures 6.19 and 6.20, reflect the degree of curvature of the α - $W_{p\,lim}$ plots, or put in other words the rate of decrease in α as a function of W_p. Parameter C can therefore be viewed as a measure of the rate of growth of the hardening flow surface. This is shown diagrammatically in Figure 6.21, which shows the influence of the accumulation of plastic work on model parameter C. For high stiffness conditions (low temperatures and fast strain rates) the level of plastic work done during inelastic hardening generally exceeds that done at low stiffness conditions (high temperature and slow strain rates), $W_p A > W_p B$ in Figure 6.21(a), and Figure 6.18. Also, with increases in

material stiffness the magnitude of parameter α has been shown to decrease, Figures 6.14 and 6.17. Plotting these trends on a α - W_p plot, Figure 6.21(b), it can be seen that this results in large curvatures of the α - W_p plots for low stiffness test conditions, and shallower curvatures for high stiffness test conditions. Parameter C controls this degree of curvature, with increases in C corresponding to increased curvatures, and hence lower mixture stiffness moduli. This effect is reflected in Figures 6.19 and 6.20, which show the change in parameter C as a function of strain rate and temperature. It can be observed from Figure 6.19 that a decrease in C is evident with decreases in temperature and increases in strain rates (increases in mixture stiffness) for the 35°C and 20°C test data. This trend is continued in Figure 6.20, for the 5°C test conditions, but only for the $0.001s^{-1}$ strain rate data. For further increases in strain rate an increase in parameter C was found, thus indicating that at high stiffness moduli the level of plastic work done during inelastic hardening reduces. This observation is also supported by Figures 6.15 and 6.16 which show dramatic reductions in the level of plastic work for the $0.1s^{-1}$, 5°C test data for both the DBM and HRA mixtures. This effect is likely to be due to the brittle response of the mixtures at these extreme test conditions, which results in a large elastic zone, and hence reduced material hardening, leading to a reduction in the measured level of plastic work.

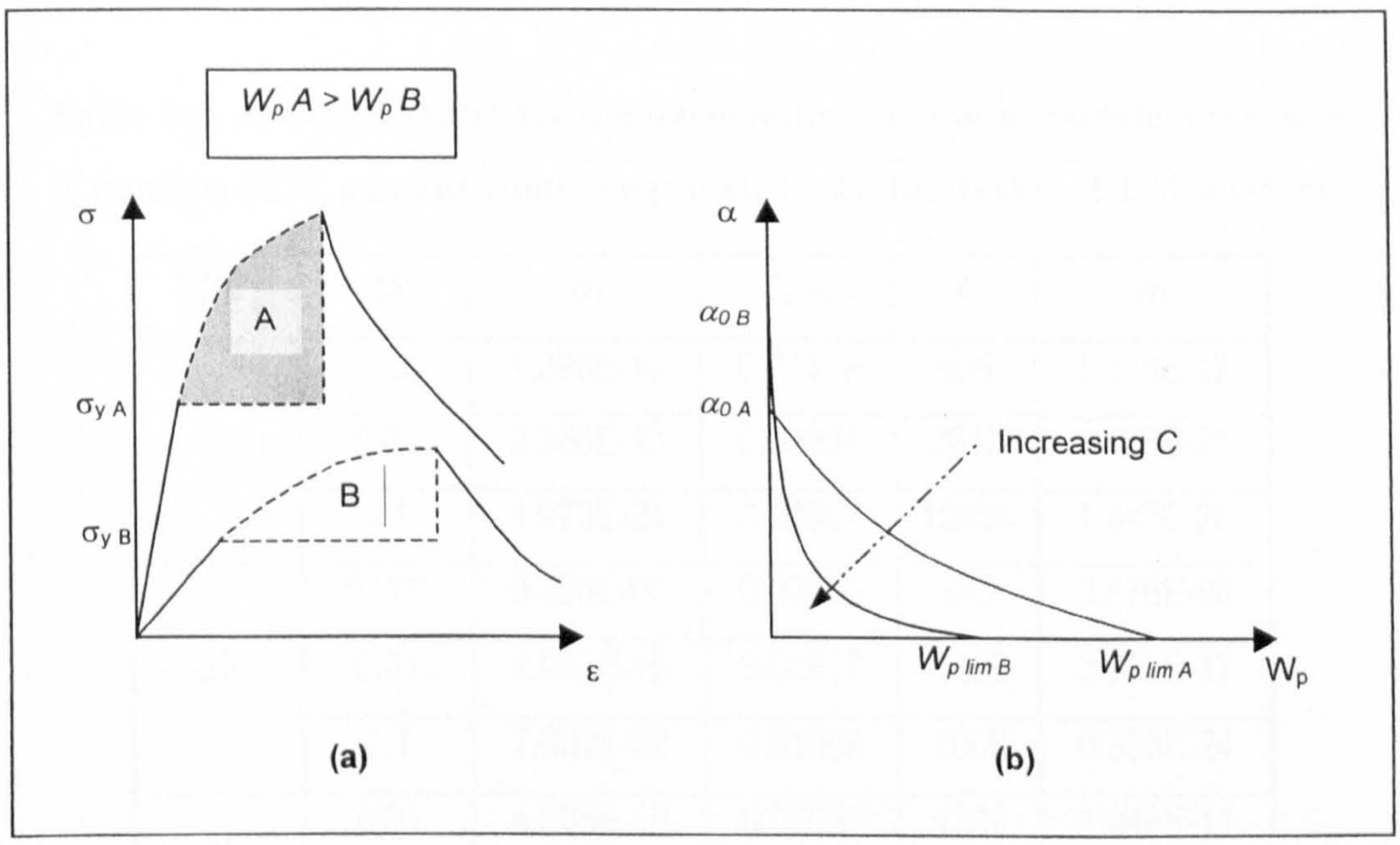

Figure 6.21: Diagram showing the influence of the accumulation of plastic work on the value of parameter *C*

6.6.4 Parameter α as a Function of Equivalent Plastic Strain

When specifying the expression for the hardening parameter α as a function of equivalent plastic strain, both axial and lateral elements of strain are used to control material response, thus providing more detailed information than is attainable when using plastic work. Figures 6.22 and 6.23 show plots of normalised alpha versus equivalent plastic strain for the DBM and HRA mixtures respectively. From these figures it is possible to observe a general trend of increasing equivalent plastic strain with increases in temperature and decreases in strain rate, i.e. the level of equivalent plastic strain increases as the mixture stiffness decreases. This was reflected in the greater level of equivalent plastic strain displayed by the HRA mixture, which is particularly noticeable for the 5°C test conditions. This is due to the larger amount of straining exhibited by the HRA mixture, compared to the less viscous, brittle behaviour observed for the DBM mixture.

Non-linear regression of Equation (6.7) over the range of experimental data allowed the average values for the hardening function parameters, for each set of experimental conditions to be determined. These values are shown graphically in Figures 6.24 to 6.26 and are given numerically in Tables 6.9 and 6.10 for the DBM and HRA mixtures respectively, along with the corresponding value for α_0.

Table 6.9: Average values for the hardening function parameters given in Equation (6.7), as a function of equivalent plastic strain – DBM mixture

T (°C)	$\dot{\varepsilon}$ (s^{-1})	α_1	$\xi_{p\,lim}$	c	α_0
5	0.001	1.396E-10	0.01379	606	1.868E-12
	0.01	2.366E-19	0.00684	2812	1.428E-21
	0.1	1.973E-24	0.00687	15554	1.347E-26
20	0.001	8.236E-07	0.03850	543	2.676E-08
	0.01	2.063E-15	0.01817	1459	3.733E-17
	0.1	7.602E-22	0.01008	2008	6.935E-24
35	0.01	4.588E-10	0.02567	1399	1.046E-11
	0.1	8.515E-14	0.01323	1800	1.146E-15

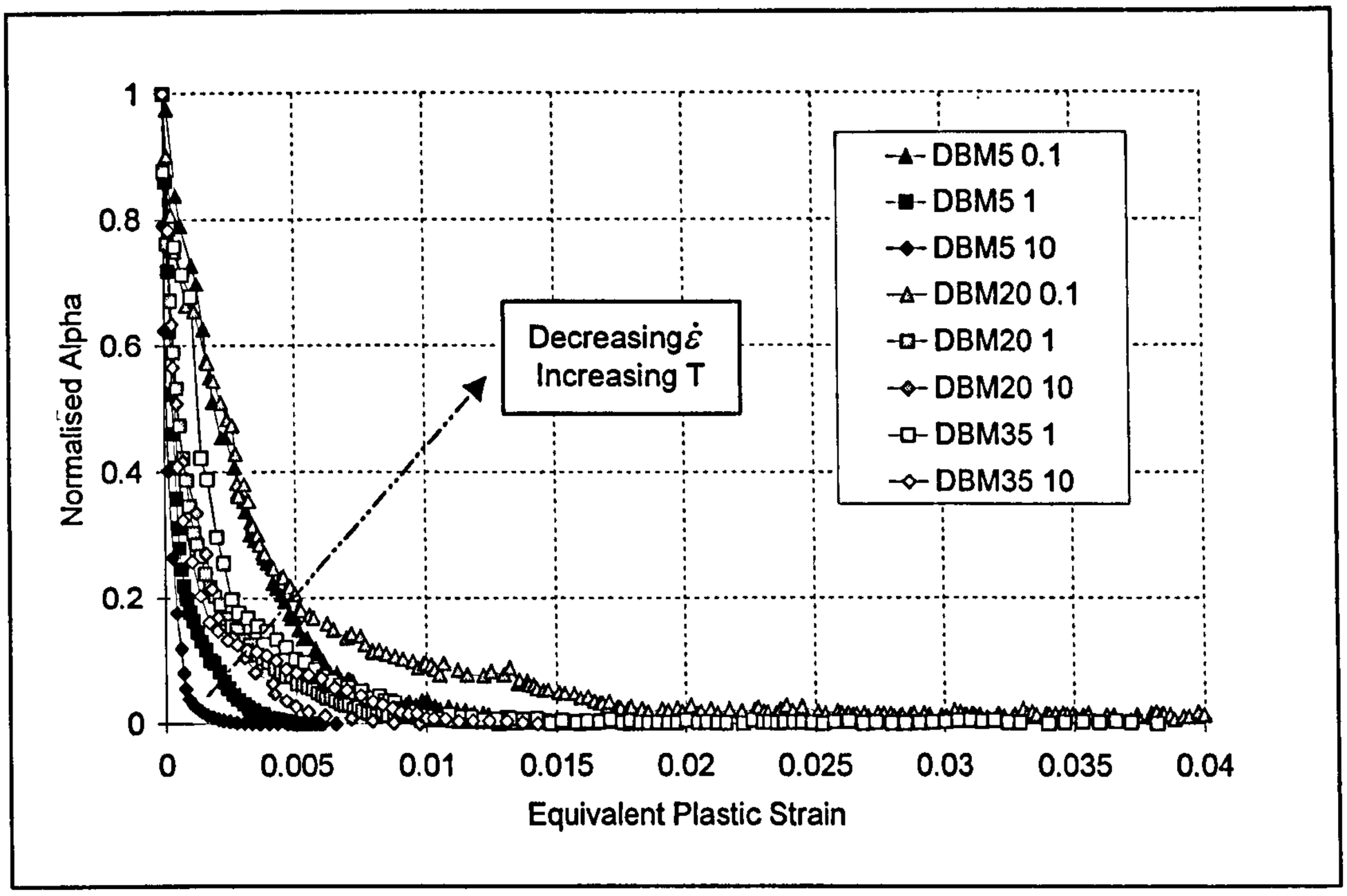

Figure 6.22: Typical plot of normalised α versus equivalent plastic strain, as a function of strain rate and temperature – DBM mixtrue

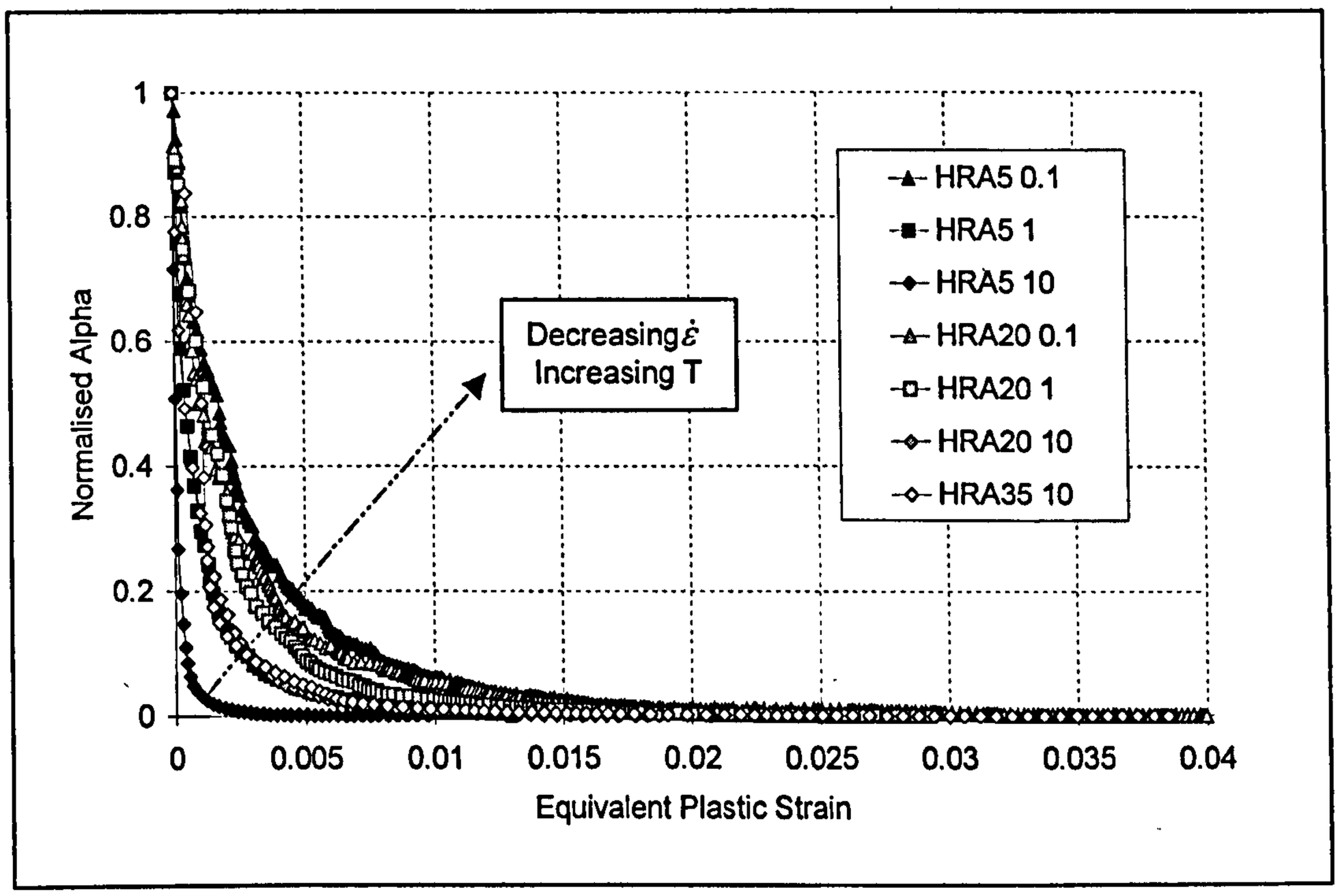

Figure 6.23: Typical plot of normalised α versus equivalent plastic strain, as a function of strain rate and temperature – HRA mixture

Table 6.10: Average values for the hardening function parameters given in Equation (6.7), as a function of equivalent plastic strain– HRA mixture

T (°C)	$\dot{\varepsilon}$ (s^{-1})	α_1	$\xi_{p\,lim}$	c	α_0
5	0.001	4.126E-10	0.02732	1000	1.134E-11
	0.01	1.015E-19	0.01498	2165	1.500E-21
	0.1	7.730E-25	0.00970	90000	5.658E-27
20	0.001	2.108E-06	0.03905	900	8.231E-08
	0.01	1.253E-14	0.03481	1900	4.225E-16
	0.1	1.036E-20	0.02200	2700	2.244E-22
35	0.1	4.913E-13	0.03334	2167	1.668E-14

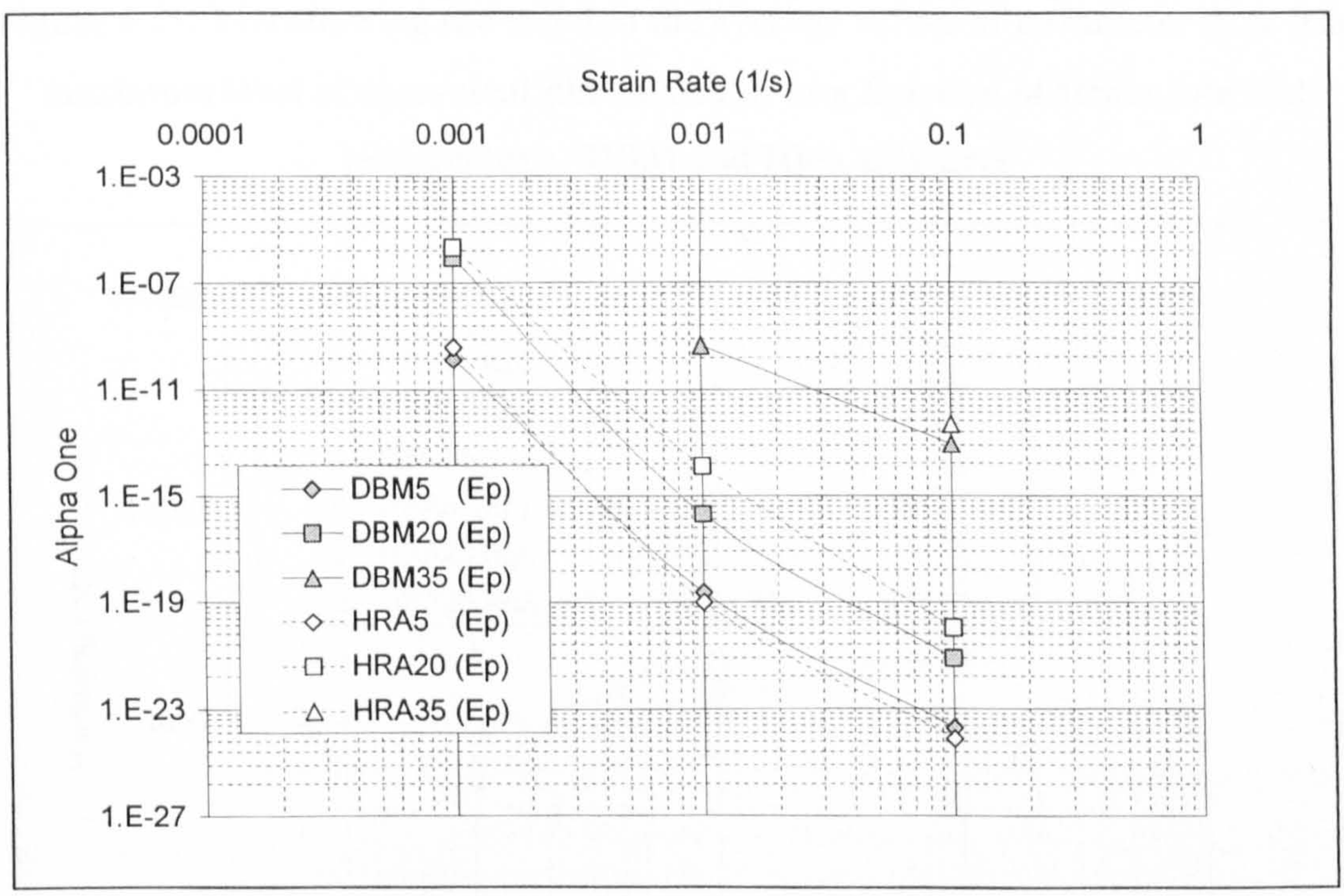

Figure 6.24: Plot showing the trend in the average values of the hardening function parameter α_1, as a function of equivalent plastic strain, with respect to changes in strain rate and temperature - DBM and HRA mixtures[4]

[4] In this chapter the symbol E_p, as used in Figures, signifies equivalent plastic strain.

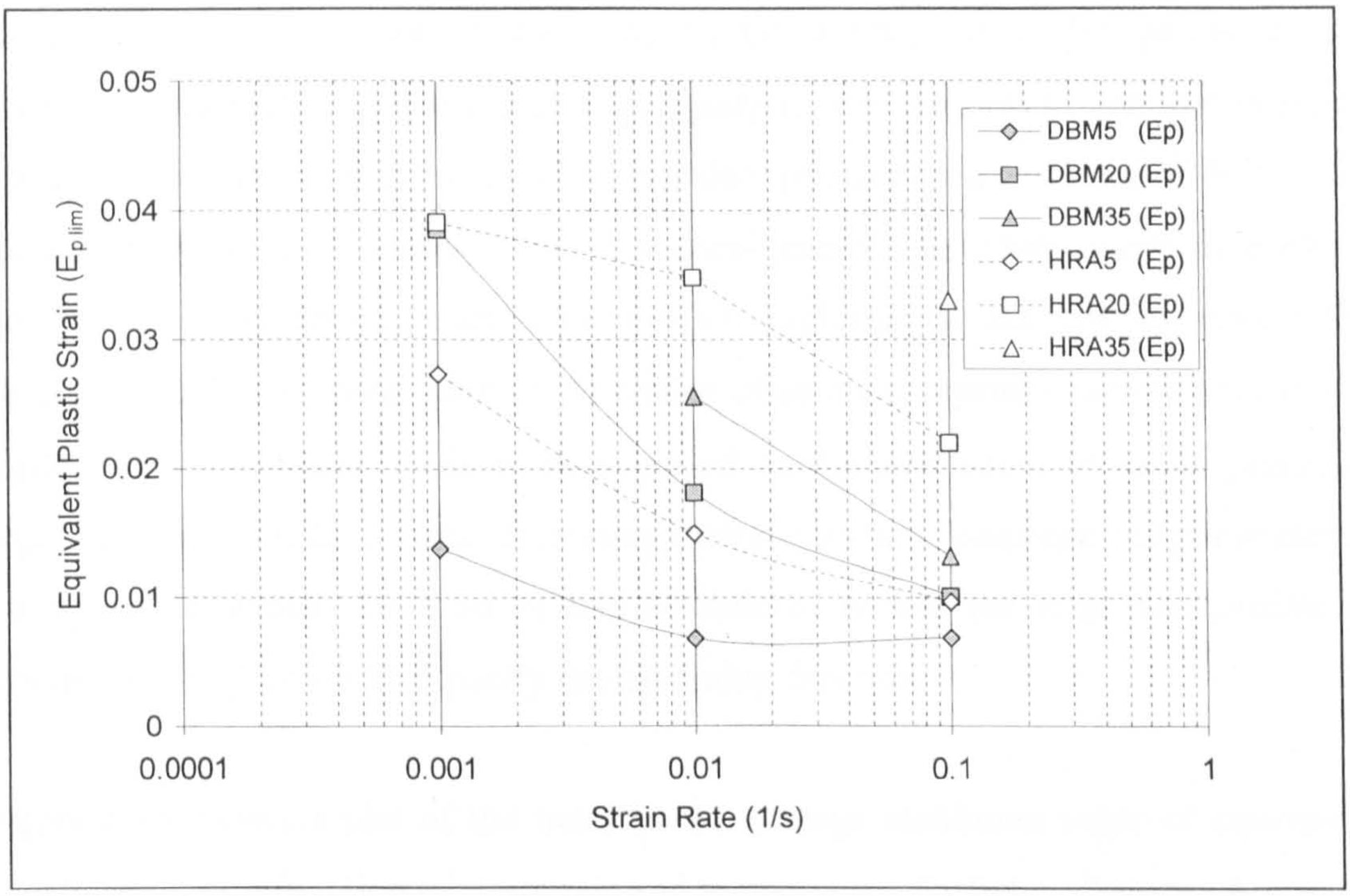

Figure 6.25: Plot showing the trend in the average values of parameter $\xi_{p\,lim}$ (the maximum level of equivalent plastic strain) as a function of strain rate and temperature - DBM and HRA mixtures

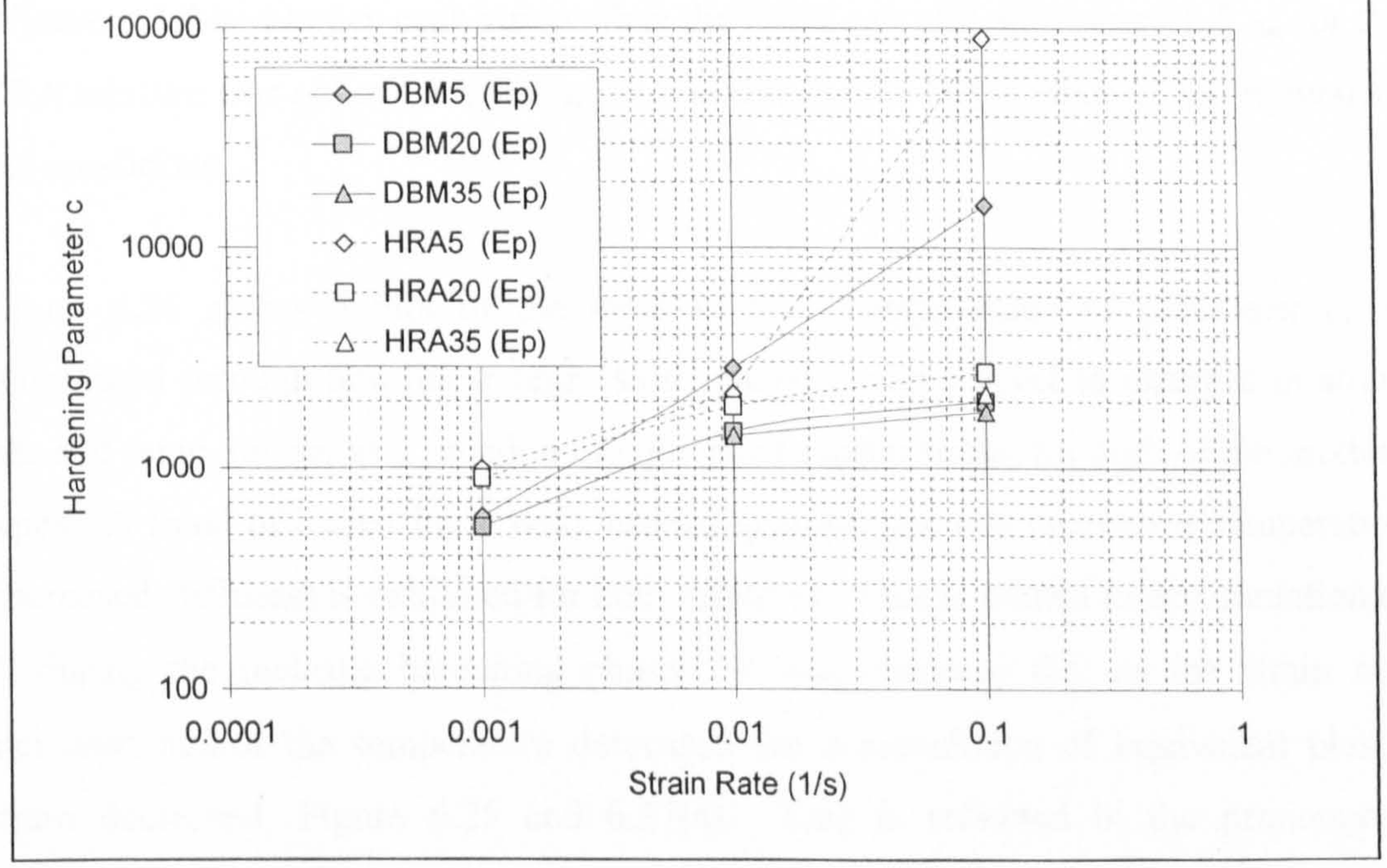

Figure 6.26: Plot showing the trend in the average values of the hardening function parameter *c*, as a function of equivalent plastic strain, with respect to changes in strain rate and temperature –DBM and HRA mixtures

Figure 6.24 shows a plot of the trend in the average value for parameter α_1, determined through non-linear regression analysis, with respect to changes in strain rate and temperature, as a function of equivalent plastic strain. A trend of decreasing values of α_1 with increasing strain rates and decreasing temperatures is evident. Comparison of Figures 6.24 and 6.17 serves to highlight the similarities between the observed trend in α_1 regardless of the choice of physical quantity used to specify the hardening relationship. This is as expected as the evaluation of α_1 is primarily dependent on the state of stress delimiting inelastic material response and parameter n, the values of which, for a set of test conditions, remain the same irrespective of whether W_p or ξ_p is used to specify the hardening function.

Figure 6.25 shows a plot of the trend in the average maximum value of equivalent plastic strain as a function of strain rate and temperature, for both mixtures. A general trend of decreasing $\xi_{p\,lim}$ with increasing strain rate and decreasing temperature can be observed for both the DBM and HRA mixtures. This plot highlights the difference in the level of straining exhibited by the two asphalt mixtures. In accordance with the experimental results presented in Chapter 5, which demonstrated that the HRA mixture exhibited larger peak strains than the DBM mixture, the value of $\xi_{p\,lim}$ for the HRA mixture was observed to be larger than that for the DBM mixture, for equivalent test conditions.

Figure 6.26 shows a plot of the trend in the average value of parameter c, as determined through non-linear regression analysis, with respect to changes in strain rate and temperature, as a function of equivalent plastic strain, for both of the mixture types. A trend of increasing c with increasing strain rate and decreasing temperature (increased stiffness) is exhibited for both mixtures. This is related to accumulation of ξ_p during the inelastic hardening phase. It was observed that as the strain rate increased and/or the temperature decreased the accumulation of equivalent plastic strain decreased, Figure 6.25 and 6.27(a). This is reflected in the pronounced curvature of the α - ξ_p plots for such test conditions, Figure 6.27(b), thus, resulting in increases in the value of parameter c with increases in mixture stiffness. It was found that for equivalent test conditions the HRA mixture exhibited greater levels of $\xi_{p\,lim}$, see Figure 6.25, than was exhibit by the DBM mixture. Therefore, as the magnitude

of parameter α was approximately the same for both mixture types, Figure 6.24, the increased level of ξ_p exhibited by the HRA mixture resulted in greater curvatures of the α - ξ_p plots for equivalent test conditions, and hence the HRA mixture is characterised by larger values for parameter c than those determined for the DBM mixture. This is reflected in Figure 6.26, which shows the values of parameter c for the HRA mixture to generally exceed those for the DBM mixture, for equivalent test conditions. The observed rapid increase in the value of the parameter for the $0.1s^{-1}$, 5°C data is a result of the brittle type response of the mixtures under these test conditions, which result in a large elastic region, followed by rapid failure. Such response is characterised by only slight inelastic hardening, and therefore the accumulation of ξ_p is small, resulting in large curvatures of the α - ξ_p plot and hence large values for parameter c.

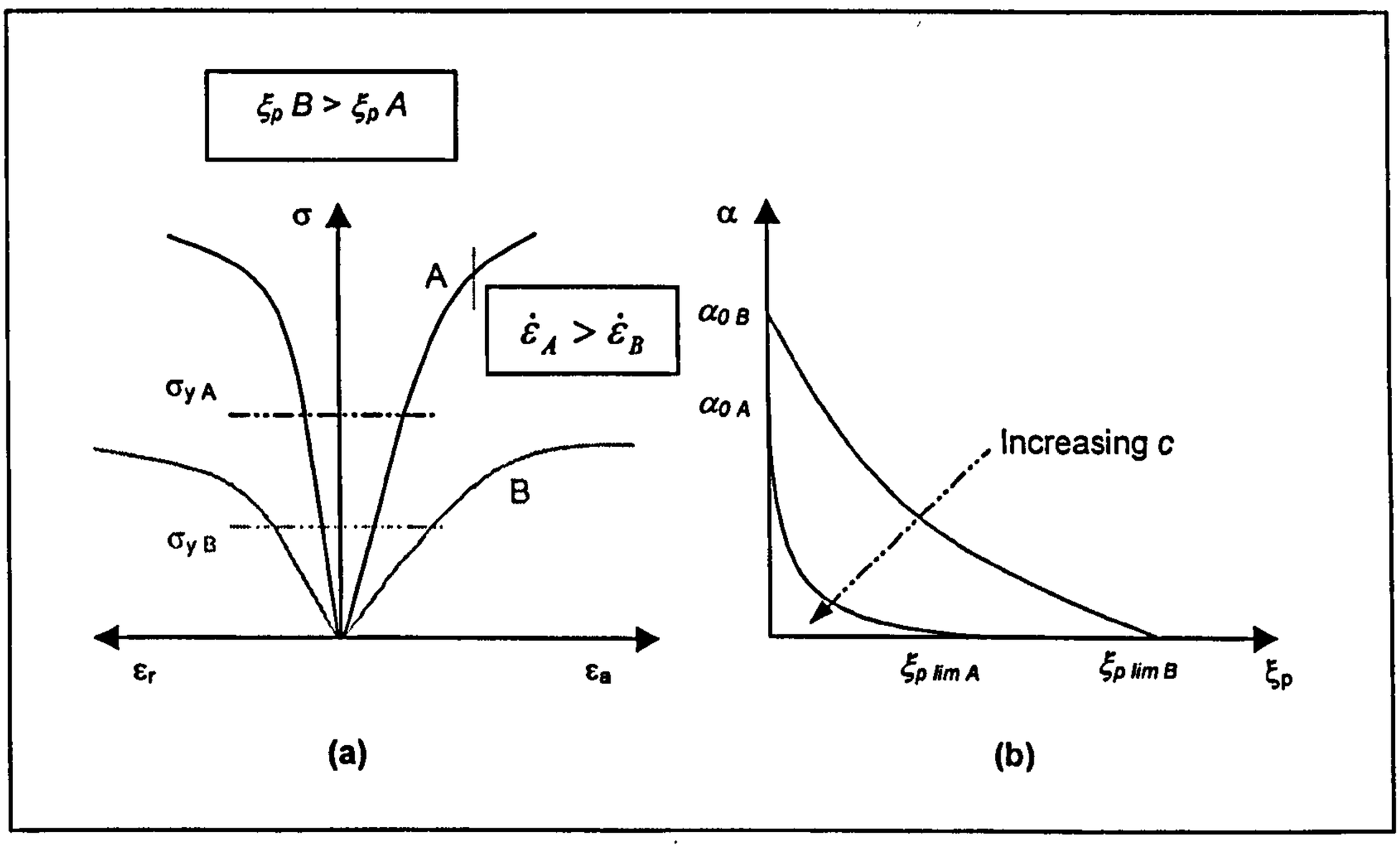

Figure 6.27: Diagram showing the influence of the accumulation of equivalent plastic strain on the value of parameter c

6.7 Material Softening Function – Model Parameter γ

During post peak response parameter γ is used to control the softening response of the Desai surface that is used to simulate the overall material strength reduction observed during compressive loading, see Section 3.3.3. Taking the initial value for γ as that

given in Tables 6.2 and 6.3, γ is re-evaluated for all states of stress during the response degradation phase (Figure 5.9, Part four), using Equation (6.3).

6.7.1 Expression for the Softening Function

By specifying γ as a decreasing function of some physical increasing quantity, the strain rate and the temperature, the size of the successive Desai flow surfaces can be diminished. In this study, in analogy to the hardening response, post fracture plastic work and post fracture equivalent plastic strain have been investigated as suitable physical quantities by which γ can be specified. In the current formulation of the ACRe model the expression given in Equation (6.9) is used to specify γ degradation.

$$\gamma = \eta \cdot \gamma_f + (1-\eta) \cdot \gamma_r \tag{6.9}$$

in which, η, is specified as a function of post fracture plastic work:

$$\eta = \left(1 + \mathrm{K} \cdot W_{pf}\right) \cdot e^{-\mathrm{K} W_{pf}} \tag{6.9a}$$

or, as a function of post fracture equivalent plastic strain [Erkens *et al.*, 2000b]:

$$\eta = \left(1 + \kappa \cdot \xi_{pf}\right) \cdot e^{-\kappa \xi_{pf}} \tag{6.9b}$$

where,

γ_f = initial gamma value (see Tables 6.2 and 6.3)

γ_r = $A \cdot \gamma_f$, the residual value for gamma (experimentally determined)

κ, K, A = material parameters

W_{pf} = current level of post fracture plastic work

ξ_{pf} = current level of post fracture equivalent plastic strain

6.7.2 Parameter γ as a Function of Post Fracture Plastic Work

The average values given in Tables 6.2 and 6.3 for the initial values of parameter γ range from 0.043 – 0.163 for the DBM mixture and 0.084 – 0.206 for the HRA

mixture. Therefore, to facilitate a comparison of the parameter as a function of temperature and strain rate, γ was normalised with respect to the initial gamma value, γ_f, for each of the test conditions, as given in Equation (6.10).

$$\gamma_{norm} = \frac{\gamma}{\gamma_f} \tag{6.10}$$

where, γ_{norm} = normalised gamma

Figures 6.28 and 6.29 show typical plots of normalised γ versus the post fracture plastic work as a function of temperature and strain rate, in which the post fracture plastic work is given by Equation (6.11).

$$W_{pf} = \int \sigma \cdot d\varepsilon_{pf} \tag{6.11}$$

where, $d\varepsilon_{pf}$ = post fracture plastic strain

From Figures 6.28 and 6.29 it is possible to observe the strain rate and temperature dependent sensitivity of W_{pf}. A trend of increasing levels of post fracture plastic work with increasing strain rate and decreasing temperature was found for both mixtures. The figures show the response exhibited by the DBM and HRA mixtures during the post fracture phase of the material response. At low stiffness conditions (slow strain rates and high temperatures) both mixtures responded similarly, exhibiting a rapid and approximately linear reduction in material strength. However, for high stiffness conditions (fast strain rates and low temperatures) the post fracture response of the two mixtures is different. The DBM mixture maintains an approximately linear decline in mixture strength, but the rate of decline decreases with increasing mixture stiffness, this is the result of the increasingly greater levels of plastic work expended during this phase of material response. Whereas, the HRA mixture displays a less pronounced decrease in the rate of material strength loss over the full range of test conditions, but exhibits increasing non-linear rates of strength reduction with increases in mixture stiffness.

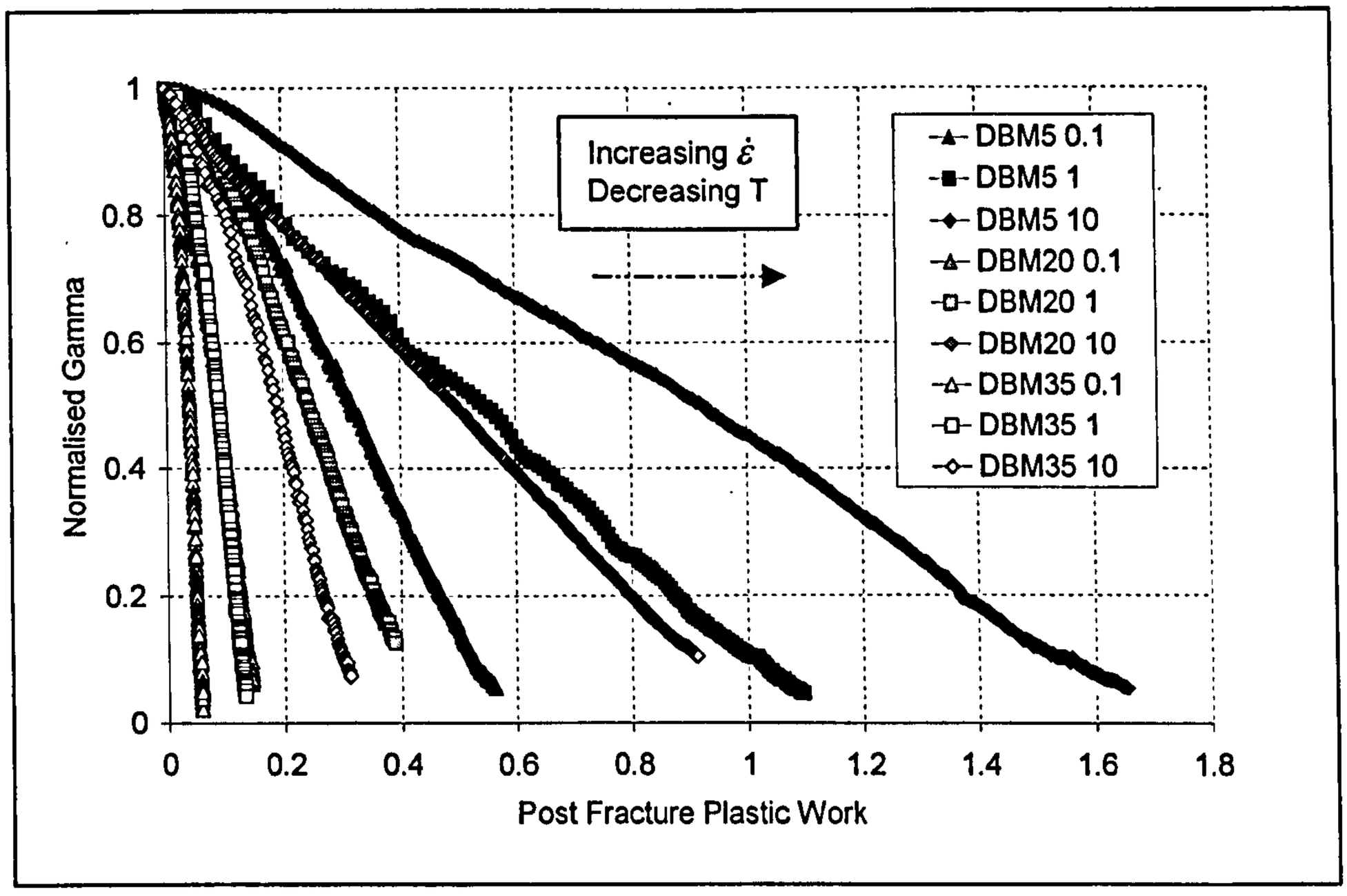

Figure 6.28: Typical plot of normalised γ versus post fracture plastic work, as a function of strain rate and temperature – DBM mixture

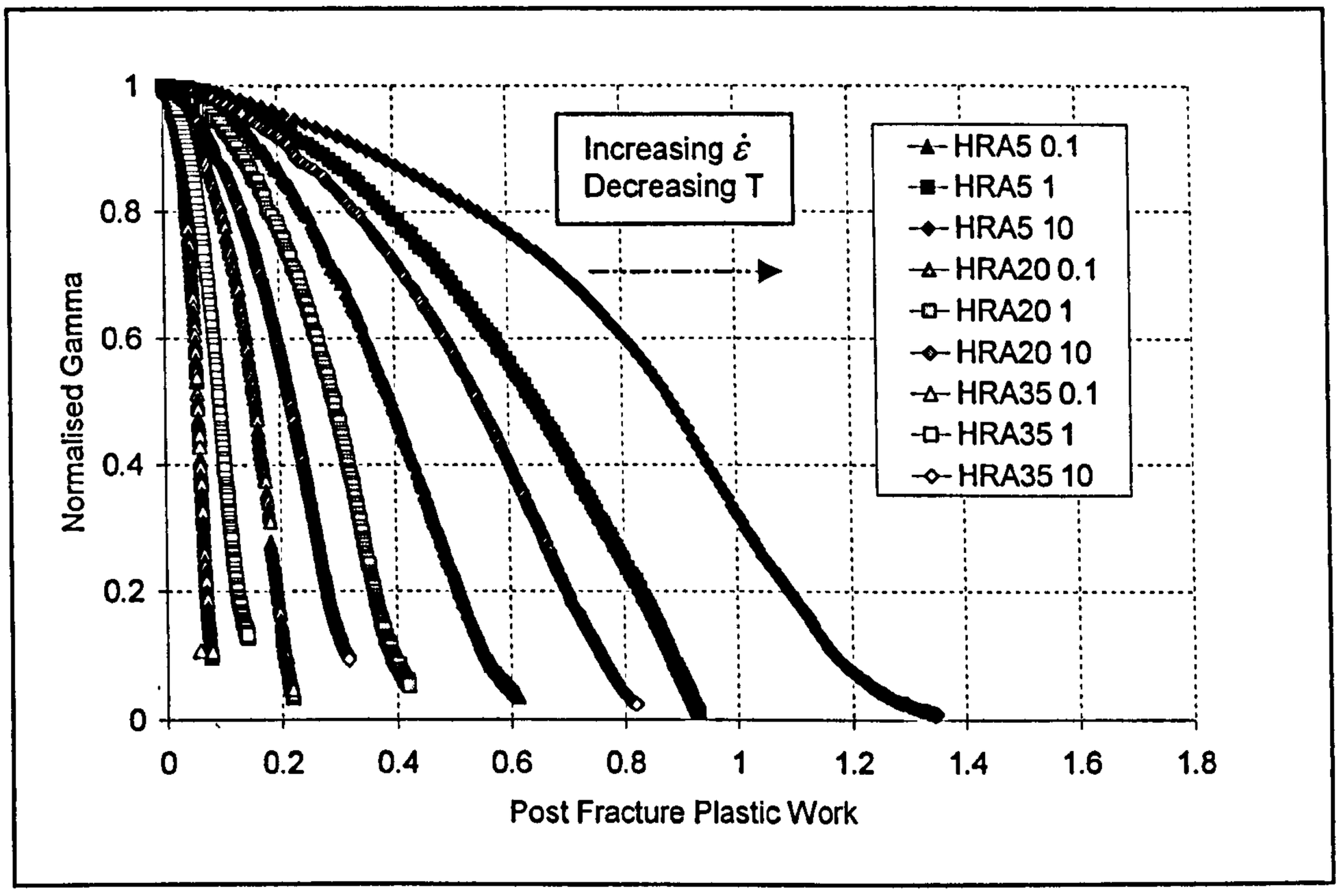

Figure 6.29: Typical plot of normalised γ versus post fracture plastic work, as a function of strain rate and temperature – HRA mixture

Using the 'Table Curve 2D' [SPSS Inc, 1996] software to perform non-linear regression of Equation (6.9a) over the experimental data allowed average values for the softening function parameters to be determined, as a function of post fracture plastic work, for each set of test conditions. These average values are given in Tables 6.11 and 6.12 for the DBM and HRA mixtures respectively, and the parameter K and A are shown graphically in Figures 6.30 and 6.31.

Table 6.11: Average values for the softening function parameters given in Equation (6.9a), derived as a function of post fracture plastic work – DBM

T (°C)	$\dot{\varepsilon}$ (s^{-1})	γ_f	A	K
5	0.001	0.0031	0.0727	6.37
	0.01	0.0031	0.0401	3.87
	0.1	0.0061	0.0425	2.32
20	0.001	0.0060	0.0823	22.05
	0.01	0.0047	0.0953	8.72
	0.1	0.0041	0.0875	4.64
35	0.001	0.0103	0.0638	57.02
	0.01	0.0074	0.0648	23.29
	0.1	0.0068	0.0749	10.18

Table 6.12: Average values for the softening function parameters given in Equation (6.9a), derived as a function of post fracture plastic work – HRA

T (°C)	$\dot{\varepsilon}$ (s^{-1})	γ_f	A	K
5	0.001	0.0034	0.0407	5.50
	0.01	0.0022	0.0274	3.49
	0.1	0.0019	0.0135	3.01
20	0.001	0.0088	0.0514	15.18
	0.01	0.0042	0.0339	7.67
	0.1	0.0023	0.0240	3.80
35	0.001	0.0157	0.0773	58.67
	0.01	0.0139	0.0791	20.93
	0.1	0.0134	0.0939	10.63

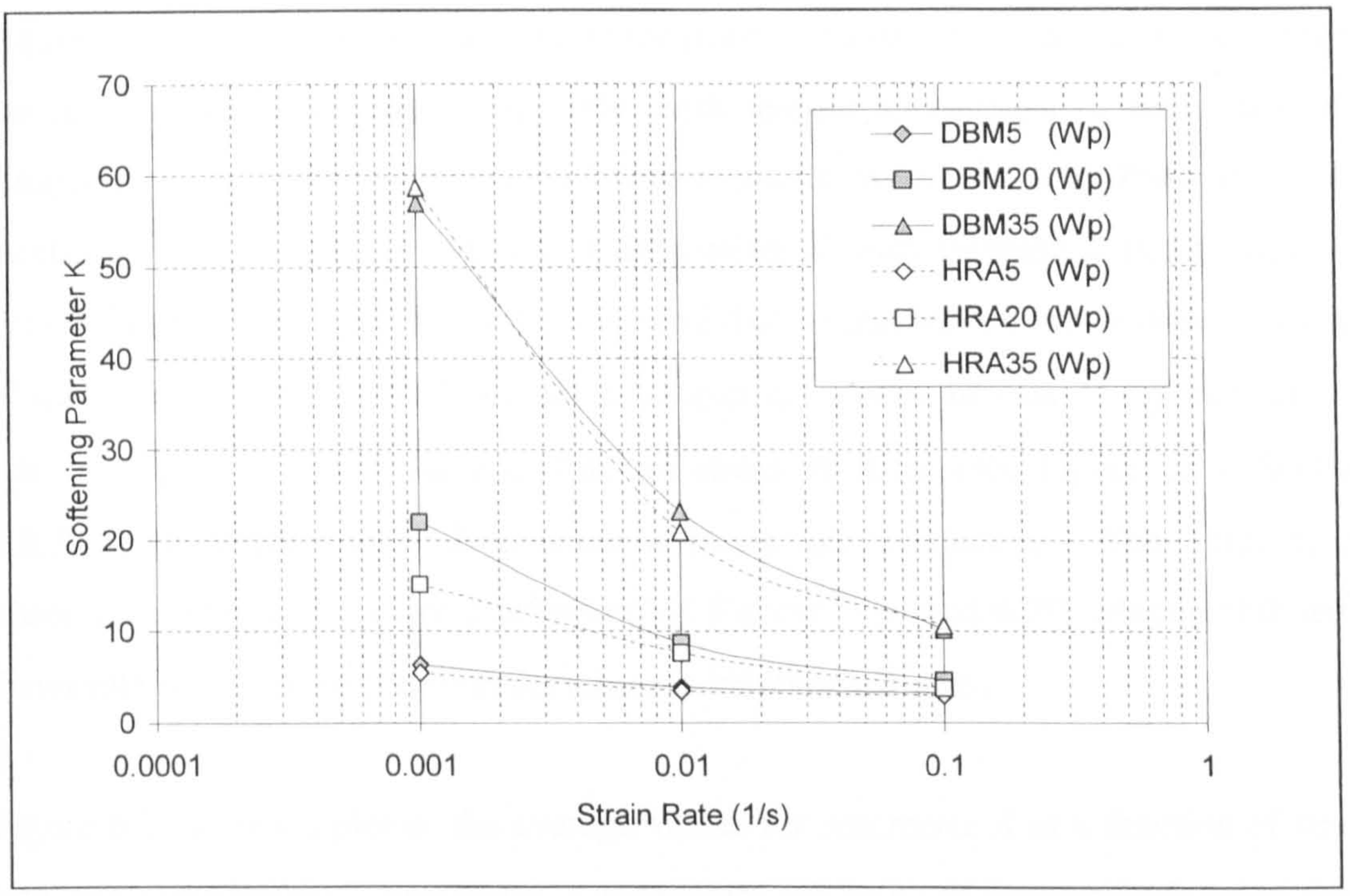

Figure 6.30: Plot showing the trend in the average values for the softening function parameter *K*, as a function of post fracture plastic work, with respect to changes in strain rate and temperature – DBM and HRA mixtures

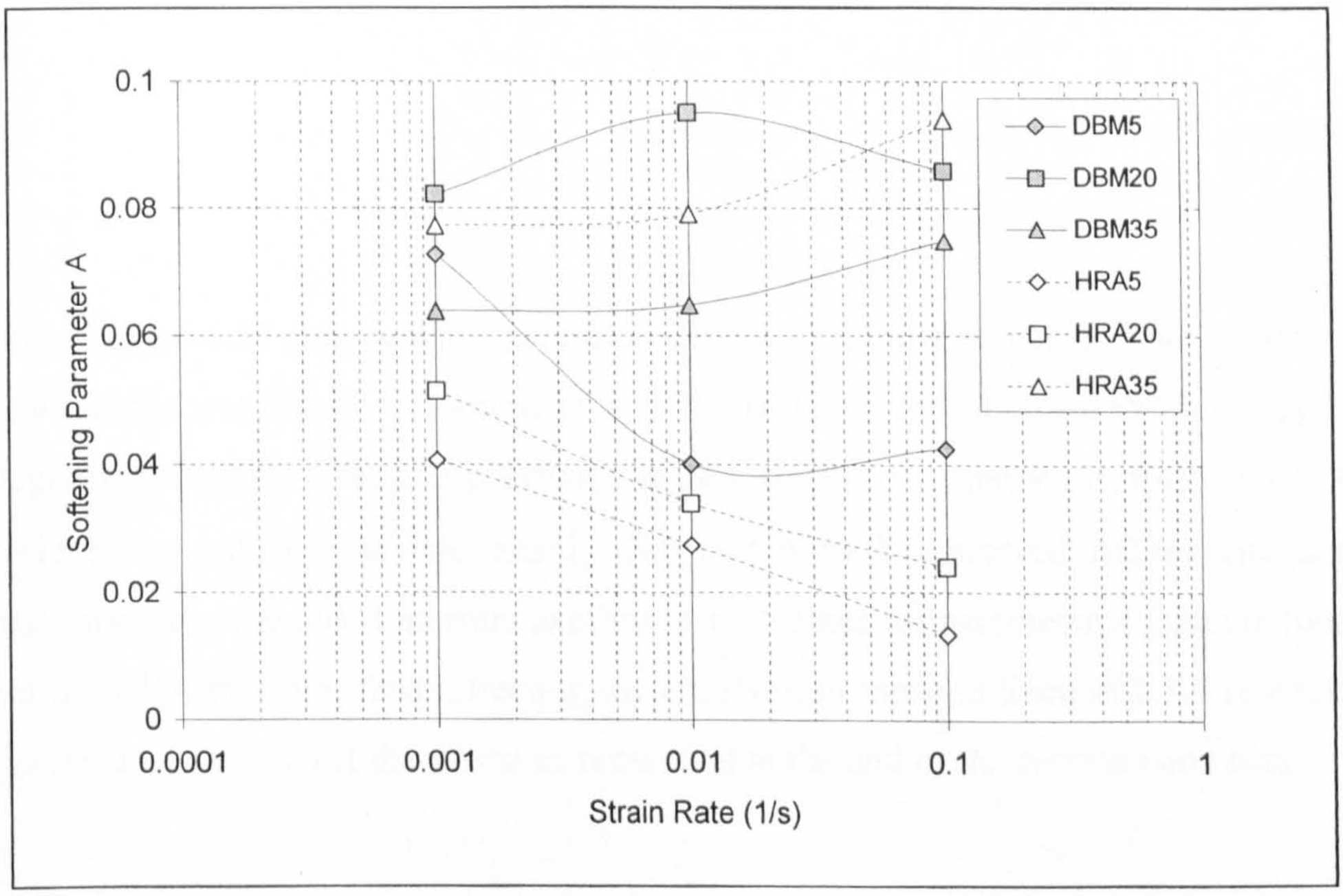

Figure 6.31: Plot showing the trend in the average values for the softening function parameter *A*, with respect to changes in strain rate and temperature – DBM and HRA mixtures

Figure 6.30 shows a plot of the trend in the average value for parameter K, determined through non-linear regression analysis, with respect to changes in strain rate and temperature, as a function of post fracture plastic work, for the DBM and HRA mixture. The plot shows a trend of decreasing K with increasing strain rates and decreasing temperatures. It can be observed that similar values are obtained for each of the mixtures. In the ACRe model parameter K (or κ in the case of ξ_{pf}) controls the rate of degradation of γ for post fracture states of stress (see Figure 6.53, Section 6.8.3), with larger values designating a faster rate of decline. The trend in K, observed above, is therefore a reflection of Figures 6.28 and 6.29, which exhibited a faster rate of γ degradation with decreases in mixture stiffness.

Figure 6.31 shows a plot of the average values for parameter A as a function of strain rate and temperature. Parameter A represents the ratio of the residual value for γ (proportional to residual strength) to the maximum value for γ (proportional to peak strength) as given in Equation (6.12), where γ_r and γ_f are determined from the experimental data.

$$A = \frac{\gamma_r}{\gamma_f} \tag{6.12}$$

From Figure 6.31 it is evident that no consistent strain rate or temperature dependent relationship was found for parameter A. This is due to the variation exhibited by the degradation phase of the compression test data, shown in Appendix E, from which the residual strength, γ_r, was determined. However, it can be observed that for equivalent test conditions the DBM mixture exhibits larger values for parameter A than are found for the HRA mixture; thus reflecting the observation made in Section 5.3.2 regarding the residual strength of the mixtures remaining at the end of the compression test.

6.7.3 Parameter γ as a Function of Post Fracture Equivalent Plastic Strain

Figures 6.32 and 6.33 show typical plots of normalised γ versus the post fracture equivalent plastic strain, as a function of temperature and strain rate, for the DBM and HRA mixtures respectively, in which the post fracture equivalent plastic strain is

given by Equation (6.13).

$$\xi_{pf} = \int \left(d\varepsilon_{ij}^{pf} \cdot d\varepsilon_{ij}^{pf} \right)^{\frac{1}{2}} \tag{6.13}$$

From these figures a general insensitivity of ξ_{pf} to temperature and strain rate can be observed for both the DBM and HRA mixtures. This is inferred from the close grouping and the slopes of the descending response curves, which for an individual mixture exhibited more or less the same gradient for all test conditions (also see Figure 6.34 showing average values of parameter κ). These observations indicated that during post fracture response, the effect of the test conditions on the level of straining exhibited by the asphalt mixtures was negligible. This may have resulted from the discontinuous nature of the test specimens, due to the opening of internal cracks, during this phase of material response.

Although approximately similar responses were observed for each of the test conditions for each mixture, overall the HRA data exhibited a slightly faster rate of response degradation.

Non-linear regression of Equation (6.9b) over the experimental data allowed average values for the softening function parameters to be determined as a function of post fracture equivalent plastic strain, for each set of test conditions. These average values are given in Tables 6.13 and 6.14 for the DBM and HRA mixtures respectively and the average values for parameter κ, determined through non-linear regression analysis, as a function of post fracture equivalent plastic strain is shown graphically in Figure 6.34.

From Figure 6.34 it can be seen that the approximate independence of ξ_{pf} to changes in strain rate and temperature, that was evident from Figures 6.32 and 6.33 is reflected in the values determined for parameter κ, which show no consistent strain rate or temperature depended trends. Although, on average the HRA mixture exhibits larger values, thus supporting the earlier observation that the rate of γ degradation is faster for the HRA mixture.

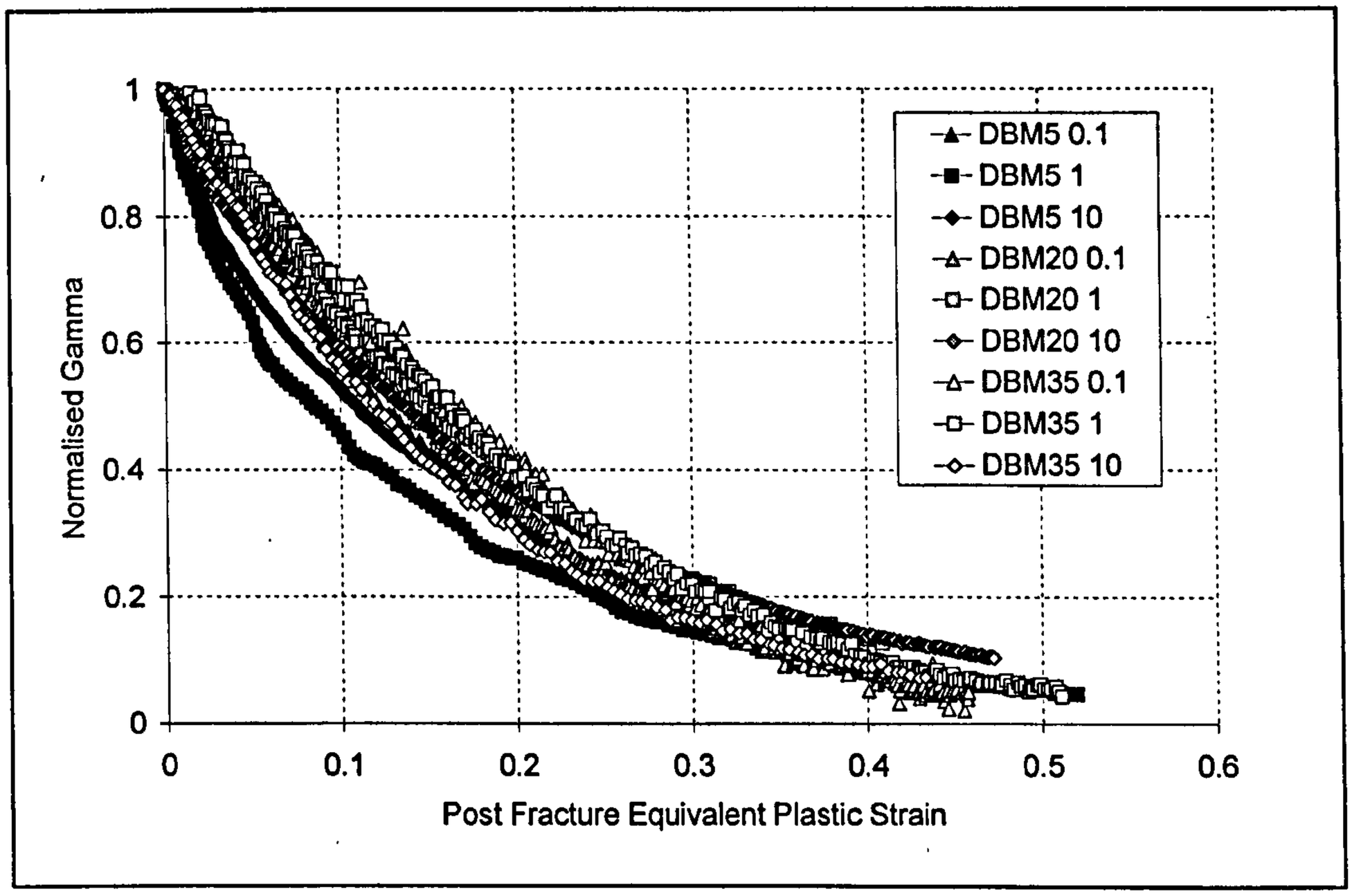

Figure 6.32: Typical plot of normalised γ versus equivalent post fracture plastic strain, as a function of strain rate and temperature – DBM mixture

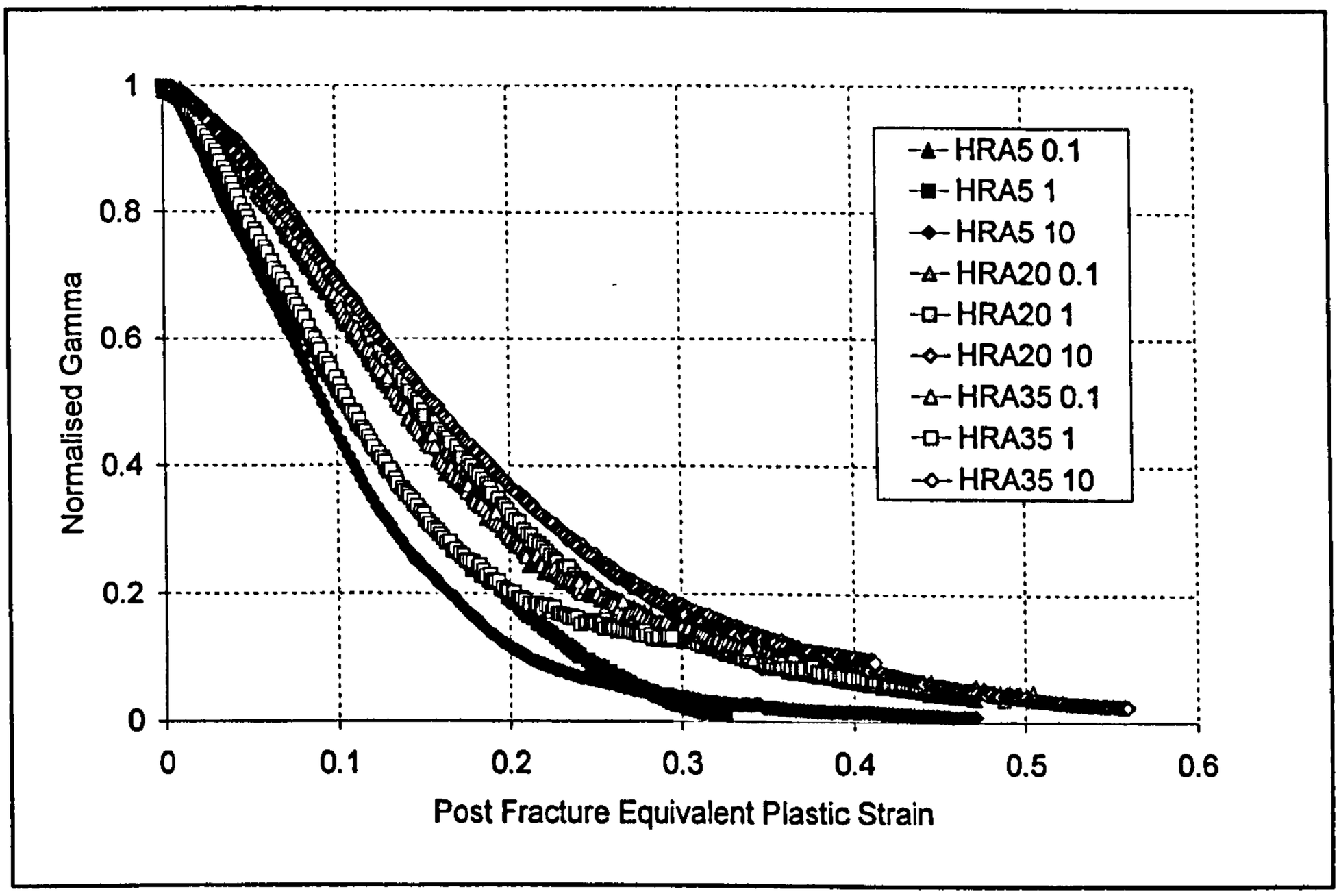

Figure 6.33: Typical plot of normalised γ versus equivalent post fracture plastic strain, as a function of strain rate and temperature – HRA mixture

Table 6.13: Average values for the softening function parameters given in Equation (6.9b), derived as a function of post fracture equivalent plastic strain – DBM mixture

T (°C)	$\dot{\varepsilon}$ (s^{-1})	γ_f	A	κ
5	0.001	0.0031	0.0727	12.85
	0.01	0.0031	0.0401	17.49
	0.1	0.0061	0.0425	14.43
20	0.001	0.0060	0.0823	11.48
	0.01	0.0047	0.0953	12.93
	0.1	0.0041	0.0875	14.69
35	0.001	0.0103	0.0638	11.26
	0.01	0.0074	0.0648	11.26
	0.1	0.0068	0.0749	12.45

Table 6.14: Average values for the softening function parameters given in Equation (6.9b), derived as a function of post fracture equivalent plastic strain – HRA mixture

T (°C)	$\dot{\varepsilon}$ (s^{-1})	γ_f	A	κ
5	0.001	0.0034	0.0407	13.41
	0.01	0.0022	0.0274	17.39
	0.1	0.0019	0.0135	18.86
20	0.001	0.0088	0.0514	12.45
	0.01	0.0042	0.0339	12.76
	0.1	0.0023	0.0240	11.46
35	0.001	0.0157	0.0773	15.41
	0.01	0.0139	0.0791	15.24
	0.1	0.0134	0.0939	13.03

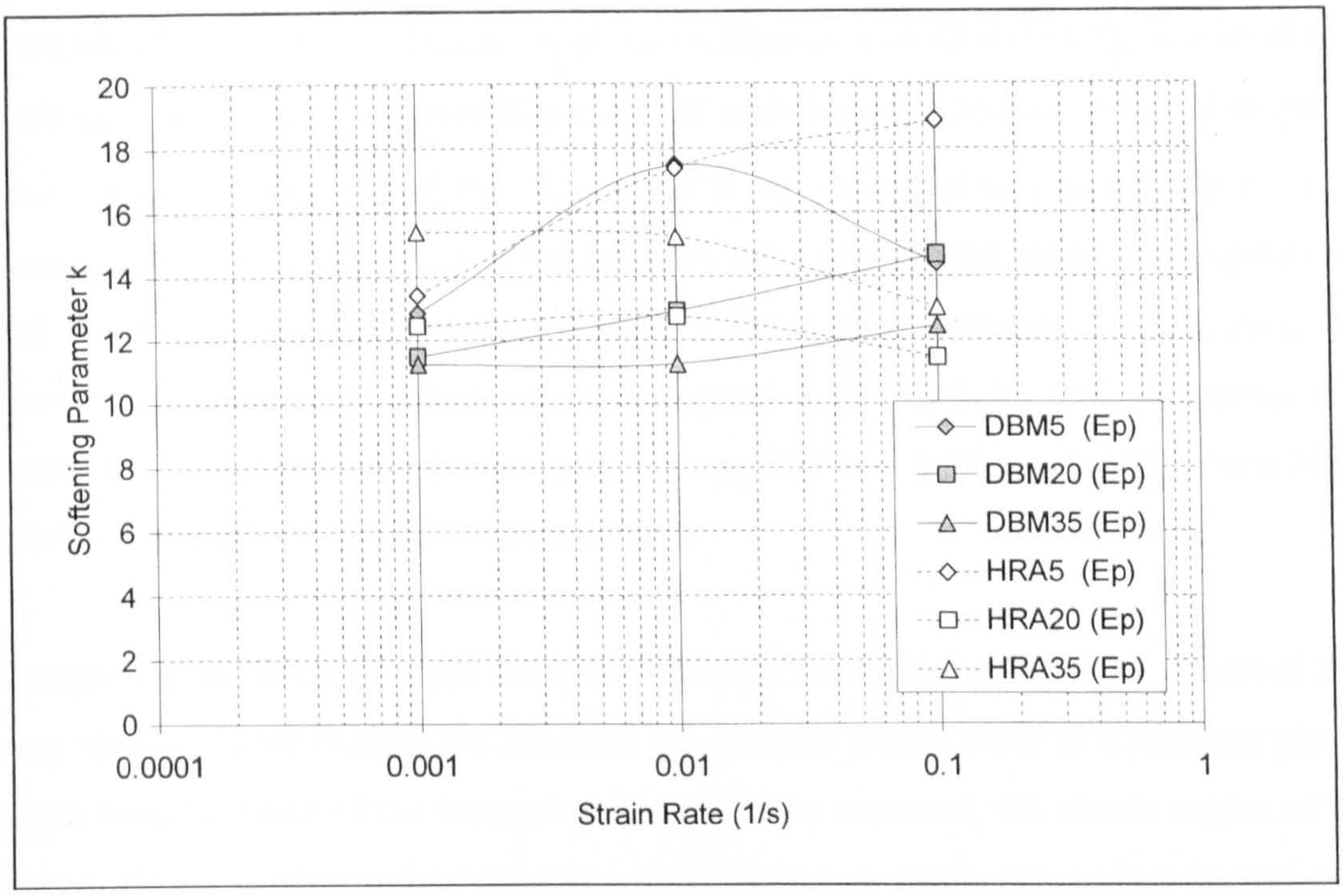

Figure 6.34: Plot showing the trend in the values for the softening function parameter κ, derived as a function of post fracture equivalent plastic strain, with respect to changes in strain rate and temperature – DBM and HRA mixtures

6.8 Simulation of Asphalt Mixture Response

Before the model is implemented in the FE code INSAP and used to simulate asphalt mixture performance in pavement structures, it is desirable to verify the predictive capabilities of the model using the derived material parameters. This has been achieved through assessment of the model flow surface characteristics and simulation of the laboratory tests that were used to compute the model parameters.

6.8.1 Characteristics of the Model Flow Surface

The characteristics of the Desai flow surface can be assessed using the model material parameters derived in this chapter. The peak response, or failure parameters, R and γ are given in Tables 6.2 and 6.3 for the DBM and HRA mixtures respectively and the values for the phase change parameter, n, are given in Table 6.6. The hardening function for α has been evaluated both as a function of plastic work and as a function of equivalent plastic strain, the parameters for which are given in Tables 6.7 and 6.9 for the DBM mixture and in Tables 6.8 and 6.10 for the HRA mixture respectively.

Evaluating the hardening functions, given in Equations (6.6) and (6.7), at their elastic limit (i.e. W_p or $\xi_p = 0$) gives the value of α delimiting inelastic material response (α_0). This allows plots of the flow surface (or yield surface) delimiting inelastic material response to be constructed for both mixtures, for the range of temperatures and strain rates investigated in this study. These plots (compression negative) are shown as a function of plastic work in Figures 6.35 and 6.36, and are shown as a function of equivalent plastic strain in Figures 6.37 and 6.38 for the DBM and HRA mixtures respectively, for all test conditions.

Comparing the fields of yield surfaces shown in these figures it can be observed that very similar elastic regions are obtained using either plastic work or equivalent plastic strain specifications of the hardening function. As expected, the elastic region of the flow surfaces is observed to expand with increases in strain rate and/or decreases in temperature (increase in mixture stiffness) for both the DBM and HRA mixtures. Contrasting the shapes of the yield surfaces for the two mixtures it can be seen that at 5°C they are similar, but as the temperature increases, the surfaces for the HRA mixture become compact but more erect compared to the more elongated but shallower surfaces for the DBM mixture. This is demonstrated more clearly in Figures 6.39 to 6.44, which show detailed plots of the fields of yield surfaces (as a function of equivalent plastic strain) at each test temperature, for the range of strain rates investigated in the study. Also marked on these plots are the uniaxial compression and tension stress paths and the corresponding failure envelopes at each of the test conditions. From Figures 6.39 to 6.44 the following important observations can be made with regard to the characteristics of the model flow surfaces using the parameters derived from the experimental work undertaken in this thesis.

- For all uniaxial compressive test conditions, for both mixtures, it can be observed that the flow surface exhibits growth potential (from the edge of the elastic zone, or yield surface, up to failure surface), and is therefore suitable for modelling the observed compressive hardening response of asphalt mixtures.
- For all uniaxial tensile test conditions, for both mixtures, it can be observed that the elastic zone (yield surface) and the failure surface coincide, and therefore the flow surface exhibits no potential for growth in the tensile zone.

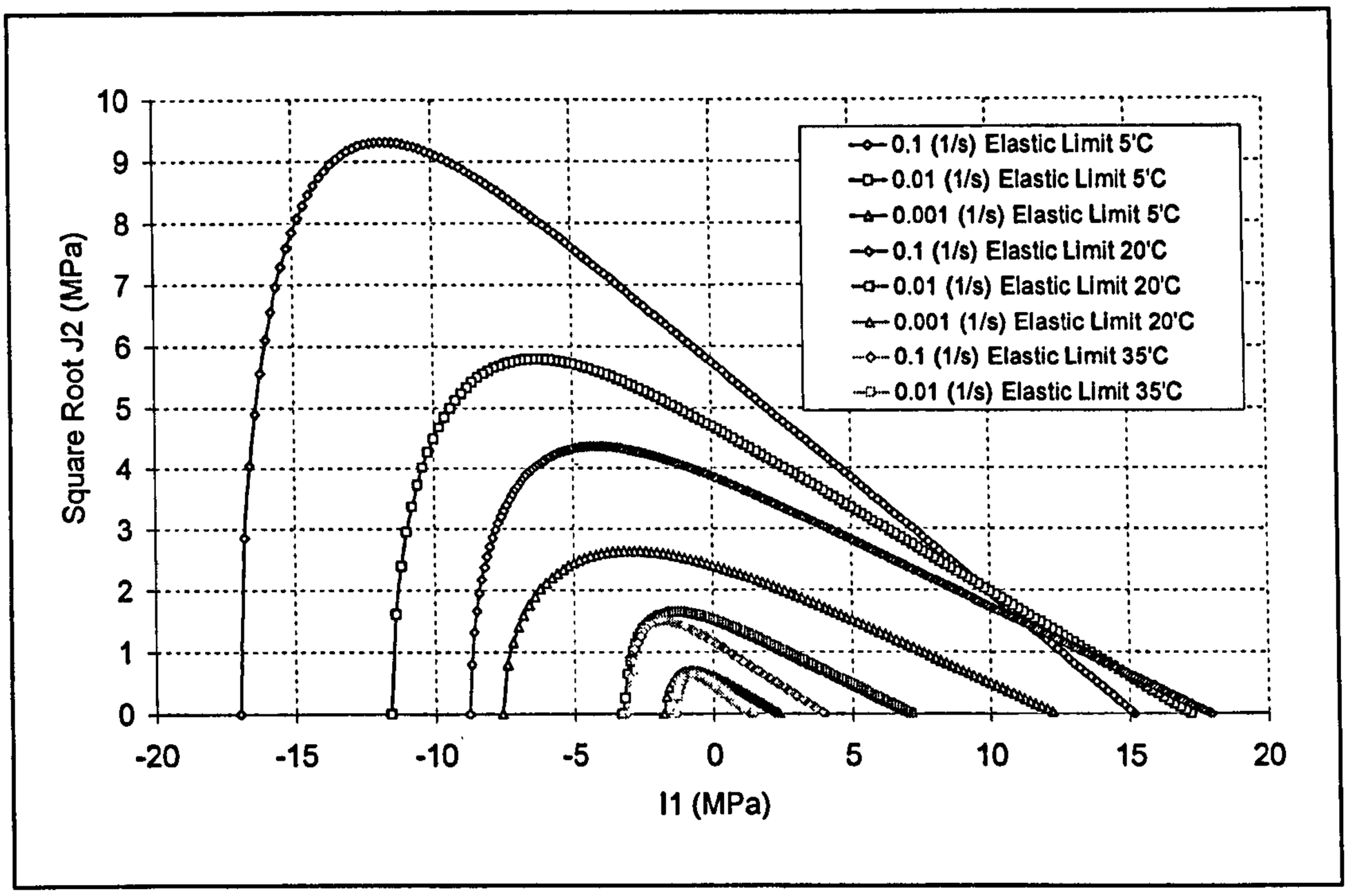

Figure 6.35: Yield surfaces showing elastic limit for DBM mixture derived as a function of plastic work

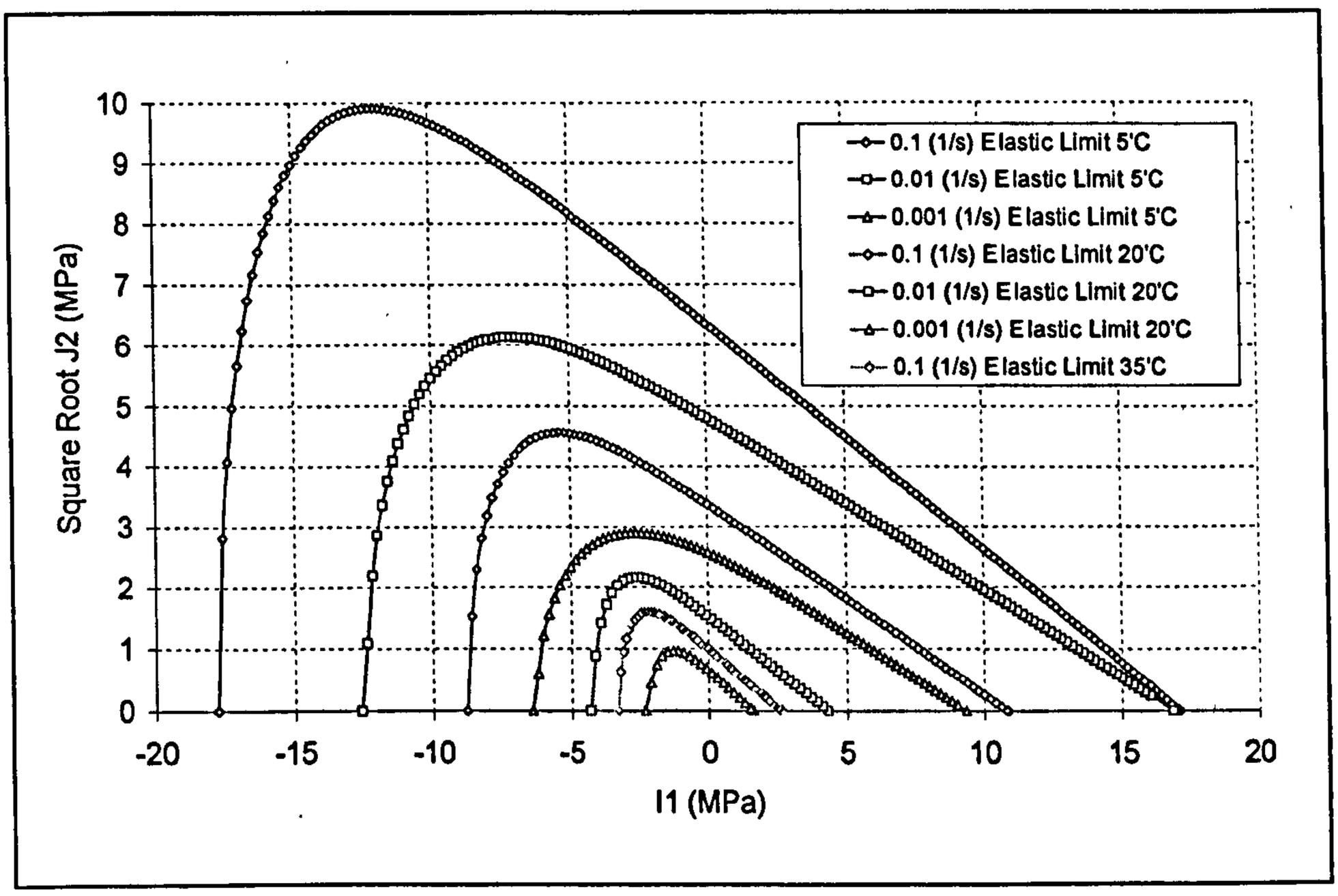

Figure 6.36: Yield surfaces showing elastic limit for HRA mixture derived as a function of plastic work

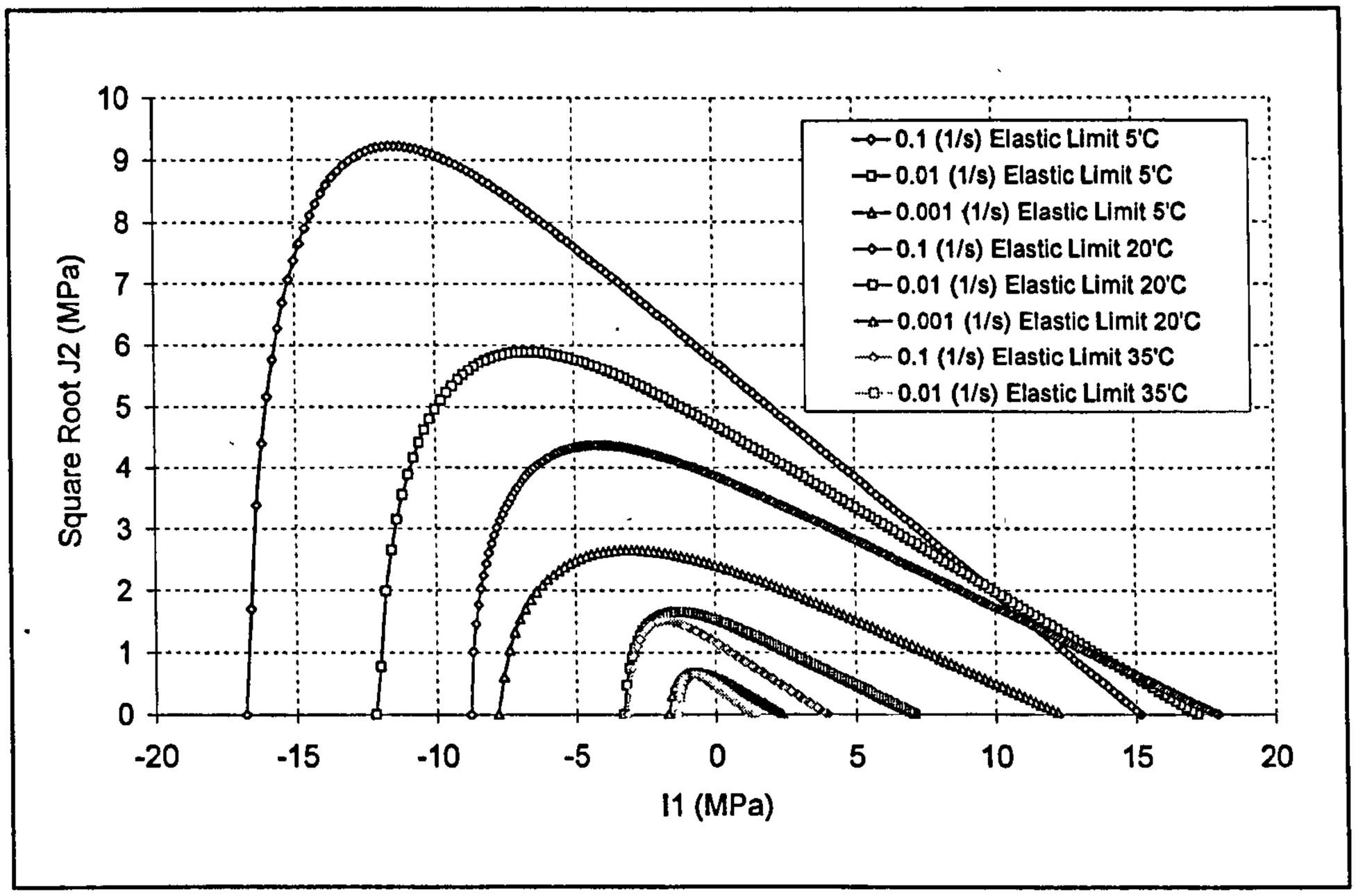

Figure 6.37: Yield surfaces showing elastic limit for DBM mixture derived as a function of equivalent plastic strain

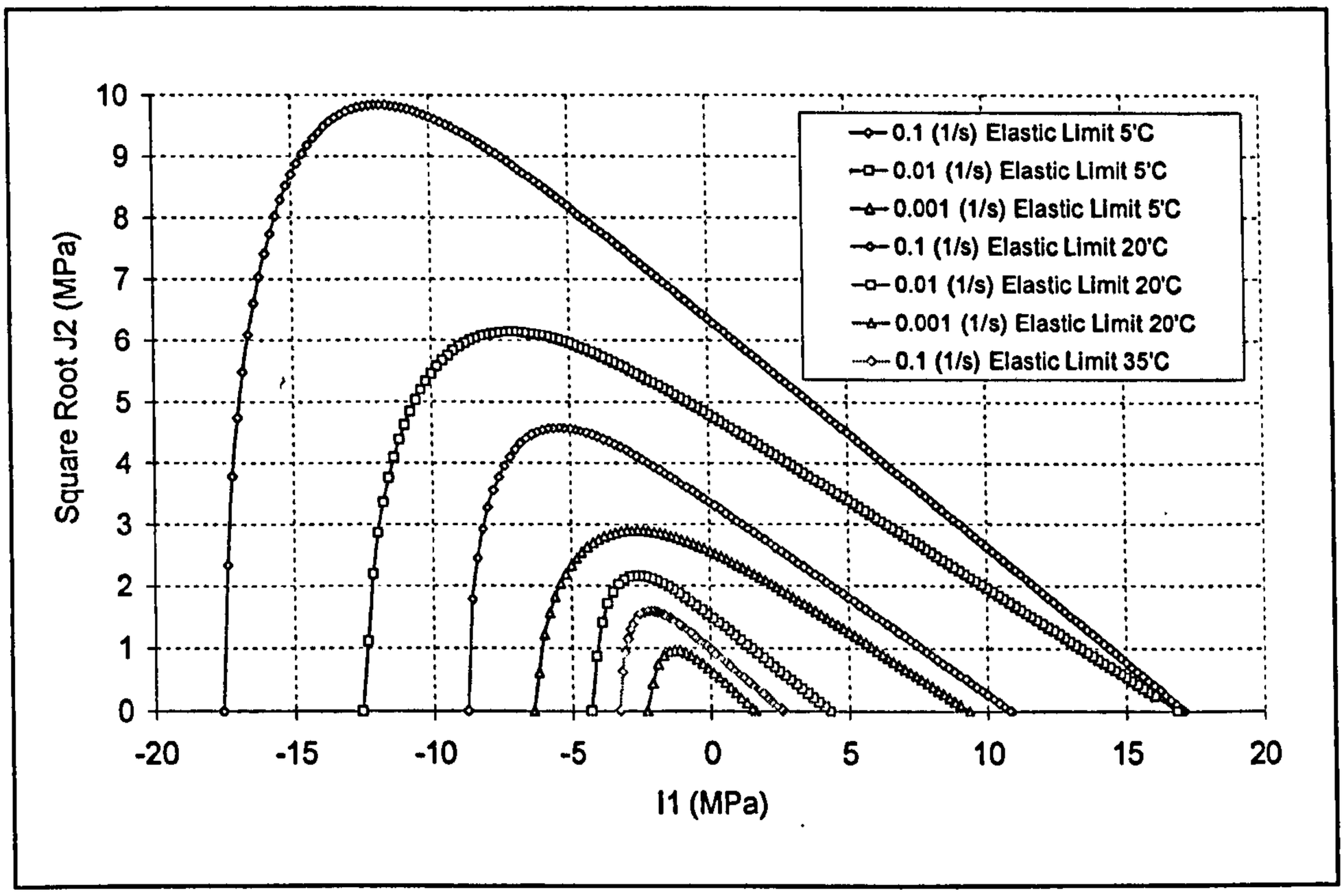

Figure 6.38: Yield surfaces showing elastic limit for HRA mixture derived as a function of equivalent plastic strain

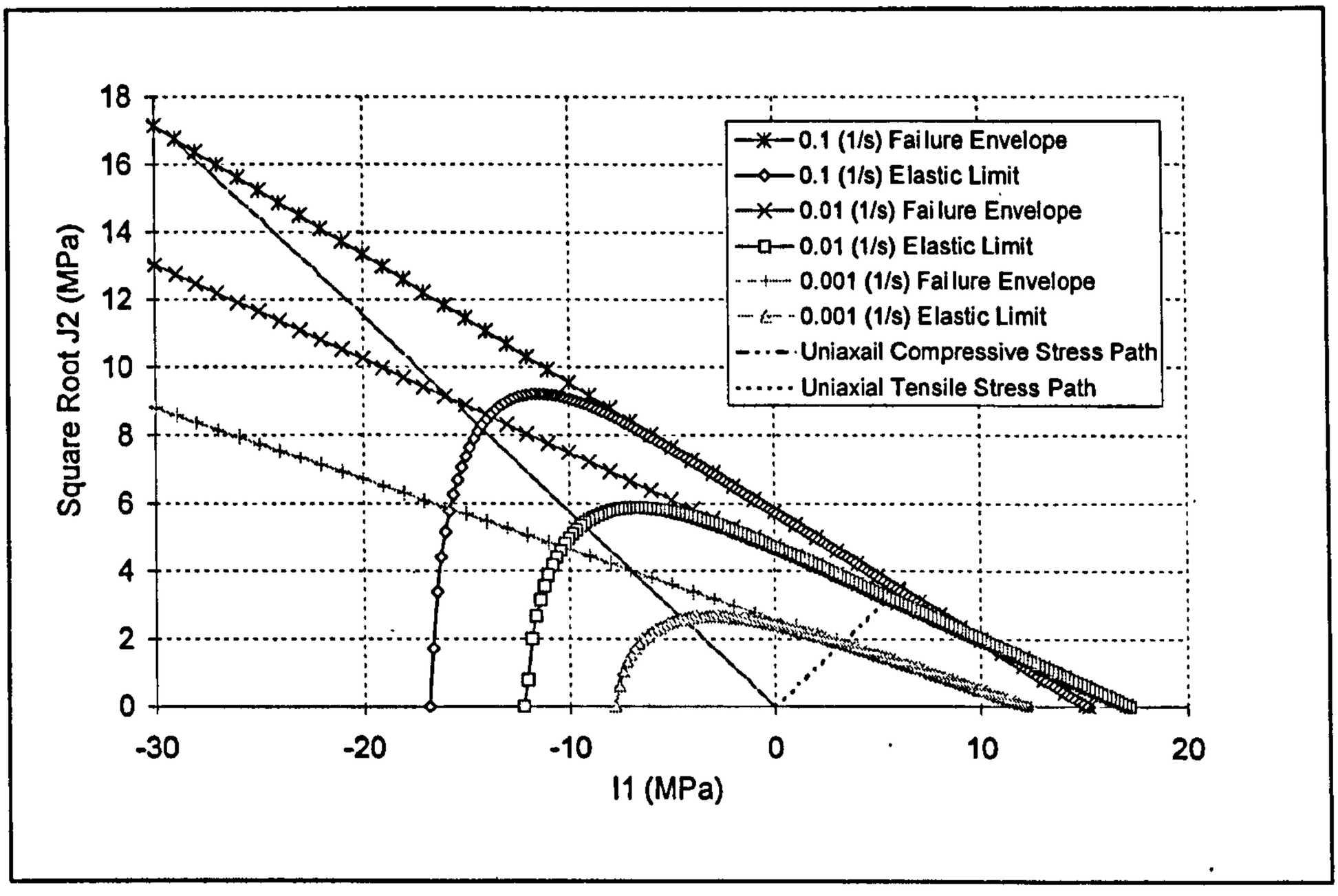

Figure 6.39: Yield surfaces and failure envelopes – DBM mixture at 5°C

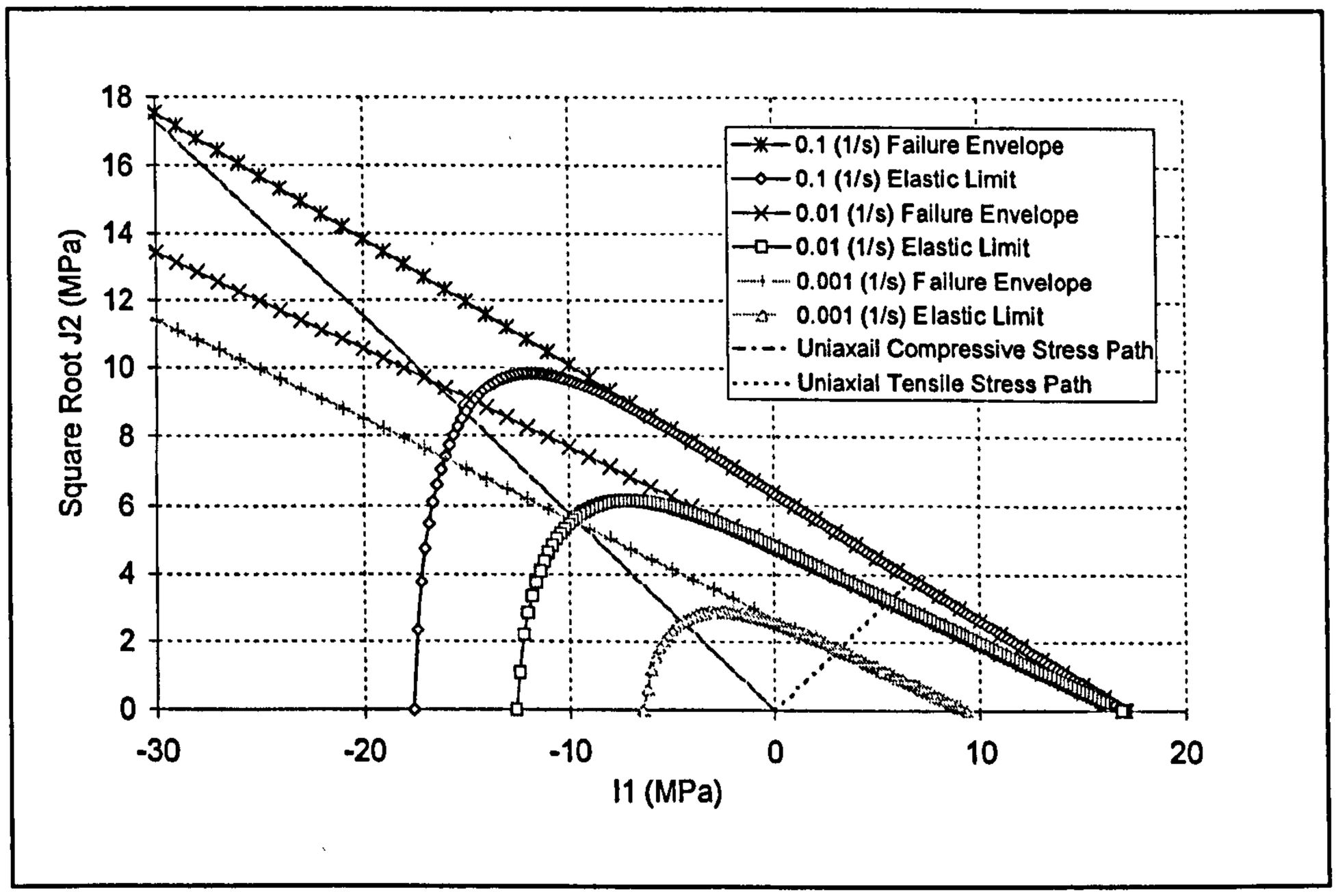

Figure 6.40: Yield surfaces and failure envelopes – HRA mixture at 5°C

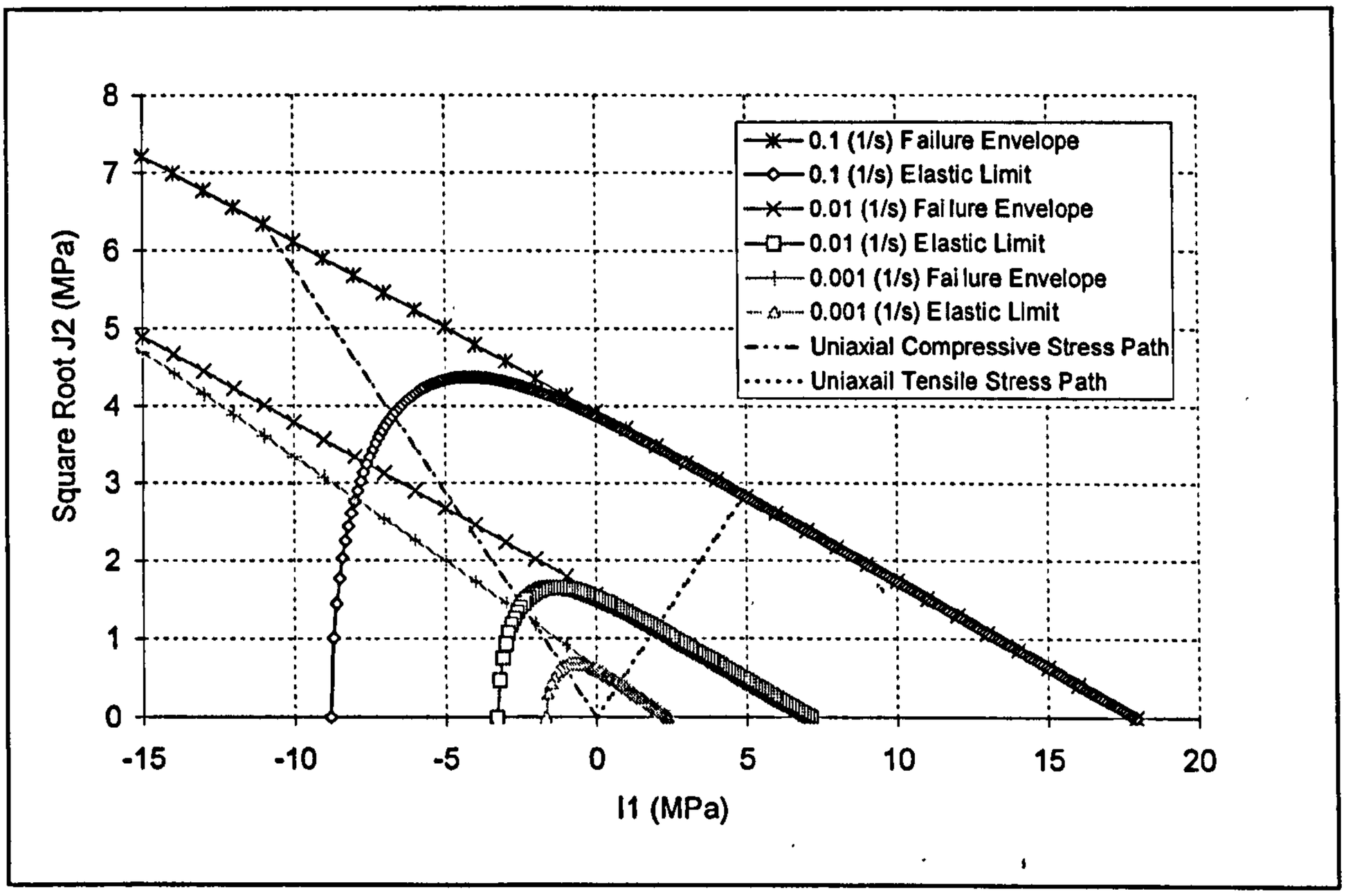

Figure 6.41: Yield surfaces and failure envelopes – DBM mixture at 20°C

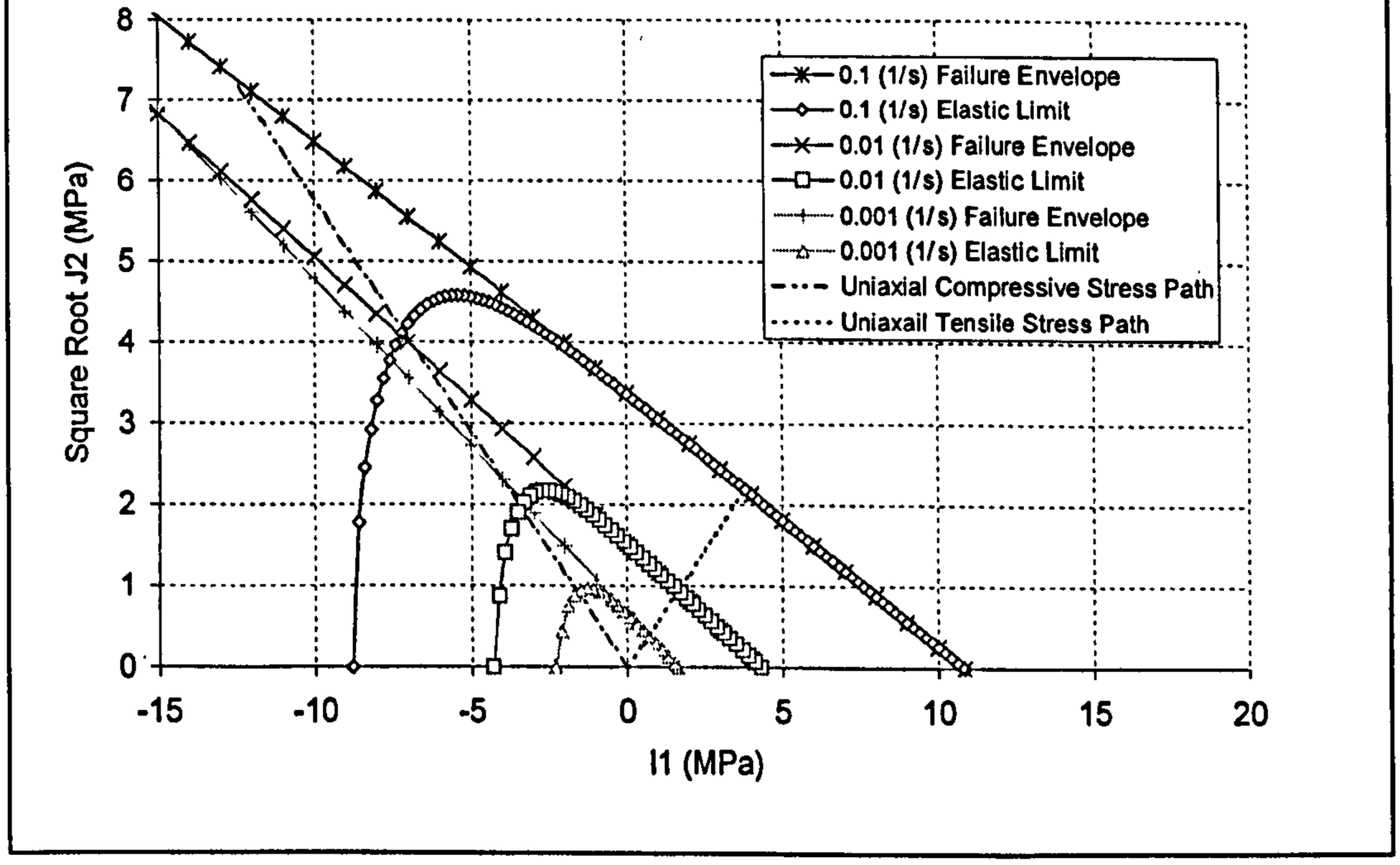

Figure 6.42: Yield surfaces and failure envelope – HRA mixture at 20°C

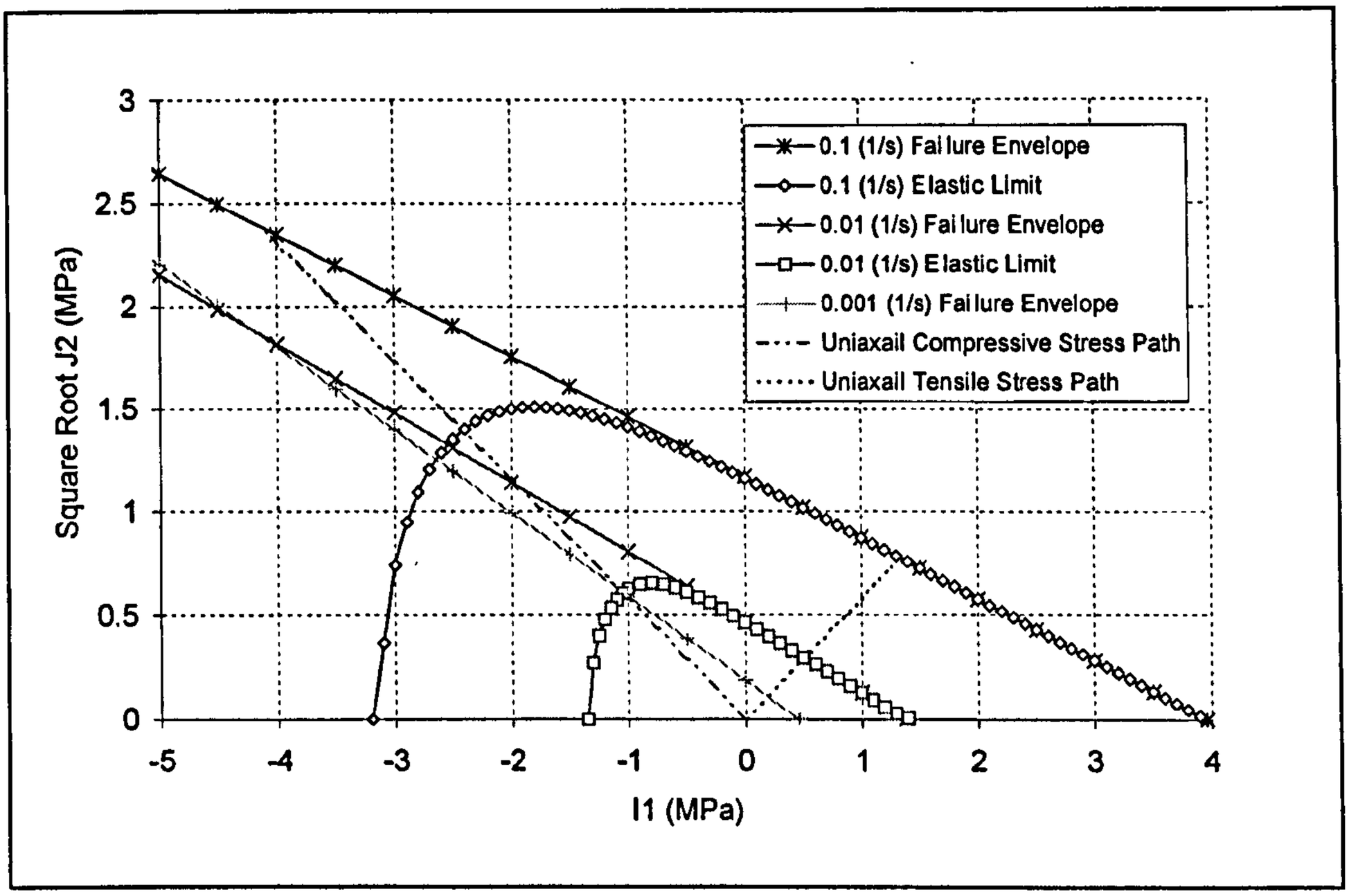

Figure 6.43: Yield surface and failure envelopes – DBM mixture at 35°C

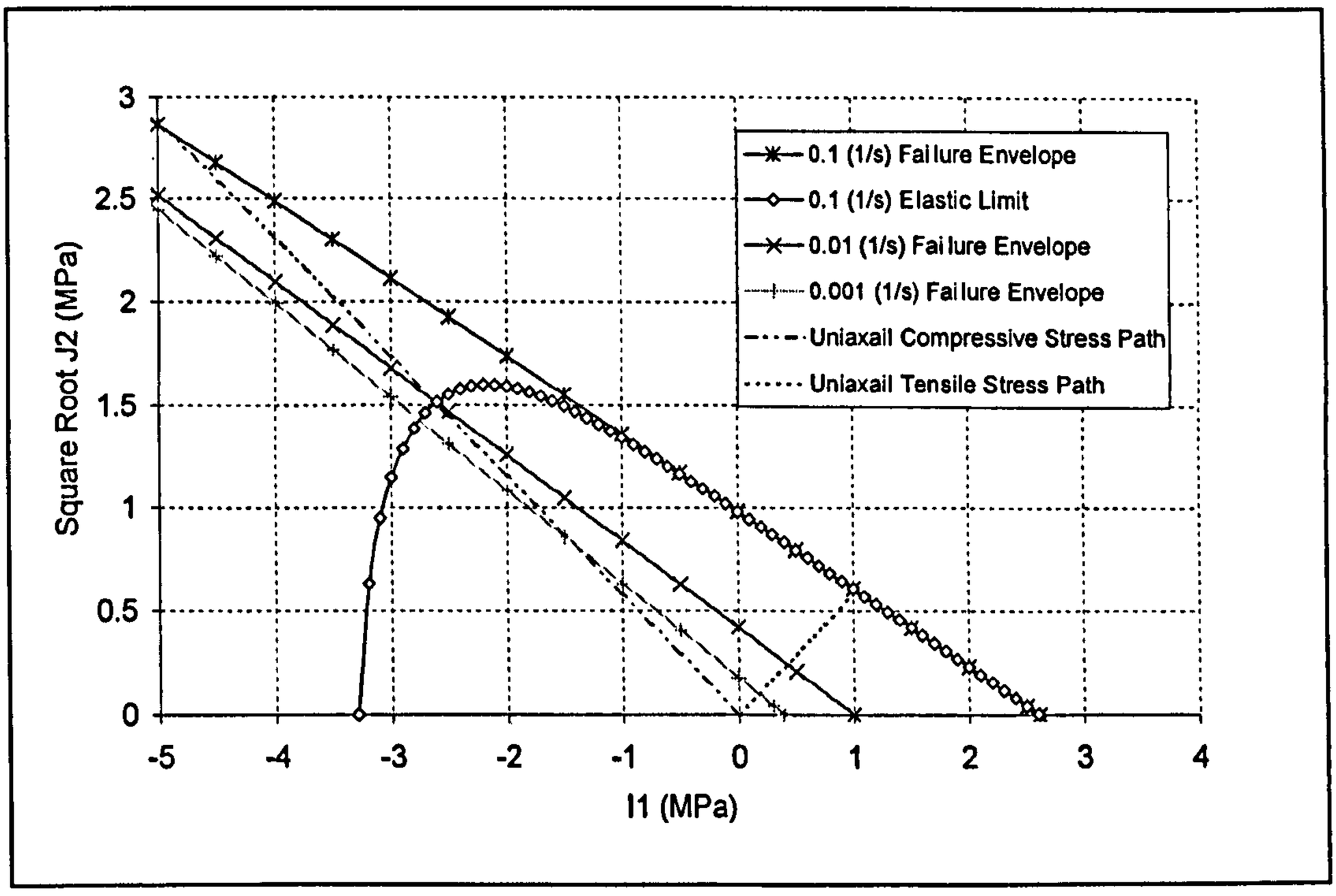

Figure 6.44: Yield surface and failure envelope – HRA mixture at 35°C

The observed coincidence of the yield and failure surfaces for tensile states of stress, would result in the prediction of purely elastic asphalt mixture responses, followed by sudden failure, exhibiting no mixture hardening, for any form of tensile loading conditions. This may be suitable for modelling the brittle type tensile response observed for high mixture stiffness moduli ($S_b \geq 60$ MPa), see Section 5.4.4, however, in Chapter 5 ductile type tensile failure conditions were reported for low stiffness conditions, ($S_b \leq 30$ MPa), during which the asphalt specimens were characterised by necking and hence exhibited material hardening. Therefore, although the constitutive model is suitable for modelling the hardening response of asphalt mixtures that is observed during compressive loading, the model is not capable of simulating the hardening response of asphalt mixtures observed during low stiffness tensile test conditions (high temperature and slow strain rates).

6.8.2 Simulation of Material Hardening Characteristics

In the current formulation of the ACRe constitutive model, either the plastic work, or the equivalent plastic strain measured during compressive loading has been utilised to derive the parameters for the hardening function. This function has then been used to specify the hardening response in both the compressive and tensile zones of the flow surface. However, as discussed above, the generalisation of the compressive hardening function for tensile states of stress results in the prediction of large elastic regions in the tensile zone. Therefore, in its present formulation the model is not suitable for predicting the ductile type stress-strain failures that have been observed for asphalt mixtures, subjected to tensile loading, at slow strain rates and high temperatures (low stiffness conditions). A possible solution to this problem would be for future contributions to utilise two independent hardening functions such as α_c and α_t to specify the growth of the flow surface for compressive and tensile states of stress respectively. For tension-compression states of stress between these two extremes, a weighted average value for α such as that suggested in Equation (6.14), could be used, where the weighting value, w, depends on the exact stress conditions.

$$\alpha = w \cdot \alpha_c + (1 - w) \cdot \alpha_t \tag{6.14}$$

6.8.3 Numerical Simulation of Experimental Compression Response

Notwithstanding the observed limitations regarding the tensile response characteristics, the ACRe model's current capabilities can be demonstrated. This has been achieved through comparison of the simulated compressive response predicted using the model, compared to the actual experimental uniaxial compression test data. These simulations were undertaken using software supplied by the Section of Structural Mechanics group, within the Department of Civil Engineering and GeoSciences at Delft University of Technology in the Netherlands. The software uses a single point method (SPM), which through integration of the incremental forms of the stress-strain relationships, can be used to simulate material response along a specific stress path. In this case, using the expressions and material parameters derived in this chapter, the software has been utilised to simulate the response of the DBM and HRA asphalt mixtures to uniaxial compressive stress paths, over the range of temperatures and strain rates undertaken in the experimental programme. Figures 6.45 to 6.50 show typical examples of the simulated compressive response predicted using the SPM using both W_p and ξ_p specification of the hardening and softening functions, compared to the observed responses recorded during the actual laboratory experiments. The model parameters used for these simulations are given in Tables 6.15 and 6.16 for the DBM and HRA mixtures respectively. A complete range of plots comparing the predicted and experimental data, for all test conditions, for both W_p and ξ_p specifications of the hardening and softening functions, using the material parameters derived in this chapter are given in Appendix J for both the DBM and HRA mixtures.

Figures 6.45 to 6.50 show a selection of the stress-axial-strain, stress-radial-strain response curves for a cross-section of DBM and HRA mixture stiffness moduli. The plots display the overall stress-strain response of the mixtures and provide a detailed view of the hardening response, shown in the top right hand corner of each figure. In addition, Figures 6.51 to 6.53 show the model sensitivity to variations in the hardening function parameters $\xi_{p\ lim}$ or $W_{p\ lim}$, c or C, and to the softening function parameter κ or K.

Table 6.15: Constitutive model material parameters for the DBM mixture

Model Parameters			Tests Conditions		
			High Stiffness	Mid-range Stiffness	Low Stiffness
			$0.1s^{-1}$, 5 ℃	$0.1s^{-1}$, 20 ℃	$0.001s^{-1}$, 20 ℃
Elastic	E (MPa)		6414	2451	378
	ν		0.30	0.35	0.35
Compressive Strength f_c	a		-76		
	b		-63.66		
	c		18014		
	d		0.39		
Tensile Strength f_t	e		6.08	26.4	
	f		-56.41	-67.66	
	g		17653	19490	
	h		0.97	0.44	
Phase Change	n		12	11	6
Atmospheric Pressure	pa (MPa)		-0.1		
Hardening	W_p	α_1	1.060E-25	6.932E-24	5.863E-07
		$W_{p\,lim}$	0.11527	0.05581	0.04279
		C	918	229	463
	ξ_p	α_1	1.976E-24	7.602E-22	8.236E-07
		$\xi_{p\,lim}$	0.00687	0.01008	0.03850
		c	15554	2008	543
Softening	W_{pf}	K	2.32	4.64	22.05
	ξ_{pf}	κ	14.43	14.69	11.48
Residual Strength	A		0.0425	0.0875	0.0823

Table 6.16: Constitutive model material parameters for the HRA mixture

Model Parameters			Tests Conditions		
			High Stiffness	Mid-range Stiffness	Low Stiffness
			$0.1s^{-1}$, 5℃	$0.1s^{-1}$, 20℃	$0.001s^{-1}$, 20℃
Elastic	E (MPa)		5162	1779	349
	ν		0.3	0.35	0.35
Compressive Strength f_c	a		-106		
	b		-67.28		
	c		18572		
	d		0.32		
Tensile Strength f_t	e		7.07	32.4	
	f		-66.93	-74.82	
	g		20441	21119	
	h		0.68	0.40	
Phase Change	n		12	11	6
Atmospheric Pressure	pa (MPa)		-0.1		
Hardening	$\dot{W}_p$	α_1	2.781E-26	1.310E-21	1.191E-06
		$W_{p\,lim}$	0.18675	0.17567	0.06910
		C	1404	350	950
	ξ_p	α_1	7.730E-25	1.036E-20	2.108E-06
		$\xi_{p\,lim}$	0.00970	0.02200	0.03905
		c	90000	2700	900
Softening	W_{pf}	K	3.01	3.80	15.18
	ξ_{pf}	κ	18.86	11.46	12.45
Residual Strength	A		0.0135	0.0240	0.0514

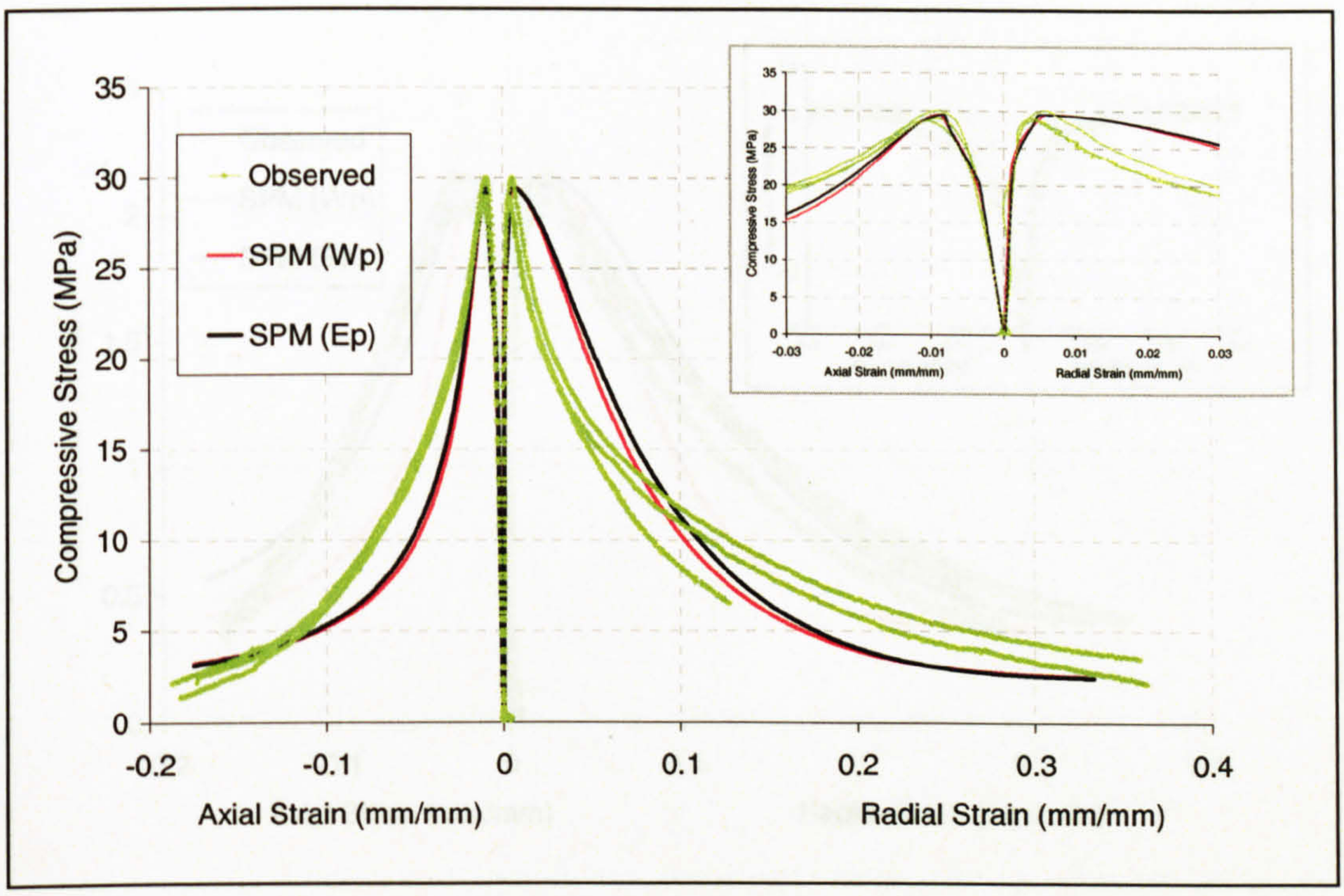

Figure 6.45: High stiffness predicted stress-strain response – DBM 5°C at 0.1s^{-1}

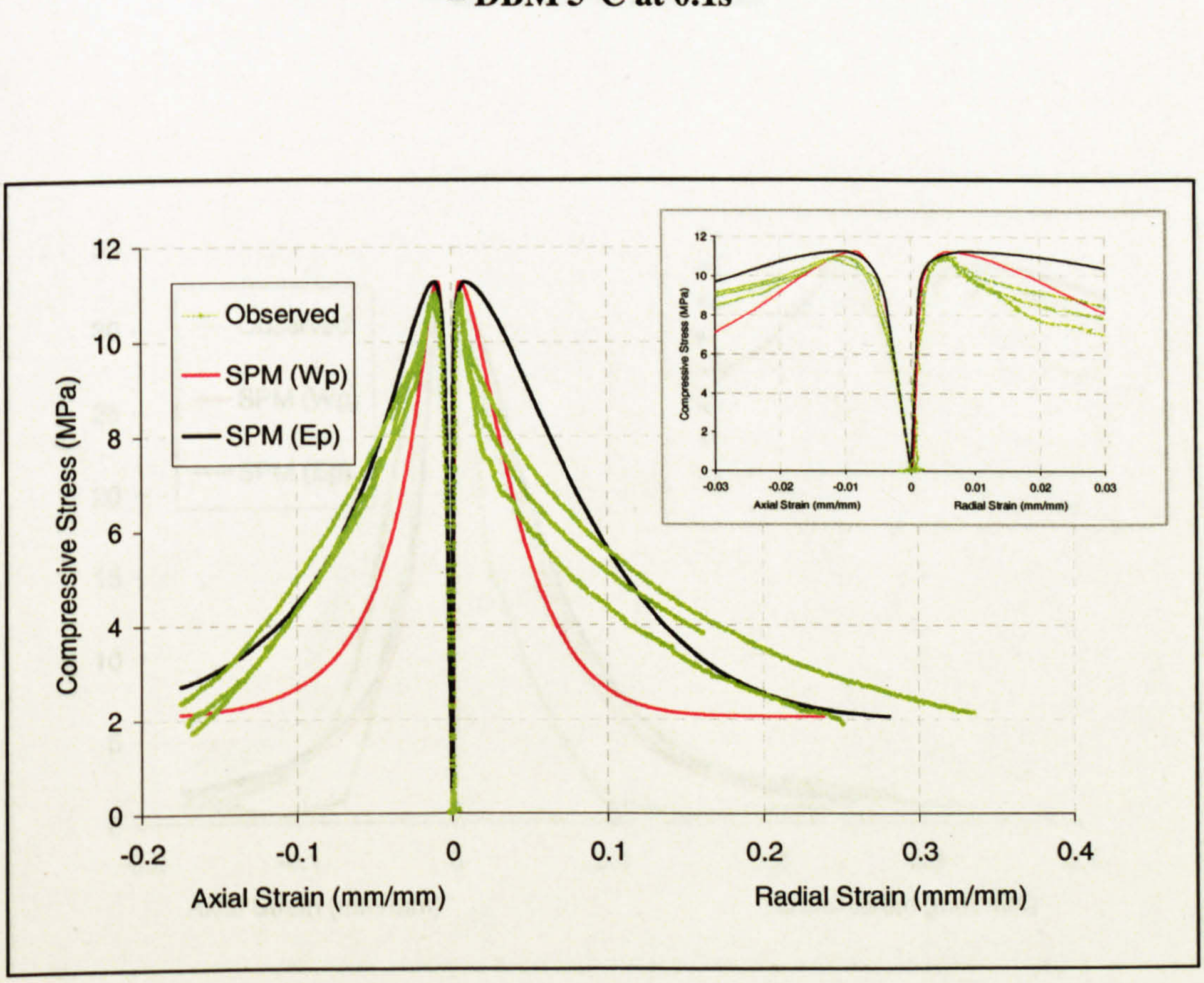

Figure 6.46: Mid-range stiffness predicted stress-strain response - DBM 20°C at 0.1s^{-1}

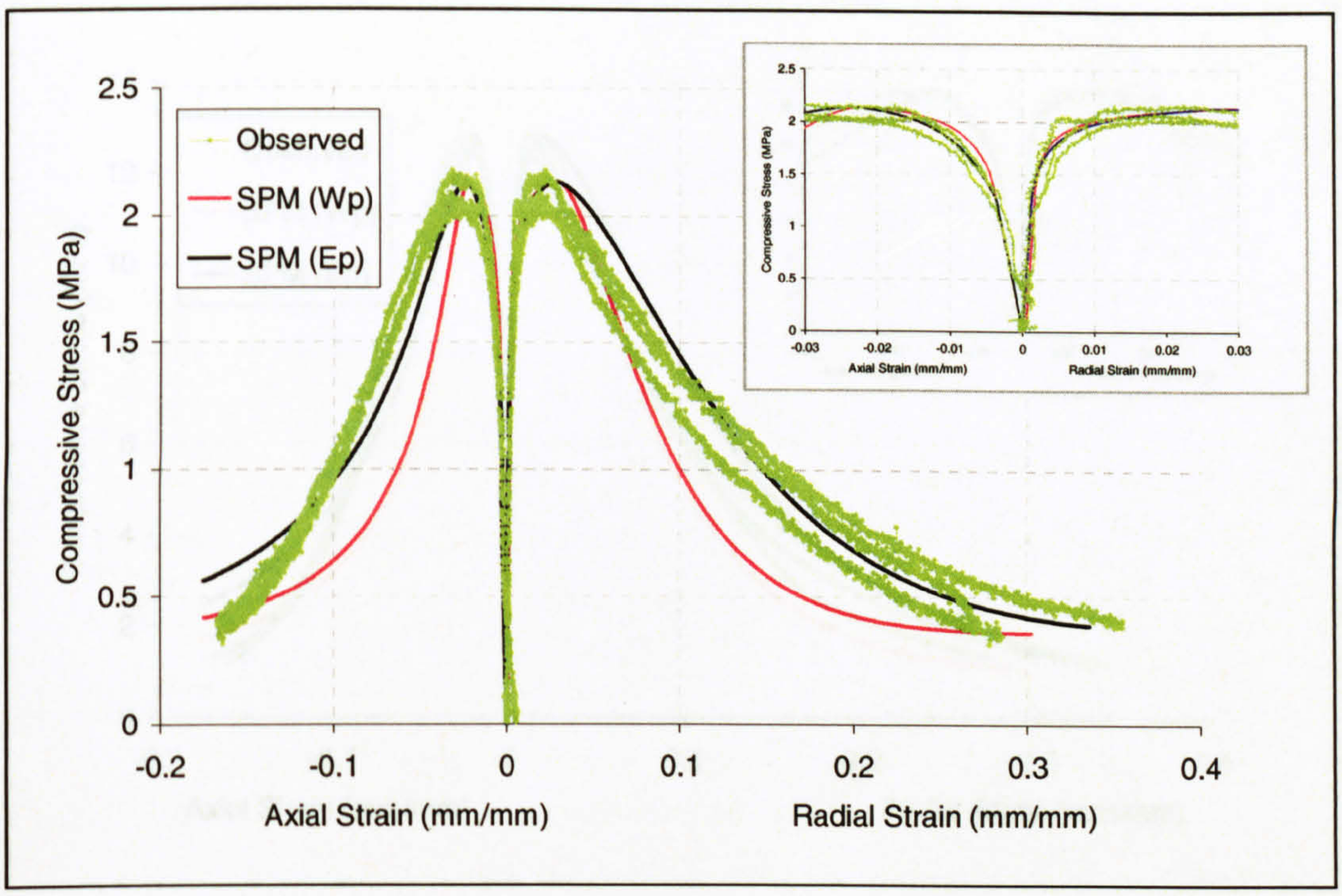

Figure 6.47: Low stiffness predicted stress-strain response – DBM 20°C at 0.001s^{-1}

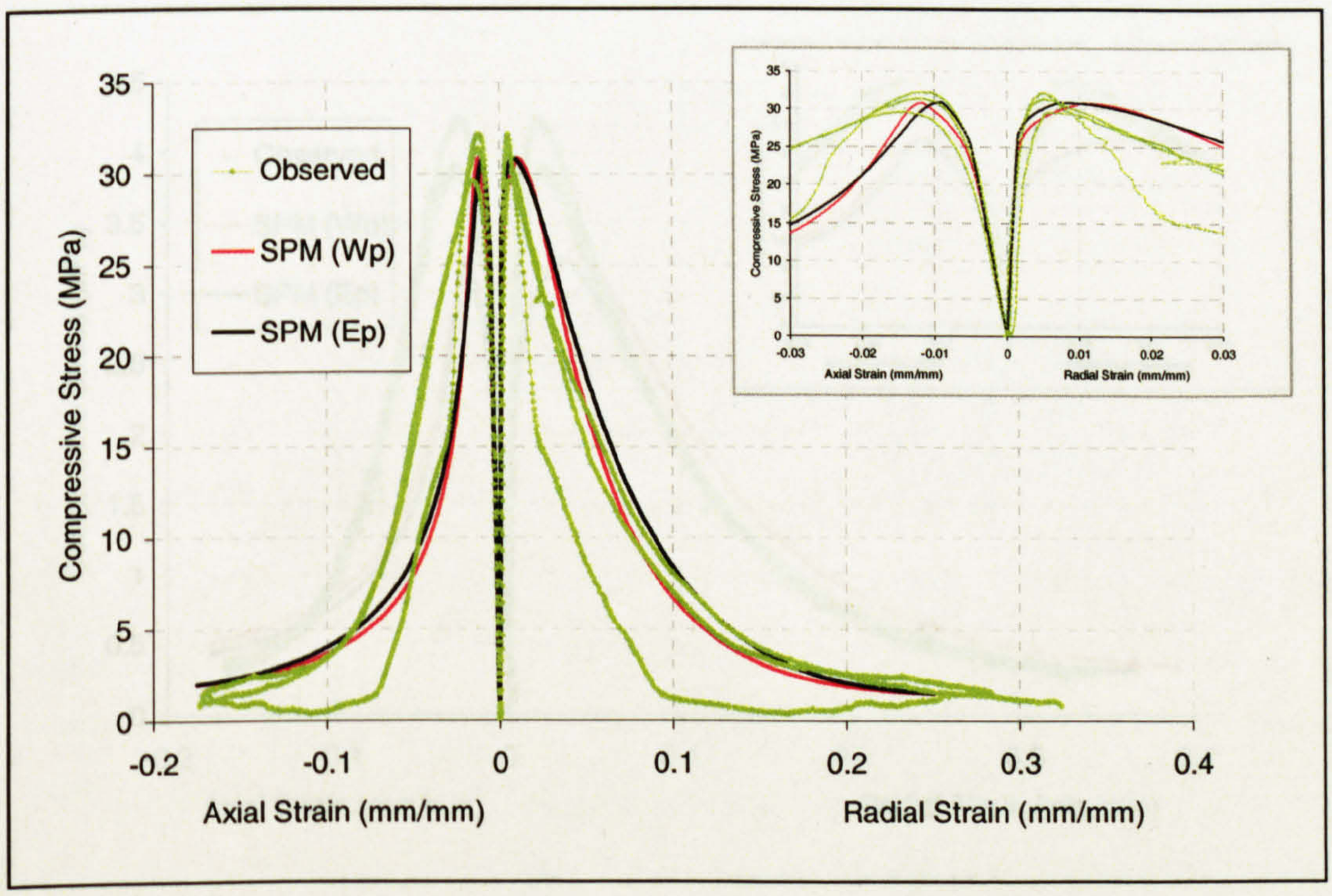

Figure 6.48: High stiffness predicted stress-strain response – HRA 5°C at 0.1s^{-1}

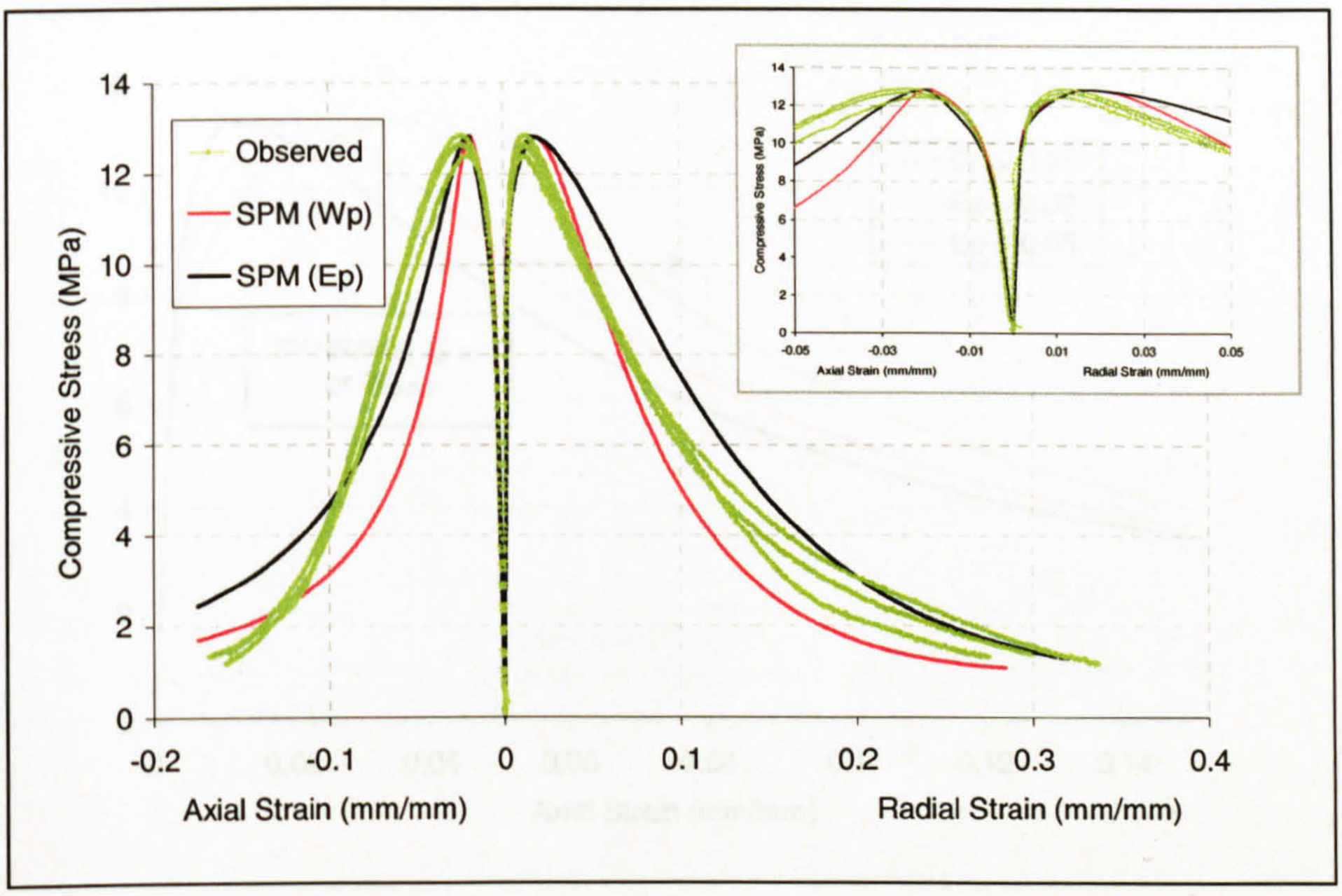

Figure 6.49: Mid-range stiffness predicted stress-strain response – HRA 20°C at $0.1s^{-1}$

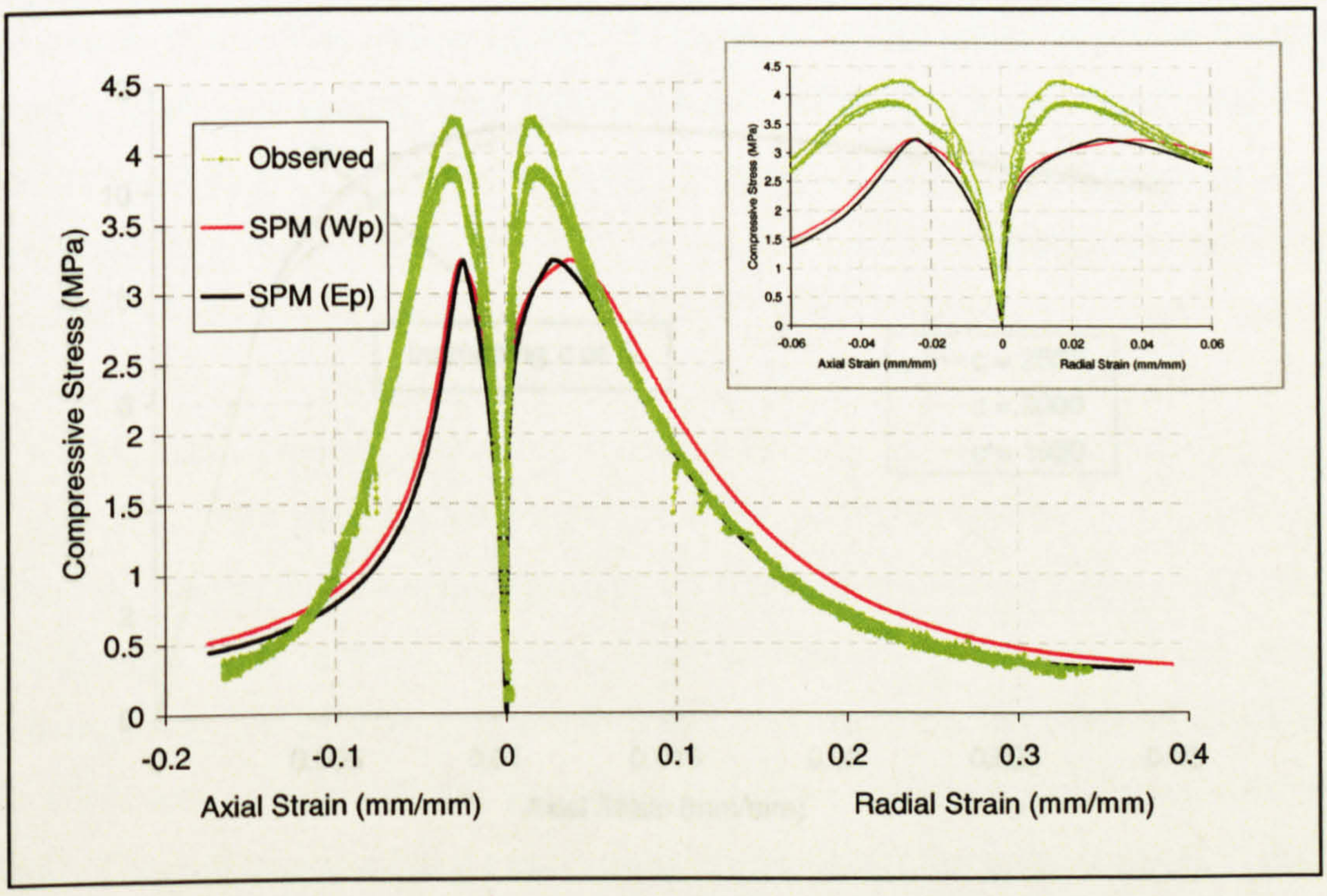

Figure 6.50: Low stiffness predicted stress-strain response – HRA 20°C at $0.001s^{-1}$

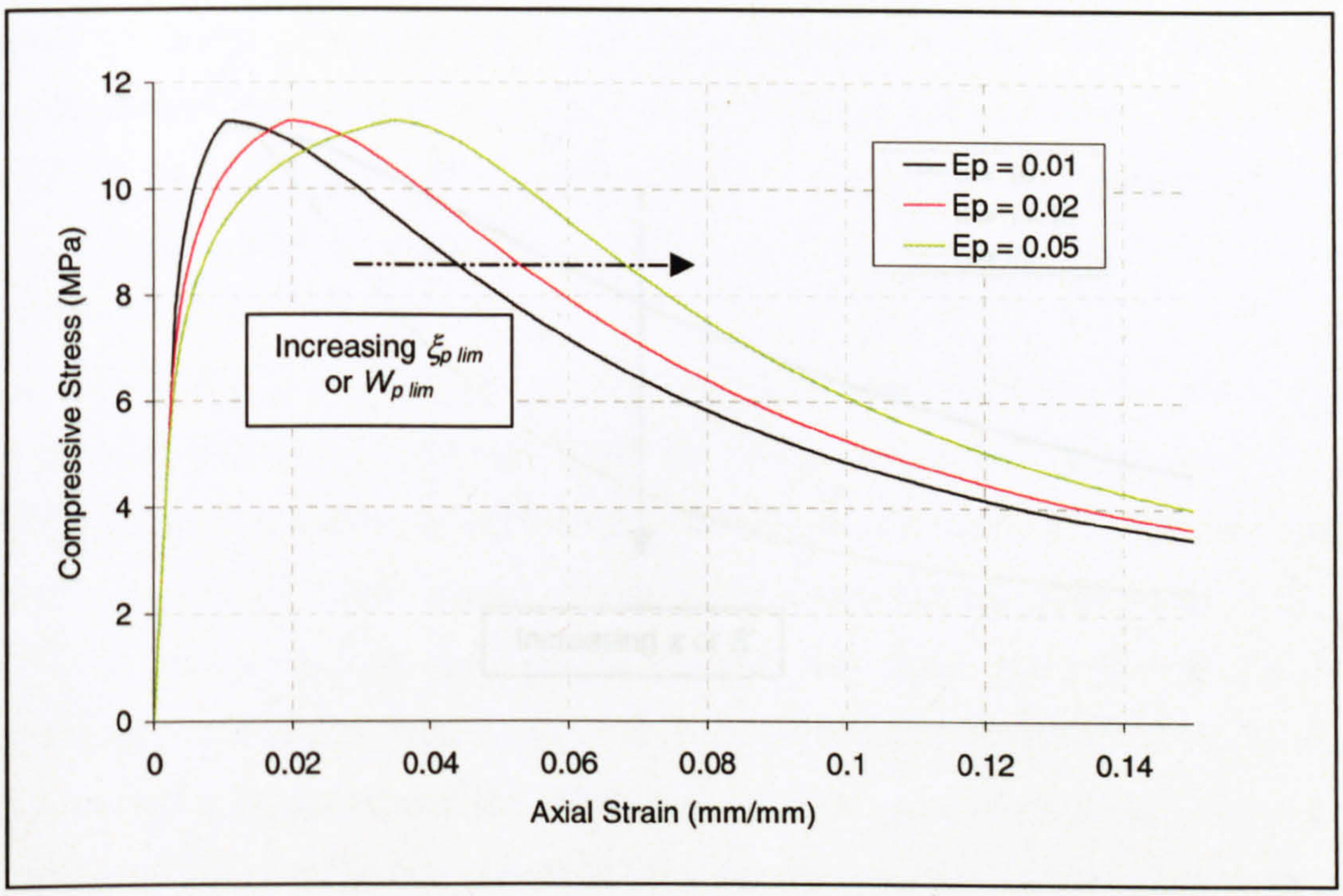

Figure 6.51: Sensitivity of model predicted response to variations in the hardening function parameter $\xi_{p\,lim}$ or $W_{p\,lim}$

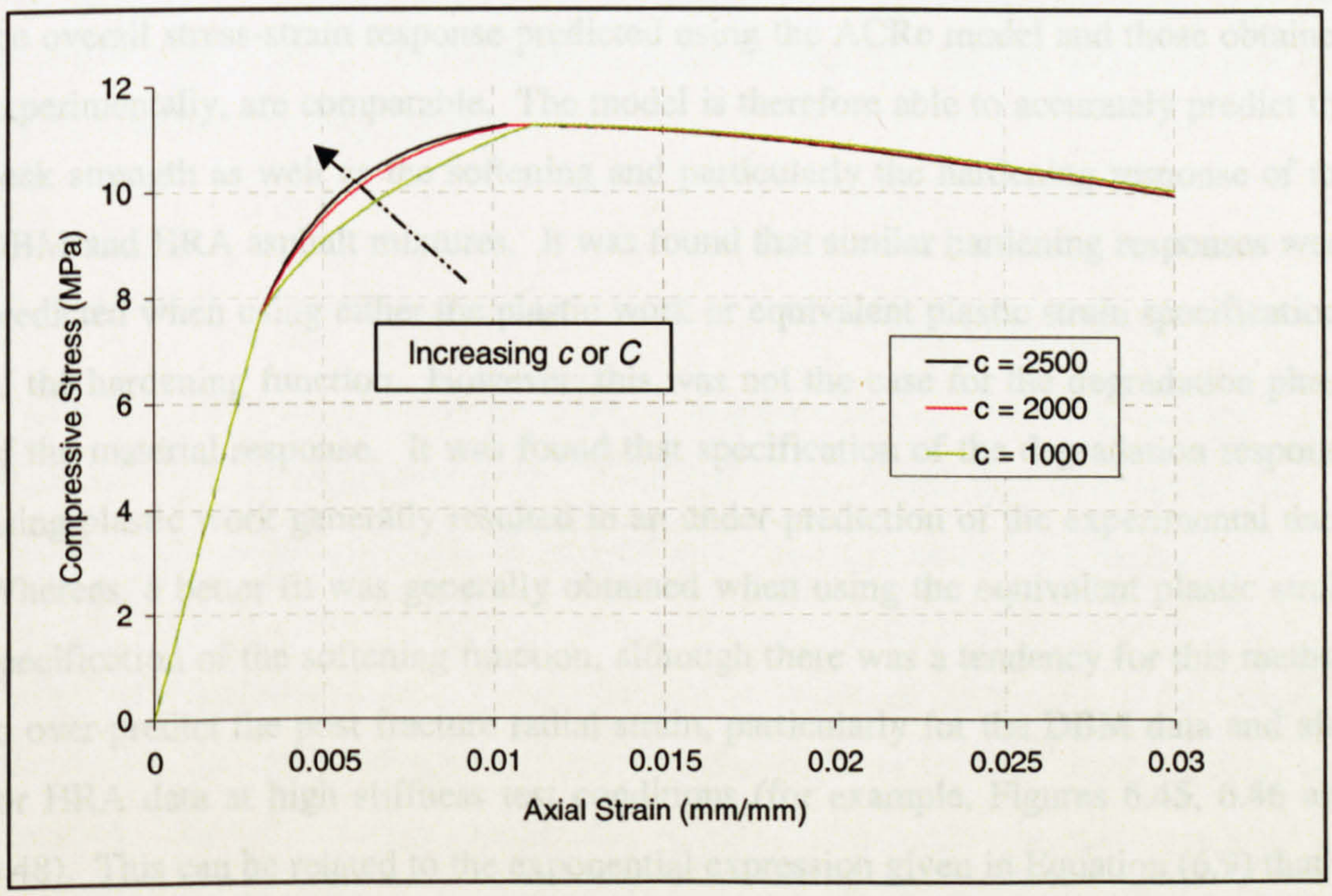

Figure 6.52: Sensitivity of model predicted response to variations in the hardening function parameter *c* or *C*

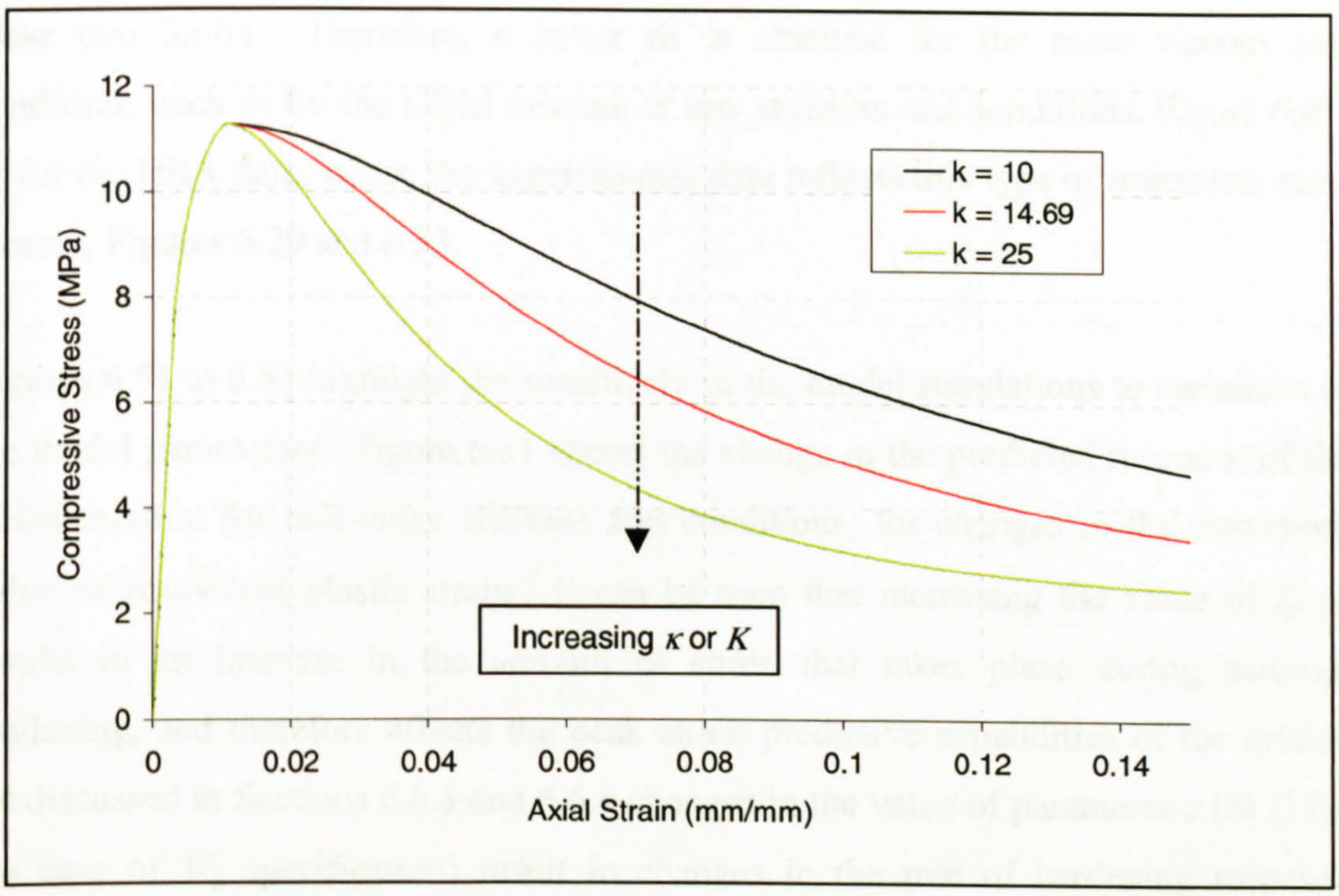

Figure 6.53: Sensitivity of model predicted response to variations in the softening function parameter κ or K

From Figures 6.45 to 6.50 and with reference to Appendix J it can be observed that the overall stress-strain response predicted using the ACRe model and those obtained experimentally, are comparable. The model is therefore able to accurately predict the peak strength as well as the softening and particularly the hardening response of the DBM and HRA asphalt mixtures. It was found that similar hardening responses were predicted when using either the plastic work or equivalent plastic strain specifications of the hardening function. However, this was not the case for the degradation phase of the material response. It was found that specification of the degradation response using plastic work generally resulted in an under-prediction of the experimental data. Whereas, a better fit was generally obtained when using the equivalent plastic strain specification of the softening function, although there was a tendency for this method to over-predict the post fracture radial strain, particularly for the DBM data and also for HRA data at high stiffness test conditions (for example, Figures 6.45, 6.46 and 6.48). This can be related to the exponential expression given in Equation (6.9) that is currently used to specify the softening function. During the non-linear regression analysis of Equation (6.9), an iterative process that simultaneously attempts to fit the values of γ_f and γ_r is undertaken. This results in a reverse S shape transition between

these two limits. Therefore, a better fit is obtained for the more viscous test conditions such as for the DBM mixture at low stiffness test conditions, Figure 6.47, or for the HRA data, where the experimental data reflects this type of transition more closely, Figures 6.29 and 6.33.

Figures 6.51 to 6.53 highlight the sensitively of the model simulations to variations in the model parameters. Figure 6.51 shows the change in the predicted response of the DBM mixture for mid-range stiffness test conditions, for changes in the maximum value of equivalent plastic strain. It can be seen that increasing the value of $\xi_{p\ lim}$ results in an increase in the amount of strain that takes place during material hardening, and therefore affects the peak strain predictive capabilities of the model. As discussed in Sections 6.6.3 and 6.6.4 changes in the value of parameter c (or C for the case of W_p specification) result in changes in the rate of hardening response exhibited during a simulation. This is shown in Figure 6.52 for changes in c as a function of equivalent plastic strain. It can be seen that increasing the value of parameter c is reflected in a decrease in the rate of hardening response in the model simulation. Finally, Figure 6.53 shows the change in the predicted response of the DBM mixture for mid-range stiffness test conditions for changes in the value of parameter κ (or K for W_p specifications). It can be observed that for increases in κ the rate of material softening also increases.

6.9 Summary

In this chapter the results from uniaxial compression and uniaxial tension tests conducted on a 10 mm DBM and a 30/10 HRA asphalt mixture have been used to evaluate the basic parameters for the constitutive model presented in Chapter 3.

The peak (failure) parameters R and γ have been evaluated from plots of the material uniaxial test failure envelopes and the expressions used in their determination are presented. The volumetric characteristics of both mixtures have been shown, after an initial compaction phase, to be dilative in response. Evaluation of the phase change parameter resulted in the selection of strain rate and temperature dependent values for parameter n.

An expression for the hardening function α has been presented, specified as a function of plastic work or equivalent plastic strain. The uniaxial compressive test data has then been used to evaluate the hardening function parameters for both specifications of the expression. The evaluated material parameters are presented and any observed trends discussed. Each of the hardening function parameters showed some form of strain rate and temperature dependency.

An expression for the softening function γ has been presented and also specified as a function of plastic work or equivalent plastic strain. The softening function material parameters have been evaluated using data from the degradation phase of the uniaxial compression test. The softening function parameter, K, evaluated on the basis of plastic work, was found to exhibit strain rate and temperature dependent characteristics. However, due to variations in the degradation phase of the uniaxial compressive test, the residual strength parameter, A, was found to demonstrate no consistent strain rate or temperature dependent trends. Evaluation of the softening parameter κ as a function of equivalent plastic strain revealed an insensitivity to changes in the temperature and strain rate. This is likely to be due to the discontinuous nature of the material specimens during the degradation phase of material response, which is caused by dilation (opening of internal cracks) of the mixtures.

Using the model parameters derived in this thesis the predictive capabilities of the model were verified through assessment of the model flow surface characteristics and through simulation of uniaxial compression tests over a range of test temperatures and strain rates.

Chapter 7 - Conclusions and Recommendations for Future Research

7.1 Conclusions

The research presented in this thesis has been concerned with the use of uniaxial quasi-static laboratory tests to determine the model parameters required for the characterisation of UK asphalt mixtures, for use in a constitutive model to simulate paving material response. In the following sections the main conclusions that were drawn from each of the chapters are presented.

7.1.1 Literature Review

The main aim of the literature review, presented in Chapter 2, was to provide the reader with the relevant background knowledge applicable to this study. Therefore, the chapter was divided into three main sections reviewing 'Pavement Engineering', 'Constitutive Relationships', and the use of 'Plasticity Based Models for Asphalt Mixtures'. From the literature presented in these sections the following conclusions can be drawn.

- Asphaltic materials only satisfy the assumptions of traditional linear elastic theory under limited conditions. These are at low temperatures and short loading times where asphaltic materials act as glassy solids, or at high temperatures and long loading times where asphaltic materials behave as Newtonian fluids.
- At intermediate temperatures and loading times, typical of in-service pavement conditions, asphaltic materials exhibit non-linear effects, which become more marked with increases in deformations, and display not only elastic but also plastic and time dependent viscous properties, including strain (or work) hardening characteristics.
- Pavements do not generally fail suddenly, but gradually deteriorate over a period of time, until a terminal level is reached. In traditional analytical flexible pavement design two classical strain criteria, the vertical compressive strain at the subgrade surface and horizontal tensile strain at the bottom of the asphalt layer, are used as

the performance criteria to design against permanent deformation and fatigue cracking respectively. However these linear elastic design methods do not fully describe the complex behaviour of asphaltic materials, are only valid within the confines of present experience and often involve the simplification of the pavement structure and loading conditions.

- Advances in computing power now facilitate the implementation of more complex models for pavement structures into incremental numerical techniques such as finite element (FE) methods. An important factor influencing the use of FE methods in pavement engineering is the identification of appropriate constitutive models to describe the behaviour of asphalt mixtures and other paving materials.
- The use of plasticity based constitutive models is well established in many fields of engineering, such as soil mechanics, where such classes of models have been identified as offering both realism and robust numerical performance. Therefore, a pre-requisite to enable greater accuracy in the description of the behaviour of asphaltic paving materials and pavement structures, is the availability of loading rate sensitive and temperature dependent plasticity based constitutive models for asphaltic materials.

7.1.2 Asphalt Concrete Response Model

Chapter 3 presented the framework for the dynamic plasticity based asphalt concrete response (ACRe) model, which has been used in this research to simulate the behaviour of asphalt mixtures. From the information presented in this chapter the following observations regarding the constitutive model, its use in this research project and the experimental work required for determination of the model material parameters can be made.

- Addressing the need for a viable model for asphaltic materials, a team at Delft University of Technology have been working on the development and three-dimensional finite element implementation of a strain rate sensitive and temperature dependent constitutive model for the characterisation of the material response of asphalt mixtures.
- By retaining the fundamental classical plasticity notions of flow surface, decomposition of strains, hardening and/or softening, a unified modelling

approach for materials such as asphalts, that exhibit rate dependent inelastic deformations, has been presented.

- The model utilises two independent flow surfaces, the first, based on work by Desai *et al.* [1986], to control material hardening and overall material softening and the second to control the tensile cracking response. In this study, research focus was placed on the determination of the model parameters concerned with the first flow surface.
- The use of more advanced constitutive models, such as the ACRe model, marks the move away from traditional pavement models where only specific forms of pavement distress are considered, to models that have the ability to identify the type of damage, including its location, extent and interaction with other concurrent types of distress.
- Monotonic uniaxial compression and tension tests were identified as suitable laboratory tests from which the model parameters necessary for the characterisation of UK asphalt mixtures could be determined. In order that the constitutive model incorporates the significant influence of loading rate and temperature on the response of asphalt mixtures, the uniaxial tests should be undertaken over a range of displacement rates and temperatures.

Chapter 3 also included a brief review of experimental work undertaken by previous researchers investigating the response of bitumen and asphalt mixtures to quasi-static loading conditions. From this review the following conclusions were drawn.

- For pure bitumens the elongation at break of tensile test specimens is a decreasing function of stiffness modulus, and the tensile strength of bitumens at break is also a function of stiffness modulus. The strength of both bitumen binders and asphalt mixtures increases with increasing binder stiffness until a peak strength is attained for binder stiffness moduli in the range of 40 to 50 MPa.
- For constant strain rate tension tests carried out on pure bitumens, fracture is controlled by the tensile stress applied to the specimen. For an applied strain rate, the stress increases with strain but at a decreasing rate until a maximum value is attained. If this maximum value is smaller than the fracture stress, the specimen necks rather that breaks. Conversely, whenever the applied strain rate is large

enough to sustain a stress that is comparable to the fracture stress, the specimen breaks before it necks.

- The observed failure mode in constant rate compression tests carried out on plain bitumens is that of cracking in the direction of the applied stress. This type of failure, cracks running parallel to the applied compressive stress along planes perpendicular to the maximum principal tensile stress, is termed axial splitting. Axial splitting is also observed in brittle materials such as concrete and rock.
- The uniaxial compressive strength of asphalt mixtures has been observed to increase with binder stiffness in a manner analogous to tensile strength, reaching a maximum value ranging from 34 to 63 MPa, at binder stiffness moduli of approximately 588 MPa.

7.1.3 Experimental Work

Chapter 4 presented details of the manufacture and development of the experimental specimens, apparatus, instrumentation and test procedures required for the experimental work undertaken in this study to enable the characterisation of UK asphalt mixtures for use in the constitutive model presented in Chapter 3.

A continuously graded 10 mm dense bitumen (DBM) macadam wearing course mixture and a gap graded 30/10 type F hot rolled asphalt (HRA) wearing course mixture were chosen for characterisation in the constitutive model. These mixtures were selected to reflect the two generic types of asphalt mixtures commonly utilised in the construction of UK lightly trafficked roads. To enable an unbiased investigation into the effect of aggregate gradation on the mixture response, and hence material parameters, the same penetration grade bitumen binder was used. Therefore, both mixtures comprised limestone aggregate and 100 penetration grade bitumen, with a binder content by mass of 5.5 % and 7 % for the DBM and HRA mixtures respectively. A 0/3 type F hot rolled asphalt mortar wearing course mixture, binder content 10.3 % by mass, was also selected for additional compressive testing to provide further data on the influence of both aggregate and binder properties, and to allow a comparison with similar data to that available for a Dutch sand asphalt mixture.

From the work presented in Chapter 4 the following conclusions regarding specimen manufacture and laboratory apparatus can be drawn.

- A process for the manufacture of cylindrical compression test specimens has been developed. A series of manufacturing trials determined that homogeneous specimens should be manufactured by taking horizontal cores, longitudinally through slabs produced using the Nottingham Roller Compactor.
- A process for the manufacture of 'dog bone' tension test specimens has been developed. The process uses a converted concrete cube mould into which steel inserts are placed to given the sample the desired shape. Compaction trials, using a vibrating hammer, identified the appropriate compaction time to achieve homogeneous test specimens.
- Use of a lubrication system based on the work undertaken by Erkens *et al.* [1998], comprising a soap - plastic film - soap sandwich, at each of the specimen/loading platen interfaces during the uniaxial compressive tests, ensured a true measure of the material properties. Tests conducted with this arrangement were observed to display up to a 25 % reduction in peak load and to exhibit a change in the mode of failure from barrelling followed by shear failure, to a more uniform dilation of the compressive specimen, followed by vertical axial splitting.

7.1.4 Experimental Results

Chapter 5 presented the results from the experimental programme undertaken in this research. The testing programme comprised monotonic uniaxial compression and monotonic uniaxial tension tests, undertaken on the DBM and HRA specimens, carried out at three displacement rates of 0.1, 1 and 10 mm/s with each displacement rate undertaken at three temperatures of 5, 20 and 35°C. Additional compression tests, at each displacement rate, at 20°C, were also carried out on the HRA mortar. Three repeats per set of test conditions were undertaken resulting in a data set of 63 uniaxial compressive test results and 54 uniaxial tension test results.

From the analysis of the data presented in Chapter 5 the following conclusions can be drawn with regard to the uniaxial compressive test data.

- The observed failure mode for the compressive specimens during the initial phase of the specimen response, up to and past peak load, was that of axial splitting.
- The HRA mixture was found to have the larger compressive strengths ranging from 1.42 MP to 31.09 MPa compared to 1.07 MPa to 29.20 MPa for the DBM mixture.
- Each of the mixtures displayed an increase in compressive strength with increasing strain rate and/or decreasing temperature. The data indicated that the apparent strength of asphalt mixtures was sensitive to both binder content and binder type (penetration grade), with increases in binder content/decreases in binder penetration grade producing increases in the compressive strength of a mixture.
- Comparison of the DBM, HRA, HRA mortar and a Dutch sand asphalt mixture indicated that the observed binder dominance of the asphalt mixtures during compressive loading was more pronounced at high stiffness conditions (lower temperature and/or fast displacement rates).
- At low stiffness conditions (high temperatures and/or slow displacement rates) the apparent strengths of all the asphalt mixtures were comparable.
- For each of the mixtures, and for all test conditions, the stress-stain response is similar, comprising an ascending portion until peak stress, followed by a descending portion. It is therefore possible to generalise the stress-strain response of the asphalt mixtures.
- Although a pre-load was applied to the test specimens prior to the start of the uniaxial compression tests the data was still subject to a load introduction phase. This is likely to be due to settling down of the lubrication system, or possibly due to internal restructuring of the bitumen films during the initial stages of loading.
- The stress-strain response curves for the DBM mixture generally exhibited more pronounced, sharply defined (brittle) peak stress-strain response curves compared to the less pronounced and more rounded (ductile) peak stress-strain response curves of the HRA and HRA mortar mixtures. This is reflected in the substantially lower peak strain values obtained for the DBM mixture compared to those found for the HRA and HRA mortar mixtures.
- The strain rate and temperature dependent relationship developed by Erkens *et al.* [2000a] to describe the strength response of a Dutch Sand asphalt mixture has been successfully used to describe the strength response of the UK DBM and HRA asphalt mixtures. However, on the basis of the analysis of the non-linear

regression parameters it was recommend that at this stage in the model development the regression parameters are considered valid only within or close to the strain rates and temperatures used in the experimental testing programme.

- The apparent stiffness of the mixtures was found, as expected, to increase as a function of decreasing temperature and/or increasing displacement rate. It was therefore possible to utilise a similar relationship as that employed for the compressive strength to describe the apparent stiffness modulus of the DBM and HRA mixtures.
- An approximately linear relationship was found to exist between compressive strength and apparent stiffness; thus providing the possible opportunity to define the apparent stiffness modulus of the mixtures based on the more easily measurable mixture compressive strength.
- Similar values for Poisson's ratio were found for both the DBM and HRA mixtures. The values ranged from 0.2 to 0.46 for the DBM mixture and 0.22 to 0.46 for the HRA mixture. A slight trend of increasing Poisson's ratio with decreasing mixture stiffness was found. Based on this observed trend, temperature dependent values for Poisson's ratio were proposed.

From analysis of the data presented in Chapter 5 the following conclusions can be drawn with regard to the uniaxial tensile test data.

- The tensile stress-strain response curves displayed a trend of increasing tensile strength with increasing displacement rate and/or decreasing temperature, up until peak fracture strengths of approximately 6.1 MPa and 6.8 MPa were reached for the DBM and HRA mixture respectively, after which a decrease in strength was observed with further increases in stiffness.
- It is possible to distinguish two main modes of tensile failure. Ductile failures, at high temperatures and slow displacement rates, and brittle failures, at low temperatures and fast displacement rates.
- The type of failure mode (ductile or brittle) was linked to binder stiffness. Brittle type failures occurred for test conditions where binder stiffness was greater than or equal to 60 MPa. Ductile type failures where observed to occur if test conditions resulted in binder stiffness moduli less than or equal to 30 MPa. For intermediate

stiffness ranges mixed failure conditions occurred. The response of the DBM and HRA mixtures are therefore dependent on the applied stress in a manner analogous to that for bituminous binders, i.e. if the test conditions are sufficient to induce large stiffness moduli, the specimen will fail in a brittle manner, otherwise for low stiffness moduli, failure will take place in a ductile manner.

- The same strain rate and temperature dependent relationship that was used to describe the compressive strength response was used to describe the tensile strength response of the asphalt mixtures. However, a dual set of non-linear regression parameters, segregated on the basis of binder stiffness was used to describe the tensile failure response in the ductile and brittle zones.

In addition to the main points given above the following general conclusions can also be drawn from Chapter 5.

- The assessment of the response of asphalt mixtures should be independent of specimen geometry. Therefore, future contributions should ensure that equivalent compressive and tensile tests are undertaken at the appropriate displacement rate to achieve the same strain rate within the respective test specimens.
- It has been shown that the dominant failure mode in a well lubricated uniaxial compression test is that of axial splitting, and that the type of failure mode exhibited in a tension test is dependent on the stress applied to the test specimen. It has also been shown that the magnitude of the tensile strain for the HRA mixture is concurrent with the measured radial strain at failure during a compression test. From this it can be deduced that the governing mode of failure for the HRA mixture is the same whether loaded in compression or in tension.

7.1.5 Determination of Model Material Parameters

In Chapter 6 the results from uniaxial compression and tension tests conducted on the DBM and HRA asphalt mixtures have been used to evaluate the basic material parameters for the constitutive model presented in Chapter 3.

Based on the work presented in Chapter 6 the following conclusions regarding the evaluation of the material parameters can be drawn.

- The peak strength data has been used to define failure envelopes for each of the test conditions from which the model parameters γ and R have been evaluated, and general expressions for these parameters as functions of uniaxial strength, temperature and strain rate have been produced.
- The volumetric response of both mixtures, after a small initial compaction phase, was found to be dilative for all test conditions. Based on evaluation of parameter n at the state of stress delimiting this dilative response, temperature and strain rate dependent values for model parameter n were determined. It was found that for states of stress close to the uniaxial compressive strength, the evaluated values for parameter n display large variations. Similar values for n were proposed for both the DBM and HRA mixtures.
- Due to the relatively large size of the load introduction phase for the 35°C test data, it was not possible to reliably determine the hardening parameters at strain rates of $0.001s^{-1}$ for the DBM data, and 0.01 and $0.001s^{-1}$ for the HRA data. Therefore, this data was not used in the evaluation of the hardening function parameters.
- Performing non-linear regression analysis on the inelastic hardening phase of the experimental data, the parameters describing the hardening functions were determined both as a function of plastic work and as a function of equivalent plastic strain. The same general trend for parameter α was found to exist for all test conditions, however the relative magnitudes varied for different test conditions. The evaluated parameters for the hardening function were found to exhibit both temperature and strain rate dependent characteristics, for both specifications of the expression.
- Performing non-linear regression analysis on the degradation phase of the experimental data, the parameters describing the softening function were determined both as a function of post fracture plastic work and as a function of post fracture equivalent plastic strain. The parameter K, evaluated as a function of post fracture plastic work, was found to exhibit a strong strain rate and temperature dependency. However, the residual strength parameter A, and parameter κ, evaluated as a function of post fracture equivalent plastic strain were found to exhibit no consistent strain rate or temperature dependencies.

The following conclusions can be drawn regarding the characteristics of the model hardening flow surface based on the model parameters derived in Chapter 6.

- Similar fields of flow surfaces are obtained for the DBM and HRA mixtures, particularly for high stiffness test conditions (low temperatures and slow strain rates), where the mixture binder properties dominate mixture response.
- Similar yield and hardening surfaces are obtained for either plastic work or equivalent plastic strain specifications of the hardening function.
- For all uniaxial compressive test conditions, for both the DBM and HRA mixtures, the model flow surface exhibits growth potential and therefore is suitable for modelling the observed compressive hardening response of asphalt mixtures.
- For all uniaxial tensile test conditions, for both the DBM and HRA mixtures, the yield and failure surfaces coincide. Therefore, the model exhibits no potential growth capabilities for tensile states of stress. This may be suitable for simulating the observed tensile response of the asphalt mixture for high stiffness conditions ($S_b \geq 60$ MPa), where the mixtures exhibit little material hardening. However, it is not suitable for simulating the ductile type tensile response for low stiffness conditions ($S_b \leq 30$ MPa), during which the response of the asphalt mixtures were observed to be characterised by necking and hence exhibited material hardening.

Notwithstanding the observed limitations regarding the tensile response characteristics, the following conclusions can be drawn regarding the present capabilities of the ACRe model to simulate the compressive response of asphalt mixtures using the parameters derived in Chapters 5 and 6 of this thesis.

- The overall predicted compressive stress-strain response was found to be comparable to the experimental data for both mixtures, for all test conditions.
- The model was found to successfully predict the peak strength as well as the softening and particularly the hardening response of the asphalt mixtures.
- Similar hardening responses were predicted irrespective of whether plastic work or equivalent plastic strain was used to specify the hardening parameters.
- A better predicted fit for the degradation response was generally obtained when the post fracture equivalent plastic strain was used to define the softening parameters,

although this was found to over-predict the post peak radial strains for high stiffness test conditions, particular for the DBM mixture.

7.2 Recommendations for Future Research

7.2.1 Recommendations for Experimental Work

One of the original goals of the research presented in this thesis was to investigate the effects of mixture composition, particularly aggregate gradation, on the model parameters of the constitutive model. This was reflected in the choice of materials. However, the work presented in this thesis has shown that the properties of the bituminous binder dominate the response of the mixtures for the range of test conditions (stiffnesses) investigated in this study. Therefore, to enable a true assessment of the effect of aggregate gradation on the model parameters it is recommended that further research should be conducted on asphalt mixtures with the same binder content and penetration grade, but with different aggregate gradations at elevated temperatures (+35°C) and/or slow strain rates.

The work undertaken in this thesis has focused on the use of uniaxial compression and tension tests to provide the data required for the determination of the material parameters for the constitutive model. Although this testing methodology constitutes the recommended minimum for determination of the model parameters, it was selected to allow a large number of tests to be included in the testing programme, hence permitting the characterisation of two asphalt mixtures over a broad range of test conditions. However, the absence of additional data describing the response of the asphalt mixtures to triaxial loading conditions has meant the generalisation of the uniaxial stress states to predict any three-dimensional material response, such as would be required for the use of the constitutive model in the FE code INSAP. The availability of data characterising the response of the asphalt mixtures to triaxial or multi-axial stress states would provide additional information permitting the effect of Lode angle and hence parameter β to be incorporated into the constitutive model, thus allowing the full capabilities of the model to be investigated.

7.2.2 Recommendations for Constitutive Model Development

It has been shown in this study that the type of failure mode exhibited by asphalt mixtures when subject to uniaxial tensile loading is dependent on the applied stress, and hence can be characterised by binder or mixture stiffness. It has been shown in the literature review, that for a range of asphaltic binders and mixtures, the relationship between tensile strength and binder stiffness is similar, reaching a maximum strength at binder stiffness moduli of approximately 40 MPa to 60 MPa. This has also been shown to be true for the DBM and HRA asphalt mixtures characterised in this study. It was found that for low binder stiffness moduli ($S_b \leq 30$ MPa) the failure mode was ductile. At intermediate stiffness moduli ($S_b = 30$ MPa to 60 MPa) both ductile and brittle fracture modes occur. At high binder stiffness moduli ($S_b \geq 60$ MPa) the fracture strengths of the mixtures were attained and the failure mode was brittle. Based on these observations it is recommended that binder stiffness be used as the criterion to segregate any multiple functions used to describe the tensile strength response, where the binder stiffness could be calculated in a programme subroutine, using the Van der Poel [1954] equations for binder stiffness.

The research undertaken in this thesis has shown that the ACRe model, in its current formulation, is suitable for simulating compressive and brittle tensile asphaltic mixture response. However, it has been shown that due to the coincidence of the yield and failure surfaces in the tensile zone, the model is not capable of simulating the tensile hardening material characteristics of asphalt mixtures. This is a result of the current specification for the hardening function α, the parameters for which are derived from the compression test data alone. An alternative approach would to be specify two independent expressions to control the hardening response in the compressive and tensile zones respectively, which would utilise both the compressive and tensile test data to derive the respective hardening parameters. A weighted average of the two expressions, the values of which would depend on the loading conditions, could then be used to specify the hardening function that would be used to control the overall growth of the flow surface.

If the ACRe model is to be eventually used in laboratory and road construction analysis, then it is necessary that the model parameters be described by general

expressions. This has been achieved in this study through specification of the model parameters through Equations (5.7), (5.8), (5.9), (5.11), (6.2a) and (6.3), which are functions of mixture strength, temperature and strain rate. By development of the model in this manner, future input parameters could be limited to the type of mixture or mixture composition, the temperature profile and the strain rate. From these inputs FE analysis could be used to determine the temperature and strain rate at each integration point in the structure from which the parameters for the model could be determined. Therefore, the next phase in the development of the constitutive model should be the development of strain rate and temperature dependent expressions for the hardening and softening function model parameters presented in Chapter 6.

References

Abdulshafi A. and Majidzadeh K., 'Combo Viscoelastic-Plastic Modelling and Rutting of Asphaltic Mixtures'. Transportation Research Record 968, Asphalt Mixtures and Performance, TRB, 1984, pp 19-31.

Airey G.D., 'Rheological Characteristics of Polymer Modified and Aged Bitumens'. Ph.D. Thesis, School of Civil Engineering, The University of Nottingham, 1997.

Airey G.D, Dunhill S.T. and Collop A.C., 'A Constitutive Material Modelling Methodology for Asphalt Mixtures'. Proceedings of the Ninth International Conference on Asphalt Pavements, Copenhagen, Denmark, 2002, (accepted for publication).

Alavi S.H. and Monismith C.L., 'Time and Temperature Dependent Properties of Asphalt Concrete Mixes as Hollow Cylinders and Subjected to Dynamic Axial and Shear Loads'. Proceeding of the Association of Asphalt Paving Technologists, Technical Sessions, Volume 63, 1994, pp 152-181.

Al-khoury R.I.N., '3-Dimensional Non-linear Soil Modelling'. M.Sc. Thesis, International Institute for Infrastructure, Hydraulic and Environmental Engineering, Delft University of Technology, Report No. Trend IP 029, 1993.

Almedia J.C.G.R., 'Analytical Techniques for the Structural Evaluation of Pavements'. Ph.D. Thesis, School of Civil Engineering, The University of Nottingham, 1993.

AMADEUS, 'Advanced Models for Analytical Design of European Pavement Structures'. Finial Report, 2000.

Asphalt Institute, 'Mix Design Methods for Asphalt Concrete and Other Hot-Mix Types'. Manual Series No. 2 (MS-2), 1988.

Becker A.A., 'Introduction to Non-linear Finite Element Analysis'. Advanced Non-linear Finite Element Analysis, Course Notes, 22-24 May, 2001.

Bonaquist R.F. and Witczat M.W., 'A Comprehensive Constitutive Model for Granular Materials in Flexible Pavement Structures'. International Society for Asphalt Pavements, Eighth International Conference on Asphalt Pavements, Volume 1 Proceeding. University of Washington, Seattle, Washington, 1997, pp 783-802.

Bonnaure F., Gest G., Gravois A. and Uge P., 'A New Method of Predicting the Stiffness of Asphalt Paving Mixtures'. Proceeding of the Association of Asphalt Paving Technologists, Technical Sessions, Volume 46, 1977, pp 64-104.

Bowles J.E., 'Physical and Geotechnical Properties of Soils'. McGraw-Hill Book Company, 1979.

British Road Federation, 'Roads and Accessibility'. Road Fact 99, 1999.

British Standards Institution, 'Hot Rolled Asphalt for Roads and Other Paved Areas'. BS 594: Part 1, 1985.

British Standards Institution, 'Sampling and Examination of Bituminous mixtures for Roads and Other Paved Areas. Part 104: Methods of Test for the Determination of the Density and Compaction'. BS 598, Part 104, 1989.

British Standards Institution, 'Hot Rolled Asphalt for Roads and Other Paved Areas'. BS 594: Part 1, 1992.

British Standards Institution, 'Coated Macadams for Roads and Other Paved Areas'. BS 4987: Part 1, 1993.

Brown S.F. and Cooper K.E., 'A Fundamental Study of the Stress-Strain Characteristics of a Bituminous Material'. Proceeding of the Association of Asphalt Paving Technologists, Volume 49, 1980, pp 476-498.

Brown S.F. and Cooper K.E., 'The Mechanical Properties of Bituminous Materials for Road Bases and Basecourses'. Proceeding of the Association of Asphalt Paving Technologists, Volume 53, 1984, pp 415-438.

Brown S.F. and Brunton J.M., 'An Introduction to the Analytical Design of Bituminous Pavements'. 3rd Edition, 1986.

Brown S.F., 'Achievements and Challenges in Asphalt Pavement Engineering'. Keynote Address, International Society for Asphalt Pavements, Eighth International Conference on Asphalt Pavements, Seattle, 1997.

Cheung C.Y., 'Mechanical Behaviour of Bitumens and Bituminous Mixes'. Ph.D. Thesis, Cambridge University Engineering Department, 1995.

Croney D. and Croney P., 'Design and Performance of Road Pavements'. 3rd Edition, McGraw-Hill, 1998.

Department of the Environment and Road Research Laboratory, 'Road Note 29 – A Guide to the Structural Design of Pavements for New Roads'. HMSO, 1960.

Department of the Environment and Road Research Laboratory, 'Road Note 29 – A Guide to the Structural Design of Pavements for New Roads 3rd Edition'. HMSO, 1970.

Department of Transport, 'Design Manual for Roads and Bridges – Volume 7: Pavement Design and Maintenance'. HMSO, 1994.

Desai C.S. and Abel J.F., 'Introduction to the Finite Element Method – A Numerical Method for Engineering Analysis'. Van Nostrand Reinhold Company, New York, 1972.

Desai C.S. and Christain J.T., 'Numerical Methods in Geotechnical Engineering'. McGraw-Hill Book Company, 1977.

Desai C.S., 'A General Basis for Yield, Failure and Potential Functions in Plasticity'. International Journal for the Numerical and Analytical Methods in Geomechanics, Volume 4, 1980, pp 361-387.

Desai C.S., Somasundaram S. and Frantziskonis G., 'A Hierarchical Approach for the Constitutive Modelling of Geologic Materials'. International Journal for the Numerical and Analytical Methods in Geomechanics, Volume 10, 1986, pp 225-257.

Desai C.S., 'Modelling and Testing – Implementation of Numerical Models and their Application in Practice'. International Centre for Mechanical Sciences, Courses and Lectures - No. 311, Numerical Methods and Constitutive Modelling in Geomechanics. Springer Verlay, New York, 1990, pp 1-168.

Dunhill S.T., 'Modelling the Deterioration Mechanisms of UK Lightly Trafficked Roads'. Report PGR 99031, School of Civil Engineering, The University of Nottingham, 1999.

Dunhill S.T., Airey G.D., Collop A.C. and Brown S.F., 'An Investigation into the Deterioration Mechanisms of Lightly Trafficked Roads'. 2nd Eurasphalt and Eurobitume Congress, Barcelona, Spain, 20 – 22 September, 2000, pp 122-129.

Earle J.B.F., 'Black Top: A History of the Flexible Roads Industry'. Basil Blackweel, Oxford, 1974.

Erkens S.M.J.G. and Poot M.R., 'The Uniaxial Compression Test - Asphalt Concrete Response (ACRe)'. Report 7-98-117-4, Delft University of Technology, 1998.

Erkens S.M.J.G and Poot M.R., 'Additional Compression Test – Asphalt Concrete Response (ACRe)'. Report 7-00-117-5, Delft University of Technology, 2000a.

Erkens S.M.J.G, Liu X. and Scarpas A., '3D Finite Element Model for Asphalt Concrete Response Simulation'. Finite Element Modelling of Pavement Structures, Preproceedings of the Second International Symposium on 3D Finite Element for

Pavement Analysis, Design and Research. Charleston, West Virginia, 2000b, pp 291-327.

Gibb J.M., 'Evaluation of Resistance to Permanent Deformation in the Design of Bituminous Paving Mixtures'. Ph.D. Thesis, School of Civil Engineering, The University of Nottingham, 1996.

Heukelom W., 'Observations on the Rheology and Fracture of Bitumens and Asphalt Mixes'. Proceeding of the Association of Asphalt Paving Technologists, Volume 35, 1966, pp 358-399.

Highway Research Board, 'The AASHO Road Test - Special Report 61E'. 1962.

Hill R., 'The Mathematical Theory of Plasticity'. Oxford University Press, New York, 1950.

Hinton E., 'Introduction to Nonlinear Finite Element Analysis'. National Agency for Finite Element Methods and Standards, Bell and Bain Ltd, Glasgow, 1992.

Hopman P. and Scarpas A., 'Multiaxial Response of Asphalt Concrete: Identification of Material Parameters'. Report 7-93-500-6, Delft University of Technology, 1993.

Hopman P., Nilsson R.N. and Pronk A.C., 'Theory, Validation and application of the Visco-Elastic Multilayer Program VEROAD'. International Society for Asphalt Pavements, Eighth International Conference on Asphalt Pavements, Volume 1 Proceeding. University of Washington, Seattle, Washington, 1997, pp 693-705.

Khanzada S., 'Permanent Deformation in Bituminous Mixtures'. Ph.D. Thesis, School of Civil Engineering, The University of Nottingham, 1999.

Lade P.V. and Kim M.K., 'Single Hardening Constitutive Model for Soil, Rock and Concrete'. International Journal of Solids and Structures, Volume 32, No. 14, 1995, pp 1963-1978.

McDowell G.R., 'Soil Mechanics'. Lecture Notes Module H2CG05, University of Nottingham, School of Civil Engineering, 2000.

Monismith C.L. and Salam Y.M., 'Distress Characteristics of Asphalt Concrete Mixes'. Proceeding of the Association of Asphalt Paving Technologists, Volume 42, 1973, pp 320-350.

NAFEMS., 'National Agency for Finite Element Methods and Standards, Guidelines to Finite Element Practice'. Department of Trade and Industry, National Engineering Laboratory, Glasgow, 1984.

Neville A.M., 'Properties of Concrete'. Longman, 1981.

Nijboer L.W., 'Plasticity as a factor in the Design of Dense Bituminous Carpets'. Elsevier publishing Company Inc, 1948.

Nunn M.E., 'The Characterisation of Bituminous Macadams by Indirect Tensile Stiffness Modulus'. TRL Project Report 160, 1995.

Owen D.R.J. and Hinton E., 'Finite Elements in Plasticity: Theory and Practice'. Pineridge Press Limited, Swansea, UK, 1980.

Pain H. J., 'The Physics of Vibrations and Waves'. John Wiley and Sons Ltd., 1970.

Paute J.-L., Dawson A.R. and Galjaard P.J., 'Recommendations for Repeated Load Triaxial Test Equipment and Procedure for Unbound Granular Materials'. In the Proceedings of the European Symposium Euroflex, Lisbon/Portugal, 20 – 22 September, 1993, pp 23–34.

Perl M., Uzan J. and Sides A., 'Visco-Elasto-Plastic Constitutive Law for a Bituminous Mixture Under Repeated Loading'. Transportation Research Record 911, Asphalt Materials, Mixtures, Construction, Moisture Effects, and Sulfur, TRB, 1981, pp 20-27.

Perzyna P., 'Fundamental Problems in Viscoplasticity'. Advances in Applied Mechanics, Volume 9, Academic Press, New York and London, pp 244-368.

Potts D.M. and Zdravkovic L., 'Finite Element Analysis in Geotechnical Engineering: Theory'. Thomas Telford, 1999.

Powell W.D., Potter J.F., Mayhew H.C. and Nunn M.E., 'The Structural Design of Bituminous Roads'. Transport and Road Research Laboratory, Report LR1132, 1984.

Read J.M., 'Fatigue Cracking of Bituminous Paving Materials'. Ph.D. Thesis, School of Civil Engineering, The University of Nottingham, 1996.

Read J.M., 'Pavement Evaluation and Advanced Bituminous Materials: Specification Developments'. ICE, Thomas Telford Services Ltd, 1998.

Rowe G.M., 'Application of the Dissipated Energy Concept to Fatigue Cracking in Asphalt Pavements'. Ph.D. Thesis, School of Civil Engineering, The University of Nottingham, 1996.

Rowe G. and Brown S.F., 'Fatigue Prediction Using Visco-Elastic Analysis'. International Society for Asphalt Pavements, Eighth International Conference on Asphalt Pavements, Volume 2 Proceeding. University of Washington, Seattle, Washington, 1997, pp 1109-1122.

Scarpas A. and Blaauwendraad J., 'Non-local Plasticity Softening Models for Brittle Materials'. Fracture and Damage of Concrete and Rock. H.P. Rossamanith, 1992, pp 44 –53.

Scarpas A., Al-Khoury R., Gurp C.A.P.M. and Erkens S.M.J.G., 'Finite Element Simulation of Damage Development in Asphalt Concrete Pavements'. International Society for Asphalt Pavements, Eighth International Conference on Asphalt Pavements, Volume 1 Proceeding. University of Washington, Seattle, Washington, 1997, pp 673-692.

Scarpas A. and Blaauwendraad J., 'Experimental Calibration of a Constitutive Model for Asphaltic Concrete'. Proceedings of the Euro-C Conference on the Computational Modelling of Concrete Structures, Bagastein, Ostenrijk, 31 March – 3 April, 1998a, pp 193 – 202.

Scarpas A. and Blaauwendraad J., 'Issues in the Numerical Simulation of Strain-Rate and Pressure Sensitive Cementitious Granular Materials'. Fifth International Conference on Structures under Shock and Impact, 1998b, pp 501-512.

Scarpas A., Personal Correspondence, October 1999.

Shell Global Solutions, 'BANDS 2.0, BISAR 3.0, SPDM 3.0, Software and Users Manual'. 1998.

Shell International Petroleum Company Limited, 'Shell Pavement Design Manual, Asphalt Pavements and Overlays for Road Traffic'. 1978.

Sprague de Camp L., 'The Ancient Engineers'. Souvenir Press, 1963.

SPSS Inc., 'Table Curve 2D'. Version 4, 1989 – 1996.

Starodubsky S., Blechmen I. and Livneh M., 'Stress-Strain Relationships for Asphalt Concrete in Compression'. Materials and Structures, Issue 172, 1994, pp 474-482.

Tan S.-A., Low B.-H. and Fwa T.-F., 'Behaviour of Asphalt Concrete Mixtures in Triaxial Compression'. Journal of Testing and Evaluation, Volume 22, No. 3, 1994, pp 195-203.

Uzan J., Sides A. and Perl M., 'Viscoelastoplastic Model for Predicting Performance of Asphaltic Mixtures'. Transportation Research Record 1043, Pavement System Analysis, TRB, 1985, pp 78-89.

Van der Poel C., 'A General System Describing the Visco-elastic Properties of Bitumens and its Relation to Routine Test Data'. Journal of Applied Chemistry, Volume 4, 1954, pp 221-236.

Van Vilet M.R.A. and Van Mier J.G.M., 'Size Effect of Concrete and Sandstone'. Heron, Netherlands School for Advanced Studies in Construction, Volume 45, 2000, pp 91-108.

Varadarajan A., Sharma K.G., Desai C.S. and Hashemi M., 'Constitutive Modelling of a Schistose Rock in the Himalaya.' The International Journal of Geomechanics, Volume 1, Number 1, 2001, pp 83-107.

Vardoulakis I., Labuz J.F., Papamichos E. and Tronvoll J., 'Continuum Fracture Mechanics of Uniaxial Compression on Brittle Materials'. International Journal of Solids and Structures, Volume 35, 1998, pp 4313 – 4335.

Whiteoak D., 'The Shell Bitumen Handbook'. Shell Bitumen UK, 1990.

Witczak M.W., Bonaquist R., Von Quintus H. and Kaloush K., 'Specimen Geometry and Aggregate Size Effects in Uniaxial Compression and Constant Height Shear Tests'. Association of Asphalt Paving Technologists, Volume 69, 2000, pp 733-793.

Appendix A - Visco-Plasticity

A.1 Introduction

Visco-plasticity has emerged as an attempt to provide a realistic phenomenological modelling approach to materials exhibiting both plastic and creep deformations. In service conditions, asphaltic materials exhibit permanent strain. Therefore, some measure of this plastic behaviour should be accounted for when attempting to model a pavement structure. However, one of the fundamental assumptions of classical plasticity, that of time independence of the equations of state, makes the simultaneous description of the plastic and rheological properties of a material impossible. Therefore, for asphaltic materials that display time dependent viscous properties the application of visco-plasticity is a great advantage [Perzyna, 1966].

A.2 Uniaxial Elasto-visco-plastic Behaviour

Figure A.1 shows a Bingham model that can be used to represent elastic visco-plastic material behaviour. It can be observed that visco-elastic response can be obtained as a special case of elastic visco-plastic behaviour. This is achieved when the yield stress in the friction slider element, which controls the onset of visco-plastic effects, is reduced to zero, thus reducing the rheological model arrangement to that of a Maxwell model. Elastic material behaviour can also be obtained as a special case, by specifying a very large yield stress for the friction slider, thereby inhibiting viscous movement of the damper.

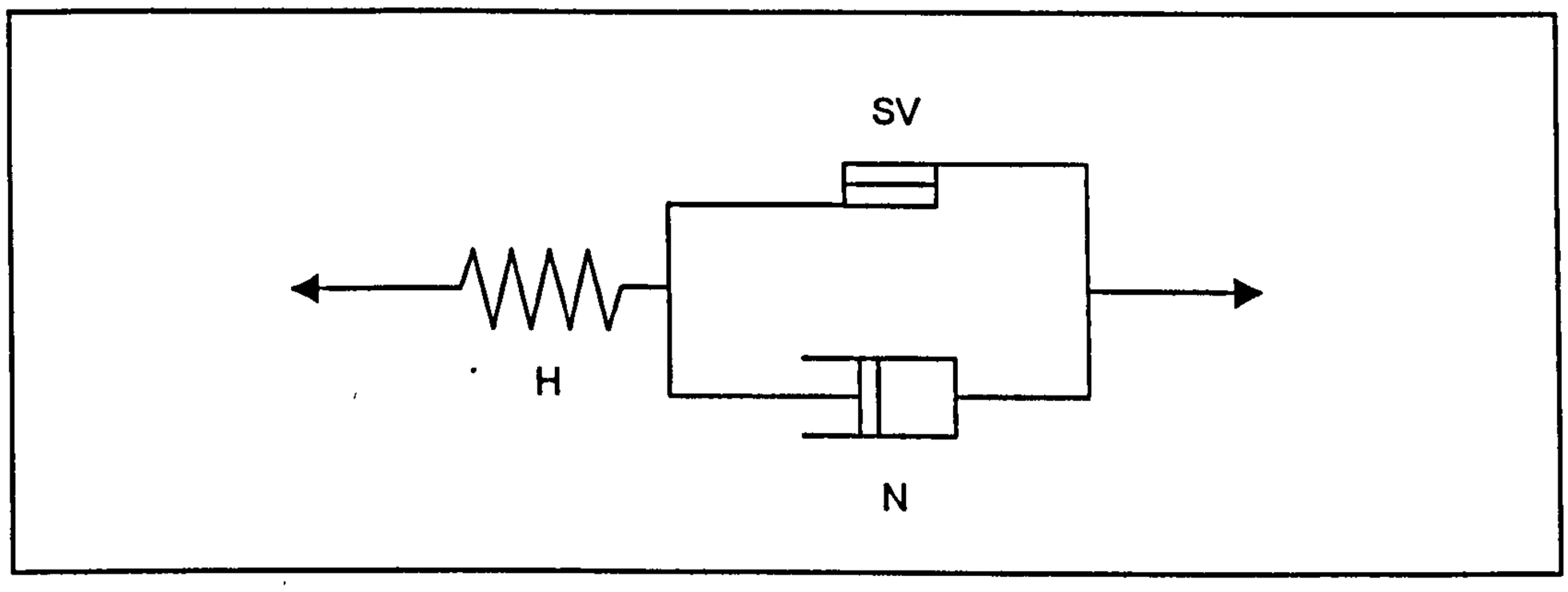

Figure A.1: Elasto-visco-plastic Bingham model

Al-khoury [1993] presents a description of the Perzyna [1966] formulation as applied to a one-dimensional elastic visco-plastic solid. In this description elastic visco-plastic behaviour is represented by the Bingham body shown in Figure A.1. The parallel combination of the friction slider and Newtonian damper represents the visco-plastic component. The series combination with the Hooken spring allows the total strain, ε, and rate of total strain, $\dot{\varepsilon}$, to be decomposed into elastic and visco-plastic components:

$$\varepsilon = \varepsilon_e + \varepsilon_{vp} \tag{A.1}$$

$$\dot{\varepsilon} = \dot{\varepsilon}_e + \dot{\varepsilon}_{vp} \tag{A.2}$$

where,

ε_e = elastic strain

ε_{vp} = visco-plastic strain

$\dot{\varepsilon}_e$ = rate of change of elastic strain

$\dot{\varepsilon}_{vp}$ = rate of change of visco-plastic strain

However, if it is assumed that for stress levels up to the yield stress, σ_y, the slider remains rigid, then $\varepsilon_{vp} = 0$ and the material behaves elastically. It is only at stress levels greater than σ_y that viscous effects occur; mobilisation of the slider allows deformation of the Newtonian damper and the generation of visco-plastic strains. Then, within the visco-plastic component of the model the applied stress is resisted by the combination of the slider and the damper:

$$\sigma = \sigma_p + \sigma_d \tag{A.3}$$

in which

$$\sigma_p = \sigma_y \tag{A.3a}$$

where,

σ_p = friction slider contribution

σ_d = Newtonian damper contribution

Due to the viscous response of the Newtonian damper component, its stress depends on the rate of straining and can be expressed as:

$$\sigma_d = \eta . \dot{\varepsilon}_{vp} \tag{A.4}$$

where, η = viscosity of the material

Substituting σ_p and σ_d with their equivalents into Equation (A.3) and rearranging:

$$\eta . \dot{\varepsilon}_{vp} = \sigma - \sigma_y \tag{A.5}$$

$$\dot{\varepsilon}_{vp} = \Gamma [\sigma - \sigma_y] \tag{A.6}$$

in which $$\Gamma = \frac{1}{\eta} \tag{A.6a}$$

where, Γ = fluidity of the material

Once $\dot{\varepsilon}_{vp}$ is known, the change in visco-plastic strain generated within an increment of time Δt, can be computed as:

$$\Delta \varepsilon_{vp} = \dot{\varepsilon}_{vp} . \Delta t \tag{A.7}$$

From Equation (A.6) it is possible to deduce that visco-plastic flow will continue as long as the imposed stress σ exceeds the threshold value σ_y. In can also be determined that the rate of increase of visco-plastic strain is a function of the excess stress $[\sigma - \sigma_y]$:

$$[\sigma - \sigma_y] = \begin{cases} 0 & if\ \sigma \leq \sigma_y \\ \sigma - \sigma_y & if\ \sigma > \sigma_y \end{cases} \tag{A.8}$$

Figure A.2 shows the uniaxial time-strain response of two different viscous materials. If subjected to a suddenly applied constant stress, the first material, Figure A.2(a), shows a strain that approaches a steady value and viscous flow stops as the time tends to infinity. This type of material behaviour has been reported for asphaltic materials

[Scarpas *et al.*, 1997]. The second material, Figure A.2(b), on the other hand shows no arrest of viscous flow, and strains will continue to develop with increasing time. Equation (A.6) can adequately describe the time-strain response of material (b), since for a constant stress test where $\sigma > \sigma_y$, the rate of visco-plastic strain $\dot{\varepsilon}_{vp}$ is always non-zero. However for material (a), a steady value is reached and viscous flow stops. This implies that after some time period, the rate of visco-plastic strain $\dot{\varepsilon}_{vp}$ becomes zero. For a constant stress test the only way this is possible is to consider that the value of σ_y does not remain constant in time, but increases as a function of some physical variable. Then as σ_y increases, the excess stress $[\sigma - \sigma_y]$ decreases and eventually $\dot{\varepsilon}_{vp}$ becomes zero.

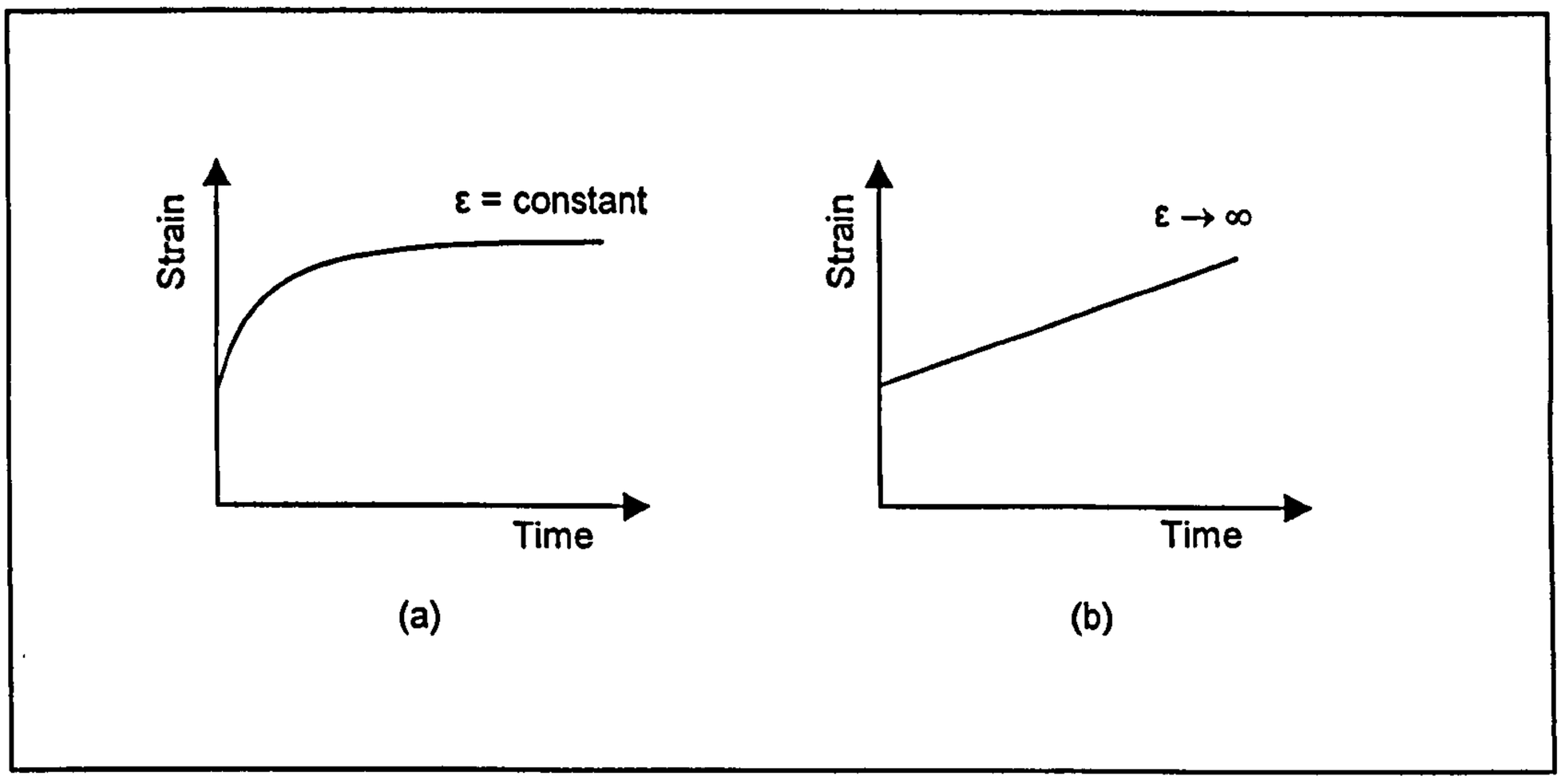

Figure A.2: Uniaxial visco-plastic response under constant load

A.3 Visco-plasticity for Multi-axial States of Stress

To generalise the uniaxial visco-plastic model to multi-axial stress-strain behaviour it is necessary to use the concepts of yield function, F, and plastic potential, Q, which have been previously introduced with respect to classical incremental plasticity in Sections 2.3.5 and 2.3.6 respectively.

As was the case for one-dimensional visco-plasticity, and in analogy with incremental plasticity, the total strain rate can be divided into elastic and visco-plastic components:

$$\dot{\varepsilon}_{ij} = \dot{\varepsilon}_{ij}^{e} + \dot{\varepsilon}_{ij}^{vp} \tag{A.9}$$

where the dot represents differentiation with respect to time (or strain rate). The elastic strain component is related to the total stress rate component by:

$$\{\dot{\sigma}\} = [D]\{\dot{\varepsilon}^{e}\} \tag{A.10}$$

where [D] is a constitutive matrix of the form given in Section 2.3.1 Utilising the concept of the plastic potential function, Q, the visco-plastic strain rate component, defined in Equation (A.6) for a uniaxial state, can be formulated for a general multi-axial state as:

$$\dot{\varepsilon}_{ij}^{vp} = \Gamma\langle\Phi(F)\rangle\frac{\partial Q}{\partial \sigma_{ij}} \tag{A.11}$$

in which Γ is the fluidity parameter controlling the plastic flow rate. The term $\langle\Phi(F)\rangle$ is a visco-plastic flow function, where the McCauley brackets indicate that visco-plastic effects only develop for positive values of $\langle\Phi(F)\rangle$. It is analogous to the excess stress function $[\sigma - \sigma_y]$ for the one-dimensional case:

$$\langle\Phi(F)\rangle = \begin{cases} 0 & for\ F \le 0 \\ \Phi(F) & for\ F > 0 \end{cases} \tag{A.12}$$

Comparison of Equation (A.11) with (2.13) shows the similarity between the flow rule for non-associated plasticity and the analogous definition for the visco-plastic flow rate. If $F \equiv Q$ is assumed, i.e. associative visco-plasticity, then Equation (A.11) can be expressed as:

$$\dot{\varepsilon}_{ij}^{vp} = \Gamma\langle\Phi(F)\rangle\frac{\partial F}{\partial \sigma_{ij}} \tag{A.13}$$

Different definitions are possible for the function, Φ, which can be selected to represent the characteristics of the material under investigation [Perzyna, 1966]. Two of the more general forms are given in Equations (A.14a) and (A.14b) [Owen *et al.*, 1980].

$$\Phi(F) = e^{M\left(\frac{F-F_0}{F_0}\right)} - 1 \qquad \text{(A.14a)}$$

$$\Phi(F) = \left(\frac{F - F_0}{F_o}\right)^N \qquad \text{(A.14b)}$$

where,

F = some function of the state of stress

F_o = a normalising factor, depending on the yield criterion

M, N = experimentally determined material parameters

An important distinction between the theories of classical plasticity and visco-plasticity is that in visco-plasticity, stresses outside the yield surface are permitted and are consistent with Equations (A.6, A.11 and A.14) in the generating cause of visco-plastic effects.

Appendix B - Specimen and Aggregate Size Selection Process

B.1 Factors Effecting the Selection Process

The link between nominal stone size and specimen geometry was used to determine the mixture type (i.e. roadbase, basecourse, or wearing course) that would be incorporated in the study. In composite materials like asphalt, the dimensions of the ideal test specimen must be large relative to the size of the individual aggregate particles. A general rule commonly used in asphalt, soils and concrete technology, recommends the minimum specimen dimensions to be 4 to 6 times the maximum aggregate size when test specimens are compacted in the laboratory [Witczak *et al.*, 2000]. Assuming a height to diameter ratio of 2 and selecting the ratio of the minimum specimen dimension to maximum aggregate size of 5, a typical macadam roadbase, comprising 28 mm size course aggregate, would require a test specimen 140 mm in diameter by 280 mm in height. In a similar manner a typical macadam basecourse comprising 20 mm stone, or wearing course comprising 10 mm stone, would require specimens 100 mm by 200 mm or 50 mm by 100 mm respectively.

The compression test, which is an integral part of the testing programme, involves the displacement controlled loading of the test specimens up to and past their peak strength. Therefore, it was important to ascertain the maximum specimen size, and hence maximum stone size, that could be loaded safely to peak strength using the available servo-controlled hydraulic test equipment, which in this case has a maximum loading capacity of 100 kN. To save time in the laboratory it was decided to determine the maximum specimen size theoretically, based on previous research.

B.2 Estimation of the Required Compressive Load Relative to Specimen Geometry

The following method was used to give an approximate estimation of the likely loads that would be encountered when carrying out the tests in the uniaxial compression testing programme. The main programme consisted of testing two material types (DBM and HRA) at three displacement rates and three temperatures.

Khanzada [1999] in this Ph.D thesis carried out a series of laboratory experiments investigating the steady-state deformation behaviour of a range of asphalt mixtures.

From these experiments he was able to construct plots of steady-state strain rate versus steady-state creep stress. Figure B.1 shows one such plot for a 10 mm DBM mixture with 100 penetration grade bitumen tested at 20°C. Using the plot it is possible to estimate from the strain rate, the corresponding induced stress. It is then possible to convert the stress to the applied load for a range of specimen sizes. Table B.1 shows the estimated loads for the range of specimen sizes previously discussed, for a range of displacement rates, at 20°C.

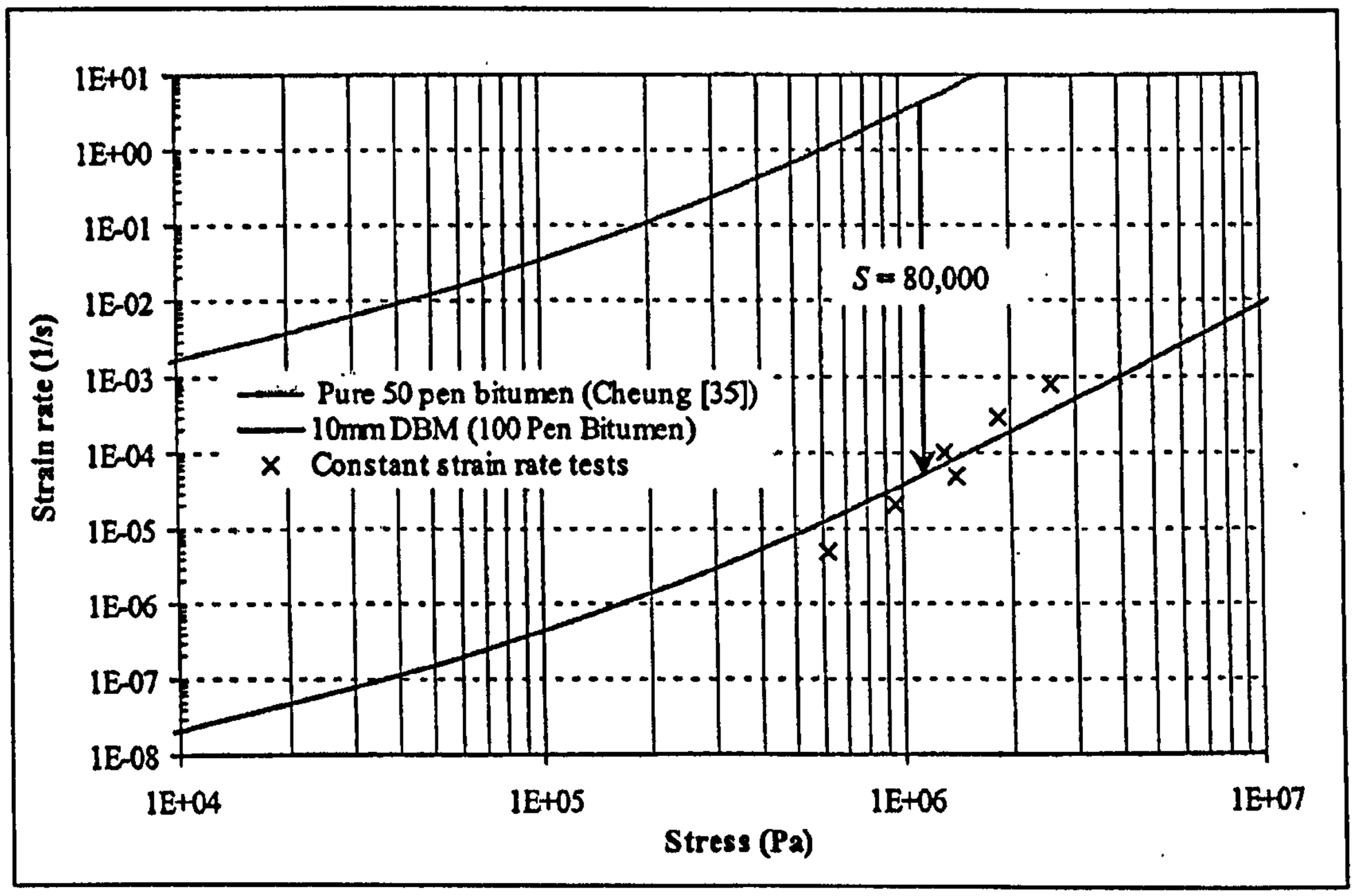

Figure B.1: Steady-state deformation behaviour of 10 mm DBM with 100 pen binder at 20°C [Reproduced from Khanzada, 1999]

Method:

a) Convert displacement rate to equivalent strain rate using Equation (B.1),

$$\dot{\varepsilon} = \frac{\dot{\delta}}{h} \tag{B.1}$$

where, $\dot{\varepsilon}$ = strain rate

$\dot{\delta}$ = displacement rate

h = specimen height in mm

b) Using Figure B.1 read off corresponding stress for the calculated strain rate,

c) Estimate the applied load using Equation (B.2).

$$P = \frac{\sigma \cdot d^2 \cdot \pi}{4} \qquad \text{(B.2)}$$

where, P = applied load

σ = stress in kPa

d = specimen diameter in metres

Table B.1: Estimated loads relative to specimen geometry and displacement rate at 20°C

Specimen Diameter (mm)	*Displacement Rate*		
	0.1 mm/s	*1 mm/s*	*10 mm/s*
140	17 kN	34 kN	100 kN
100	10 kN	26 kN	70 kN
50	8 kN	19 kN	50 kN

B.3 Conclusions

By using the simple method described above an estimation of the magnitude of loads that will be encountered when testing the DBM mixture in compression at 20°C has been possible. The results in Table B.1 show that at the faster loading rates only the 100 mm (20 mm stone size) or smaller diameter specimen sizes could be tested safely with the loading capacity of the available hydraulic equipment. However, as tests were also to be undertaken at 5°C, where higher loads would be expected, it was decided to restrict the specimen size to a 50 mm diameter (10 mm maximum stone size) and hence the choice of mixture type was restricted to wearing course designs.

Appendix C - Determination of the Average Radial Strain from the Radial Variable Differential Transformer Data

C.1 Introduction

The radial variable differential transformer (RVDT) unit was used in the uniaxial compression test to measure the average radial strain exhibited by the specimen during a test. The unit measures the increase in the circumference of the specimen at mid-height throughout the duration of a test. Figure C.1 shows that this is possible, as the extensible wire that is used to measure the circumferential increase in the specimen, is allowed to pivot at the RVDT end as the specimen is compressed.

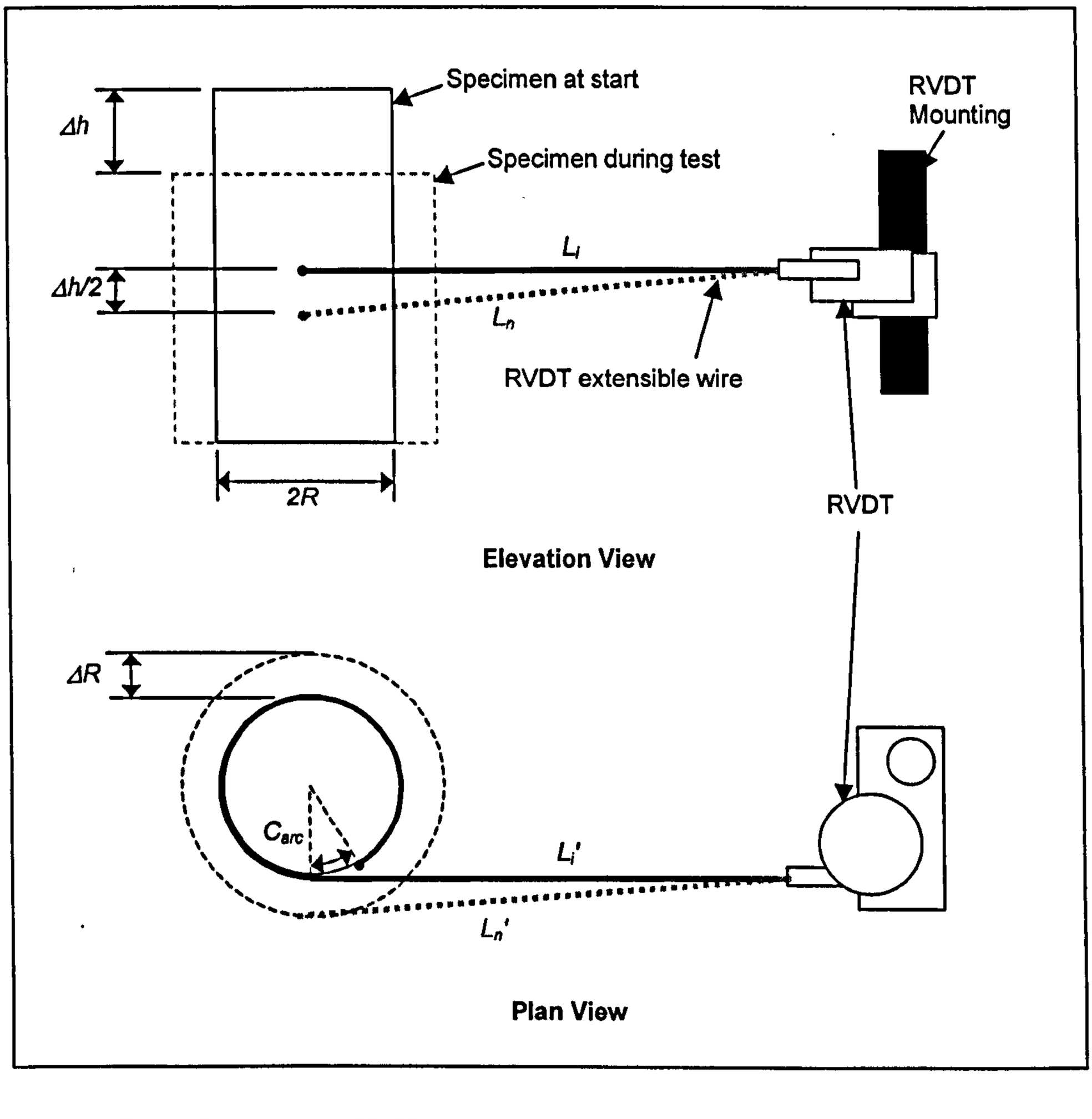

Figure C.1: Movement of RVDT extensible wire in relation to specimen during the uniaxial compression test [Adapted from Erkens *et al.*, 1998]

Therefore the RVDT system measures the increase in the extension of wire due to an increase in the radius of the specimen, but also the increase in the extension of the

wire due to the displacement in both the vertical and horizontal positions of the wire. To determine the actual increase in the radius of the specimen, these displacements need to be taken into account.

C.2 Determination of the Average Radial Strain from the RVDT Measurement

From Figure C.1, the change in the extension of the wire due to vertical displacement, ΔL_v, can be expressed as:

$$\Delta L_v = L_n - L_i = \left[L_i^2 + \left(\frac{\Delta h}{2} \right)^2 \right]^{\frac{1}{2}} - L_i \qquad \text{(C.1)}$$

and the change in the extension of the wire due to the horizontal displacement, ΔL_h, can be expressed as:

$$\Delta L_h = L_n' - L_i' = \left(L_i'^2 + \Delta R^2 \right)^{\frac{1}{2}} - L_i' \qquad \text{(C.2)}$$

where the distances L_i, L_n, L_i', L_n', Δh and ΔR are as defined in Figure C.1. The change in the circumference of the specimen, ΔC, is given by:

$$\Delta C = 2\pi\Delta R - \theta\Delta R \qquad \text{(C.3)}$$

where, $$\theta = \frac{C_{arc}}{R} \qquad \text{(C.3a)}$$

in which R is the radius of the specimen and C_{arc} is as defined in Figure C.1.

Treating the horizontal and vertical changes in the position of the wire as geometrically independent events, and by making the assumption that the vertical

displacement occurs first, $L_i' = L_n$, the total change in the extension of wire, ΔL_{Total}, can by described by Equation (C.4) [Erkens *et al.*, 1998].

$$\Delta L_{Total} = L_n' - L_i = \left(L_i'^2 + \Delta R^2\right)^{\frac{1}{2}} - L_i \qquad \text{(C.4)}$$

which substituting the expression for L_n from Equation (C.1) into Equation (C.4) gives:

$$\Delta L_{Total} = \left[\left(\left(L_i^2 + \left(\frac{\Delta h}{2}\right)^2\right)^{\frac{1}{2}}\right)^2 + \Delta R^2\right]^{\frac{1}{2}} - L_i = \left[L_i^2 + \left(\frac{\Delta h}{2}\right)^2 + \Delta R^2\right]^{\frac{1}{2}} - L_i \qquad \text{(C.5)}$$

The RVDT system measures the change in the extension of wire due to the increase in the radius of the specimen, and the change in the extension of wire due to the change in the position of the wire. Therefore the RVDT reading, P, comprises two parts:

$$P = \Delta C + \Delta L_{Total} \qquad \text{(C.6)}$$

Substituting Equations (C.3) and (C.5) for their respective equivalents in Equation (C.6) and rearranging to solve for ΔR gives Equation (C.7), which can then be solved iteratively to obtain ΔR.

$$\Delta R = \frac{P - \left[\left(L_i^2 + \left(\frac{\Delta h}{2}\right)^2 + \Delta R^2\right)^{\frac{1}{2}} + L_i\right]}{2\Pi - \left(\frac{C_{arc}}{R}\right)} \qquad \text{(C.7)}$$

As the RVDT extensible wire runs around the specimen on plastic guides (see Section 4.6.1) a final correction ratio, given in Equation (C.8) is applied to obtain the actual

average radial strain of the test specimen.

$$\varepsilon_r = \frac{\Delta R}{R} \cdot \frac{\phi_s}{\phi_{sg}} \tag{C.8}$$

where ε_r = average radial strain

ϕ_s = diameter of the specimen

ϕ_{sg} = diameter of the specimen with guides

Appendix D - Compression Test Data Filtering

D.1 Problem Outline

Analysis of the compressive test data revealed that for some data sets interference was disrupting the LVDT signals, and therefore use of a filtering system would be required. Figure D.1 shows a typical plot of the LVDT signals from a compression test. The figure shows the axial and radial stress-strain curves for a test conducted on a HRA mixture specimen, at 20°C at a displacement rate of 1 mm/s. It can be seen from the plot that both LVDT signals display a sinusoidal oscillation of approximately 3.5 Hz.

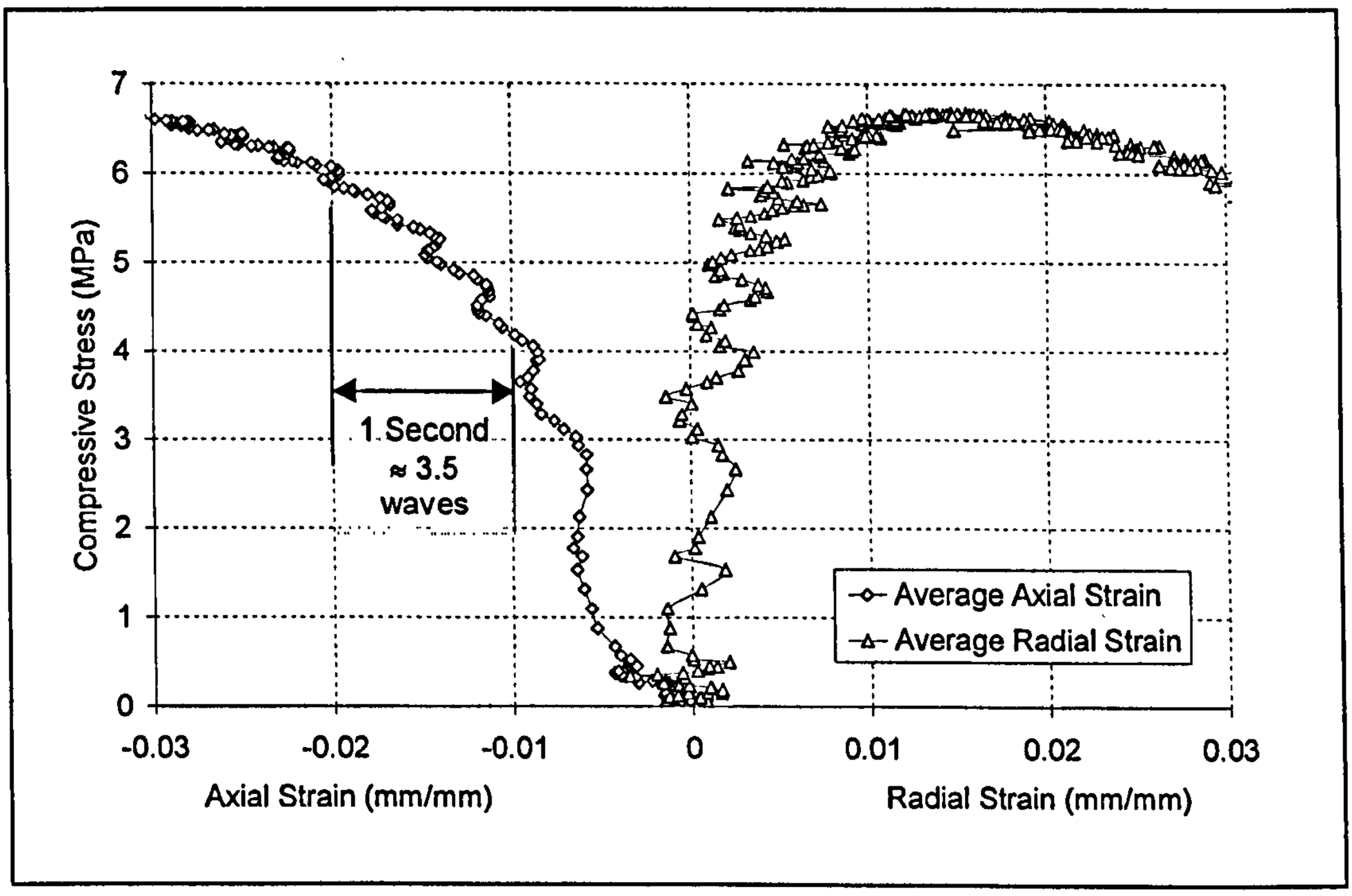

Figure D.1: Plot showing LVDT interference – HRA mixture at 20°C and 1 mm/s

A definitive cause for the interference shown in Figure D.1 could not be identified. However, an investigation into this type of phenomena revealed the interference to be consistent with that produced by spurious beat frequencies [Pain, 1970]. Beats are caused when two or more waves of different frequency interact. The alternatively constructive and destructive interference causes the beat phenomena, see Figure D.2. The number of beats per second is equal to the difference in frequency, given by Equation (D.1)

$$f_{beat} = |f_2 - f_1| \qquad \text{(D.1)}$$

where, f_{beat} = beat frequency

$f_{1,2}$ = interacting wave frequencies

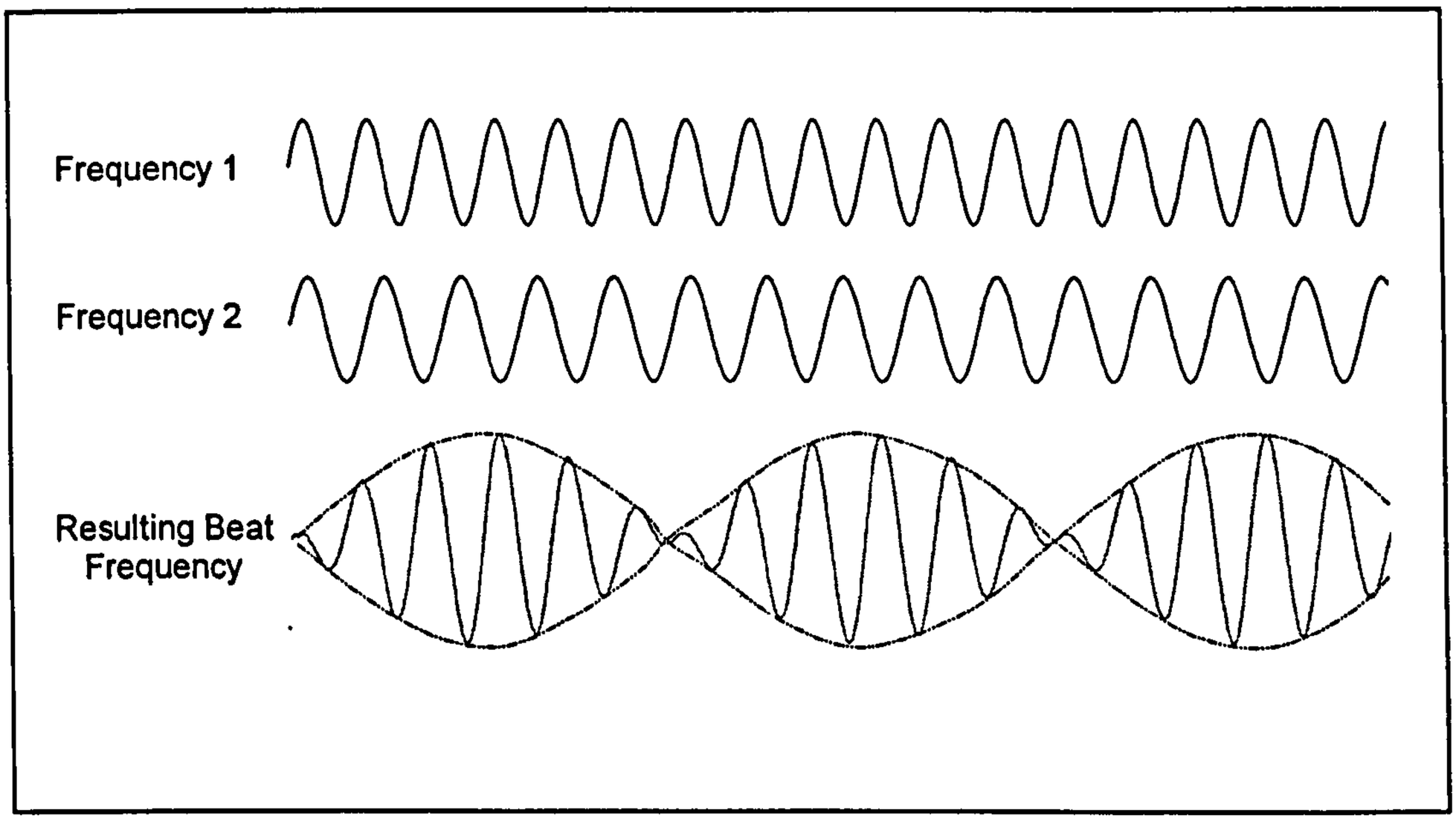

Figure D.2: Schematic showing beat interference

When more than one AC energised LVDT is being used in a measurement arrangement, where the instruments are contiguously mounted or the transducer cabling is in a common conduit, beat frequencies may be produced. In the case of the compression test arrangement it is likely that a beat frequency arose from the 5-kHz oscillators used in the instrumentation to develop the excitation. To prevent beat frequencies from occurring it is necessary to designate one unit the master, with the remaining units being driven from the oscillator contained within the master unit, therefore ensuring a common wave frequency for all four LVDT's. However, as this problem was not recognised until the completion of the compression testing programme, an alternative post data correction solution was sought.

D.2 Data Smoothing

As can be seen from Figure D.1, the signal interference manifested as a sine wave of 3.5 Hz superimposed on the test data. In order to minimise this interference a data-

smoothing package was used. The package employed was part of a data analysis program entitled 'Table Curve 2D' [SPSS Inc, 1996]. An automated Loess smoothing algorithm, that performed a least-squares fit for each data point was used on each compressive data set. Figure D.3 shows an example of a typical compressive data set before and after data smoothing. The figure shows the axial and radial stress-strain curves for a test conducted on an HRA mixture specimen, at 20°C at displacement rate of 1 mm/s.

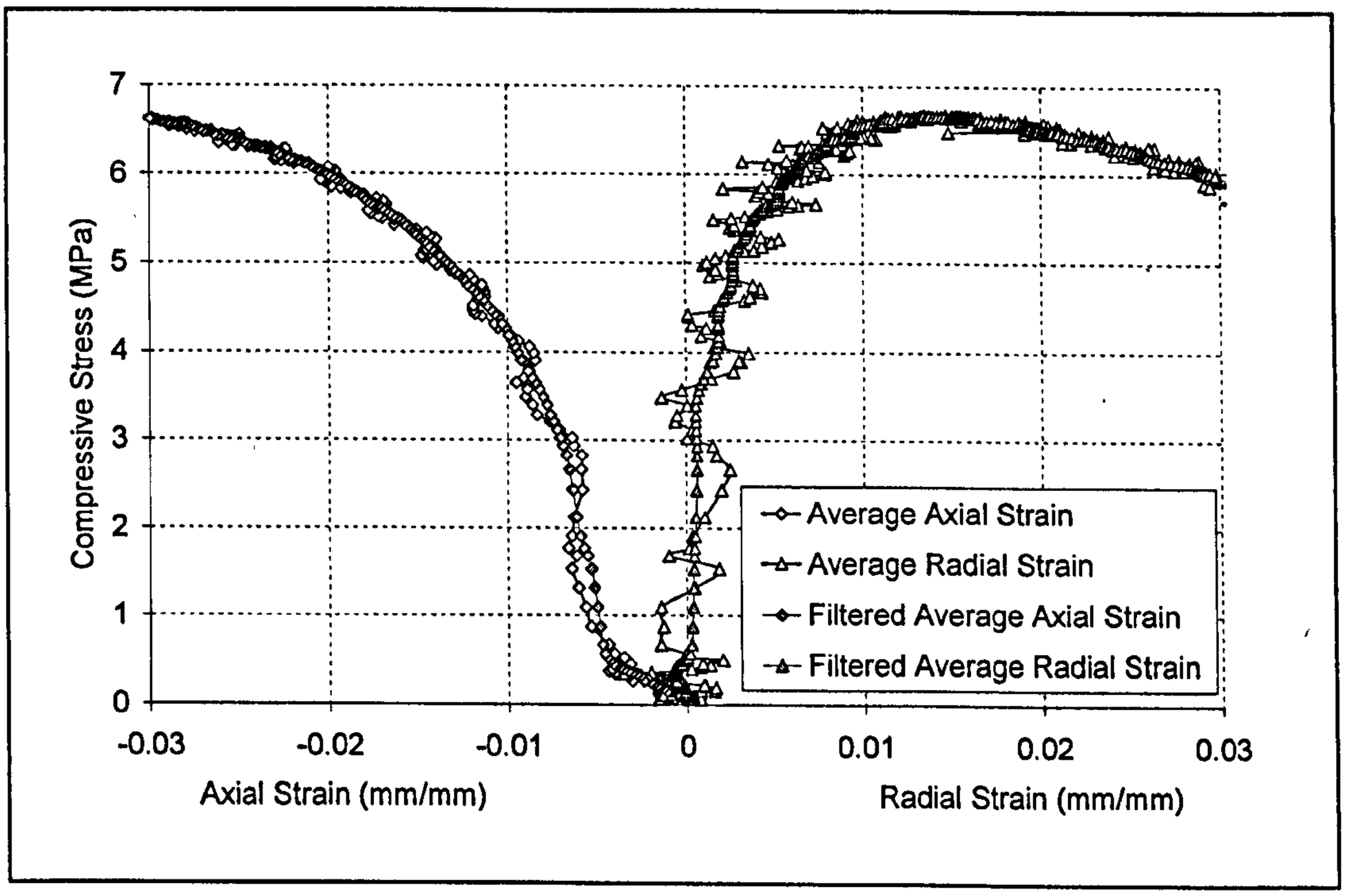

Figure D.3: Plot showing LVDT signal before and after data filtering – HRA mixture at 20°C and 1 mm/s

As can be seen from Figure D.3 this method of data smoothing proved effective in minimising the sinusoidal wave interference, and was therefore used on any compressive data set displaying such a phenomenon.

Appendix E - Uniaxial Compression Test Results

E.1 Uniaxial Compression Test Results - DBM Mixture

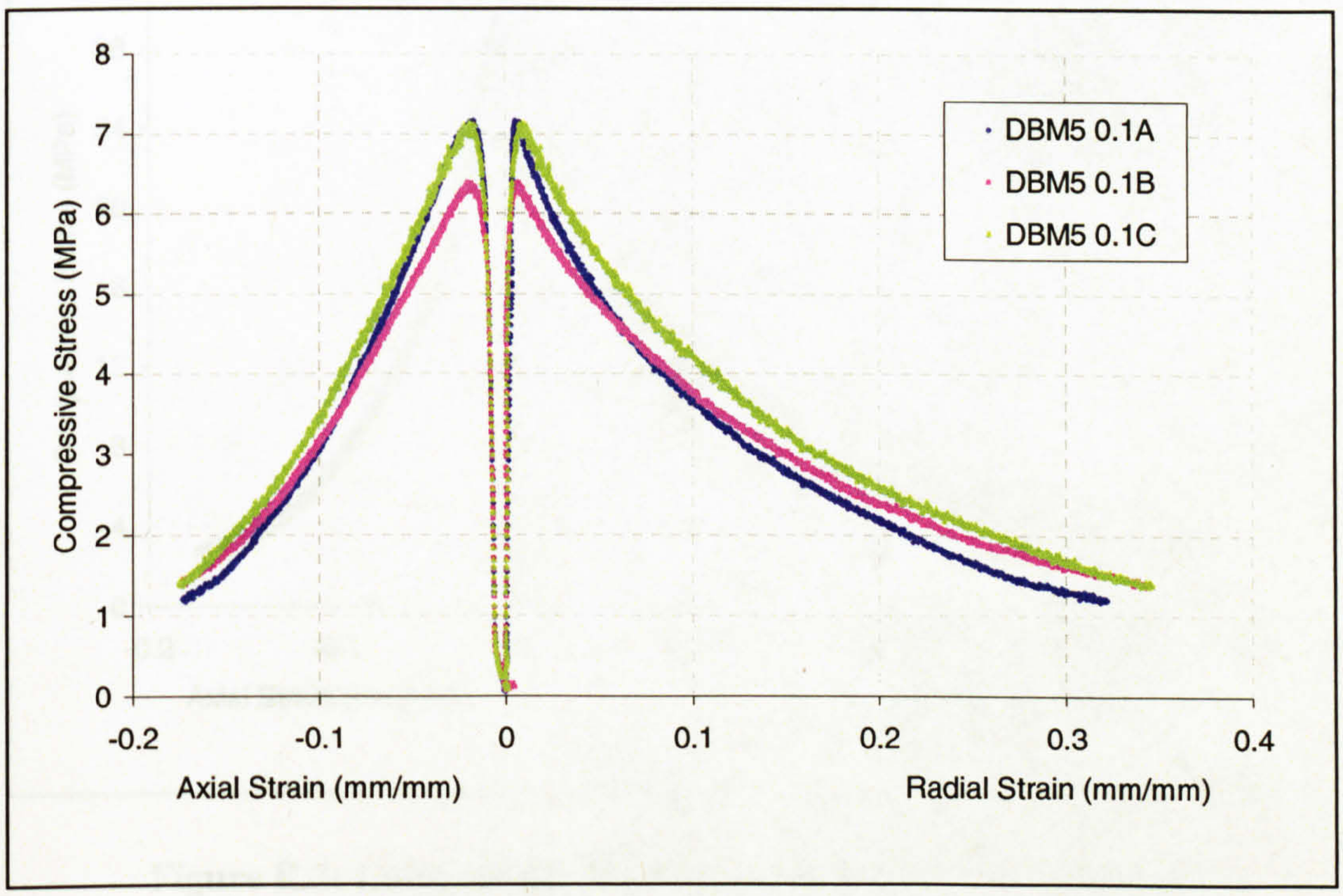

Figure E.1: Compression Test Data - DBM at 5°C at 0.1 mm/s

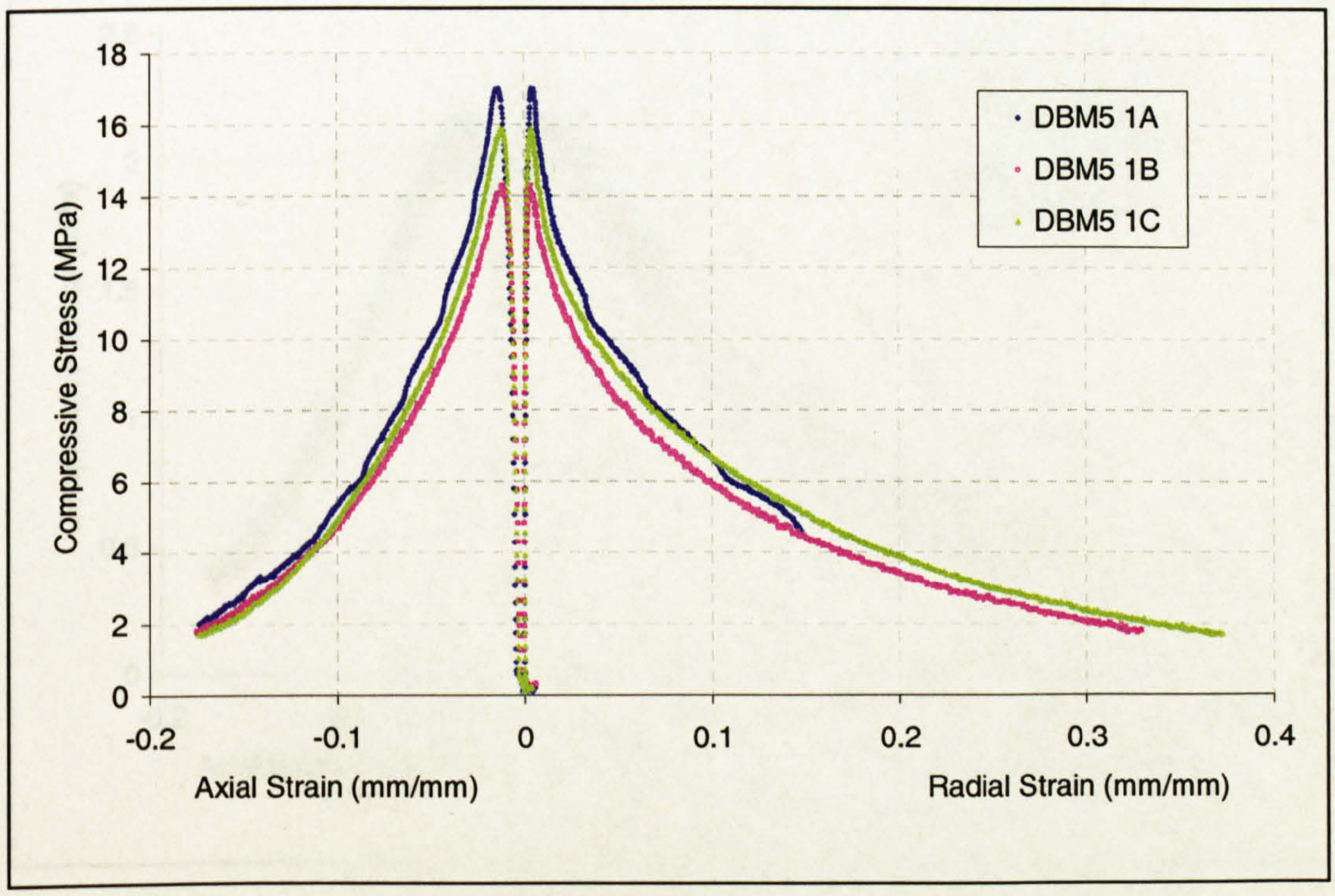

Figure E.2: Compression Test Data - DBM at 5°C at 1 mm/s

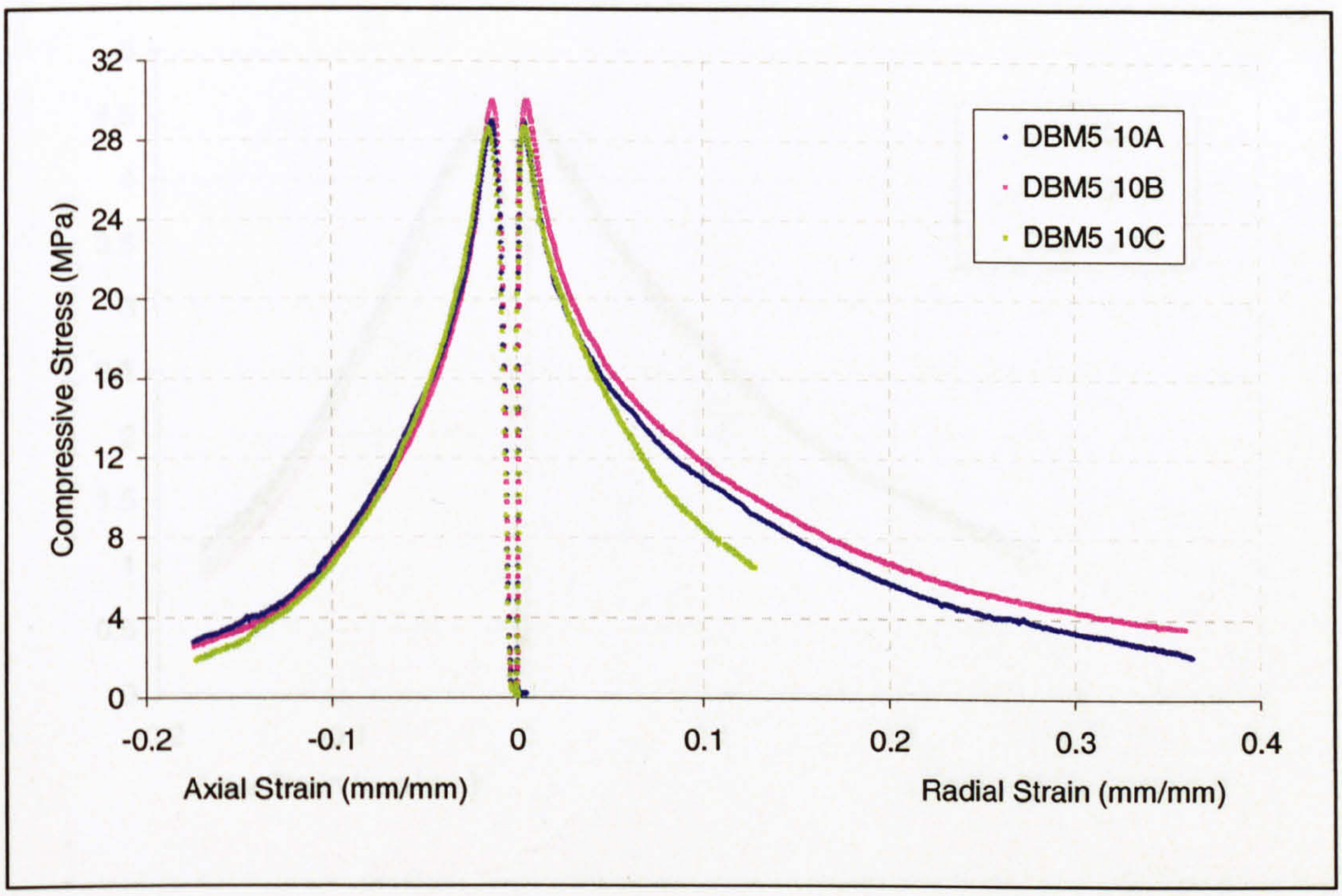

Figure E.3: Compression Test Data – DBM at 5°C at 10 mm/s

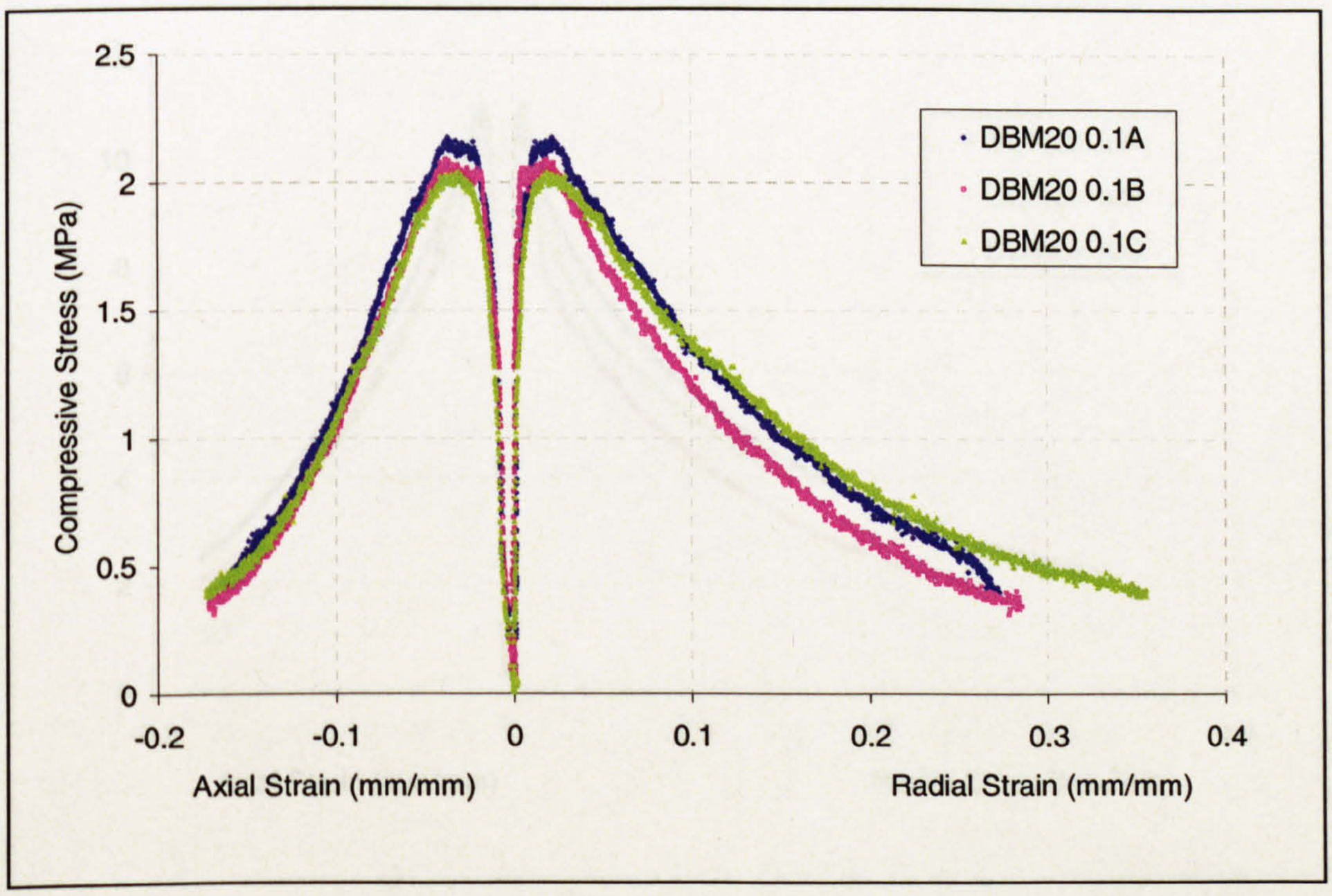

Figure E.4: Compression Test Data – DBM at 20°C at 0.1 mm/s

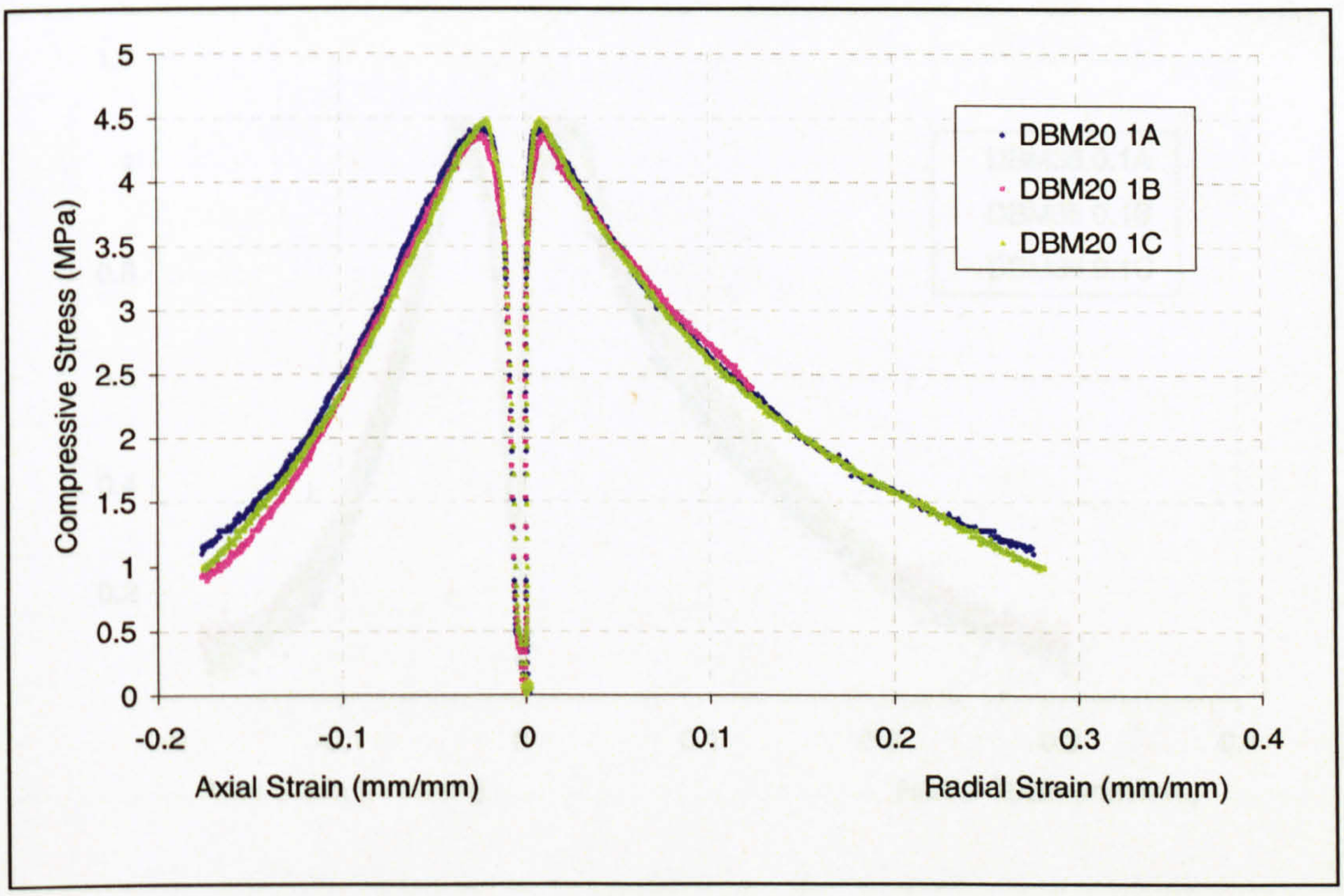

Figure E.5: Compression Test Data – DBM at 20°C at 1 mm/s

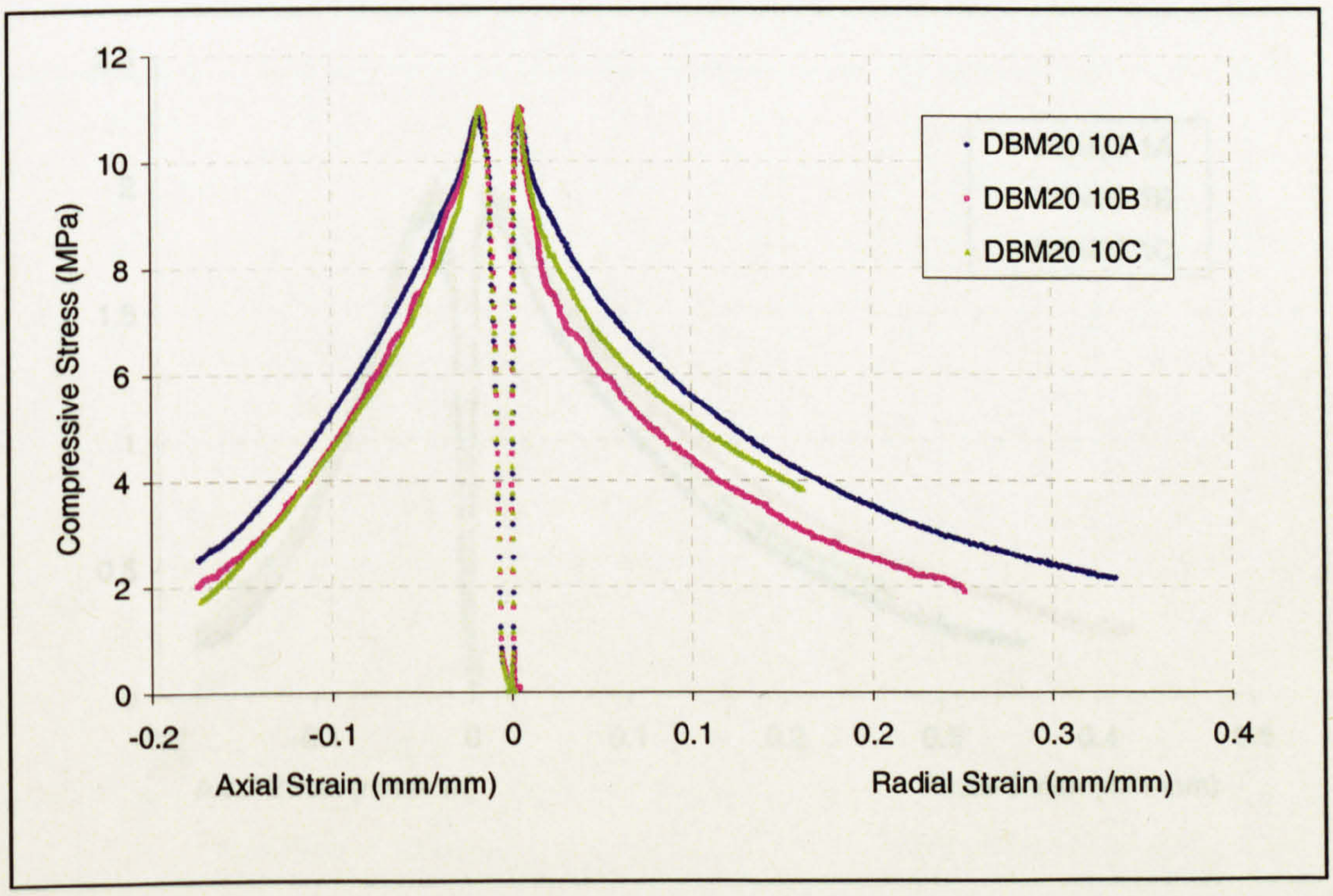

Figure E.6: Compression Test Data – DBM at 20°C at 10 mm/s

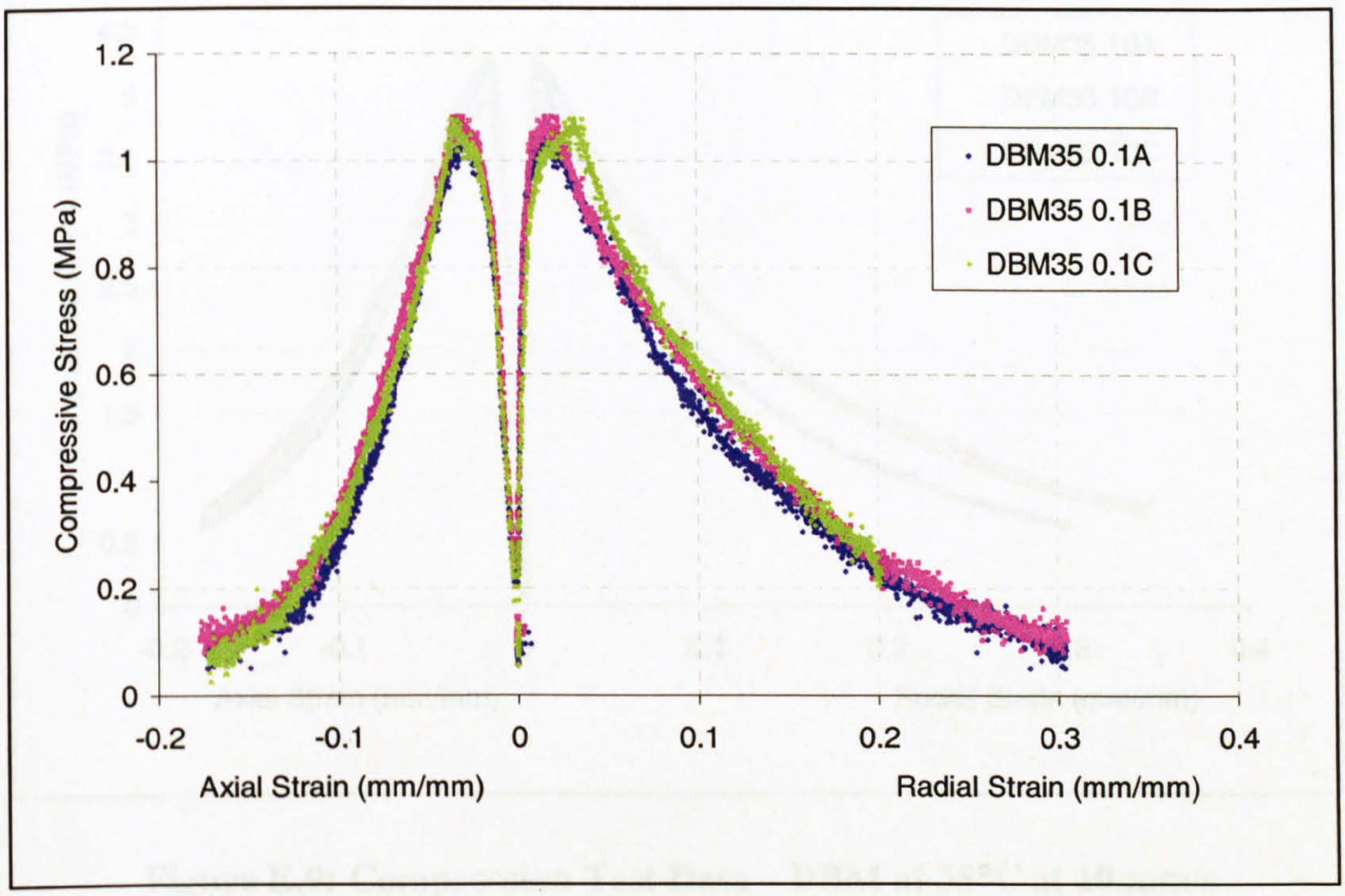

Figure E.7: Compression Test Data – DBM at 35°C at 0.1 mm/s

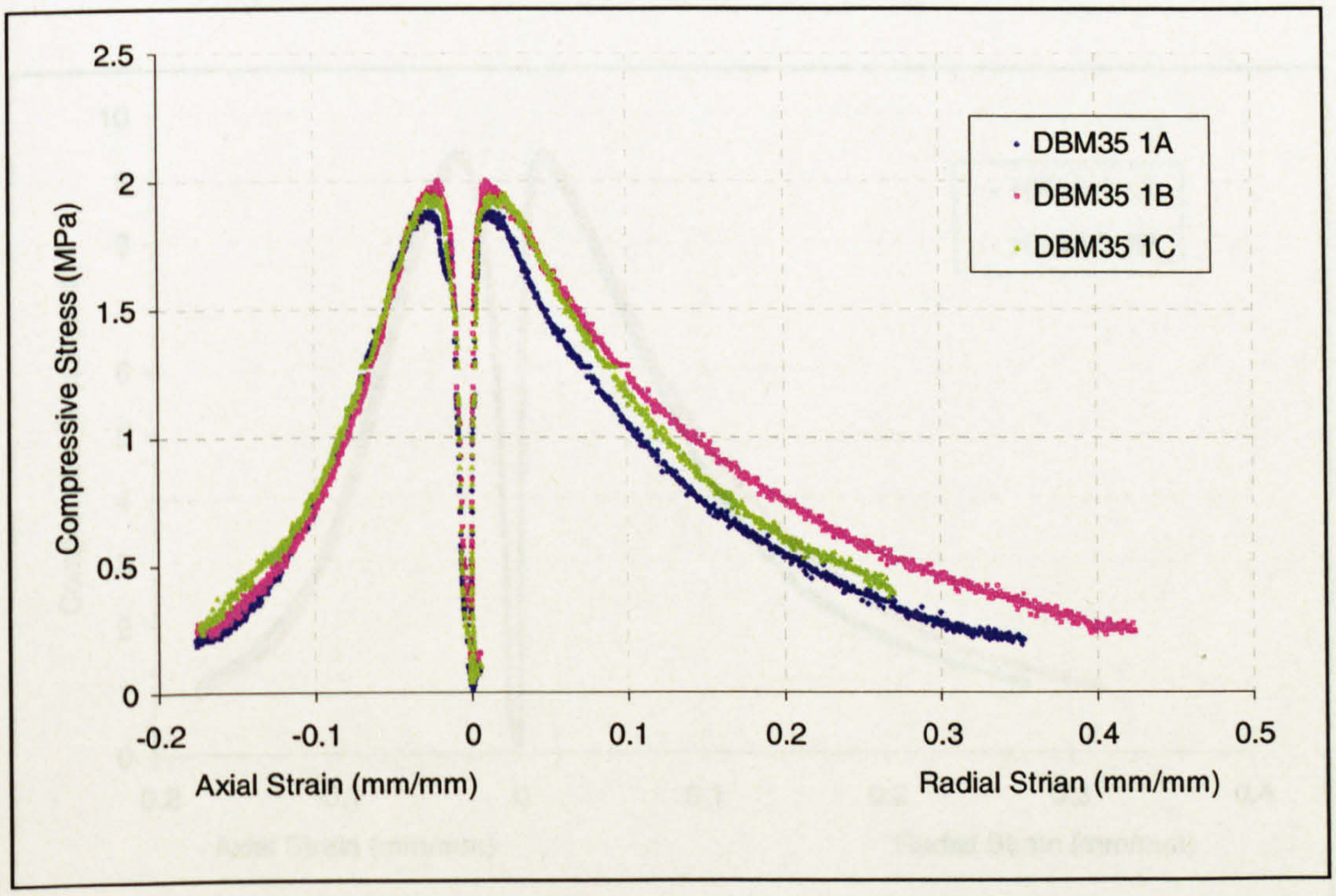

Figure E.8: Compression Test Data – DBM at 35°C at 1 mm/s

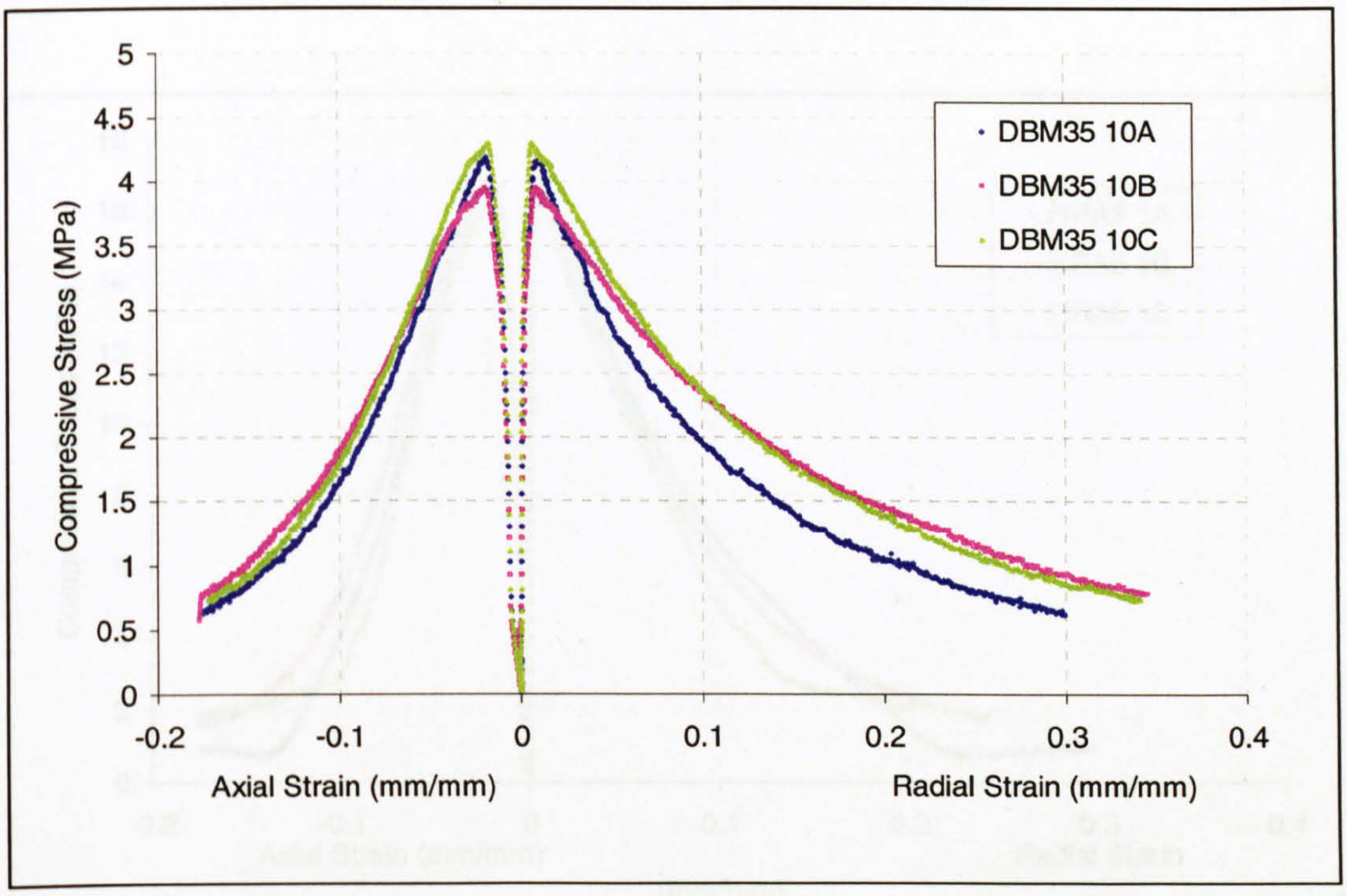

Figure E.9: Compression Test Data – DBM at 35°C at 10 mm/s

E.2 Uniaxial Compression Test Results – HRA Mixture

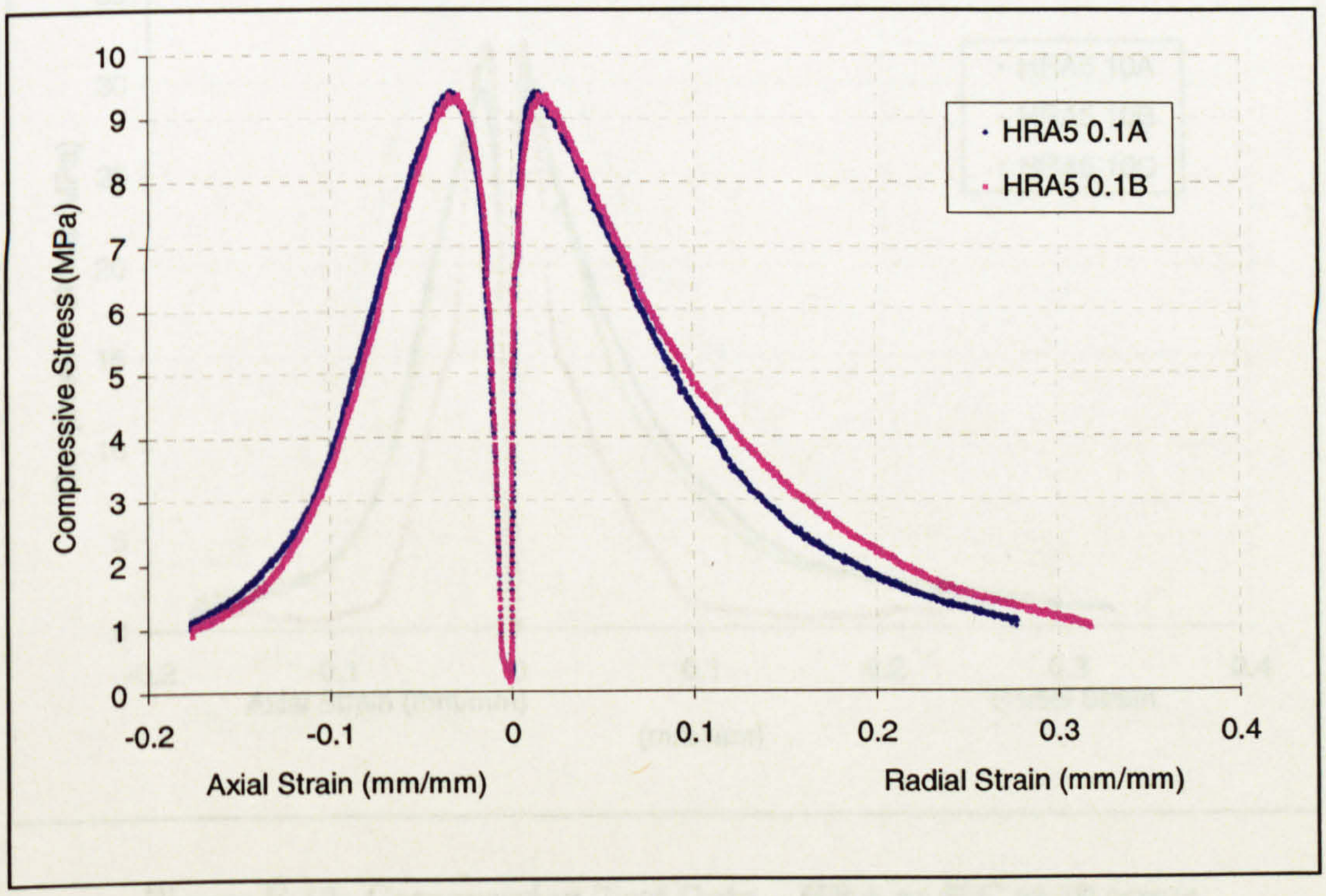

Figure E.10: Compression Test Data – HRA at 5°C at 0.1 mm/s

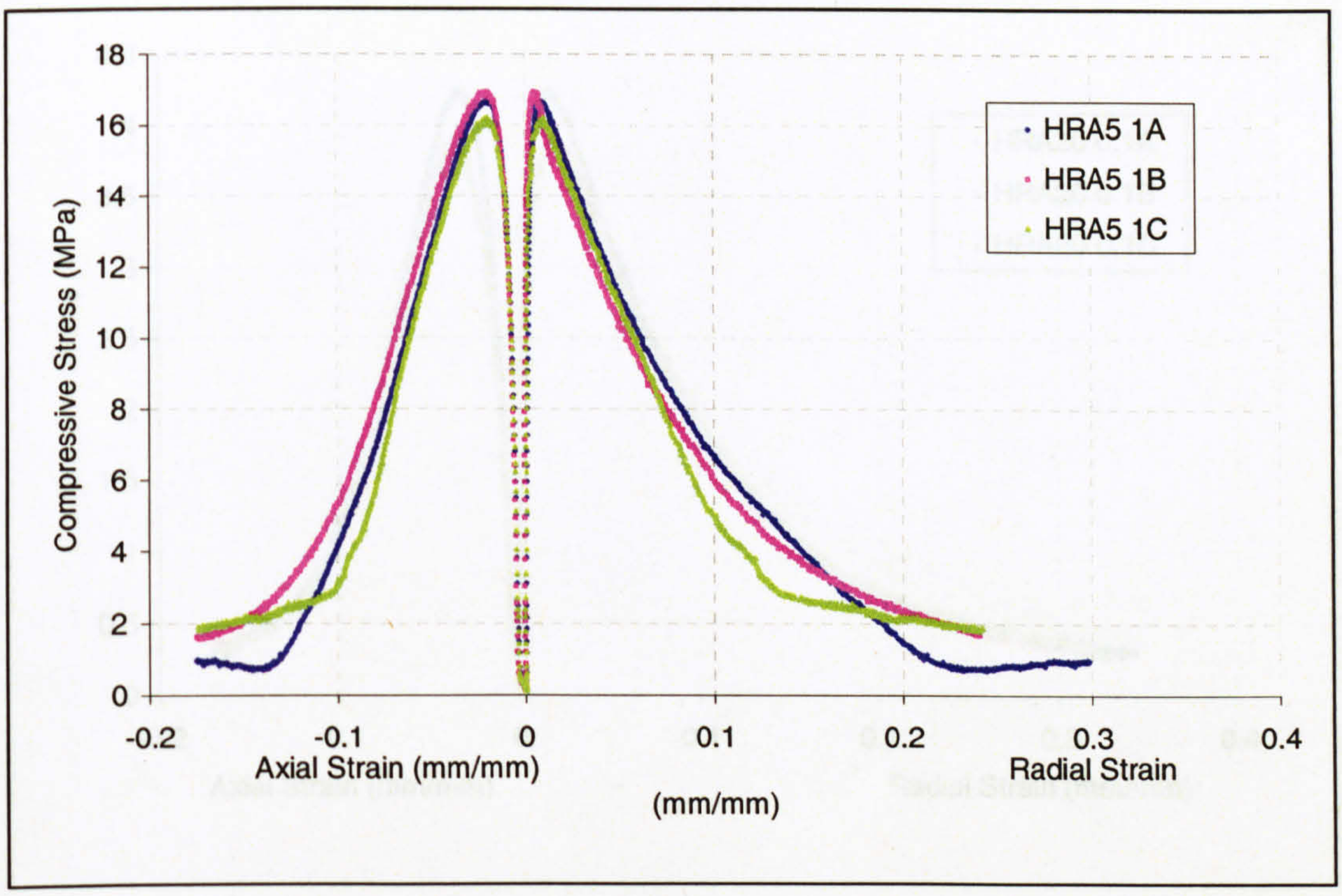

Figure E.11: Compression Test Data – HRA at 5°C at 1 mm/s

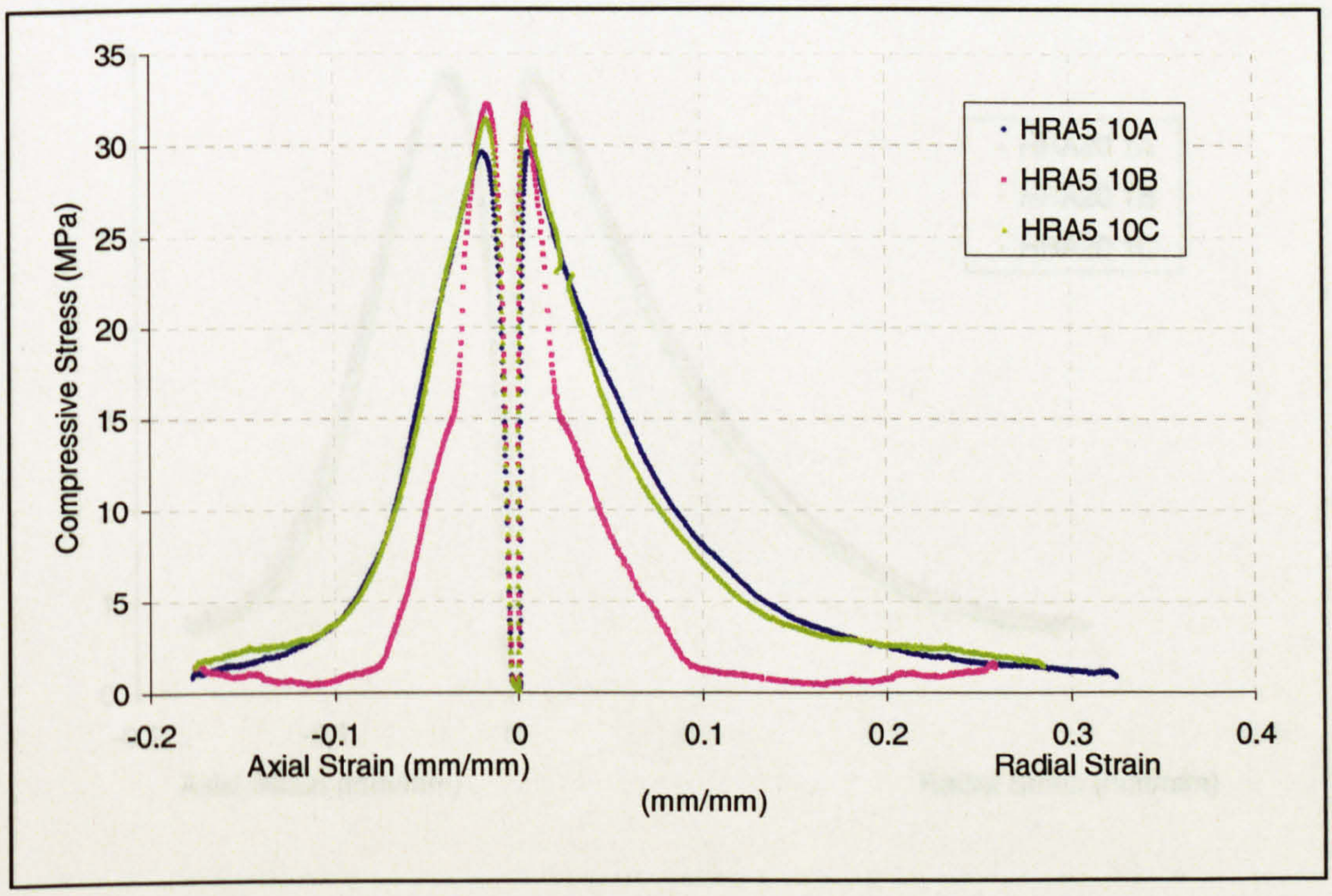

Figure E.12: Compression Test Data – HRA at 5°C at 10 mm/s

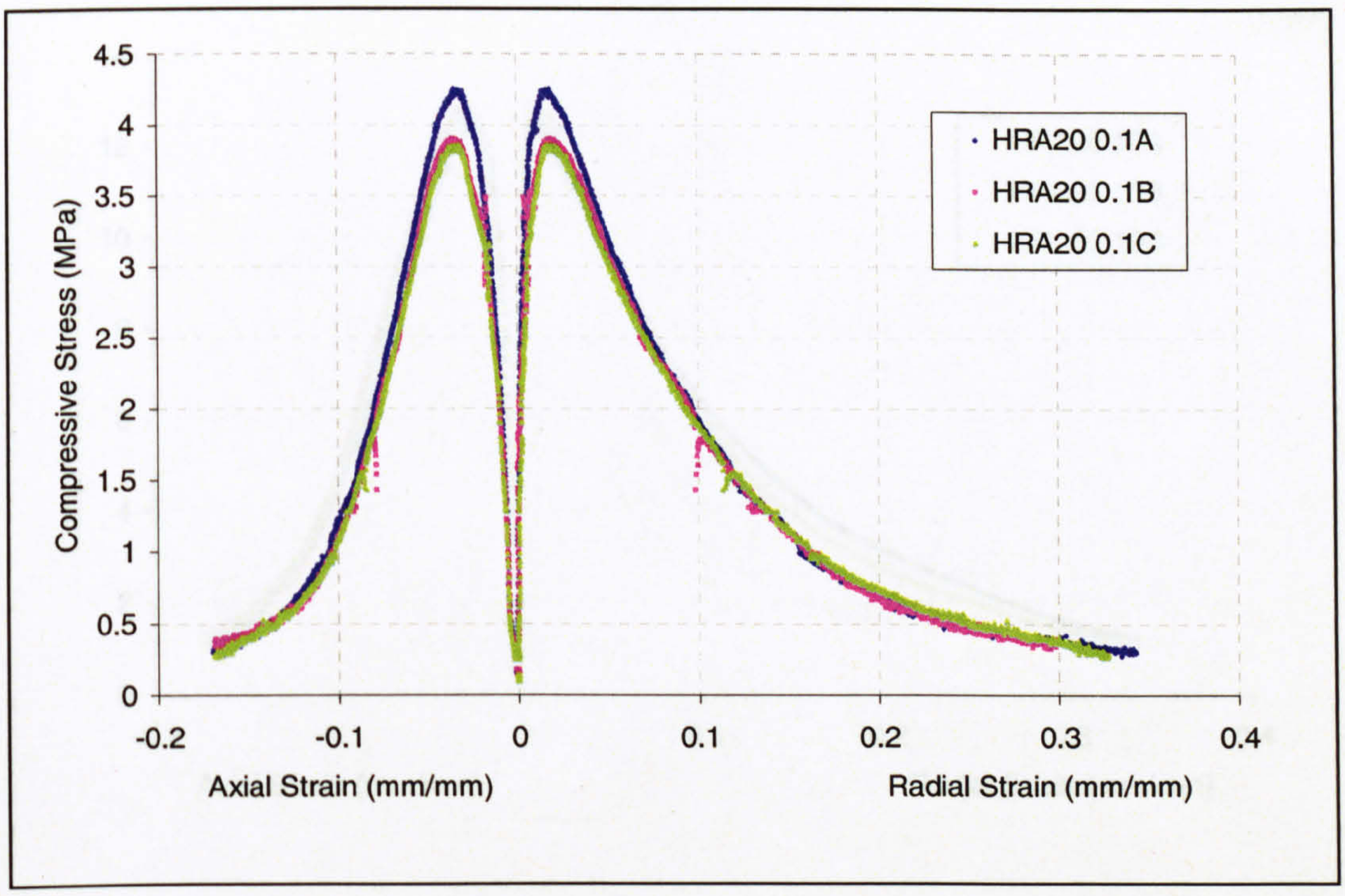

Figure E.13: Compression Test Data – HRA at 20°C at 0.1 mm/s

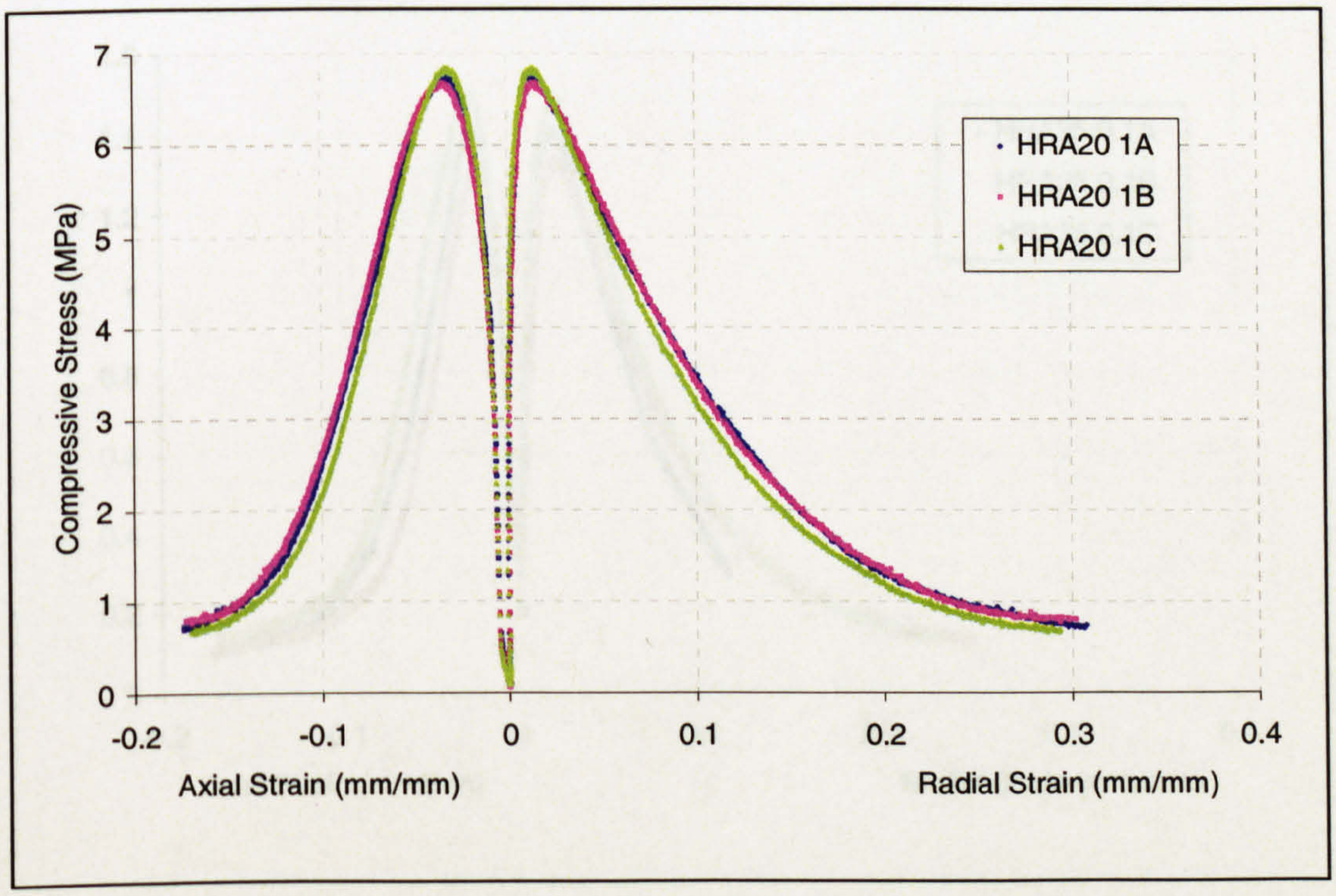

Figure E.14: Compression Test Data – HRA at 20°C at 1 mm/s

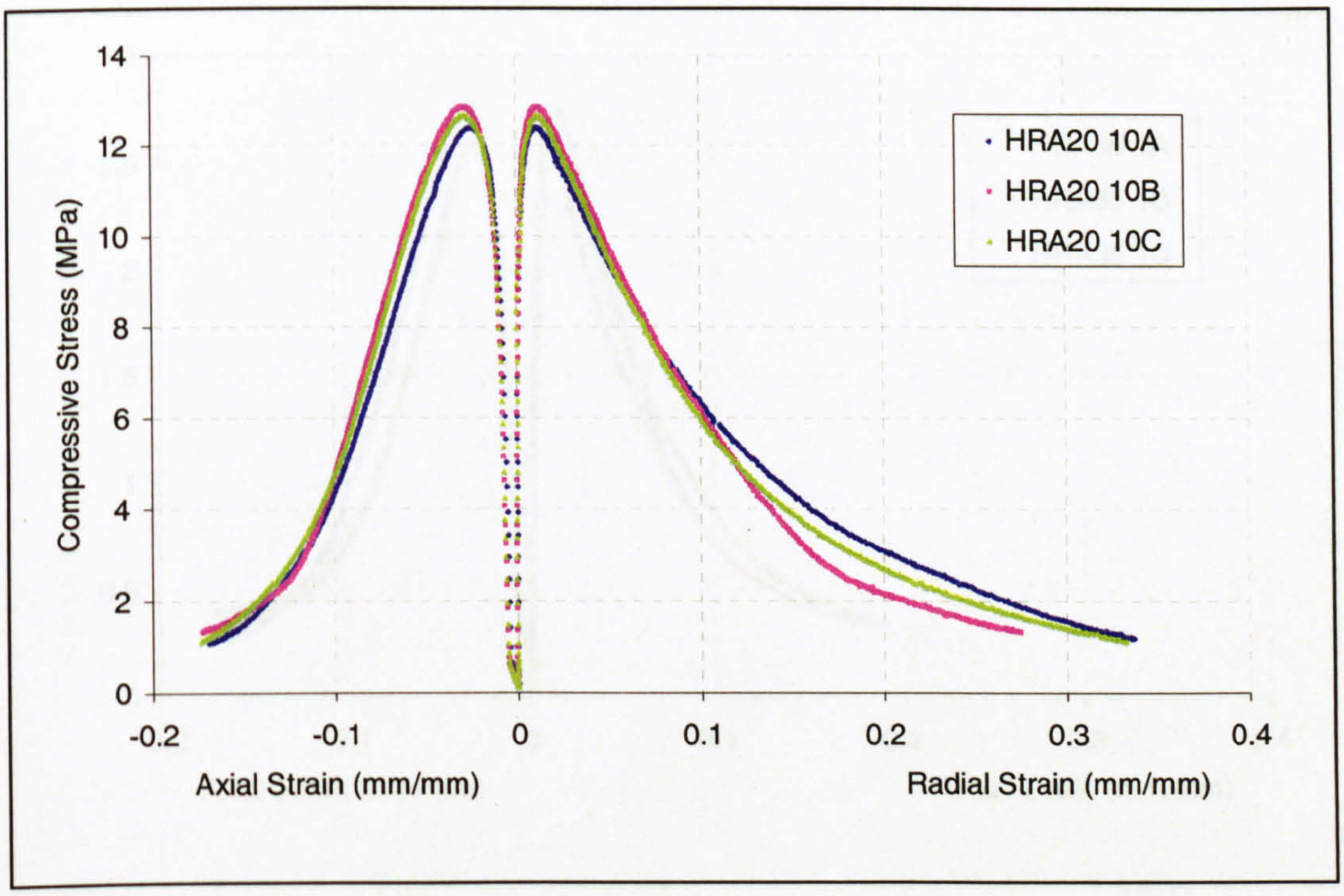

Figure E.15: Compression Test Data – HRA at 20°C at 10 mm/s

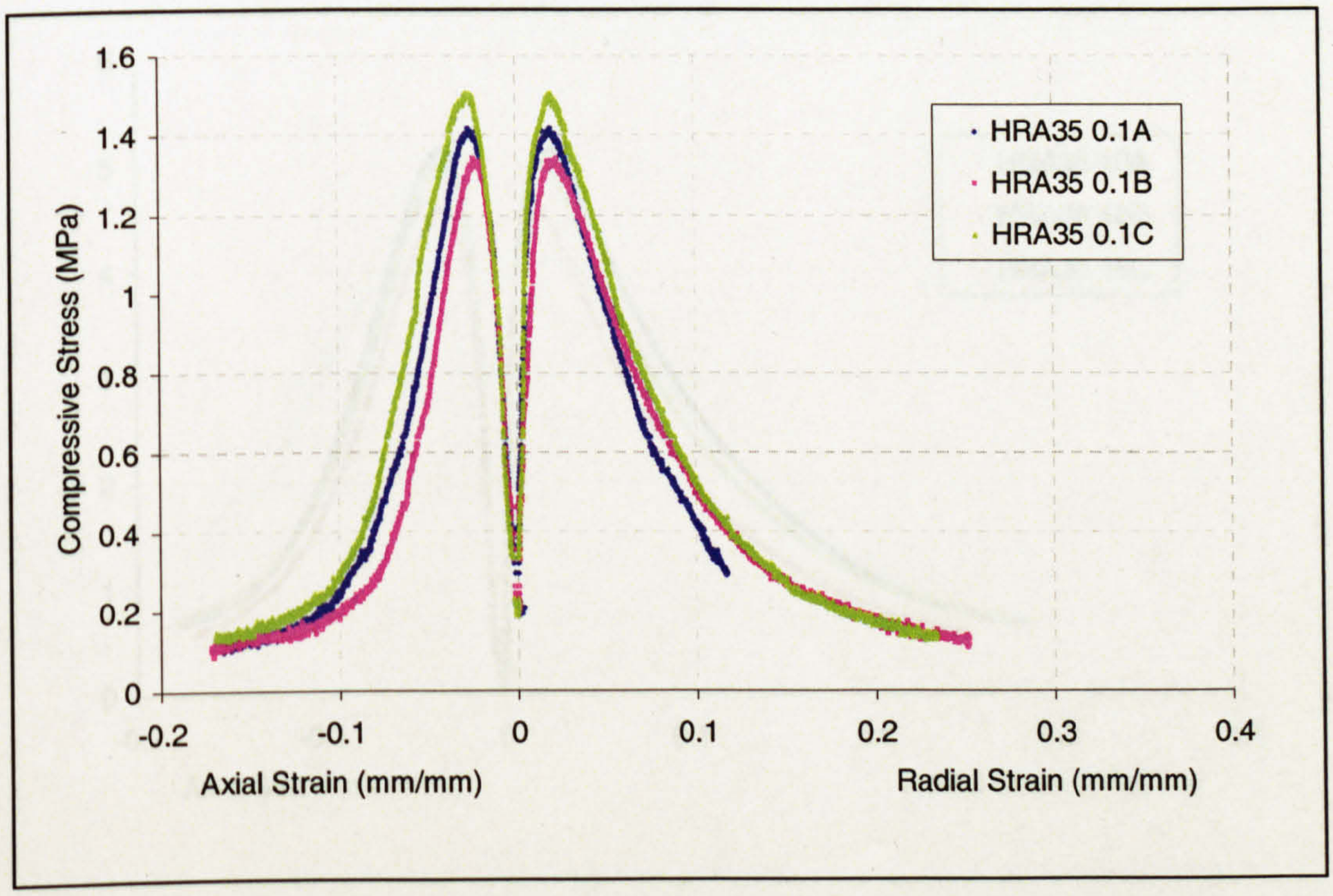

Figure E.16: Compression Test Data – HRA at 35°C at 0.1 mm/s

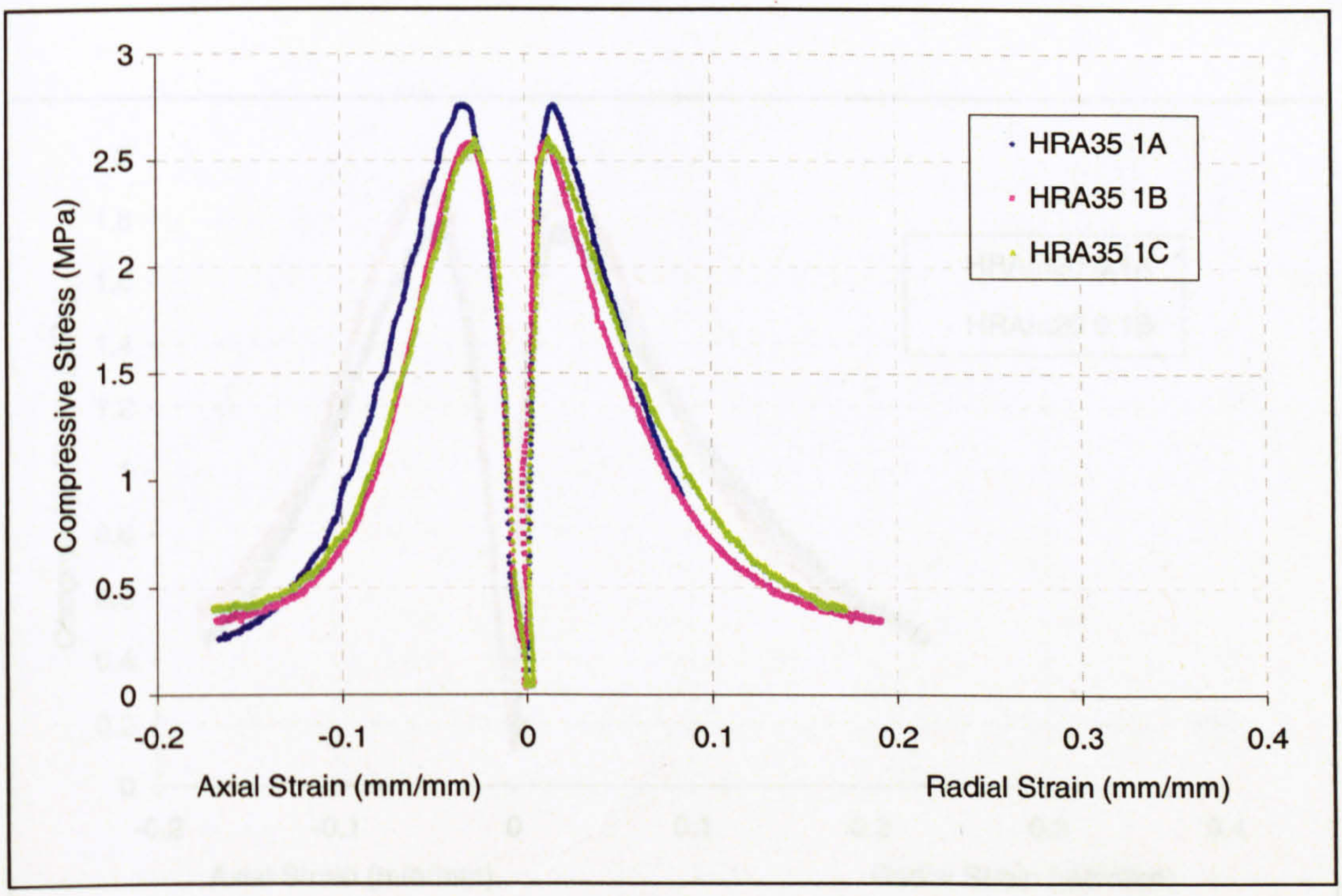

Figure E.17: Compression Test Data – HRA at 35°C at 1 mm/s

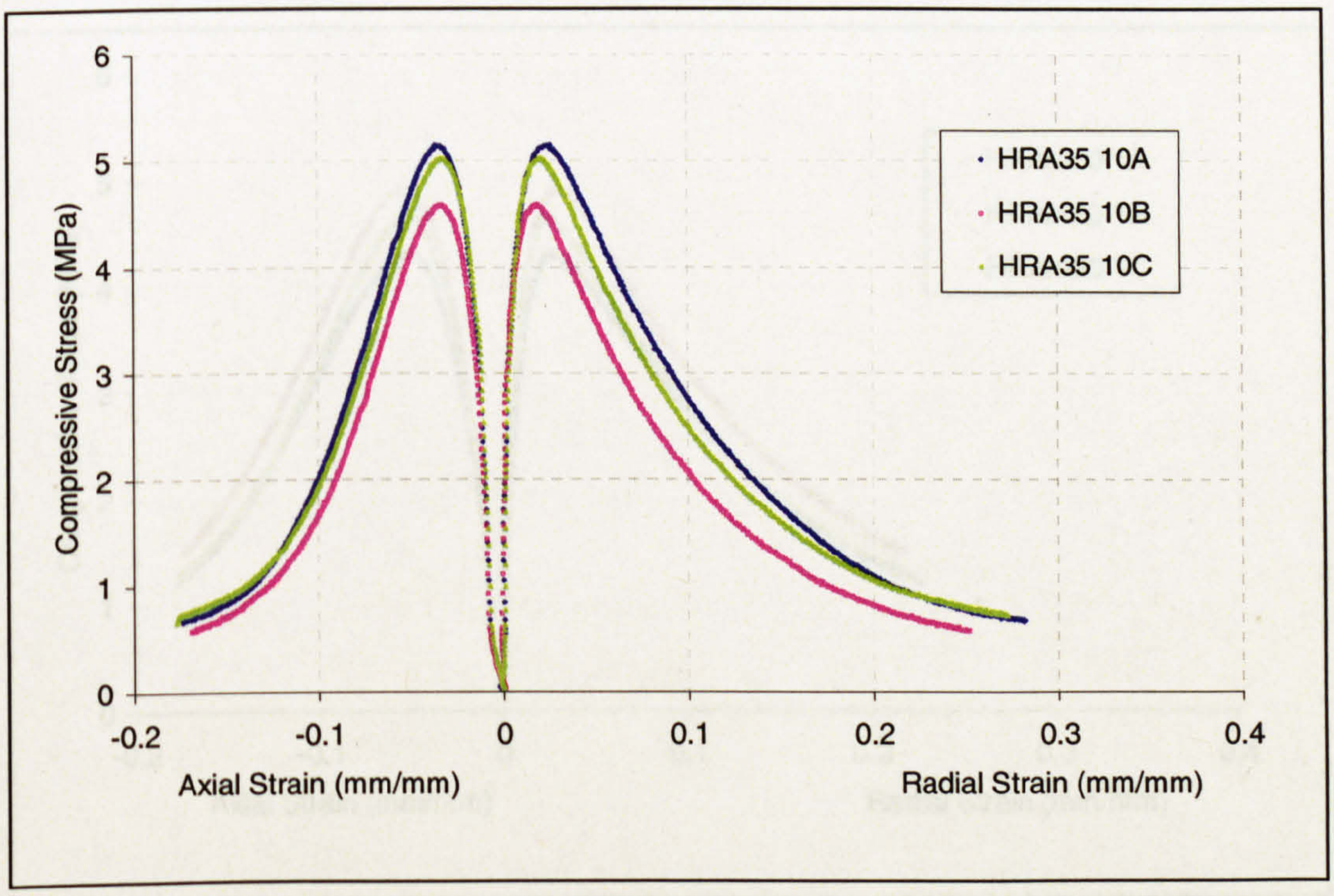

Figure E.18: Compression Test Data – HRA at 35°C at 10 mm/s

E.3 Uniaxial Compression Test Results – HRA Mortar Mixture

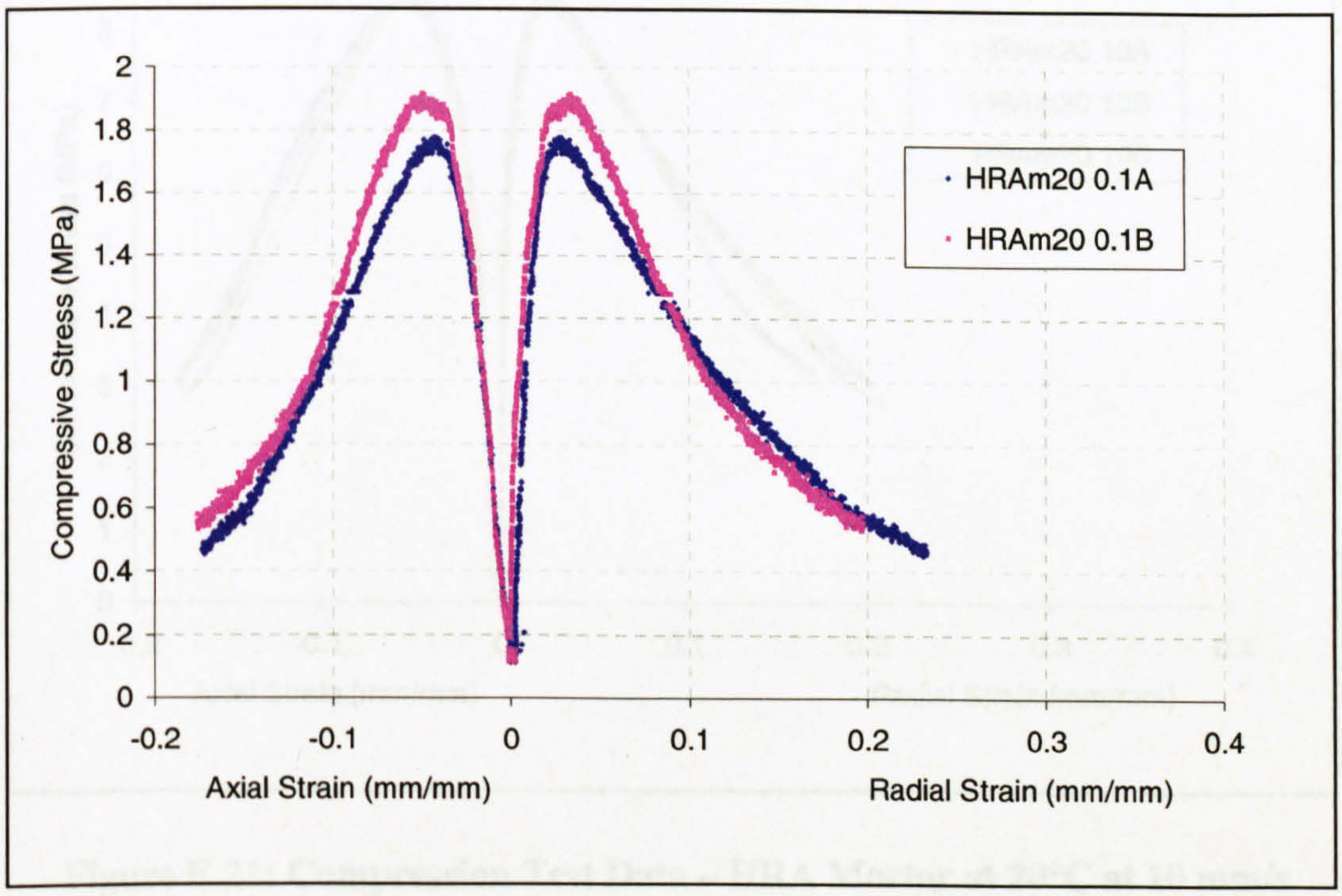

Figure E.19: Compression Test Data – HRA Mortar at 20°C at 0.1 mm/s

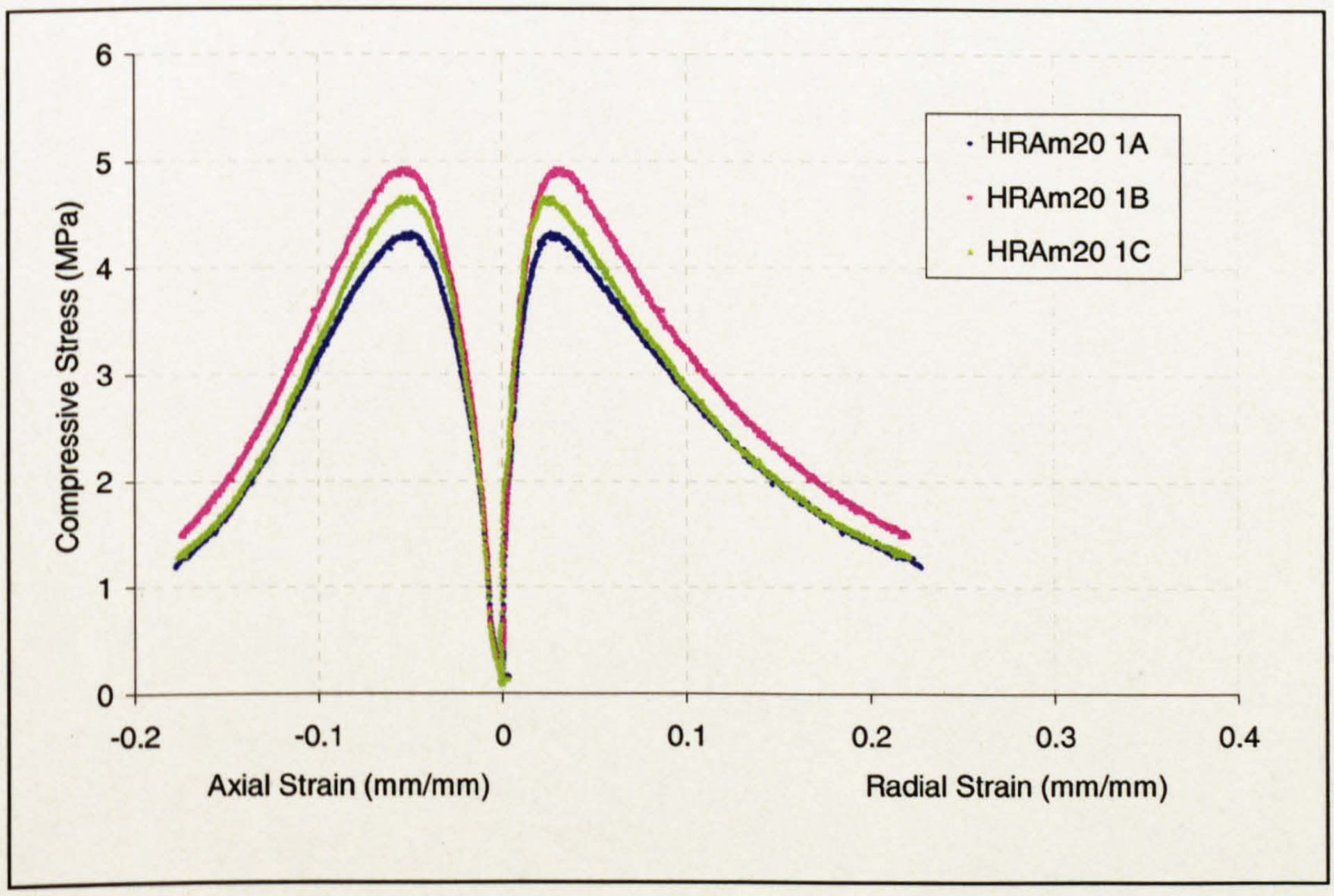

Figure E.20: Compression Test Data – HRA Mortar at 20°C at 1 mm/s

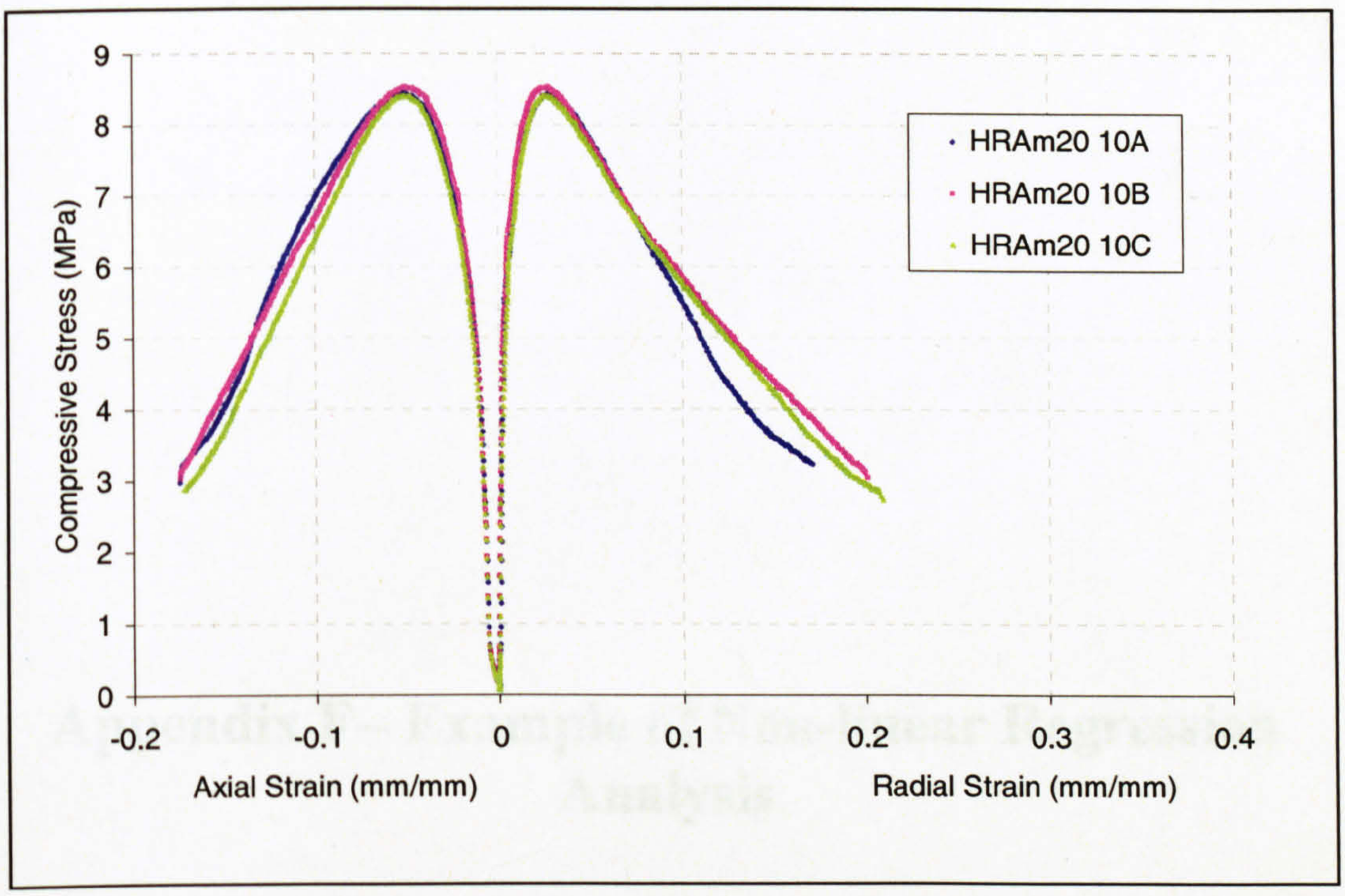

Figure E.21: Compression Test Data – HRA Mortar at 20°C at 10 mm/s

Appendix F– Example of Non-linear Regression Analysis

	t	v	fc
1	278.15	.001	-6.89
2	278.15	.010	-15.74
3	278.15	.100	-29.20
4	293.15	.001	-2.10
5	293.15	.010	-4.42
6	293.15	.100	-10.96
7	308.15	.001	-1.07
8	308.15	.010	-1.95
9	308.15	.100	-4.15

Non-linear Regression

All the derivatives will be calculated numerically.

Iteration	Residual SS	A	B	C	D
1	1305.581164	-1.0000000	.000000000	1.00000000	1.00000000
1.1	1314.097600	76.4776880	-65.515361	45112.2805	-77.731151
1.2	1314.097600	3.28505352	3.44798018	23667.1550	-44.318088
1.3	1314.097600	-29.144360	31.3147261	10080.0696	-14.273544
1.4	1314.097600	-15.030357	15.5062683	4732.93855	-6.0099638
1.5	1314.097600	-7.9411592	7.66299918	2318.78543	-2.4198820
1.6	1283.473196	-4.6755713	4.05635759	1224.29980	-.80255418
2	1283.473196	-4.6755713	4.05635759	1224.29980	-.80255418
2.1	1259.748427	-5.0225969	3.91047264	1179.24761	-.65058749
3	1259.748427	-5.0225969	3.91047264	1179.24761	-.65058749
3.1	1187.938831	-5.4562947	3.65630895	1100.74886	-.42262430
4	1187.938831	-5.4562947	3.65630895	1100.74886	-.42262430
4.1	1028.258302	-6.0849688	3.12774033	937.045943	-.18431482
5	1028.258302	-6.0849688	3.12774033	937.045943	-.18431482
5.1	849.5481348	-7.2174578	2.37058455	700.771857	.093373939
6	849.5481348	-7.2174578	2.37058455	700.771857	.093373939
6.1	546.6913976	-10.330024	3.51421970	1068.04163	.559620532
7	546.6913976	-10.330024	3.51421970	1068.04163	.559620532
7.1	528.8621431	-15.787923	.773483185	791.976638	.381803940
8	528.8621431	-15.787923	.773483185	791.976638	.381803940
8.1	453.9549386	-16.838551	1.29912005	1132.88067	.637709730
9	453.9549386	-16.838551	1.29912005	1132.88067	.637709730
9.1	425.2526653	-20.072861	-.69316882	1297.00950	.504474690
10	425.2526653	-20.072861	-.69316882	1297.00950	.504474690
10.1	373.0012406	-22.170272	-4.1489058	2246.88121	.619709625
11	373.0012406	-22.170272	-4.1489058	2246.88121	.619709625
11.1	320.3299112	-32.021705	-9.8454691	3429.44732	.440888552
12	320.3299112	-32.021705	-9.8454691	3429.44732	.440888552
12.1	156.6626635	-37.943824	-20.570536	6536.22711	.572674443
13	156.6626635	-37.943824	-20.570536	6536.22711	.572674443
13.1	65.49997513	-65.537684	-37.236062	10640.7039	.389831159
14	65.49997513	-65.537684	-37.236062	10640.7039	.389831159
14.1	8.168343278	-100.49622	-61.462761	16935.2485	.347529282
15	8.168343278	-100.49622	-61.462761	16935.2485	.347529282
15.1	2.336918949	-70.473884	-63.808993	18090.4627	.384211366
16	2.336918949	-70.473884	-63.808993	18090.4627	.384211366
16.1	.8729543761	-76.693743	-63.681868	18004.0986	.390077529
17	.8729543761	-76.693743	-63.681868	18004.0986	.390077529
17.1	.8459581791	-75.982470	-63.661784	18014.8402	.391221697
18	.8459581791	-75.982470	-63.661784	18014.8402	.391221697
18.1	.8459535548	-75.963754	-63.658052	18014.2131	.391294205
19	.8459535548	-75.963754	-63.658052	18014.2131	.391294205
19.1	,8459535453	-75.959987	-63.657848	18014.2181	.391300190
20	.8459535453	-75.959987	-63.657848	18014.2181	.391300190
20.1	.8459535452	-75.959745	-63.657827	18014.2164	.391300630

Run stopped after 45 model evaluations and 20 derivative evaluations.
Iterations have been stopped because the relative reduction between successive residual sums of squares is at most SSCON = 1.000E-08

Nonlinear Regression Summary Statistics Dependent Variable FC

Source	DF	Sum of Squares	Mean Square
Regression	4	1313.25165	328.31291
Residual	5	.84595	.16919
Uncorrected Total	9	1314.09760	
(Corrected Total)	8	664.18756	

R squared = 1 - Residual SS / Corrected SS = .99873

Parameter	Estimate	Asymptotic Std. Error	Asymptotic 95 % Confidence Interval Lower	Upper
A	-75.95974538	18.219202469	-122.7936963	-29.12579445
B	-63.65782745	2.979271616	-71.31628895	-55.99936595
C	18014.216428	692.19688126	16234.867698	19793.565158
D	.391300630	.030599475	.312642176	.469959085

Asymptotic Correlation Matrix of the Parameter Estimates

	A	B	C	D
A	1.0000	.5774	-.2636	.9278
B	.5774	1.0000	-.9394	.7521
C	-.2636	-.9394	1.0000	-.4939
D	.9278	.7521	-.4939	1.0000

Appendix G - Uniaxial Tension Test Results

G.1 Uniaxial Tension Test Results - DBM Mixture

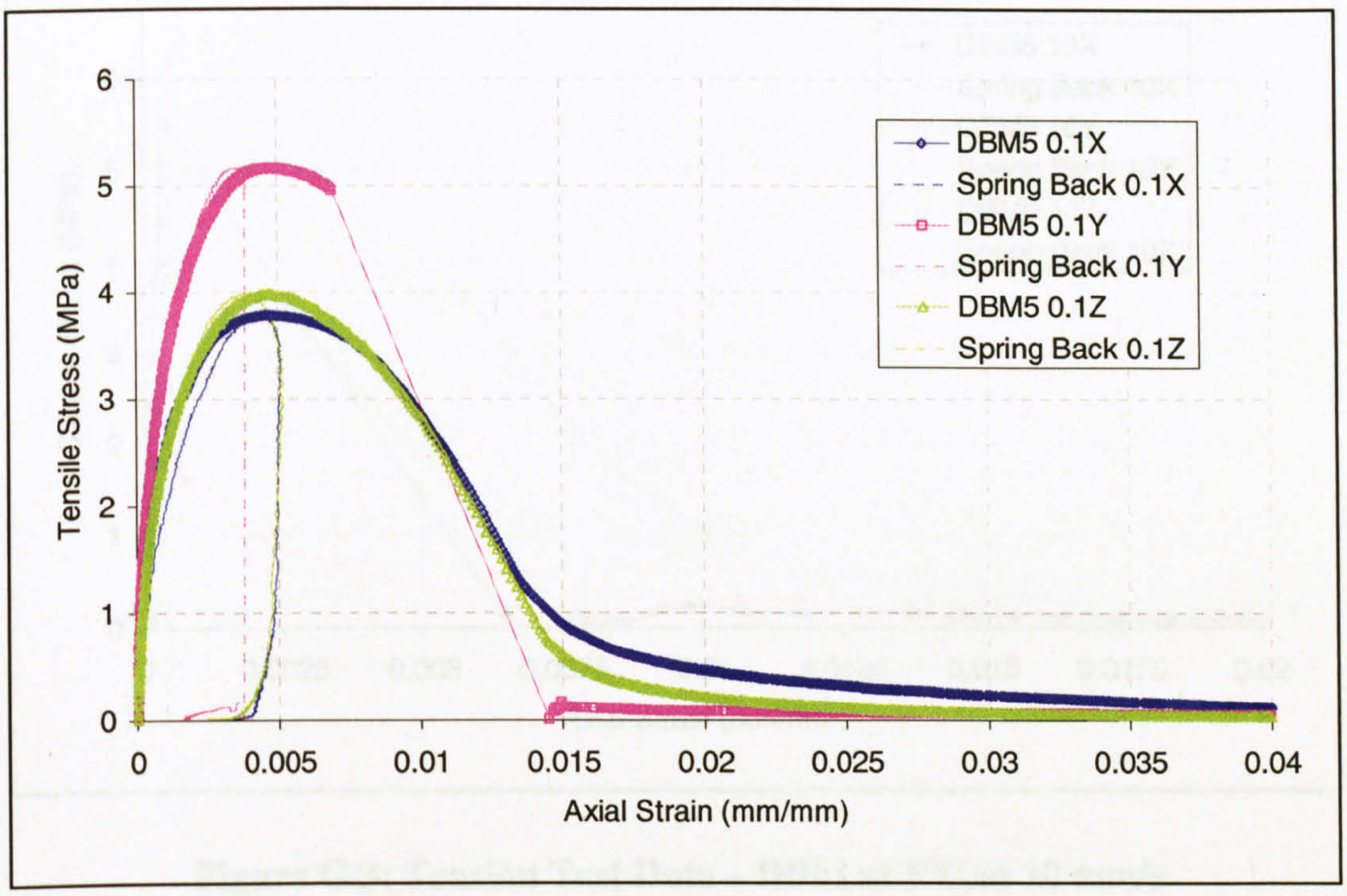

Figure G.1: Tension Test Data – DBM at 5°C at 0.1 mm/s

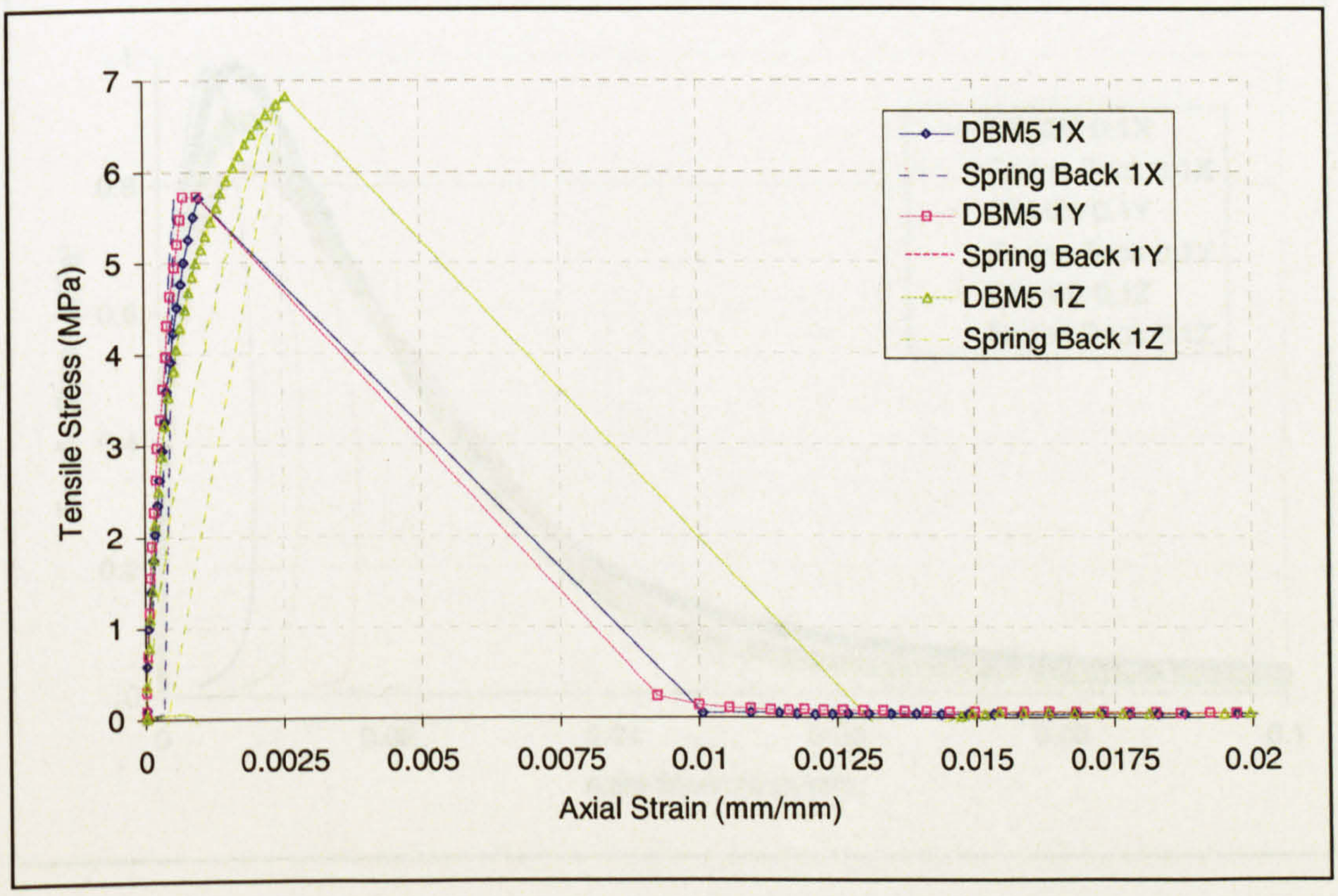

Figure G.2: Tension Test Data – DBM at 5°C at 1 mm/s

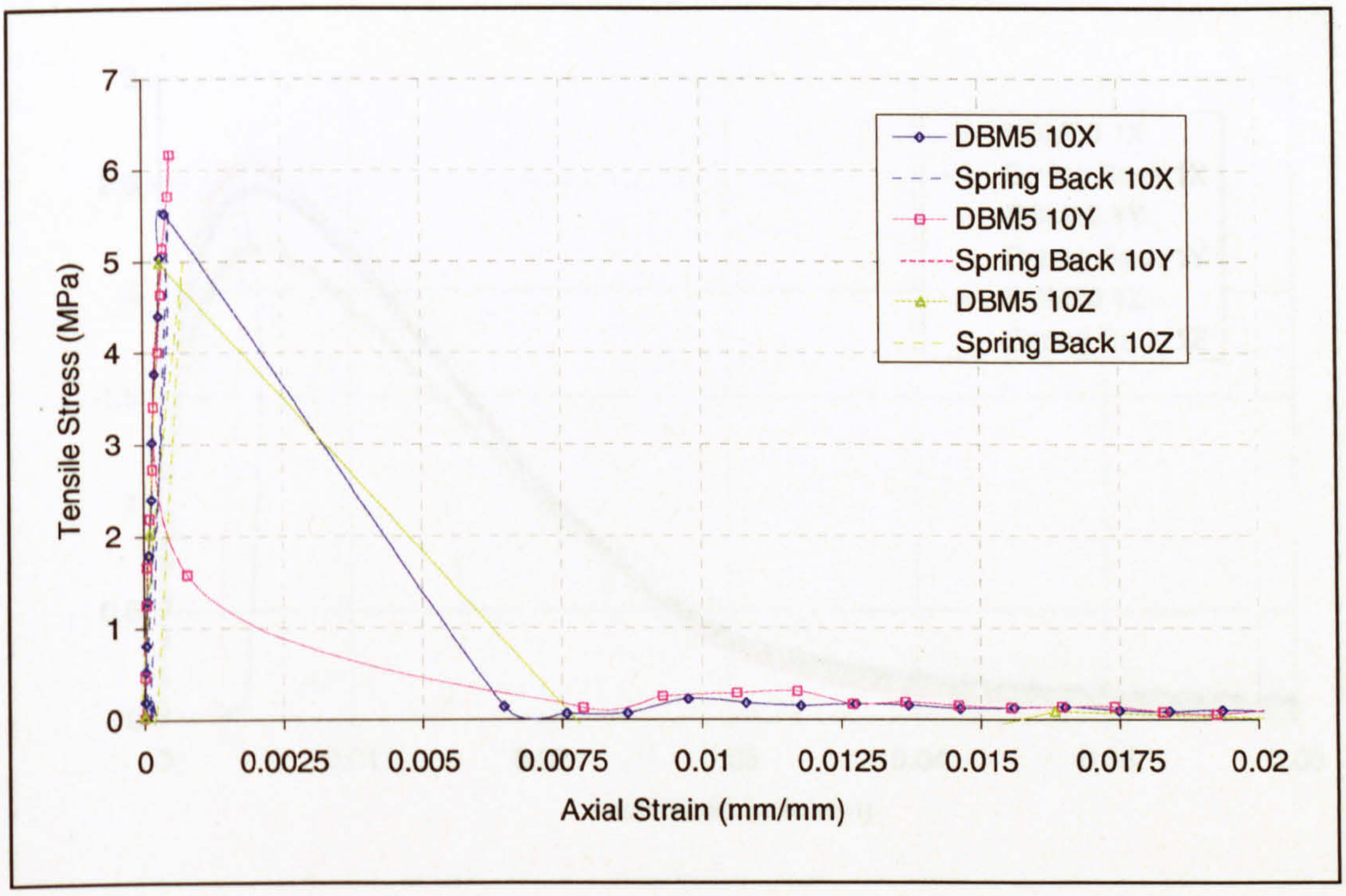

Figure G.3: Tension Test Data – DBM at 5°C at 10 mm/s

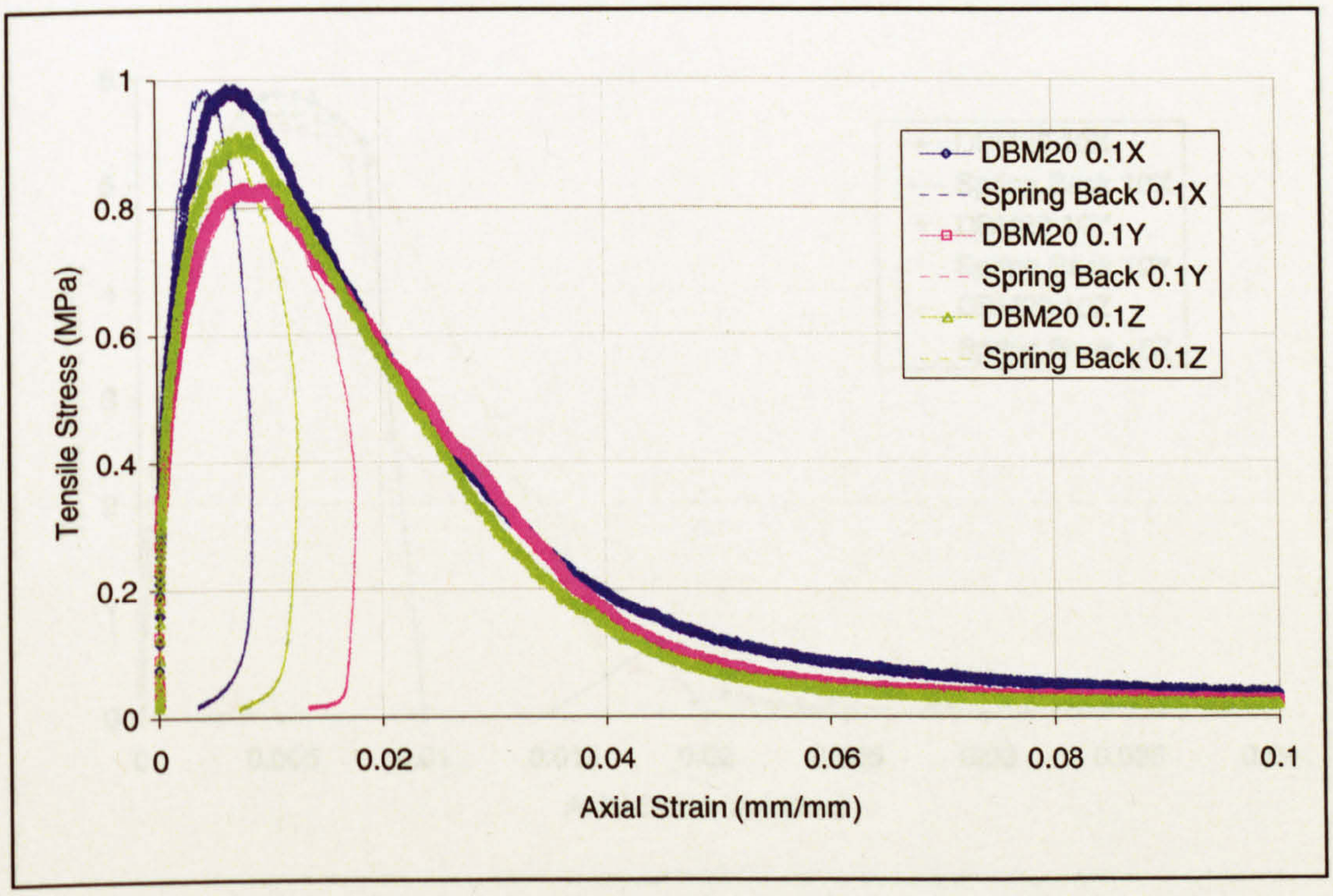

Figure G.4: Tension Test Data – DBM at 20°C at 0.1 mm/s

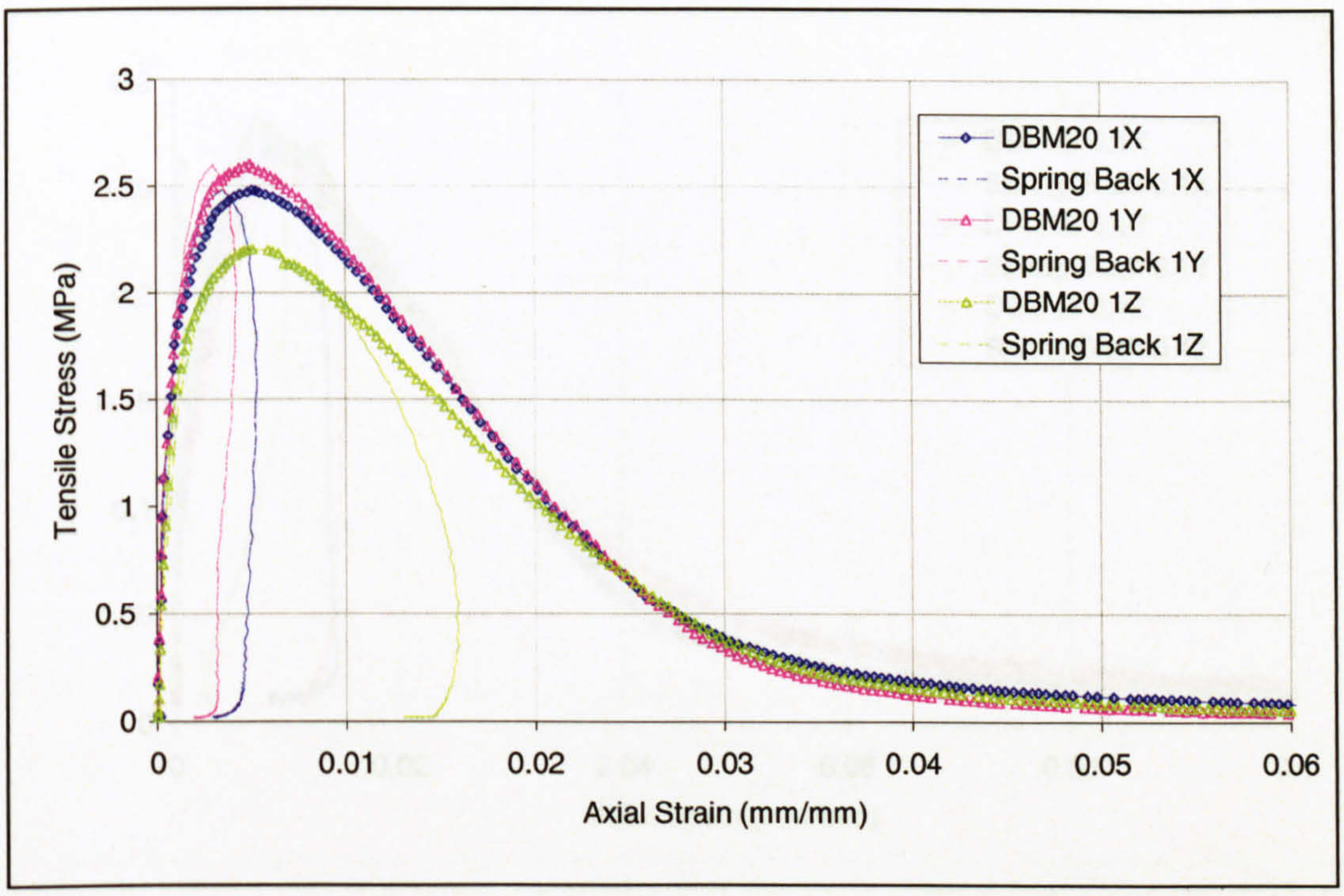

Figure G.5: Tension Test Data – DBM at 20°C at 1 mm/s

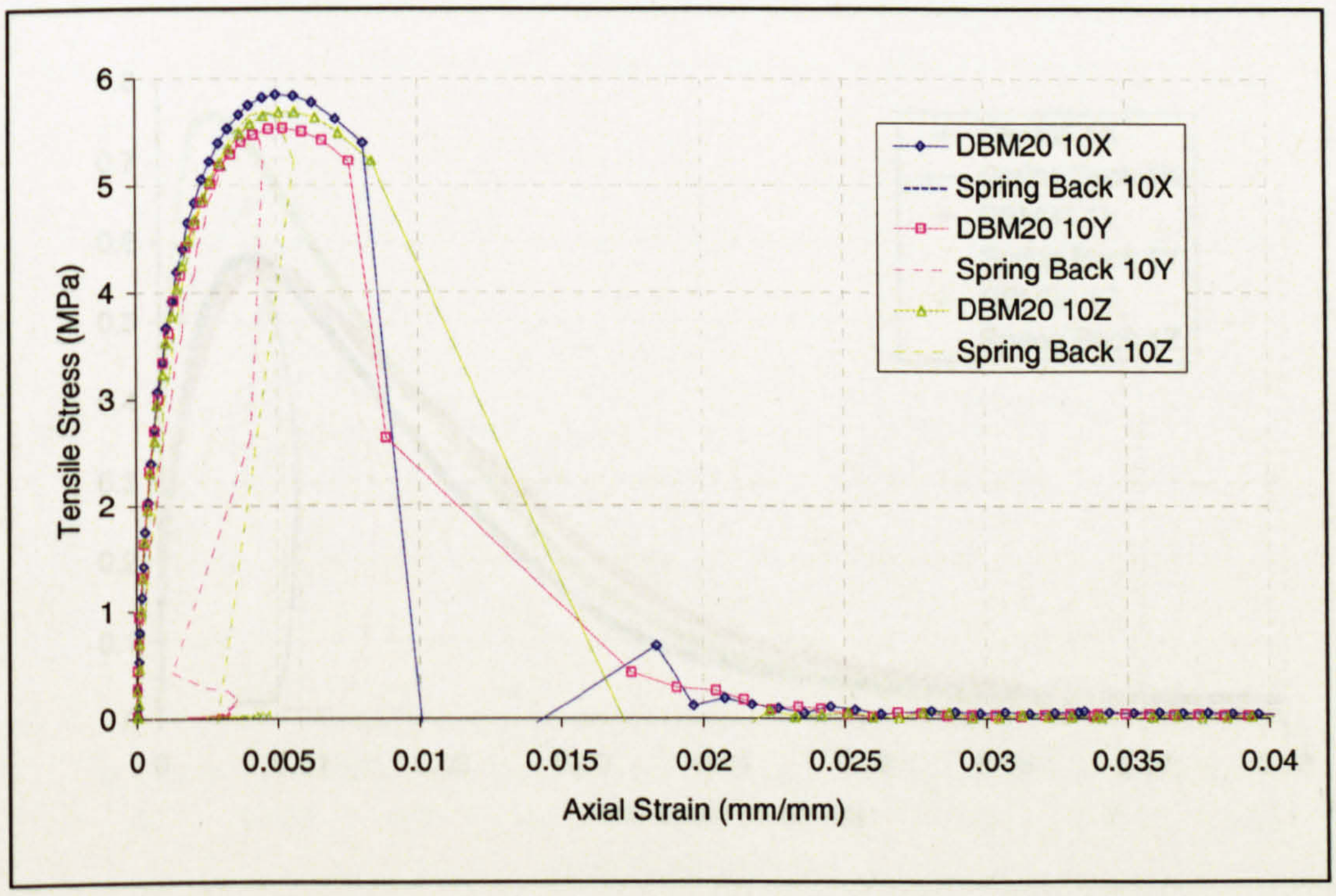

Figure G.6: Tension Test Data – DBM at 20°C at 10 mm/s

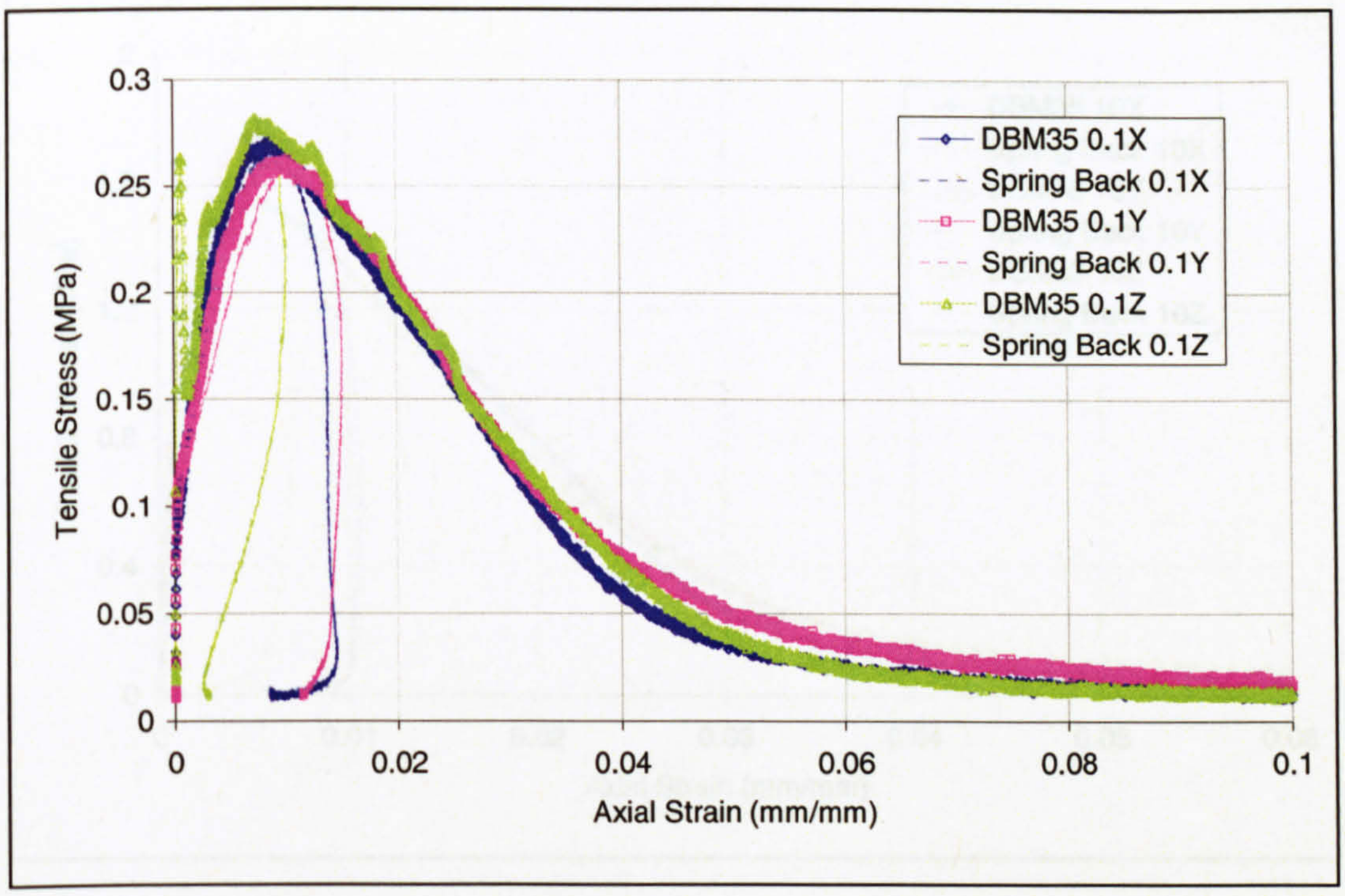

Figure G.7: Tension Test Data – DBM at 35°C at 0.1 mm/s

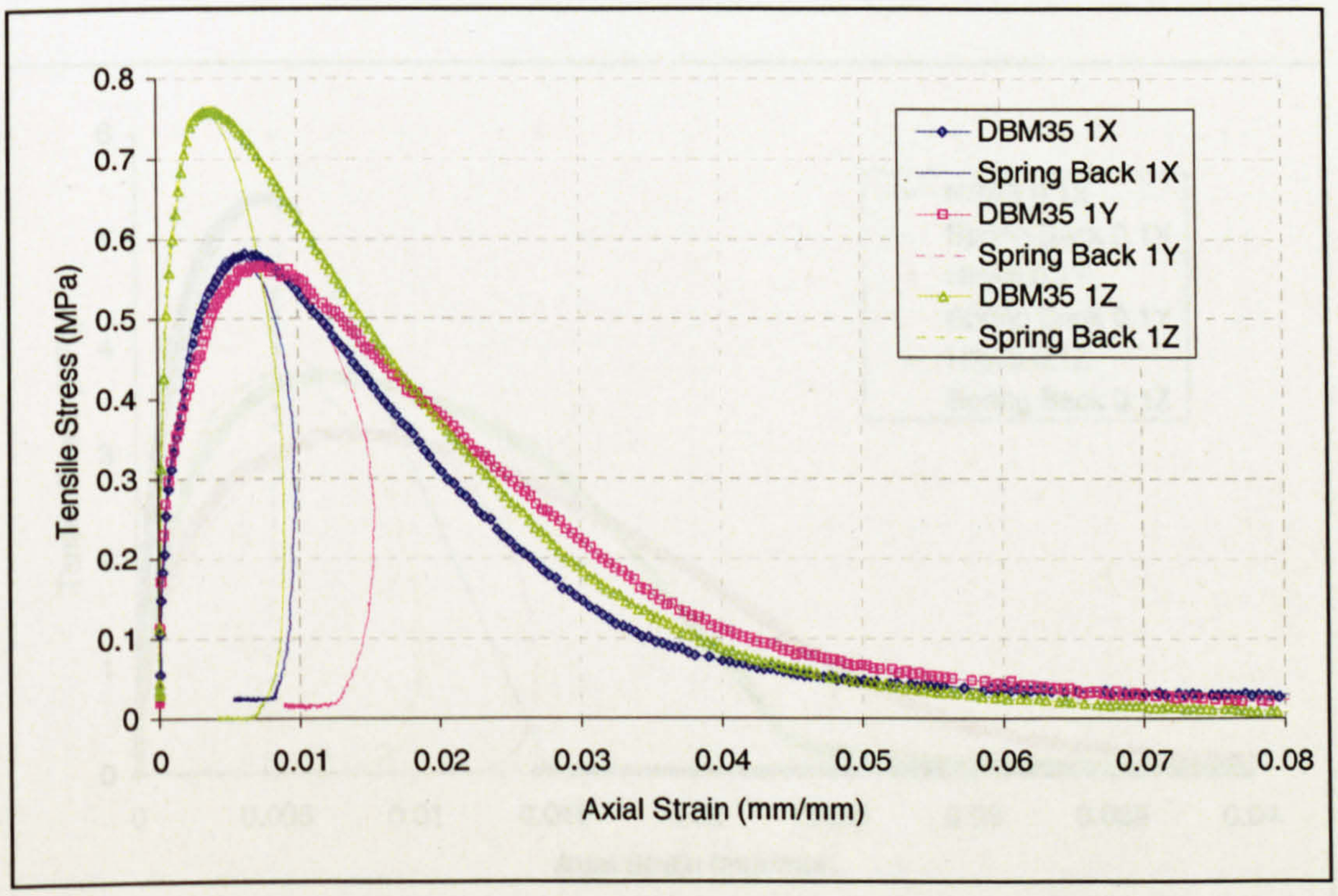

Figure G.8: Tension Test Data – DBM at 35°C at 1 mm/s

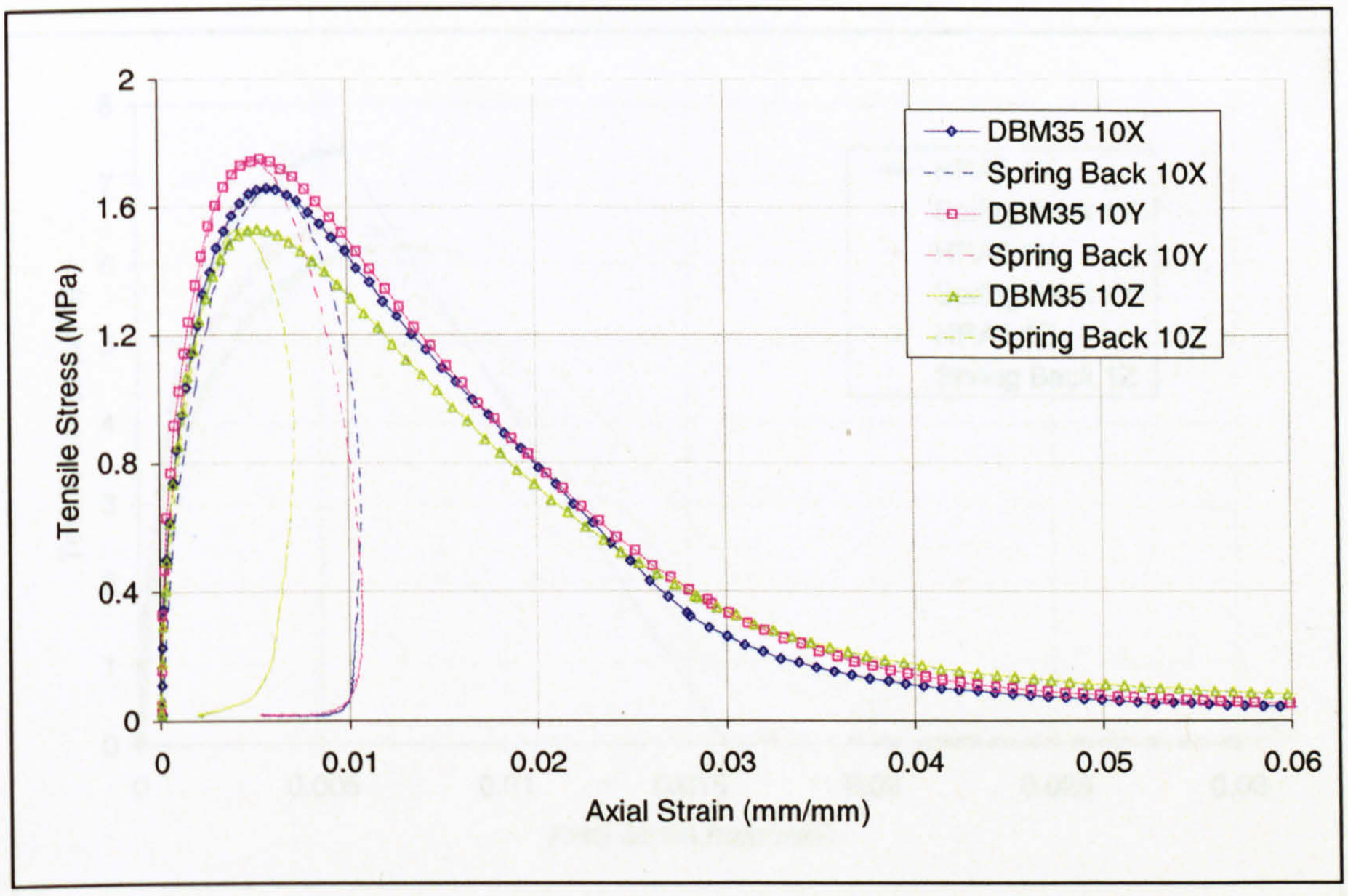

Figure G.9: Tension Test Data – DBM at 35°C at 10 mm/s

G.2 Uniaxial Tension Test Results – HRA Mixture

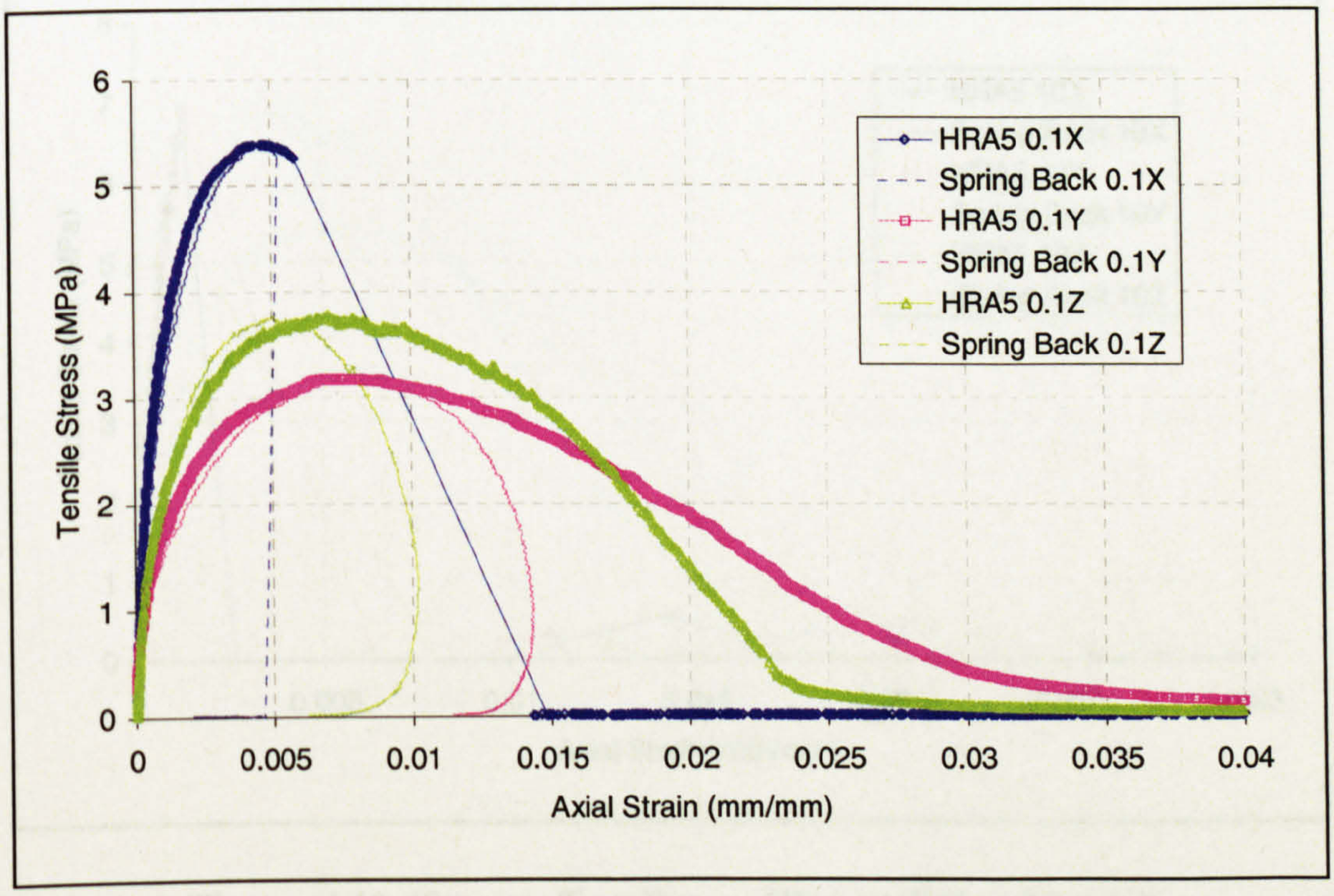

Figure G.10: Tension Test Data – HRA at 5°C at 0.1 mm/s

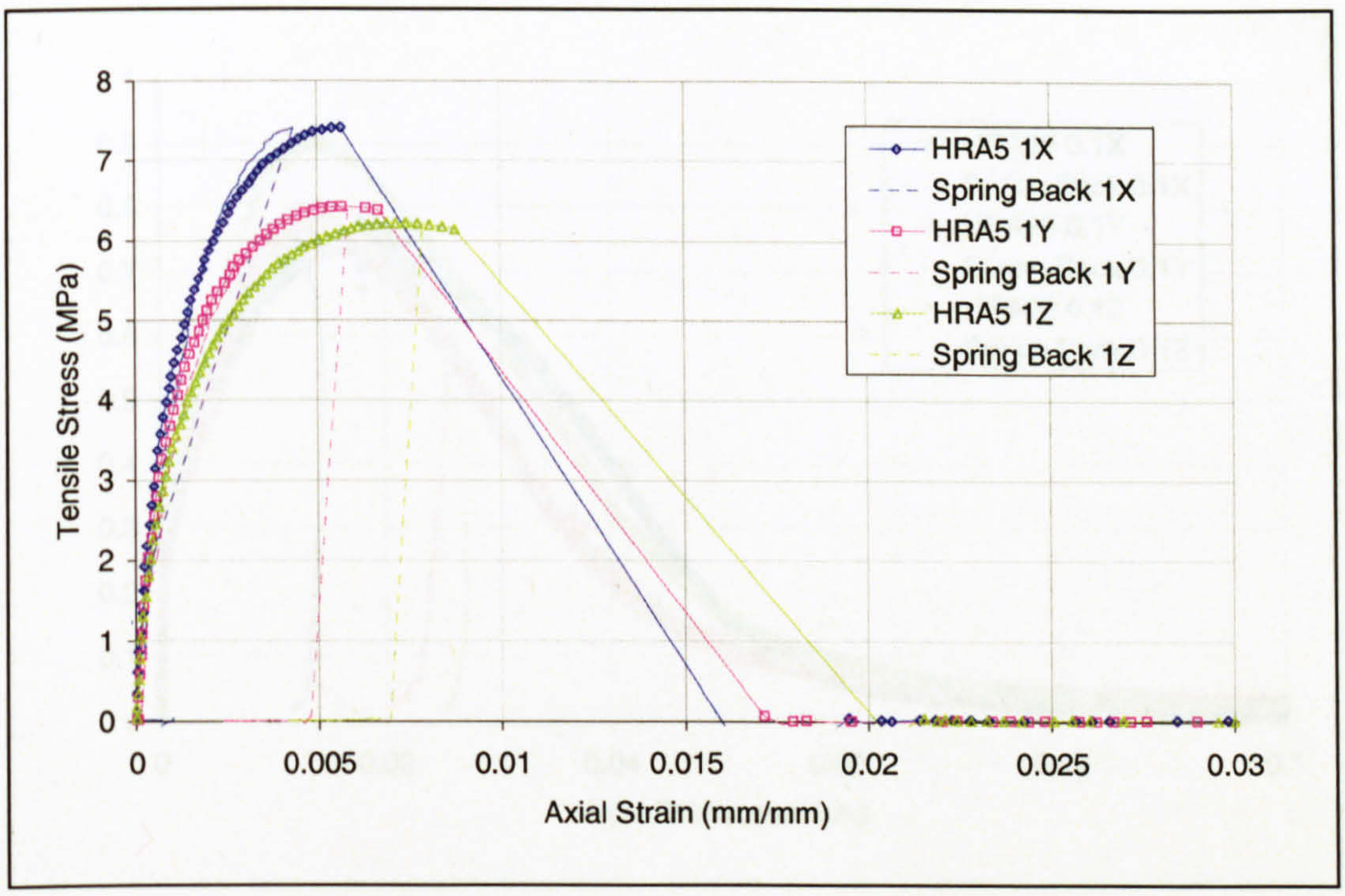

Figure G.11: Tension Test Data – HRA at 5°C at 1 mm/s

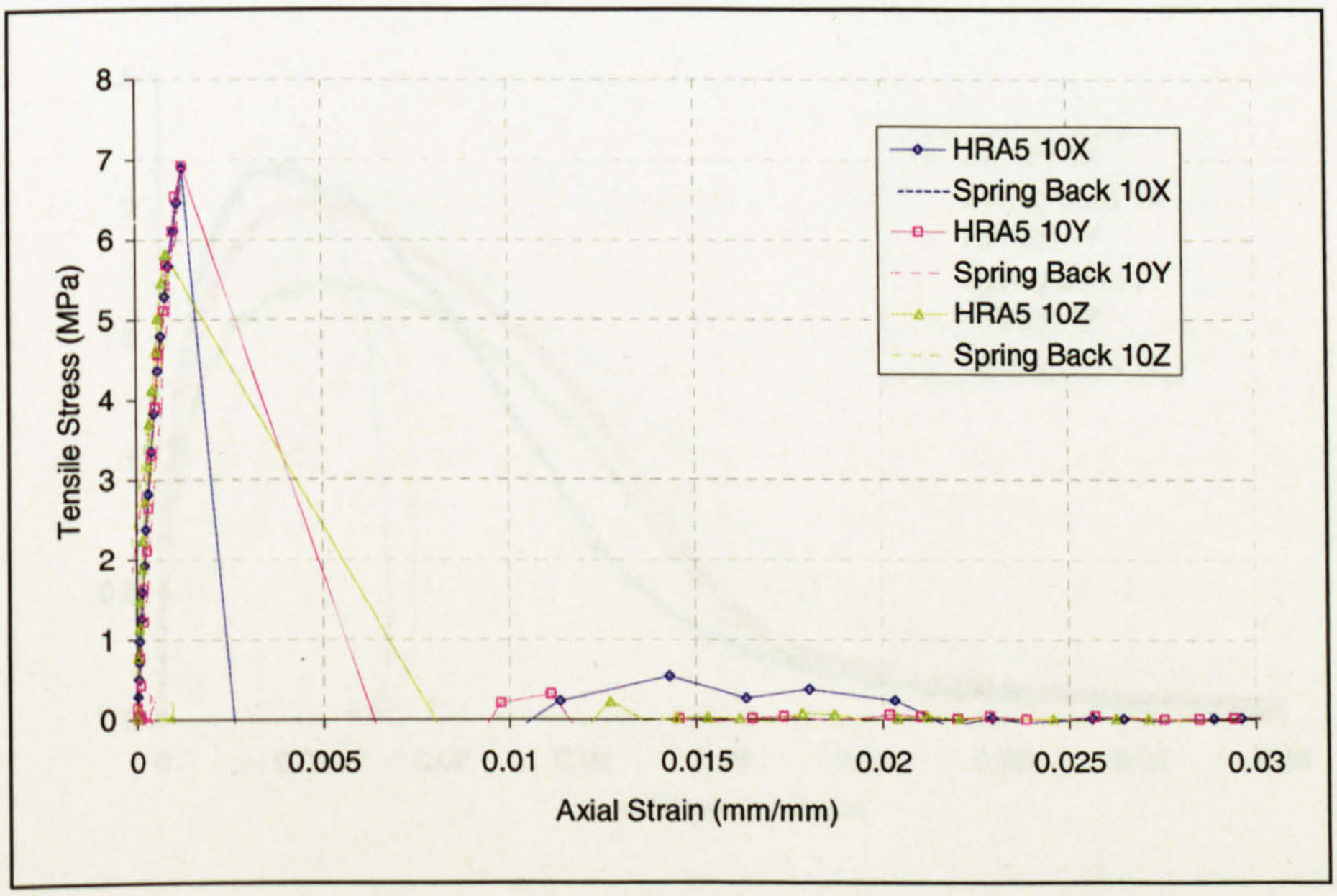

Figure G.12: Tension Test Data – HRA at 5°C at 10 mm/s

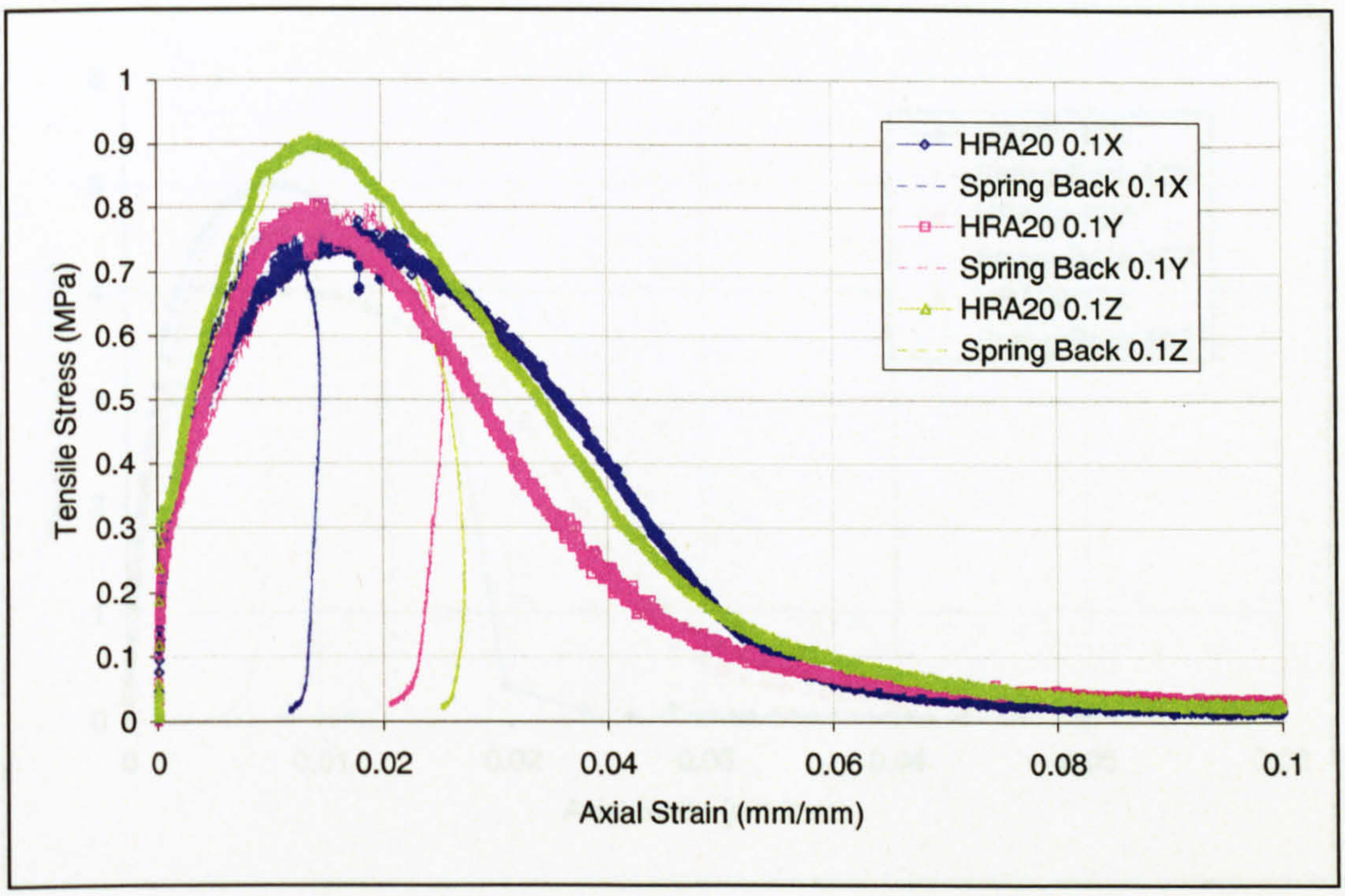

Figure G.13: Tension Test Data – HRA at 20°C at 0.1 mm/s

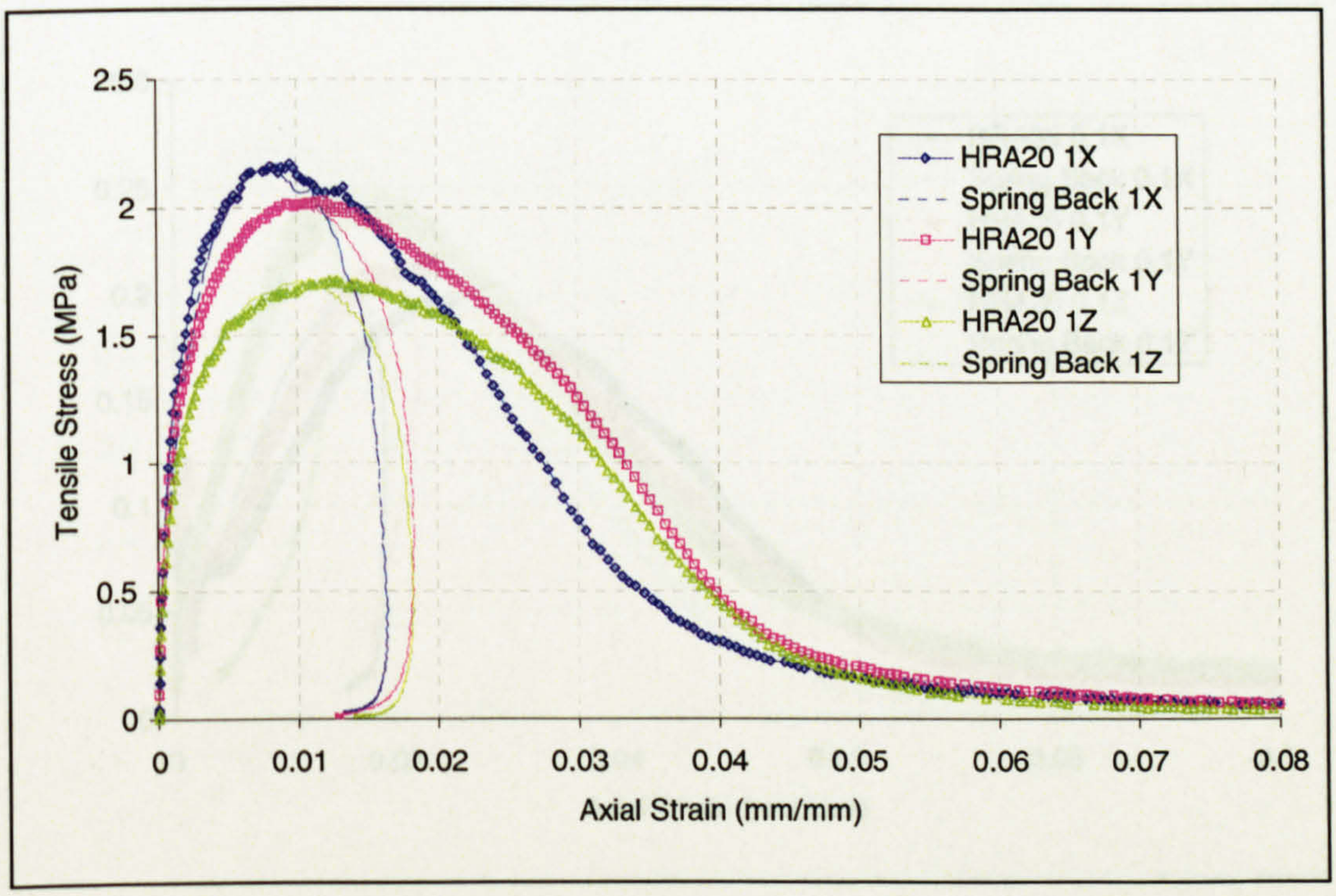

Figure G.14: Tension Test Data – HRA at 20°C at 1 mm/s

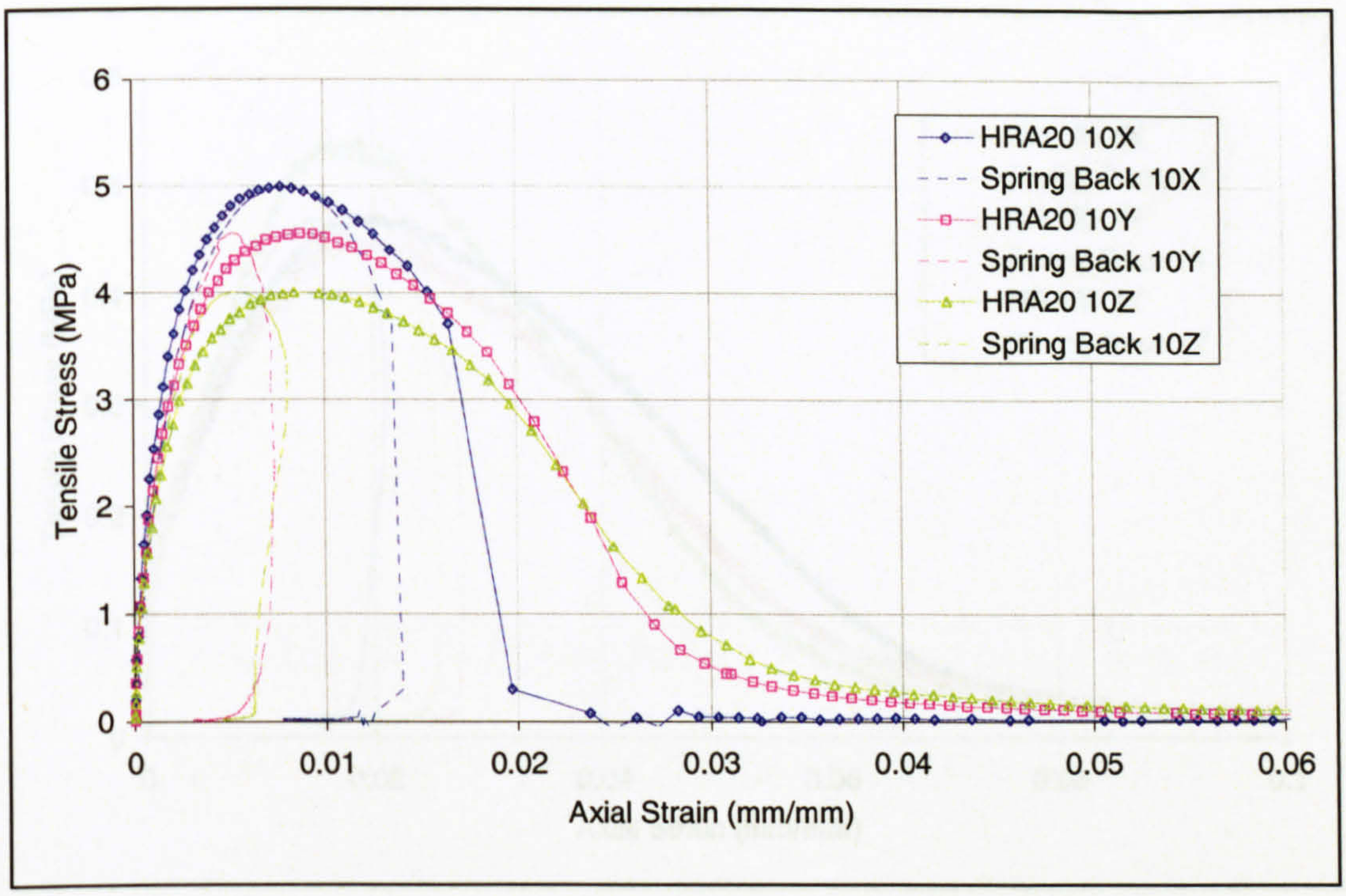

Figure G.15: Tension Test Data – HRA at 20°C at 10 mm/s

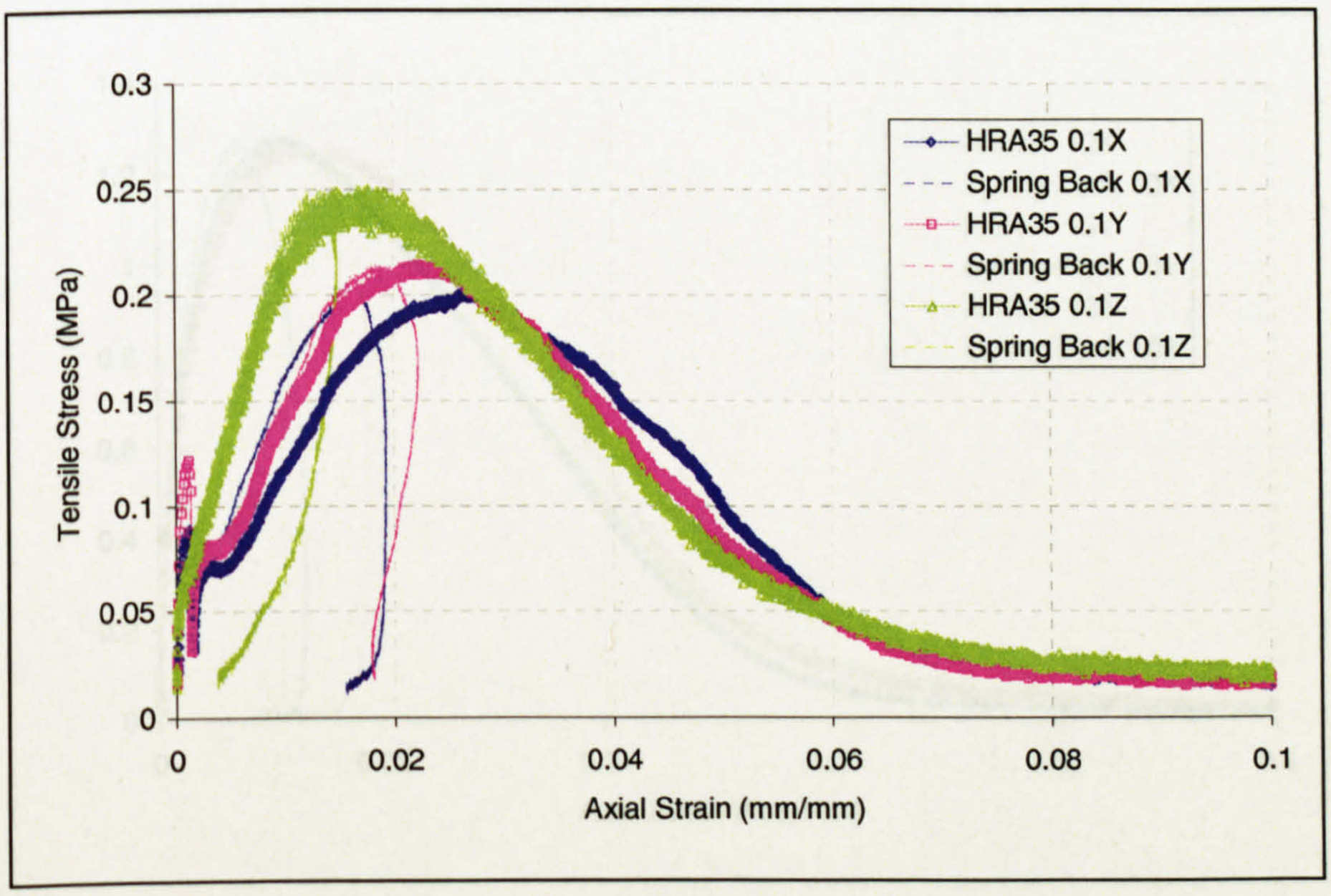

Figure G.16: Tension Test Data – HRA at 35°C at 0.1 mm/s

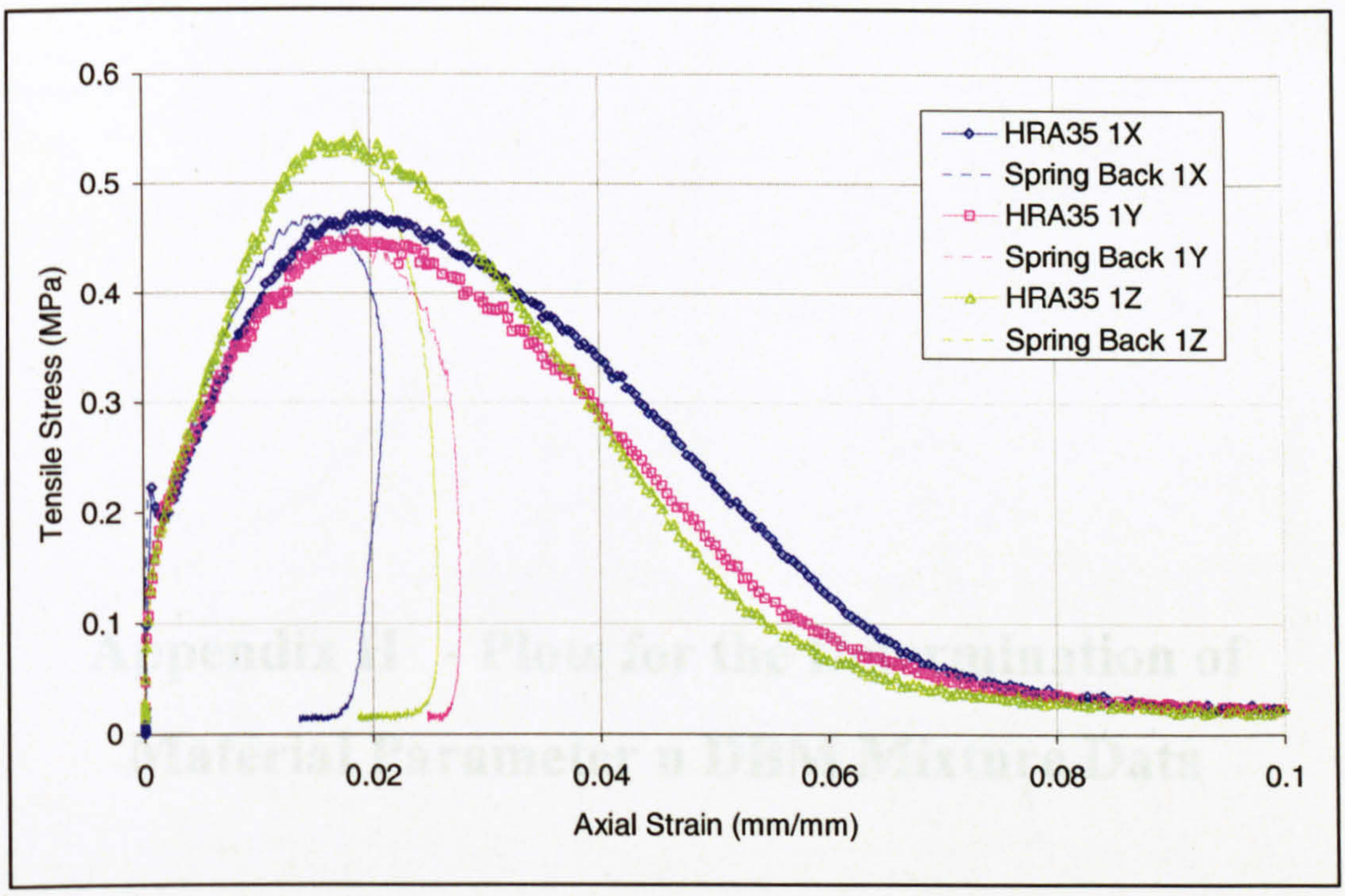

Figure G.17: Tension Test Data – HRA at 35°C at 1 mm/s

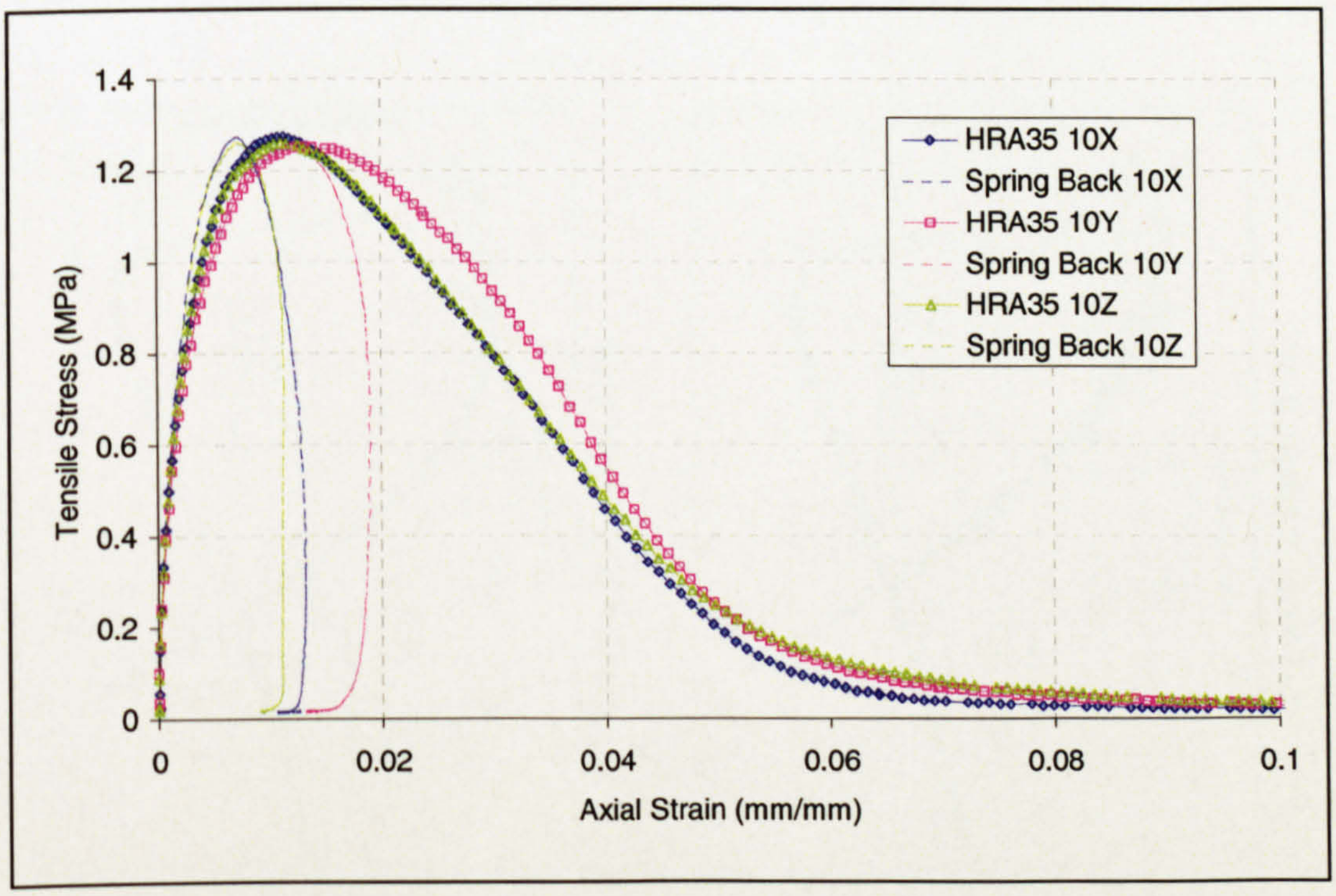

Figure G.18: Tension Test Data – HRA at 35°C at 10 mm/s

Appendix H - Plots for the Determination of Material Parameter n DBM Mixture Data

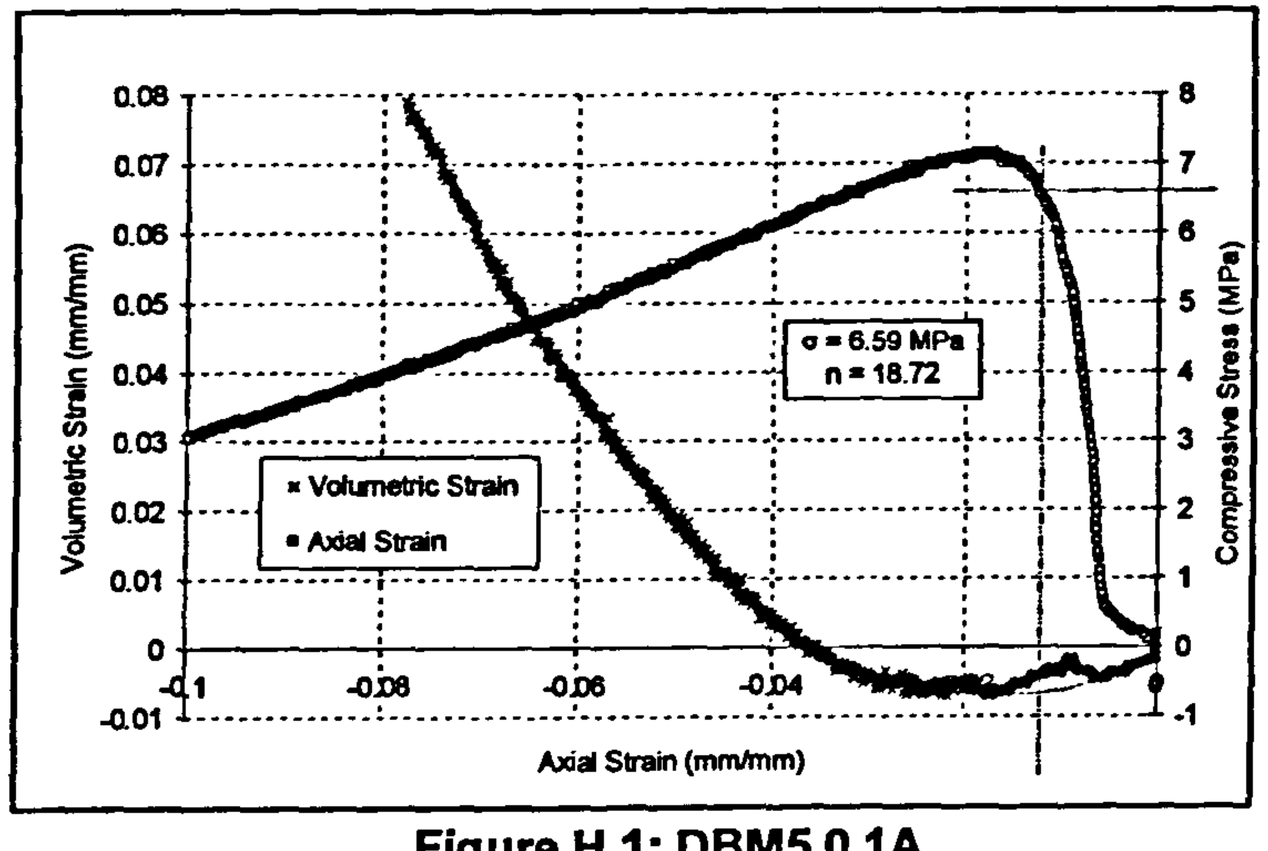

Figure H.1: DBM5 0.1A

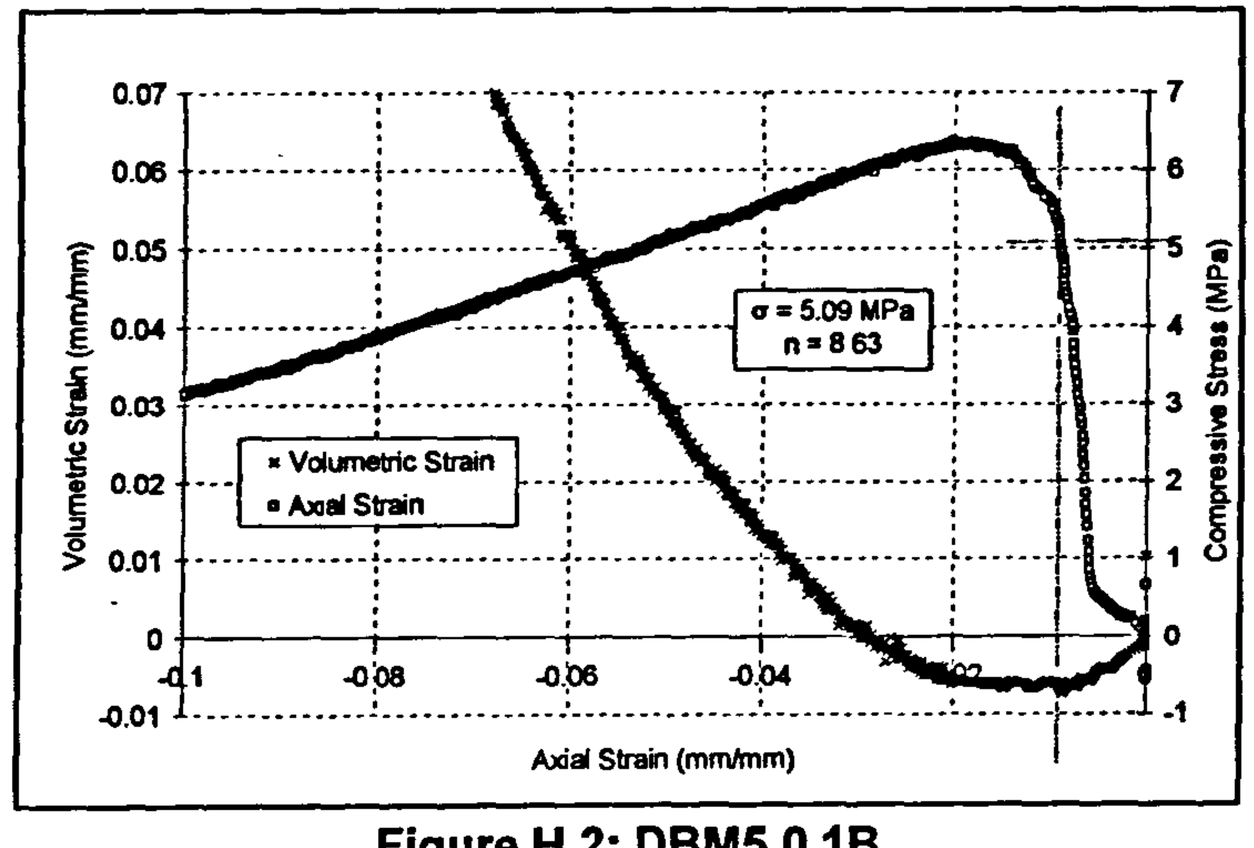

Figure H.2: DBM5 0.1B

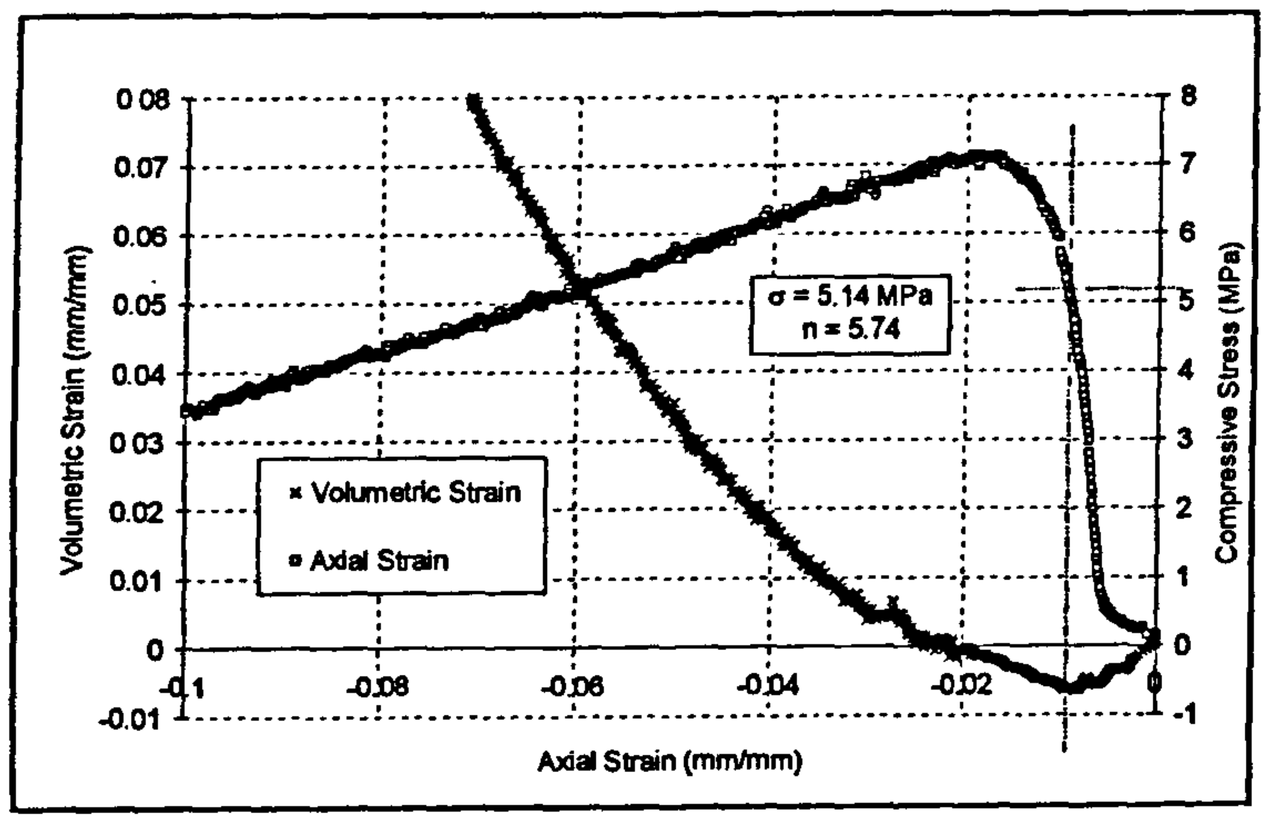

Figure H.3: DBM5 0.1C

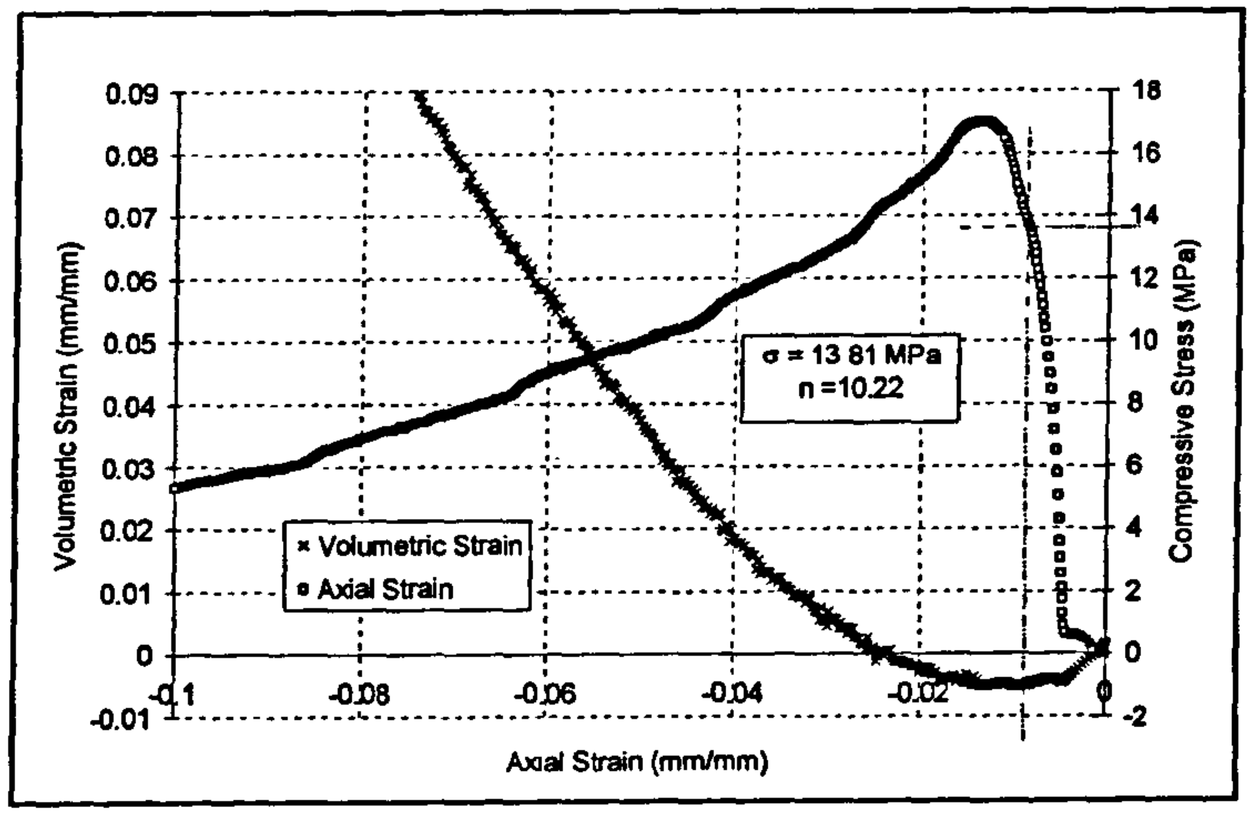

Figure H.4: DBM5 1A

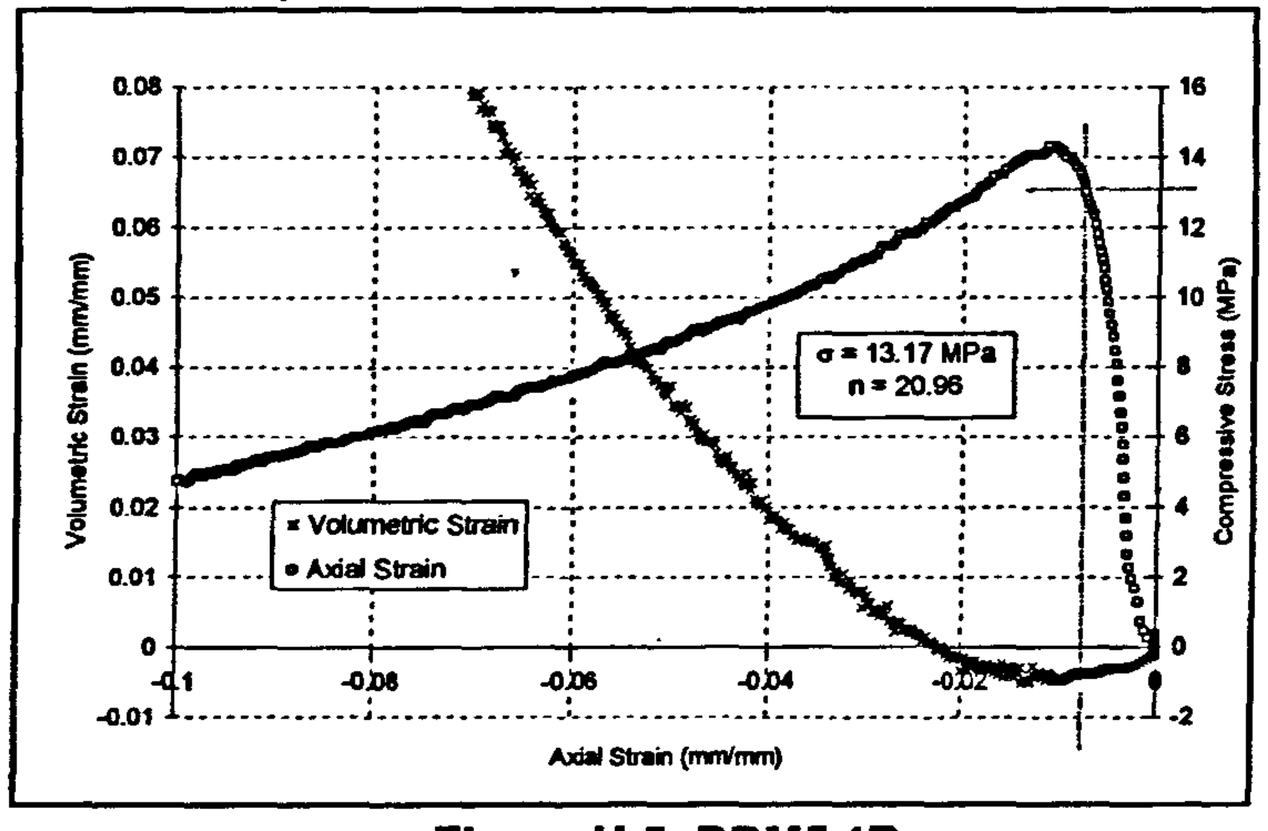

Figure H.5: DBM5 1B

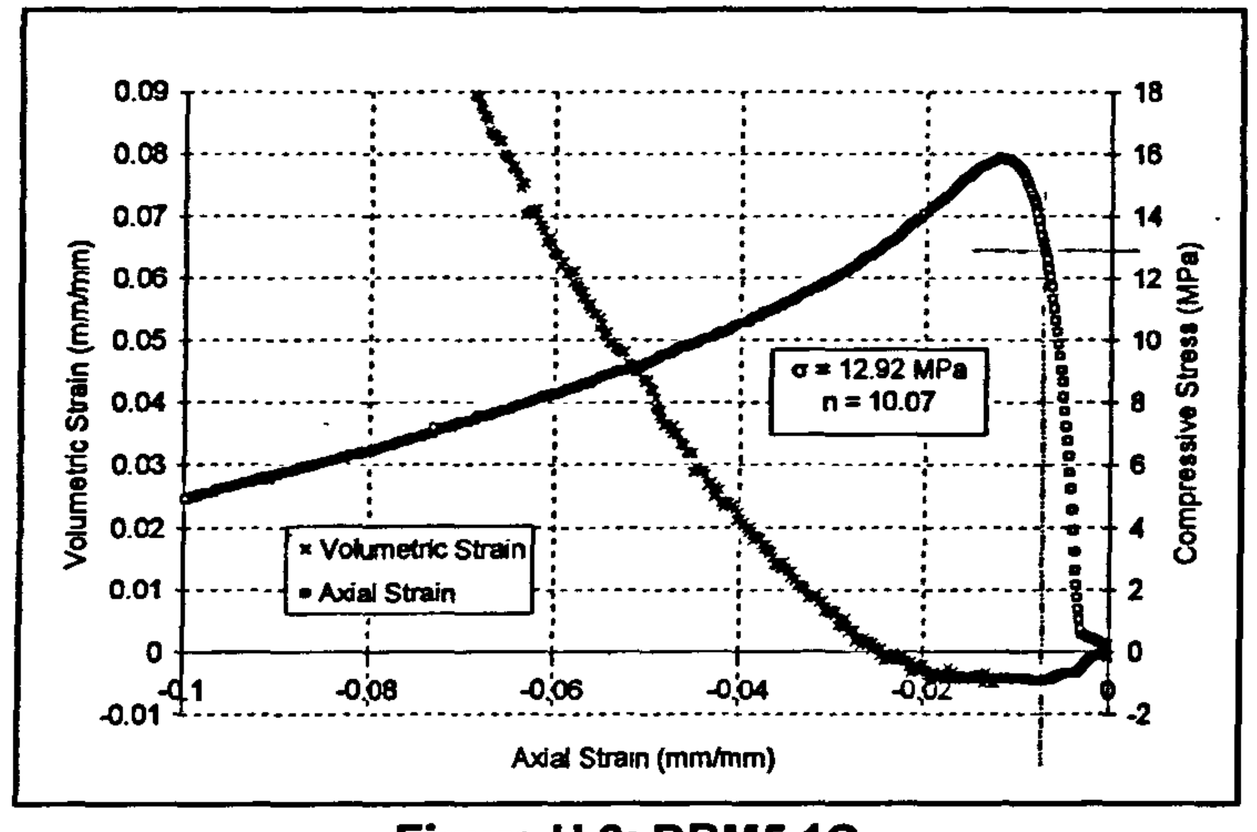

Figure H.6: DBM5 1C

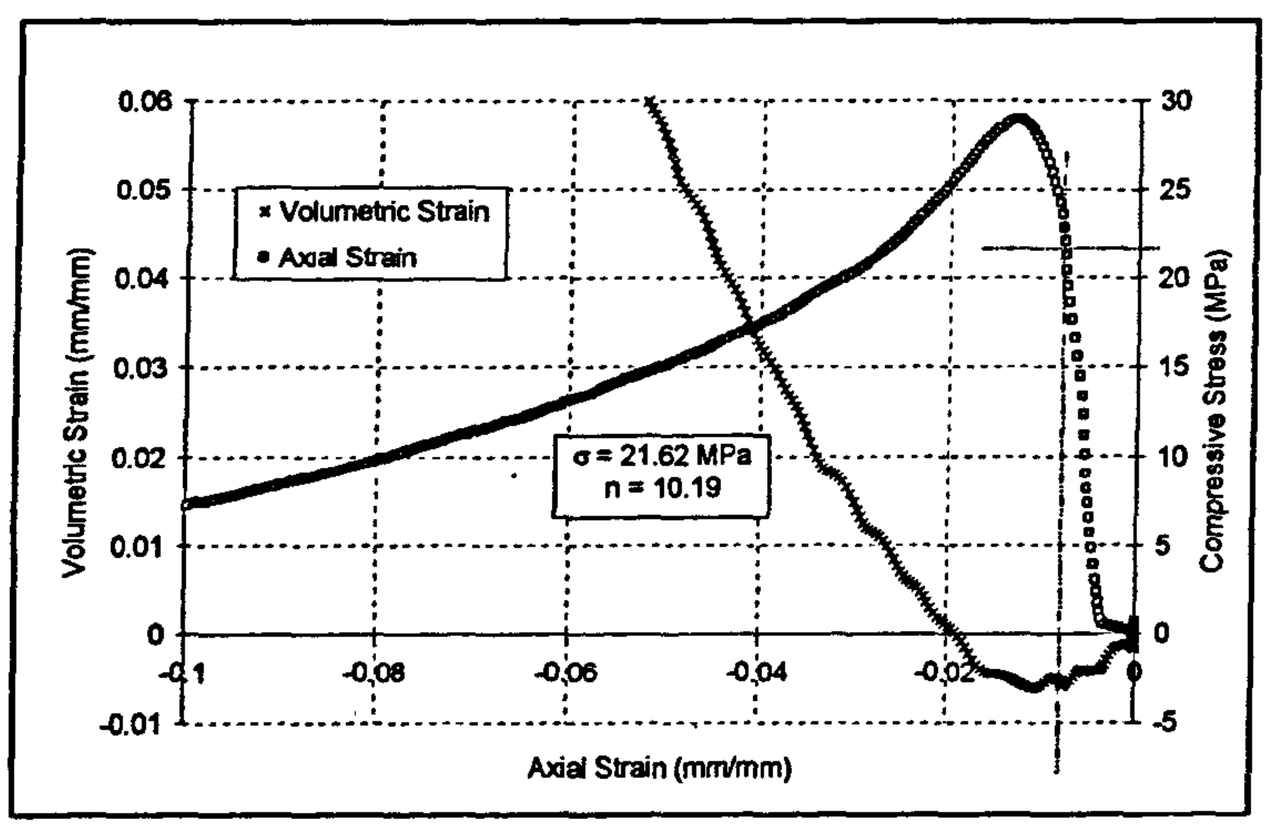

Figure H.7: DBM5 10A

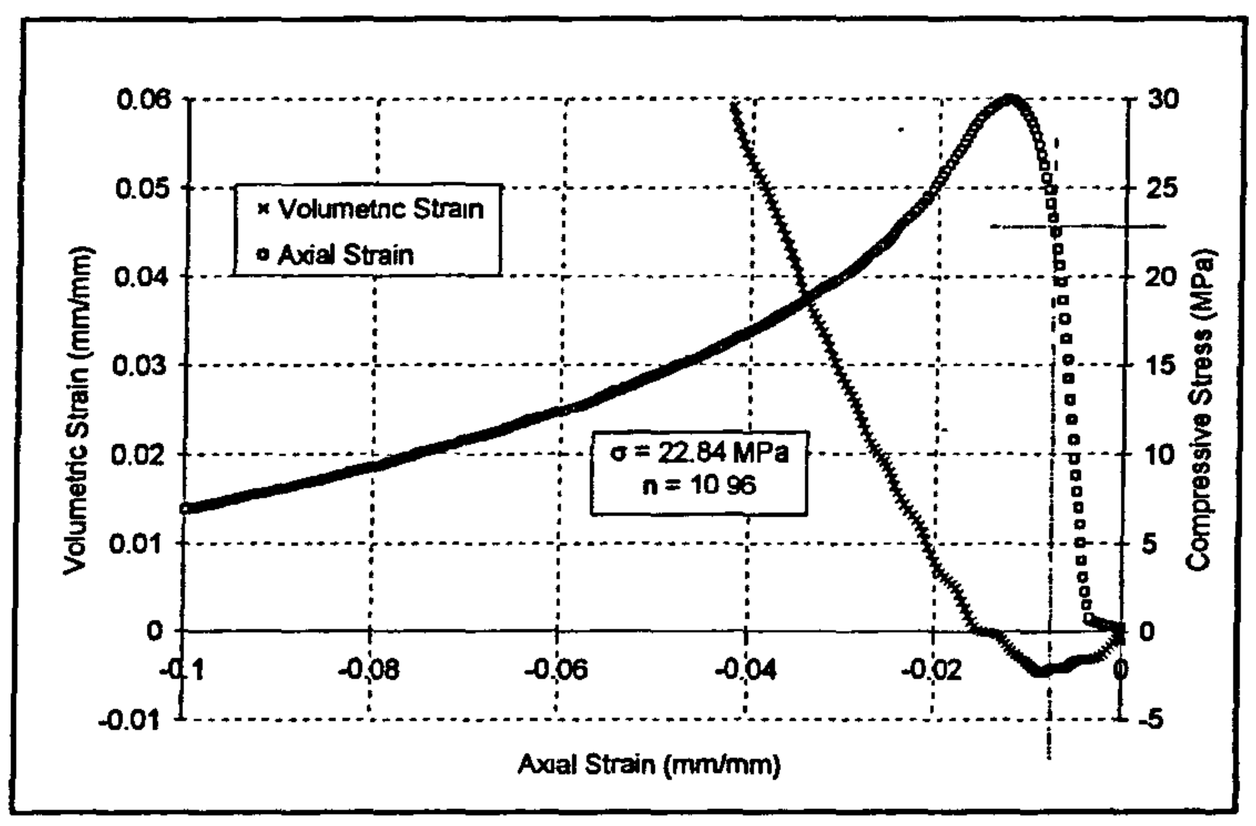

Figure H.8: DBM5 10B

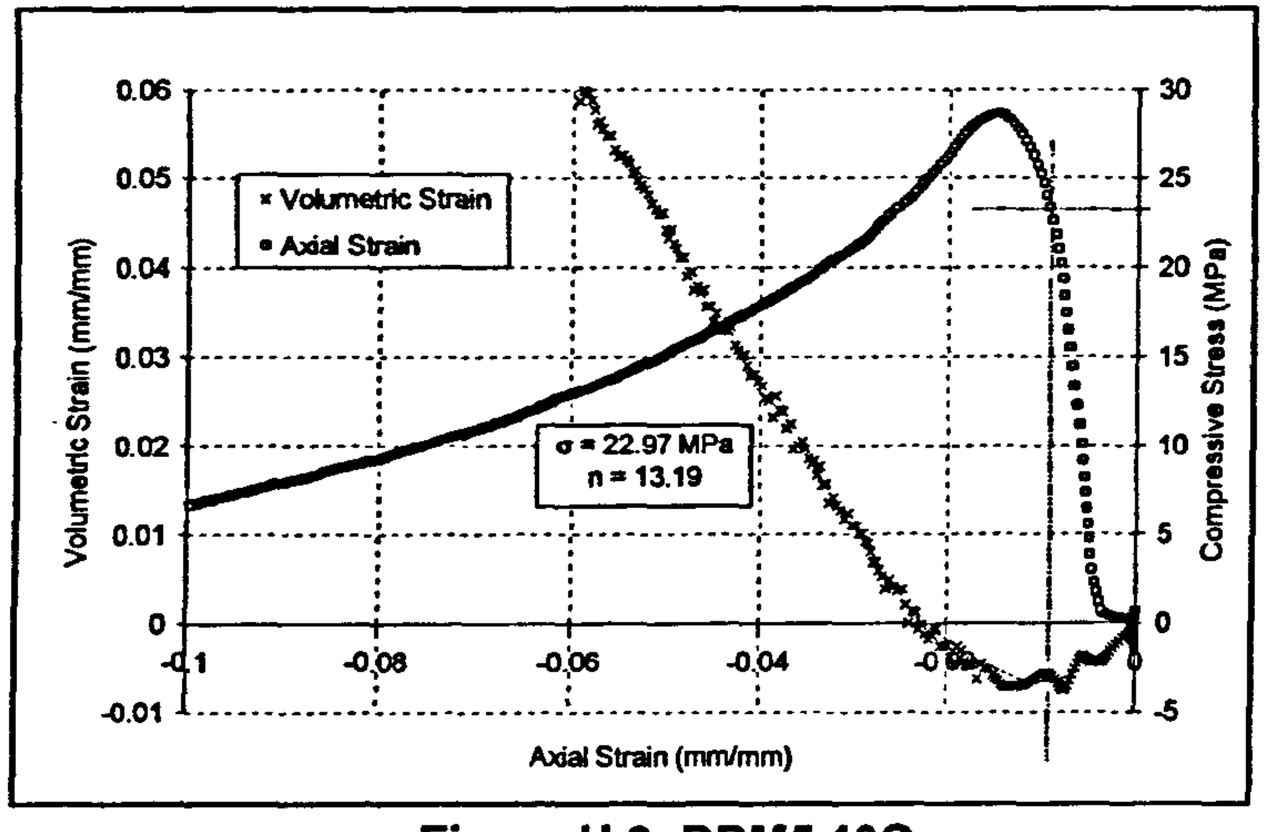

Figure H.9: DBM5 10C

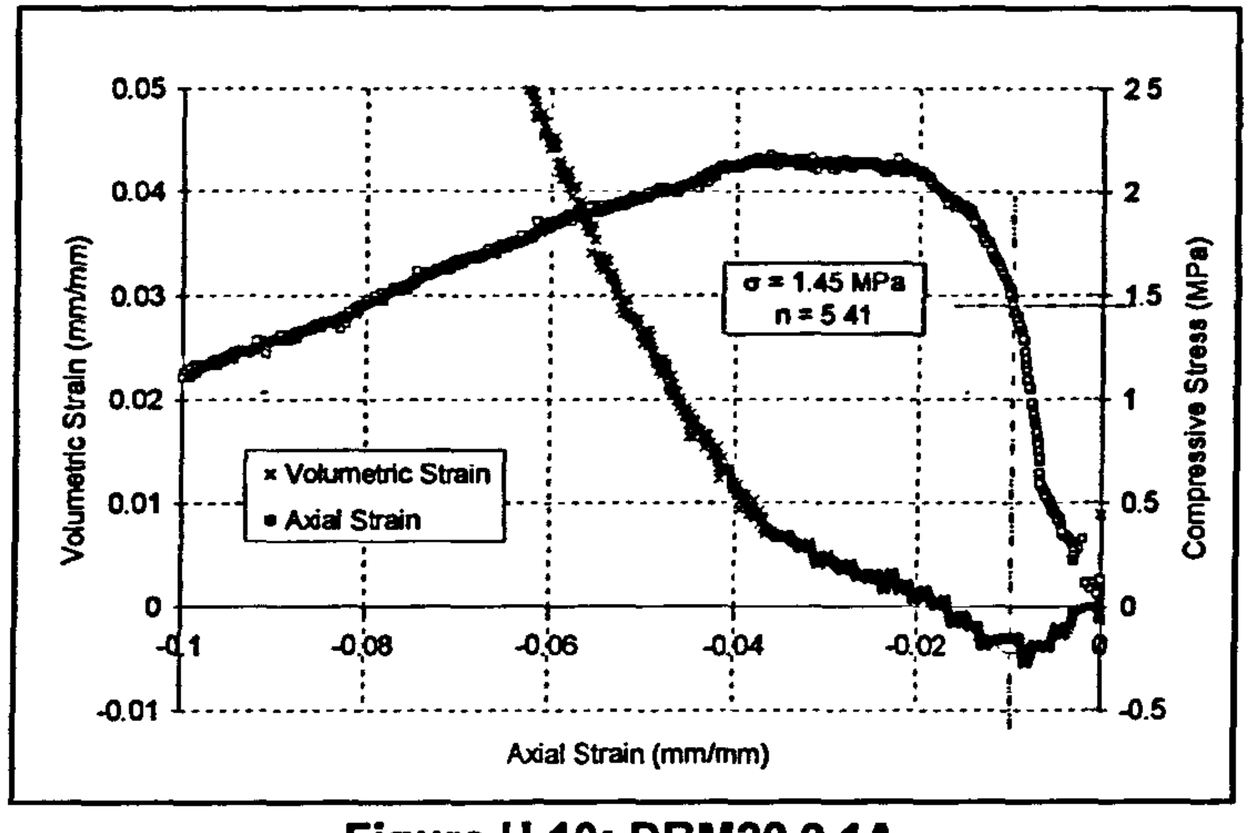

Figure H.10: DBM20 0.1A

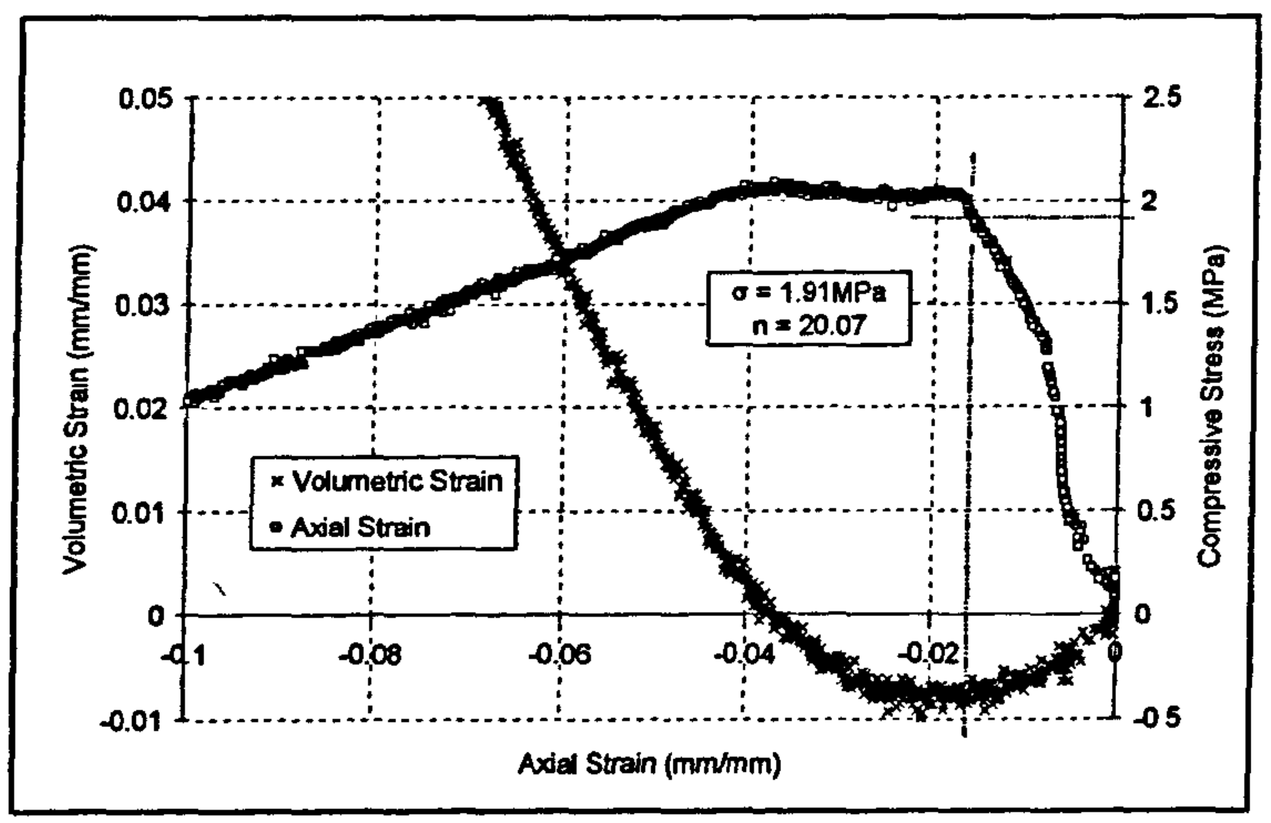

Figure H.11: DBM20 0.1B

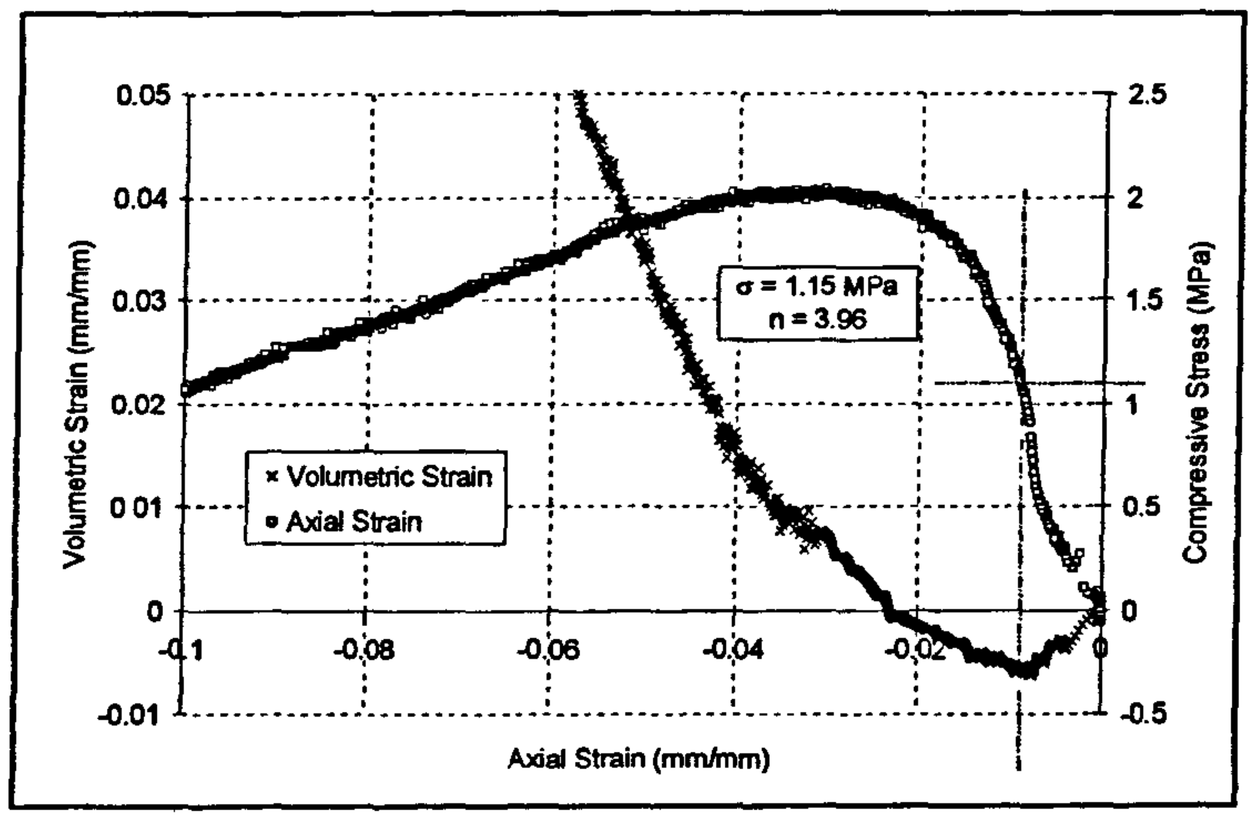

Figure H.12: DBM20 0.1C

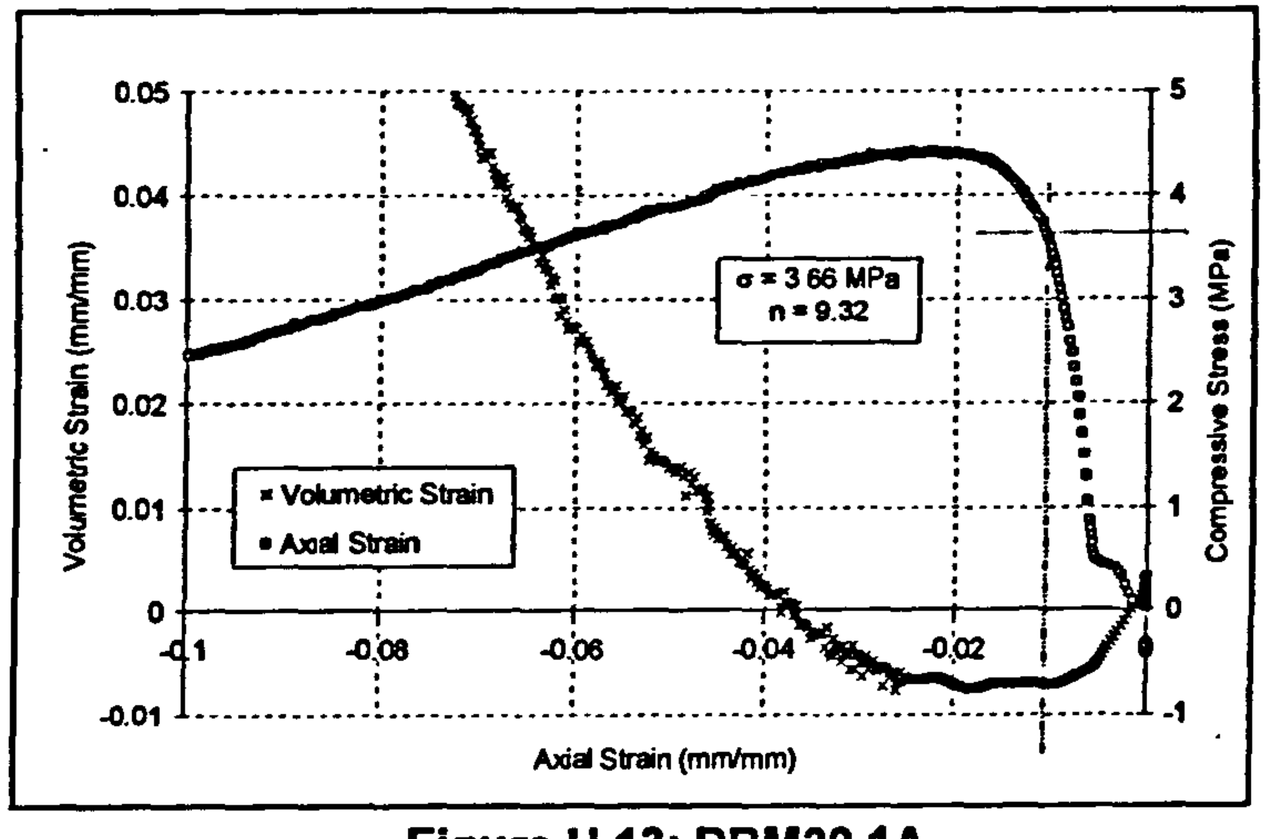

Figure H.13: DBM20 1A

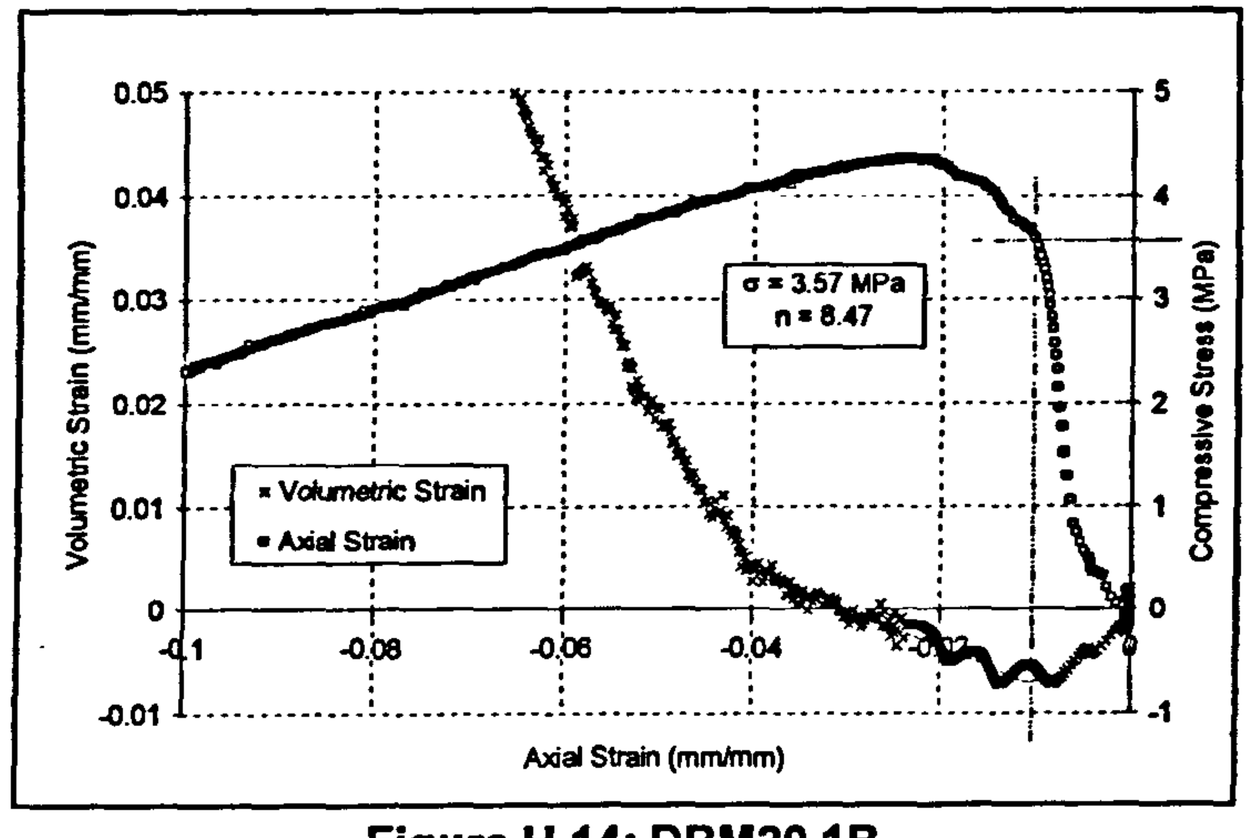

Figure H.14: DBM20 1B

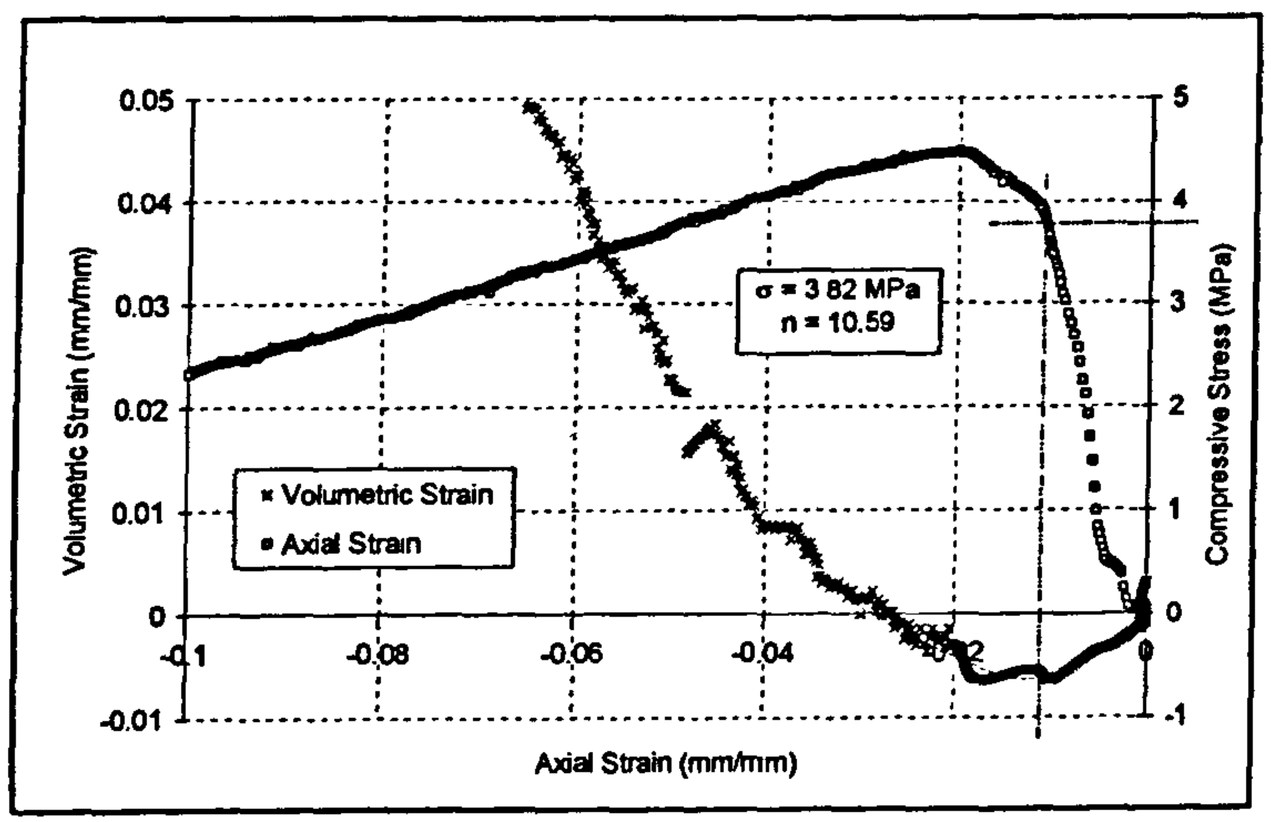

Figure H.15: DBM20 1C

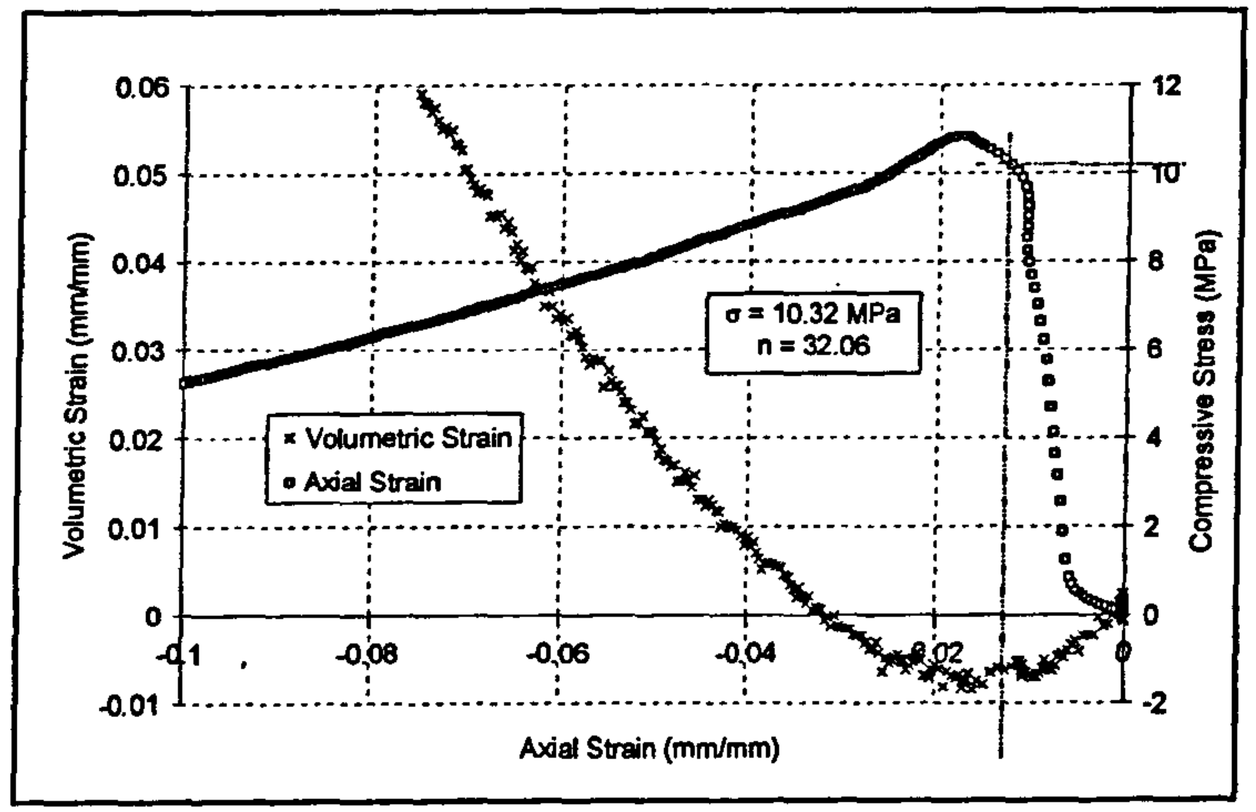

Figure H.16: DBM20 10A

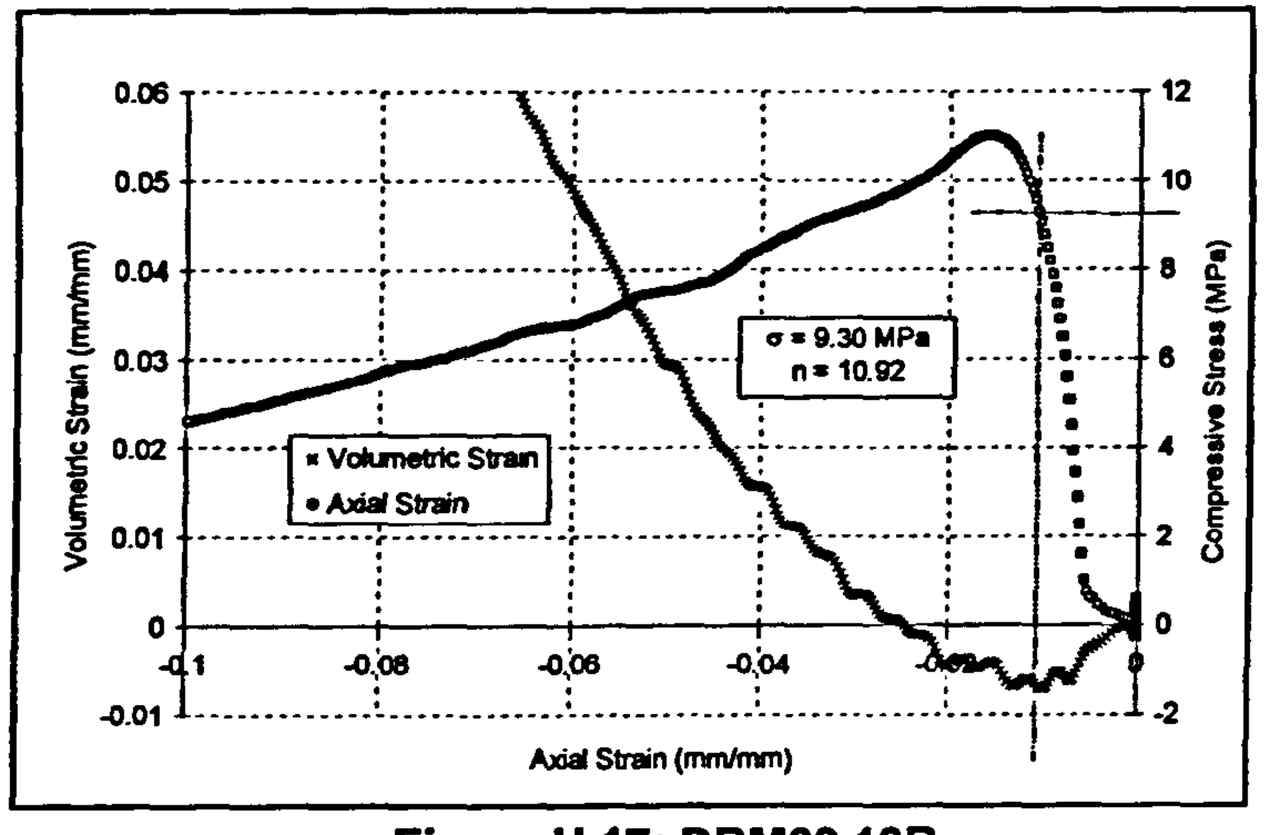

Figure H.17: DBM20 10B

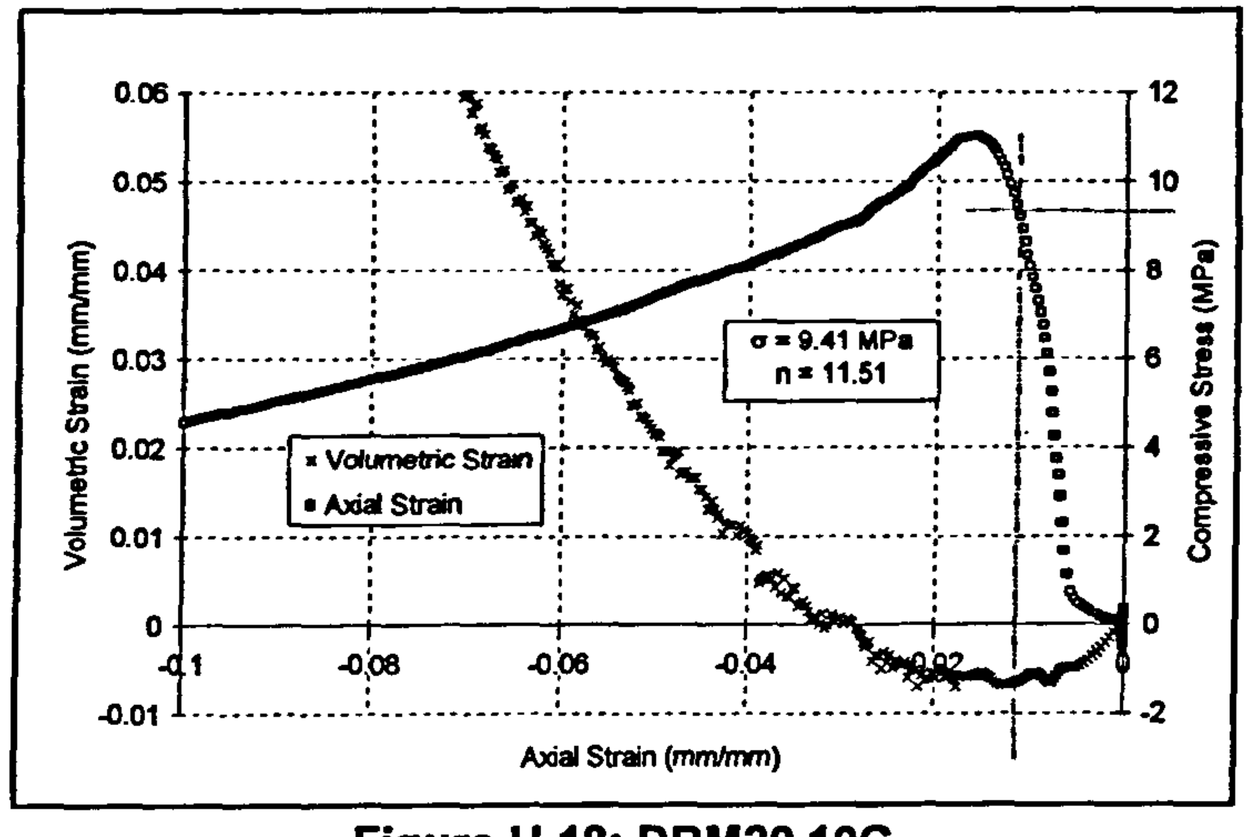

Figure H.18: DBM20 10C

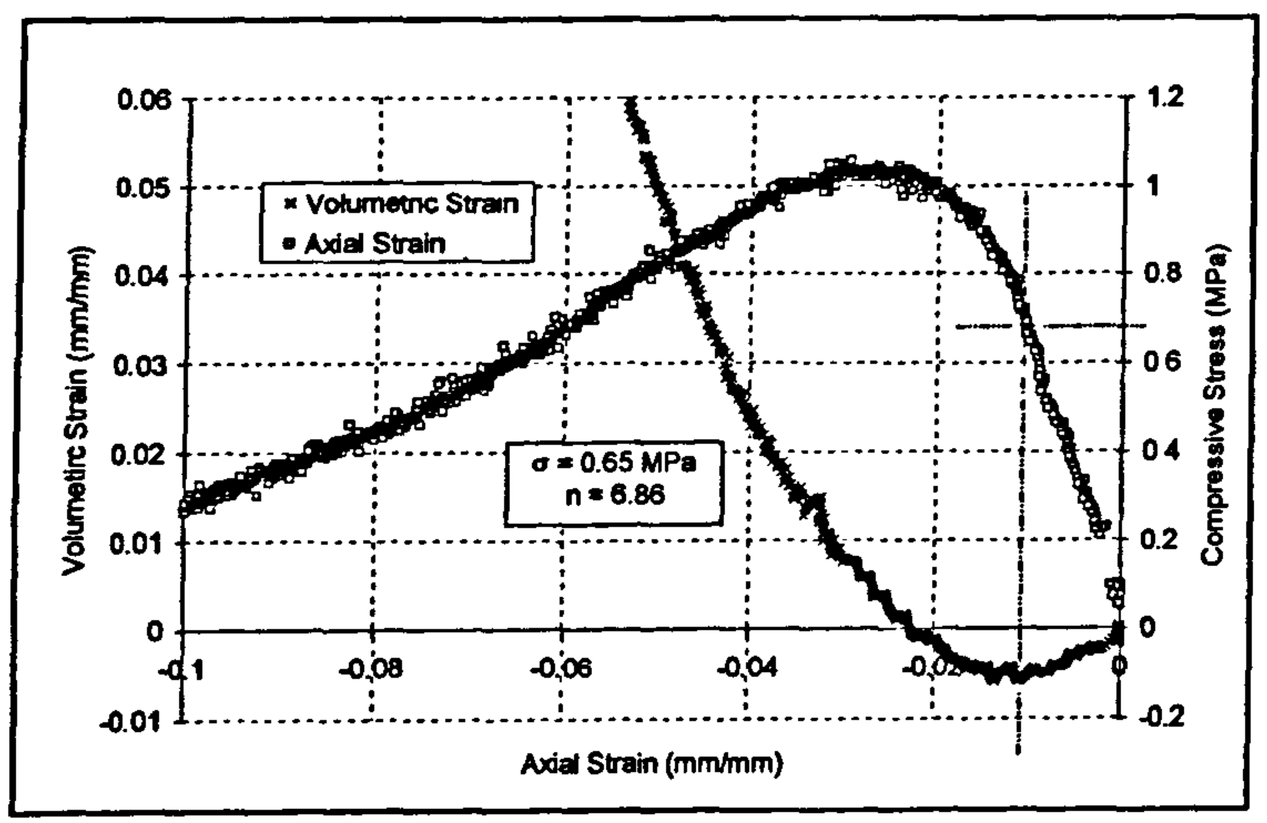

Figure H.19: DBM35 0.1A

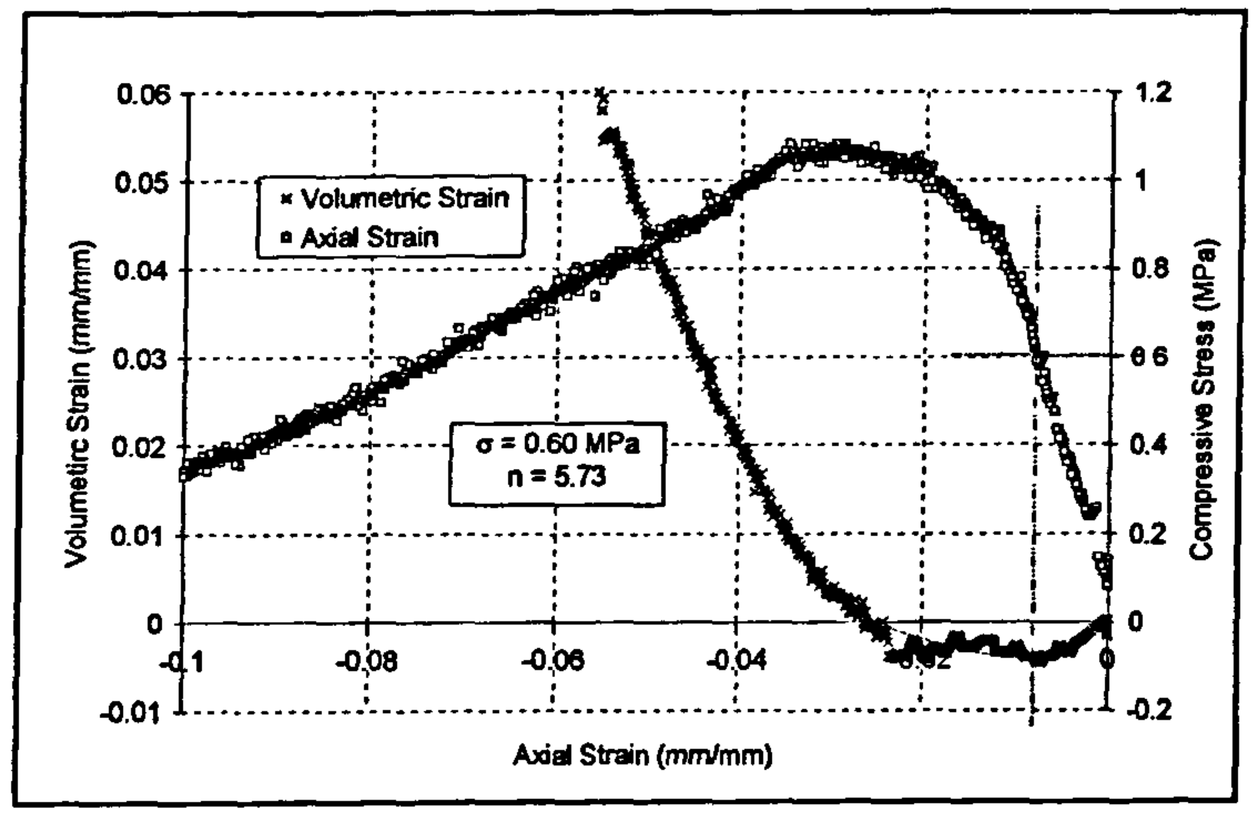

Figure H.20: DBM35 0.1B

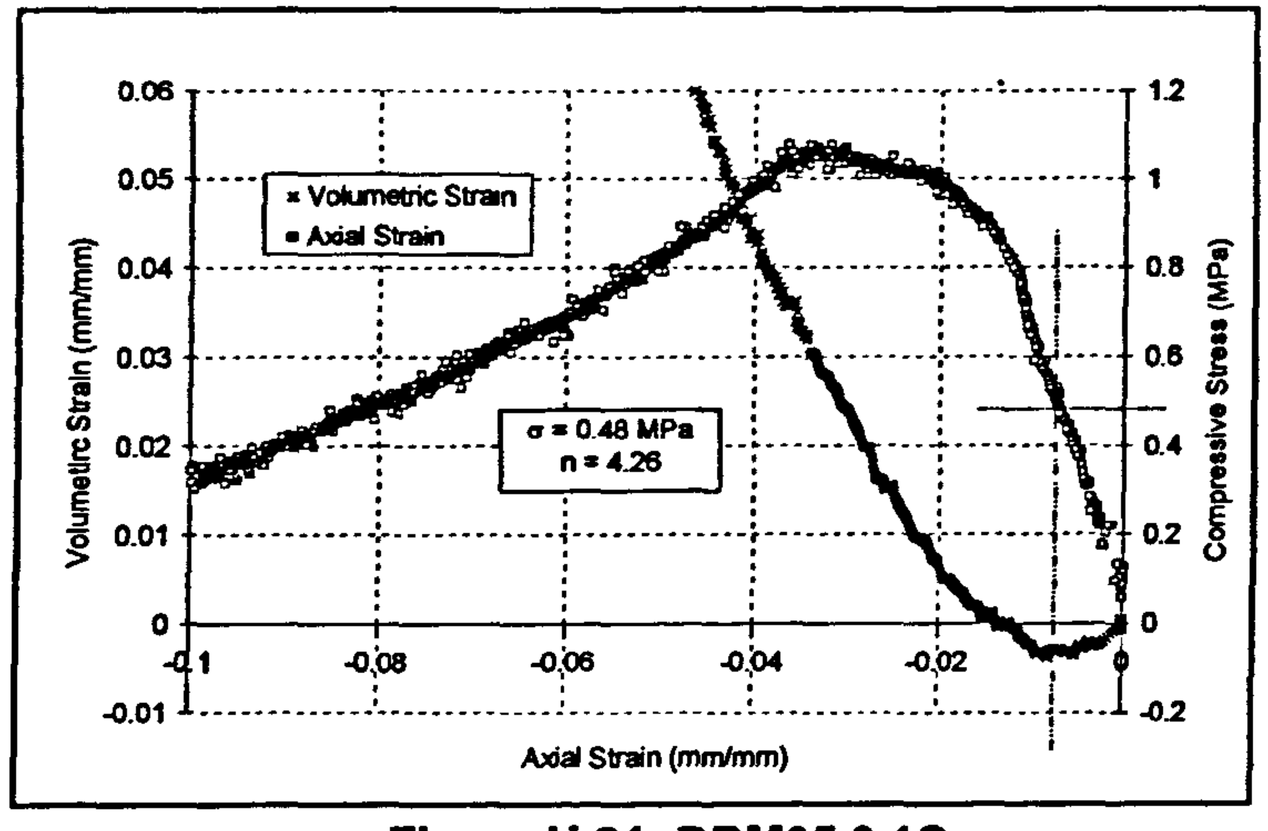

Figure H.21: DBM35 0.1C

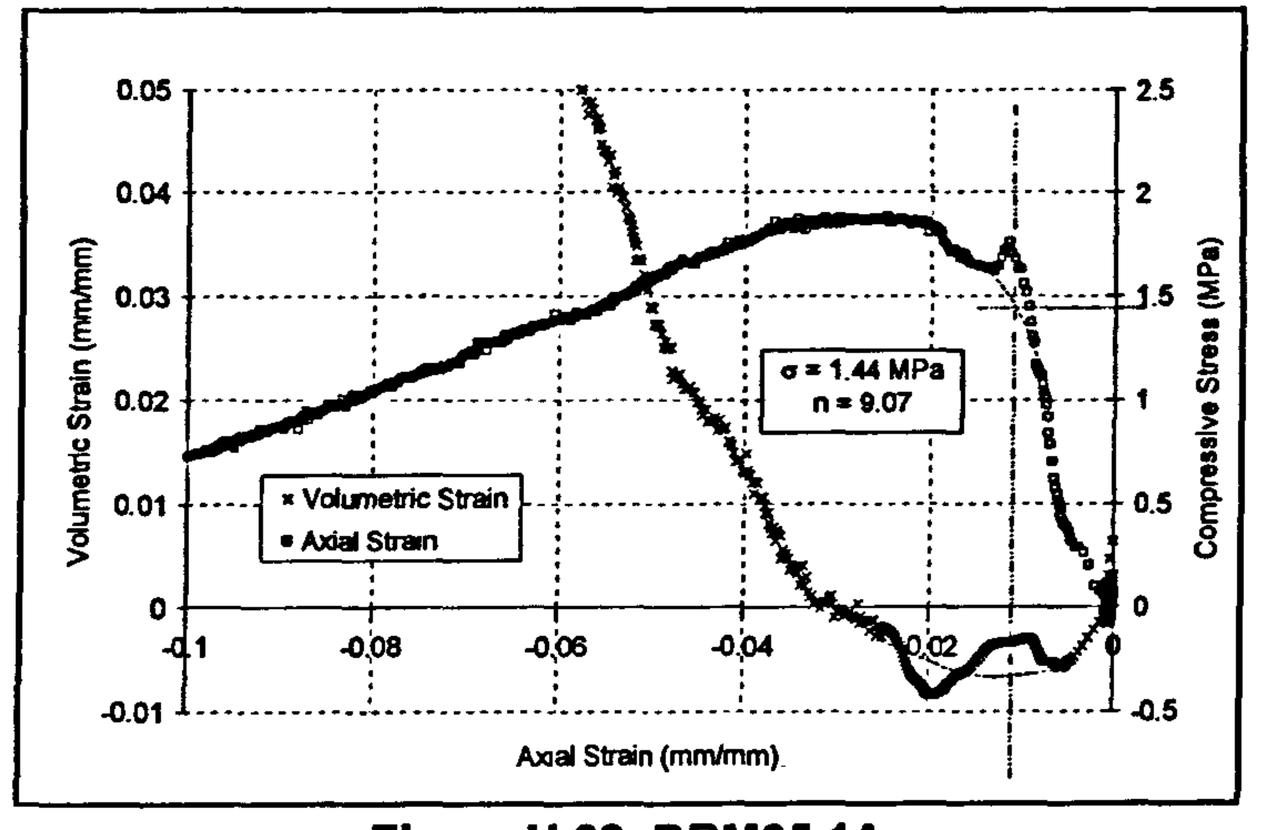

Figure H.22: DBM35 1A

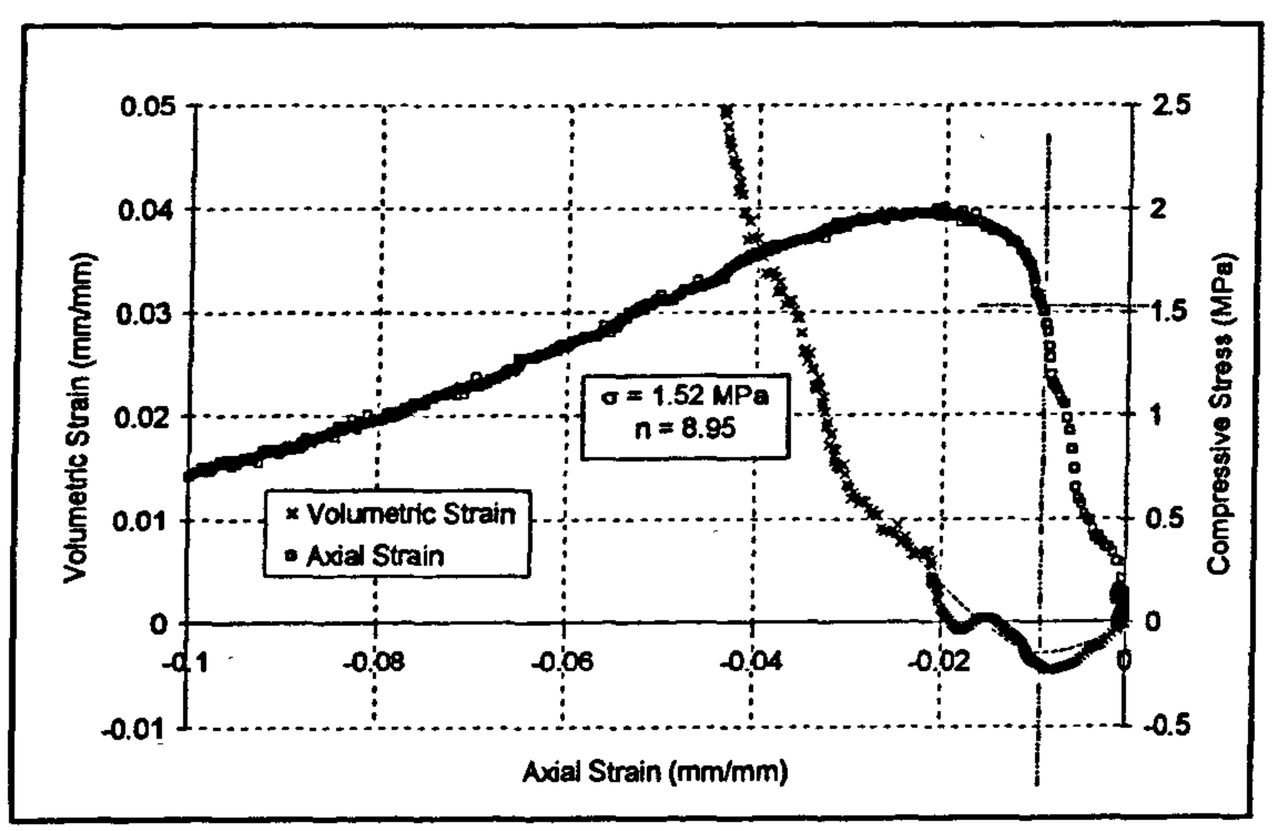

Figure H.23: DBM35 1B

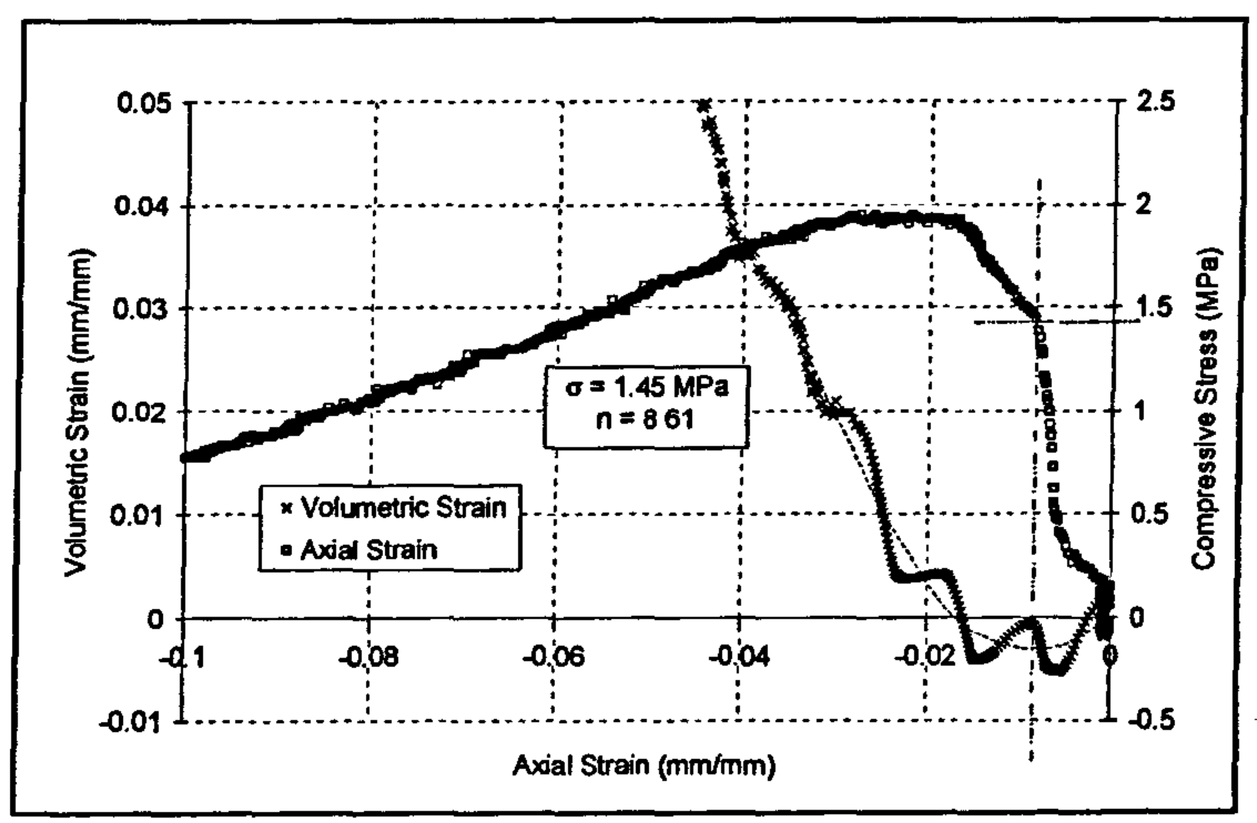

Figure H.24: DBM35 1C

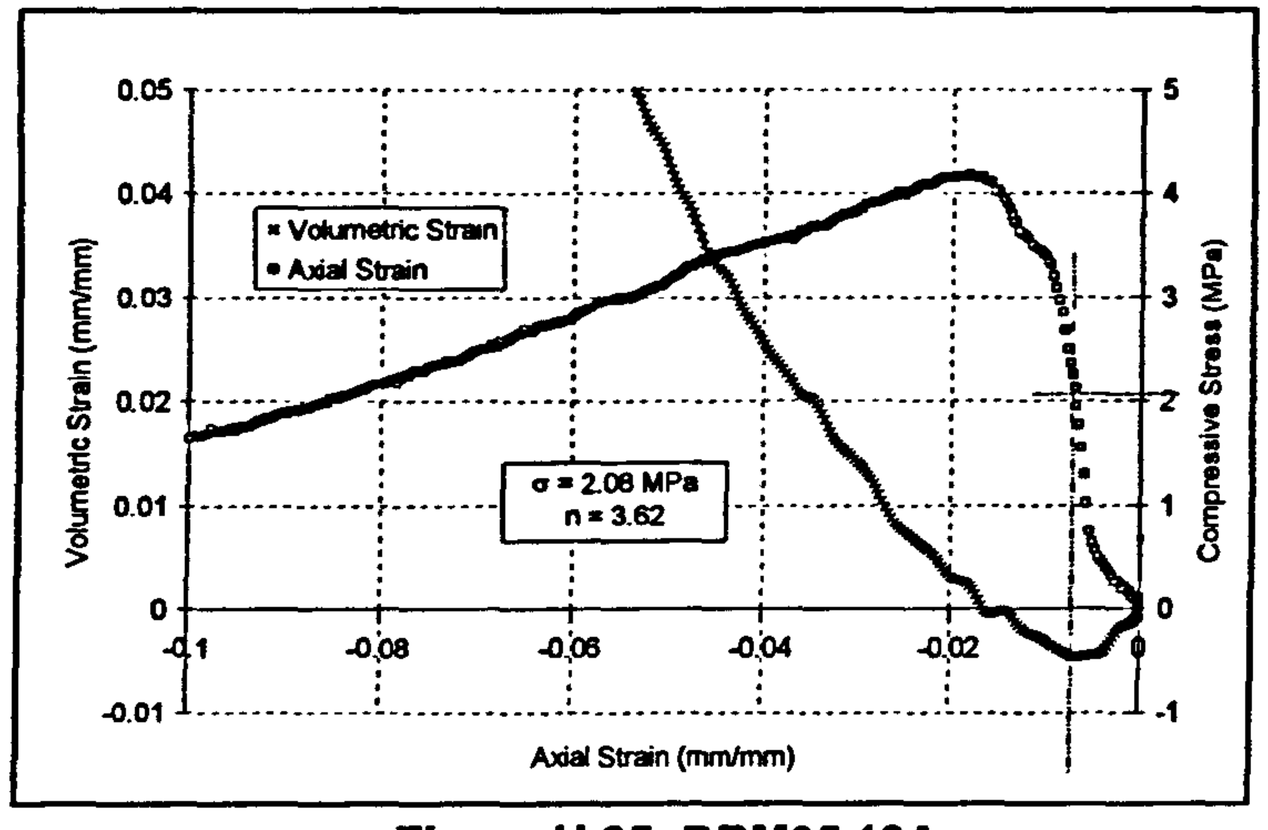

Figure H.25: DBM35 10A

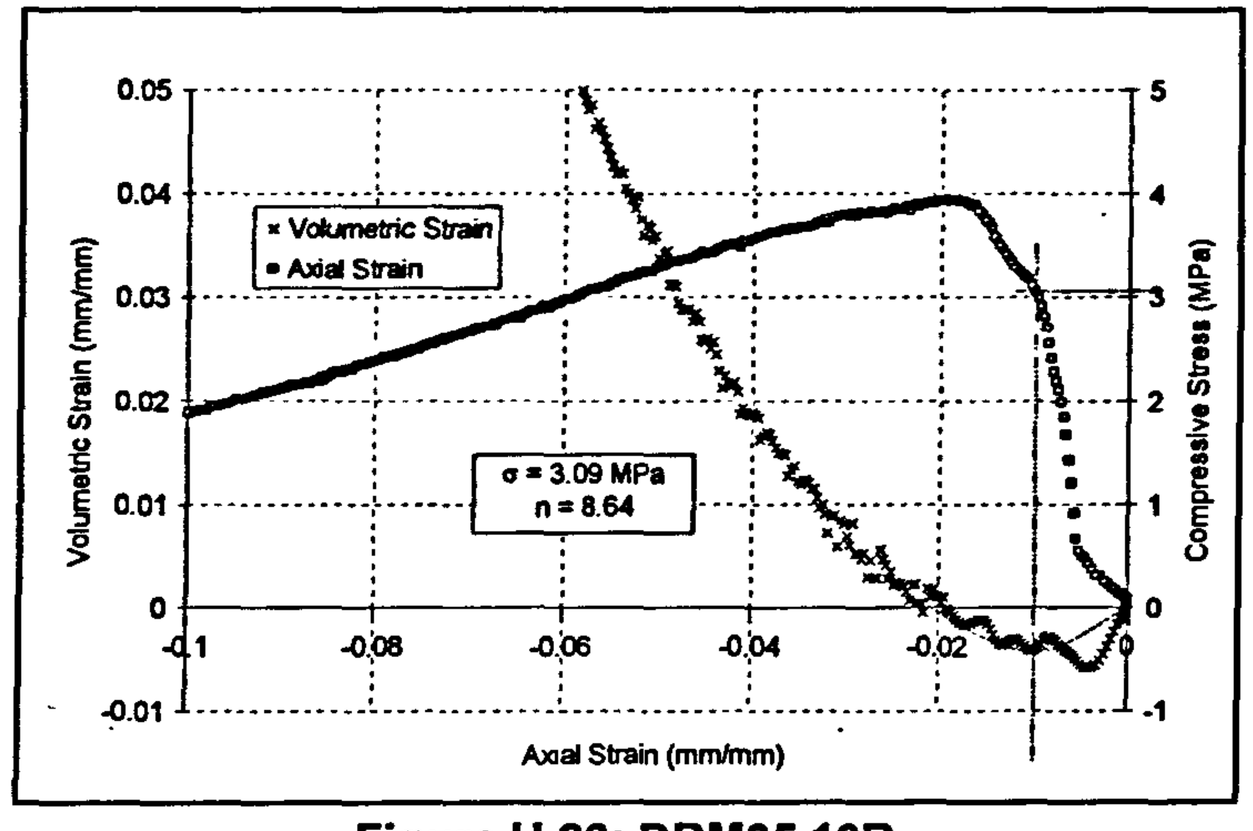

Figure H.26: DBM35 10B

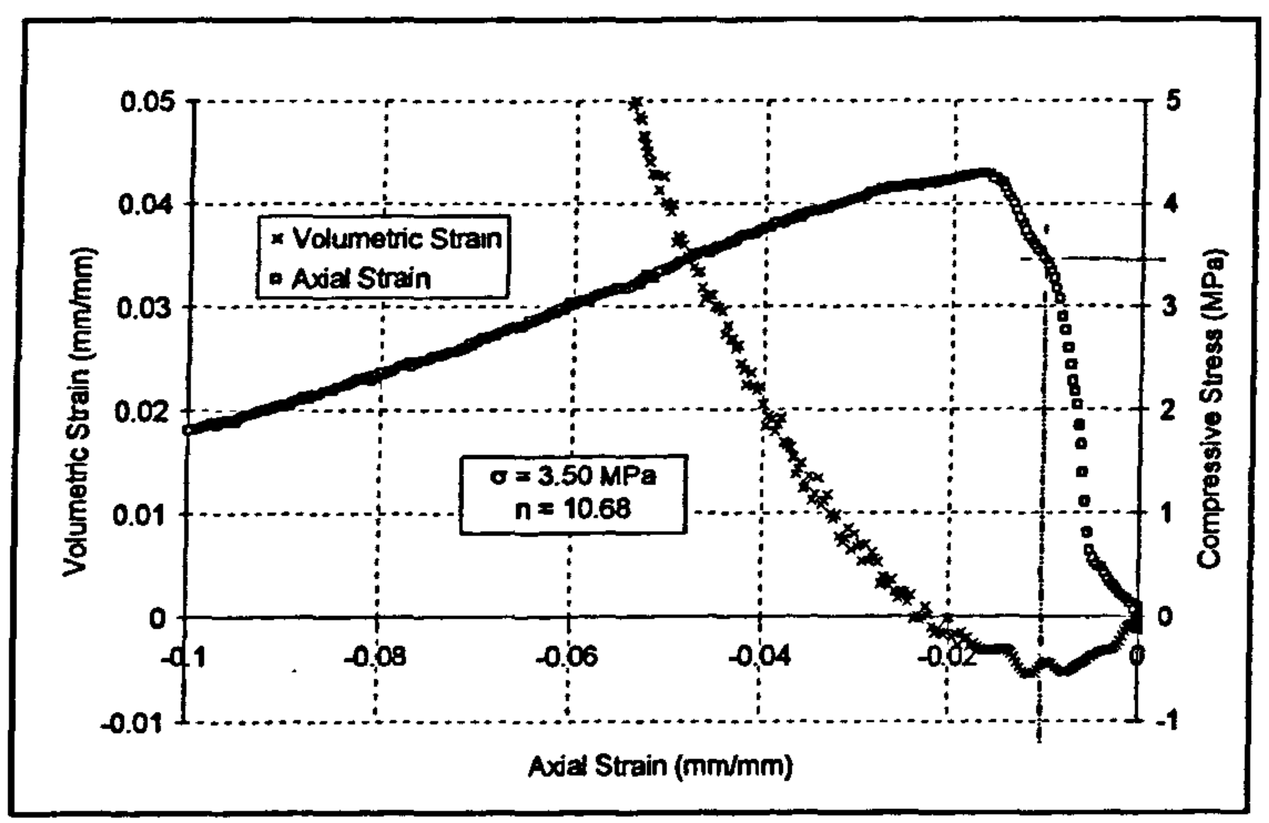

Figure H.27: DBM35 10C

Appendix I - Plots for the Determination of Material Parameter n HRA Mixture Data

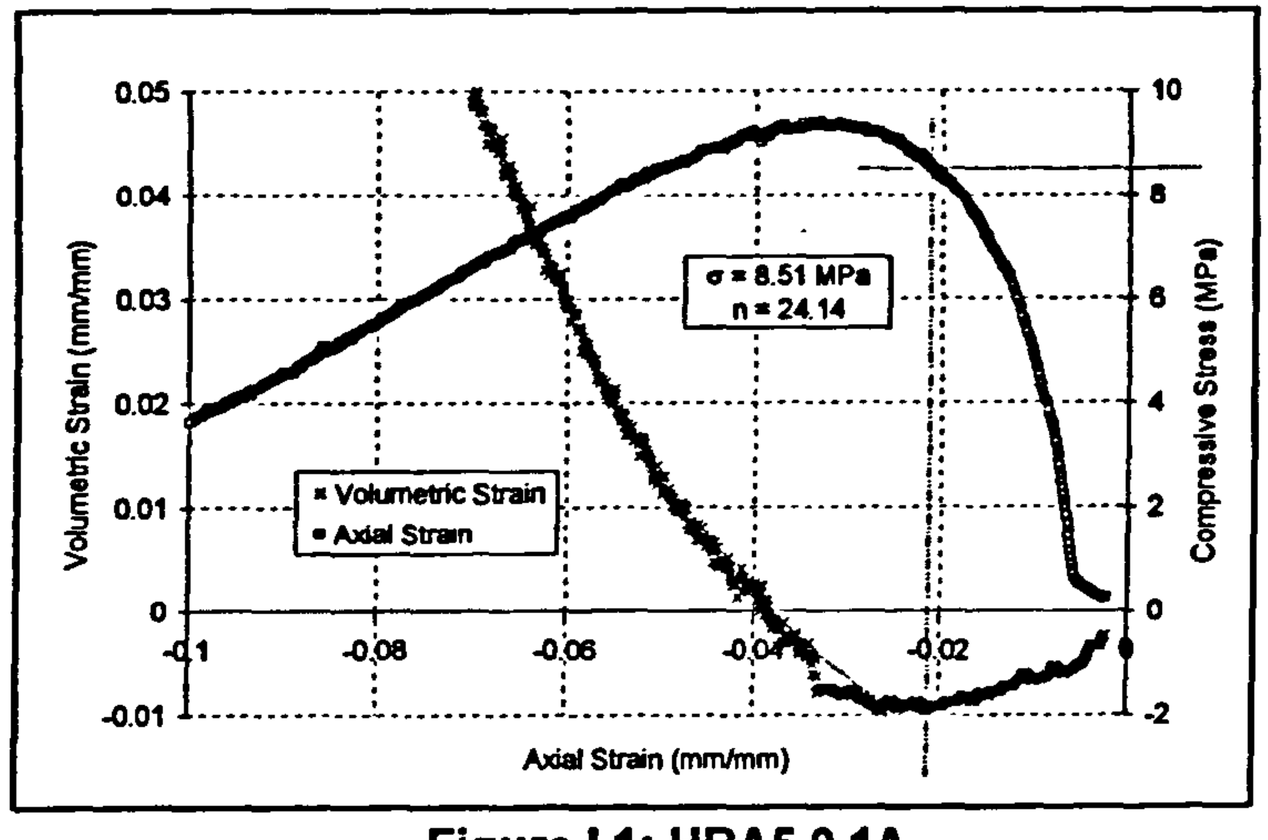

Figure I.1: HRA5 0.1A

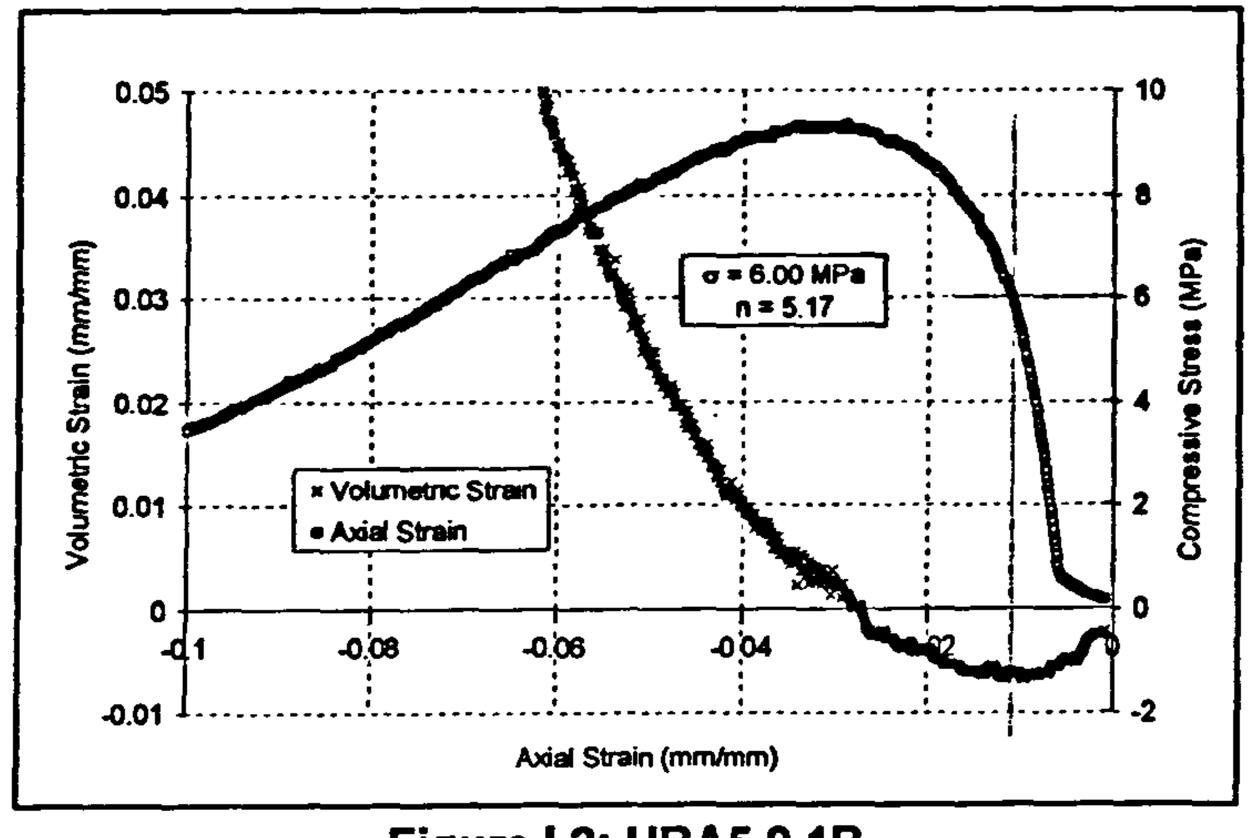

Figure I.2: HRA5 0.1B

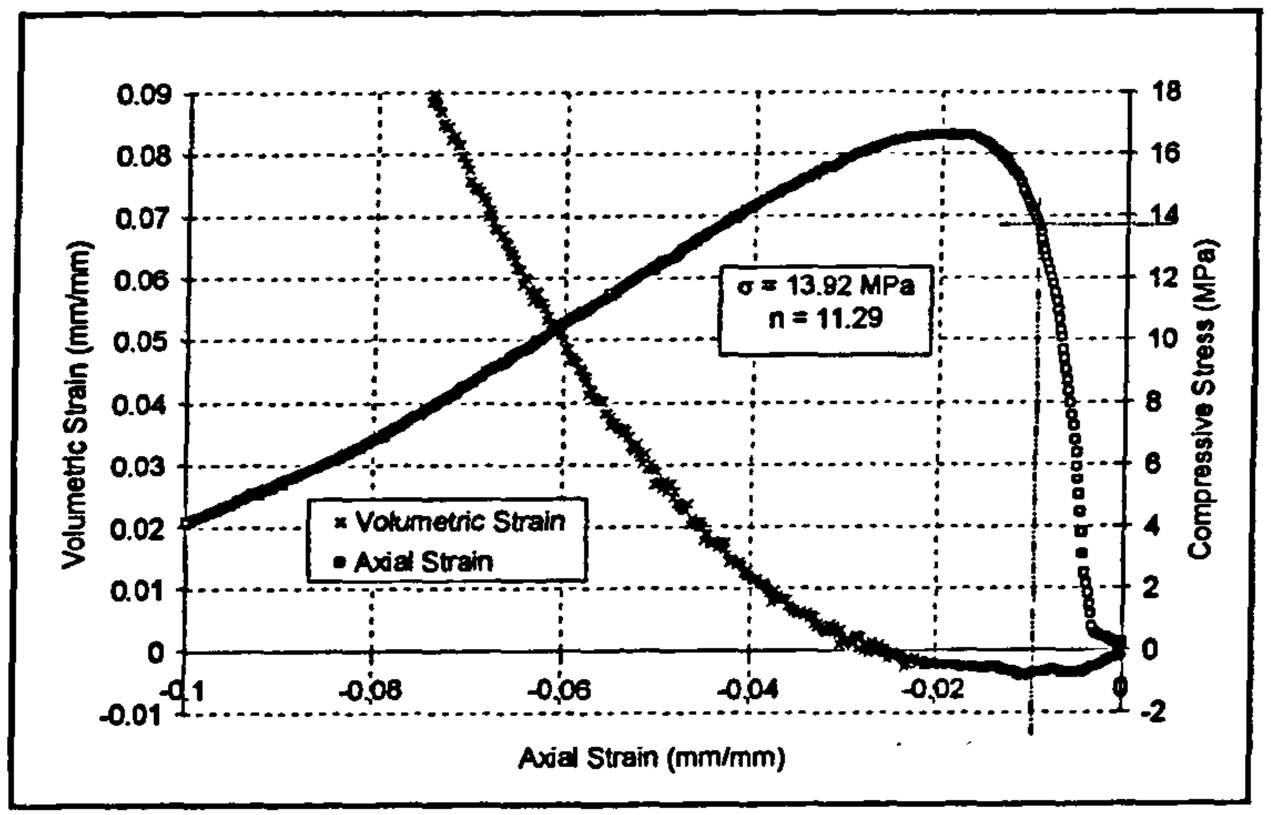

Figure I.3: HRA5 1A

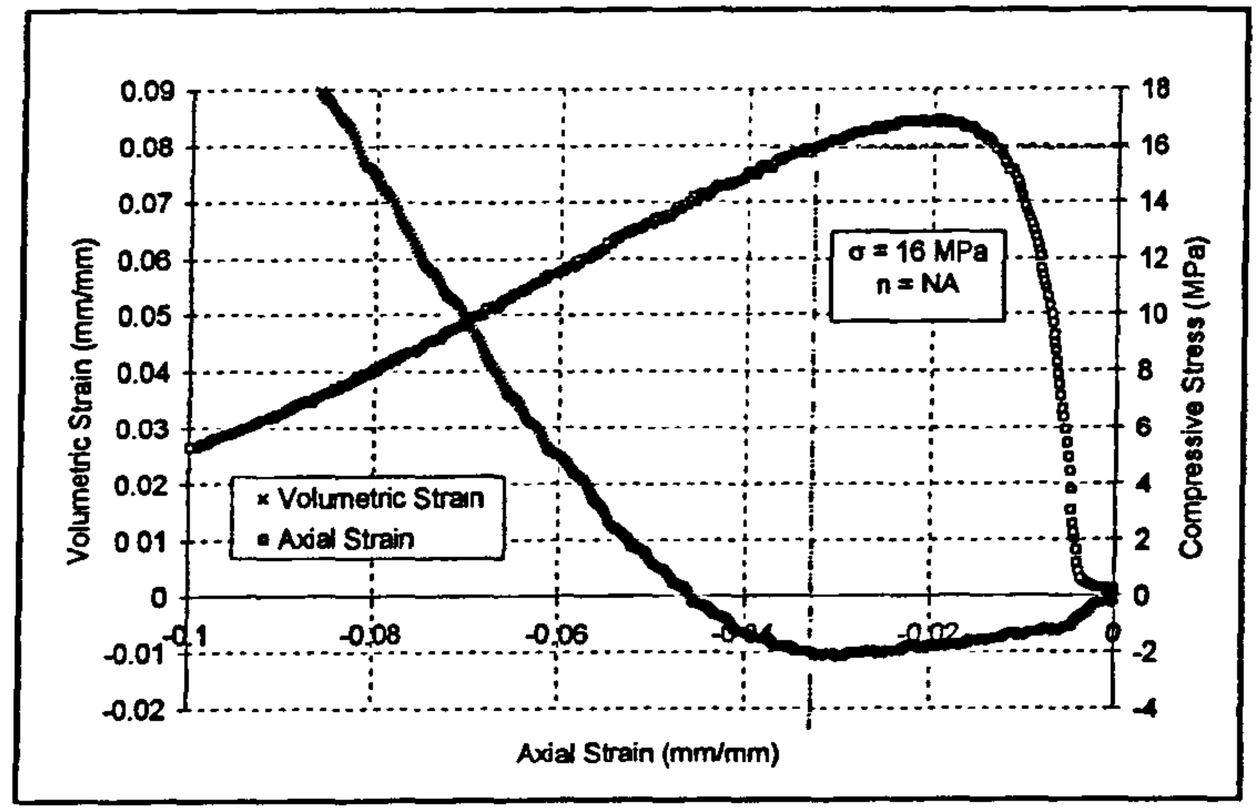

Figurel.4: HRA5 1B

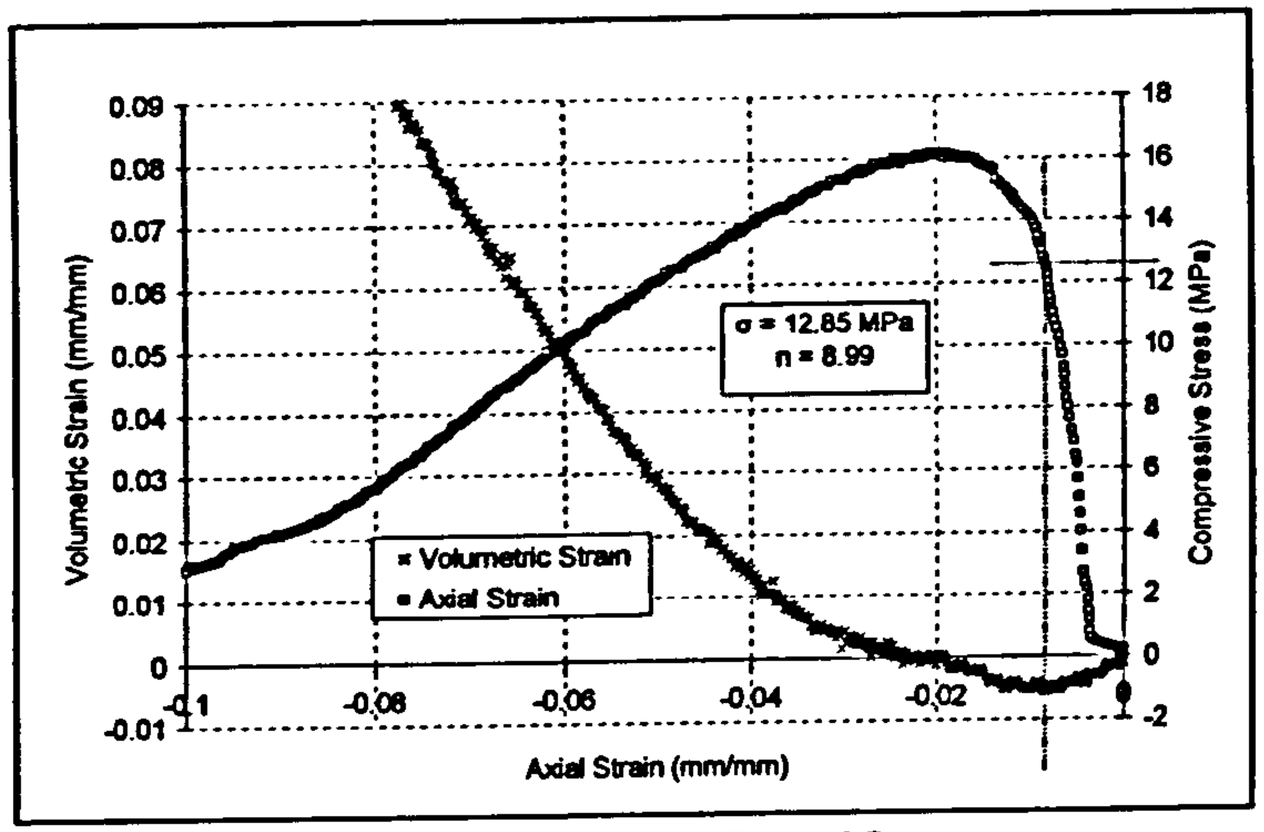

Figure I.5: HRA5 1C

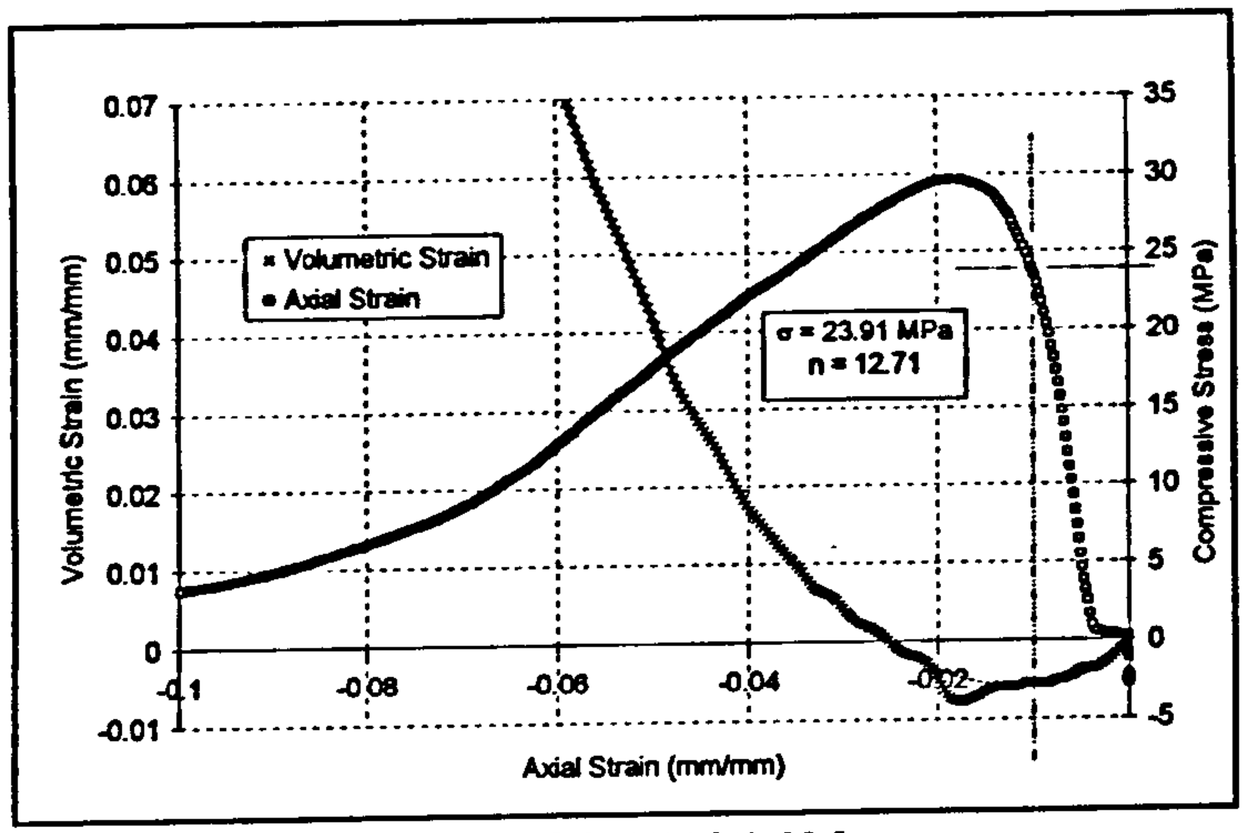

Figure I.6: HRA5 10A

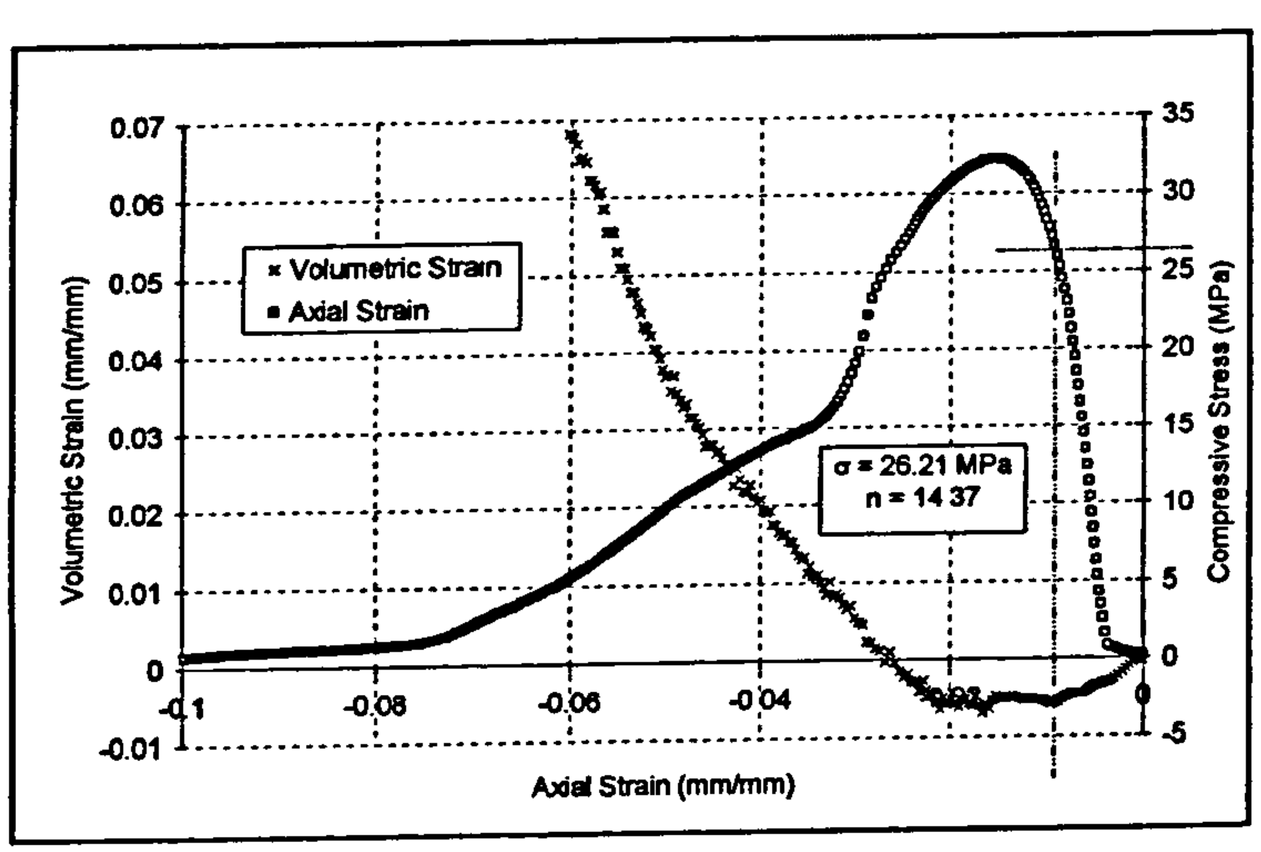

Figure I.7: HRA5 10B

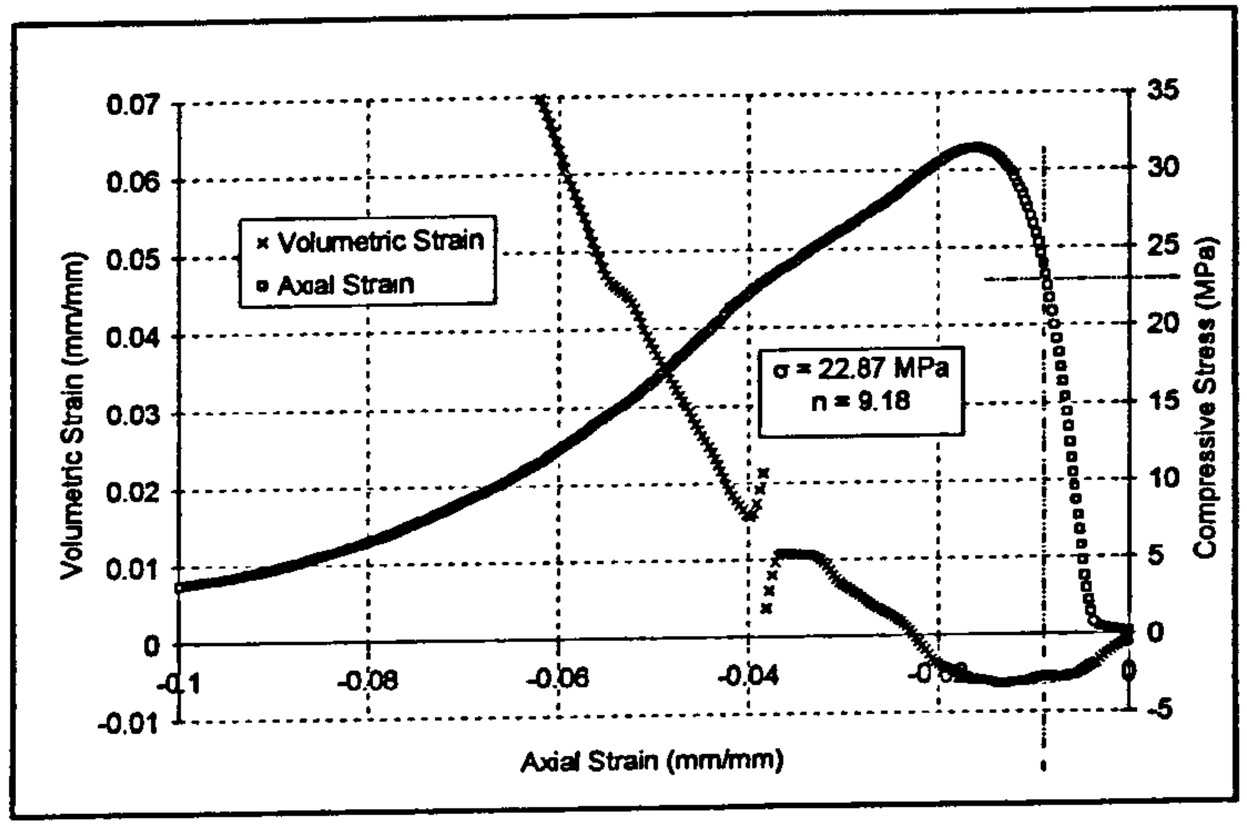

Figure I.8: HRA5 10C

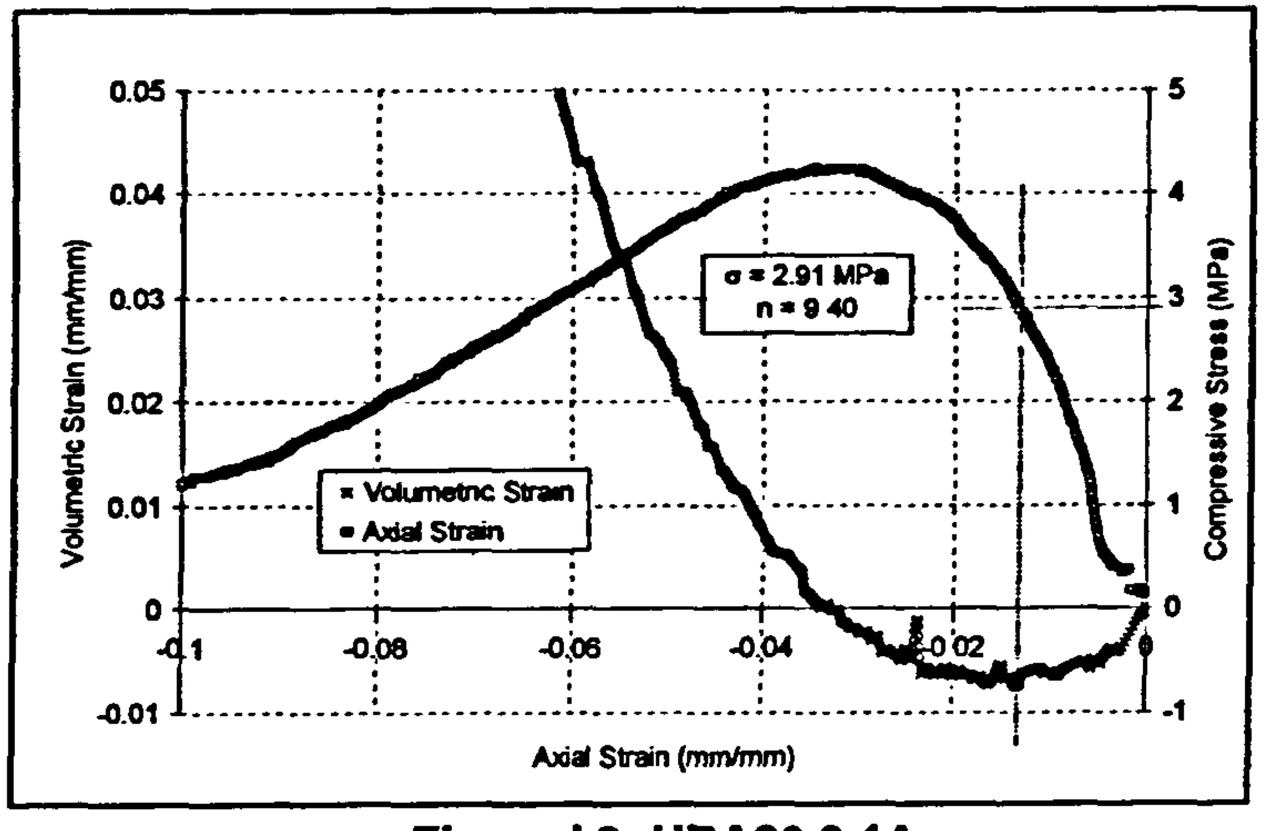

Figure I.9: HRA20 0.1A

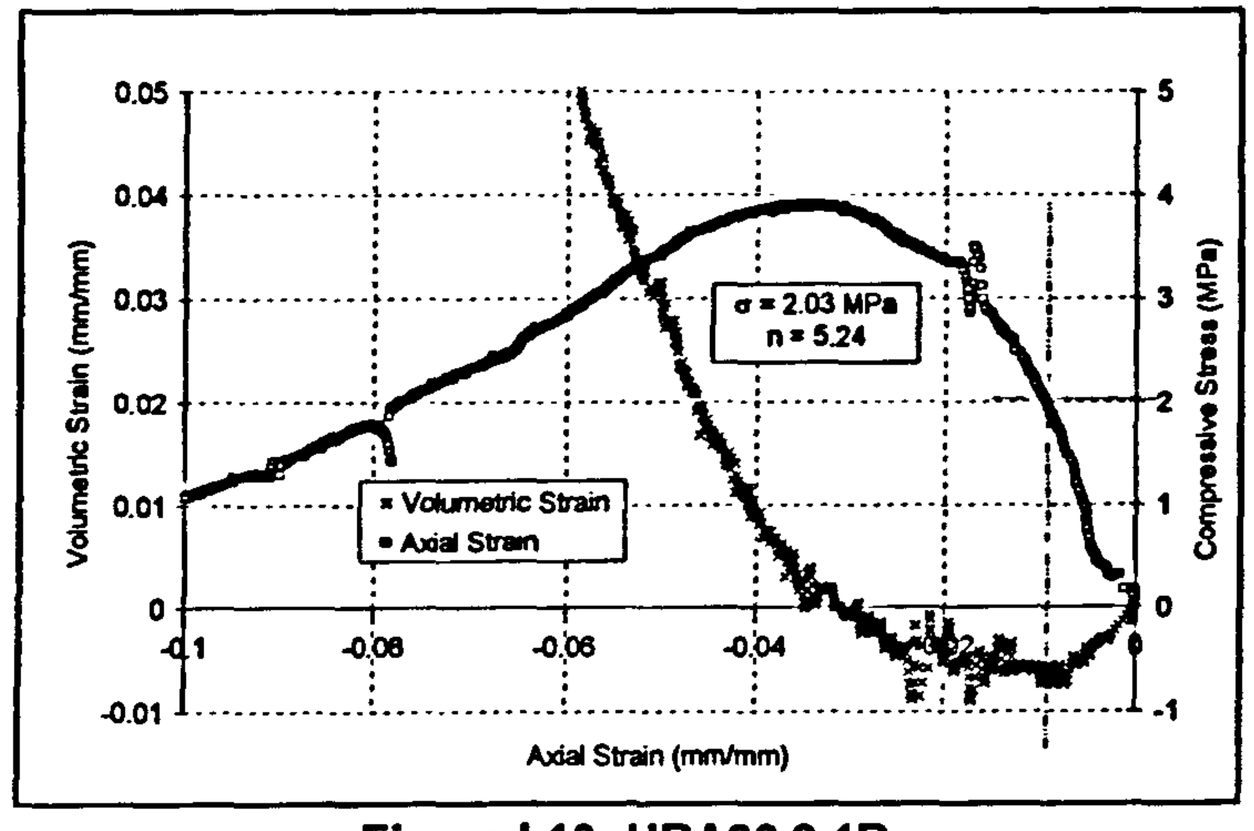

Figure I.10: HRA20 0.1B

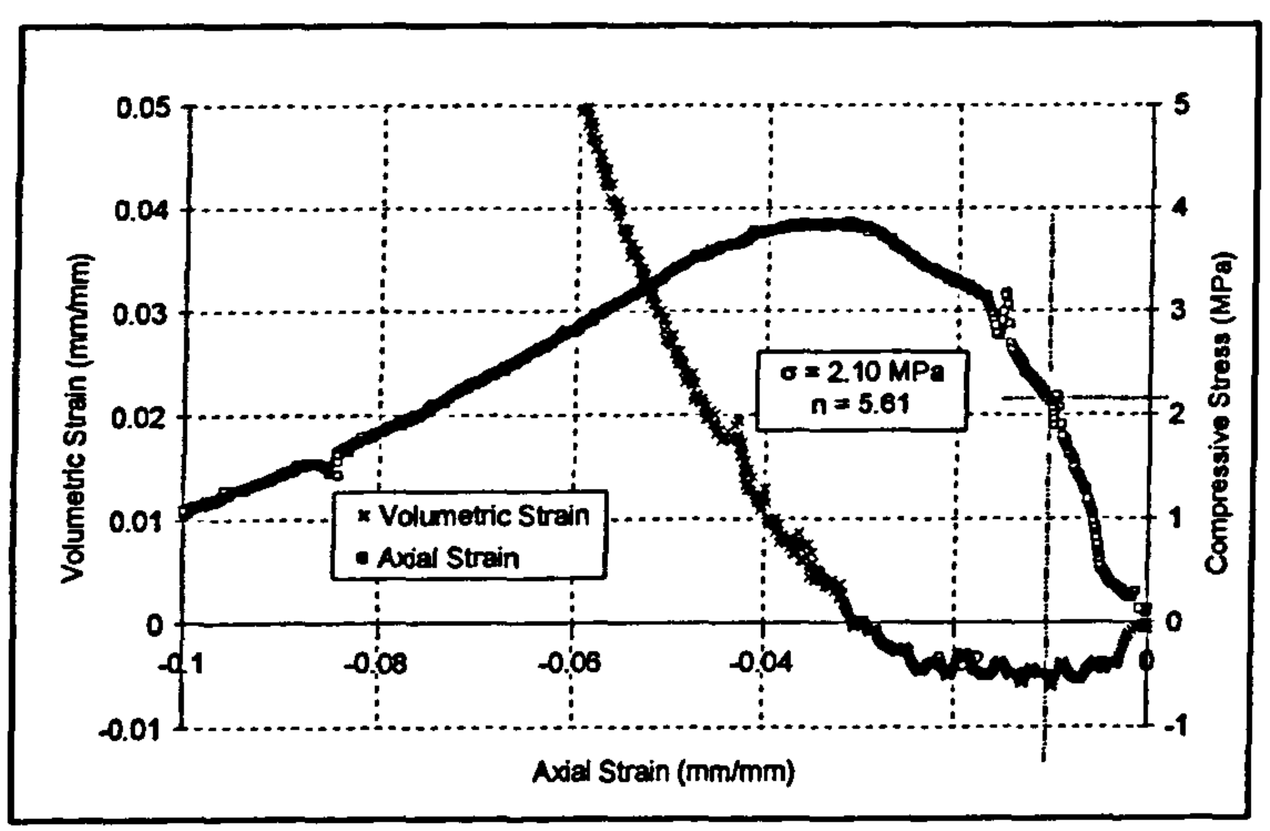

Figure I.11: HRA20 0.1C

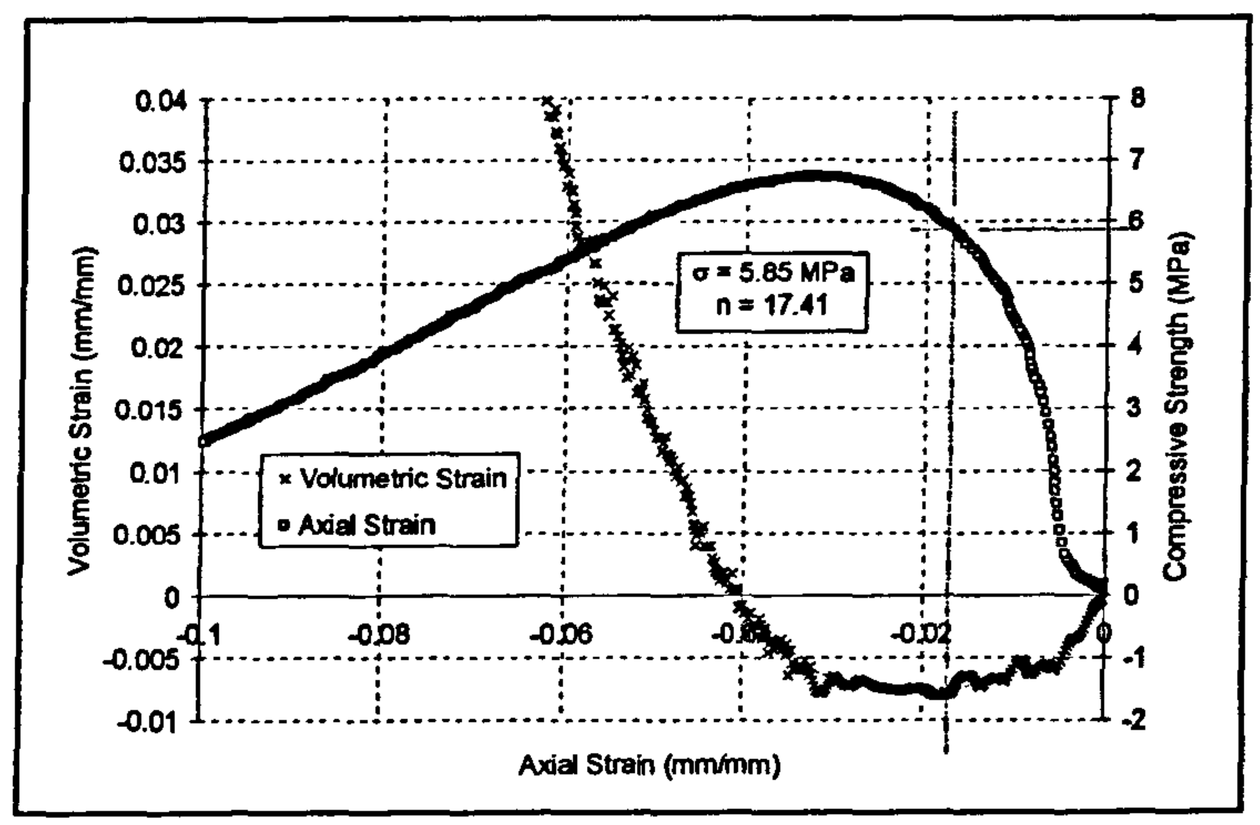

Figure I.12: HRA20 1A

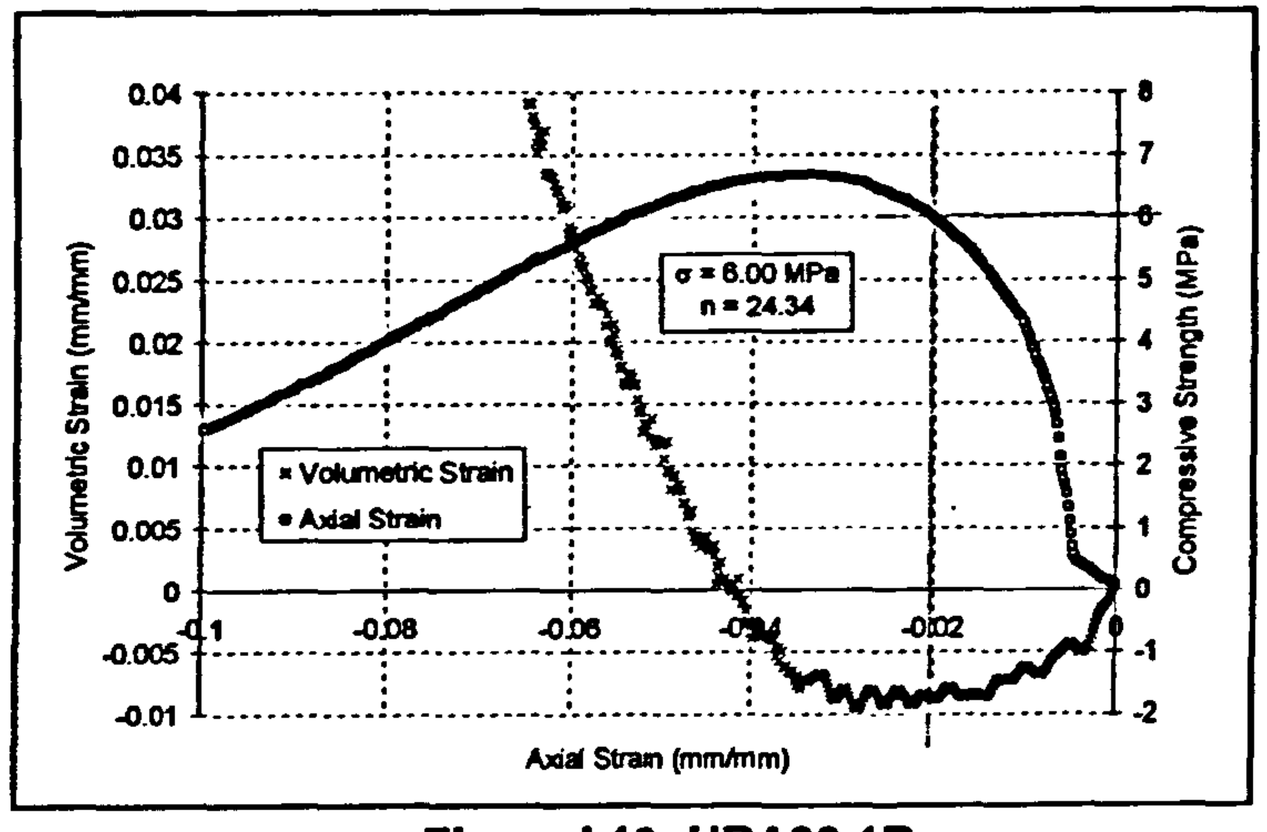

Figure I.13: HRA20 1B

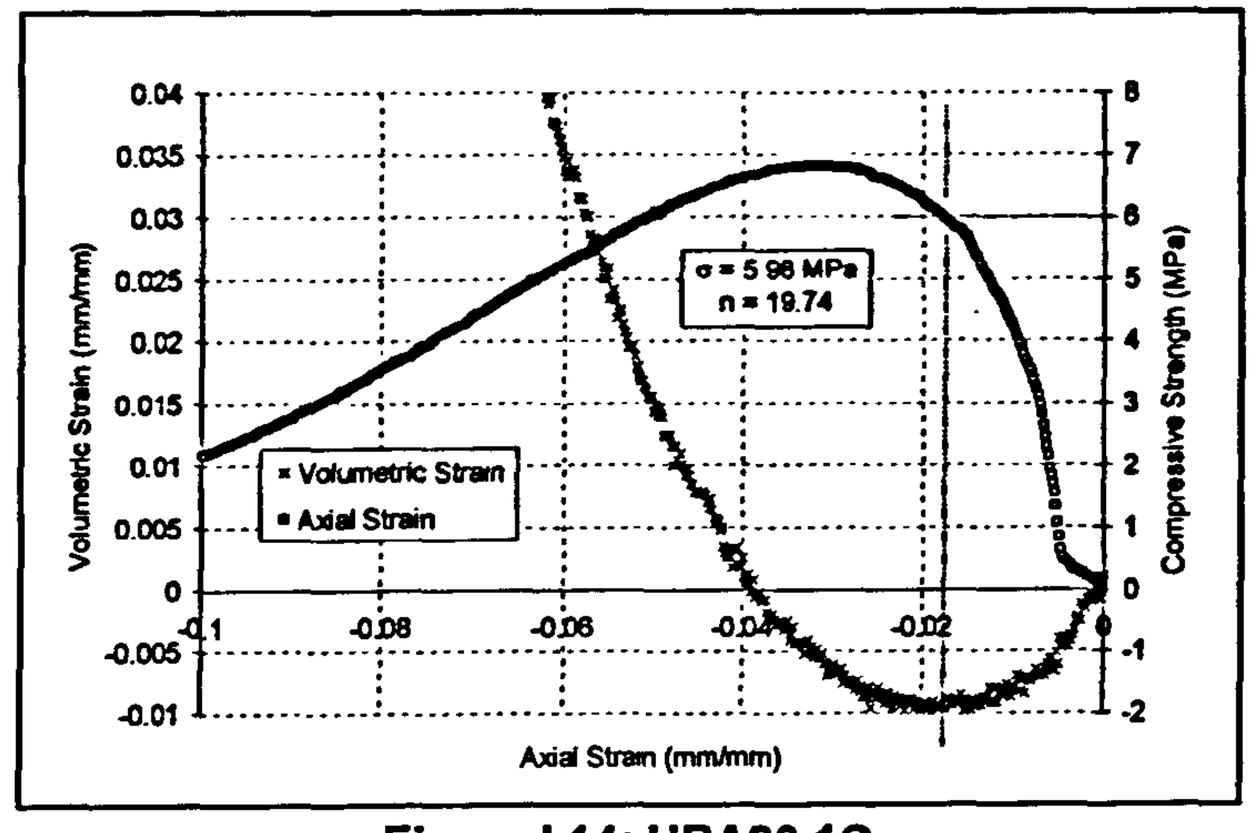

Figure I.14: HRA20 1C

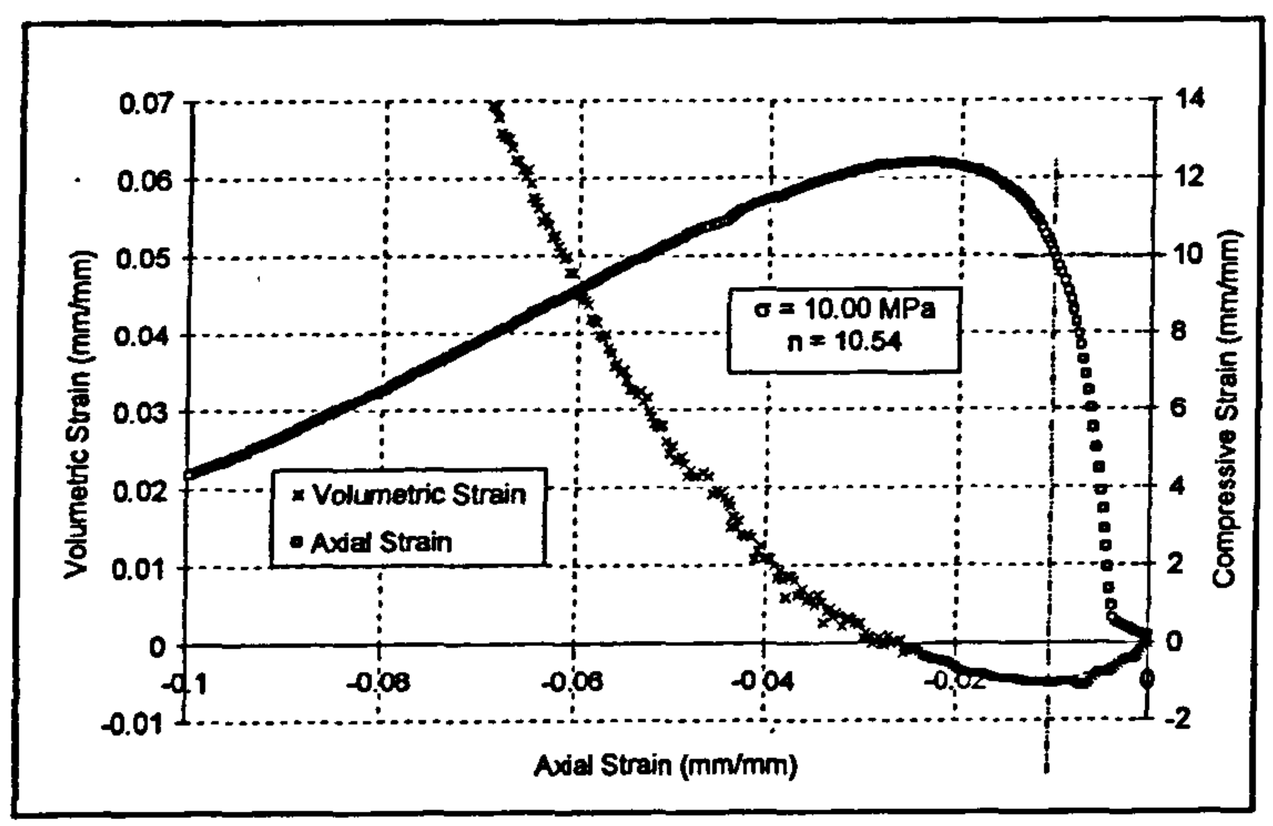

Figure I.15: HRA20 10A

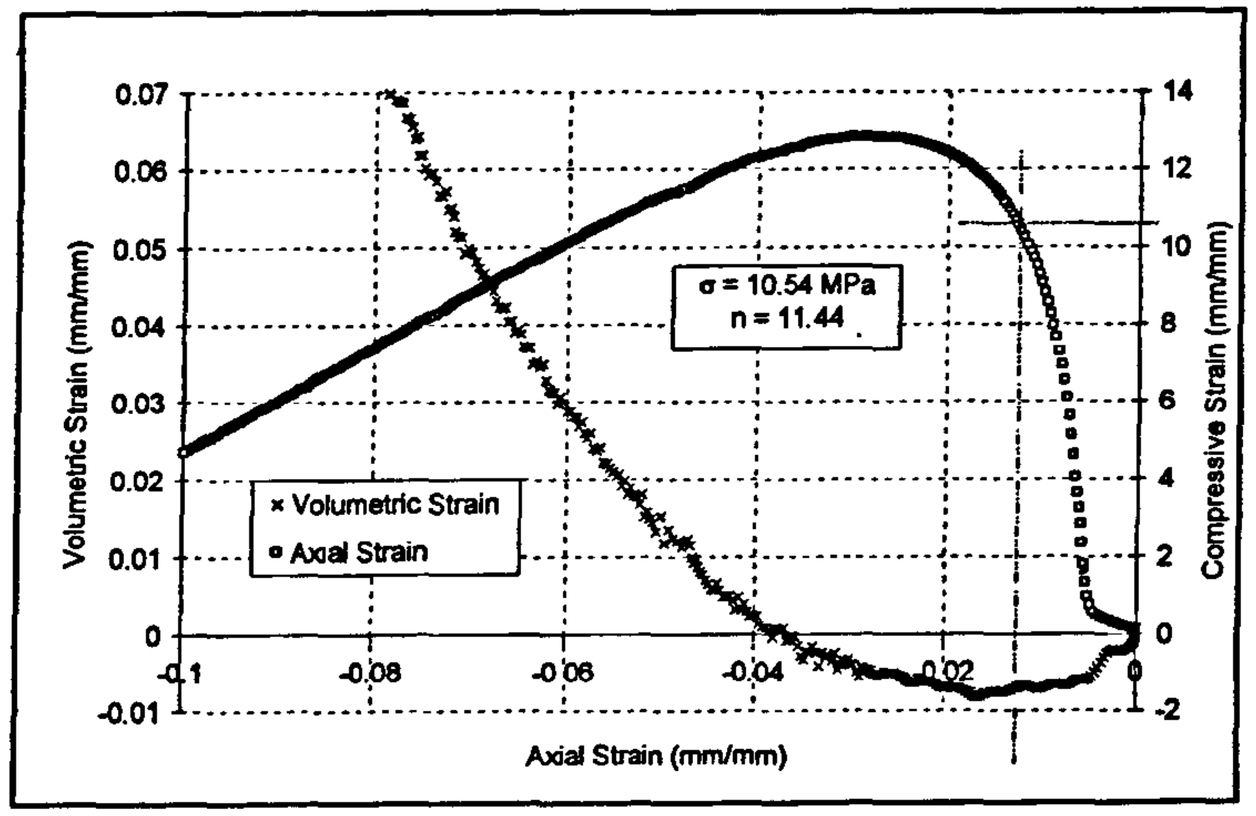

Figure I.16: HRA20 10B

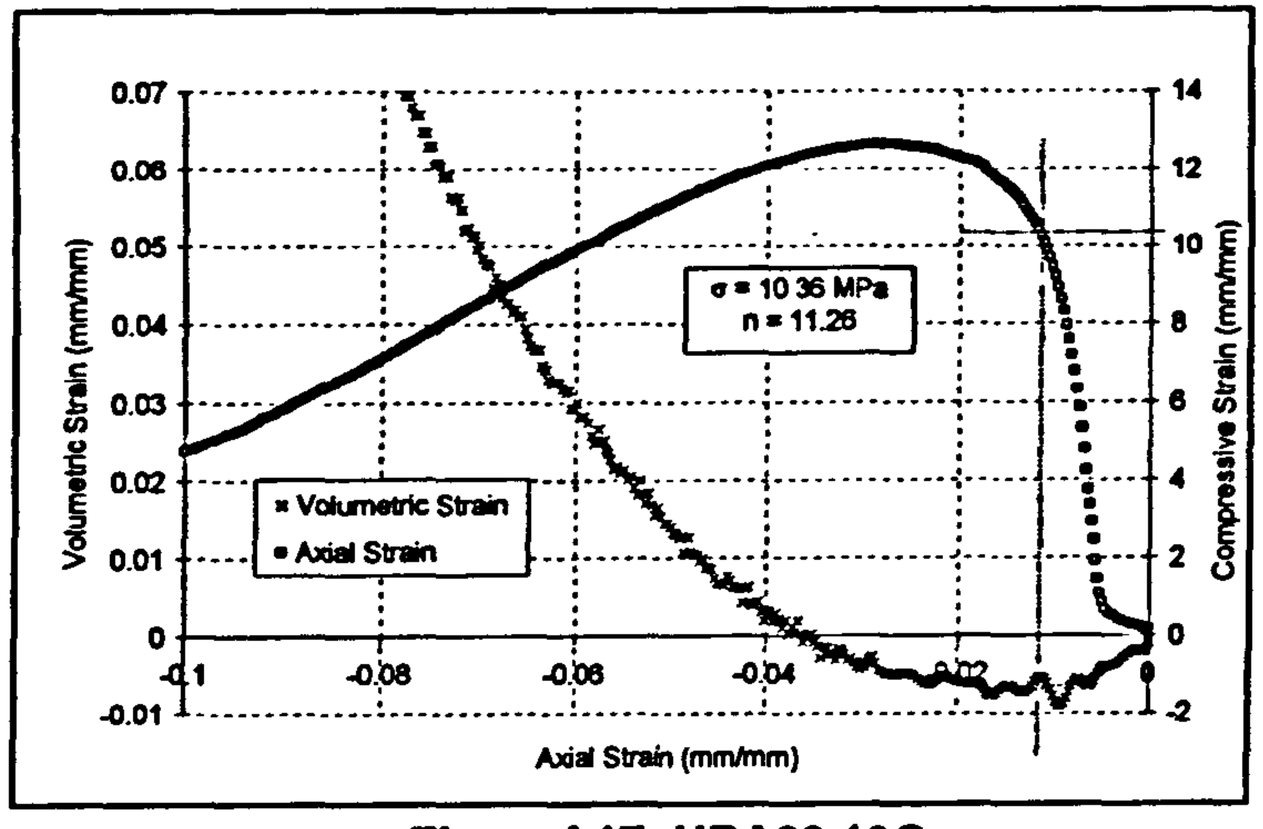

Figure I.17: HRA20 10C

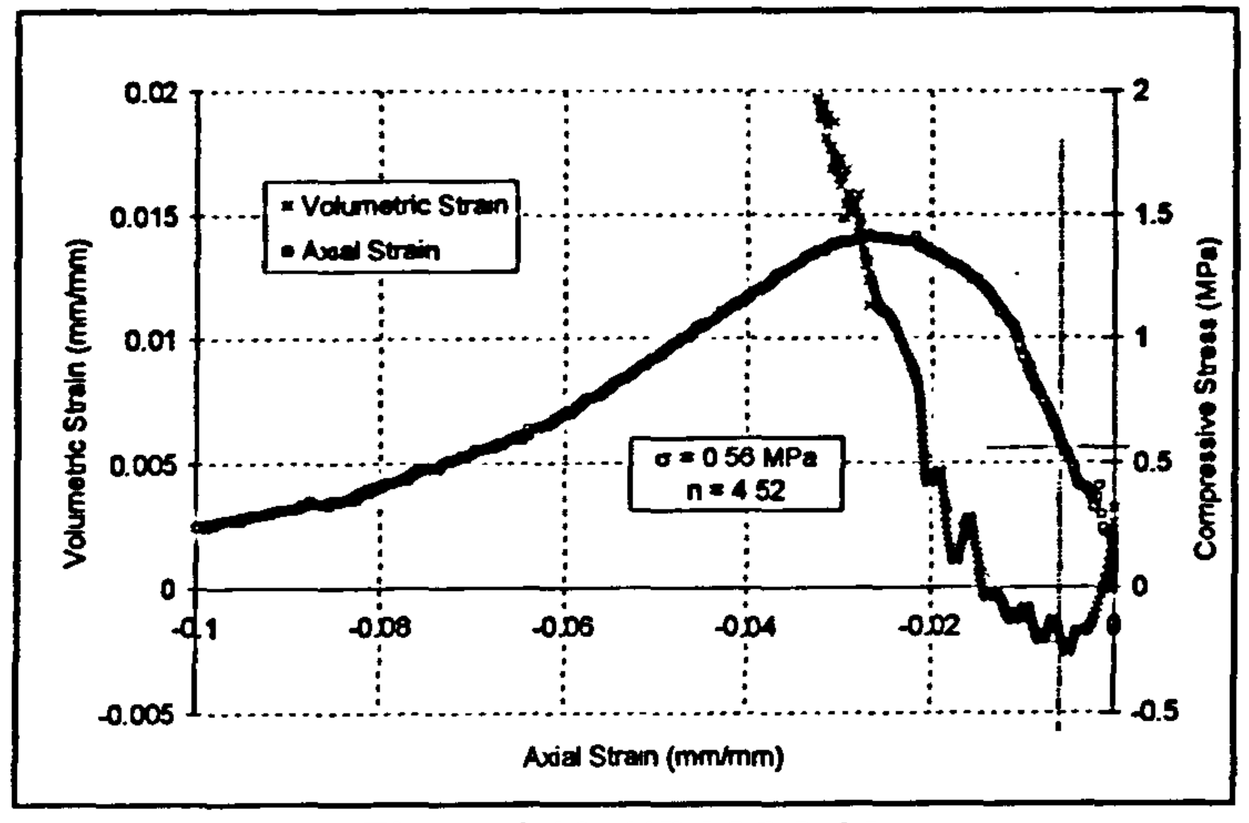

Figure I.18: HRA35 0.1A

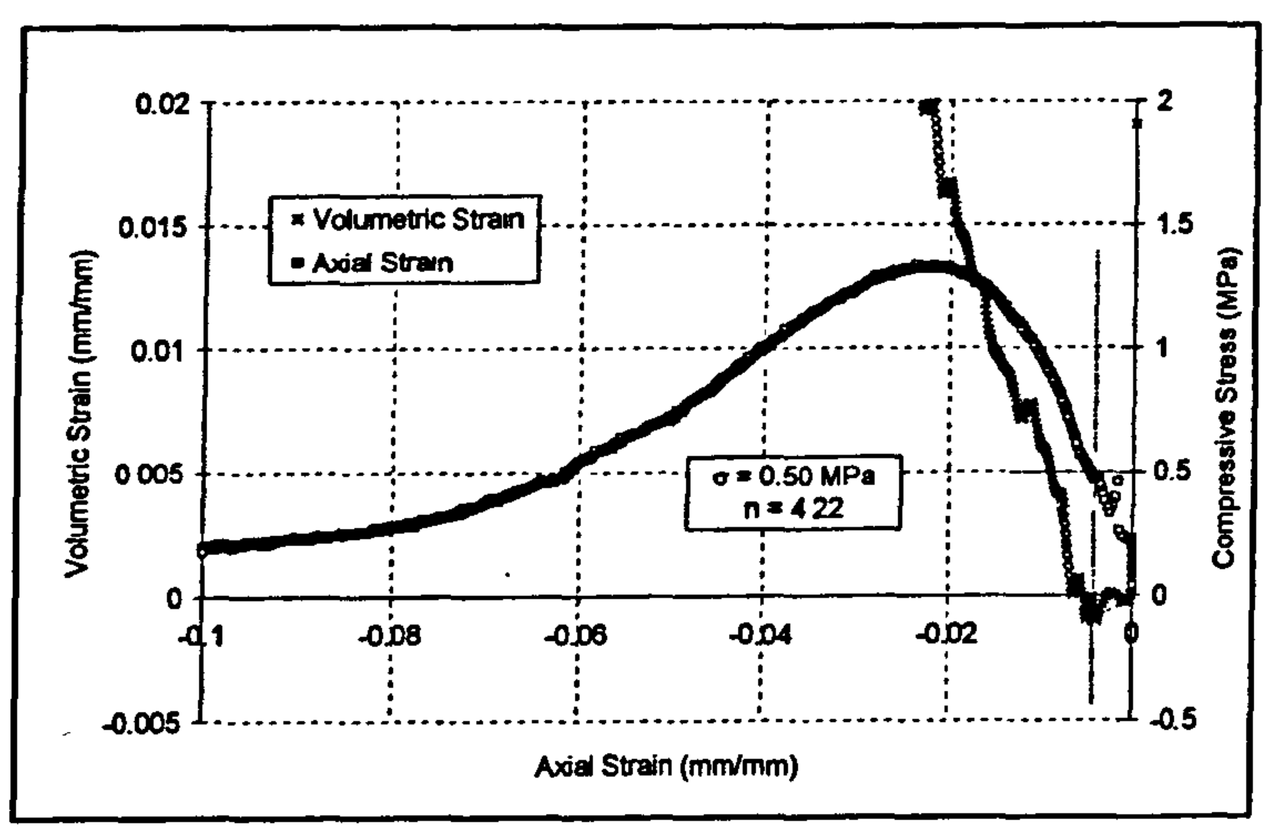

Figure I.19: HRA35 0.1B

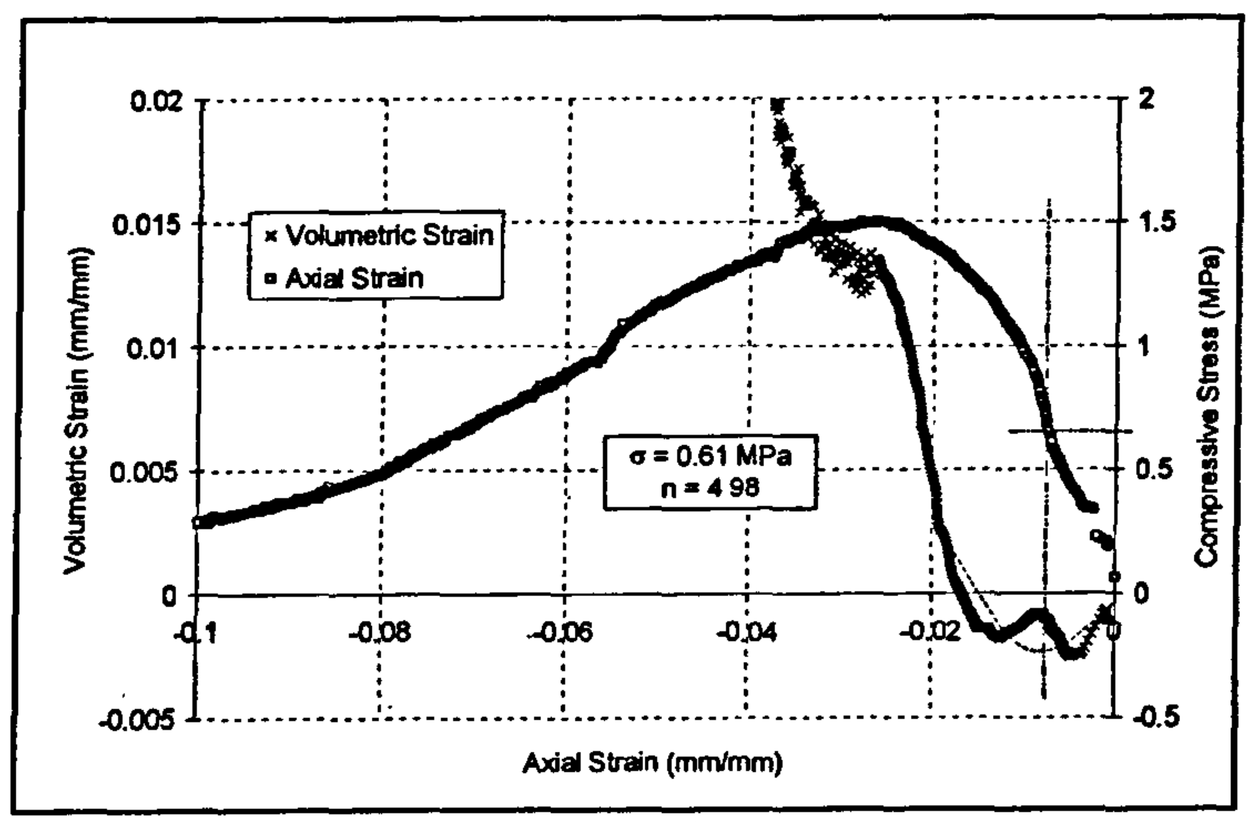

Figure I.20: HRA35 0.1C

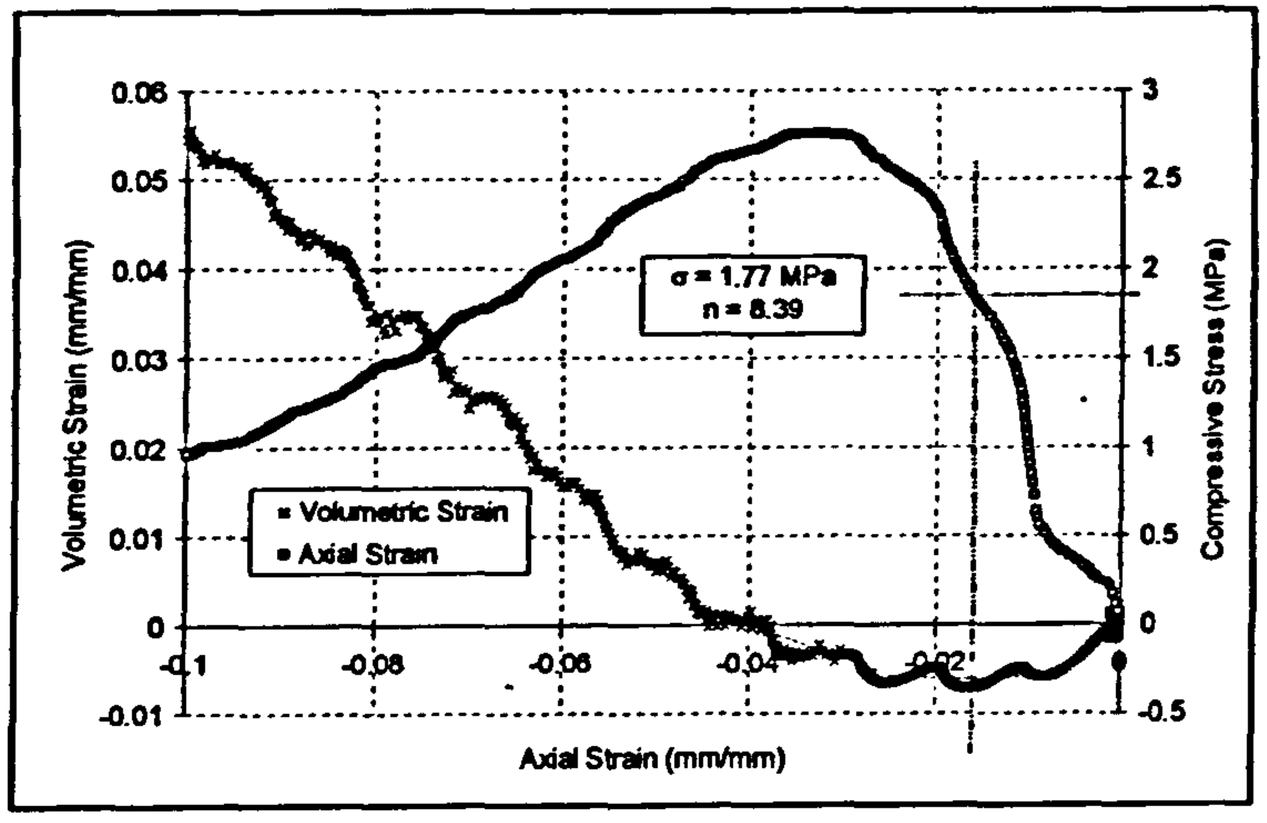

Figure I.21: HRA35 1A

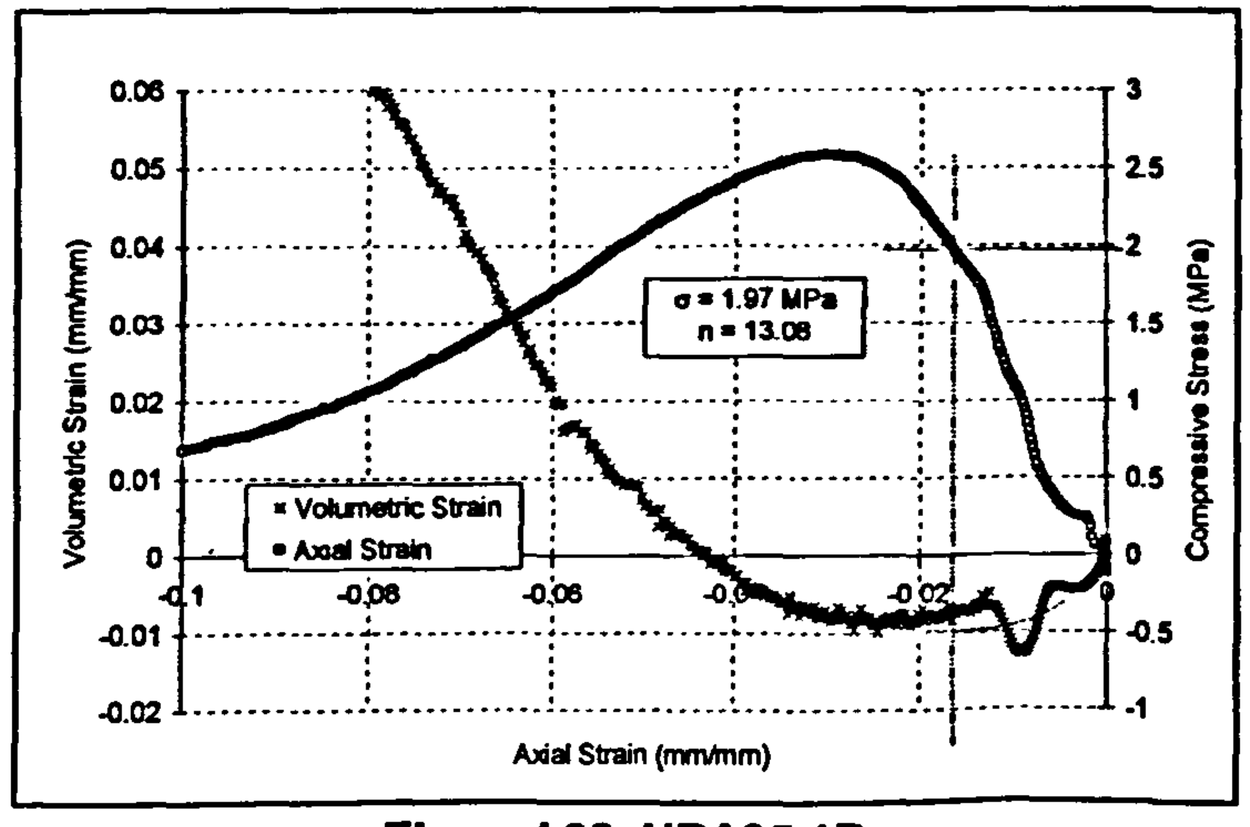

Figure I.22: HRA35 1B

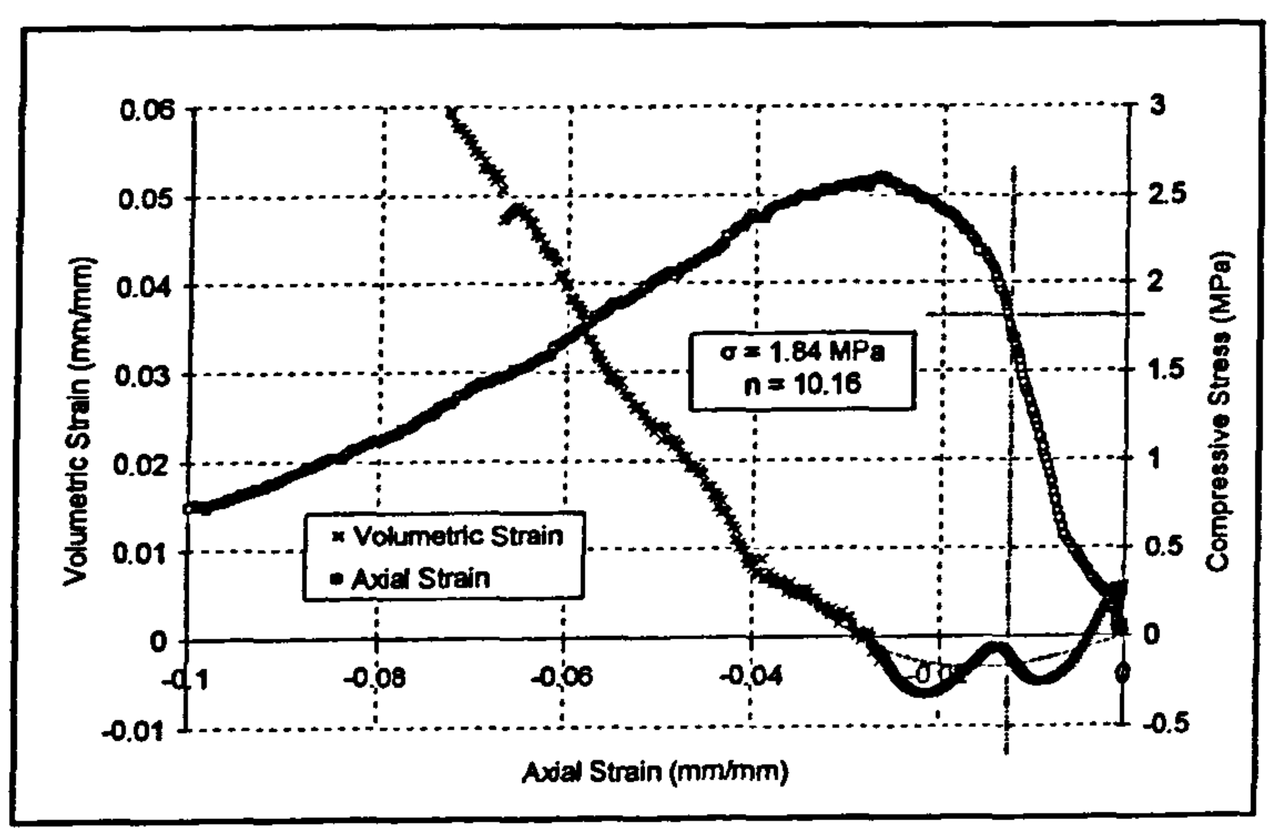

Figure I.23: HRA35 1C

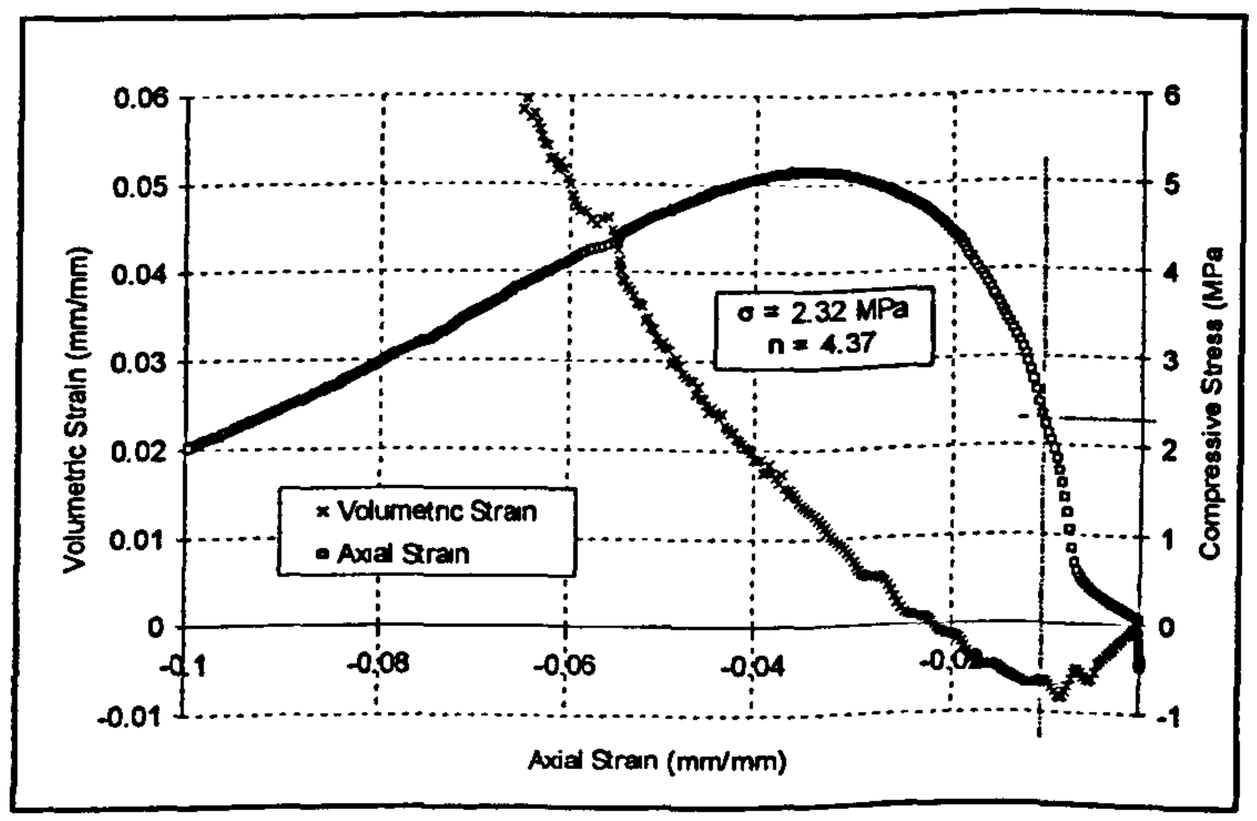

Figure I.24: HRA35 10A

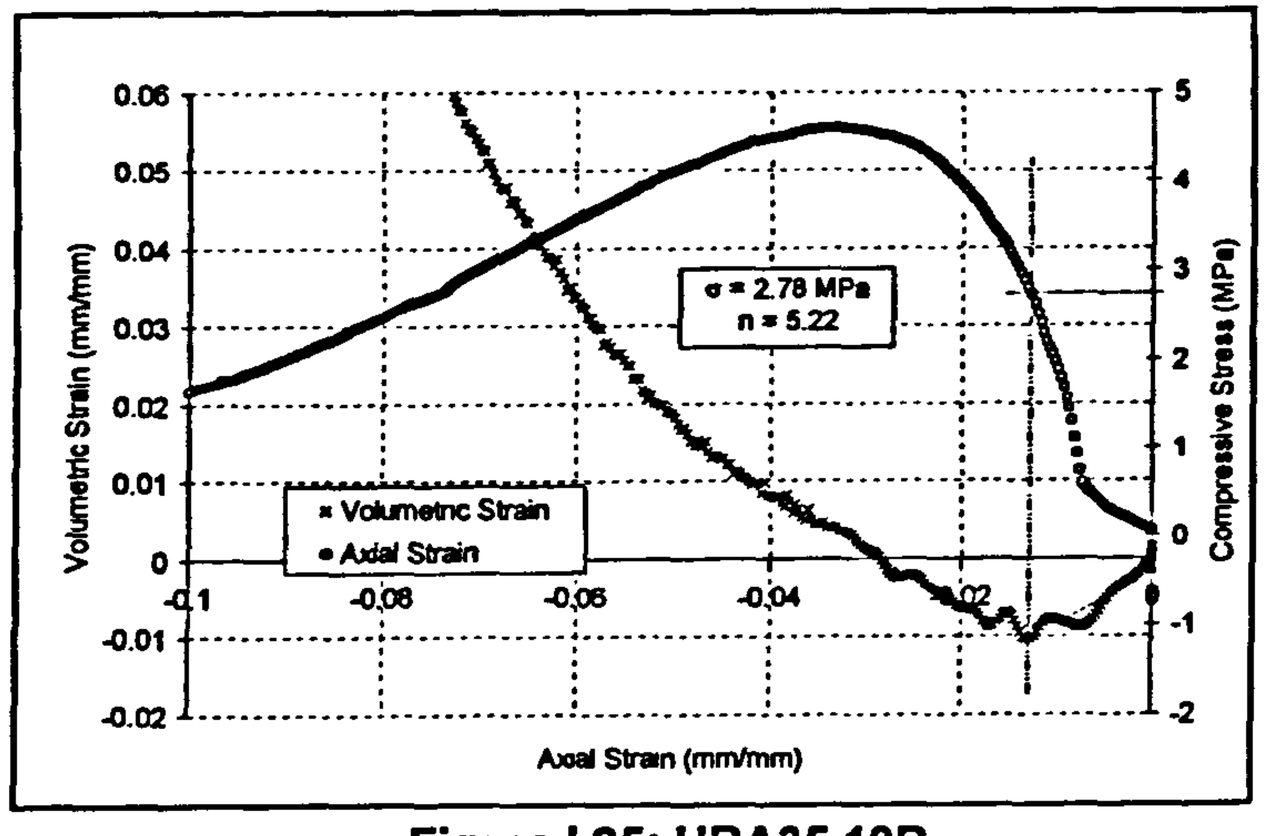

Figure I.25: HRA35 10B

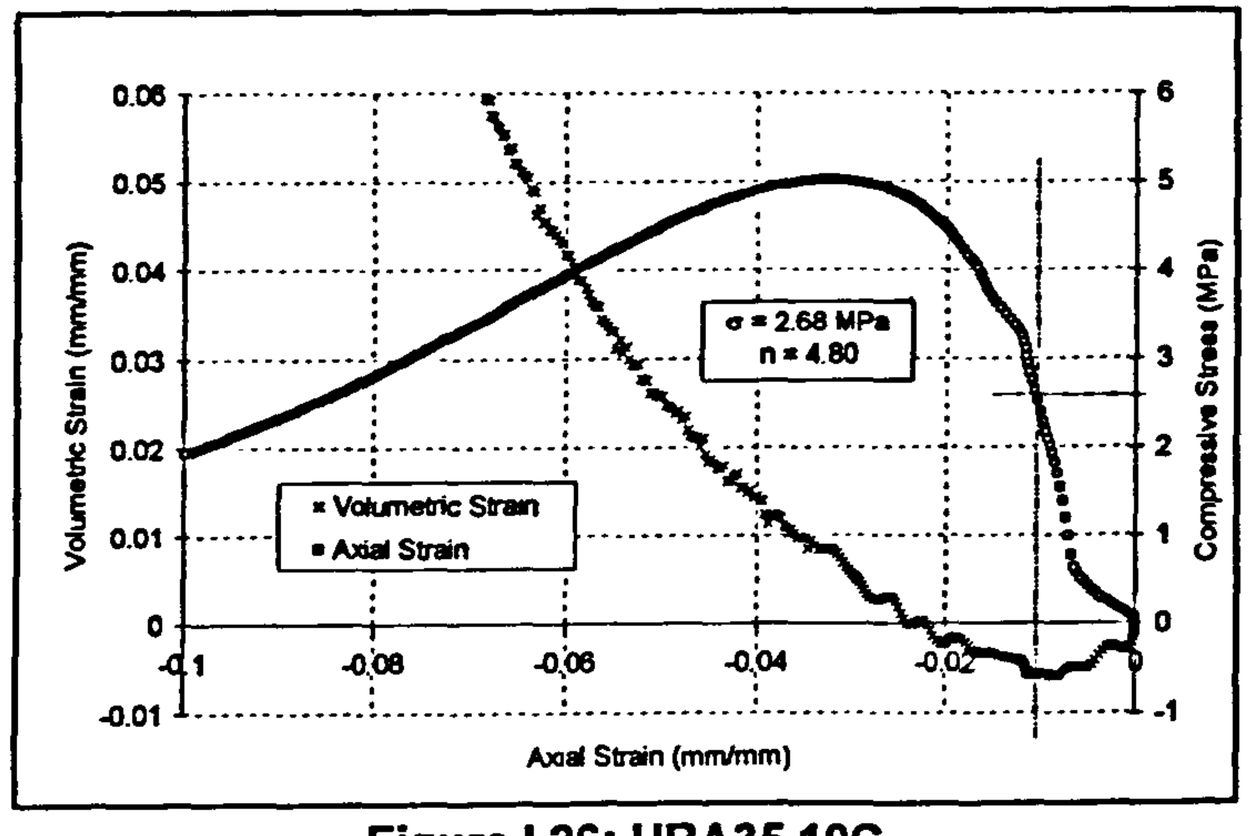

Figure I.26: HRA35 10C

Appendix J- Comparison of Observed and Predicted Compression Test Results

J.1 Comparison of Observed to Predicted Data – DBM Mixture

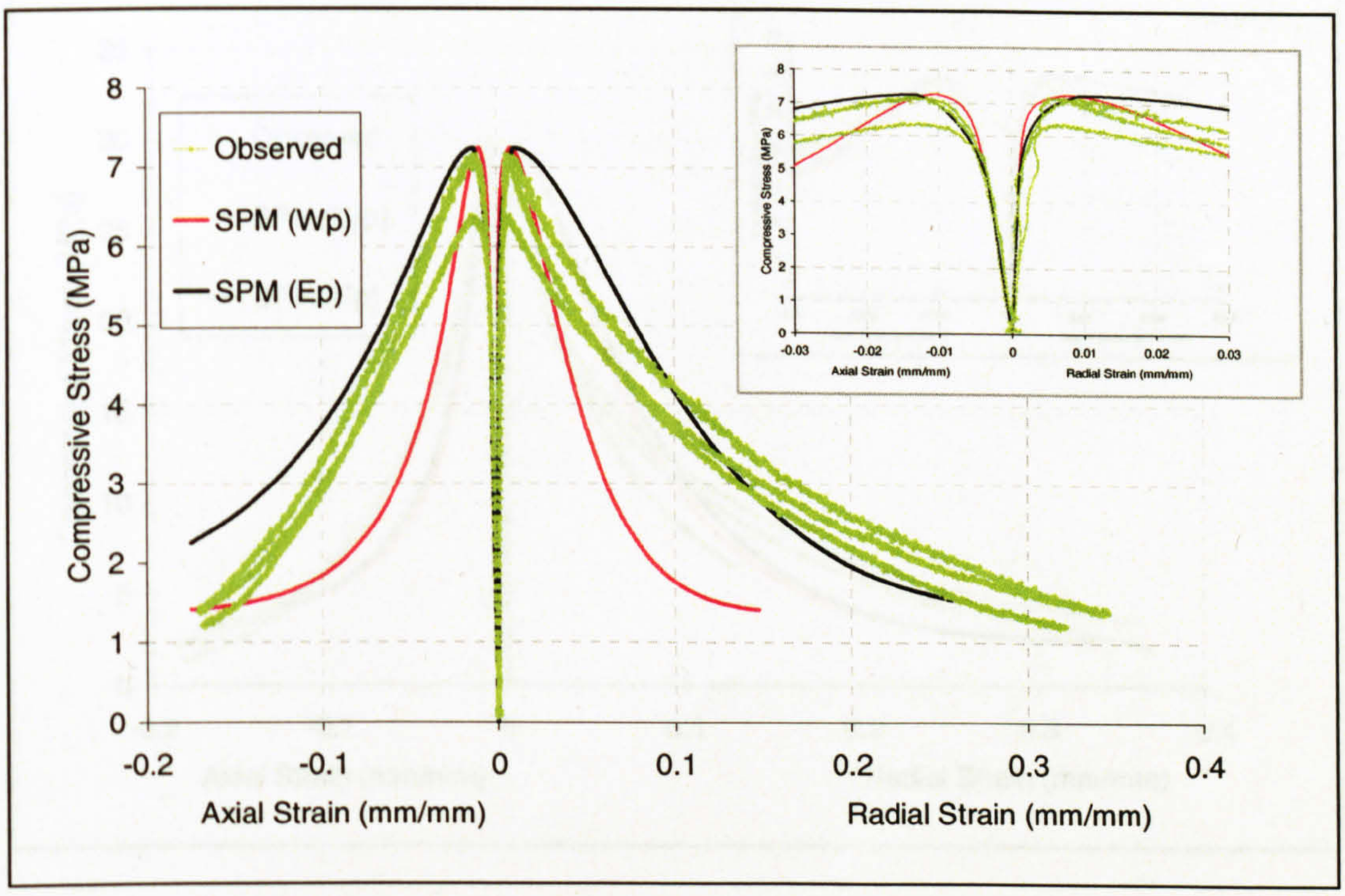

Figure J.1: Predicted stress-strain response – DBM at 5°C at 0.001 s^{-1}

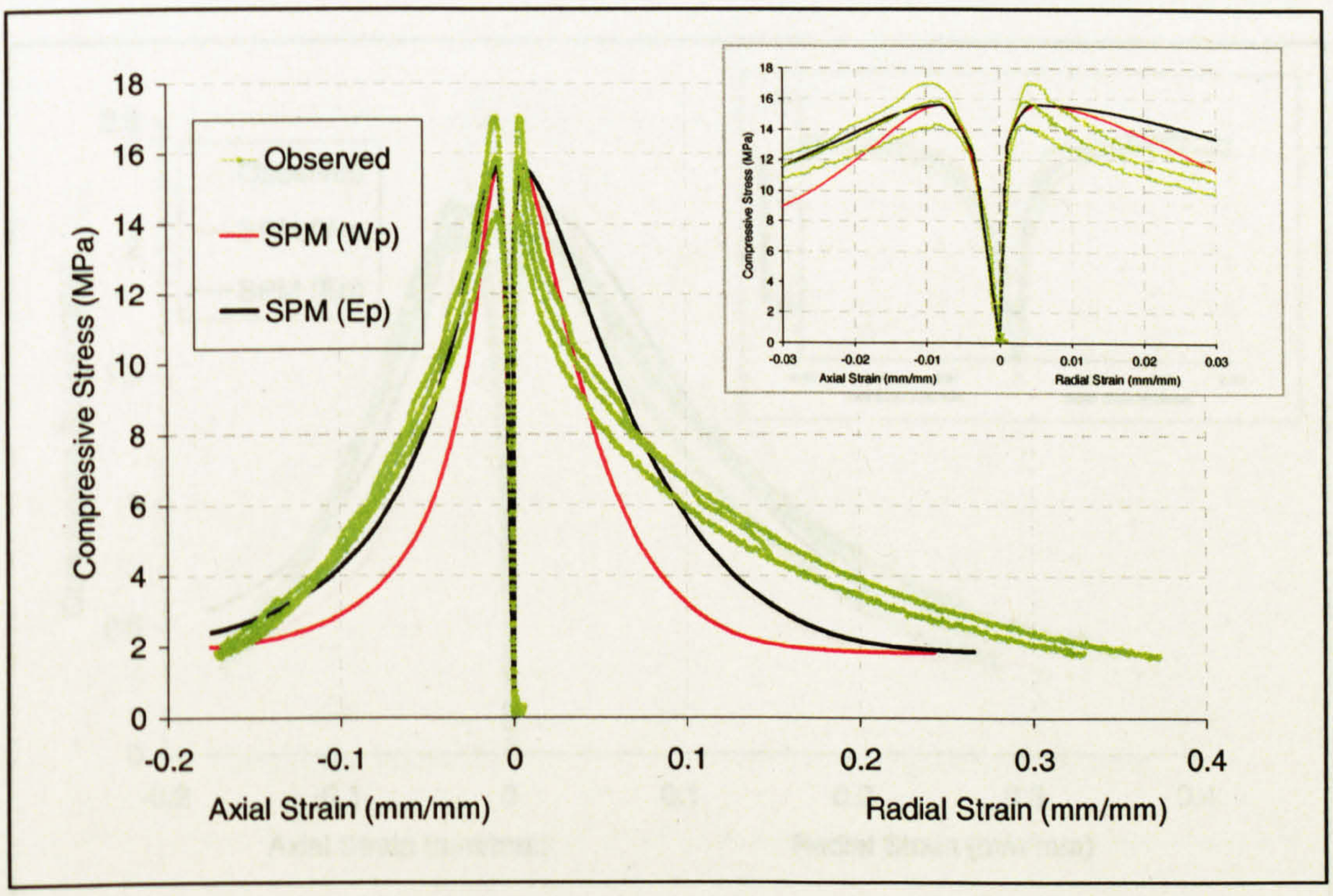

Figure J.2: Predicted stress-strain response – DBM at 5°C at 0.01 s^{-1}

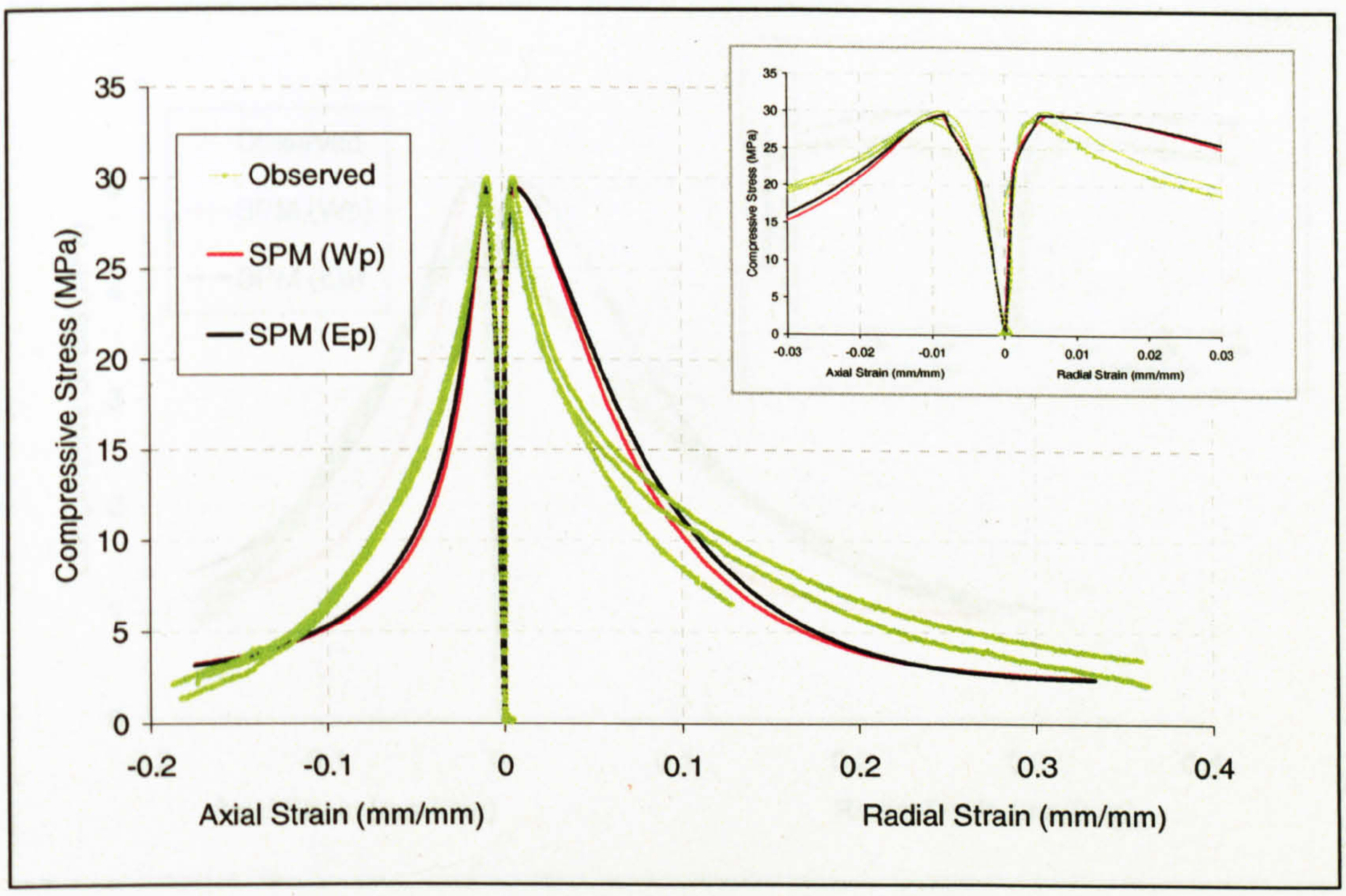

Figure J.3: Predicted stress-strain response – DBM at 5°C at 0.1 s^{-1}

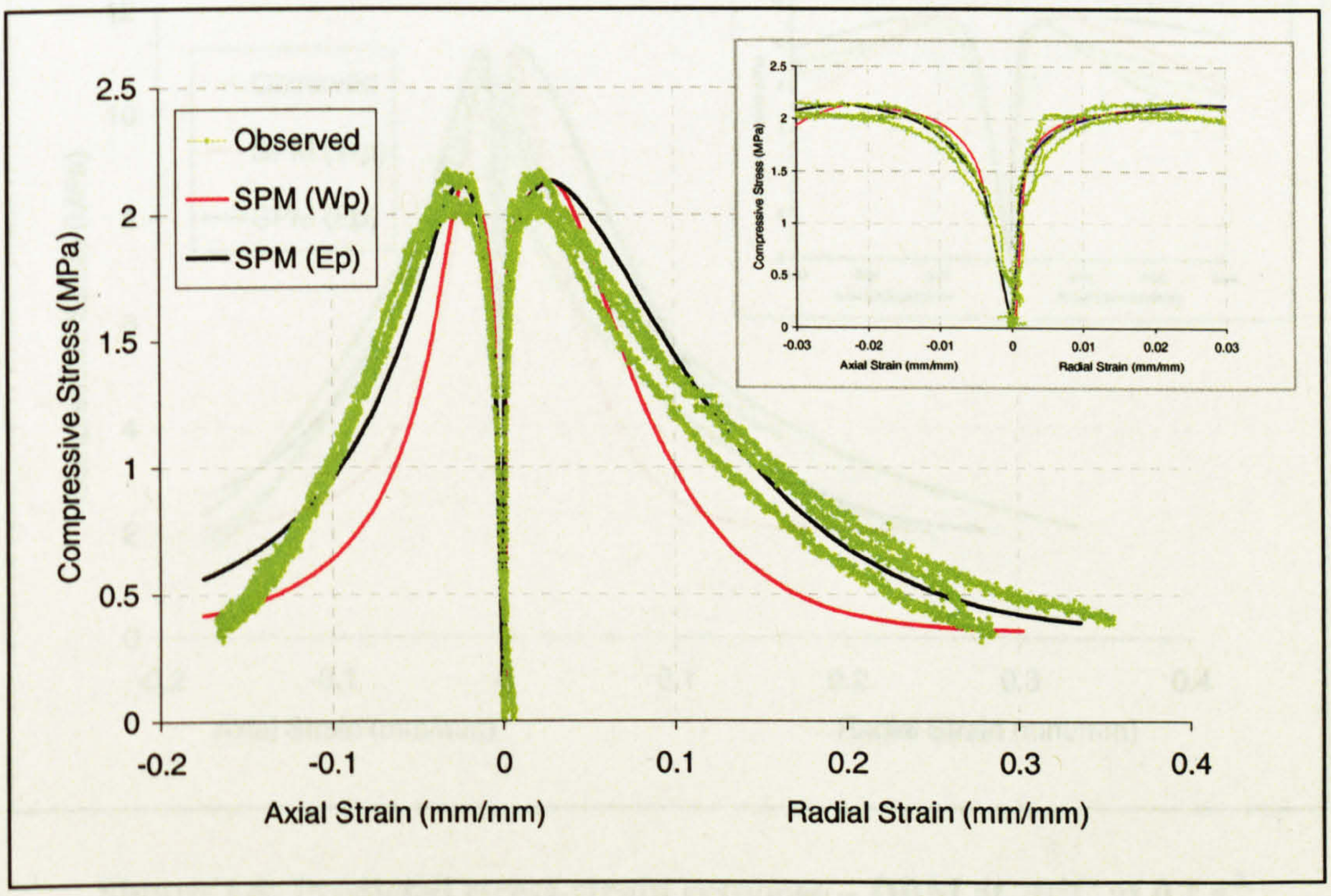

Figure J.4: Predicted stress-strain response – DBM at 20°C at 0.001 s^{-1}

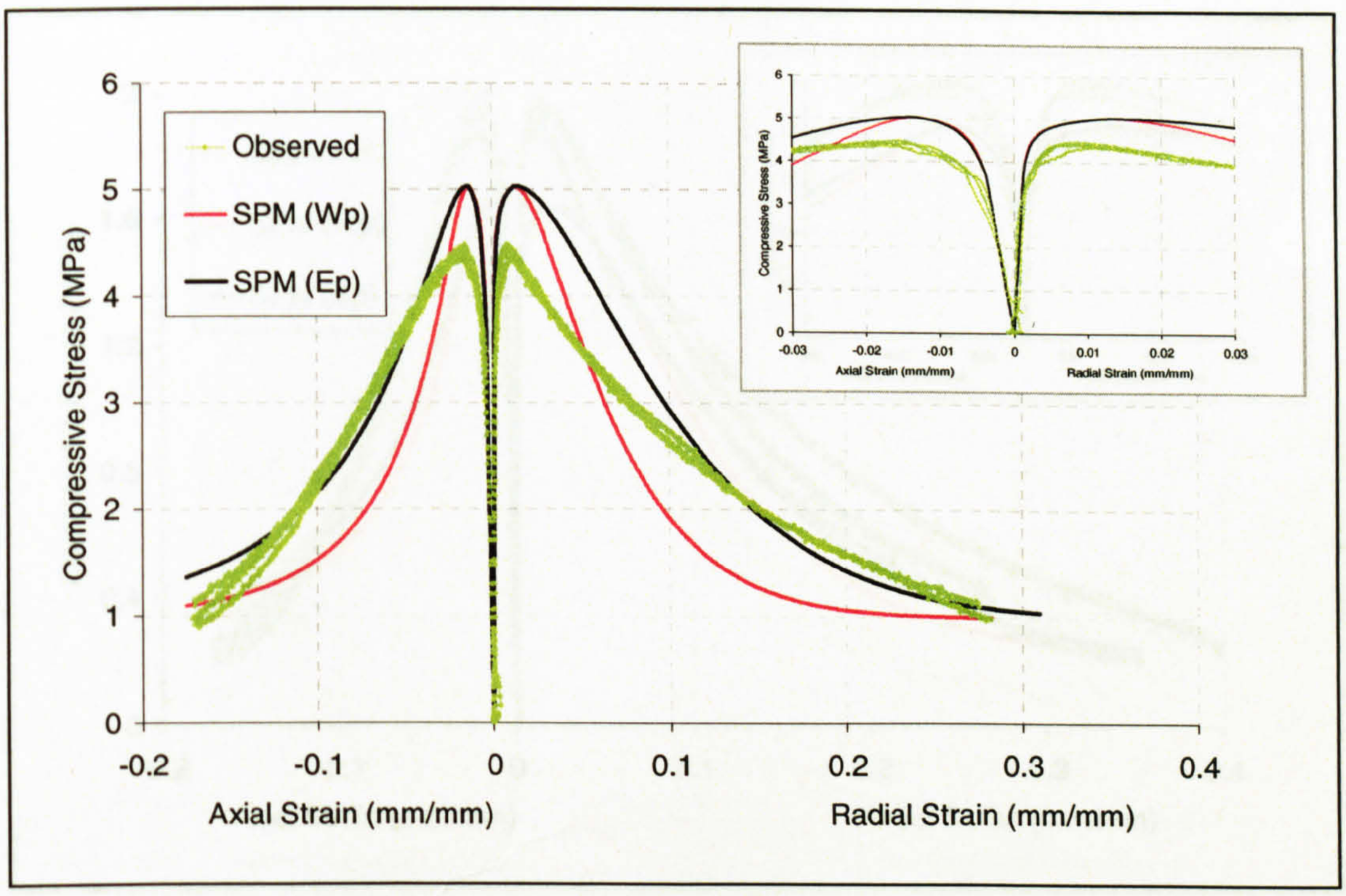

Figure J.5: Predicted stress-strain response – DBM at 20°C at 0.01 s^{-1}

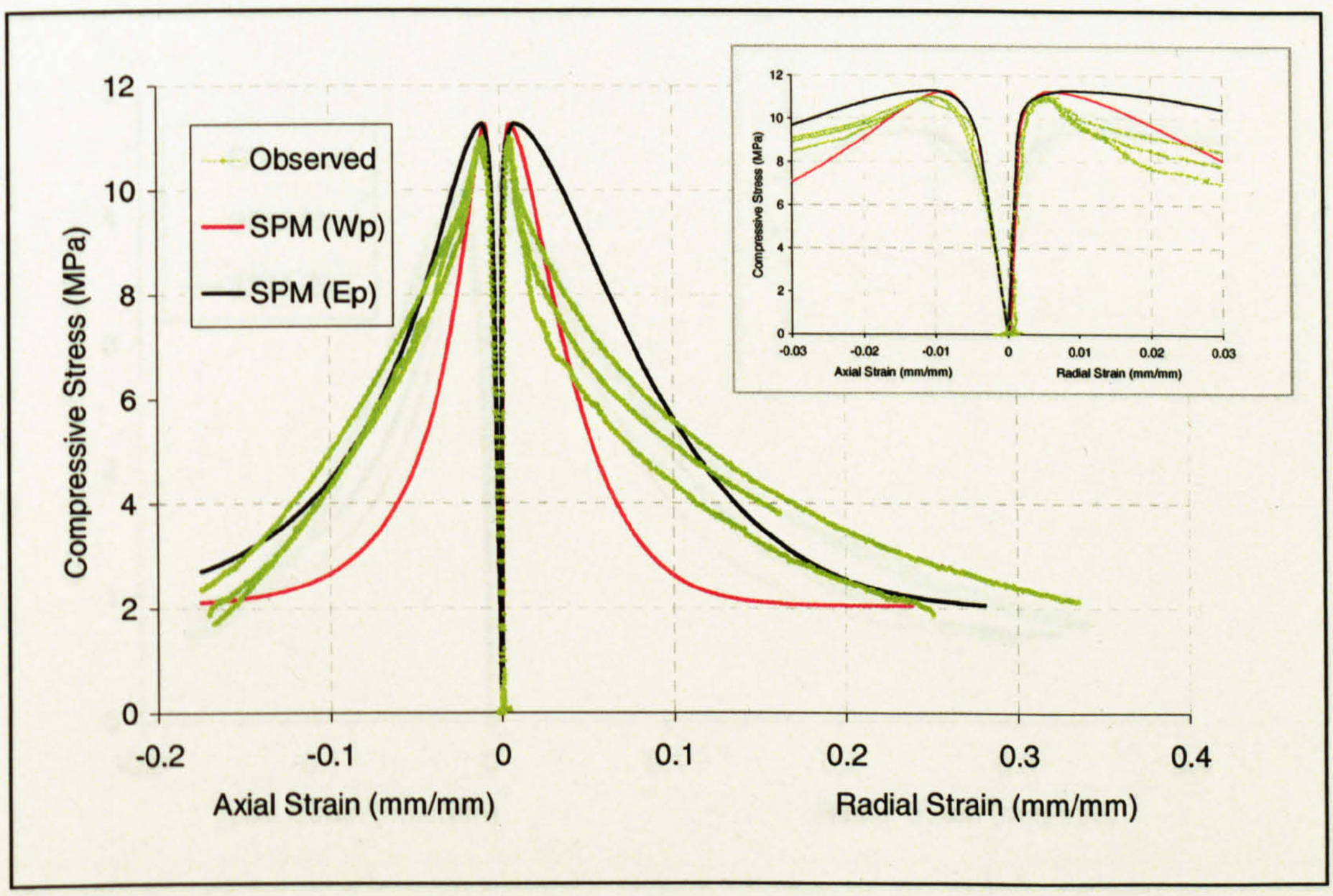

Figure J.6: Predicted stress-strain response – DBM at 20°C at 0.1 s^{-1}

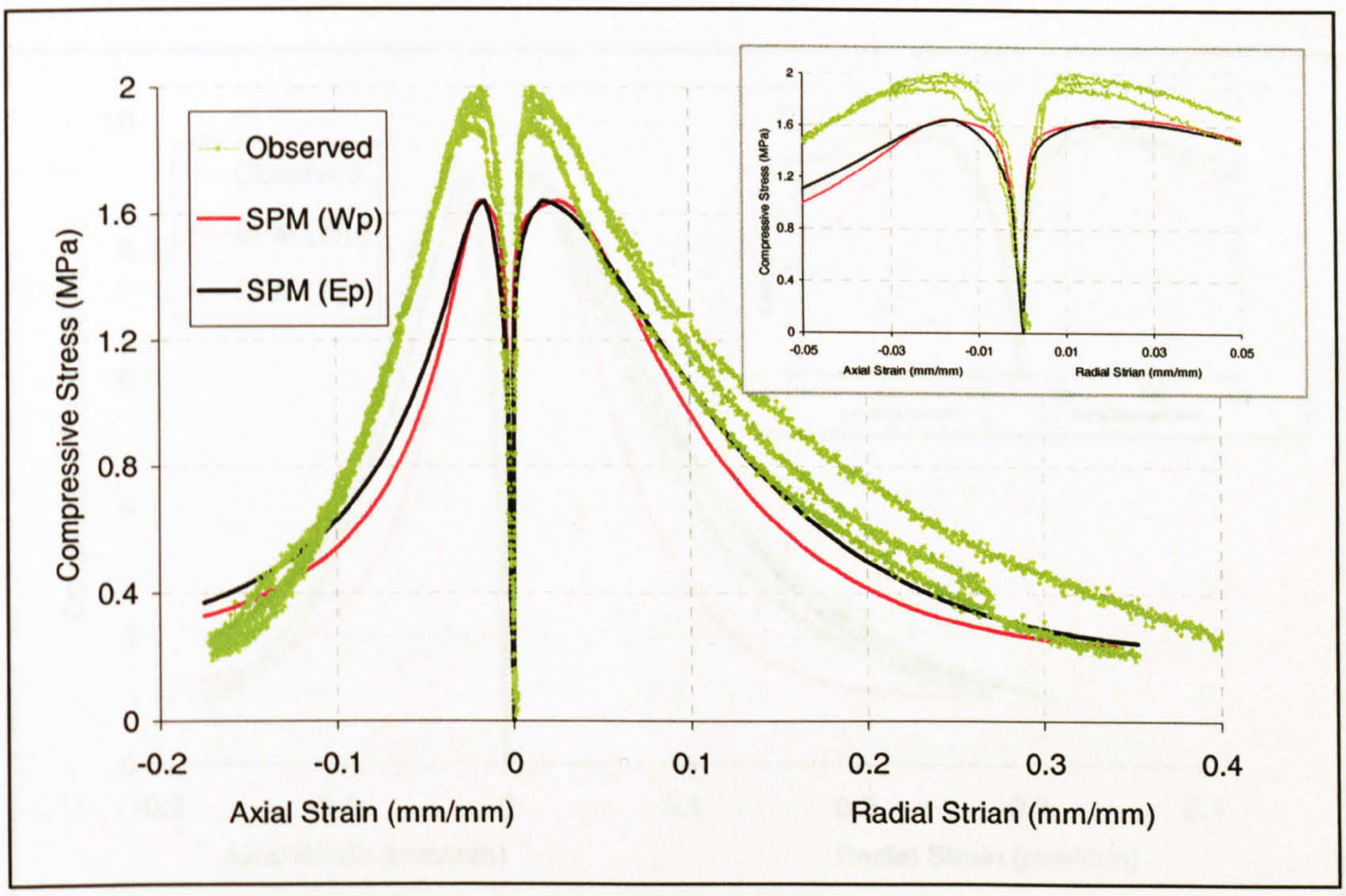

Figure J.7: Predicted stress-strain response – DBM at 35°C at 0.01 s^{-1}

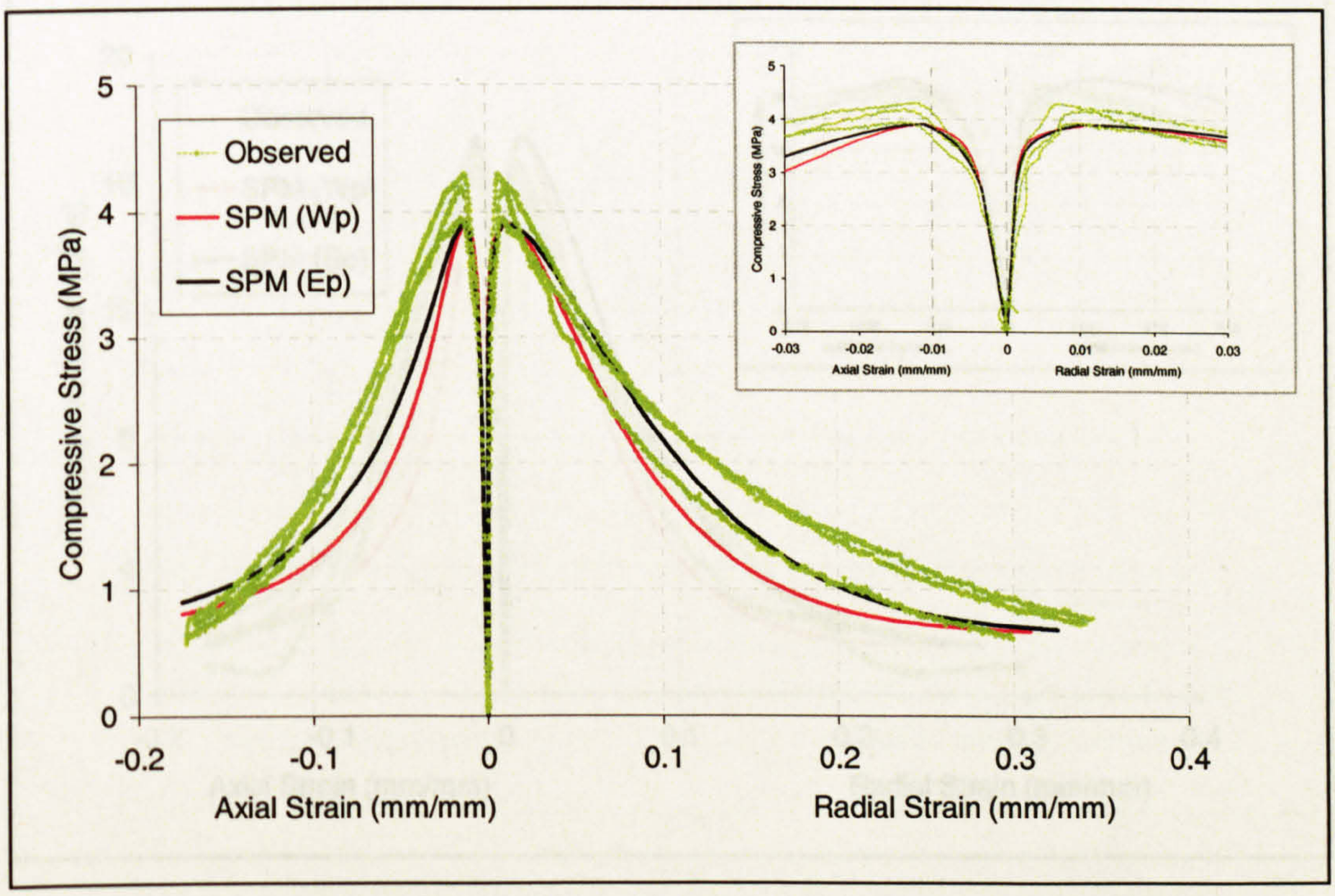

Figure J.8: Predicted stress-strain response – DBM at 35°C at 0.1 s^{-1}

J.2 Comparison of Observed to Predicted Data– HRA Mixture

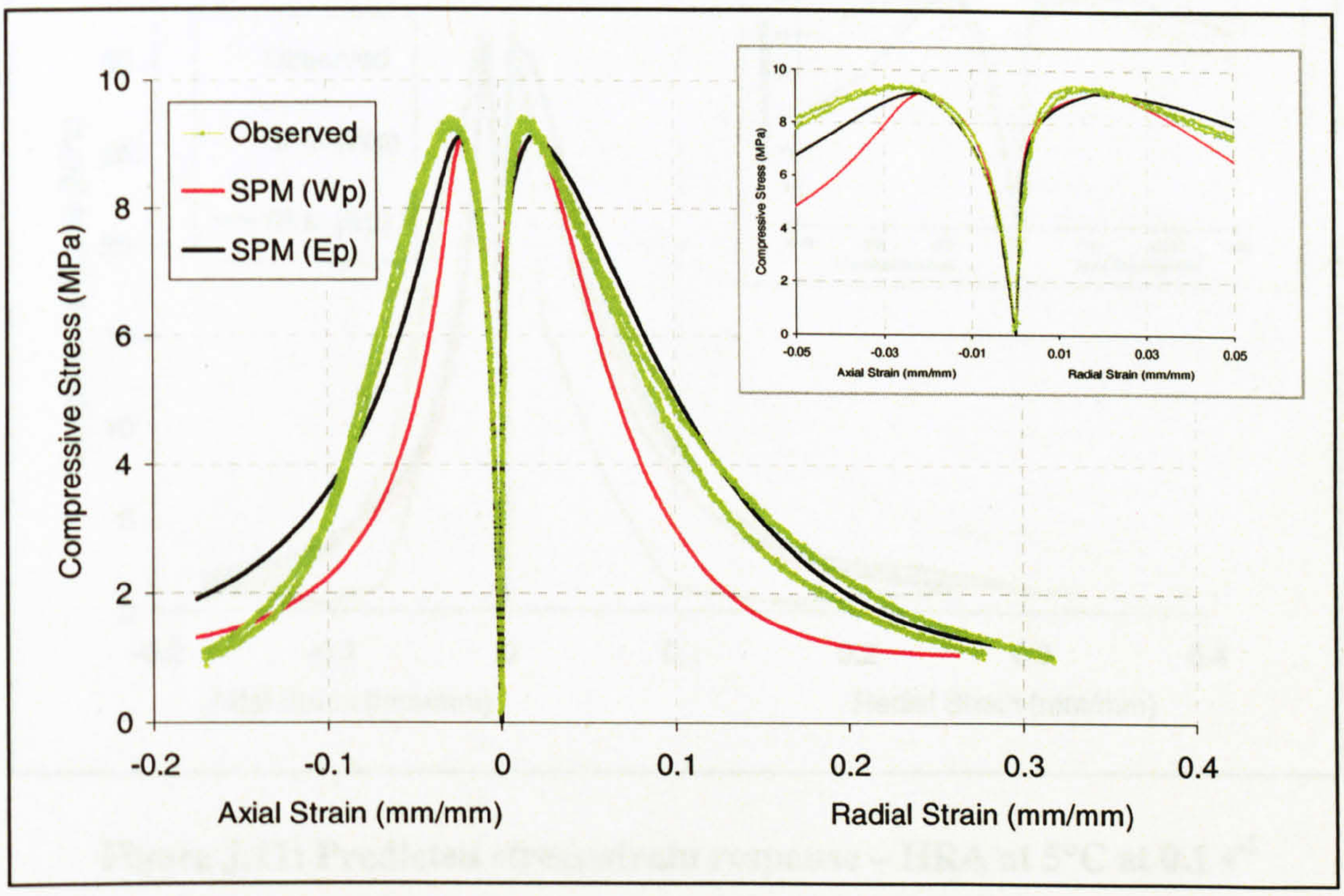

Figure J.9: Predicted stress-strain response – HRA at 5°C at 0.001 s^{-1}

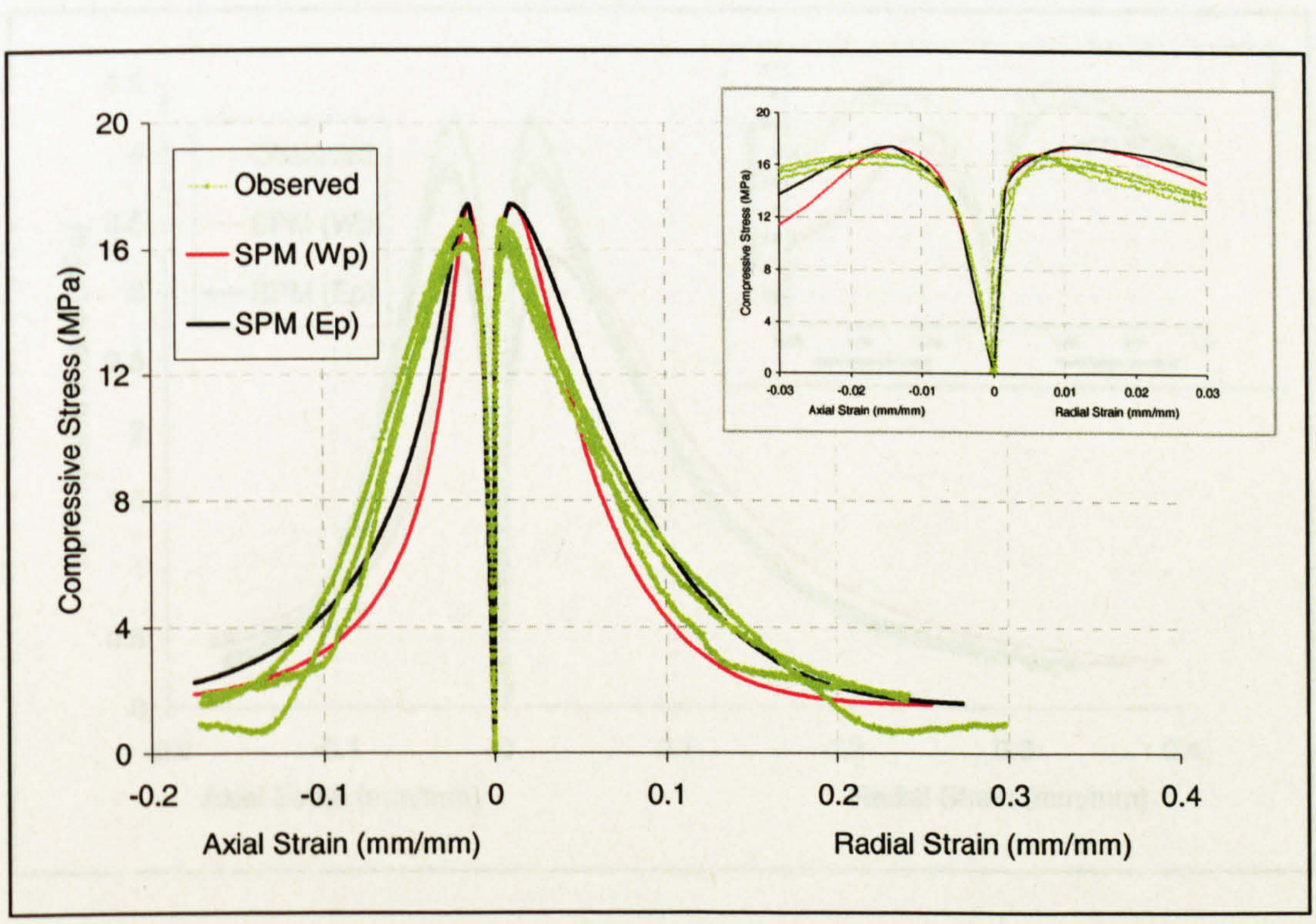

Figure J.10: Predicted stress-strain response – HRA at 5°C at 0.01 s^{-1}

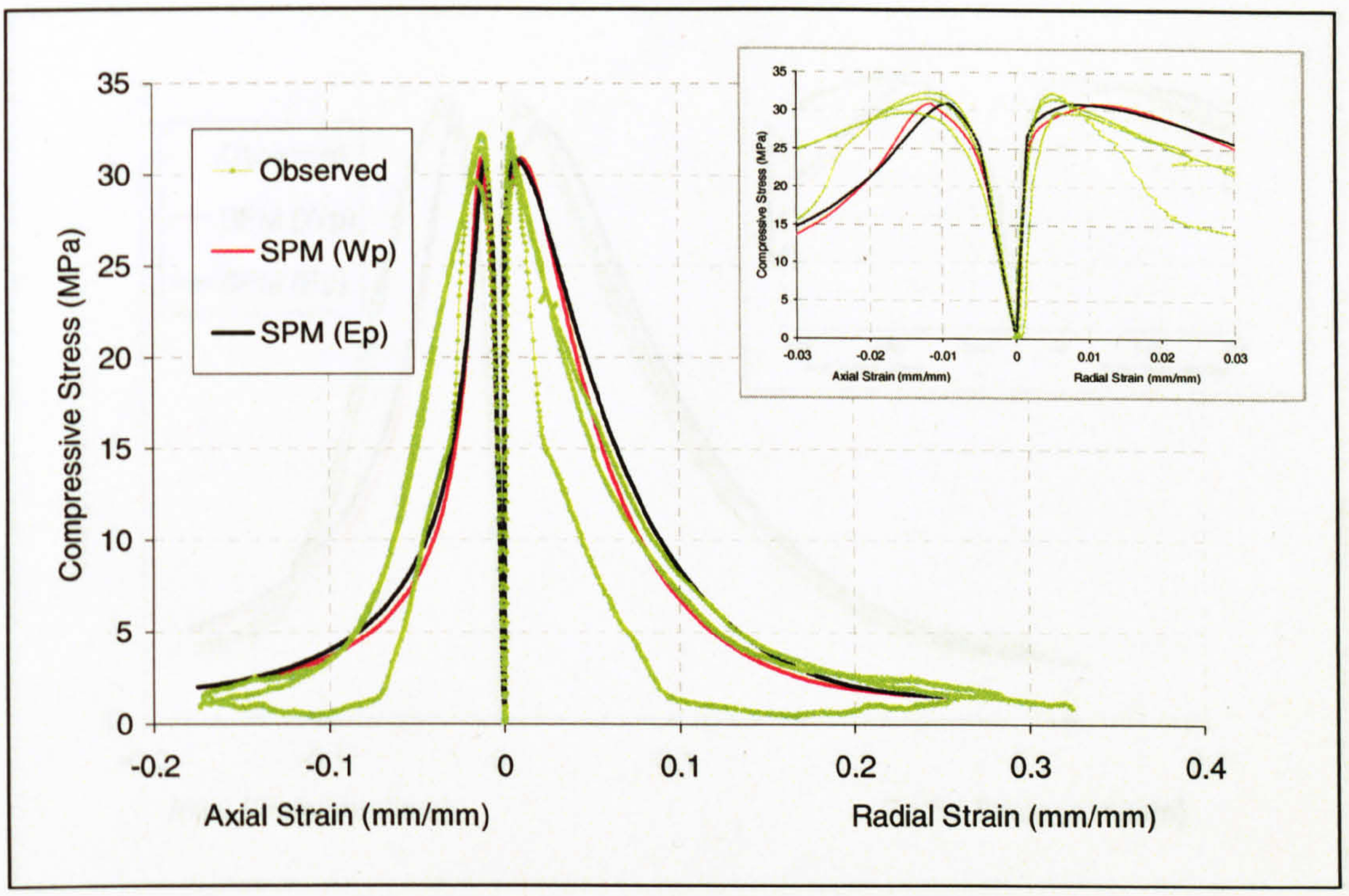

Figure J.11: Predicted stress-strain response – HRA at 5°C at 0.1 s^{-1}

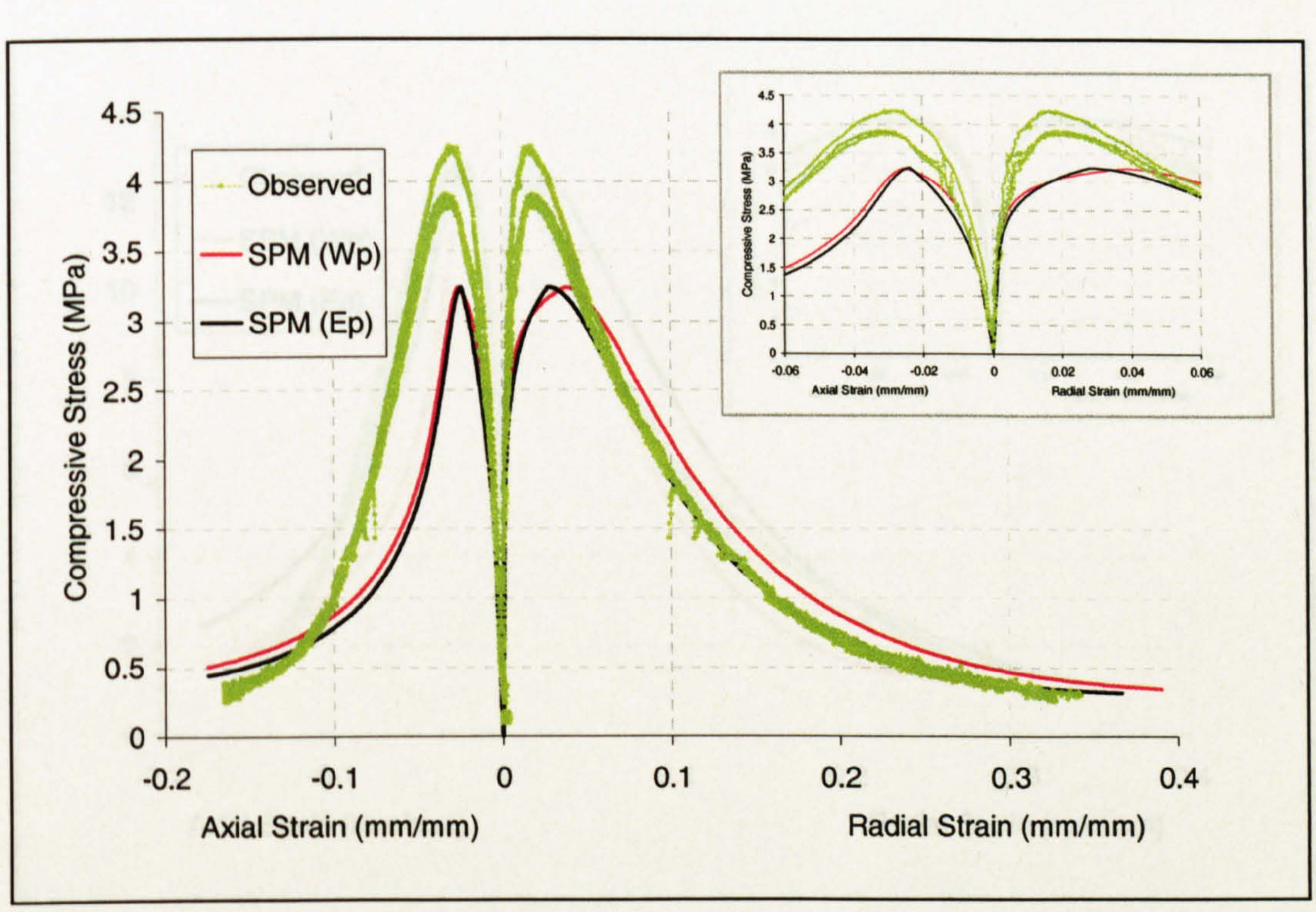

Figure J.12: Predicted stress-strain response – HRA at 20°C at 0.001 s^{-1}

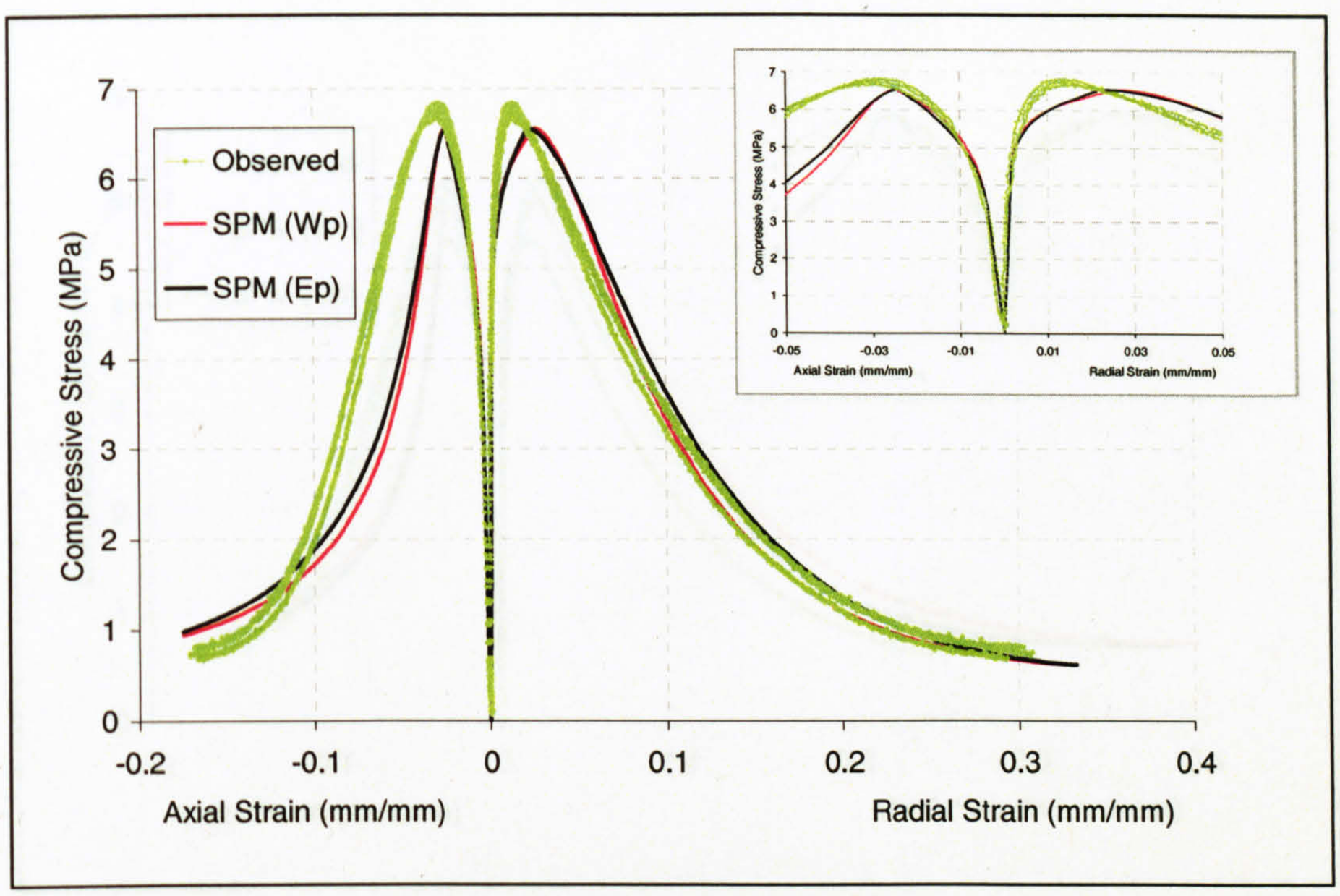

Figure J.13: Predicted stress-strain response – HRA at 20°C at 0.01 s^{-1}

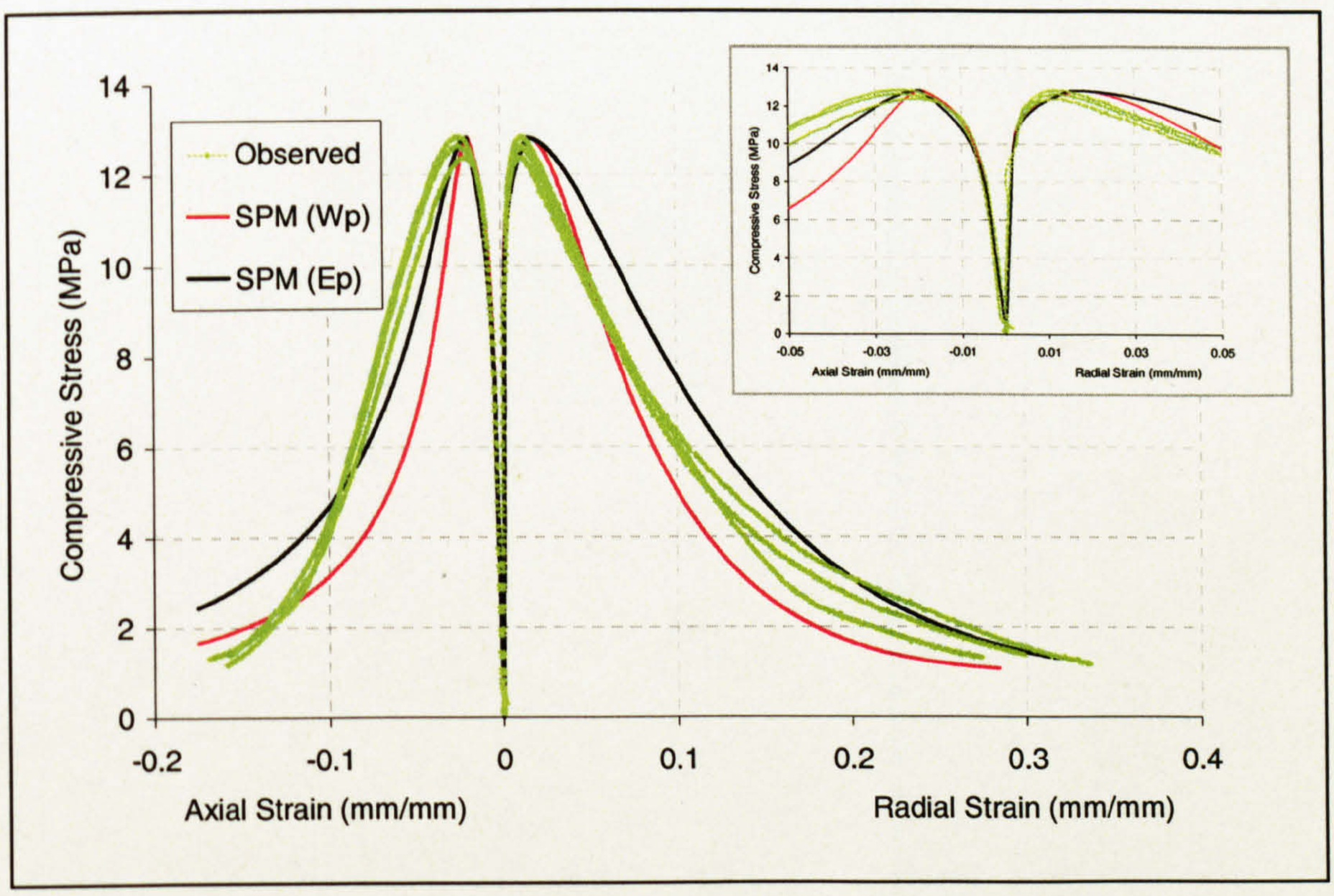

Figure J.14: Predicted stress-strain response – HRA at 20°C at 0.1 s^{-1}

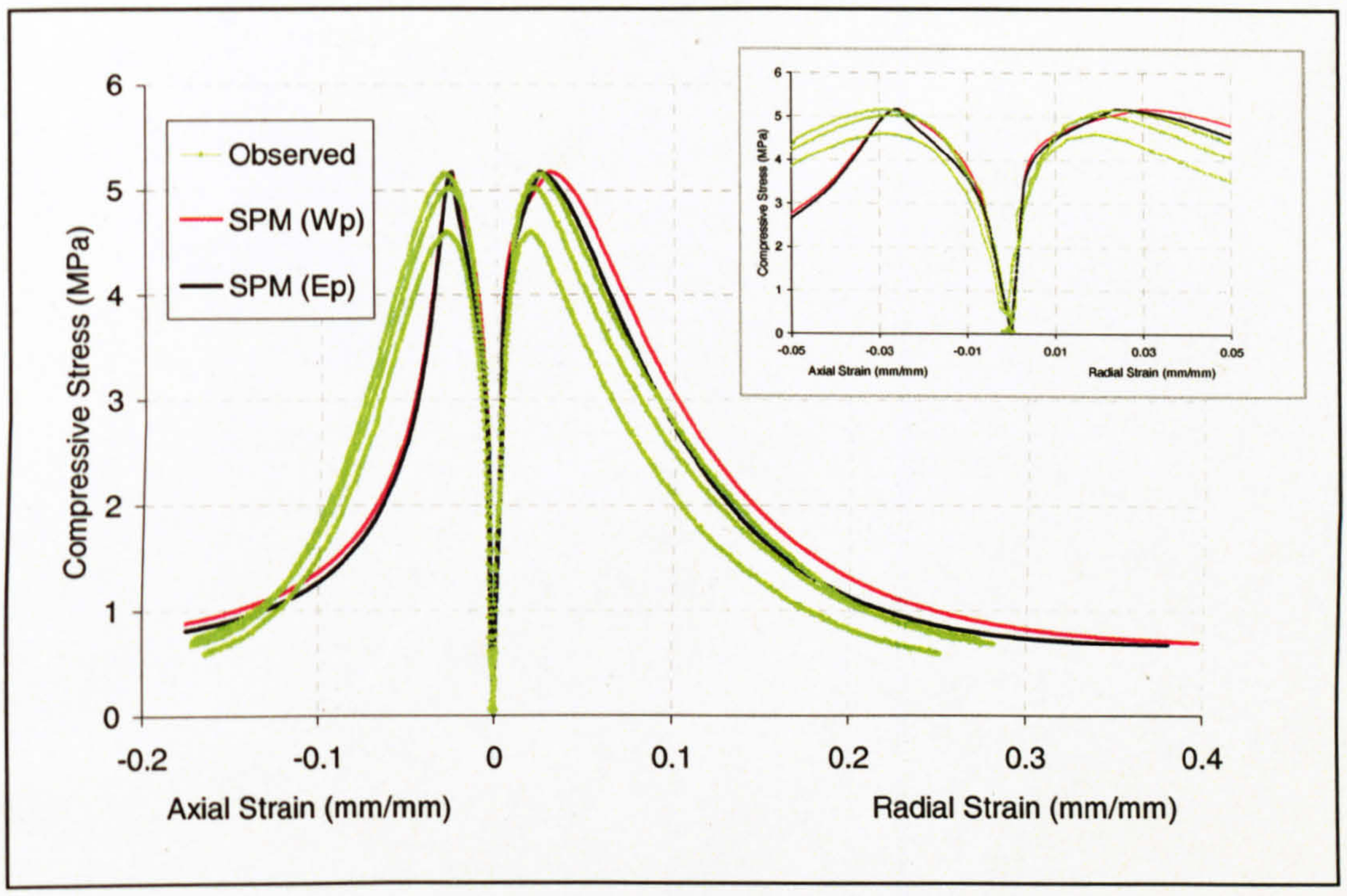

Figure J.15: Predicted stress-strain response – HRA at 35°C at 0.1 s^{-1}